Pertanika Journal of

SCIENCE & TECHNOLOGY

JST

VOL. 28 (3) JUL. 2020

A scientific journal published by Universiti Putra Malaysia Press

Journal of Science & Technology

Journal of Science & Technology

Journal of Science & Technology

About the Journal

Overview

Pertanika Journal of Science & Technology (JST) is the official journal of Universiti Putra Malaysia published by UPM Press. It is an open-access online scientific journal which is free of charge. It publishes the scientific outputs. It neither accepts nor commissions third party content.

Recognized internationally as the leading peer-reviewed interdisciplinary journal devoted to the publication of original papers, it serves as a forum for practical approaches to improving quality in issues pertaining to science and engineering and its related fields.

JST is a **quarterly** (January, April, July and October) periodical that considers for publication original articles as per its scope. The journal publishes in **English** and it is open to authors around the world regardless of the nationality.

The Journal is available world-wide.

Aims and scope

Pertanika Journal of Science and Technology aims to provide a forum for high quality research related to science and engineering research. Areas relevant to the scope of the journal include: bioinformatics, bioscience, biotechnology and bio-molecular sciences, chemistry, computer science, ecology, engineering, engineering design, environmental control and management, mathematics and statistics, medicine and health sciences, nanotechnology, physics, safety and emergency management, and related fields of study.

History

Pertanika was founded in 1978. A decision was made in 1992 to streamline Pertanika into three journals as Journal of Tropical Agricultural Science, Journal of Science & Technology, and Journal of Social Sciences & Humanities to meet the need for specialised journals in areas of study aligned with the interdisciplinary strengths of the university.

After almost 28 years, as an interdisciplinary Journal of Science & Technology, the revamped journal now focuses on research in science and engineering and its related fields.

Goal of *Pertanika*

Our goal is to bring the highest quality research to the widest possible audience.

Quality

We aim for excellence, sustained by a responsible and professional approach to journal publishing. Submissions are guaranteed to receive a decision within 14 weeks. The elapsed time from submission to publication for the articles averages 5-6 months.

Abstracting and indexing of *Pertanika*

The journal is indexed in SCOPUS (Elsevier), Clarivate-Emerging Sources Citation Index [ESCI (Web of Science)], BIOSIS, National Agricultural Science (NAL), Google Scholar, MyCite and ISC.

Future vision

We are continuously improving access to our journal archives, content, and research services. We have the drive to realise exciting new horizons that will benefit not only the academic community, but society itself.

Citing journal articles

The abbreviation for Pertanika Journal of Science & Technology is *Pertanika J. Sci. Technol.*

Publication policy

Pertanika policy prohibits an author from submitting the same manuscript for concurrent consideration by two or more publications. It prohibits as well publication of any manuscript that has already been published either in whole or substantial part elsewhere. It also does not permit publication of manuscript that has been published in full in Proceedings.

Code of Ethics

The Pertanika Journals and Universiti Putra Malaysia takes seriously the responsibility of all of its journal publications to reflect the highest in publication ethics. Thus all journals and journal editors are expected to abide by the Journal's codes of ethics. Refer to Pertanika's **Code of Ethics** for full details, or visit the Journal's web link at http://www.pertanika.upm.edu.my/code_of_ethics.php

International Standard Serial Number (ISSN)

An ISSN is an 8-digit code used to identify periodicals such as journals of all kinds and on all media–print and electronic. All Pertanika journals have ISSN as well as an e-ISSN.

Journal of Science & Technology: ISSN 0128-7680 (*Print*); ISSN 2231-8526 (*Online*).

Lag time

A decision on acceptance or rejection of a manuscript is reached in 3 to 4 months (average 14 weeks). The elapsed time from submission to publication for the articles averages 5-6 months.

Authorship

Authors are not permitted to add or remove any names from the authorship provided at the time of initial submission without the consent of the Journal's Chief Executive Editor.

Manuscript preparation

Refer to Pertanika's **Instructions to Authors** at the back of this journal.

Editorial process

Authors are notified with an acknowledgement containing a *Manuscript ID* on receipt of a manuscript, and upon the editorial decision regarding publication.

Pertanika follows a **double-blind peer-review** process. Manuscripts deemed suitable for publication are usually sent to reviewers. Authors are encouraged to suggest names of at least three potential reviewers at the time of submission of their manuscript to Pertanika, but the editors will make the final choice. The editors are not, however, bound by these suggestions.

Notification of the editorial decision is usually provided within ten to fourteen weeks from the receipt of manuscript. Publication of solicited manuscripts is not guaranteed. In most cases, manuscripts are accepted conditionally, pending an author's revision of the material.

The Journal's peer-review

In the peer-review process, three referees independently evaluate the scientific quality of the submitted manuscripts.

Peer reviewers are experts chosen by journal editors to provide written assessment of the **strengths** and **weaknesses** of written research, with the aim of improving the reporting of research and identifying the most appropriate and highest quality material for the journal.

Journal of Science & Technology
Journal of Science & Technology
Journal of Science & Technology

Journal of Science & Technology
Journal of Science & Technology
Journal of Science & Technology

Operating and review process

What happens to a manuscript once it is submitted to *Pertanika*? Typically, there are seven steps to the editorial review process:

1. The Journal's Chief Executive Editor (CEE) and the Editorial Board Members (EBMs) examine the paper to determine whether it is appropriate for the journal and should be reviewed. If not appropriate, the manuscript is rejected outright and the author is informed.

2. The CEE sends the article-identifying information having been removed, to three reviewers who are specialists in the subject matter represented by the article. The CEE requests them to complete the review in three weeks.

   Comments to authors are about the appropriateness and adequacy of the theoretical or conceptual framework, literature review, method, results and discussion, and conclusions. Reviewers often include suggestions for strengthening of the manuscript. Comments to the editor are in the nature of the significance of the work and its potential contribution to the field.

3. The CEE, in consultation with the Editor-in-Chief (EiC), examines the reviews and decides whether to reject the manuscript, invites the author(s) to revise and resubmit the manuscript. The CEE may seek additional reviews. Final acceptance or rejection rests with the CEE and EiC, who reserve the right to refuse any material for publication. In rare instances, the manuscript is accepted with almost no revision. Almost without exception, reviewers' comments (to the author) are forwarded to the author. If a revision is indicated, the editor provides guidelines for attending to the reviewers' suggestions and perhaps additional advice about revising the manuscript.

4. The authors decide whether and how to address the reviewers' comments and criticisms and the editor's concerns. The authors return a revised version of the paper to the chief executive editor along with specific information describing how they have answered' the concerns of the reviewers and the editor, usually in a tabular form. The author(s) may also submit a rebuttal if there is a need especially when the author disagrees with certain comments provided by reviewer(s).

5. The CEE sends the revised paper out for re-review. Typically, at least one of the original reviewers will be asked to examine the article.

6. When the reviewers have completed their work, the CEE in consultation with the EiC and EBMs examine their comments and decide whether the paper is ready to be published, needs another round of revisions, or should be rejected.

7. If the decision is to accept, an acceptance letter is sent to all the author(s), the paper is sent to the Press. The article should appear online in approximately three months.

   The Publisher ensures that the paper adheres to the correct style (in-text citations, the reference list, and tables are typical areas of concern, clarity, and grammar). The authors are asked to respond to any minor queries by the Publisher. Following these corrections, page proofs are mailed to the corresponding authors for their final approval. At this point, **only essential changes are accepted**. Finally, the article appears in the pages of the Journal and is posted online.

Pertanika Journal of

SCIENCE & TECHNOLOGY

Vol. 28 (3) Jul. 2020

A scientific journal published by Universiti Putra Malaysia Press

JST
Journal of Science & Technology
AN INTERNATIONAL PEER-REVIEWED JOURNAL

EDITOR-IN-CHIEF
Luqman Chuah Abdullah
Chemical Engineering

CHIEF EXECUTIVE EDITOR
Abu Bakar Salleh
Biotechnology and Biomolecular Science

CHAIRMAN
UNIVERSITY PUBLICATIONS COMMITTEE
Zulkifli Idrus

EDITORIAL STAFF

Journal Officers:
Kanagamalar Silvarajoo, *ScholarOne*
Siti Zuhaila Abd Wahid, *ScholarOne*
Tee Syin Ying, *ScholarOne*
Ummi Fairuz Hanapi, *ScholarOne*

Editorial Assistants:
Siti Juridah Mat Arip
Zulinaardawati Kamarudin

PRODUCTION STAFF
Pre-press Officers:
Nur Farrah Dila Ismail
Wong Lih Jiun

WEBMASTER
IT Officer:
To be appointed

PUBLICITY & PRESS RELEASE
Magdalene Pokar *(ResearchSEA)*

Adress:
EDITORIAL OFFICE
JOURNAL DIVISION
Putra Science Park
1st Floor, IDEA Tower II
UPM-MTDC Technology Centre
Universiti Putra Malaysia
43400 Serdang, Selangor Malaysia.
Gen Enq.: +603 9769 1622 | 1616
E-mail:
executive_editor.pertanika@upm.edu.my
URL: www.journals-jd.upm.edu.my

PUBLISHER
UPM Press
Universiti Putra Malaysia
43400 UPM, Serdang, Selangor, Malaysia.
Tel: +603 9769 8851
E-mail: penerbit@putra.upm.edu.my
URL: http://penerbit.upm.edu.my

EDITORIAL BOARD
2018-2020

Adem Kilicman
Mathematical Sciences
Universiti Putra Malaysia, Malaysia.

Ali A. Moosavi-Movahedi
Biophysical Chemistry
University of Tehran, Tehran, Iran.

Amu Therwath
Oncology, Molecular Biology,
Université Paris, France.

Angelina Chin
Mathematics, Group Theory and Generalisations, Ring Theory,
University of Malaya, Malaysia.

Bassim H. Hameed
Chemical Engineering: Reaction Engineering, Environmental Catalysis & Adsorption,
Universiti Sains Malaysia, Malaysia.

Biswa Mohan Biswal
Medical, Clinical Oncology, Radiotherapy
Universiti Sains Malaysia, Malaysia.

Christopher G. Jesudason
Mathematical Chemistry, Molecular Dynamics Simulations, Thermodynamics and General Physical Theory,
University of Malaya, Malaysia.

Hari M. Srivastava
Mathematics and Statistics,
University of Victoria, Canada.

Ivan D. Rukhlenko
Nonliner Optics, Silicon Photonics, Plasmonics and Nanotechnology
Monash University, Australia.

Kaniraj R. Shenbaga
Geotechnical Engineering,
India.

Kanury Rao
Senior Scientist & Head, Immunology Group, International Center for Genetic Engineering and Biotechnology, Immunology, Infectious Disease Biology and System Biology
International Centre for Genetic Engineering & Biotechnology, New Delhi, India.

Ki-Hyung Kim
Computer and Wireless Sensor Networks
AJOU University, Korea.

Kunnawee Kanitpong
Transportation Engineering-Road Traffic Safety, Highway Materials and Construction
Asian Institute of Technology, Thailand.

Megat Mohd Hamdan Megat Ahmad
Mechanical and Manufacturing Engineering
Universiti Pertahanan Nasional Malaysia, Malaysia.

Mirnalini Kandiah
Public Health Nutrition, Nutritional Epidemiology
UCSI University, Malaysia.

Mohamed Othman
Communication Technology and Network, Scientific Computing
Universiti Putra Malaysia, Malaysia

Mohd. Ali Hassan
Bioprocess Engineering, Environmental Biotehnology
Universiti Putra Malaysia, Malaysia.

Mohd Sapuan Salit
Concurrent Engineering and Composite Materials
Universiti Putra Malaysia, Malaysia.

Narongrit Sombatsompop
Engineering & Technology: Materials and Polymer Research
King Mongkut's University of Technology Thonburi (KMUTT), Thailand.

Prakash C. Sinha
Physical Oceanography, Mathematical Modelling, Fluid Mechanics, Numerical Techniques
Universiti Malaysia Terengganu, Malaysia.

Rajinder Singh
Biotechnology, Biomolecular Sciences, Molecular Markers/ Genetic Mapping
Malaysia Palm Oil Board, Kajang, Malaysia.

Renuganth Varatharajoo
Engineering, Space System
Universiti Putra Malaysia, Malaysia.

Riyanto T. Bambang
Electrical Engineering, Control, Intelligent Systems & Robotics
Bandung Institute of Technology, Indonesia.

Roslan Abd-Shukor
Physics & Materials Physics, Superconducting Materials
Universiti Kebangsaan Malaysia, Malaysia.

Sabira Khatun
Engineering, Computer Systems & Software Engineering, Applied Mathematics
Universiti Malaysia Pahang, Malaysia.

Shiv Dutt Gupta
Director, IIHMR, Health Management, Public Health, Epidemiology, Chronic and Non-communicable Diseases
Indian Institute of Health Management Research, India.

Suan-Choo Cheah
Biotechnology, Plant Molecular Biology
Asiatic Centre for Genome Technology (ACGT), Kuala Lumpur, Malaysia.

Wagar Asrar
Engineering, Computational Fluid Dynamics, Experimental Aerodynamics
International Islamic University, Malaysia.

Wing Keong Ng
Aquaculture, Aquatic Animal Nutrition, Aqua Feed Technology
Universiti Sains Malaysia, Malaysia.

Yudi Samyudia
Chemical Engineering, Advanced Process Engineering
Curtin University of Technology, Malaysia.

INTERNATIONAL ADVISORY BOARD
2018-2021

Adarsh Sandhu
Editorial Consultant for Nature Nanotechnology and Contributing Writer for Nature Photonics, Physics, Magnetoresistive Semiconducting Magnetic Field Sensors, Nano-Bio-Magnetism, Magnetic Particle Colloids, Point of Care Diagnostics, Medical Physics, Scanning Hall Probe Microscopy, Synthesis and Application of Graphene
Electronics-Inspired Interdisciplinary Research Institute (EIIRIS), Toyohashi University of Technology, Japan.

Graham Megson
Computer Science
The University of Westminster, U.K.

Kuan-Chong Ting
Agricultural and Biological Engineering
University of Illinois at Urbana-Champaign, USA.

Malin Premaratne
Advanced Computing and Simulation
Monash University, Australia.

Mohammed Ismail Elnaggar
Electrical Enginering
Ohio State University, USA.

Peter J. Heggs
Chemical Engineering
University of Leeds, U.K.

Ravi Prakash
Vice Chancellor, JUIT, Mechanical Engineering, Machine Design, Biomedical and Materials Science
Jaypee University of Information Technology, Indian.

Said S.E.H. Elnashaie
Environmental and Sustainable Engineering
Penn. State University at Harrisburg, USA.

Suhash Chandra Dutta Roy
Electrical Engineering
Indian Institute of Technology (IIT) Delhi, India.

Vijay Arora
Quantum and Nano-Engineering Processes
Wilkes University, USA.

Yi Li
Chemistry, Photochemical Studies, Organic Compounds, Chemical Engineering
Chinese Academy of Sciences, Beijing, China.

ABSTRACTING AND INDEXING OF PERTANIKA JOURNALS

Pertanika has reached **40 years old**; this accumulated knowledge has resulted in the journals being abstracted and indexed in SCOPUS (Elsevier), Clarivate-Emerging Sources Citation Index [ESCI (Web of Science)], BIOSIS, National Agricultural Science (NAL), Google Scholar, MyCite and ISC.

The publisher of Pertanika will not be responsible for the statements made by the authors in any articles published in the journal. Under no circumstances will the publisher of this publication be liable for any loss or damage caused by your reliance on the advice, opinion or information obtained either explicitly or implied through the contents of this publication.

All rights of reproduction are reserved in respect of all papers, articles, illustrations, etc., published in Pertanika. Pertanika provides free access to the full text of research articles for anyone, web-wide. It does not charge either its authors or author-institution for refereeing/publishing outgoing articles or user-institution for accessing incoming articles.

No material published in Pertanika may be reproduced or stored on microfilm or in electronic, optical or magnetic form without the written authorization of the Publisher.

Copyright © 2019 Universiti Putra Malaysia Press. All Rights Reserved.

Pertanika Journal of Science & Technology
Vol. 28 (3) Jul. 2020

Contents

Foreword

Welcome to the Third Issue of 2020 for the Journal of Science and Technology (JST)!

JST is an open-access journal for studies in Science and Technology published by Universiti Putra Malaysia Press. It is independently owned and managed by the university for the benefit of the world-wide science community.

This issue contains 20 articles; a short communication and the rest are regular articles. The authors of these articles come from different countries namely China, India, Indonesia, Iran, Iraq, Malaysia, Nigeria, Sudan, Tanzania, Thailand and Yemen.

Mohd Shahrol Abd Wahil and co-researchers from Universiti Kebangsaan Malaysia had assessed the health risk among adult and children on potential air pollutants released from the petrochemical plant in Malaysia: The result of air modelling. Hazard quotient (HQ) was used to assess non-carcinogenic risk, while lifetime cancer risk (LCR) was used to assess carcinogenic risk. The health risk assessment showed no risk of developing malignancy and non-cancer disorder among the workers and general population living surround the petrochemical plants. Further details of the article are available on page 859.

A regular article titled “Load Balancing using Enhanced Multi-Objective with Bee Colony optimization in cloud networks” was written by Abhikriti Narwal and Sunita Dhingra University Institute of Engineering and Technology, India. In their research, they found an effective adjustment of Enhanced Multi-objective task algorithm with load balancing for task scheduling. This technique was better than the earlier techniques in term of each performance attribute like average waiting time by 2.934%, processing cost by 17.6% and processing time by 20.5%. Detailed information on this study can be found on page 1049.

Another article that we wish to highlight is on “Spectrum Efficiency of Modulation Schemes for Network Optimization in 5GHz Dense Environments” by Mina Malekzadeh from Hakim Sabzevari University, Iran. They found out that utilizing wider channels and shorter guard intervals did not necessarily optimize the 802.11ax networks that were under heavy loads of many users. The modulation schemes from BPSK to 64-QAM was able to improve the network performance in line with increasing the bandwidth of channels. The best performance was accomplished by 64-QAM with 40, 80, and 160 MHz channels with 5/6 coding rate. However, for higher-order modulation including 256-QAM and 1024-QAM, the results prove otherwise. Detailed information on this study is presented on page 1063.

We anticipate that you will find the evidence presented in this issue to be intriguing, thought-provoking and useful in reaching new milestones in your own research. Please recommend the journal to your colleagues and students to make this endeavour meaningful.

All the papers published in this edition underwent Pertanika's stringent peer-review process involving a minimum of two reviewers comprising internal as well as external referees. This was to ensure that the quality of the papers justified the high ranking of the journal, which is renowned as a heavily-cited journal not only by authors and researchers in Malaysia but by those in other countries around the world as well.

We would also like to express our gratitude to all the contributors, namely the authors, reviewers, Editor-in-Chief and Editorial Board Members of JST, who have made this issue possible. JST is currently accepting manuscripts for upcoming issues based on original qualitative or quantitative research that opens new areas of inquiry and investigation.

Chief Executive Editor
Prof. Dato' Dr. Abu Bakar Salleh
executive_editor.pertanika@upm.edu.my

Pertanika J. Sci. & Technol. 28 (3): 767 - 778 (2020)

PERTANIKA JOURNALS

SCIENCE & TECHNOLOGY

Journal homepage: http://www.pertanika.upm.edu.my/

Production of Packaging Molded from Banana Sheath

Natcharee Jirukkakul

Faculty of Applied Science and Engineering, Nong Khai Campus, Khon Kaen University, Nong Khai 43000, Thailand
The Indo-China Country International Trade and Economic Research Sector, Nong Khai Campus, Khon Kaen University, Nong Khai 43000, Thailand

ABSTRACT

This research was done to study the effect of methods of making containers by hot air oven (H) and a hot press machine (C) and the ratio of banana stem fiber to binder on the properties of containers made from banana sheath fibers. The ratios between the dried banana sheath powder and the binder (banana starch solution 7.5%) were 60:40, 70:30, 80:20, and 90:10, respectively. It was found that method C had shown low amounts of oil and water absorption and a high resistance to deformation, which was due to compression and penetration. In terms of compression and penetration forces, no significant differences were found for the ratios of 80:20 and 90:10. However, the ratio of 90:10 showed lower fat and water absorption when compared to other ratios. Therefore, the ratio of 90:10 between the banana sheath fiber and the binder and the method C were found to be the best ratio to use when making containers, which are suitable to be applied for further use.

Keywords: Banana fiber, container, hot compression, molding

INTRODUCTION

Kluai Namwa (*Musa sapientum* L.) is a plant that is grown throughout the year in all regions of Thailand. The plantation area of Kluai Namwa covers 80% of the total banana plantation areas (Jirukkakul, 2016). Most of the products (both fresh and processed) are consumed domestically, such as in the form of fried bananas, dried bananas, banana powder, and banana starch (Jirukkakul, 2019). In addition, there are perennial herbs that are widely distributed in tropical and subtropical regions (Bi et al., 2017). When cutting a bunch of bananas from the tree, that tree is not able to grow a new bunch. The bananas trees, which have produced a

ARTICLE INFO

Article history:
Received: 09 December 2019
Accepted: 21 April 2020
Published: 16 July 2020

E-mail address:
pnatch@kku.ac.th

ISSN: 0128-7680
e-ISSN: 2231-8526

© Universiti Putra Malaysia Press

bunch of bananas, have to be cut down, resulting in waste materials (banana trees or banana stalks) from the plantation areas. These waste materials (10-15% of bananas) do not have commercial value, resulting in major wasting of resources (Bi et al., 2017).

In addition, because banana sheaths have a lot of fiber consisting of 50% of cellulose and 17% of lignin (Alarcon & Marzocchi., 2015), they can also be used as a raw material for paper production, just like mulberry, pineapple fiber, or elephant dung (Oliveira et al., 2009). The stalks can be utilized in the process of molding containers, which can replace plastic materials (Liu et al., 2009). The quality of the packaging can be checked by examining the following properties: tensile strength, compression and penetration resistance, and water and oil absorption. In addition, this packaging is also environmentally friendly. At present, environmentally friendly containers are being invented and being called "bio-based food packaging", which is made from natural materials that are biodegradable from renewable resources. One of the natural materials being commonly used to produce bio-based food packaging is starch, which is abundant in cassava, potatoes, corn, and bananas. In general, the production of bio-degradable food packaging has often been processed through thermal extrusion (Tiefanbacher, 1993). Research on the production of foam containers made from starch and water through hot molding revealed that the containers became fragile and were not flexible or water resistant. Therefore, they could not be used for food packaging. Shorgen et al. (2002) studied disposable food packaging made from potato starch and corn starch and found that adding the fibers of softwoods had helped to increase the strength of the starch-made foam container. Moreover, the addition of Monostearyl citrate improved the water resistance and flexibility of the containers. Soykeabkaew et al. (2004) studied the characteristics of cassava starch foam reinforced with jute and hemp fibers by extruding the foam into the hot mold at 220^{o}C for 150 s. It was found that 5 - 10% of fiber increased the bending resistance and bending modulus of the starch foam. Jute fibers have more bending resistance than hemp fibers. In addition, Cinelli (2006) studied the natural biodegradable foam containing potato starch, corn fibers, and polyvinyl alcohol as the main components. It was molded through the hot mold at a temperature of 200^{o}C for 120 - 180 s. The study revealed that the corn fiber added to the mixture had increased the density of the foam, and the addition of polyvinyl alcohol had made the foam stronger. Furthermore, the foam could better withstand the compression, and these added materials were also able to increase the water absorption resistance. Therefore, for food storage, the development of containers made from banana sheaths has become an interesting alternative. The containers were also beautiful and increased a variety of product distribution. The objective of this study is to investigate the effect of the ratio of banana fiber to binder on the properties of the food containers made by hot air oven and hot press molding techniques.

MATERIALS AND METHODS

This study used the factorial for the completely randomized design (CRD) experiment. The studied factors were the dried banana sheath containers molded by using the hot air oven and the hot press at different ratios (90:10, 80:20, 70:30 and 60:40) of the dried banana sheath powder and the binder (7.5% banana flour solution). The package properties were analyzed in relation to thickness, weight, moisture, tensile strength, compression resistance, penetration resistance, and water and oil absorption.

Banana Fiber Preparation

The banana sheaths were peeled off into sheets, which had been cut from the cultivated banana trees. The sheaths were dried in the sun for 8 h or baked in an oven at 55°C for 5 h. This condition affected the moisture content of sheets was less than 14%. The sheaths were then ground using hammer mill into a powder, screened through 80 wire mesh and then sifting was kept in a ziplock bag until needed for the further processes of mixing and extrusion.

Binder Preparation

The binder in this study was cultivated banana flour solution. The solution was created by mixing 7.5% of banana flour with water (7.5 g banana flour with 92.5 ml of water) and heating at 90°C for 10 min until it became a gel.

Testing through Extrusion

By Hot Air Oven (H). The prepared banana fiber powder was measured with the binder at ratios of 90:10, 80:20, 70:30, and 60:40, and then the materials were mixed together using a food blender for 15 min. The 100 grams of the mixed material was placed into the mold and baked for 18 h at 60°C (Sibaly & Jeetah, 2017). Then it was left in the mold to cool at room temperature. The work piece was then removed from the mold and kept in a ziplock bag until its properties were ready to be tested.

By Hot Compression (C). The banana fiber powder and the binder were measured at the ratios of 90:10, 80:20, 70:30 and 60:40. Then the materials were mixed using the food blender for 15 min. Aluminum foil was cut to the size of the mold (12 cm diameter with 1 cm edge high) and was then placed in the mold to prevent mold stickiness. The temperature of the hot compressor was set at 150°C, the empty mold was heated for 10 min. Then the mixed materials were put into the mold, and the compression pressure was increased to 700 kPa (Muratore et al., 2019). Compression on the work piece continued for 30 min, and then the mold was left to cool to room temperature. Finally, the work piece was removed from the mold and kept in a ziplock bag until its properties were ready to be tested.

Packaging Testing

Thickness. Thickness was tested using Dial Thickness gauge (model 7301, Mitutoyo, Japan) with resolution of 0.01 mm. The results of the thicknesses were used in the analysis of the tensile strength.

Weight. Weight was tested in accordance with ASTM D646 (1996) standard. The 3 samples of 20 × 25 cm were cut and stored in a temperature and relative humidity controller at 27 ± 1°C and at 65 ± 2% for at least 24 h. Then 1 cut sheet at a time was weighed. Finally, the average standard weight in grams per square meter was reported.

Moisture content. Moisture content was tested in accordance with AOAC (2000) standard. Aluminum cups with lids were heated in a hot air oven at a temperature of 105 ± 2°C for 1 h. Then the cups were left to cool in a desiccator for 30 min before being weighed with the lids. After that, sampling was carried out to store a sample cup in a temperature and relative humidity controller at 27 ± 1°C and 65 ± 2% RH for at least 24 h. The sample was then cut into the size of approximately 2 × 2 cm^2 and put in a 3 g aluminum cup to be recorded as the pre oven sample weight (W1). After that, the sample in the cup with the lid open was put into the oven at 105 ± 2°C for 24 h. The weight was recorded as the post oven sample weight (W2). This moisture content test was repeated at least 5 times per 1 sample, and the average moisture content was reported in percentage units.

Calculation:Moisture content (%) = (W1– W2) /W1 × 100

Tensile Strength and Elongation. Tensile strength and elongation were tested in accordance with the ASTM D882 (1997) standard. The container sample was cut to 1 cm in width and 12 cm in length. The sample was fixed by 1 cm clamps on both sides of the Texture Analyzer (model TA.XT plus, by Micro Systems Ltd., UK). The tensile strength was directly calculated when the force at break was divided by the area used to pull (MPa). Elongation is measured as the distance that the sample can stretch (%).

Compression Resistance. Compression resistance was tested in accordance with the ASTM D642 (2010) standard. The container sample was cut to 5 × 5 cm^2 in size and then placed on the base of the Texture Analyzer (model TA.XT plus, by Micro Systems Ltd., UK). The cylindrical P/50 probe was installed into the Texture Analyzer. The compression resistance is the maximum force (MPa) that causes a sample to transform by 10%.

Penetration Resistance. Penetration resistance or puncture test was tested in accordance with ASTM F904 (2016) standard. The sample was cut to 5 × 5 cm^2 in size and placed on

the cylindrical base of the Texture Analyzer (model TA.XT plus, by Micro Systems Ltd., UK), which had been installed with the cylindrical probe P / 6. Puncture force was the maximum force (MPa) used to penetrate the sample.

Water Absorption Property. The Water absorption property was tested in accordance with modified ASTM D 3285 (2005) standard. The sample was cut to 2.5 × 2.5 cm^2 and then stored in the temperature and relative humidity controller at a temperature of 27 ± 1°C and 65 ± 2%RH for at least 24 h. The sample was then removed from the controller and was weighed prior to the testing (W1). After that, the sample was put in a beaker containing 100 mL of distilled water, and immediately started the timer. At the 60th second, the sample was removed and placed on tissue paper. Then another tissue paper was immediately placed on top. The metal roller was used to roll over the tissue paper back and forth. Finally, the sample was weighed again (W2).

Calculation: Water absorption value (%) = (W2 –W1) / W1 × 100

Oil Absorption. Oil absorption was tested in accordance with modified ASTM D 3285 (2005) standard. The sample was cut to the size of 2.5 × 2.5 cm^2 and stored in the temperature and relative humidity controller at a temperature of 27 ± 1°C and at 65 ± 2%RH for at least 24 h. Then, it was removed from the controller and was weighted prior to the testing (W1). The sample was then put into a beaker containing 100 mL of oil, and then immediately started the timer. At the 60th second, the sample was removed and placed on tissue paper. Then immediately another piece of tissue paper was placed on the top. The metal roller was used to roll back and forth over the tissue paper. Finally, the sample was weighted again (W2).

Calculation:Oil absorption value (%) = (W2 –W1) / W1 × 100

Analysis of Results. Three (3) replications were done, and the average value was calculated. The package properties were analyzed by using SPSS: one - way Analysis of Variance (ANOVA) and Duncan's Multiple Range Test (DMRT) at a confidence level of 95%.

RESULTS AND DISCUSSIONS

Physical Properties

The physical properties of the paper were determined from thickness, standard weight, and moisture content. According to the current study, the container molded by Method C had lower thickness and moisture content, but had higher standard weight per area than

Table 1
Thickness, standard weight and moisture content of packaging molded from banana sheath

Fiber:Binder	Thickness (mm)	Weight (g/m^2)	Moisture content (%)
Hot air			
60:40	5.63±0.09	2266.67±47.29	10.60±4.31
70:30	5.47±0.32	2426.67±28.77	12.15±0.24
80:20	5.71±0.30	2834.67±56.21	12.44±0.32
90:10	6.57±0.45	2901.33±84.66	10.80±0.29
Compression			
60:40	4.18±0.18	2762.67±46.19	8.80±0.12
70:30	4.10±0.28	3200.00±144.00	8.23±0.30
80:20	4.04±0.27	3354.67±88.12	8.88±0.64
90:10	3.91±0.11	3584.00±204.27	9.48±0.54

the container molded by Method H as shown in Table 1. An identical surface area of the package, Method C had higher mass content than Method H because of their short edge.

Since the container molded by Method C received compression resulting in high density of the structure, it had more weight per area, but less thickness than the container molded by Method H. Neither container had a statistically significant difference ($p>0.05$) in the amount of banana sheath fibers at 60-90%, but the standard weight was in the range of 2762-3584 g / m^2. The weight increase was consistent with the amount of banana sheath fibers. The standard weight of the container made from banana sheath in both methods was found to be higher after the banana sheath fibers had been added. Meanwhile, the thickness and moisture content were similar. The container molded by Method H had the thickness and moisture of 5.63-6.57 mm and 10.60-12.44%, respectively, while the container molded by Method C, had the thickness and moisture content of 3.91-4.18 mm and 8.23-9.48%, respectively. The moisture content of the banana sheath container was lower than the bio-degradable starch container (25.3-28.6%) (Medina-Jaramillo et al., 2017).

For containers, the absorption properties are important when storing liquid products or storing products in humid conditions. Therefore, the packaging should have a low liquid absorption value to ensure the durability of the packaging for various uses.

Based on the water absorption test, it was found that the container molded by Method H had absorbed more water than the container from Method C ($p <0.05$) as shown in Figure 1. Due to the porous structure, water was found to infiltrate the material. Conversely, when the banana sheath fibers were added, water absorption decreased because the binder was the flour solution, which has good compatibility with water. When banana sheath fibers were added, the amount of the binder was reduced, resulting in a decrease in water absorption. However, the ratios of banana sheath fiber per binder at 70:30, 80:20 and 90:10 were not found to be significantly different ($p> 0.05$).

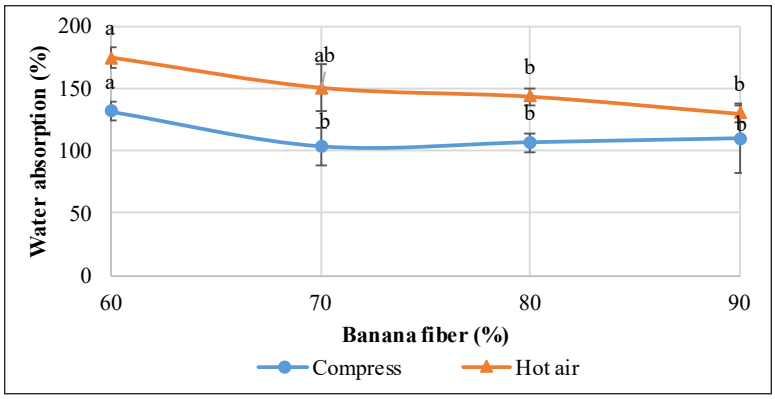

Figure 1. Water absorption of packaging molded from banana sheath

Like water absorption, Method H ($p < 0.05$) showed higher oil absorption than Method C (Figure 2) due to the loose structure which allowed oil particles to penetrate the structure more easily than in Method C. However, when the fiber content increased, the oil absorption reduced due to the close arrangement of fiber particles of the banana sheath, which had been packed up and had prevented the oil from penetrating. The container made from the ratio of 90:10 showed only 20% oil absorption. The absorption of water and fat can be improved by coating the container in order to reduce the permeability of water, oil, and other solutions.

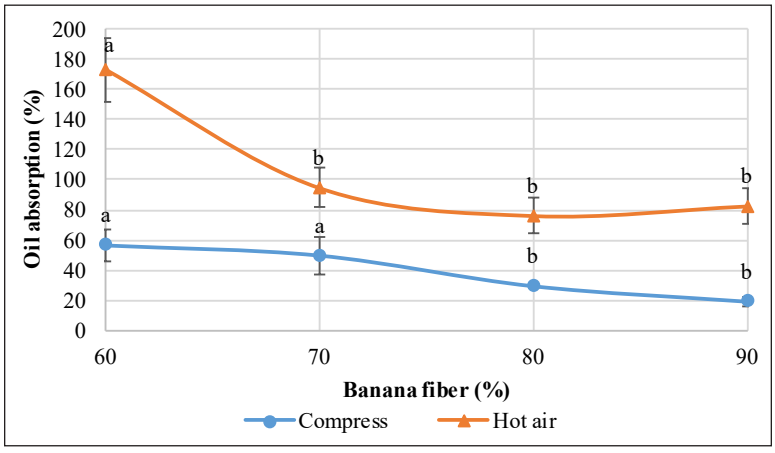

Figure 2. Oil absorption of packaging molded from banana sheath

Mechanical Properties

Mechanical properties are important properties for containers, especially during transportation when damage may be caused to agricultural products and food. Therefore, strength is essential when testing containers. When molding the container in the oven, a

mold was used and was heated along with the material. The force, resulting in deformation from compression, was in the range of 180-550 N, as shown in the Figure 3. The sample with the highest compression force had been made of 60% dried banana sheath fiber. When increasing the amount of dried banana sheath fiber, the compression resistance was found to decrease. This was due to a distribution of fibers in the materials in the molding force, causing the fiber particles to become untightened. In addition, the small particles are easily deformed (Sibaly & Jeetah, 2017).

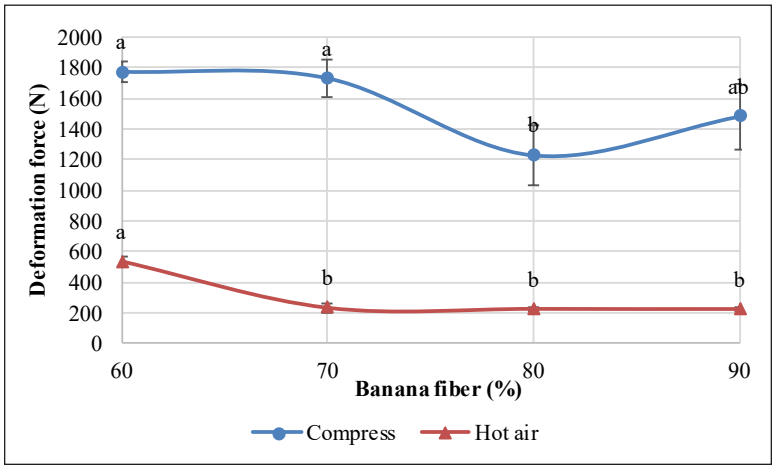

Figure 3. Compression resistance of packaging molded from banana sheath

Based on the container molded by Method C, the compression resistance required a lot of force to make the container deform because when the container was being molded, the material was pressed into the mold and heated, which resulted in a high density of the material particles. Therefore, the force that caused deformation from compression was very high. The compressive force was in the range 1200-1800 N, which decreased in contrast with increased amounts of banana sheath fiber. However, the compressive force increased when the amount of banana sheath increased to 90%. Yet, there was no difference found from the banana sheath container having 80% of banana sheath ($p > 0.05$). Higher compressive force indicated the strength of the containers to withstand deformation. In short, molding the containers by hot compressor had made the containers stronger than those containers molded by Method H.

Puncture force of the banana sheath fiber container molded by Method C increased when the fiber content was increased by 80% and decreased by 90%, which was similar to paper made from banana sheath fibers (Romdhonee & Jeetah, 2017). However, no difference was found in the penetrating force at the fiber content of 80-90% ($p > 0.05$) (Figure 4). The penetrating force of the container made from banana sheath increased when the amount of banana sheath fiber was increased. The increased penetrating force indicated a composition

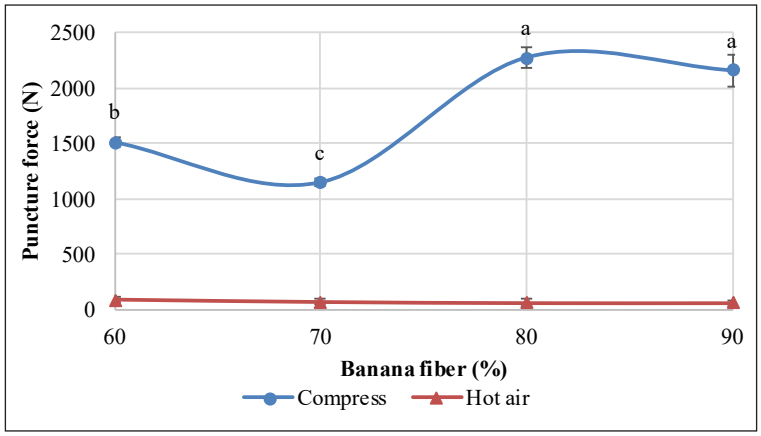

Figure 4. Penetration resistance of packaging molded from banana sheath

of alpha cellulose in larger quantities and a decrease in microfibilar angle. Moreover, the increased density contributed to resistance to the penetrating force. Likewise, the paper made from pineapple fibers (Sibaly & Jeetah, 2017) had higher penetrating force when the amount of fibers was increased. Meanwhile, the containers molded by Method H had low penetrating force and no difference was indicated when the fiber content was increased ($p > 0.05$) because the structure of the banana sheath fiber is uneven. Furthermore, the packaging had uneven thickness, which was caused by the uneven distribution of fibers. Therefore, in the areas where the fiber particles were not dense, it was easily penetrated. Also, the fact that the containers were thin had made them fragile. Moreover, the puncture force related to the deformation force which against the percentage by mass of fiber. The Method C had higher density and the stiffness. Thus, the resistance of puncture and deformation force were higher than Method H ($p<0.05$) (Sibaly & Jeetah, 2017).

The dried and crushed banana sheath fibers, which had been used as a material in the banana sheath containers, increased the adhesion efficiency between the fiber particles and the binder. When increasing the amount of fiber, the tensile strength resistance was also increased, making the containers to become stronger (Zhao et al., 2019) (Figure 5) due to the cross-linking of the cellulose molecular chain (Muratore et al., 2019) which can be attributed to higher cellulose crosslinking as their cellulose chains reacts each other. There was also the bonding strength between the sheath fiber and banana starch solution during the molding process. The tensile strength of Method H was greater than Method C because of the molding method was used in the experiment. Method H affected the tough but not tight while Method C affected high density and resistant puncture. This is similar to pineapple fiber paper and banana fiber paper, which had shown greater tensile strength resistance when the amount of fibers was increased (Sibaly & Jeetah, 2017; Ramdhonee & Jeetah, 2017). However, it was still less than the biological material PHBV (28.1 MPa) (Zhao et al., 2019) and the paper (321.20 MPa) (Muratore et al., 2019).

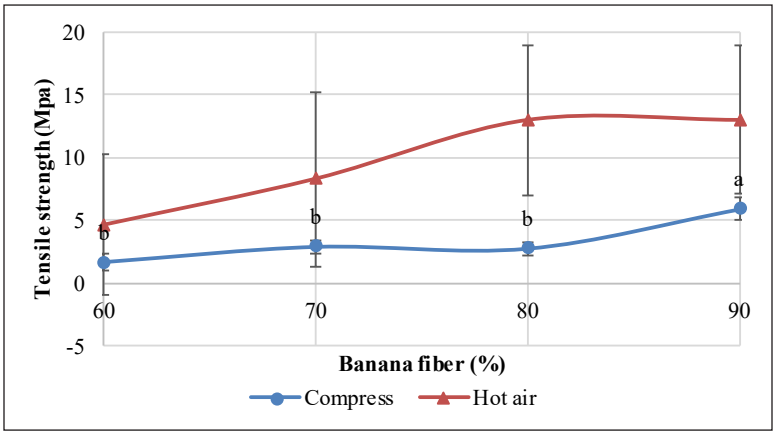

Figure 5. Tensile strength resistance of packaging molded from banana sheath

The elongation of the banana sheath containers was found to increase along with an increase in the amounts of banana sheath fibers. However, the variation of elongation at break with fiber content is so small, less than 1%. The containers molded by Method H were different at 70-90% of banana sheath. In contrast, for the containers molded by Method C, there was no difference found between 60-80% of the banana sheath fiber. However, elongation increased when the banana sheath fiber was increased to 90%. Because the molded containers were hard, they were found to be strong, but less flexible. This contributed to the low elongation of the containers, making the containers strong with an elongation value of not more than 1.4% (Figure 6).

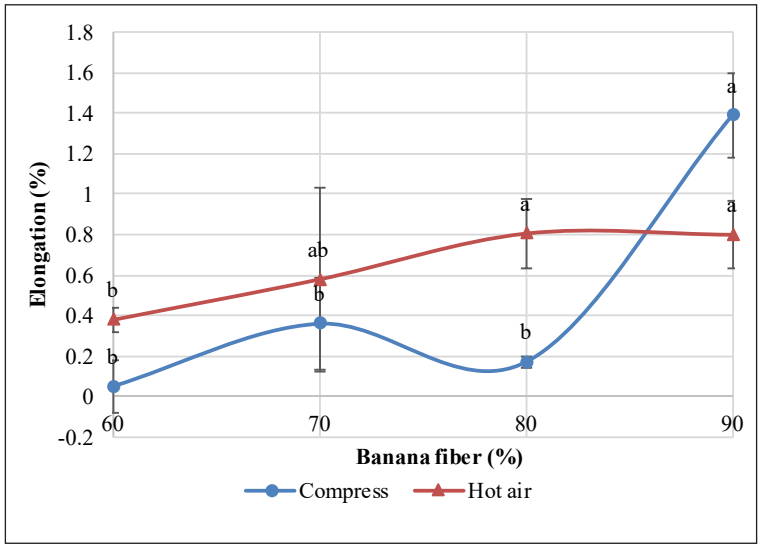

Figure 6. Elongation of packaging molded from banana sheath

CONCLUSIONS

The ground dried banana sheath powder, which was used as a material for making the containers had contributed to an even distribution in the structure, as well as the adhesion of the particles. The containers, molded by the hot compression, indicated that the mechanical properties had consisted of resistance values in compression, penetration, and tensile strength. It was found that the samples containing 90% of banana sheath fibers and the hot press method were resistant to deformation, penetration and tensile strength, and had shown lower water and oil absorption. However, further experiment will be to improve the water and oil absorption by coating with edible film.

ACKNOWLEDGEMENTS

The authors would like to thank the National Research Council of Thailand (NRCT) and Division of Research Administration, Khon Kaen University for financial support. All facilities from the Faculty of Applied science and Engineering were also acknowledged.

REFERENCES

Alarcon, L. C., & Marzocchi, V. A. (2015). Evaluation for paper ability to pseudo stem of banana tree. *Procedia Materials Science, 8*, 814-823.

AOAC. (2000). *Official methods of analysis of AOAC international*. Gaithersburg, USA: Association of Official Agricultural Chemists.

ASTM D3285. (2005). *Standard test method for water absorptiveness of nonbibulous paper and paperboard (Cobb Test)*. American Standard Testing Method. West Conshohocken, PA: ASTM International.

ASTM D642. (2010). *Standard test method for determining compressive resistance of shipping containers, components and unit loads*. American Standard Testing Method. West Conshohocken, PA: ASTM International.

ASTM D646. (1996). *Standard test method for grammage of paper and paperboard (Mass Per Unit Area)*. American Standard Testing Method. West Conshohocken, PA: ASTM International.

ASTM D882. (1997). *Standard test method for tensile properties of thin plastic sheeting*. American Standard Testing Method. West Conshohocken, PA: ASTM International.

ASTM F904. (2016). *Standard test method for comparison of bond strength or ply adhesion of similar laminated mode from flexible materials*. American Standard Testing Method. West Conshohocken, PA: ASTM International.

Bi, Y., Zhang, Y., Jiang, H., Hong, Y., Gu, Z., Cheng, L., … & Li, C. (2017). Molecular structure and digestibility of banana flour and starch. *Food Hydrocolloids.*, *72*, 219-227.

Cinelli, P., Chiellini, E., Lawtom, J. W., & Imam, S. H. (2006). Foamed articles based on potato starch, corn fibers and poly (vinyl alcohol). *Polymer Degradation and Stability, 91*(5), 1147-1155.

Jirukkakul, N. (2016). The study of edible film production from unriped banana flour and riped banana puree. *International Food Research Journal, 23*(1), 95-101.

Jirukkakul, N. (2019). Physical properties of banana stem and leaf papers laminated with banana film. *Walailak Journal of Science and Technology (WJST), 16*(10), 753-763.

Liu, H., Wu, Q., & Zhang, Q. (2009). Preparation and properties of banana fiber-reinforced composites based on high density polyethylene (HDPE)/Nylon-6 blends. *Bioresource Technology, 100*(23), 6088-6097.

Medina-Jaramillo, C., Ochoa-Yepes, O., Bernal, C., & Fama, L. (2017). Active and smart biodegradable packaging based on starch and natural extracts. *Carbohydrate Polymers, 176*, 187-194.

Muratore, F., Barbosa, S. E., & Martini, R. E. (2019). Development of bioactive paper packaging for grain-based food products. *Food Packaging and Shelf Life, 20*, 1-7.

Oliveira, L., Evtuguin, D., Cordeiro, N., & Silvestre, A. J. D. (2009). Structural characterization of stalk lignin from banana plant. *Industrial Crops and Products, 29*(1), 86-95.

Ramdhonee, A., & Jeetah, P. (2017). Production of wrapping paper from banana fibres. *Journal of Environmental Chemical Engineering, 5*(5), 4298-4306.

Shogren, R. L., Lawton, J. W., & Tiefenbacher, K. F. (2002). Baked starch foams: Starch modifications and additives improve process parameters, structure and properties. *Industrial Crop and Products, 16*(1), 69-79.

Sibaly, S., & Jeetah, P. (2017). Production of paper from pineapple leaves. *Journal of Environmental Chemical Engineering, 5*(6), 5978-5986.

Soykeabkaew, N., Supaphol, P., & Rujiravanit, R. (2004). Preparation and characterization of jute and flax-reinforced starch-based composite foams. *Carbohydrate Polymers, 58*(1), 53-63.

Tiefenbacher, K. F. (1993). Starch-based foamed materials-use and degradation properties. *Journal of Macromolecular Science, Part A: Pure and Applied Chemistry, 30*(9-10), 727-731.

Zhao, X., Ji, K., Kurt, K., Cornish, K., & Vodovotz, Y. (2019). Optimal mechanical properties of biodegradable natural rubber-toughened PHBV bioplastics indended for food packaging applications. *Food Packaging and Shelf Life, 21*, 1-11.

Pertanika J. Sci. & Technol. 28 (3): 779 - 795 (2020)

PERTANIKA JOURNALS

SCIENCE & TECHNOLOGY

Journal homepage: http://www.pertanika.upm.edu.my/

Rice Chlorophyll Content Monitoring using Vegetation Indices from Multispectral Aerial Imagery

Ang Yuhao[1], Nik Norasma Che'Ya[2]*, Nor Athirah Roslin[2] and Mohd Razi Ismail[3]

[1]Department of Civil Engineering, Faculty of Engineering, Universiti Putra Malaysia, 43400 UPM, Serdang, Selangor, Malaysia.
[2]Department of Agriculture Technology, Faculty of Agriculture, Universiti Putra Malaysia, 43400 UPM, Serdang, Selangor, Malaysia.
[3]Department of Crop Science, Faculty of Agriculture, Universiti Putra Malaysia, 43400 UPM, Serdang, Selangor, Malaysia

ABSTRACT

Precision agriculture is a concept of agricultural management, based on analyzing, measuring, and reacting to inter and intra-field variability in crops. One of the tools deployed for crop monitoring in precision agriculture is the use of an unmanned aerial vehicle, able to obtain high flexibility with fewer restrictions, and high spatial and spectral resolution in comparison to airborne and spaceborne system. In this paper, the assessment of various vegetation indices were performed for paddy stress monitoring using red edge band from multispectral imagery. The objective of the study was to create rice field maps with the use of aerial imagery and object-based image analysis technique to validate vegetative indices in rice field maps by using soil plant analysis development (SPAD) data. The result showed Normalized Difference Vegetation Index (R=0.957), Normalized Difference Red Edge (NDRE) (R=0.974), Soil Adjusted Vegetation Index (R=0.964), and Optimized Soil Adjusted Vegetation Index (R=0.966), all of which provided positive linear correlations with SPAD readings. NDRE showed higher correlation compared with other vegetation indices, exhibiting a better measure ment for farmers to make decisions. This paper has demonstrated how aerial imagery can be used to collect an accurate mapping in real time that can be analyzed to monitor

ARTICLE INFO

Article history:
Received: 28 March 2020
Accepted: 14 May 2020
Published: 16 July 2020

E-mail addresses:
vincentangkhun@gmail.com; vincentangkhun@gmail.com (Ang Yuhao)
niknorasma@upm.edu.my (Nik Norasma Che'Ya)
norathirahroslin@gmail.com (Nor Athirah Roslin)
razi@upm.edu.my (Mohd Razi Ismail)
* Corresponding author

ISSN: 0128-7680
e-ISSN: 2231-8526

© Universiti Putra Malaysia Press

conditions of crop and chlorophyll content by using SPAD to enable farmers to make informed decisions. Further investigations need to be carried out by validating the real chlorophyll content to improve existing correlations.

Keywords: Multispectral imagery, object-based analysis, red edge band, vegetation index

INTRODUCTION

Rice (*Oryza sativa* L.) is the most important source of livelihood and income of rural population. Currently, the self-sufficiency level (SSL) of rice is 71.5% and SSL needs to be increased up to 80% to feed country's population by 2020. However, rice productivity is too low due to lack of technical efficiency which can be brought to effect for agricultural households (Arellano & Reyes, 2019). Precision farming offer an alternative choice for the farming community for farm productivity improvement. Site-specific crop management is a technique that is designed to integrate various technologies to provide spatially referenced data for better decision making (Norasma et al., 2013; Mukherjee et al., 2019). Crop monitoring and assessment is one of the crucial problems related to yield in agricultural crops. Timely and accurate crop monitoring can provide early treatment to unhealthy crops and can maintain the amount of yield production in agriculture. Traditionally, crop assessment had relied on ground-based field survey and visual observation to measure plant status by collecting a small sample size (Sim & Gamon, 2012). Common techniques, including manual inspection and perimeter scouting, are inefficient methods for data collection and validation process (Valente et al., 2011). For instance, ground assessment is to ascertain crop status which involves measurement of a plant by using its leaf. However, the crop assessment for an agricultural field requires an up-scaled information beyond the canopy level. Moreover, the collection of ground samplings in the field was slow and costly. According to Zhang et al. (2015), implementing this type of collection for crop assessment in the field would be tedious. Regular remote sensing technique by placing a sensor on a stronghold over crop fields, as well as weather constraints, was a limitation for data collection (Nguy-Robertson et al., 2012). Likewise, using a satellite and piloted aircraft demonstrated a constraint with temporal and spatial resolution for agricultural assessment (Maes & Steppe, 2019).

Therefore, applying a quick, efficient, and accurate method for crop monitoring and assessment is crucial in increasing productivity and efficiency in the field. Remote sensing technology is a reliable tool to assess crop health and status, such as chlorophyll collection (Haboudane et al., 2002), leaf area indicator (Wang et al., 2019; Liu et al., 2017), and biomass (Fu et al., 2014), which can effectively be correlated with remote sensing information. In precision agriculture, crop condition can be monitored using remote sensing based on the crop parameter. In general, remote sensing is a means of obtaining

and interpreting information of an object from a distance, an area phenomenon by acquiring the data using sensors or devices without physical touch (Johnson et al., 2003). Remote sensing typically uses sensors to reach aerial, satellite, and orbital observations on the surfaces and the targeted objects (Zulfa & Norizah, 2018; Ren et al., 2018). Satellite images have been used as the primary source of information for analyzing crop health in precision farming (Auernhammer, 2001). However, satellite and aerial remote sensing have their own limitations. In contrast, UAV technology can identify the details of an area because of higher spatial resolution and this type of imagery provides new solutions for crop management and monitoring in agricultural fields (Abdullah et al., 2019). High-resolution imagery and real-time satellite imagery are expensive. The limitation of satellite remote sensing is cloud cover, which contributes to low pixels resolution in unclear imagery (Verger et al., 2014).

The Development and UAV-based Application for Crop Management and Monitoring

The advanced development of UAV has provided another alternative for crop management and monitoring in large areas (Li et al., 2019). The application of UAV technology in crop assessment has functions in various crops for monitoring health status of crops. This would ease farmers in managing their farms and provide more accurate data regarding their crop conditions in the field. UAVs equipped with visible band and multispectral scanning sensors can provide enough information for analysing crop growth, health status, maturity, and morphology. Imagery from UAV, using different sensors like RGB (Red Green Blue), multispectral, hyperspectral, and thermal camera have been used to estimate leaf area indicator (LAI) (Wang et al., 2019), biomass (Bendig et al., 2015), carotenoid (Zarco-Tejada et al., 2012), and temperature (Tokekar et al., 2013). Shafri et al. (2006) demonstrated the usefulness of a multispectral camera mounted UAV to examine the emergence of wheat during early season from UAV imagery applying vegetation index. Louis et al. (2005) had proven that the use of UAV technology with a multispectral sensor provided a higher spatial resolution for wheat monitoring in the emergence stage. This was supported by Sullivan et al. (2007) who investigated hyperspectral data acquired from UAV platform to perform quantitative analysis for rootstock performance in walnut trees.

The developmental progress of UAV has improved from slow-flying UAV (Berni et al., 2009) to fixed wing and rotary-UAV, where the advantage is that flight characteristics due to their natural gliding capabilities with no power. In addition, Norasma et al. (2018) experimented on crop status using UAV with optical sensors and had successfully identified stressed area using water flow analysis at the early season of rice growth. Table 1 shows the types of UAV application for different purposes of crop assessment.

Table 1
Different types of UAV application in crop assessment

UAV type	Objective	Camera	Crop	Reference
RCTAS/APV-3 Unmanned aircraft	Usefulness of UAV's for precision agriculture	Hyper-spectral	Grapevine	Kira et al. (2015)
Unmanned helicopter	Tree canopy conductance, crop water stress index	Airborne Hyper-spectral Scanner	Corn Olive Peach and olive	Berni et al. (2009)
Unmanned helicopter	Development small UAV for agriculture surveillance Assess water stress	Thermal	Turf grass	Xue & Su (2017)
Fixed- wing	Water stress	Narrow-band multi-spectral Thermal	Grapevine	Zarco-Tejada et al. (2012)
Multirotor UAV	Weed detection	MCA 6 Multi-spectral	Sorghum	Norasma (2016)

Berni et al. (2009) found that thermal sensing could be used for irrigation management and the sensor can read characterization of water stress in the orchards. However, the sensor is expensive and needs an expert pilot to fly the UAV to collect the data. This is similar to Kira et al. (2015) that also used hyperspectral sensor and found that VI gave the highest results compared to NN and PLS model. Zarco-Tejada et al. (2012) experimented the effectiveness of narrow-band indices such as chlorophyll indices like fluorescence indices (FLD2) and xanthophyll, showed promising result than NDVI for water stress detection. The result indicated the spectral index that comprised the wavelength near red edge region such as 747nm, 762nm and 780nm were the best indicators in monitoring crop status. Therefore, the use of VI is important to improve the sensitivity of the greenness of the plants (Xue & Su, 2017) and consistently with Norasma (2016) that also used VI and OBIA to detect weed in sorghum crop. Norasma (2016) and Xue and Su (2017) suggested to develop new VIs for the broadening of the research areas. In addition, Norasma (2016) found that the overall accuracy for weed detection using OBIA was more than 80%. These results are considered high and moderate for the effectiveness in discrimination respectively (Norasma, 2016). Therefore, the OBIA technique was used and calculated the VIs for accurate rice mapping using multispectral sensor due the cost effectiveness.

Chlorophylls is a major and integral part for the reaction of photosynthesis, and this is suitable as remote sensing could assess plant physiological development (Yongjun & Jingjing, 2016). The quantity of chlorophyll per unit leaf area in a plant is a key status of the entire plant's health. Healthy plants with the capability of displaying growth rates until optimal extent is estimated to have higher amounts of chlorophyll than unhealthy plants. Thus, the identification and detection of chlorophyll content in a leaf can be used to detect and study plant stress, based on its nutritional form, contributing a crucial effect

on crop status and conditions, the level of severity, and the amount of nutrients, especially in precision agriculture practices (Zarco-Tejada et al., 2013). Vegetation indices and red edge-based indices are the most general techniques that can be used in plant stress detection. Vegetation indices are widely used for the estimation of crop status based on the amount of chlorophyll content by using visible and near-infrared (NIR) regions of the electromagnetic spectrum. Chlorophylls have strong absorption peaks in the red region and high reflectance peaks in the near-infrared region (Shamshiri et al., 2017). Maximal absorbance in the red region occurs between 660 nm and 680 nm. This is because absorption range of 660 – 680 nm tends to be saturated at low chlorophyll quantities and reflect in the near-infrared region, thus reducing the sensitivity of the spectral indices based on this wavelength, except for high chlorophyll content (Singh et al., 2017)

In recent years, numerous spectral indices from UAV have been proven to calculate plant disease detection and crop monitoring (Garcia-Ruiz et al., 2013; Hunt et al., 2018; Yoder & Pettigrew-Crosby, 1995). Multispectral (MS) and hyperspectral sensors mounted on UAVs have been extensively used to assess plant health and conditions for several vegetation indices, which involved integrated R515/ R570 (band ratioing) and TCARI/ OSAVI narrow-band indices for leaf chlorophyll estimation with a hyperspectral camera mounted on UAV (Liang et al., 2015; Wang et al., 2019). Hunt et al. (2003) proved that colour-infrared film used with a low-cost automatic camera produced a Normalized Difference Vegetation Index (NDVI) map that can be used in crop monitoring. Table 2 shows the sensor of different remote sensing platforms in crop disease inspection.

Ranganath et al. (2004) proved near-infrared region had shown considerable reduction in reflectance in differentiating diseased rubber from healthy rubber using multi-date satellite data of IRS-1C. This is similar to the work of Shaw and Kelly (2005), using multispectral satellite imagery in classifying soybean anomalies from infestation. This is attributed to differences in colouration of soybean plants with iron chlorosis and lack of full canopy coverage of stunted soybean. However, previous studies were not sufficient for crop

Table 2
Example of disease detection of crop by various remote sensing methods

Crop types	Sensor	References
Rubber plantation	Indian remote sensing satellite (IRS-IC)	Ranganath et al. (2004)
Soybean	Multispectral sensor	Shaw & Kelly (2005)
Paddy	Hyperspectral radiometer (ASD fieldspec pro FR)	Ren et al. (2008)
Oil palm	Hyperspectral sensor, APOGEE spectroradiometer	Shafri & Anuar (2008)
Wheat aphids	Handheld cropscan radiometer	Yang et al. (2009)
Oil palm	AISA airborne hyperspectral sensor	Shafri et al. (2011)
Grapevine	Narrow-band multispectral thermal UAV	Zarco-Tejada et al. (2013)
Onion Cultures	Multispec 4C protype (Ebee) UAV	Nebiker et al. (2016)
Walnut trees	Hyperspectral sensor	Singh et al. (2017)

monitoring due to lack of narrower spectral bands such as hyperspectral data. Therefore, Ren et al. (2008) and Shafri et al. (2011) proved that hyperspectral crop reflectance data could be used in monitoring crop growth and development using VI and spectral signatures. Nebiker et al. (2016) showed that NDRE index showed an average correlation and had better performance than NDVI in detecting disease in onion using light-weight multispectral UAV sensor. Singh et al. (2017) had further proven that red-edge position index, which fell in the wavelength of 680-780 nm was a better preference in monitoring rootstock growth in walnut trees using UAV-based remote sensing.

Singh et al. (2017) had shown how a multispectral sensor could be used to examine the emergence and growth stages of wheat from UAV technology using a sequence of vegetation indices. Andre et al. (2013), had reported a stronger relationship between vegetation and leaf area index (LAI). Moreover, vegetation indices made up of red edge band (720 nm) and near-infrared band (800 nm) were found to be more effective in estimating yield and amount of chlorophyll present at higher state. In this study, multispectral images in the early season of rice growth were obtained using UAV technology, and vegetation indices were correlated to SPAD chlorophyll meter readings to assess the potential of several vegetation indices for examining amount of chlorophyll concentration present in rice. The objective of this study was to examine four vegetation indices using aerial images and object image analysis (OBIA), and to correlate with the vegetation indices in paddy field maps using the chlorophyll data from SPAD meters.

MATERIAL AND METHODS

The research was carried out at Ladang Merdeka, Ketereh, Kelantan, located in the east coast of Peninsular Malaysia (Figure 1). The whole coverage of the study area is twenty acres. The coordinates of the study location are 6.076184°, 102.184315°. The plots were thoroughly prepared and levelled using a leveler machine. Rice variety called PadiU putra, which is resistant to leaf blight disease (S1) was used in this present study.

This study was developed and managed by UPM researchers for a single season from January 2018 until May 2018. The cultivated medium of PadiU Putra (S1) was planted on 30th January 2018. Figure 2

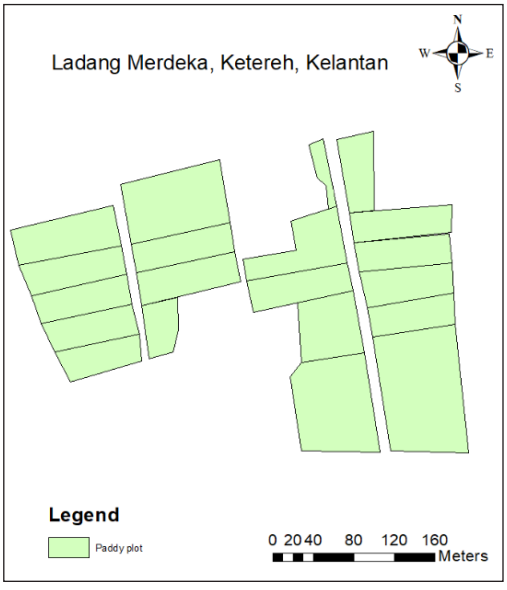

Figure 1. The experimental plot in Ladang Merdeka

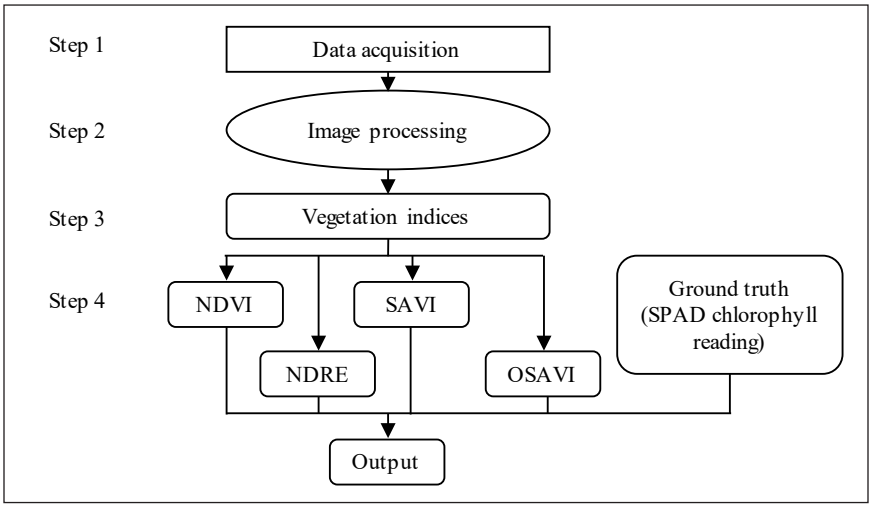

Figure 2. The methods steps in this study

shows the flow chart of this research, indicating the performance of difference vegetation indices at early season of rice growth.

Data Acquisition

Step 1: Collection of Ground Samples. The ground chlorophyll diagnostic tool used in this study was SPAD 502 chlorophyll meter (Konica Minolta Sensing, Inc., Osaka, Japan). Five samples from eight points within 1 m radius were scanned using SPAD chlorophyll meter and these samples were then recorded and averaged to obtain the accurate result.

Image Acquisition

For image collection, a multirotor UAV and multispectral camera were used. The flight plan was designed prior to data acquisition by using Mission Planner software (http://ardupilot.org/planner/index.html). Mission planner is a ground control station for ArduPilot created by Oborne (2019), providing setup and flying support, as well as reviewing recorder flights. The multispectral sensor mounted on the drone was Parrot Sequoia, which was manufactured in Paris, France. It was able to capture 4 types of wavebands, and they were green band, red band, red edge, and NIR (Markengold PR, 2016). The data collection was conducted at daytime under less cloudy and windy conditions, between 08:30 a.m. until 12:00 p.m. (+8 GMT) on 10th of February 2018 on the 11th Day After Planting (DAP). Agisoft Photoscan software (Agisoft LLC, St. Petersburg, Russia) was used to build and arrange the imagery mosaic using Structure from Motion (SfM) algorithms. Table 3 shows specification of the multispectral camera used.

Table 3
Basic parameters for multispectral camera on UAV

Sensor	Spectral bands (nm)	Resolution (pixels)	Weight (g)
Parrot Sequoia	530, 640, 730, 770	1280 × 960	107g

Step 2: Image Processing. Pre-processing of raw images involved downloading them from the SD memory card to the computer and then further processing them in Agisoft Photoscan Professional software (Agisoft LLC, St. Petersburg, Russia) to produce orthophoto map. Then, the orthophoto map was geo-rectified using the control points at the field. The geo-rectified process use ArcMap software to validate the orthophoto map. Subsequently, the orthophoto map was analysed using eCognition software. eCognition software (Definiens AG, Munich, Germany) is a development environment for object-based image analysis (Andre et al., 2013).

Data Analysis

Step 3: Vegetation Analysis for Different Vegetation Indices. Four types of vegetation indices were used for monitoring the crop condition in the rice field. Normalized Difference Vegetation Index (NDVI), Normalized Difference Red-Edge Index (NDRE), Soil Adjusted Vegetation Index (SAVI), and Optimized Soil Adjusted Vegetation Index (OSAVI) indices were chosen for the multispectral images such as green band, red band, red edge, and NIR images. Vegetative maps for different vegetation indices were produced for NDVI, NDRE, SAVI, and OSAVI. Table 4 provides information on vegetation indices including red-edge indices were applied in this this UAV-imagery. This processing step was performed using eCognition software.

Table 4
Vegetation indices and red edge algorithms were applied in this UAV-imagery

Vegetative Index	Algorithm formula	Author
NDVI	(NIR-RED) / (NIR+RED)	Rouse et al. (1974)
NDRE	(NIR-RED EDGE) / (NIR+RED EDGE)	Fitzgerald et al. (2006)
SAVI	(1+L) * (NIR-RED) / (NIR+RED+L)	Huete (1988)
OSAVI	(1+l) * (NIR-RED) / (NIR+RED+L) Where L= 0.16	Rondeaux et al. (1996)

Step 4: Statistical Analysis between Vegetative Indices (NDVI/ NDRE/ SAVI/ OSAVI) with SPAD Readings. Statistical analysis between NDVI/ NDRE/ SAVI/ and OSAVI values obtained from multispectral imagery were correlated with ground samples (SPAD chlorophyll values). Vegetative indices were correlated and validated to compare two different vegetative indices, such as NDVI/ NDRE/ SAVI/ OSAVI with SPAD units using

Pearson correlation analysis. Besides, the root mean squared error (RMSE) for each iteration was computed and averaged to determine coefficient of variation (CV). The lower the value of the CV, the more precise the estimate is. This analysis was run by Minitab® 17 Statistical Software.

RESULT AND DISCUSSION

Vegetation Analysis

Figure 3 shows the VI map at early season of rice growth. The range of values for the NDVI/ NDRE/ SAVI/ OSAVI is -1 to 1 where -1.0 represents very low level of vegetation greenness and 1.0 represents very high level of vegetation greenness. Vegetation indices, such as NDVI, NDRE, SAVI, and OSAVI, usually have values closer to 0, indicating lesser canopy density, whereas values closer to 1 indicate more canopy density for crops (Xiang & Tian, 2011). Since four different VI were used, the outcomes were different because each indices is for different purpose. This project shows that the results were as expected based on the literature. In the early phase of rice growth, the canopy area of the rice crop was small, and most of the reflectance were affected by soil and water factors, which could influence the result on vegetation indices (Garcia-Ruiz et al., 2013). Most rice crop in the early season fall in the yellow zone, with NDVI values ranging from 0.3 to 0.5 because soil background effects during the growth stage of the rice plants. This is consistently found where NDVI is sensitive to the effects of soil brightness, soil color, atmosphere, cloud and cloud shadow, and leaf canopy shadow (Xue & Su, 2017). Whereas OSAVI and NDRE showed promising indices that were able to capture some smaller plants inside the paddy field, due to elimination of soil background

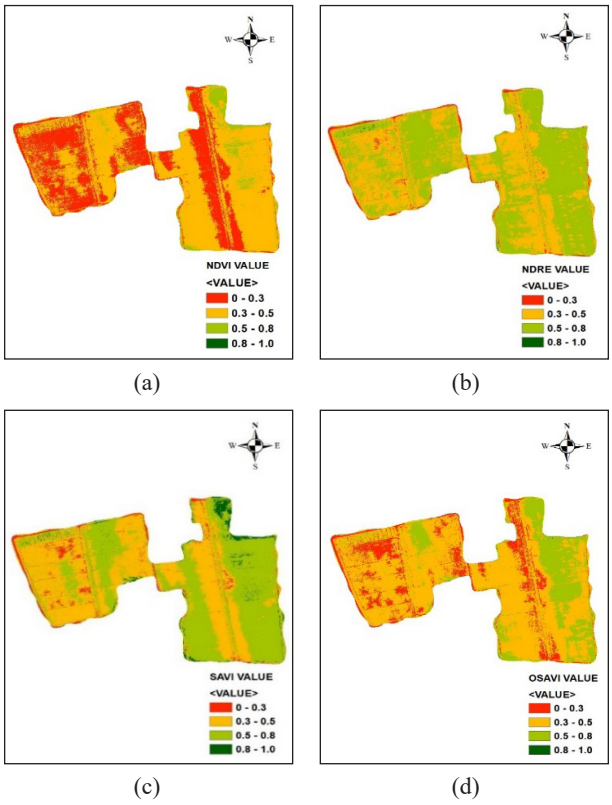

Figure 3. Vegetation indices map generated during early season (on the 11`th Day After Planting (DAP) of rice growth: (a) NDVI map; (b) NDRE map; (c) SAVI map; and (d) OSAVI map

effects and larger the effect of photosynthesis even though it fell at the early season of growth (Li et al., 2019; Rouse et al., 1974).

Relationship Between Vegetation Indices and SPAD Chlorophyll Readings

There was a positive linear correlation between NDVI and SPAD readings. NDVI shows higher correlation with SPAD readings (R = 0.957; RMSE= 0.74) (Figure 4). This relationship is consistent with those of other studies which also reported a positive and linear relationship between vegetation index (NDVI) and ground data such as SPAD chlorophyll readings and nutrient content. Zhou et al. (2017) suggested that vegetation index, such as Normalized Difference Vegetation Index (NDVI), could be used to identify rice crops' characteristics. Likewise, there was a positive linear correlation between NDRE and SPAD readings. NDRE showed a high correlation with SPAD readings (R = 0.974; RMSE= 0.576) (Figure 4). Additionally, the result supports the theory that green and red edge region are highly responsive to a broad range of chlorophyll levels in red region only (Carter & Knapp, 2001). Figure 3 shows NDRE values, which indicate the status of chlorophyll content in the early stage of the rice plants' growth between red edge conversions. The normalized difference of the red edge index (NDRE) is made of red edge band (700-740 nm). A conversion area of rapid shift in leaf reflectance, caused by higher chlorophyll absorption in the red region and leaf scattering in the near-infrared spectrum, has been found to be related to plant health (Niinemets & Tenhunen, 1997). NDRE values can show the chlorophyll content in the early phase of rice growth, as the value range is between 0.5 and 0.8 as shown in Figure 3(b). This was because soil and water background factors were not considered. Furthermore, this is related to the distinct emission in the red edge region, which penetrates deeply into the crop canopy and plant leaves compared to visible light (especially blue and red radiation) because of the lower chlorophyll absorption in this region. This is useful in monitoring crop N status based on the amount of chlorophyll content but does not perform well in examining crop growth stage when there is less fluctuation in plant N concentration (Li et al., 2012). Particularly, the sensitivity of absorbance could be linked to plant chlorophyll content that is higher than that of the red edge region (Niinemets & Tenhunen, 1997). The red edge band is a spectral reflectance feature whereby the characterization of red portion showing in red portion of the visible spectrum, due to the absorption by chlorophyll. In contrast, high reflectance in the NIR due to light scattering from refraction along interfaces between leaf cells and air spaces inside the leaf (Zhang et al., 2015). Also, Soil-adjusted vegetation index (SAVI) showed higher correlation with SPAD readings (R = 0.964; RMSE= 0.676) (Figure 4). Soil-adjusted vegetation index (SAVI) can be another adjusted index for NDVI, as NDVI has its own limitation when connections are being made across various soil types that may reflect different amounts of light in the red and near infrared wavelengths (Li et al., 2014).

Soil-adjusted vegetation index (SAVI) was developed as an improvement of the NDVI to reduce the influence of soil brightness when vegetative area is sparsely distributed (Huete, 1988). In addition, soil-adjusted vegetation index SAVI (Figure 4) reduces soil background noise effects. This was further supported by Ren et al. (2018), showing that the negative soil adjustment factor was the factor of the increase of the slope of vegetation contour and the positive intersected points between vegetation isolines and soil. For example, it happened in the first quadrant of the NIR-red plane. Optimized soil adjusted vegetation index (OSAVI) indicates high correlation with SPAD readings (R = 0.966; RMSE= 0.664) (Figure 4). In this analysis, the performance of OSAVI was similar to SAVI, as the standardized vegetation indices, to further fit the purpose of this study and to reduce the possibility of soil background effect; this was in agreement with other vegetation studies (Rondeaux et al., 1996). The validation was done using SPAD value, where it showed higher correlation and validated method were supported by the work of Basca et al. (2019). Table 5 shows the summary of the relationship between ground data (chlorophyll readings) and vegetation indices as well as RMSE. Spatial trend of SPAD chlorophyll map is shown in Figure 5. Bato (2018) stated that GIS-based suitability mapping was momentous to enable the creation of a spatially accurate suitability map like spatial distribution of nitrogen in this study and contributing of great moment in decision making process for farmers.

Table 5
Relationship between NDVI, NDRE, SAVI and OSAVI with chlorophyll readings (SPAD) using Pearson correlation and RMSE

	SPAD	
Vegetation index	R	RMSE
NDVI	0.957	0.74
NDRE	0.974	0.576
SAVI	0.964	0.676
OSAVI	0.966	0.664

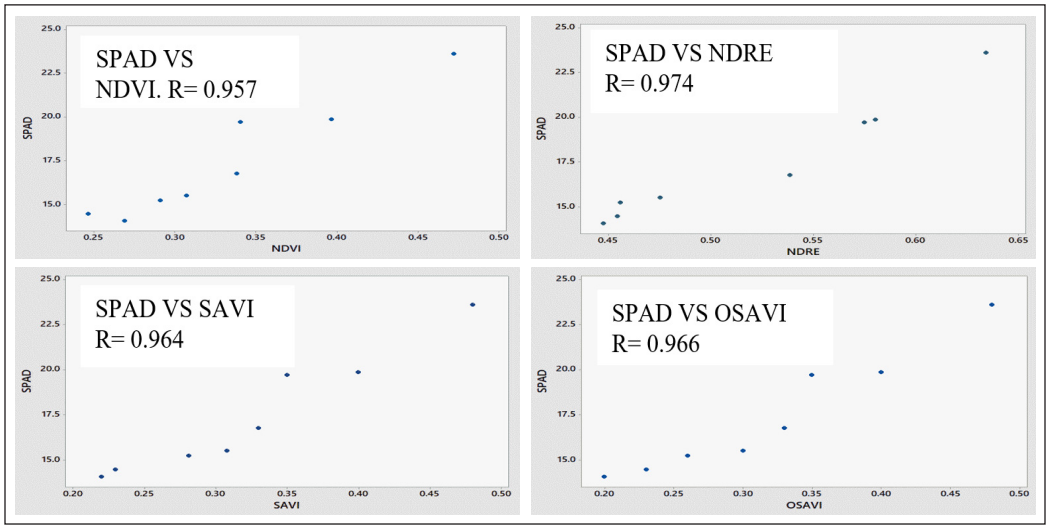

Figure 4. Relationship between SPAD chlorophyll readings, NDVI, NDRE, SAVI and OSAVI using Pearson correlation analysis in scatter plot

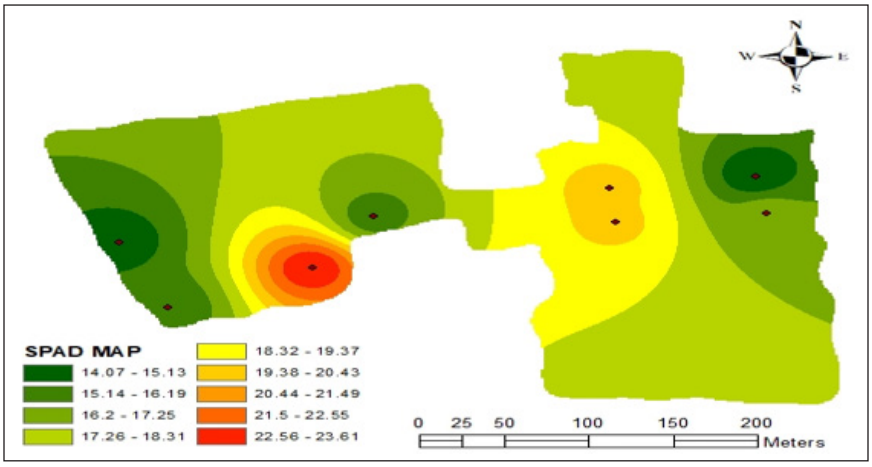

Figure 5. SPAD chlorophyll map for Ladang Merdeka

CONCLUSION

Vegetation indices, known as NDVI, NDRE, SAVI, and OSAVI, were tested in this study to investigate their ability in the estimation of the amount of chlorophyll by the multispectral sensors, which comprised only four spectral bands (530nm, 640nm, 730nm, 770nm). The findings showed the strongest correlation is NDRE (R=0.974; RMSE= 0.576), followed by OSAVI (R=0.966; RMSE= 0.664) and SAVI (R=0.964; RMSE= 0.676). The lowest correlation is NDVI (R= 0.957; RMSE= 0.74). NDRE was among the best indicators in estimating the status of chlorophyll content in paddy, while providing an overall map for farmers to calibrate their agricultural input, such as increasing the input to stressed areas while reducing the input to the healthy areas, where necessary. Future research needs to focus on sensors with lesser gap of spectral bands (hyperspectral). Namely in the red edge region, specifically the blue shift of the red edge, which has potential for crop monitoring in agriculture. By having a vegetation index map, farmers can easily track the crop growth and the condition of the paddy in real-time (Figure 3). However, more points should be added for SPAD data collection in the future to acquire good variable maps and accurate spatial distribution. Studies need to be done for further assessment and validation to test the accuracy and efficiency of this technology. With that, the goal of applying the concept of precision agriculture can be achieved in the operation. By that, it helps farmers in their management and crop condition monitoring. It fulfills the gap of crop monitoring in agricultural practices and sustainable production in real time.

FUTURE DIRECTION

The future potential of UAV technology can serve as a powerful tool to collect accurate and high-resolution images for spatial data. Meanwhile, image processing can be adopted

with more advanced computer vision and machine learning algorithms. Several machine learning algorithms can be further applied on UAV based multispectral imaging using programming application such as python and other related web-based programmed cloud processing should be applied in the near future due to the size of the data. The analysis output then can be transferred to the automation and robotics in real-time for decision-making process and quick responses.

ACKNOWLEDGEMENT

The authors wish to thank Dr. Mashitah Jusoh for statistical advice and acknowledge the financial support from the Ministry of Higher Education, Malaysia, under the Translational PADIU PUTRA Research Grant, Universiti Putra Malaysia (Vote No: 5526500) and UPM GP-IPM (Vote No: 9611400).

REFERENCES

Abdullah, S., Tahar, K. N., Rashid, M. F. A., & Osoman, M. A. (2019). Camera calibration performance on different non-metric cameras. *Pertanika Journal of Science and Technology*, *27*(3), 1397-1406.

Andre, M., Mahy, G., Lejeune, P., & Bogaert, J. (2013, September 5-6). City pattern as a factor influencing the impact of urbanization on ecosystems-A diachronic analysis of the dynamic of two cities: Kisangani and Lubumbashi (Democratic Republic of Congo). In *International Colonial and postcolonial urban planning in Africa* (pp. 1-49). Lisbon, Portugal.

Arellano, C. A., & Reyes, J. A. D. (2019). Effects of farmer-entrepreneurial competencies on the level of production and technical efficiency of rice farms in Laguna, Philippines. *Journal of the International Society for Southeast Asian Agricultural Sciences*, *25*(2), 45-57.

Auernhammer, H. (2001). Precision farming – The environmental challenge. *Computers and Electronics in Agriculture*, *30*, 41-33.

Bacsa, C. M., Martorillas, R. M., Balicanta, L. P., & Tamondong, A. M. (2019). Correlation of UAV-based multispectral vegetation indices and leaf color chart observations for nitrogen concentration assessment on rice crops. *The International Archives of Photogrammetry, Remote Sensing and Spatial Information Sciences, 42*, 31-38.

Bato, V. A. (2018). GIS-based suitability mapping of banana in the Philippines. *Journal of the International Society for Southeast Asian Agricultural Sciences*, *24*(1), 1-13.

Bendig, J., Yu, K., Aasen, H., Bolten, A., Bennertz, S., Broscheit, J., … & Bareth, G. (2015). Combining UAV-based plant height from crop surface models, visible, and near infrared vegetation indices for biomass monitoring in barley. *International Journal of Applied Earth Observations and Geoinformation*, *39*, 79-87.

Tejada, P. J., Sepulcre-Cantó, G., Fereres, E., & Villalobos, F. (2009). Mapping canopy conductance and CWSI in olive orchards using high resolution thermal remote sensing imagery. *Remote Sensing of Environment*, *113*(11), 2380-2388. *American Journal of Botany*, *88*(4), 677-84.

Fitzgerald, G. J., Rodriguez, D., Christensen, L. K., Belford, R., Sadras, V. O., & Clarke, T. R. (2006). Spectral and thermal sensing for nitrogen and water status in rainfed and irrigated wheat environments. *Precision Agriculture*, *7*(4), 233-248.

Fu, Y., Yang, G., Wang, J., Song, X., & Feng, H. (2014). Winter wheat biomass estimation based on spectral indices, band depth analysis and partial least squares regression using hyperspectral measurements. *Computers and Electronics in Agriculture, 100*, 51-59.

Garcia-Ruiz, F., Sankaran, S., Maja, J. M., Lee, W. S., Rasmussen, J., & Ehsani, R. (2013). Comparison of two aerial imaging platforms for identification of Huanglongbing-infected citrus trees. *Computers and Electronics in Agriculture*, *91*, 106-115.

Haboudane, D., Miller, J. R., Tremblay, N., Zarco-Tejada, P. J., & Dextraze, L. (2002). Integrated narrow-band vegetation indices for prediction of crop chlorophyll content for application to precision agriculture. *Remote Sensing of Environment*, *81*(2–3), 416-426.

Huete, A. R. (1988). A soil-adjusted vegetation index (SAVI). *Remote Sensing of Environment*, *25*(3), 295-309.

Hunt, E. R., Everitt, J. H., Ritchie, J. C., Moran, M. S., Booth, D. T., Anderson, G. L., & Seyfried, M. S. (2003). Applications and research using remote sensing for rangeland management. *Photogrammetric Engineering and Remote Sensing, 69*(6), 675-693.

Hunt, E. R., Horneck, D. A., Spinelli, C. B., Turner, R. W., Bruce, A. E., Gadler, D. J., & Hamm, P. B. (2018). Monitoring nitrogen status of potatoes using small unmanned aerial vehicle. *Precision Agriculture*, *19*(10), 314-333.

Johnson, L. F., Herwitz, S., Dunagan, S., Lobitz, B., Sullivan, D., & Sly, R. (2003, November 10-14). Collection of ultra-high spatial and spectral resolution image data over California vineyards with a small UAV. In *Proceedings of the 30th International Symposium on Remote Sensing of Environment* (pp. 10-14). Honolulu, HI, USA.

Kira, O., Linker, R., & Gitelson, A. (2015). Non-destructive estimation of foliar chlorophyll and carotenoid contents: focus on informative spectral bands. *International Journal of Applied Earth Observation & Geoinformation*, *38*, 251-260.

Li, C., Li, H., Li, J., Lei, Y., Ii, C., Manevski, K., & Shen, Y. J. (2019). Using NDVI percentiles to monitor real-time crop growth. *Computers and Electronics in Agriculture*, *162*, 357-363.

Li, F., Miao, Y., Feng, G., Yuan, F., Yue, S., Gao, X., & Chen, X. (2014). Improving estimation of summer maize nitrogen status with red edge-based spectral vegetation indices. *Field Crops Research*, *157*, 111-123.

Li, X., Lee, W. S., Li, M., Ehsani, R., Mishra, A. R., Yang, C., & Mangan, R. L. (2012). Spectral difference analysis and airborne imaging classification for citrus greening infected trees. *Computers and Electronics in Agriculture*, *83*, 32-44.

Liang, L., Di, L., Zhang, L., Deng, M., Qin, Z., Zhao, S., & Lin, H. (2015). Estimation of crop LAI using hyperspectral vegetation indices and a hybrid inversion method. *Remote Sensing of Environment*, *165*, 123-34.

Liu, S., Baret, F., Andrieu, B., Burger, P., & and Hemmerlé, M. (2017). Estimation of wheat plant density at early stages using high resolution imagery. *Frontiers in Plant Science, 8*, 1-10.

Louis, J., Ounis, A., Ducruet, J. M., Evain, S., Laurila, T., Thum, T., & Moya, I. (2005). Remote sensing of sunlight-induced chlorophyll fluorescence and reflectance of scots pine in the boreal forest during spring recovery. *Remote Sensing of Environment*, *96*(1), 37-48. Perspectives for remote sensing with unmanned aerial vehicles in precision agriculture. *Trends in Plant Science*, *24*(2), 152-164.

Markengold PR. (2016, February 8). *Parrot revolutionizes precision agriculture with Sequoia: A miniaturized high-tech multispectral sensor, compatible with all civil drones*. Retrieved January 10, 2019, from https://www.markengold.de/parrot-revolutionizes-precision-agriculture-with-sequoia-a-miniaturized-high-tech-multispectral-sensor-compatible-with-all-civil-drones/

Mukherjee, A., Misra, S., & Raghuwanshi, N. S. (2019). A survey of unmanned aerial sensing solutions in precision agriculture. *Journal of Network and Computer Applications*, *148*, 1-24.

Nebiker, S., Lack, N., Abächerli, M., & Läderach, S. (2016, July 12-19). Light-weight multispectral UAV sensors and their capabilities for predicting grain yield and detecting plant diseases. In *International Archives of the Photogrammetry, Remote Sensing and Spatial Information Sciences* (pp. 963-970). Prague, Czech Republic.

Nguy-Robertson, A., Gitelson, A., Peng, Y., Viña, A., Arkebauer, T., & Rundquist, D. (2012). Green leaf area index estimation in maize and soybean: Combining vegetation indices to achieve maximal sensitivity. *Agronomy Journal Abstract – Biometry, Modeling and Statistics*, *104*(5), 1336-1347.

Niinemets, Ü., & Tenhunen, J. D. (1997). A model separating leaf structural and physiological effects on carbon gain along light gradients for the shade-tolerant species *Acer saccharum*. *Plant, Cell and Environment*, *20*(7), 845-866.

Norasma, C. Y. N. (2016). *Site-specific weed management using remote sensing* (PhD Thesis). The University of Queensland, Gatton, Australia. *IOP Conference Series: Earth and Environmental Science* (Vol. 169, No. 1, p. 012095). Bristol, UK: IOP Publishing.

Norasma, C. Y. N., Shariff, A. R. M., Jahanshiri, E., Amin, M. S. M., Khairunniza-Bejo, S., & Mahmud, A. R. (2013). Web-based decision support system for paddy planting management. *Pertanika Journal of Science and Technology*, *21*(2), 343-364.

Oborne, M. (2019). *ArduPilot: Mission planner home*. Retrieved December 15, 2019, from https://ardupilot.org/planner/

Ranganath, B. K., Pradeep, N., Manjula, V. B., Balakrishna, G., Rajanna, M. D., & Nageswara, R. P. P. (2004). Detection of diseased rubber plantations using satellite remote sensing. *Journal of the Indian Society of Remote Sensing*, *32*, 49-58.

Ren, H. Y., Zhuang, D. F., Pan, J. J., Shi, X. Z., & Wang, H. J. (2008). Hyper-spectral remote sensing to monitor vegetation stress. *Journal of Soils and Sediments*, *8*(5), 323-326.

Ren, H., Zhou, G., & Zhang, F. (2018). Using negative soil adjustment factor in soil-adjusted vegetation index (SAVI) for aboveground living biomass estimation in arid grasslands. *Remote Sensing of Environment*, *209*(79), 439-445.

Rondeaux, G., Steven, M., & Baret, F. (1996). Optimization of soil-adjusted vegetation indices. *Remote Sensing of Environment*, *55*(2), 95-107.

Rouse, J. W., Haas, R. H., Scheel, J. A., & Deering, D. W. (1974) Monitoring vegetation systems in the great plains with ERTS. In *Third Earth Resources Technology Satellite-1 Symposium: Section AB. Technical presentations* (Vol. 1, pp. 309-318). Washington, USA: National Aeronautics and Space Administration.

Shafri, H. Z. M., & Anuar, M. I. (2008, December 20-22). Hyperspectral signal analysis for detecting disease infection in oil palms. In *International Conference on Computer and Electrical Engineering* (pp. 312-316). Phuket, Thailand.

Shafri, H. Z. M., Anuar, M. I., Seman, I. A., & Noor, N. M. (2011). Spectral discrimination of healthy and Ganoderma - infected oil palms from hyperspectral data. *International Journal of Remote Sensing*, 32(22), 7111-7129.

Shafri, H. Z. M., Salleh, M. A. M., & Ghiyamat, A. (2006). Hyperspectral remote sensing of vegetation using red edge position techniques. *American Journal of Applied Science*, *3*(6), 1864-1871.

Shamshiri, R. R., Mahadi, M. R., Ahmad, D., Bejo, S. K., Aziz, S. A., Ismail, W. I. W., & Che Man, H. (2017, July 16-19). Controller design for an osprey drone to support precision agriculture research in oil palm plantations. In *2017 ASABE Annual International Meeting* (pp. 2-13). Washington, USA.

Shaw, D. R., & Kelley, F. S. (2005). Evaluating remote sensing for determining and classifying soybean anomalies. *Precision Agriculture*, *6*, 421-429.

Sims, D. A., & Gamon, J. A. (2002). Relationships between leaf pigment content and spectral reflectance across a wide range of species, leaf structures and developmental stages. *Remote Sensing of Environment*, *81*(2-3), 337-354.

Singh, K. D., Starnes, R., Kluepfel, D. A., & Nansen, C. (2017, April 24). Qualitative analysis of walnut trees rootstock using airborne remote sensing. In *Sixth Annual Plant Science Symposium* (p. 1). UC Davis, CA, USA.

Sullivan, D. G., Fulton, J. P., Shaw, J. N., & Bland, G. (2007). Evaluating the sensitivity of an unmanned thermal infrared aerial system to detect water stress in a cotton canopy. *Transactions of the ASABE*, *50*(6), 1963-1969.

Tokekar, P., Hook, J. V., Mulla, D., & Isler, V. (2013). Sensor planning for a symbiotic UAV and UGV system for precision agriculture. *IEEE Transactions on Robotics*, *32*(6), 5321-5326.

Valente, J., Sanz, D., Barrientos, A., del Cerro, J., Ribeiro, A., & Rossi, C. (2011). An air-ground wireless sensor network for crop monitoring. *Sensors*, *11*(6), 6088-6108.

Verger, A., Vigneau, N., Chéron, C., Gilliot, J. M., Comar, A., & Baret, F. (2014). Green area index from an unmanned aerial system over wheat and rapeseed crops. *Remote Sensing of Environment*, *152*, 654-664.

Wang, K., Huggins, D. R., & Tao, H. (2019). Rapid mapping of winter wheat yield, protein, and nitrogen uptake using remote and proximal sensing. *International Journal of Applied Earth Observation and Geoinformation*, *82*, 1-10.

Xiang, H., & Tian, L. (2011). Development of a low-cost agricultural remote sensing system based on an autonomous unmanned aerial vehicle (UAV). *Biosystem Engineering*, *108*(2), 174-190.

Xue, J., & Su, B. (2017). Significant remote sensing vegetation indices: A review of development and applications. *Journal of Sensors*, *2017*, 1-17.

Yang, Z., Rao, M. N., Elliott, N. C., Kindler, S. D., & Popham, T. W. (2009). Differentiating stress induced by greenbugs and Russian wheat aphids in wheat using remote sensing. *Computers and Electronics in Agriculture, 67*(1-2), 64-70.

Yoder, B. J., & Pettigrew-Crosby, R. E. (1995). Predicting nitrogen and chlorophyll content and concentrations from reflectance Spectra (400-2500 Nm) at leaf and canopy scales. *Remote Sensing of Environment*, *53*(3), 199-211.

Yongjun, D., & Jingjing, Z. (2016). Extraction of REPs from leaves reflectance spectrum for estimation of chlorophyll content. *IFAC-PapersOnLine*, *49*(16), 205-208.

Zarco-Tejada, P. J., Gonzalez-Dugo, V., & Berni, J. A. J. (2012). Fluorescence, temperature and narrow-band indices acquired from a UAV platform for water stress detection using a micro-hyperspectral imager and a thermal camera. *Remote Sensing of Environment*, *117*, 322-337.

Zarco-Tejada, P. J., Guillén-Climent, M. L., Hernández-Clemente, R., Catalina, A., González, M. R., & Martín, P. (2013). Estimating leaf carotenoid content in vineyards using high resolution hyperspectral imagery acquired from an unmanned aerial vehicle (UAV). *Agricultural and Forest Meteorology*, *171*, 281-294.

Zhang, G., Xiao, X., Dong, J., Kou, W., Jin, C., Qin, Y., … & Biradar, C. (2015). Mapping paddy rice planting areas through time series analysis of MODIS land surface temperature and vegetation index data. *ISPRS Journal of Photogrammetry and Remote Sensing*, *106*, 157-171.

Zhou, X., Zheng, H. B., Xu, X. Q., He, J. Y., Ge, X. K., Yao, X., … & Tian, Y. C. (2017). Predicting grain yield in rice using multi-temporal vegetation indices from UAV-based multispectral and digital imagery. *ISPRS Journal of Photogrammetry and Remote Sensing*, *130*, 246-255.

Zulfa, A. W., & Norizah, K. (2018). Remotely sensed imagery data application in mangrove forest: A review. *Pertanika Journal of Science and Technology*, *26*(3), 899-922.

Pertanika J. Sci. & Technol. 28 (3): 797 - 828 (2020)

PERTANIKA JOURNALS

SCIENCE & TECHNOLOGY

Journal homepage: http://www.pertanika.upm.edu.my/

A Study of the Parameters That Effect the Quality of the Estimated Modal Parameters in Automated Enhanced Frequency Domain Decomposition Algorithm

Muhammad Danial Bin Abu Hasan[1*], Zair Asrar Bin Ahmad[2], Mohd Salman Leong[1] and Lim Meng Hee[1]

[1]*Institute of Noise and Vibration, Universiti Teknologi Malaysia, 54100 UTM, Kuala Lumpur, Malaysia*
[2]*School of Mechanical Engineering, Universiti Teknologi Malaysia, 81310 UTM, Skudai, Johor Bahru, Malaysia*

ABSTRACT

This paper presents parameters analysis for the estimated modal damping ratio using a new version of the automated enhanced frequency domain decomposition (AEFDD). The purpose of this study is to provide a better choice of a maximum number of points of time segments and modal assurance criterion (MAC) index number regarding to the variable level of system damping (low and high damped structure) and degree of freedom of the system. According current literature, frequency domain (FD) methods seem to have the problem with providing a correct identification of the modal damping ratio, since the correct estimate of modal damping is still an open problem and often leads to biased estimates. This technique is capable of providing consistent modal parameters estimation, particularly for modal frequencies and mode shapes. As a necessary fundamental condition, the algorithm has been assessed first from computed numerical responses according to random white noise, acting on different shear-type frame structures and corrupted with noise. Results indicate that reducing the value of natural frequencies and modal damping ratios of the modes under analysis demands longer time segments and a high value of the maximum number of points for adequate information on the decaying

ARTICLE INFO

Article history:
Received: 6 February 2020
Accepted: 14 May 2020
Published: 16 July 2020

E-mail addresses:
muhd_danial200@yahoo.com (Muhammad Danial Bin Abu Hasan)
zair@utm.my (Zair Asrar Bin Ahmad)
salman.leong@gmail.com (Mohd Salman Leong)
limmenghee@gmail.com (Lim Meng Hee)
*Corresponding author

ISSN: 0128-7680
e-ISSN: 2231-8526

© Universiti Putra Malaysia Press

correlation functions when computing a modal damping ratio. In addition, the results also prove that the MAC index does not significantly affect the results for the low damped system. However, the use of a high MAC index value for the high damped system significantly introduces large error bound and it becomes worse, particularly for the higher modes, as the standard deviation of percentage error increases gradually. Furthermore, the use of a MAC index for a high number of points of time segments significantly increases the standard deviation of the percentage error.

Keywords: Automated OMA, automatization, frequency domain decomposition, operational modal analysis

INTRODUCTION

The present structural modal identification method, operational modal analysis (OMA) is widely and normally used within various engineering fields due to its ability to perform cost-effective and fast tests that depend solely on structural response signals generated by ambient excitations without affecting its operating conditions (Rainieri & Fabbrocino, 2015). This means that OMA techniques have major advantages compared to classical experimental modal analysis (EMA), which requires input excitations for structural modal identification (Mironov et al., 2015; Zhang et al., 2005). In the literature, the classical frequency domain decomposition (FDD) was originally proposed by Brincker et al. (2001a) and this technique is based on the singular value decomposition (SVD) of the power spectral density (PSD) matrix of the response signals (Brincker et al., 2001b; Gade et al., 2005). With simple execution and user-friendly characteristics, this technique is also capable of providing consistent modal parameters estimation, particularly for modal frequencies and mode shapes; however, modal damping value was not clarified in their work. Later, the second generation of FDD, known as enhanced frequency domain decomposition (EFDD), was introduced to enhance the accuracy of modal frequencies and explain how to estimate modal damping ratios (Brincker et al., 2001a). The third generation of FDD, frequency-spatial domain decomposition (FSDD), was proposed in the following years to overcome some problems in EFDD algorithms (Brincker & Zhang, 2009; Wang et al., 2005; Zhang et al., 2010). According to the existing literature, frequency domain (FD) methods are capable of detecting modal frequencies and mode shapes in terms of closely spaced modes or even repeated modes, since SVD can isolate the signal from noise (Zhang & Tamura, 2003). However, frequency domain (FD) methods seem to have the problem of providing a correct identification of the modal damping ratio, since the actual estimation of modal damping is still an open problem and frequently leads to biased estimates, although natural frequencies and mode shapes can be estimated confidently (Rainieri & Fabbrocino, 2014; Rainieri & Fabbrocino, 2015).

Most of the researchers have tried to improve modal damping estimation by introducing a variety of techniques for modal damping estimation in FDD-type procedures such as logarithmic decrement (LogDec) method (Brincker et al., 2001a; Gade et al., 2005), Hilbert transform (HT) (Zhang & Tamura, 2003), natural excitation techniques (NExt) ie cross-covariance function, Ibrahim time domain, and Polyreference (Bajrić et al., 2015a) as well as the optimal wavelet (Tarinejad & Damadipour, 2014). Furthermore, a new approach involving hybrids or combinations of two methods together is also introduced to improve modal damping estimation such as Enhanced FDD Algorithm in-operation modal appropriation (EFDD-INOPMA) (Ghalishooyan et al., 2019), Frequency Domain Decomposition-Natural Excitation Technique (FDD-NExT) (Frans & Arfiadi, 2019), Frequency Domain State Space-Based Mode Decomposition Framework (Hwang et al., 2019) and Frequency Domain Stochastic Subspace Identification (Chou & Chang, 2020). However, this issue is still considered as an open problem, even though some researchers have also tried to tackle the signal processing issue by making improvements using their proposed method since, the signal processing also denoted as the contributing factor for estimation errors comprising estimates of correlation function (CF) and the spectral density (SD) (Bajric et al., 2015b). After throughout critical reviews and pilot tests, there is another factor that contributes to this error which is caused by parameter extraction, particularly in term of proper selection of the correct time window, extrema picking of single degree of freedom (SDOF) auto-correlation function and modal assurance criterion (MAC) index selection which turn out to be the most challenging part of the algorithm. Time window, extrema picking of SDOF auto-correlation function and MAC index selection need to be carefully chosen, otherwise it will lead to random and bias errors. Therefore, particular attention is needed for proper selection of the correct time window, MAC index selection and extrema picking of a single degree of freedom (SDOF) auto-correlation function. Currently, some researchers have tried to address this problem by introducing iterative loop optimization in the selection of the correct time window, extrema picking of single degree of freedom (SDOF) auto-correlation function and MAC index selection. The refined FDD is a new version of EFDD. However, they can only improve the estimation of modal damping ratios up to 75% and 95% for the natural frequencies but ineffective for a very high noise and only reported for the high damped system (Brincker et al., 2001b; Pioldi et al., 2016; Pioldi et al., 2017; Pioldi & Rizzi, 2015; Pioldi & Rizzi, 2017; Pioldi & Rizzi, 2018; Pioldi et al., 2014).

The proposed method which is an automated EFDD method tried to improvise the recent method, Refined FDD by introducing a new approach of iterative loop optimization in the selection of the correct time window and extrema picking of single degree of freedom (SDOF) auto-correlation function. Meanwhile for MAC index selection, further analysis is needed to identify the appropriate range of MAC index value for a different level of system

damping (low and high damped structure) because the study on refined FDD is limited to the high damped structure only.

Therefore, the purpose of this study is to evaluate the performance of the automated version of the EFDD method by performing parameter analysis for the estimated modal damping ratio to provide a better choice of a maximum number of points of time segments and modal assurance criterion (MAC) index number regarding the variable level of system damping (low and high damped structure) and degree of freedom of the system.

MATERIALS AND METHODS

All the frequency domain methods in OMA share similar characteristics in terms of the spectral density (SD) function assessment from the output responses, but each of them has a different way of extracting structural modal parameters. Further information on the automated EFDD method algorithm is discussed in this section.

The overall schematic illustration of the automated EFDD method procedure is shown in Figure 1. At first, each method in OMA including the FD method is required to go through signal processing before the modal identification process takes place. This is because all the modal information generally is suppressed in the mess made by the randomness of the measured signals. Thus, signal processing is used to provide a clearer picture of the physical problem being dealt with. Signal processing consists of correlation functions (CF) and spectral densities (SD) function. The CF matrix was estimated using the direct method, as given by Equation 1.

$$\hat{R}(k) = (1/(N-k))Y_{(1:N-k)}{Y^T}_{(k+1:N)} \quad (1)$$

Where the measured responses are arranged as a column in data series, N is the total number of data points in the time series, k corresponds to the time lag $\tau = k\Delta t$ and $(N-k)\Delta t$ corresponds to $T-\tau$, T is the total length of the time series. Before estimating SD, the fast Fourier transform (FFT) algorithm requires time windows to reduce leakage by forcing the endpoints of each signal sample data to zero. In this study, the flat-triangular window with $\alpha = 0.5$ was chosen. Next, the singular value decomposition (SVD) is applied to decompose the output SD into auto SD that represents an SDOF system. The singular value data that are identified around a resonance peak by using modal assurance criterion (MAC) filtering, which is also known as spectral bell identification (Gade et al., 2005; Zhang & Tamura, 2003), are transfered back to the time domain (TD) using the inverse FFT (Gade et al., 2005; Zhang & Tamura, 2003).

Considering two different vectors φ_r and φ_s, that are to be considered as two different estimates of the same experimental mode shape vector (Bricker & Venture, 2015), we can calculate the correlation between the two vectors according to the MAC normally formulated as in Equation 2:

$$MAC(\{\varphi_r\}\{\varphi_s\}) = \frac{|\{\varphi_r\}^{*t}\{\varphi_s\}|^2}{(\{\varphi_r\}^{*t}\{\varphi_r\})(\{\varphi_s\}^{*t}\{\varphi_s\})} \quad (2)$$

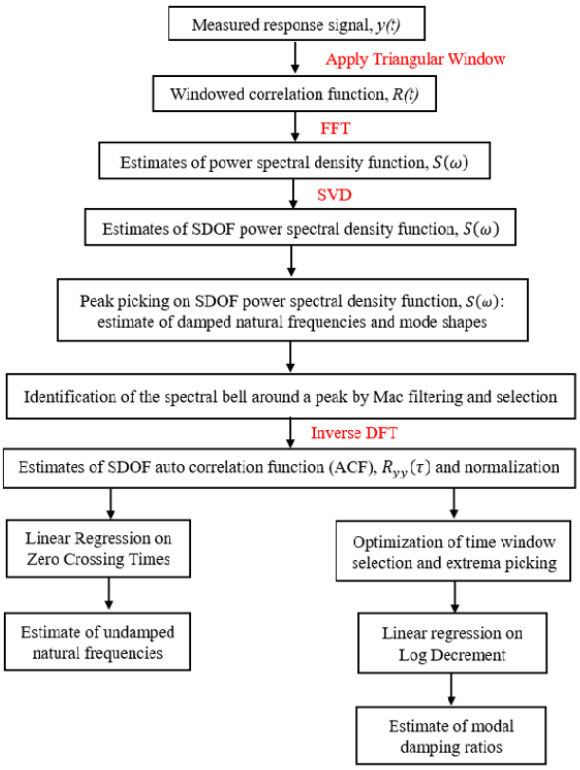

Figure 1. Schematic illustration of FDD procedure

If a linear relationship exists (i.e., the vectors move the same way) between the two complex vectors, the MAC value will be near to one. If they are linearly independent, the MAC value will be small (near zero).

Then, all extrema of the free decay that within an appropriate time window were used to implement the subsequent linear regression operations for assessing the logarithmic decrement (LogDec), δ as characterized in Equation 3 and Equation 4 below:

$$\delta = \frac{2}{k}\ln\left(\frac{r_0}{|r_k|}\right) \tag{3}$$

$$2\ln(|r_k|) = 2\ln(r_0) - \delta k \tag{4}$$

where k is an integer counter of the kth extreme of the auto-correlation function, $k = 1,2,3, \ldots$, while r_0 and r_k are the initial and the kth extreme value of the auto-correlation function, respectively. Then, modal damping ratio can be obtained in Equation 5.

$$\zeta_q = \frac{\delta_q}{\sqrt{4\pi^2 + {\delta_q}^2}} \tag{5}$$

Meanwhile, the damped natural frequency, ω_d was estimated by linear regression on the zero-crossing times of the equivalent SDOF correlation function. Then, the undamped

natural frequency, ω_n was computed by using the following Equation 6:

$$\omega_n = \frac{\omega_d}{\sqrt{1-\varsigma^2}} \tag{6}$$

Further information on all alternative FD methods can be found in (Jacobsen et al., 2008; Pioldi et al., 2016; Rodrigues et al., 2004).

Validation with Numerical Simulations

As a fundamentally necessary condition, the algorithm had been assessed first from computed numerical responses according to random white noise, acting on different ideal shear-type frame structures. The proposed algorithms were validated via simulated data from a series of multi-storey shear-type models consisting of two, three and six degrees of freedom (DOF) as illustrated in Figure 2. All these structural features with different DOFs are examined first (Zanchi, 2011; Pioldi, 2012; Pioldi, 2013).

The characteristics of the simulated multi-storey shear-type models which present well-separated modes are provided in Figure 3 by the stiffness (K), mass (M) and damping (C) matrices.

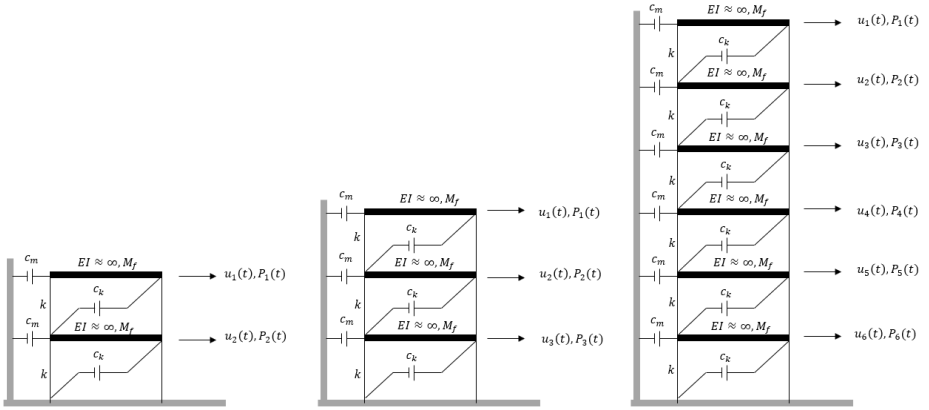

Figure 2. Two-, three and six -storey frame models.

The well-separated modes and different DOFs were used in this study to discover the efficiency of the proposed approach for the diversity of features and type of structure. The system matrices were defined with to achieve modal parameters with values of the same order of magnitude as the ones generally found in present civil engineering structures. Mass and stiffness matrices were set fixed for every frame as reported below. Damping matrices have been assumed to be diagonal in modal coordinates and represented by different modal damping ratios in the numerical tests. The damping of the structure is viscous (damping forces proportional to velocity) and proportional Rayleigh damping, the prescribed modal damping ratios for multi-storey shear-type models are set to $\zeta_k=\zeta_j=1\%$, 3% and 5% of critical damping which consists of low and high values of damping in a structure. In the

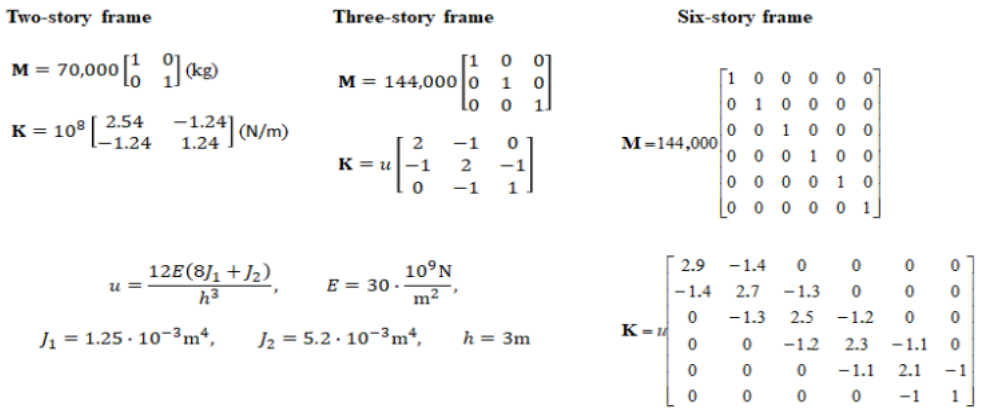

Figure 3. Dynamic system models: the main features of ideal shear-type frames.

literature, only lightly damped structures that contain modal damping ratios below 2% are considered for analysis (Brewick & Smyth, 2013; Brincker et al., 2001a; Brincker et al., 2001b; Gade et al., 2005; Magalhães et al., 2010; Zhang & Tamura, 2003). Input is taken as a stationary broadband ambient excitation with normally distributed random numbers assuming independent inputs for all DOF of the models. It has a constant PSD which can cover a wide range of frequencies and is adequate to excite all the structural modes. The random input excitation, which is also known as zero-mean Gaussian white noise, takes the assumption of the excitation system to be linear and time-invariant. The response of the system was simulated using Newmark's method with constant average acceleration (i.e. γ=12 and β=14) (Chopra, 2001). The adopted parameters in the analysis are shown in Table 1.

The simulated outputs, which are time series with the accelerations of all the DOFs of the models, are corrupted with noise that mimics the influence of the sensors and measuring chain noise. This was simulated by normally distributed random numbers with a standard deviation equal to 10% of the standard deviation of the simulated outputs [this percentage of noise is quite conservative in the case of well-conducted ambient vibration tests (Magalhães, 2010)].In this numerical simulation, the eigenvalue problem analysis was

Table 1
The adopted parameters for the multi-storey frame in the processing

Parameters	Two-storey frame	Three-storey frame	Six-storey frame
Length of time series, t(s)	400	600	1000
Sampling frequency, f_s(Hz)	200	200	200
Adopted frequency resolution, Δf f*(Hz)*	0.0025	0.00167	0.001

used to validate the effectiveness of the proposed approach. By taking the values of the stiffness K, mass M, and damping C, the modal parameters (modal damping ratio, natural frequency and mode shape) can be estimated.

The automated version of the EFDD method was tested on multi-storey shear-type models which consisted of two, three and six DOF and different levels of damping (1%, 3% and 5% of critical damping, which consisted of low and high damped systems) with the appropriate variation of the MAC index ranging from 0.70 to 0.99 based on a literature review (Pioldi et al., 2016) and using ten alternative time segment lengths that led to spectra with different frequency resolution. Table 2 characterises 70 scenarios (named from 1a to 10g) that involved varying the maximum number of points considered in the time segments from 1024 to 10240 and using a variation of the MAC index that ranges from 0.70 to 0.99. The 70 scenarios are the percentage deviation (error) of estimate modal damping ratios.

The use of multi-storey shear-type models for this analysis requires a large number of simulations and datasets and forced the use of an automated procedure, which is presented in the last section. The automated version of the EFDD method is a robust procedure and adequate for this particular application.

Table 2

Scenarios for the application of the FDD method

Maximum number of points in the time segments	MAC Index						
	0.70	0.75	0.80	0.85	0.90	0.95	0.99
1024*1	1a	1b	1c	1d	1e	1f	1g
1024*2	2a	2b	2c	2d	2e	2f	2g
1024*3	3a	3b	3c	3d	3e	3f	3g
1024*4	4a	4b	4c	4d	4e	4f	4g
1024*5	5a	5b	5c	5d	5e	5f	5g
1024*6	6a	6b	6c	6d	6e	6f	6g
1024*7	7a	7b	7c	7d	7e	7f	7g
1024*8	8a	8b	8c	8d	8e	8f	8g
1024*9	9a	9b	9c	9d	9e	9f	9g
1024*10	10a	10b	10c	10d	10e	10f	10g

RESULTS AND DISCUSSION

Low Level of Damping (1%)

Percentage deviations (errors) of modal damping ratio for the low damped of two, three and six-storey frame (1%) are shown in Figures 4, 5 and 6.

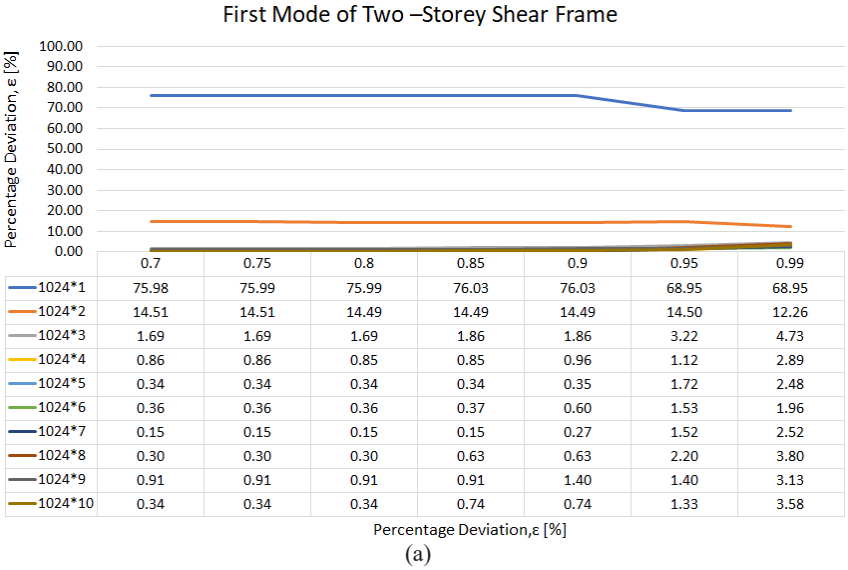

	0.7	0.75	0.8	0.85	0.9	0.95	0.99
1024*1	75.98	75.99	75.99	76.03	76.03	68.95	68.95
1024*2	14.51	14.51	14.49	14.49	14.49	14.50	12.26
1024*3	1.69	1.69	1.69	1.86	1.86	3.22	4.73
1024*4	0.86	0.86	0.85	0.85	0.96	1.12	2.89
1024*5	0.34	0.34	0.34	0.34	0.35	1.72	2.48
1024*6	0.36	0.36	0.36	0.37	0.60	1.53	1.96
1024*7	0.15	0.15	0.15	0.15	0.27	1.52	2.52
1024*8	0.30	0.30	0.30	0.63	0.63	2.20	3.80
1024*9	0.91	0.91	0.91	0.91	1.40	1.40	3.13
1024*10	0.34	0.34	0.34	0.74	0.74	1.33	3.58

(a)

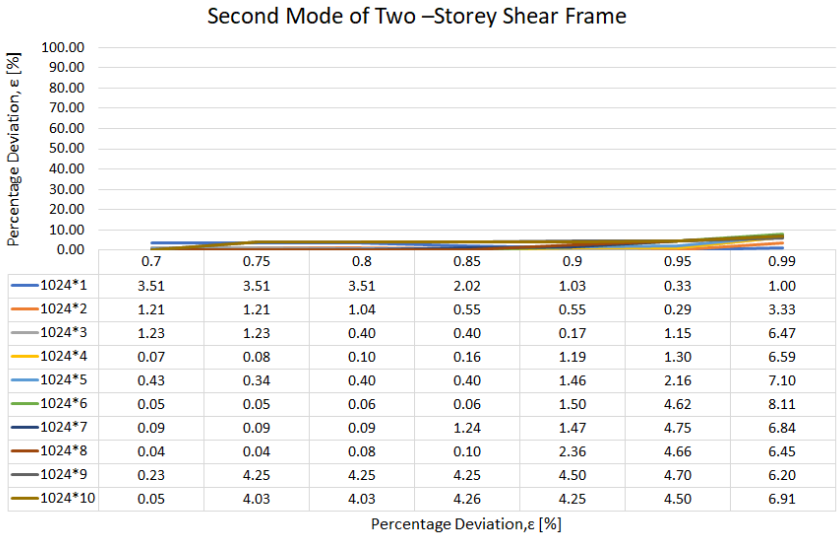

	0.7	0.75	0.8	0.85	0.9	0.95	0.99
1024*1	3.51	3.51	3.51	2.02	1.03	0.33	1.00
1024*2	1.21	1.21	1.04	0.55	0.55	0.29	3.33
1024*3	1.23	1.23	0.40	0.40	0.17	1.15	6.47
1024*4	0.07	0.08	0.10	0.16	1.19	1.30	6.59
1024*5	0.43	0.34	0.40	0.40	1.46	2.16	7.10
1024*6	0.05	0.05	0.06	0.06	1.50	4.62	8.11
1024*7	0.09	0.09	0.09	1.24	1.47	4.75	6.84
1024*8	0.04	0.04	0.08	0.10	2.36	4.66	6.45
1024*9	0.23	4.25	4.25	4.25	4.50	4.70	6.20
1024*10	0.05	4.03	4.03	4.26	4.25	4.50	6.91

(b)

Figure 4. Percentage deviation (error) of modal damping ratio for the low damped two-storey frame (1%): (a) the first mode; (b) the second mode.

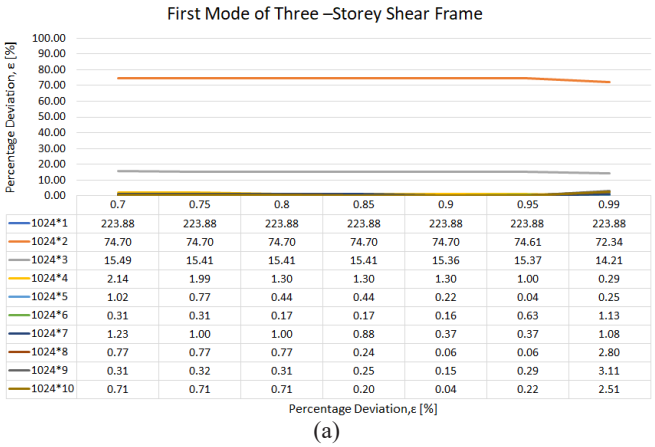

	0.7	0.75	0.8	0.85	0.9	0.95	0.99
1024*1	223.88	223.88	223.88	223.88	223.88	223.88	223.88
1024*2	74.70	74.70	74.70	74.70	74.70	74.61	72.34
1024*3	15.49	15.41	15.41	15.41	15.36	15.37	14.21
1024*4	2.14	1.99	1.30	1.30	1.30	1.00	0.29
1024*5	1.02	0.77	0.44	0.44	0.22	0.04	0.25
1024*6	0.31	0.31	0.17	0.17	0.16	0.63	1.13
1024*7	1.23	1.00	1.00	0.88	0.37	0.37	1.08
1024*8	0.77	0.77	0.77	0.24	0.06	0.06	2.80
1024*9	0.31	0.32	0.31	0.25	0.15	0.29	3.11
1024*10	0.71	0.71	0.71	0.20	0.04	0.22	2.51

(a)

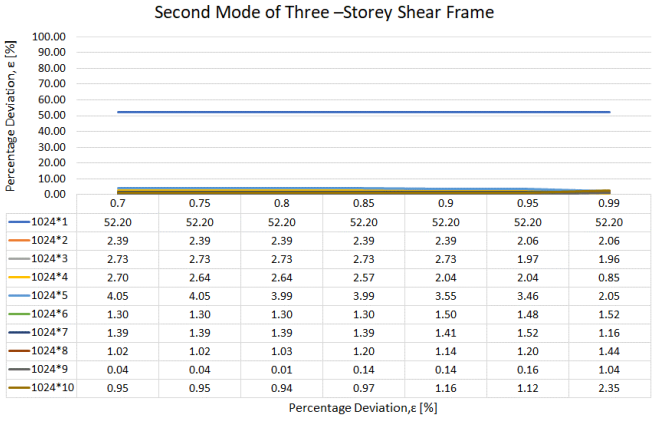

	0.7	0.75	0.8	0.85	0.9	0.95	0.99
1024*1	52.20	52.20	52.20	52.20	52.20	52.20	52.20
1024*2	2.39	2.39	2.39	2.39	2.39	2.06	2.06
1024*3	2.73	2.73	2.73	2.73	2.73	1.97	1.96
1024*4	2.70	2.64	2.64	2.57	2.04	2.04	0.85
1024*5	4.05	4.05	3.99	3.99	3.55	3.46	2.05
1024*6	1.30	1.30	1.30	1.30	1.50	1.48	1.52
1024*7	1.39	1.39	1.39	1.39	1.41	1.52	1.16
1024*8	1.02	1.02	1.03	1.20	1.14	1.20	1.44
1024*9	0.04	0.04	0.01	0.14	0.14	0.16	1.04
1024*10	0.95	0.95	0.94	0.97	1.16	1.12	2.35

(b)

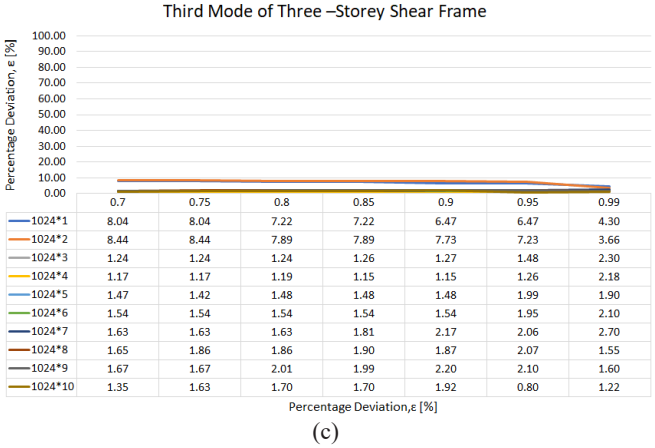

	0.7	0.75	0.8	0.85	0.9	0.95	0.99
1024*1	8.04	8.04	7.22	7.22	6.47	6.47	4.30
1024*2	8.44	8.44	7.89	7.89	7.73	7.23	3.66
1024*3	1.24	1.24	1.24	1.26	1.27	1.48	2.30
1024*4	1.17	1.17	1.19	1.15	1.15	1.26	2.18
1024*5	1.47	1.42	1.48	1.48	1.48	1.99	1.90
1024*6	1.54	1.54	1.54	1.54	1.54	1.95	2.10
1024*7	1.63	1.63	1.63	1.81	2.17	2.06	2.70
1024*8	1.65	1.86	1.86	1.90	1.87	2.07	1.55
1024*9	1.67	1.67	2.01	1.99	2.20	2.10	1.60
1024*10	1.35	1.63	1.70	1.70	1.92	0.80	1.22

(c)

Figure 5. Percentage deviation (error) of modal damping ratio for the low damped three-storey frame (1%): (a) the first mode; (b) the second mode; (c) the third mode.

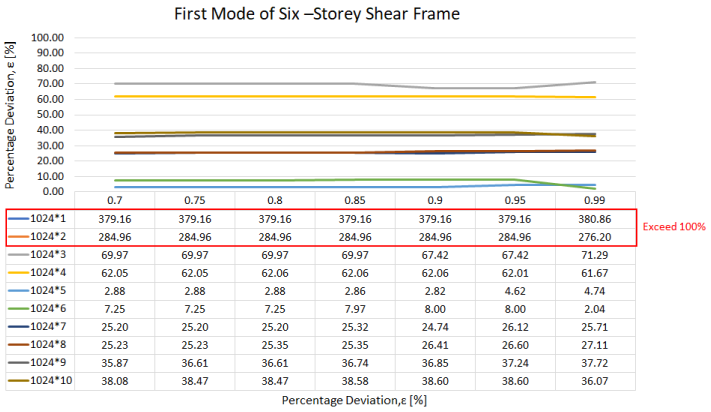

	0.7	0.75	0.8	0.85	0.9	0.95	0.99	
1024*1	379.16	379.16	379.16	379.16	379.16	379.16	380.86	Exceed 100%
1024*2	284.96	284.96	284.96	284.96	284.96	284.96	276.20	
1024*3	69.97	69.97	69.97	69.97	67.42	67.42	71.29	
1024*4	62.05	62.05	62.06	62.06	62.06	62.01	61.67	
1024*5	2.88	2.88	2.88	2.86	2.82	4.62	4.74	
1024*6	7.25	7.25	7.25	7.97	8.00	8.00	2.04	
1024*7	25.20	25.20	25.20	25.32	24.74	26.12	25.71	
1024*8	25.23	25.23	25.35	25.35	26.41	26.60	27.11	
1024*9	35.87	36.61	36.61	36.74	36.85	37.24	37.72	
1024*10	38.08	38.47	38.47	38.58	38.60	38.60	36.07	

(a)

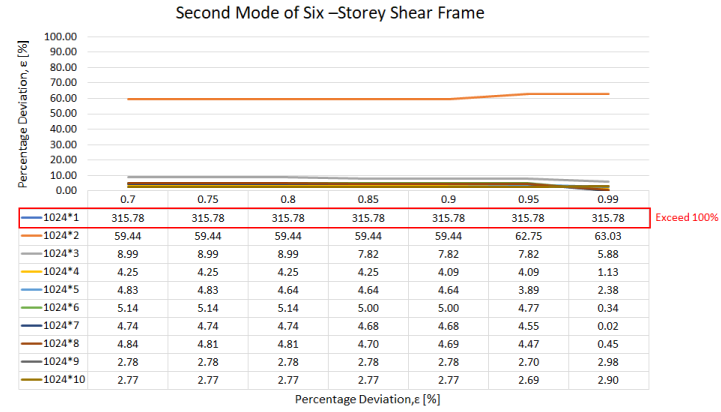

	0.7	0.75	0.8	0.85	0.9	0.95	0.99	
1024*1	315.78	315.78	315.78	315.78	315.78	315.78	315.78	Exceed 100%
1024*2	59.44	59.44	59.44	59.44	59.44	62.75	63.03	
1024*3	8.99	8.99	8.99	7.82	7.82	7.82	5.88	
1024*4	4.25	4.25	4.25	4.25	4.09	4.09	1.13	
1024*5	4.83	4.83	4.64	4.64	4.64	3.89	2.38	
1024*6	5.14	5.14	5.14	5.00	5.00	4.77	0.34	
1024*7	4.74	4.74	4.74	4.68	4.68	4.55	0.02	
1024*8	4.84	4.81	4.81	4.70	4.69	4.47	0.45	
1024*9	2.78	2.78	2.78	2.78	2.78	2.70	2.98	
1024*10	2.77	2.77	2.77	2.77	2.77	2.69	2.90	

(b)

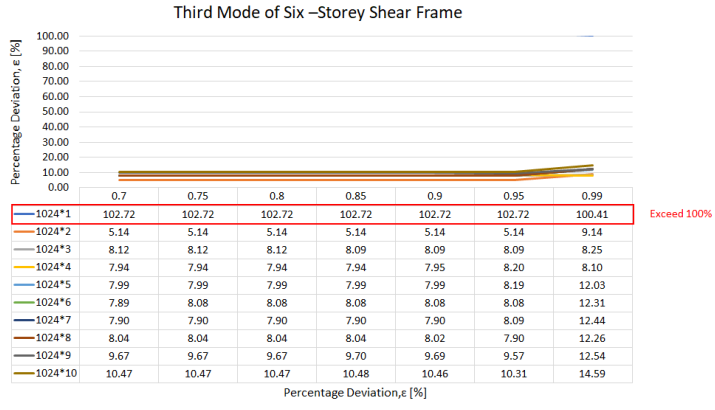

	0.7	0.75	0.8	0.85	0.9	0.95	0.99	
1024*1	102.72	102.72	102.72	102.72	102.72	102.72	100.41	Exceed 100%
1024*2	5.14	5.14	5.14	5.14	5.14	5.14	9.14	
1024*3	8.12	8.12	8.12	8.09	8.09	8.09	8.25	
1024*4	7.94	7.94	7.94	7.94	7.95	8.20	8.10	
1024*5	7.99	7.99	7.99	7.99	7.99	8.19	12.03	
1024*6	7.89	8.08	8.08	8.08	8.08	8.08	12.31	
1024*7	7.90	7.90	7.90	7.90	7.90	8.09	12.44	
1024*8	8.04	8.04	8.04	8.04	8.02	7.90	12.26	
1024*9	9.67	9.67	9.67	9.70	9.69	9.57	12.54	
1024*10	10.47	10.47	10.47	10.48	10.46	10.31	14.59	

(c)

Figure 6. Percentage deviation (error) of modal damping ratio for the low damped six-storey frame (1%): (a) the first mode; (b) second mode; (c) the third mode

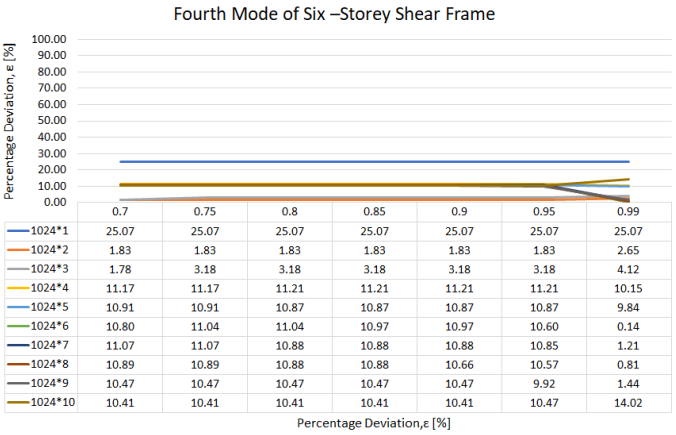

	0.7	0.75	0.8	0.85	0.9	0.95	0.99
1024*1	25.07	25.07	25.07	25.07	25.07	25.07	25.07
1024*2	1.83	1.83	1.83	1.83	1.83	1.83	2.65
1024*3	1.78	3.18	3.18	3.18	3.18	3.18	4.12
1024*4	11.17	11.17	11.21	11.21	11.21	11.21	10.15
1024*5	10.91	10.91	10.87	10.87	10.87	10.87	9.84
1024*6	10.80	11.04	11.04	10.97	10.97	10.60	0.14
1024*7	11.07	11.07	10.88	10.88	10.88	10.85	1.21
1024*8	10.89	10.89	10.88	10.88	10.66	10.57	0.81
1024*9	10.47	10.47	10.47	10.47	10.47	9.92	1.44
1024*10	10.41	10.41	10.41	10.41	10.41	10.47	14.02

(d)

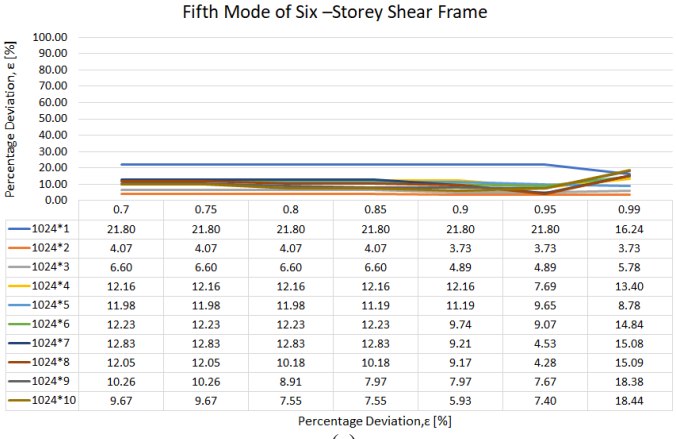

	0.7	0.75	0.8	0.85	0.9	0.95	0.99
1024*1	21.80	21.80	21.80	21.80	21.80	21.80	16.24
1024*2	4.07	4.07	4.07	4.07	3.73	3.73	3.73
1024*3	6.60	6.60	6.60	6.60	4.89	4.89	5.78
1024*4	12.16	12.16	12.16	12.16	12.16	7.69	13.40
1024*5	11.98	11.98	11.98	11.19	11.19	9.65	8.78
1024*6	12.23	12.23	12.23	12.23	9.74	9.07	14.84
1024*7	12.83	12.83	12.83	12.83	9.21	4.53	15.08
1024*8	12.05	12.05	10.18	10.18	9.17	4.28	15.09
1024*9	10.26	10.26	8.91	7.97	7.97	7.67	18.38
1024*10	9.67	9.67	7.55	7.55	5.93	7.40	18.44

(e)

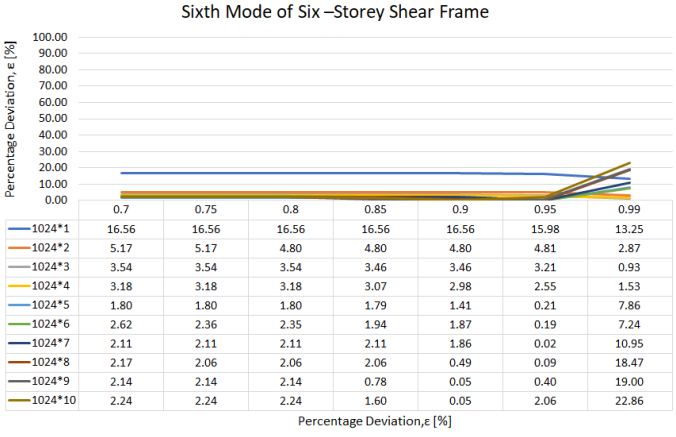

	0.7	0.75	0.8	0.85	0.9	0.95	0.99
1024*1	16.56	16.56	16.56	16.56	16.56	15.98	13.25
1024*2	5.17	5.17	4.80	4.80	4.80	4.81	2.87
1024*3	3.54	3.54	3.54	3.46	3.46	3.21	0.93
1024*4	3.18	3.18	3.18	3.07	2.98	2.55	1.53
1024*5	1.80	1.80	1.80	1.79	1.41	0.21	7.86
1024*6	2.62	2.36	2.35	1.94	1.87	0.19	7.24
1024*7	2.11	2.11	2.11	2.11	1.86	0.02	10.95
1024*8	2.17	2.06	2.06	2.06	0.49	0.09	18.47
1024*9	2.14	2.14	2.14	0.78	0.05	0.40	19.00
1024*10	2.24	2.24	2.24	1.60	0.05	2.06	22.86

(f)

Figure 6. Percentage deviation (error) of modal damping ratio for the low damped six-storey frame (1%): (d) the fourth mode; (e) the fifth mode; (f) the sixth mode.

High Level of Damping (3%)

Percentage deviations (errors) of modal damping ratio for the high damped of two, three and six-storey frame (3%) are shown in Figures 7, 8 and 9.

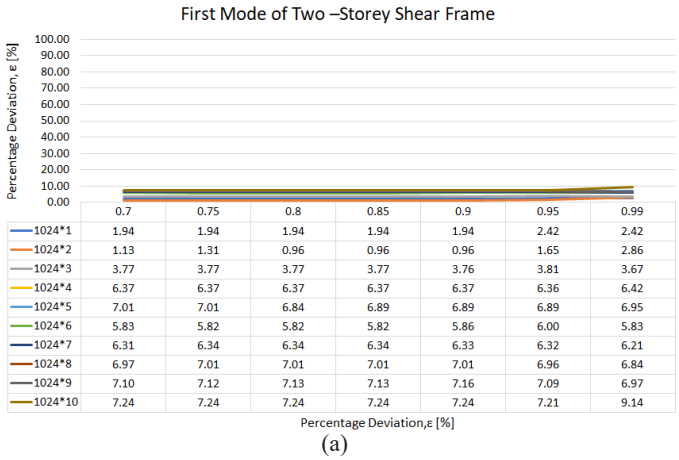

	0.7	0.75	0.8	0.85	0.9	0.95	0.99
1024*1	1.94	1.94	1.94	1.94	1.94	2.42	2.42
1024*2	1.13	1.31	0.96	0.96	0.96	1.65	2.86
1024*3	3.77	3.77	3.77	3.77	3.76	3.81	3.67
1024*4	6.37	6.37	6.37	6.37	6.37	6.36	6.42
1024*5	7.01	7.01	6.84	6.89	6.89	6.89	6.95
1024*6	5.83	5.82	5.82	5.82	5.86	6.00	5.83
1024*7	6.31	6.34	6.34	6.34	6.33	6.32	6.21
1024*8	6.97	7.01	7.01	7.01	7.01	6.96	6.84
1024*9	7.10	7.12	7.13	7.13	7.16	7.09	6.97
1024*10	7.24	7.24	7.24	7.24	7.24	7.21	9.14

(a)

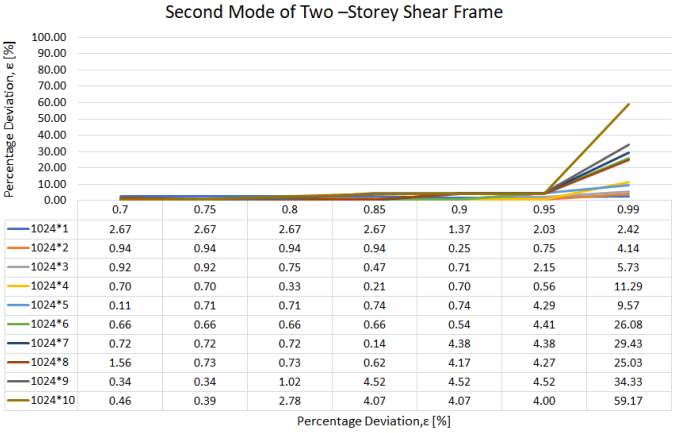

	0.7	0.75	0.8	0.85	0.9	0.95	0.99
1024*1	2.67	2.67	2.67	2.67	1.37	2.03	2.42
1024*2	0.94	0.94	0.94	0.94	0.25	0.75	4.14
1024*3	0.92	0.92	0.75	0.47	0.71	2.15	5.73
1024*4	0.70	0.70	0.33	0.21	0.70	0.56	11.29
1024*5	0.11	0.71	0.71	0.74	0.74	4.29	9.57
1024*6	0.66	0.66	0.66	0.66	0.54	4.41	26.08
1024*7	0.72	0.72	0.72	0.14	4.38	4.38	29.43
1024*8	1.56	0.73	0.73	0.62	4.17	4.27	25.03
1024*9	0.34	0.34	1.02	4.52	4.52	4.52	34.33
1024*10	0.46	0.39	2.78	4.07	4.07	4.00	59.17

(b)

Figure 7. Percentage deviation (error) of modal damping ratio for the high damped two-storey frame (3%): (a) the first mode; (b) the second mode.

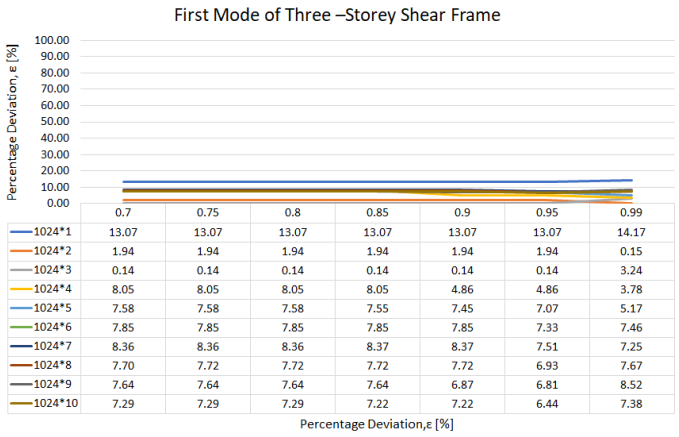

	0.7	0.75	0.8	0.85	0.9	0.95	0.99
1024*1	13.07	13.07	13.07	13.07	13.07	13.07	14.17
1024*2	1.94	1.94	1.94	1.94	1.94	1.94	0.15
1024*3	0.14	0.14	0.14	0.14	0.14	0.14	3.24
1024*4	8.05	8.05	8.05	8.05	4.86	4.86	3.78
1024*5	7.58	7.58	7.58	7.55	7.45	7.07	5.17
1024*6	7.85	7.85	7.85	7.85	7.85	7.33	7.46
1024*7	8.36	8.36	8.36	8.37	8.37	7.51	7.25
1024*8	7.70	7.72	7.72	7.72	7.72	6.93	7.67
1024*9	7.64	7.64	7.64	7.64	6.87	6.81	8.52
1024*10	7.29	7.29	7.29	7.22	7.22	6.44	7.38

(a)

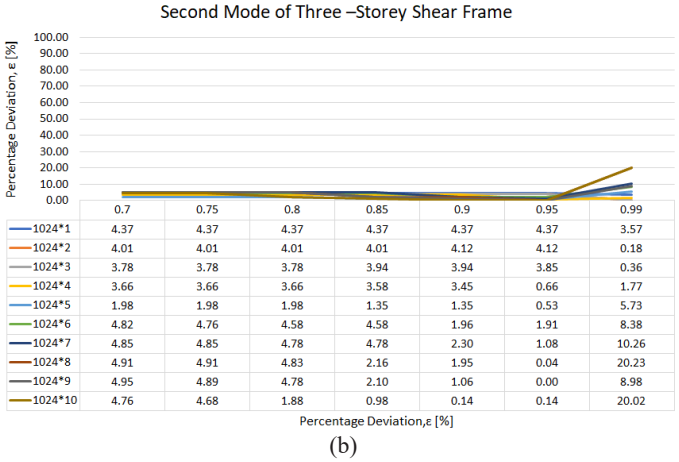

	0.7	0.75	0.8	0.85	0.9	0.95	0.99
1024*1	4.37	4.37	4.37	4.37	4.37	4.37	3.57
1024*2	4.01	4.01	4.01	4.01	4.12	4.12	0.18
1024*3	3.78	3.78	3.78	3.94	3.94	3.85	0.36
1024*4	3.66	3.66	3.66	3.58	3.45	0.66	1.77
1024*5	1.98	1.98	1.98	1.35	1.35	0.53	5.73
1024*6	4.82	4.76	4.58	4.58	1.96	1.91	8.38
1024*7	4.85	4.85	4.78	4.78	2.30	1.08	10.26
1024*8	4.91	4.91	4.83	2.16	1.95	0.04	20.23
1024*9	4.95	4.89	4.78	2.10	1.06	0.00	8.98
1024*10	4.76	4.68	1.88	0.98	0.14	0.14	20.02

(b)

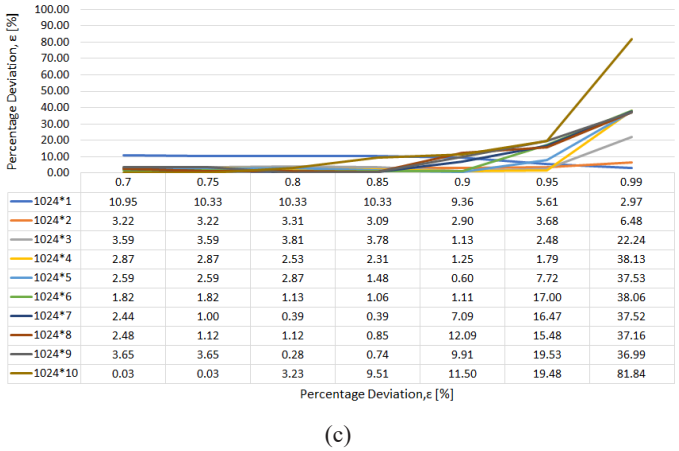

	0.7	0.75	0.8	0.85	0.9	0.95	0.99
1024*1	10.95	10.33	10.33	10.33	9.36	5.61	2.97
1024*2	3.22	3.22	3.31	3.09	2.90	3.68	6.48
1024*3	3.59	3.59	3.81	3.78	1.13	2.48	22.24
1024*4	2.87	2.87	2.53	2.31	1.25	1.79	38.13
1024*5	2.59	2.59	2.87	1.48	0.60	7.72	37.53
1024*6	1.82	1.82	1.13	1.06	1.11	17.00	38.06
1024*7	2.44	1.00	0.39	0.39	7.09	16.47	37.52
1024*8	2.48	1.12	1.12	0.85	12.09	15.48	37.16
1024*9	3.65	3.65	0.28	0.74	9.91	19.53	36.99
1024*10	0.03	0.03	3.23	9.51	11.50	19.48	81.84

(c)

Figure 8. Percentage deviation (error) of modal damping ratio for the high damped three-storey frame (3%): (a) the first mode; (b) the second mode; (c) the third mode.

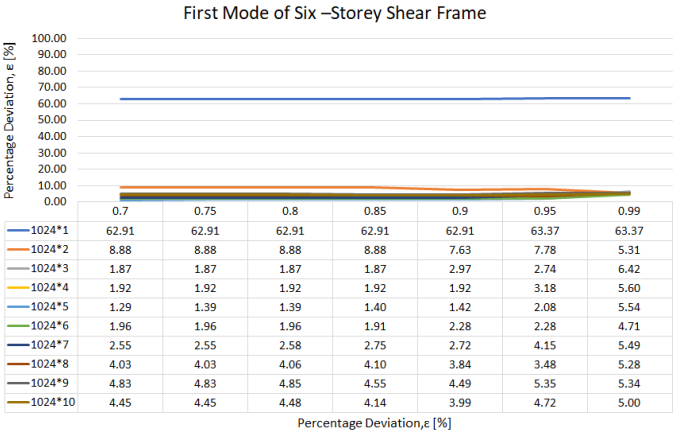

	0.7	0.75	0.8	0.85	0.9	0.95	0.99
1024*1	62.91	62.91	62.91	62.91	62.91	63.37	63.37
1024*2	8.88	8.88	8.88	8.88	7.63	7.78	5.31
1024*3	1.87	1.87	1.87	1.87	2.97	2.74	6.42
1024*4	1.92	1.92	1.92	1.92	1.92	3.18	5.60
1024*5	1.29	1.39	1.39	1.40	1.42	2.08	5.54
1024*6	1.96	1.96	1.96	1.91	2.28	2.28	4.71
1024*7	2.55	2.55	2.58	2.75	2.72	4.15	5.49
1024*8	4.03	4.03	4.06	4.10	3.84	3.48	5.28
1024*9	4.83	4.83	4.85	4.55	4.49	5.35	5.34
1024*10	4.45	4.45	4.48	4.14	3.99	4.72	5.00

(a)

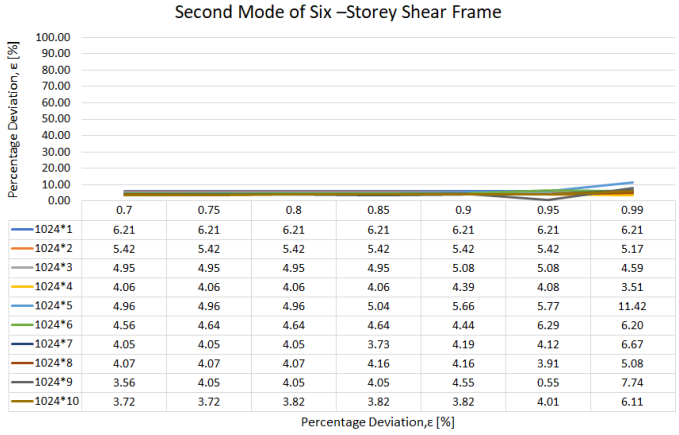

	0.7	0.75	0.8	0.85	0.9	0.95	0.99
1024*1	6.21	6.21	6.21	6.21	6.21	6.21	6.21
1024*2	5.42	5.42	5.42	5.42	5.42	5.42	5.17
1024*3	4.95	4.95	4.95	4.95	5.08	5.08	4.59
1024*4	4.06	4.06	4.06	4.06	4.39	4.08	3.51
1024*5	4.96	4.96	4.96	5.04	5.66	5.77	11.42
1024*6	4.56	4.64	4.64	4.64	4.44	6.29	6.20
1024*7	4.05	4.05	4.05	3.73	4.19	4.12	6.67
1024*8	4.07	4.07	4.07	4.16	4.16	3.91	5.08
1024*9	3.56	4.05	4.05	4.05	4.55	0.55	7.74
1024*10	3.72	3.72	3.82	3.82	3.82	4.01	6.11

(b)

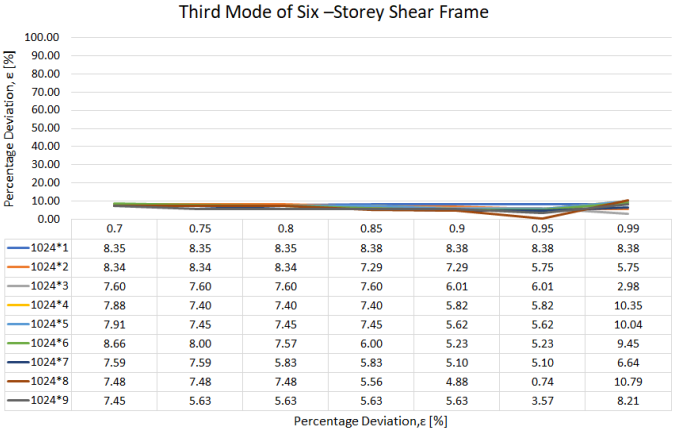

	0.7	0.75	0.8	0.85	0.9	0.95	0.99
1024*1	8.35	8.35	8.35	8.38	8.38	8.38	8.38
1024*2	8.34	8.34	8.34	7.29	7.29	5.75	5.75
1024*3	7.60	7.60	7.60	7.60	6.01	6.01	2.98
1024*4	7.88	7.40	7.40	7.40	5.82	5.82	10.35
1024*5	7.91	7.45	7.45	7.45	5.62	5.62	10.04
1024*6	8.66	8.00	7.57	6.00	5.23	5.23	9.45
1024*7	7.59	7.59	5.83	5.83	5.10	5.10	6.64
1024*8	7.48	7.48	7.48	5.56	4.88	0.74	10.79
1024*9	7.45	5.63	5.63	5.63	5.63	3.57	8.21

(c)

Figure 9. Percentage deviation (error) of modal damping ratio for the high damped six-storey frame (3%): (a) the first mode; (b) second mode; (c) the third mode

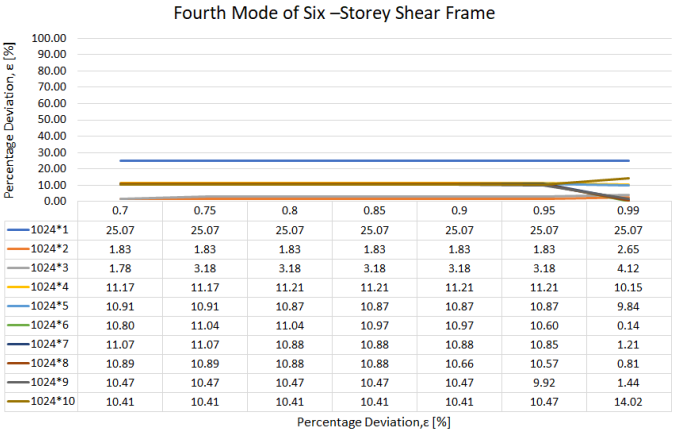

	0.7	0.75	0.8	0.85	0.9	0.95	0.99
1024*1	25.07	25.07	25.07	25.07	25.07	25.07	25.07
1024*2	1.83	1.83	1.83	1.83	1.83	1.83	2.65
1024*3	1.78	3.18	3.18	3.18	3.18	3.18	4.12
1024*4	11.17	11.17	11.21	11.21	11.21	11.21	10.15
1024*5	10.91	10.91	10.87	10.87	10.87	10.87	9.84
1024*6	10.80	11.04	11.04	10.97	10.97	10.60	0.14
1024*7	11.07	11.07	10.88	10.88	10.88	10.85	1.21
1024*8	10.89	10.89	10.88	10.88	10.66	10.57	0.81
1024*9	10.47	10.47	10.47	10.47	10.47	9.92	1.44
1024*10	10.41	10.41	10.41	10.41	10.41	10.47	14.02

(d)

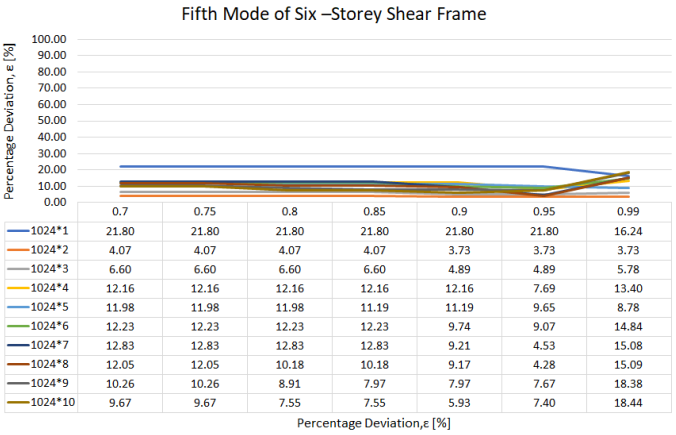

	0.7	0.75	0.8	0.85	0.9	0.95	0.99
1024*1	21.80	21.80	21.80	21.80	21.80	21.80	16.24
1024*2	4.07	4.07	4.07	4.07	3.73	3.73	3.73
1024*3	6.60	6.60	6.60	6.60	4.89	4.89	5.78
1024*4	12.16	12.16	12.16	12.16	12.16	7.69	13.40
1024*5	11.98	11.98	11.98	11.19	11.19	9.65	8.78
1024*6	12.23	12.23	12.23	12.23	9.74	9.07	14.84
1024*7	12.83	12.83	12.83	12.83	9.21	4.53	15.08
1024*8	12.05	12.05	10.18	10.18	9.17	4.28	15.09
1024*9	10.26	10.26	8.91	7.97	7.97	7.67	18.38
1024*10	9.67	9.67	7.55	7.55	5.93	7.40	18.44

(e)

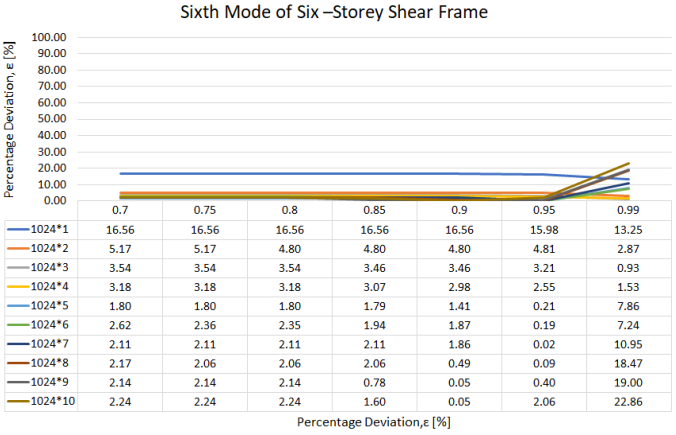

	0.7	0.75	0.8	0.85	0.9	0.95	0.99
1024*1	16.56	16.56	16.56	16.56	16.56	15.98	13.25
1024*2	5.17	5.17	4.80	4.80	4.80	4.81	2.87
1024*3	3.54	3.54	3.54	3.46	3.46	3.21	0.93
1024*4	3.18	3.18	3.18	3.07	2.98	2.55	1.53
1024*5	1.80	1.80	1.80	1.79	1.41	0.21	7.86
1024*6	2.62	2.36	2.35	1.94	1.87	0.19	7.24
1024*7	2.11	2.11	2.11	2.11	1.86	0.02	10.95
1024*8	2.17	2.06	2.06	2.06	0.49	0.09	18.47
1024*9	2.14	2.14	2.14	0.78	0.05	0.40	19.00
1024*10	2.24	2.24	2.24	1.60	0.05	2.06	22.86

(f)

Figure 9. Percentage deviation (error) of modal damping ratio for the high damped six-storey frame (3%): (d) the fourth mode; (e) the fifth mode; (f) the sixth mode.

High Level of Damping (5%)

Percentage deviations (errors) of modal damping ratio for the high damped of two, three and six-storey frame (5%) are shown in Figures 10, 11 and 12.

This analysis reveals that a maximum number of points of the time segment or frequency resolution play a major role in presenting high bias results (sometimes above 100%) in cases when this parameter is not well chosen. The frequency resolution and the correct choice of the number of points of the time segments are both interrelated; increasing the number of points means increasing the frequency resolution. The biased estimate of the modal damping ratio is influenced by estimated auto-correlation. The correct selection of a maximum number of time segments for estimating auto-correlation should require some points after the disappearance of the decay to ensure that the length of the estimated

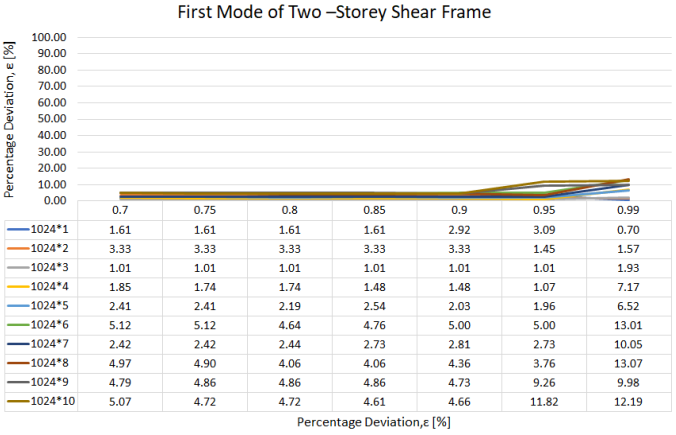

	0.7	0.75	0.8	0.85	0.9	0.95	0.99
1024*1	1.61	1.61	1.61	1.61	2.92	3.09	0.70
1024*2	3.33	3.33	3.33	3.33	3.33	1.45	1.57
1024*3	1.01	1.01	1.01	1.01	1.01	1.01	1.93
1024*4	1.85	1.74	1.74	1.48	1.48	1.07	7.17
1024*5	2.41	2.41	2.19	2.54	2.03	1.96	6.52
1024*6	5.12	5.12	4.64	4.76	5.00	5.00	13.01
1024*7	2.42	2.42	2.44	2.73	2.81	2.73	10.05
1024*8	4.97	4.90	4.06	4.06	4.36	3.76	13.07
1024*9	4.79	4.86	4.86	4.86	4.73	9.26	9.98
1024*10	5.07	4.72	4.72	4.61	4.66	11.82	12.19

(a)

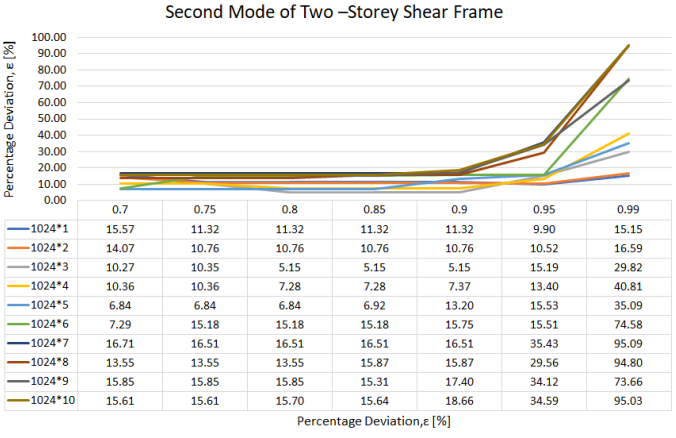

	0.7	0.75	0.8	0.85	0.9	0.95	0.99
1024*1	15.57	11.32	11.32	11.32	11.32	9.90	15.15
1024*2	14.07	10.76	10.76	10.76	10.76	10.52	16.59
1024*3	10.27	10.35	5.15	5.15	5.15	15.19	29.82
1024*4	10.36	10.36	7.28	7.28	7.37	13.40	40.81
1024*5	6.84	6.84	6.84	6.92	13.20	15.53	35.09
1024*6	7.29	15.18	15.18	15.18	15.75	15.51	74.58
1024*7	16.71	16.51	16.51	16.51	16.51	35.43	95.09
1024*8	13.55	13.55	13.55	15.87	15.87	29.56	94.80
1024*9	15.85	15.85	15.85	15.31	17.40	34.12	73.66
1024*10	15.61	15.61	15.70	15.64	18.66	34.59	95.03

(b)

Figure 10. Percentage deviation (error) of modal damping ratio for the high damped two-storey frame (5%): (a) the first mode; (b) the second mode.

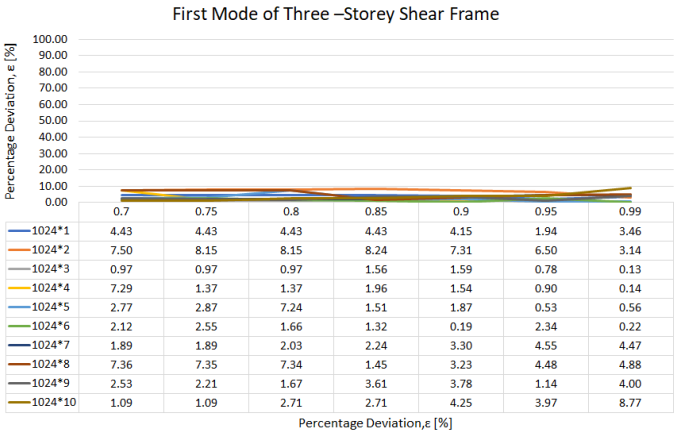

	0.7	0.75	0.8	0.85	0.9	0.95	0.99
1024*1	4.43	4.43	4.43	4.43	4.15	1.94	3.46
1024*2	7.50	8.15	8.15	8.24	7.31	6.50	3.14
1024*3	0.97	0.97	0.97	1.56	1.59	0.78	0.13
1024*4	7.29	1.37	1.37	1.96	1.54	0.90	0.14
1024*5	2.77	2.87	7.24	1.51	1.87	0.53	0.56
1024*6	2.12	2.55	1.66	1.32	0.19	2.34	0.22
1024*7	1.89	1.89	2.03	2.24	3.30	4.55	4.47
1024*8	7.36	7.35	7.34	1.45	3.23	4.48	4.88
1024*9	2.53	2.21	1.67	3.61	3.78	1.14	4.00
1024*10	1.09	1.09	2.71	2.71	4.25	3.97	8.77

(a)

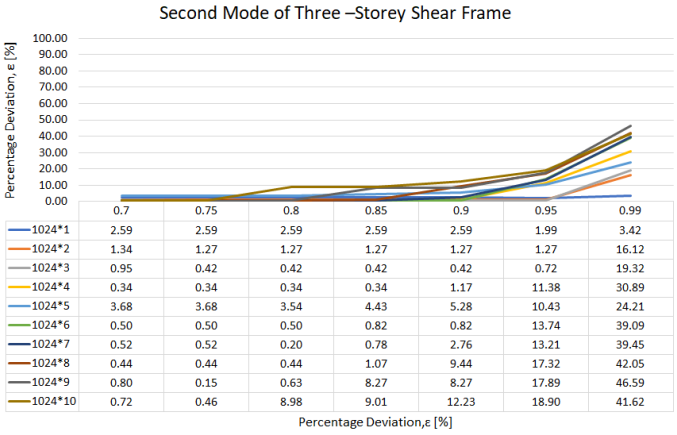

	0.7	0.75	0.8	0.85	0.9	0.95	0.99
1024*1	2.59	2.59	2.59	2.59	2.59	1.99	3.42
1024*2	1.34	1.27	1.27	1.27	1.27	1.27	16.12
1024*3	0.95	0.42	0.42	0.42	0.42	0.72	19.32
1024*4	0.34	0.34	0.34	0.34	1.17	11.38	30.89
1024*5	3.68	3.68	3.54	4.43	5.28	10.43	24.21
1024*6	0.50	0.50	0.50	0.82	0.82	13.74	39.09
1024*7	0.52	0.52	0.20	0.78	2.76	13.21	39.45
1024*8	0.44	0.44	0.44	1.07	9.44	17.32	42.05
1024*9	0.80	0.15	0.63	8.27	8.27	17.89	46.59
1024*10	0.72	0.46	8.98	9.01	12.23	18.90	41.62

(b)

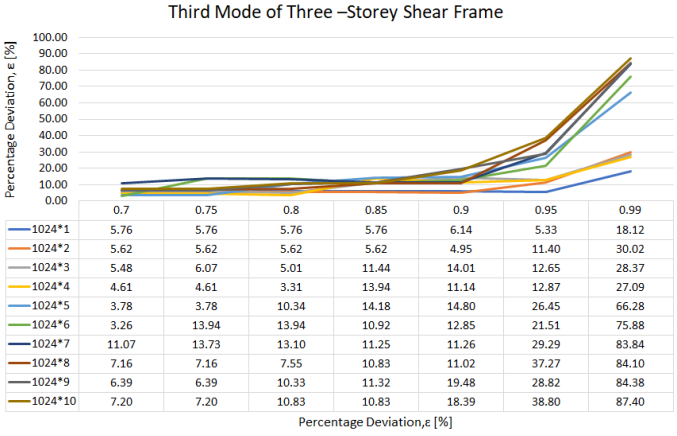

	0.7	0.75	0.8	0.85	0.9	0.95	0.99
1024*1	5.76	5.76	5.76	5.76	6.14	5.33	18.12
1024*2	5.62	5.62	5.62	5.62	4.95	11.40	30.02
1024*3	5.48	6.07	5.01	11.44	14.01	12.65	28.37
1024*4	4.61	4.61	3.31	13.94	11.14	12.87	27.09
1024*5	3.78	3.78	10.34	14.18	14.80	26.45	66.28
1024*6	3.26	13.94	13.94	10.92	12.85	21.51	75.88
1024*7	11.07	13.73	13.10	11.25	11.26	29.29	83.84
1024*8	7.16	7.16	7.55	10.83	11.02	37.27	84.10
1024*9	6.39	6.39	10.33	11.32	19.48	28.82	84.38
1024*10	7.20	7.20	10.83	10.83	18.39	38.80	87.40

(c)

Figure 11. Percentage deviation (error) of modal damping ratio for the high damped three-storey frame (5%): (a) the first mode; (b) the second mode; (c) the third mode.

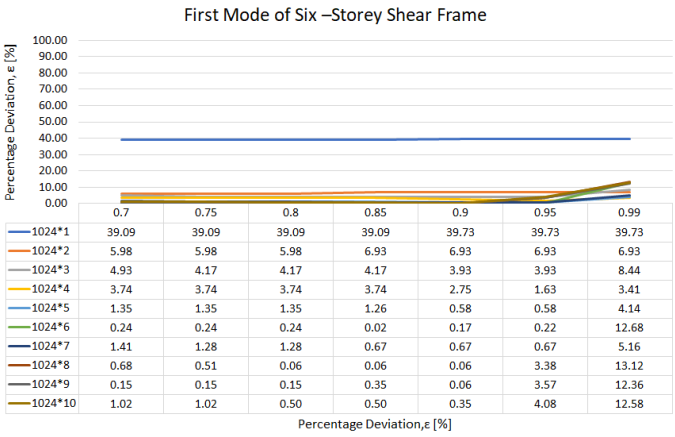

	0.7	0.75	0.8	0.85	0.9	0.95	0.99
1024*1	39.09	39.09	39.09	39.09	39.73	39.73	39.73
1024*2	5.98	5.98	5.98	6.93	6.93	6.93	6.93
1024*3	4.93	4.17	4.17	4.17	3.93	3.93	8.44
1024*4	3.74	3.74	3.74	3.74	2.75	1.63	3.41
1024*5	1.35	1.35	1.35	1.26	0.58	0.58	4.14
1024*6	0.24	0.24	0.24	0.02	0.17	0.22	12.68
1024*7	1.41	1.28	1.28	0.67	0.67	0.67	5.16
1024*8	0.68	0.51	0.06	0.06	0.06	3.38	13.12
1024*9	0.15	0.15	0.15	0.35	0.06	3.57	12.36
1024*10	1.02	1.02	0.50	0.50	0.35	4.08	12.58

(a)

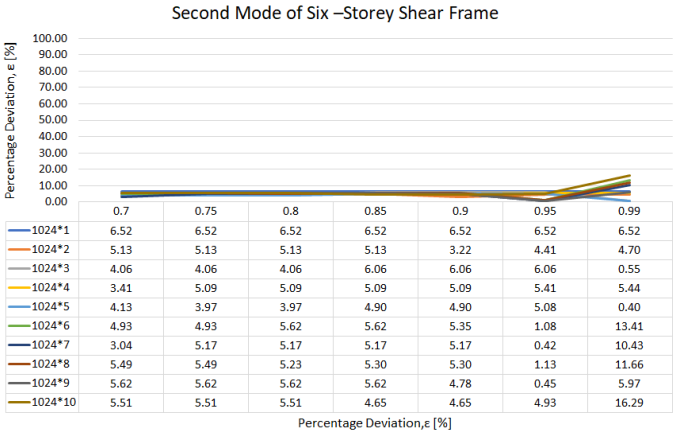

	0.7	0.75	0.8	0.85	0.9	0.95	0.99
1024*1	6.52	6.52	6.52	6.52	6.52	6.52	6.52
1024*2	5.13	5.13	5.13	5.13	3.22	4.41	4.70
1024*3	4.06	4.06	4.06	6.06	6.06	6.06	0.55
1024*4	3.41	5.09	5.09	5.09	5.09	5.41	5.44
1024*5	4.13	3.97	3.97	4.90	4.90	5.08	0.40
1024*6	4.93	4.93	5.62	5.62	5.35	1.08	13.41
1024*7	3.04	5.17	5.17	5.17	5.17	0.42	10.43
1024*8	5.49	5.49	5.23	5.30	5.30	1.13	11.66
1024*9	5.62	5.62	5.62	5.62	4.78	0.45	5.97
1024*10	5.51	5.51	5.51	4.65	4.65	4.93	16.29

(b)

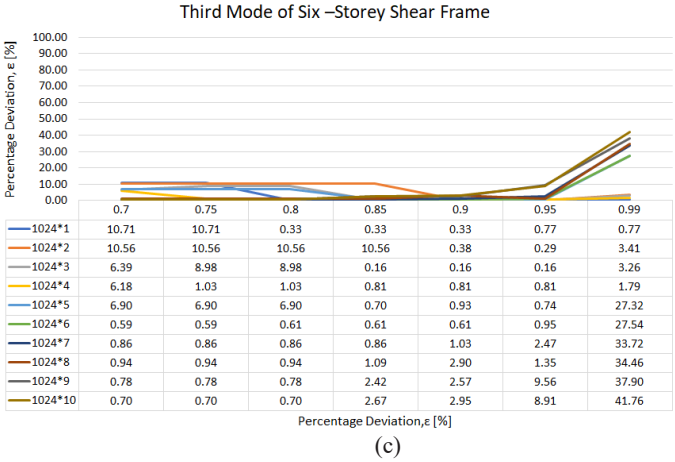

	0.7	0.75	0.8	0.85	0.9	0.95	0.99
1024*1	10.71	10.71	0.33	0.33	0.33	0.77	0.77
1024*2	10.56	10.56	10.56	10.56	0.38	0.29	3.41
1024*3	6.39	8.98	8.98	0.16	0.16	0.16	3.26
1024*4	6.18	1.03	1.03	0.81	0.81	0.81	1.79
1024*5	6.90	6.90	6.90	0.70	0.93	0.74	27.32
1024*6	0.59	0.59	0.61	0.61	0.61	0.95	27.54
1024*7	0.86	0.86	0.86	0.86	1.03	2.47	33.72
1024*8	0.94	0.94	0.94	1.09	2.90	1.35	34.46
1024*9	0.78	0.78	0.78	2.42	2.57	9.56	37.90
1024*10	0.70	0.70	0.70	2.67	2.95	8.91	41.76

(c)

Figure 12. Percentage deviation (error) of modal damping ratio for the high damped six-storey frame (5%): (a) the first mode; (b) second mode; (c) the third mode

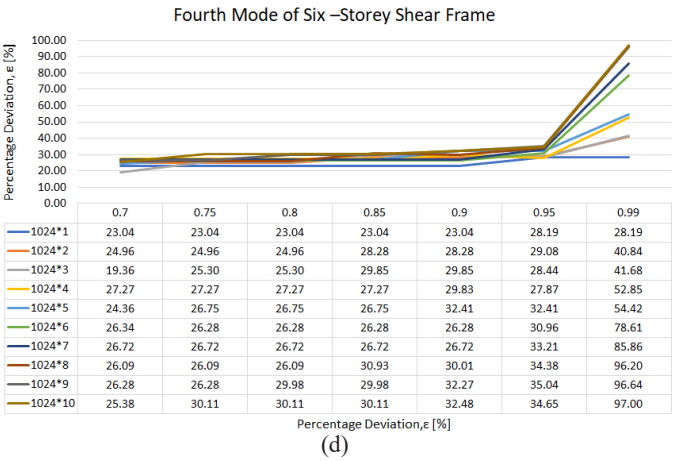

	0.7	0.75	0.8	0.85	0.9	0.95	0.99
1024*1	23.04	23.04	23.04	23.04	23.04	28.19	28.19
1024*2	24.96	24.96	24.96	28.28	28.28	29.08	40.84
1024*3	19.36	25.30	25.30	29.85	29.85	28.44	41.68
1024*4	27.27	27.27	27.27	27.27	29.83	27.87	52.85
1024*5	24.36	26.75	26.75	26.75	32.41	32.41	54.42
1024*6	26.34	26.28	26.28	26.28	26.28	30.96	78.61
1024*7	26.72	26.72	26.72	26.72	26.72	33.21	85.86
1024*8	26.09	26.09	26.09	30.93	30.01	34.38	96.20
1024*9	26.28	26.28	29.98	29.98	32.27	35.04	96.64
1024*10	25.38	30.11	30.11	30.11	32.48	34.65	97.00

(d)

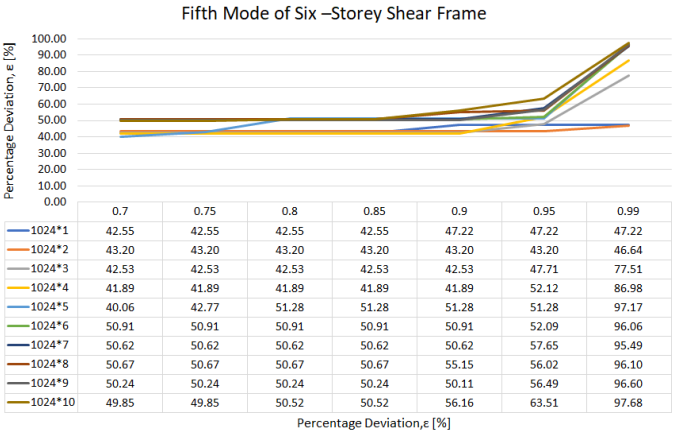

	0.7	0.75	0.8	0.85	0.9	0.95	0.99
1024*1	42.55	42.55	42.55	42.55	47.22	47.22	47.22
1024*2	43.20	43.20	43.20	43.20	43.20	43.20	46.64
1024*3	42.53	42.53	42.53	42.53	42.53	47.71	77.51
1024*4	41.89	41.89	41.89	41.89	41.89	52.12	86.98
1024*5	40.06	42.77	51.28	51.28	51.28	51.28	97.17
1024*6	50.91	50.91	50.91	50.91	50.91	52.09	96.06
1024*7	50.62	50.62	50.62	50.62	50.62	57.65	95.49
1024*8	50.67	50.67	50.67	50.67	55.15	56.02	96.10
1024*9	50.24	50.24	50.24	50.24	50.11	56.49	96.60
1024*10	49.85	49.85	50.52	50.52	56.16	63.51	97.68

(e)

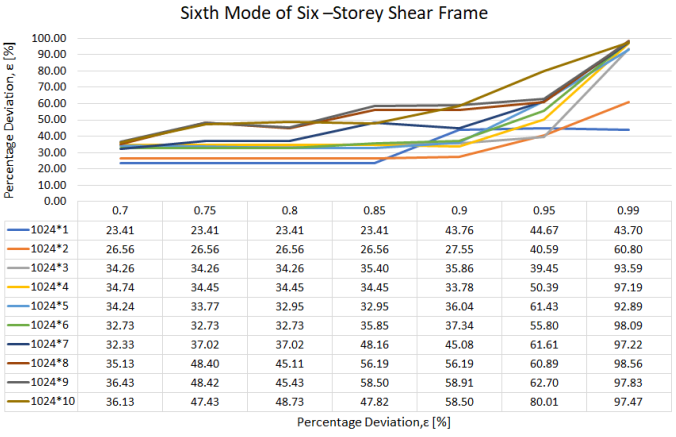

	0.7	0.75	0.8	0.85	0.9	0.95	0.99
1024*1	23.41	23.41	23.41	23.41	43.76	44.67	43.70
1024*2	26.56	26.56	26.56	26.56	27.55	40.59	60.80
1024*3	34.26	34.26	34.26	35.40	35.86	39.45	93.59
1024*4	34.74	34.45	34.45	34.45	33.78	50.39	97.19
1024*5	34.24	33.77	32.95	32.95	36.04	61.43	92.89
1024*6	32.73	32.73	32.73	35.85	37.34	55.80	98.09
1024*7	32.33	37.02	37.02	48.16	45.08	61.61	97.22
1024*8	35.13	48.40	45.11	56.19	56.19	60.89	98.56
1024*9	36.43	48.42	45.43	58.50	58.91	62.70	97.83
1024*10	36.13	47.43	48.73	47.82	58.50	80.01	97.47

(f)

Figure 12. Percentage deviation (error) of modal damping ratio for the high damped six-storey frame (5%): (d) the fourth mode; (e) the fifth mode; (f) the sixth mode.

correlation is adequate and able to successfully capture all full modal decay that contains an adequate amount of information about the decaying CF, otherwise the likely presence of noise and errors in the results for the modal damping estimate will be caused by the spectral estimation. Since the identification of the modal damping ratio using logarithmic decrement is fully reliant on modal decay, the accurate maximum number of time segment lengths becomes a crucial step for accurate estimation of the modal parameter. The results of this analysis for the percentage deviation of the estimated modal damping ratio are illustrated in Figures 4 to 12.

Meanwhile, results of theoretical modal decay of the first mode and limits of the auto-correlation functions calculated using the time segment lengths defined in Table 2 for two, three and six-storey frame are shown in Figures 13, 14 and 15.

This is proven with the scheme presented in Figure 13, 14 and 15, which display the theoretical modal decay of the first mode and the limits of the auto-correlation functions calculated using the time segment lengths defined in Table 2 for multi-storey shear-type models and a variable level of damping (1%, 3% and 5% of critical damping, which consists of low and high damped systems). The red vertical lines that are clearly observed before the end of the decay, consequently, lead to the bias estimates. The effect of the introduced errors can also be observed by comparing, for instance, the auto-correlation estimated using time segments with 2048 points (Figure 16 with its theoretical counterpart Figure 14a): the estimated decay vanishes just at the end of the estimated segment, approximately at 5 seconds or 6 seconds, but the estimated correlation does not contain some points after the

Table 2

Scenarios for the application of the FDD method

Maximum number of points in the time segments	MAC Index						
	0.70	0.75	0.80	0.85	0.90	0.95	0.99
1024*1	1a	1b	1c	1d	1e	1f	1g
1024*2	2a	2b	2c	2d	2e	2f	2g
1024*3	3a	3b	3c	3d	3e	3f	3g
1024*4	4a	4b	4c	4d	4e	4f	4g
1024*5	5a	5b	5c	5d	5e	5f	5g
1024*6	6a	6b	6c	6d	6e	6f	6g
1024*7	7a	7b	7c	7d	7e	7f	7g
1024*8	8a	8b	8c	8d	8e	8f	8g
1024*9	9a	9b	9c	9d	9e	9f	9g
1024*10	10a	10b	10c	10d	10e	10f	10g

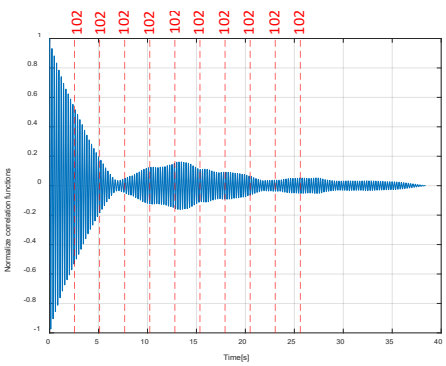

(a)

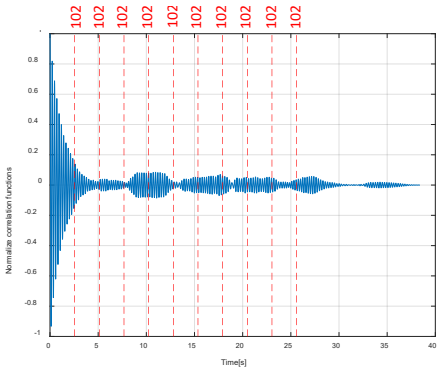

(b)

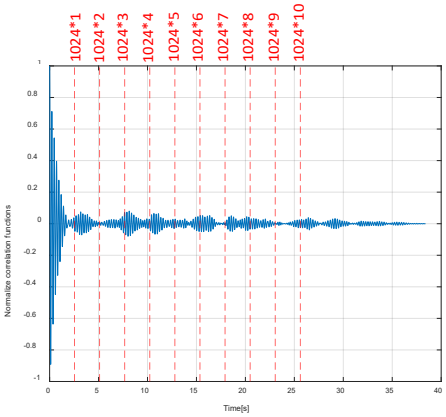

(c)

Figure 13. Theoretical modal decay of the first mode and limits of the auto-correlation functions calculated using the time segment lengths defined in Table 2 for two-storey frame: (a) low damped (1%); (b) high damped (3%); (c) high damped (5%) system.

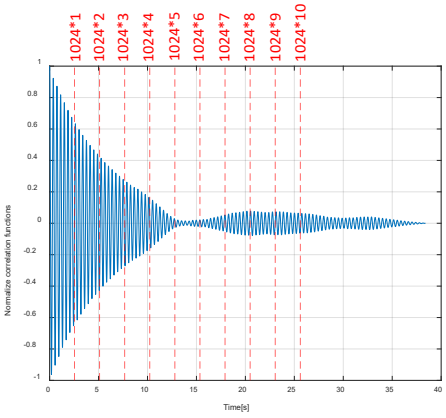

(a)

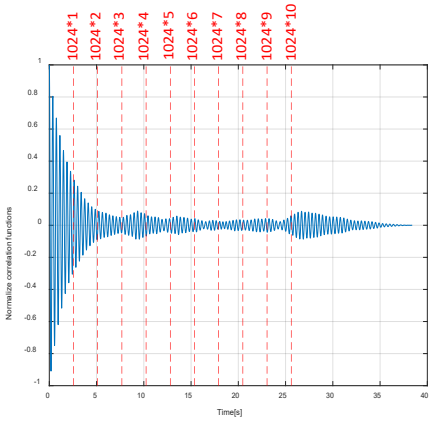

(b)

Figure 14. Theoretical modal decay of the first mode and limits of the auto-correlation functions calculated using the time segment lengths defined in Table 2 for three-storey frame: (a) low damped (1%); (b) high damped (3%)

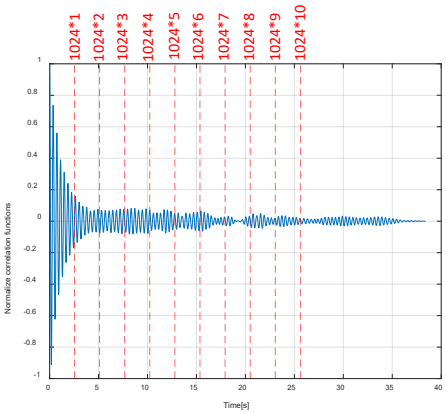

(c)

Figure 14. Theoretical modal decay of the first mode and limits of the auto-correlation functions calculated using the time segment lengths defined in Table 2 for three-storey frame: (c) high damped (5%) system

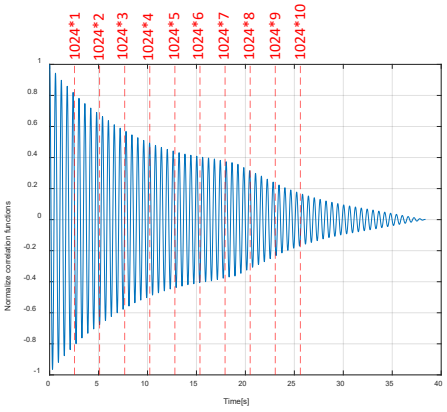

(a)

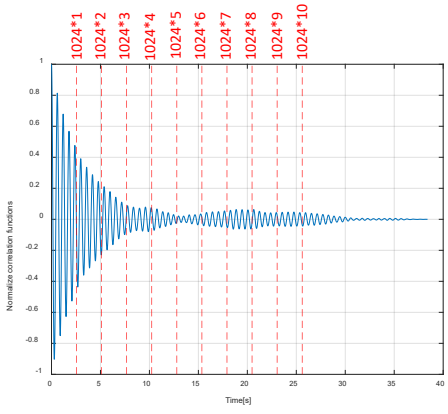

(b)

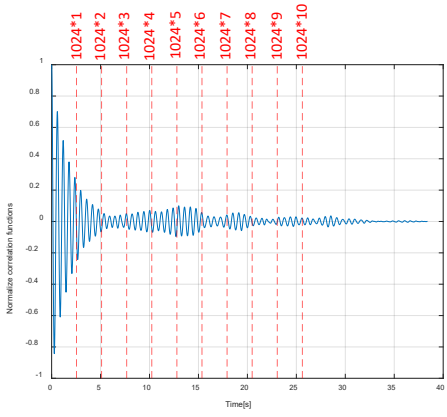

(c)

Figure 15. Theoretical modal decay of the first mode and limits of the auto-correlation functions calculated using the time segment lengths defined in Table 2 for six-storey frame: (a) low damped (1%); (b) high damped (3%); (c) high damped (5%) system.

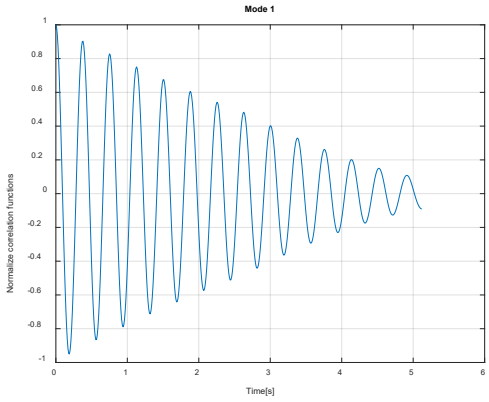

Figure 16. Modal decay estimated using time segments with 2048 points for the first mode of the three-storey frame (1% of critical damping)

disappearance of the decay. This indicates that the length of the estimated correlation is not long enough to characterise the full decay.

In the case of the various levels of damping of the system, the appropriate maximum number of points of the time segment become a crucial decision and need to be defined properly, particularly for low damped systems where the response will decay at a slower rate and thus requiring the high number of points of time segments when compared to a high damped structure. Table 3 provides the appropriate adopted number of points of time segments for the first mode of the multi-storey frame based on the results provided in Figures 4 to 12. The first mode becomes a key point to determine the maximum number of points of the time segments. This has proven that the accurate selection of the time segment length does not rely solely on modal damping ratios; instead, natural frequencies also need to be taken into account because each first mode of multi-storey shear-type models has a different value of natural frequencies. This indicates that reducing the value of natural frequencies and modal damping ratios of the modes under analysis demands longer time segments and a high value of the maximum number of points for an adequate amount of information of the decaying CF when estimating modal damping (examples are shown in Figure 6a and Figure 15a for the first the mode of the six-storey shear model with 1% of critical damping). Furthermore, if the maximum number of points of the time segment is too high, it will cause bias errors. Thus, from this analysis, the maximum number of points of the time segment suitable to be used for both low and high damped systems (1%–5% of critical damping and from frequency 1.5 Hz and above) for multi-storey shear-type models is 5120 (1024*5) or more, as outlined in Table 3. Instead of an increasing number of points of time segments, another way to enhance the frequency resolution is through interpolation of the spectrum by zero-padding the time window to increase the length of recordings (Ewins, 2000).

Table 3

The appropriate adopted number of points of time segments for the multi-storey frame

Storey frame	Natural frequency [Hz]	Modal damping ratio [%]	Appropriate no. of point of time segments
Two	4.211	1	≥ 1024*3 @ (3072)
		3	≥ 1024*1 @ (1024)
		5	≥ 1024*1 @ (1024)
Three	2.657	1	≥ 1024*4 @ (4096)
		3	≥ 1024*2 @ (2048)
		5	≥ 1024*1 @ (1024)
Six	1.666	1	≥ 1024*5 @ (5120)
		3	≥ 1024*3 @ (3072)
		5	≥ 1024*2 @ (2048)

In addition, the supplementary set of analysis involving the parameters of the MAC index with different levels of system damping and the number of points of the time segments revealed that the results yield small variations of the percentage deviation of the modal damping ratio (around 1.23% standard deviation) for multi-storey shear-type models with 1% (low damped system) as shown in Figures 4, 5 and 6. This proves that the MAC index does not significantly affect the results of the low damped system. The use of a high MAC index value for the high damped system (5% of critical damping) will significantly introduce large error bound about 8.71% standard deviation of percentage error. It became worse, particularly for the higher modes, as the standard deviation of percentage error increased gradually. Furthermore, the use of a MAC index for a high number of points of time segments significantly increases the standard deviation of the percentage error. The plots in Figures 7 to 12 also revealed that the use of a high number of points of time segments as well as a high MAC index lead to an increased percentage deviation of estimate modal damping ratio, which can be up to 30% of standard deviation when the level of damping is higher. The selection of the auto-spectra based on the MAC index using values higher than 0.8 is preferred by most researchers (Magalhães, 2010; Magalhães et al., 2010) but it is unsuitable, particularly for the higher modes of the high damped system.

Therefore, this analysis also provides the appropriate range for the MAC index for each mode with different levels of damping according to the trend, as illustrated in Figure 4 to 12. The results of the analysis are provided in Tables 4, 5 and 6 with respect to two-, three- and six-storey frames. Table 7 comprises all the appropriate range of MAC indexes with different levels of damping from multi-storey models according to each mode, based on the results in Figures 4 to 12. This Table 7 clearly shows that the higher modes require lower MAC index values and vice versa for lower modes.

Table 4

The appropriate adopted range of MAC index for the two-storey frame

Mode	Natural frequency [Hz]	Modal damping ratio [%]	Appropriate MAC index
First	4.211	1	0.70–0.90
		3	0.80–0.99
		5	0.70–0.95
Second	10.911	1	0.70–0.95
		3	0.70–0.90
		5	0.70–0.85

Table 5

The appropriate adopted range of MAC index for the three-storey frame

Mode	Natural frequency [Hz]	Modal damping ratio [%]	Appropriate MAC index
First	2.657	1	0.75–0.99
		3	0.70–0.99
		5	0.85–0.99
Second	7.445	1	0.80–0.99
		3	0.85–0.95
		5	0.70–0.85
Third	10.759	1	0.70–0.90
		3	0.70–0.90
		5	0.70–0.75

Table 6

The appropriate adopted range of MAC index for the six-storey frame

Mode	Natural frequency [Hz]	Modal damping ratio [%]	Appropriate MAC index
First	1.666	1	0.70–0.90
		3	0.70–0.90
		5	0.70–0.95
Second	4.672	1	0.70–0.99
		3	0.70–0.95
		5	0.70–0.80
Third	7.448	1	0.70–0.95
		3	0.70–0.95
		5	0.70–0.95

Table 6 *(Continued)*

Mode	Natural frequency [Hz]	Modal damping ratio [%]	Appropriate MAC index
Fourth	9.789	1	0.70–0.99
		3	0.70–0.90
		5	0.70–0.85
Fifth	11.587	1	0.70–0.99
		3	0.70–0.95
		5	0.70–0.75
Sixth	13.082	1	0.70–0.95
		3	0.70–0.75
		5	0.70–0.85

Table 7

The appropriate adopted range of MAC index for each mode

Mode	Modal damping ratio [%]	Appropriate Range of MAC index	Appropriate MAC index
First	1	0.75–0.90	
	3	0.80–0.90	0.85–0.90
	5	0.85–0.95	
Second	1	0.80–0.95	
	3	0.85–0.90	0.85–0.90
	5	0.70–0.80	
Third	1	0.70–0.90	
	3	0.70–0.90	0.70–0.75
	5	0.70–0.75	
Fourth	1	0.70–0.99	
	3	0.70–0.90	0.70–0.85
	5	0.70–0.85	
Fifth	1	0.70–0.99	
	3	0.70–0.95	0.70–0.75
	5	0.70–0.75	
Sixth	1	0.70–0.95	
	3	0.70–0.75	0.70–0.75
	5	0.70–0.85	

CONCLUSIONS

In this study, the results of the parameters that have a bigger effect on the performance of the automated EFDD method are presented involving the maximum number of points considered in the time segments used for the spectra calculation, selection of MAC index and the variable level of damping of the system. The results indicate that reducing the value of natural frequencies and modal damping ratios of the modes under analysis demands longer time segments and a high value of the maximum number of points for adequate information of the decaying CF when estimating modal damping. In addition, the supplementary set of analyses involving the parameters of the MAC index with different levels of system damping and number of points of the time segments revealed that the results proved that the MAC index did not significantly affect the results for the low damped system. However, the use of a high MAC index value for the high damped system (5% of critical damping) significantly introduced large error bound. It became worse, particularly for the higher modes, as the standard deviation of percentage error increased gradually. Furthermore, the use of a MAC index for a high number of points of time segments significantly increased the standard deviation of the percentage error. Therefore, a careful treatment of a maximum number of points of time segments and MAC index numbers regarding the variable level of system damping and degree of freedom of the system are an important element in achieving an accurate estimate of modal parameters. Therefore, the attempted simulations have confirmed the efficacy of the implemented analysis. This research serves as a base for future studies in enhancing the performance of the automated EFDD method as a modal information engine in structural health monitoring (SHM) systems by providing a better choice of a maximum number of points of time segments and MAC index number regarding the variable level of system damping and degree of freedom of the system.

ACKNOWLEDGMENTS

The authors would like to extend their greatest gratitude to the Institute of Noise and Vibration UTM for funding the current study under the Higher Institution Centre of Excellence (HICoE) Grant Scheme (R.K130000.7843.4J227 and R.J130000.7824.4J234). Additional funding for this research came from the UTM Research University Grant (Q.K130000.2543.11H36) and the Fundamental Research Grant Scheme (R.K130000.7840.4F653) from The Ministry of Higher Education, Malaysia.

REFERENCES

Bajrić, A., Georgakis T. C., & Brincker, R. (2015a, February 2-5). Evaluation of damping using frequency domain operational modal analysis techniques. In *Proceedings of the 33rd International Modal Analysis Conference* (pp. 351-355). Orlando, USA.

Bajric, A., Brincker, R., & Thöns, S. (2015b, May 12-14). Evaluation of damping estimates in the presence of closely spaced modes using operational modal analysis techniques. In *Proceedings of the 6th International Operational Modal Analysis Conference* (pp. 1-13). Gijon, Spain.

Brewick, P. T., & Smyth, A. W. (2013). An investigation of the effects of traffic induced local dynamics on global damping estimates using operational modal analysis. *Mechanical Systems and Signal Processing*, *41*(1-2), 433-453.

Bricker, R., & Venture, C. (2015). *Introduction to operational modal analysis*. Chichester, England: John Wiley and Sons, Ltd.

Brincker, R., Ventura, C. E., & Andersen, P. (2001a, February 5-8). Damping estimation by frequency domain decomposition. In *Proceedings of the 19th International Modal Analysis Conference* (pp. 698-703). Hyatt Orlando, USA.

Brincker, R., Zhang, L., & Andersen, P. (2001b). Modal identification of output-only systems using frequency domain decomposition. *Smart Materials and Structures*, *10*(3), 441-445.

Brincker, R., & Zhang, L. (2009, May 4-6). Frequency domain decomposition revisited. In *Proceedings of the 3rd International Operational Modal Analysis Conference* (pp. 615-626). Portonovo, Italy.

Chopra, A. K. (2001). *Dynamics of Structures: Theory and applications to earthquake engineering*. New Jersey, USA: Prentice Hall

Chou, J. Y., & Chang, C. M. (2020). Modal property extraction based on frequency domain stochastic subspace identification. In *Proceedings of the 13th International Conference on Damage Assessment of Structures* (pp. 303-313). Singapore: Springer.

Ewins, D. J. (2000). *Modal testing: Theory, practice, and application*. Hertfordshire, England: Research Studies Press.

Frans, R., & Arfiadi, Y. (2019). Structural system identification of plane frames based on frequency domain decomposition-natural excitation technique (FDD-NExT). *IOP Conference Series: Materials Science and Engineering*, *615*(1), 1-10.

Gade, S., Møller, N. B., Herlufsen, H., & Konstantin-Hansen, H. (2005, April 26-27). Frequency domain techniques for operational modal analysis. In *Proceedings of the 1st International Operational Modal Analysis (IOMAC) Conference* (pp. 261-271). Copenhagen, Denmark.

Ghalishooyan, M., Shooshtari, A., & Abdelghani, M. (2019). Output-only modal identification by in-operation modal appropriation for use with enhanced frequency domain decomposition method. *Journal of Mechanical Science and Technology*, *33*(7), 3055-3067.

Hwang, J. S., Kwon, D. K., & Kareem, A. (2019). Frequency domain state space–based mode decomposition framework. *Journal of Engineering Mechanics*, *145*(7), 1-45.

Jacobsen, N., Andersen, P., & Bricker, R. (2008, February 4-7). Applications of frequency domain curve-fitting in the EFDD technique. In *Proceedings of the 26th International Modal Analysis Conference* (pp. 1-13). Orlando, Florida.

Magalhães, F. (2010). *Operational modal analysis for testing and monitoring of bridges and special structures* (PhD Thesis). University of Porto, Portugal.

Magalhães, F., Cunha, Á., Caetano, E., & Brincker, R. (2010). Damping estimation using free decays and ambient vibration tests. *Mechanical Systems and Signal Processing*, *24*(5), 1274-1290.

Mironov, A., Doronkin, P., Priklonsky, A., & Kabashkin, I. (2015). Condition monitoring of operating pipelines with operational modal analysis application. *Transport and Telecommunication Journal*, *16*(4), 305-319.

Pioldi, F. (2012). *Sulla stima dello smorzamento modale mediante algoritmo frequency domain decomposition* [On the estimation of modal damping by frequency domain decomposition algorithm] (BSc. Thesis). Università di Bergamo, Italy.

Pioldi, F. (2013). *Sulla formulazione di algoritmi ottimizzati di identificazione dinamica modale e loro applicazione in ambito sismico* [On the formulation of optimized modal dynamic identification algorithms and their application in seismic fields] (MSc. Thesis). University of Bergamo, Italy.

Pioldi, F., Ferrari, R., & Rizzi, E. (2014, September 15-17). A refined FDD algorithm for operational modal analysis of buildings under earthquake loading. In *Proceedings of the 26th International Conference on Noise and Vibration Engineering* (pp. 3353-3368). Leuven, Belgium.

Pioldi, F., Ferrari, R., & Rizzi, E. (2016). Output-only modal dynamic identification of frames by a refined FDD algorithm at seismic input and high damping. *Mechanical Systems and Signal Processing*, *68*, 265-291.

Pioldi, F., Ferrari, R., & Rizzi, E. (2017). Earthquake structural modal estimates of multi-storey frames by a refined Frequency Domain Decomposition algorithm. *Journal of Vibration and Control*, *23*(13), 2037-2063.

Pioldi, F., & Rizzi, E. (2015, September 14-17). On modal identification of structures from earthquake response signals by a refined frequency domain decomposition approach. In *Proceedings of the 22nd Conference of the Associazione Italiana Di Meccanica Teorica E Applicata (AIMETA 2015)* (pp. 307-316). Genova, Italy.

Pioldi, F., & Rizzi, E. (2017). A refined frequency domain decomposition tool for structural modal monitoring in earthquake engineering. *Earthquake Engineering and Engineering Vibration*, *16*(3), 627-648.

Pioldi, F., & Rizzi, E. (2018). Earthquake induced structural response output only identification by two different operational modal analysis techniques. *Earthquake Engineering and Structural Dynamics*, *47*(1), 257-264.

Rainieri, C., & Fabbrocino, G. (2014). *Operational modal analysis of civil engineering structures*. New York, NY: Springer.

Rainieri, C., & Fabbrocino, G. (2015, May 12-14). Learning operational modal analysis in four steps. In *Proceeding of the 6th International Operational Modal Analysis Conference* (pp. 1-12). Gijón, Spain.

Rodrigues, J., Brincker, R., & Andersen, P. (2004, January 26-29). Improvement of frequency domain output-only modal identification from the application of the random decrement technique. In *Proceedings of the 23rd International Modal Analysis Conference* (pp. 92-100). Dearborn, Michigan, USA.

Tarinejad, R., & Damadipour, M. (2014). Modal identification of structures by a novel approach based on FDD-wavelet method. *Journal of Sound and Vibration*, *333*(3), 1024-1045.

Wang, T., Zhang, L., & Tamura, Y. (2005). An operational modal analysis method in frequency and spatial domain. *Earthquake Engineering and Engineering Vibration*, *4*(2), 295-300.

Zanchi, D. Z. (2011). *Identificazione dinamica modale di strutture mediante tecniche basate sul solo segnale di risposta* [Dynamic modal identification of structures using techniques based on the response signal only] (MSc. Thesis). Università di Bergamo, Italy.

Zhang, L., Brincker, R., & Andersen, P. (2005, April 26-27). An overview of operational modal analysis: Major development and issues. In *Proceedings of the 1st International Operational Modal Analysis Conference* (pp. 179-190). Copenhagen, Denmark.

Zhang, L., & Tamura, Y. (2003, September 16-18). Damping estimation of engineering structures with ambient response measurements. In *Proceedings of the 21st International Modal Analysis Conference* (pp. 226-233). Kissimmee, Florida.

Zhang, L., Wang, T., & Tamura, Y. (2010). A frequency-spatial domain decomposition (FSDD) method for operational modal analysis. *Mechanical Systems and Signal Processing*, *24*(5), 1227-1239.

APPENDIX

Nomenclature list

FDD	Frequency Domain Decomposition
SDOF	Single Degree of Freedom
MAC	Modal Assurance Criterion
SSI	Stochastic Subspace-Based Algorithms
OMA	Operational Modal Analysis
EMA	Experimental Modal Analysis
SVD	Singular Value Decomposition
PSD	Power Spectrum Density
LogDec	Logarithmic Decrement
HT	Hilbert Transform
NExt	Natural Excitation Techniques
CF	Correlation Function
SD	Spectral Density
SHM	Structural Health Monitoring
RUL	Remaining Useful Life

Pertanika J. Sci. & Technol. 28 (3): 829 - 838 (2020)

PERTANIKA JOURNALS

SCIENCE & TECHNOLOGY

Journal homepage: http://www.pertanika.upm.edu.my/

Simple Parallel Probe as Soil Moisture Sensor for Sandy Land in Tropical-Coastal Areas

Arief Sudarmaji[1]*, Saparso[2], Hadi Supriyo[3] and Anteng Widodo[4]

[1]Department of Agricultural Engineering, Faculty of Agriculture, Universitas Jenderal Soedirman, Jl. Dr. Soeparno, Karangwangkal Purwokerto 53123, Indonesia
[2]Department of Agrotechnology, Faculty of Agriculture, Universitas Jenderal Soedirman, Jl. Dr. Soeparno, Karangwangkal Purwokerto 53123, Indonesia
[3]Department of Agrotechnology , Faculty of Agriculture, Universitas Muria Kudus, Jl. Lingkar Utara UMK, Gondang Manis, Bae, Kudus,59327, Indonesia
[4]Department of Information System, Faculty of Engineering, Universitas Muria Kudus, Jl. Lingkar Utara UMK, Gondang Manis, Bae, Kudus,59327, Indonesia

ABSTRACT

One potential land in marginal areas able to be utilized for keeping the sustainability of agriculture in Indonesia is coastal areas. However it requires optimum treatment, especially in using the water for plants efficiently due to the factors of land characteristics and climate. This paper describes the use of simple and low-cost soil moisture probe for sandy land in the coastal area. The probe is a parallel plate which separated at a certain distance. The principle is based on soil electrical conductivity, which delivers the electrical current from one plate to another. Two designs (single and double) and two distances (3 mm and 5 mm) of probes were tested to measure the sandy soil at the moisture content of 0%, 5%, 10%, 15%, 20%, 25%, 30%, 35% and 40%. It was found that the resistance of probes was inversely proportional to water content, but not linear. The best fit of probe resistance (X) to the moisture of sandy soil (Y) was of the 5 mm double parallel probe, with the equation $Y = -10.33 \ln(X) + 128.13$ (R^2 is 0.9199) and non-linearity of 62.88%. The probes and a built soil moisture logger/ controller were applied for sandy soil of

ARTICLE INFO

Article history:
Received: 6 March 2020
Accepted: 14 May 2020
Published: 16 July 2020

E-mail addresses:
arief.sudarmaji@unsoed.ac.id (Arief Sudarmaji)
parso.fpunsoed@yahoo.co.id (Saparso)
hsupriyo@gmail.com (Hadi Supriyo)
anteng.widodo@umk.ac.id (Anteng Widodo)
*Corresponding author

ISSN: 0128-7680
e-ISSN: 2231-8526

© Universiti Putra Malaysia Press

Shallot cultivation land at coastal area in Empurancak Beach, Jepara (located about 150 m from the foreshore).

Keywords: Coastal area, parallel probe, sandy soil, soil moisture content

INTRODUCTION

In a developing country, like Indonesia, the decrease of agricultural land also occurs as an impact of a large number of land conversion functions becoming industrial or residential areas (Anandita & Patria, 2016). One potential land that can be utilized for agriculture is marginal land in the coastal area. Indonesia is an archipelagic country that has many islands, wide beaches, and coastal areas. Many marginal lands are scattered across islands which most not been explored and managed properly (Hutomo & Moosa, 2005). The development of coastal areas as agricultural land has strategic potency to overcome the decrease of agricultural land and to keep food sustainability as well.

However, the natural conditions of tropical-coastal area, such as the climate (dry and hot), the physical properties of soil (very high percolation and low water holding capacity), and hydrological conditions, require farmers to always monitor and keep the availability of water for plants intensively (Ray et al., 2014). Unfortunately, many farmers often give the water to plants irregularly either the amount or the time. The watering is not based on the availability of water in the soil. Meanwhile, the way to get water is mostly traditional and the watering is very costly.

Therefore, a simple device able to measure the soil moisture content *in-situ* rapidly and reliably is needed which can be applied in automated irrigation for water use efficiency. Irrigation is based on the soil moisture. Efficient irrigation will lead the least amount of water used directly to the plants to replenish the moisture of the root zone before water stress adversely impacts the plant. Automated irrigation systems can help to optimize water use by using soil moisture content and plant-specific information to provide irrigation application amount and timing decisions. Efficient irrigation conserves water and reduces potential leaching of agrichemicals (Ray et al., 2014; Sample et al., 2016).

The moisture of the soil depends upon various factors such as type of soil whether sandy, clay, or loam, and type of salts present in the soil such as iron, manganese, calcium, phosphorus, nitrogen and sulfur. It also depends upon temperature (Sample et al., 2016).

Soil water content can be measured directly or indirectly. Direct measurement is laboratory-based measurement. It is commonly known as the gravimetric method, measuring its weight as a fraction of the total soil weight. However, it is impracticable in the field. Recently there are many indirect methods/measurements that have been developed over the years to determine the soil moisture for automatic irrigation systems. They include

tension-measurement, neutron scattering measurement, spectrometric measurement (such as infra-red, near infra-red, and visible spectrometers), galvanic cell, dielectric/electromagnetic measurement (such as Time Domain Reflectometry, Frequency Domain Reflectometry, Time Domain Transmissometry, ADR, and Capacitance), and resistivity measurement (such as gypsum block, four-probe resistance, and ohm-probe electrode) (Bittelli, 2011; Gaikwad et al., 2015; Robinson, 2014; Sample et al., 2016).

Presently most commercial soil water sensors available today infer soil dielectric properties either from measured soil capacitance or impedance. It is based on the soil dielectric permittivity as the basis for determining soil water content. However mostly their techniques are costly and difficult to be adopted by farmers. Among others, resistance-based technique offers a simple, lower cost and reliable solution. Principally it is based on the conductivity properties of water contained in the soil. This paper presents an application of "easy self-made" resistance-based probe to measure the moisture sandy soil in tropical areas. Some constructions of the probe to examine its reliability were tested.

METHODS

Design of Soil Moisture Probe

The design of the soil moisture probe is shown in Figure 1. It is a parallel probe, which is separated at a certain distance by an acrylic block which keeps the probes apart. The probe is made of single-layer PCB coated by solder wire. Solder wire, made of silver-tin alloy, has high conductive properties and strength to being buried in the soil for a long time. It does not get corroded easily in the sandy soil. The length (L) and width (W) of the probe are 10 cm and 1 cm, respectively. The tip of the probe is made into a triangular shape, so that the probe can be easily inserted into the soil. The design is based on the probe construction of Tyagi et al. (2011).

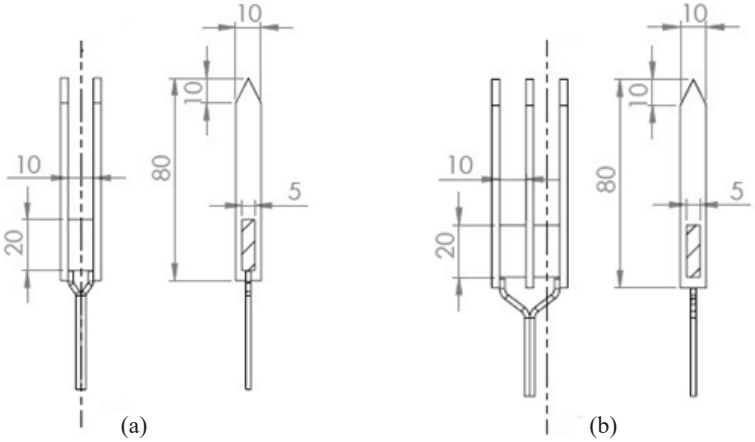

Figure 1. Design of 5 mm soil moisture probes: (a) single parallel and (b) double parallel, scale in mm

Two types of probes (i.e. single parallel and double parallel) with two distances of probes (i.e. 3 mm and 5 mm) were constructed and tested. Basically, double parallel probe is two parallel single probes joined in series. The distance of the probe is separated by 3 mm or 5 mm acrylic. Two cables are mounted as pinouts of the probes to be connected to the circuit of the sensor. A simple DC voltage divider is used as a conditioning circuit, with 56 kΩ fixed resistor to all probes.

The principle of the probe is the determination of soil moisture by measurement of electrical resistance of soil and porous media imbedded in the soil. Hence, a simple circuit of the voltage divider was applied as a conditioning circuit to convert the resistance of probe into direct voltage proportionally. And, an acquisition unit based on Arduino Mega2560 was built to acquire the array of probes which employ RTC-1302 as timer and 3.5 inch LCD 320x480 pixels as display. The data of measurements were logged into SPI-SD Card. The firmware of Arduino Mega2560 was built under Arduino Software (IDE) 1.8.12. Figure 2 shows the schematic of soil moisture measurement.

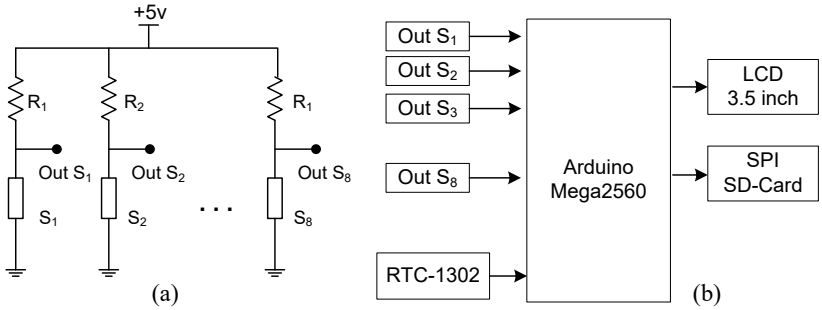

Figure 2. (a) Sensor circuit (where R is fixed 56 kΩ, S is soil moisture probe), and (b) diagram of soil moisture measurement

Sample of Sandy soil and Measurement Steps

Sandy soils were taken from coastal areas in Empurancak Beach, Jepara, Central Java, Indonesia. It is located at 6°29'09.7" S, 110°41'46.6" E. The water content of sandy soil was conditioned into the desired condition. Figure 3 shows the samples of sandy soil in certain water content. The Soil Water Content (SWC) is expressed in a dry-weight base. It is defined with the gravimetric method by measuring its weight as a fraction of the total soil weight as shown in Equation 1, where W_W is the weight of water and W_S is the weight of solid soil.

$$SWC = \frac{W_W}{W_S} x100\% \quad [1]$$

Samples of sandy soils were prepared to represent the soil condition from dried to saturated conditions, namely 0%, 5%, 10%, 15%, 20%, 25%, 30%, 35% and 40%. The

sample of sandy soil used was 1 kg for each experiment. The steps to prepare the sample of sandy soil in a certain value of SWC is as follow: firstly dry the soil using a drying oven at a temperature of 105°C and weight the soil repeatedly until the weight of the soil is constant (there is no difference of weight between any two consecutive measurements), which means that there is no water contained in soil (0% SWC). Secondly the weight of water added was calculated into the soil to get the desired value of SWC and finally adding water until evenly mixed.

After preparing the soil in particular SWC, the measurement of the probe to the SWC was done by means of the Arduino Mega2560 based-soil moisture acquisition device. The probes were placed inside the sandy soil horizontally. The sampling of resistance acquisition was set every two seconds in one minute. The measured resistance of probe was stored in a micro SD-card according to the date of measurement.

The tested treatments of the probe were the types of probe (i.e. single parallel and double parallel) and the distances of probes (i.e. 3 mm and 5 mm). Thus there were four kinds of probes tested. Each probe was made as many as eight units and the resistance of probe measured simultaneously using the built soil moisture acquisition device. Each measurement was repeated five times. Regression analysis was used as the statistical method to interpret the correlation between the resistance of probe and soil moisture. The flowchart of testing process is shown if Figure 4.

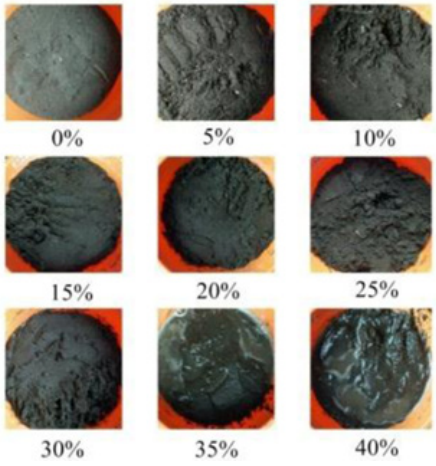

Figure 3. Samples of sandy soil in various water moistures

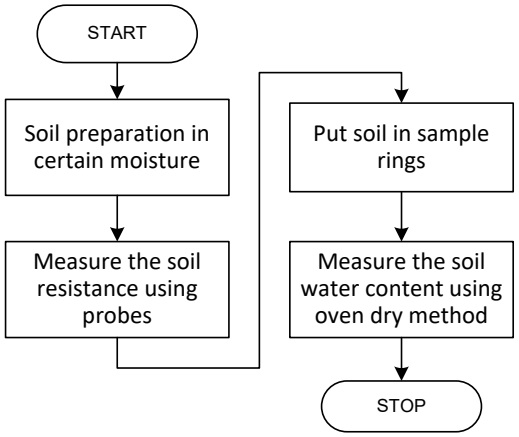

Figure 4. Testing process of the probes to moisture of sandy soil

RESULTS AND DISCUSSION

The Single and Double Parallel Probes

The shape and dimension of single and double parallel probes are shown in Figure 5. They are simple and hand-made probes. Basically, double parallel probe is two parallel single

probes joined in series. The probe transfers the electron from one probe to another and soil acts as the barrier of electron flow regarding to SWC of sandy soil. The value of probe resistivity is then obtained by acquiring the changes in voltage. It is an indirect method that measures another variable that is affected by the amount of soil water, and then it relates its changes to the SWC changes, through physically-based or empirical relationships called calibration curves (Bittelli, 2011).

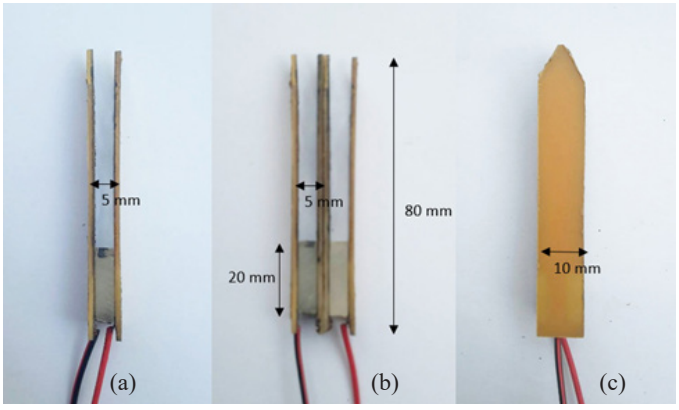

Figure 5. Photo of 5 mm (a) single and (b) double parallel probes, and (c) the side shape of probe

The electrical resistance of soil material is highly sensitive to small variations in water content and forms the basis of the parallel probe technique of measuring the soil moisture. Comparing to the gypsum block technique, the parallel probe gives simplicity and direct measurement to soil material. Gypsum block installation requires coring, taking considerable time and effort (Robinson, 2014). The main disadvantage of the gypsum block is that each block has different characteristics, depending on its shape and composition of materials, thus needing to be calibrated individually. And, the calibration tends to change gradually over time, limiting the accuracy and life of the gypsum block (Robinson, 2014; Zazueta & Xin, 1994).

Figure 6 and Figure 7 show the apparatus and diagram of measurement of sandy soil moisture respectively. The soil moisture probes were applied for Shallot cultivation. The probes were put horizontally 10 cm inside the soil. A 12-volt battery was used as a power supply to provide a constant DC voltage. The battery was recharged by the solar panel system.

Response of Simple Probe Sensor to Water Content

Soil samples from the field used for a sand-specific calibration were done under laboratory conditions, to ensure the reliable measurements. At the beginning, the resistivity of soil was investigated under dry and saturation states. When SWC was at 50%, it seemed that the sandy soil was at saturated condition. It was found that the electrical resistance of

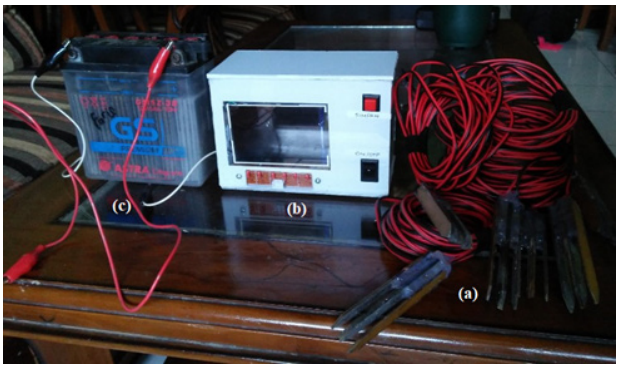

Figure 6. Measurement device of soil moisture, where a=double parallel probes, b = Arduino-based logger/ controller, and c=battery as power supply

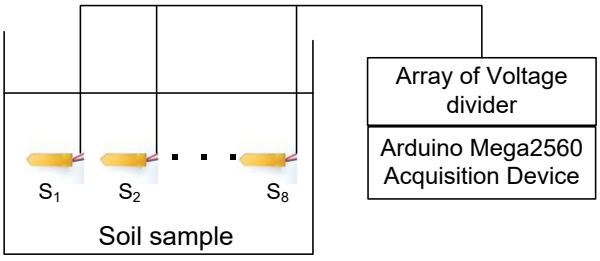

Figure 7. Measurement diagram of soil moisture

probe in a dry state (0% of SWC) and very low water content (less than 2% of SWC) was not available. The voltage output was 5 volts, the same with source voltage. It indicates there is no conduction of electron (electric current) through the soil. Electrical conduction in clean sandy soil occurs primarily in a liquid contained in the pores of soil (Jackson, 1975). Solid of the soil is usually insulators, when on the state of water contained in micro voids, it seems to be surface conduction of electrical current (Robain et al., 2003). While in state of saturation the voltage output is zero. It means no resistivity of soil, like the probe measures only the water. Therefore, the conditions of the dry state and saturated state are excluded from the correlation analysis. The steady-state time of the initial warm-up of the probe was also observed after the first installment inside the sandy soil. The responses showed that the initial response got steady at two minutes. Thus, the resistance of probe was acquired after a steady condition of probe in two minutes.

Figure 7 and Figure 8 show the responses of 3 mm and 5 mm probes to the SWC of sandy soil respectively. Generally, the responses showed a decrease in resistance in each increase in water content. That is a natural conductivity behavior of material in wet conditions. Water is conductive material to electrical current. The conduction of water contained in solid soil lies in the volume conduction phenomenon which is controlled by the electrolyte concentration in water and the geometrical structure of macro voids (Robain et al., 2003).

Figure 8 and Figure 9 reveal that the resistances of all probes are inversely proportional and nonlinear to the soil moisture. Overall the trends were similar. The experimental results obtained through laboratory tests on sandy soil samples for electrical resistance values corresponding to different moisture of sandy soil under 5V DC supply on voltage divider circuit showed that water content and electrical resistivity had a strong correlation and electrical resistivity of sandy soil was found to be decreasing with the increase of water content.

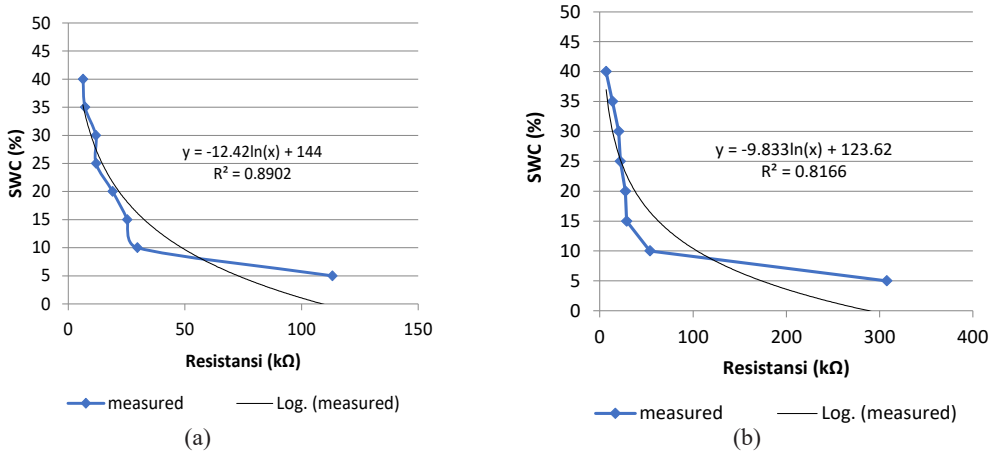

Figure 8. Response of 3 mm parallel probe to 5% to 40% of SWC, incremental in 5: (a) single probe and (b) double probe

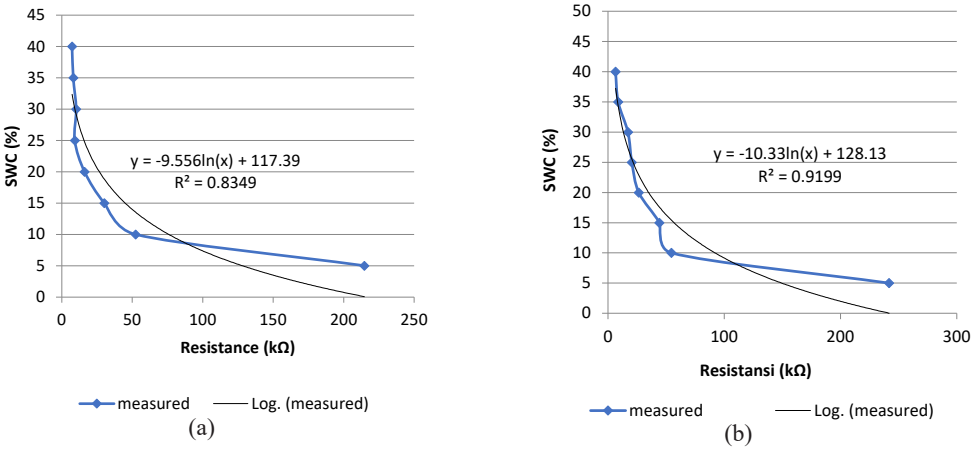

Figure 9. Response of 5 mm parallel probe to 5% to 40% of SWC, incremental in 5: (a) single probe and (b) double probe

The results of the regression analysis show that the logarithmic regression equation provides a high correlation between resistances of the probe to soil moisture content as can be seen in Table 1. This calibration outcome is closely in agreement with the result of those who applied the electrical resistivity principle to determine soil moisture level (Bhatt & Jain, 2014; Ozcep et al, 2010; Tyagi et al., 2011). Moreover, it also seems that

a 5 mm probe has a better correlation than a 3 mm probe. The fittest equation is a 5 mm double parallel probe, with 62.88% of non-linearity (Figure 10).

Table 1

The equation and correlation analysis of probes to change of SWC weight base model

Probe Type	Model	R^2
3 mm Single parallel probe	y = -12.42ln(x) + 144	0.8902
3 mm Double parallel probe	y = -9.83ln(x) + 123.62	0.8166
5 mm Single parallel probe	y = -9.56ln(x) + 117.39	0.8349
5 mm Double parallel probe	y = -10.33ln(x) + 128.13	0.9199

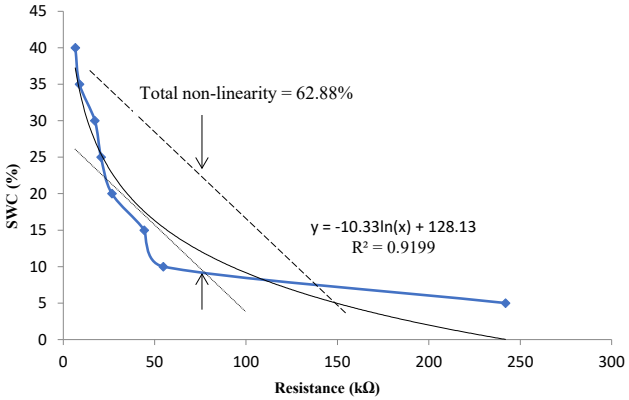

Figure 10. Non-linearity degree of 5 mm double parallel probe

CONCLUSION

A simple soil moisture sensor in parallel probe form has been successfully made from a pair of single layer PCB coated with solder wire and separated with thick acrylic. Its principle is based on the conductance properties of water contained in the soil. A simple voltage divider with 5 volt DC voltage is employed to drive the probe and a low-cost Arduino Mega2560 board is used as an acquisition device. Two types of probe (single and double) and two distances of probe (3 mm and 5 mm) were tested. The probes were tested for the sandy soil with its moisture at 0% to 40%. The results show-that the resistance of the probe is proportional inversely and nonlinear to the soil moisture. The higher moisture of soil, the lower resistance of probes. The steady conditions of the probes were in two minutes. The best fit of probe resistance (X) to the moisture of sandy soil (Y) is of the 5 mm double parallel probe, with the equation Y = -10.33 ln(X) + 128.13 (R^2 is 0.9199) and non-linearity of 62.88% of full range.

ACKNOWLEDGEMENTS

We would like to thank to Indonesian Directorate General of Higher Education (DIKTI), Universitas Jenderal Soedirman, and Universitas Muria Kudus. This research is supported by PKPT Research 2019 of the Indonesian Directorate General of Higher Education (DIKTI).

REFERENCES

Anandita, D. A., & Patria, K. Z. (2016). Agriculture challenges: Decline of farmers and farmland (study from Indonesian family life survey). *Jurnal Ilmu Ekonomi Dan Pembangunan*, *16*(1), 48-53.

Bhatt, S., & Jain, P. K. (2014). Correlation between electrical resistivity and water content of sand–a statistical approach. *American International Journal of Research in Science, Technology, Engineering and Mathematics*, *6*(2), 115-121.

Bittelli, M. (2011). Measuring soil water content: A review. *HortTechnology*, *21*(3), 293-300.

Gaikwad, P., Devendrachari, M. C., Thimmappa, R., Paswan, B., Kottaichamy, A. R., Kotresh, H. M. N., & Thotiyl, M. O. (2015). Galvanic cell type sensor for soil moisture analysis. *Analytical Chemistry*, *87*(14), 7439-7445.

Hutomo, M., & Moosa, M. K. (2005). Indonesian marine and coastal biodiversity: Present status. *Indian Journal of Marine Sciences*, *34*(1), 88-97.

Jackson, P. D. (1975). An electrical resistivity method for evaluating the *in situ* porosity of clean marine sands. *Marine Geotechnology*, *1*(2), 91-115.

Ozcep, F., Yıldırım, E., Tezel, O., Asci, M., & Karabulut, S. (2010). Correlation between electrical resistivity and soil-water content based artificial intelligent techniques. *International Journal of Physical Sciences*, *5*(1), 47-56.

Ray, P., Meena, B., & Nath, C. (2014). Management of coastal soils for improving soil quality and productivity. *Popular Kheti*, *2*(1), 95-99.

Robain, H., Camerlynck, C., Bellier, G., & Tabbagh, A. (2003). Laboratory measurements of electrical resistivity versus water content on small soil cores. *Geophysical Research Abstracts*, *5*, 1-2.

Robinson, B. (2014). *Devices for measuring soil moisture: Selecting sensors for use with the SoilWaterApp*. National Centre for Engineering in Agriculture, University of Southern Queensland, Australia: Grains Research and Development Coporation.

Sample, D. J., Owen, J. S., Fields, J. S., & Barlow, S. (2016). *Understanding soil moisture sensors: A fact sheet for irrigation professionals in Virginia*. Virginia, USA: Verginia Coorperative Extension.

Tyagi, A., Reddy, A. A., Singh, J., & Chowdhury, S. R. (2011). A low cost portable temperature-moisture sensing unit with artificial neural network based signal conditioning for smart irrigation applications. *International Journal on Smart Sensing and Intelligent Systems*, *4*(1), 94-111.

Zazueta, F. S., & Xin, J. (1994). *Soil moisture sensors* (Bulletin 292). University of Florida, USA: Florida Cooperative Extension Service.

Pertanika J. Sci. & Technol. 28 (3): 839 - 858 (2020)

PERTANIKA JOURNALS

SCIENCE & TECHNOLOGY

Journal homepage: http://www.pertanika.upm.edu.my/

Dual-Tree Complex Wavelet Packet Transform for Voice Pathology Analysis

Farah Nazlia Che Kassim[1]*, Hariharan Muthusamy[2], Vikneswaran Vijean[1], Zulkapli Abdullah[3] and Rokiah Abdullah[1]

[1]School of Mechatronic Engineering, Universiti Malaysia Perlis, Kampus Pauh Putra, 02600 UniMAP, Arau, Perlis, Malaysia
[2]Department of Biomedical-Engineering, SRM Institute of Science and Technology, SRM Nagar, Kattankulathur 603203 Kancheepuram District, Tamil Nadu, India
[3]Pusat Kejuruteraan, Universiti Malaysia Perlis, Kampus Pauh Putra 02600 UniMAP, Arau, Perlis, Malaysia

ABSTRACT

Voice pathology analysis has been one of the useful tools in the diagnosis of the pathological voice, as the method is non-invasive, inexpensive, and can reduce the time required for the analysis. This paper investigates feature extraction based on the Dual-Tree Complex Wavelet Packet Transform (DT-CWPT) using energy and entropy measures tested with two classifiers, k-Nearest Neighbors (k-NN) and Support Vector Machine (SVM). Massachusetts Eye and Ear Infirmary (MEEI) voice disorders database and Saarbruecken Voice Database (SVD) were used. Five datasets of voice samples were used from these databases, including normal and abnormal samples, Cysts, Vocal Nodules, Polyp, and Paralysis vocal fold. To the best of the authors' knowledge, very few studies were done on multiclass classifications using specific pathology database. File-based and frame-based investigation for two-class and multiclass were considered. In the two-class analysis using the DT-CWPT with entropies, the classification accuracy of 100% and 99.94% was achieved for MEEI and SVD database respectively. Meanwhile, the classification accuracy for multiclass analysis comprised of 99.48% for the MEEI database and 99.65% for SVD database. The experimental results using the proposed features provided promising accuracy to detect the presence of diseases in vocal fold.

Keywords: Dual-tree complex wavelet packet transform, file-based, frame-based, two-class and multiclass, voice pathology analysis

ARTICLE INFO

Article history:
Received: 24 February 2020
Accepted: 18 March 2020
Published: 16 July 2020

E-mail addresses:
nazlia@unimap.edu.my (Farah Nazlia Che Kassim)
hariharan.m@ktr.srmuniv.ac.in (Hariharan Muthusamy)
vikneswaran@unimap.edu.my (Vikneswaran Vijean)
zulkapli@unimap.edu.my (Zulkapli Abdullah)
rokiah@unimap.edu.my (Rokiah Abdullah)
*Corresponding author

ISSN: 0128-7680
e-ISSN: 2231-8526

© Universiti Putra Malaysia Press

INTRODUCTION

Pathological changes of the larynx are presented by the failure of the vocal fold to move continuously and properly, which can affect the voice. Voice changes may include loss of power, changes in the pitch, constriction of the voice range (i.e. displacement towards lower frequency), the addition of noises, and others (Vikram & Umarani, 2013). The precise laryngeal diagnostic methods like endoscopy and laryngoscopy used in clinical practice can cause discomfort to the patient, invasive, and expensive. By this reason, detection of the disease in its early stage is required. A precise voice signal diagnostic quantitative and non-invasive nature allows the identification and monitoring of vocal fold pathology, as well as reducing the time and cost required for detection.

Patient voice recording allows researchers to analyse a variety of parameters. The acoustics features identify the pathology based on the functioning and condition of various speech organs such as fundamental frequency, jitter, shimmer, harmonic to noise ratio, and intensity (Teixeira et al., 2013). A long duration of the signal is needed to extract the features in the time domain, which is tough to get from affected patients. For this reason, researchers start to explore the frequency domain analysis, which requires less data that offers more information. Mel Frequency Cepstral Coefficients (MFCC) has been reported as a very successful parameter for pathological voice detection (Srinivasan et al., 2014). Although MFCC is renowned and widely used, some limitations exist, such as low robustness to noisy signals (Harar et al., 2018). Mekyska et al. (2015), who studied the parameterisation techniques based on segmental features, such as MFCC and Linear Predictive Coding (LPC), provided the best classification results of 82.1%–100%. These techniques were, however, usually challenging to be clarified clinically. Among the limitations raised were identification of particular voice diseases and detection in its first stage or evaluation of its progress.

In recent times, enormous interest has emerged in wavelets approaches for pathological voice detection. Wavelet Packet Transform (WPT) was found to be an excellent tool for the analysis of non-stationary signals both in time and frequency scale (Hariharan et al., 2014). Decomposing a signal into wavelets rather than frequencies can give a much better resolution in the domain it is transformed into. Although a great deal of literature exists concerning voice pathology analysis, only a handful of them had employed time-frequency analysis for the investigation of pathology detections. This study focuses on investigating the use of DT-CWPT for voice pathology analysis. DT-CWPT produces complex coefficients using a dual-tree of wavelet filters to obtain real and imaginary coefficients. This would be useful as an effort to identify new features that can contribute to the overall best performance to detect the specific pathology.

Related Works

Voice pathology analysis focuses on employing signal processing techniques and machine learning algorithms to form a system capable of precise and accurate detection. Wavelet decomposition for feature extraction has been one of the great approaches in this field. Most works were done using file-based analysis, where the whole audio file is considered as the input signal to further classified as normal or pathological. Very few studies have been carried out as frame-based (Godino-llorente et al., 2005; Hariharan et al., 2014). Hariharan et al. (2014) proposed a new feature vector based on the WPT and singular value decomposition using four differently supervised classifiers, such as k-NN, least-square SVM, probabilistic neural network, and general regression neural network. In their paper, 100% classification accuracy was attained using the proposed features and classifiers for normal and abnormal vocal fold detection in both MEEI and MAPACI speech pathology database. Akbari and Arjmandi (2014) explored the possibility of applying the Discrete Wavelet Packet Transform (DWPT) to categorise 258 voiced samples, randomly selected from three pathologic classes and one normal class in MEEI database. The disordered voice samples comprised hyperfunction, gastric reflux, and A–P squeezing. Feature vectors optimised using Multiclass Linear Discriminant Analysis showed an average performance of 96.67% and 97.33% for Energy and entropy features, respectively classified by Multilayer Neural Network. Saidi and Almasganj (2015) obtained a good classification rate of 99.3% for normal and abnormal cases classified by SVM using extracted features from a five-band wavelet system. Features were extracted from a total of 57 normal and 653 pathological voice signals in the MEEI database containing sustained vowel /ah/ and speech sample pronounced the "Rainbow passage". Majidnezhad (2015) explored an initial feature vector based on the combination of the Wavelet Packet Decomposition (WPD) and the MFCC using a hybrid of the Artificial Neural Network (ANN) as the classifier, which gave 94.24% accuracy on the MEEI database and 95.3% accuracy on the Russian database (RusDS).

While most of the current work focuses on distinguishing normal (healthy) and abnormal (pathological) voices using various parameters, very little research on the multiclass classification system of different types of pathologies have been conducted. A study by Muhammad et al. (2017) on multiclass experimental results indicated that the Interlaced Derivative Pattern (IDP) based features using SVM gave greater accuracy than those using conventional MFCC and Multi-Dimensional Voice Program parameters in three different databases, which are the MEEI, SVD, and Arabic Voice Pathology Database (AVPD). The proposed IDP based features using SVM achieved 99.38% (MEEI), 93.2% (SVD), and 91.5% (AVPD) average accuracies for two-class classification. However, it is a

challenging task to compare between published papers, since their findings varied because of the differences in the chosen voice pathology samples from different databases, acoustic features implemented, and classifiers employed in the researches.

DT-CWPT introduced by Bayram and Selesnick (2008) had several properties such as the introduction of limited redundancy, reduced aliasing, and nearly shift-invariance, which were lacking in conventional WPT. Recently, the successful application of DT-CWPT in various fields such as mechanical fault diagnosis (Qu et al., 2016; Cao et al., 2019; Haidong et al., 2019), infant cry classification (Lim et al., 2018), speaker, and accent recognition (Abdullah et al., 2019) has been reported. Since the wavelet packet analysis has a reliable capability in identifying vocal fold pathology, this study aimed to investigate the use of DT-CWPT for analysing the voice signals using energy and entropy measures. Two-class and multiclass experiments were performed using the file-based and frame-based approach. Five datasets of voice samples for two-class and multiclass analysis from two databases were used for the investigation so that a direct comparison could be made with that of the previous studies.

METHODOLOGY

Figure 1 shows the block diagram of the proposed voice pathology analysis in this study.

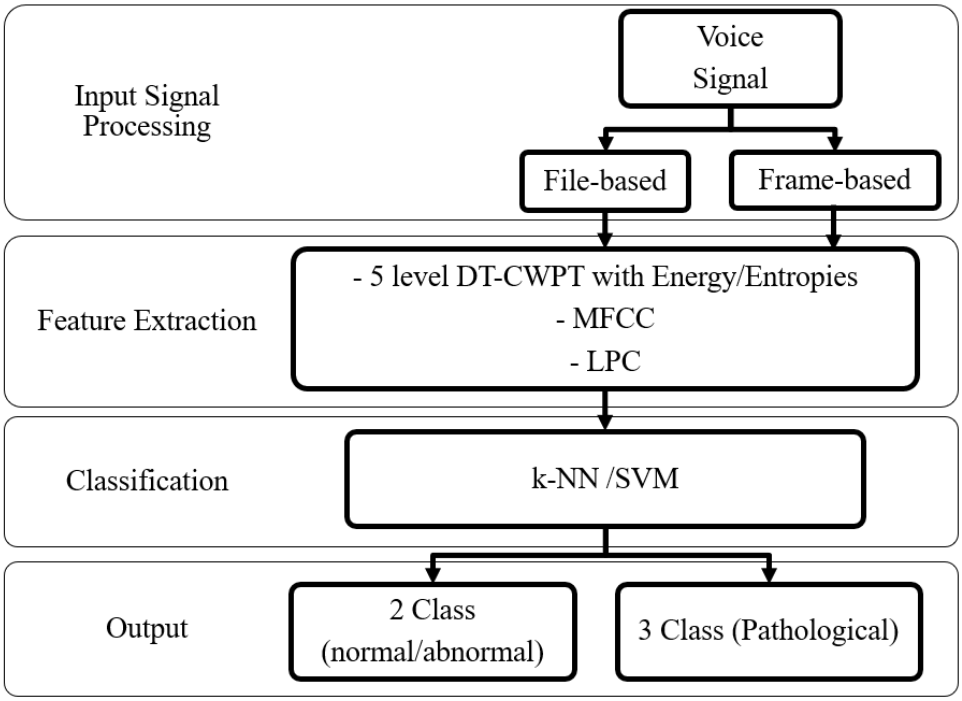

Figure 1. Block diagram of the proposed voice pathology analysis

Input Signal Processing

The voice signals from the normal person and patients suffering from disorders were acquired from the MEEI and SVD databases. Five datasets of voice samples were used from these databases, including normal and abnormal samples, Cysts, Vocal Nodules, Polyp, and Paralysis vocal folds. Table 1 shows the number of voice samples used as datasets for two-class and multiclass investigations.

Table 1

Number of samples for two-class and multiclass analysis

Dataset	Database	Analysis	Voice Sample			Total Samples
1	MEEI	Two-class	Class 1	Abnormal	173	226
			Class 2	Normal	53	
2	MEEI	Two-class	Class 1	Abnormal	106	159
			Class 2	Normal	53	
3	SVD	Two-class	Class 1	Abnormal	244	931
			Class 2	Normal	687	
4	MEEI	Multiclass	Class 1	Vocal nodules	19	106
			Class 2	Paralysis	67	
			Class 3	Polyp	20	
5	SVD	Multiclass	Class 1	Cysts	6	244
			Class 2	Paralysis	194	
			Class 3	Polyp	44	

The MEEI database, which is the most widely used and the only commercially available database, become a benchmark in the field of pathological speech analysis (Harar et al., 2018). Meanwhile, the SVD database, a freely downloadable database, was recorded by the Institute of Phonetics of Saarland University (Barry & Pützer, 2007). Only a few studies of voice pathology analysis have been explored in this database (Martinez et al., 2012; Muhammad et al., 2017). The voice signal files that only contained sustained normal pitch vowel /a/ samples were selected. All voice samples were down-sampled to have the same sampling frequency of 25 kHz due to the different recording sampling rates stored in this database. This rate was exploited because it satisfied the minimum rate specified by Nyquist and also the rate was mostly used in other referenced papers (Hariharan et al., 2014; Muhammad et al., 2017; Harar et al., 2018; Patil, 2019). This sample analysis was chosen to present outcomes comparable with previously published works. In the MEEI database, only samples of vocal nodules were available, while in SVD, cysts samples were

provided. Therefore, to investigate the three pathologies and to allow easier comparison between the MEEI and SVD databases, class 1 was represented to be either vocal nodules or cysts depending on the database employed.

However, unlike the previous works, file-based and frame-based analyses were conducted to produce a larger dataset. In the frame-based analysis, voice samples were segmented into frames of 40 ms long (as the voice are considered stationary in the period of 20–40 ms) using a Hamming window with 50% overlap (Shafik et al., 2009; Hariharan et al., 2014).

Feature Extraction

The DT-CWPT using energy and entropy measures are proposed as the feature extraction. It is an extended algorithm from the Dual-Tree Complex Wavelet Transform (DT-CWT), with two bands of DWPT operating in parallel (Bayram & Selesnick, 2008). The DT-CWT is a form of the discrete wavelet transform, which generates complex coefficients (real and imaginary) using a dual-tree of wavelet filters that offer a more productive signal analysis. This introduces limited redundancy (2m:1 for m-dimensional signals) and allows the transform to provide approximate shift-invariance and directionally selective filters (properties lacking in the traditional wavelet transform) while preserving the natural properties of perfect reconstruction and computational efficiency with good, well-balanced frequency responses (Selesnick et al., 2005). DT-CWPT has the same properties of DT-CWT i.e shift-invariance and excellent directional selectivity, with the advantage of fewer energy leakages into its negative frequency bands (Serbes et al., 2013).

As shown in Figure 2, each of the sub-bands should be repeatedly decomposed using low-pass/high-pass perfect reconstruction (PR) filter banks (FB) to construct DT-CWPT. The PR FBs should be chosen so that the response of each branch of the second wavelet packet FB is the discrete Hilbert transform of the corresponding branch of the first wavelet packet FB; thus, allowing each sub-band of the DT-CWPT to be analytic. The PR FB, which is used to decompose the first FB of the DT-CWT, should also be used to decompose the second FB to preserve the Hilbert transform relationship already satisfied by those branches. The high-pass branch of the first stage, $h_1^{(1)}(n)$ and $h'_1{}^{(1)}(n)$, satisfy $h'_1{}^{(1)}(n) = h_1^{(1)}(n-1)$, which is exactly the same relationship satisfied by the low-pass filters of the first stage, $h'_0{}^{(1)}(n) = h_0^{(1)}(n-1)$. The second wavelet packet FB is obtained by replacing the first stage filters $h_i^{(1)}(n)$ by $h_i^{(1)}(n-1)$ and by replacing $h_i(n)$ by $h'_i(n)$ for $i \in \{0,1\}$(Bayram & Selesnick, 2008).

DT-CWPT utilises dual-tree decomposition; thus, producing complex (real and imaginary) coefficients using dual-tree wavelet filters to the full binary tree. For j levels of decomposition, the wavelet packets produce 2^j different sets of coefficients. At level 5, both wavelet packet filters will generate a total of 64 sub-bands ($2^5 \times 2$). A matrix size of

64 × *M* composed of wavelet packet coefficient (sub-bands × coefficients) obtained, as described in Equation 1 below.

$$A = \left[C_5^1(M)\ \ C_5^2(M) \ldots\ C_5^{64}(M)\ \right]^T \quad [1]$$

To investigate the influence of wavelet levels, experiments using all levels from 1 to 5 ($[2^1 + 2^2 + 2^3 + 2^4 + 2^5] \times 2$), which produced 124 sub-bands were also conducted. The results just give a little difference in ±1%–2% accuracy with a longer computation time, so only the fifth level of DT-CWPT was chosen.

The Energy, Shannon and Renyi entropy measures were applied to the decomposed fifth level DT-CWPT sub-bands to extract a useful and straightforward feature vector. Those non-linear entropies were extracted to evaluate the subtle changes present in analysing non-stationary signals like speech signals and various bio-signals (Hariharan et al., 2018). The energy (EGY) of each wavelet packet sub-band coefficients was computed using Equation 2 below:

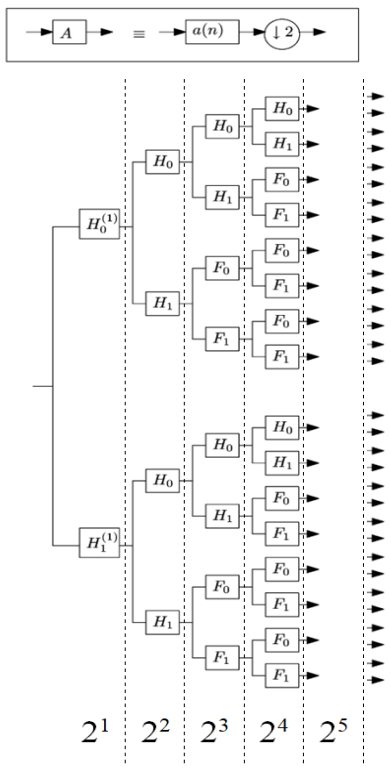

Figure 2. First wavelet packet FB of a five-level DT-CWPT. Note that the same decomposition mechanism also applies to the second wavelet FB.

$$EGY = \sum_{j,k} |C_{j,k}|^2 \quad [2]$$

The Shannon entropy defined by Equation 3, is an average information content measure that has been hidden in a signal. It's exploited to model the unpredictability and irregularities of a pathologic speech signal, as well as the possibility within a certain wavelet packet decomposition sub-band.

$$ShEn = -\sum_{j,k} C_{j,k} \log\left(C_{j,k}\right) \quad [3]$$

Renyi entropy is a well-known one-parameter generalisation of Shannon entropy. It is used to estimate the spectral complexity of a time series signal given by Equation 4 where α≠1.

$$ReEn = \frac{1}{1-\alpha} \log\left(\sum_{j,k} C_{j,k}^{\alpha}\right) \quad [4]$$

j=1, 2, 3,…*j*, where *j* is the number of decomposition level and *k*=1, 2, 3,…*N* is the number of wavelet packet coefficient in the respective sub-band.

The proposed method was then compared to the standard and well-known feature extraction methods, i.e. the MFCC and LPC (Alim & Rashid, 2018; Ankışhan, 2018). MFCC and LPC methods transform the voice signal from time-based to frequency-based domain while the DT-CWPT provides a time-frequency analysis of the voice signals. The 13 MFCC is chosen due to higher-order coefficients that represent increasing levels of spectral details; whereby depending on the sampling rate and estimation method, 12 to 20 cepstral coefficients are typically optimal for speech analysis (Huang et al.,2001; Virtanen et al., 2012). The order of ten for LPC is usually chosen since there is no significant improvement in sound quality for orders greater than ten (Ngo & Mehrubeoglu, 2010).

Classification

Two common classifiers, k-NN and SVM, were used to find the classification rate. The two-class analysis produced a result of normal or abnormal voice, while the multiclass analysis produced results according to the pathological voice. The k-NN classifier was chosen due to its simple implementation and flexibility to feature or distance choices (Abdullah et al., 2019). The classification was based on the majority of the k-Nearest Neighbor's category. In this study, k values were varied between 1 and 10. Instead of modelling the probability density of each class, SVM models the boundary between the classes. In biomedical applications, it is better to get a false alarm than a false negative, and the SVM seems to have better behaviour (Godino-Llorente et al., 2005). The best combination of two SVM parameters; cost (c) and gamma (γ) were obtained using LIBSVM Selection Tool (Chang & Lin, 2011). SVM was chosen since it has a better generalisation (less overfitting) and robust to noise.

In this work, a 10-fold cross-validation classification (CVC) scheme was used to increase the reliability of the results. Using this scheme, the extracted features were distributed into ten sets randomly, and ten times repetitive training was performed. To evaluate the two-class classifier performance, measures from the confusion matrix represented in Table 2 are considered. True positive (TP) measure of the classifier is classified as pathology when pathological samples are present, true negative (TN) classified as normal when normal samples are present, false positive (FP) classified as pathological when normal samples are present, and false negative (FN) classified as normal when pathological samples are present.

Table 2
Two-class confusion matrix

System decision	Actual diagnosis	
	Pathological	Normal
Pathological	True positive (TP)	False positive (FP)
Normal	False negative (FN)	True negative (TN)

The overall accuracy is calculated using the measures in Equation 5.

$$\text{Accuracy} = ((TP+TN)/ (\text{Total Samples})) \times 100\ \% \quad [5]$$

The performance of the multiclass analysis was evaluated by a confusion matrix represented in Table 3; where n = number of class. This matrix shows which points are correctly classified and which points are incorrectly classified. The number of test instances is shown by each matrix element for which the actual class is the row, and the predicted class is the column. Large numbers down the diagonal and small values (ideally zero) in the rest of the matrix relate to promising results.

Table 3
Multiclass confusion matrix

		Prediction			
		Class 1	Class 2	…	Class *n*
Actual	Class 1	Accuracy 1			
	Class 2		Accuracy 2		
	…			…	
	Class *n*				Accuracy *n*

The overall performance of the classifier is calculated as in Equation 6.

$$\text{Overall Accuracy} = \frac{(\text{Accuracy 1} + \text{Accuracy 2} + \ldots + \text{Accuracy n})}{\text{Total Samples}} \times 100\ \% \quad [6]$$

RESULT AND DISCUSSION

Overall, in this proposed work, the DT-CWPT based on Energy, Shannon and Renyi entropy, tested with k-NN and SVM classifiers yielded promising results. The results achieved better accuracy in the framed-based approach for all five datasets of voice samples compared to file-based analysis. Table 4 shows the two-class analysis for MEEI database (Dataset 1 and Dataset 2) and SVD database (Dataset 3). The proposed method, DT-CWPT with Shannon entropy, achieved the accuracy of 99.60% and 99.43% for Dataset 1 and 2 respectively while for Dataset 3, 94.60% obtained from DT-CWPT with Renyi entropy. From the Table 4, in the file-based approach the results outperformed the other two conventional methods (the highest accuracy of MFCC and LPC are 94.04% and 90.01% respectively). The frame-based experiment also gave good performance using the proposed method. The best performance was 100% accuracy score, achieved for both k-NN and SVM classifier in both Dataset 1 and 2, while the Dataset 3, best performance gave about 99.92% for k-NN and 99.94% for SVM.

Table 5 compares the proposed work with previous related researches for two-class analysis. The related works in Table 5 were selected because they used the same database and similar classifier as the proposed work. The difference in the feature extraction method employed would be an ideal opportunity to compare our results with those present in the

Table 4

Two-class analysis for the databases

2 CLASS	Classifier	Feature Extraction Method (no. of Coefficients)		Dataset 1 Accuracy (%) ± sd	Dataset 2 Accuracy (%) ± sd	Dataset 3 Accuracy (%) ± sd
FILE - BASED	KNN	DTCWPT (64)	Energy Entropy	88.54 ± 0.76	89.31 ± 1.22	81.34 ± 0.15
			Shannon Entropy	99.60 ± 0.14	99.43 ± 0.20	81.45 ± 0.35
			Renyi Entropy	92.83 ± 0.72	93.33 ± 0.80	82.41 ± 0.34
		MFCC (13)		82.12 ± 1.18	81.01 ± 1.51	84.61 ± 0.26
		LPC (10)		84.16 ± 0.75	83.08 ± 1.00	82.07 ± 0.40
	SVM	DTCWPT (64)	Energy Entropy	90.27 ± 0.81	88.93 ± 0.44	94.40 ± 0.30
			Shannon Entropy	99.20 ± 0.35	99.43 ± 0.20	90.01 ± 0.45
			Renyi Entropy	94.29 ± 0.64	91.76 ± 0.46	94.60 ± 0.29
		MFCC (13)		86.19 ± 0.85	85.28 ± 1.19	94.04 ± 0.35
		LPC (10)		87.21 ± 0.82	85.22 ± 0.68	90.01 ± 0.46
FRAME - BASED	KNN	DTCWPT (64)	Energy Entropy	100 ± 0.00	100 ± 0.00	99.88 ± 0.02
			Shannon Entropy	100 ± 0.00	100 ± 0.00	99.92 ± 0.02
			Renyi Entropy	100 ± 0.00	100 ± 0.00	99.88 ± 0.01
		MFCC (13)		100 ± 0.00	100 ± 0.00	99.97 ± 0.01
		LPC (10)		98.11 ± 0.10	99.53 ± 0.05	95.18 ± 0.09

Table 4 *(Continued)*

2 CLASS	Classifier	Feature Extraction Method (no. of Coefficients)		Dataset 1 Accuracy (%) ± sd	Dataset 2 Accuracy (%) ± sd	Dataset 3 Accuracy (%) ± sd
FRAME - BASED	SVM	DTCWPT (64)	Energy Entropy	99.99 ± 0.01	100 ± 0.00	99.94 ± 0.01
			Shannon Entropy	99.99 ± 0.03	99.97 ± 0.03	99.59 ± 0.03
			Renyi Entropy	100 ± 0.01	100 ± 0.00	99.94 ± 0.01
		MFCC (13)		99.99 ± 0.01	100 ± 0.00	99.92 ± 0.01
		LPC (10)		98.51 ± 0.11	99.73 ± 0.07	97.23 ± 0.05

Table 5

Overview of two-class analysis using MEEI subset (53 normal and 173 pathological)

Method	Feature	Classifier	Accuracy (%) ± sd	
			File-based	Frame-based
(Godino-Llorente et al., 2005)	MFCC with noise features	SVM	95.00 ± 2.00	94.10 ± 2.00
(Hariharan et al., 2014)	WPT	k-NN	99.65 ± 0.19	94.05 ± 0.83
		LS-SVM	99.12 ± 0.47	95.25 ± 0.12
(Majidnezhad (2015)	WPD with MFCC	ANN	94.24	-
(Muhammad et al., 2017)	IDP	SVM	99.38	-
Proposed	DT-CWPT	k-NN	99.60 ± 0.14	100 ± 0.00
		SVM	99.20 ± 0.35	100 ± 0.01

literature. Moreover, they had also analysed the data using a frame-based and file-based analysis, which is similar to the proposed work.

In the frame-based analysis, the proposed method demonstrated improvements in performance because more information in time and frequency scale was obtained from 5^{th} level proposed complex coefficients ($2\times2^5=64$) as compared to the 5^{th} level WPT coefficients

(2^5=32) proposed by Hariharan et al. (2014), thus generating real and imaginary tree fine resolution frequency sub-band data allowing for a better analysis. Moreover, a higher level of wavelet packet decomposition leads to better discriminative quality (Akbari & Arjmandi, 2014). These points contribute to better results performance compared to previous work.

These two-class accuracy results motivate the investigation of multiclass file-based and frame-based experiments for the other multiclass datasets in the databases. The complete results for multiclass analysis are shown in Table 6 and Table 7 for Dataset 4 and Dataset 5, respectively. The performance of the multiclass results was found not consistent. It is because of a limited number of pathology available and unevenly distributed number of samples from a different set of pathological voice in these databases. These limitations in the number and sample differences contribute to the accuracy performance for both databases.

It is known that the classification accuracy of vocal fold pathology detection systems is extremely dependent on the dataset and its characteristics, such as the volume of the dataset (Majidnezhad, 2015). Therefore, an adaptive synthetic (ADASYN) sampling approach is applied to imbalanced experimental datasets, to balance up the minority sample data to achieve better accuracy. ADASYN generates a weighted distribution for different minority class examples according to their level of difficulty in learning, where more synthetic data is produced for minority class examples that are harder to learn compared to those minority examples that are easier to learn. As a result, the ADASYN approach improves learning to the data distributions in two ways: reducing the bias introduced by the class imbalance, and adaptively shifting the classification decision boundary toward the difficult examples (He et al., 2008).

The proposed frame-based multiclass analysis using DT-CWPT with entropy and SVM yields a better average result ranging from 99.48%–99.65% as compared to 94.09%–98.80% obtained from its file-based analysis. However, the research on multiclass pathology analysis is lacking. The same database and almost similar datasets used by Muhammad et al. (2017) were applied in this work as a fair comparison, except for Class 1, where the authors used Cyst pathology for both MEEI and SVD database. The performances of file-based multiclass analysis of the proposed method are comparable, as indicated in Table 8.

Generally, both two-class and multiclass pathology detection using proposed DT-CWPT, produced better accuracy in the frame-based compared to the file-based analysis. This is because the frame based method framed the signal at 40ms per frame, which gives better time resolution analysis. It is known that speech signal exhibit quasi-stationary behaviour within the short period of time. In order to reduce feature loss and increase the continuity between adjacent frames in the framing, each frame is multiplied by Hamming window with 50% overlapped.

Nonetheless, the drawback of the frame-based analysis is that it takes a longer processing time due to more information obtained from all of the frames. The proposed feature methods also exhibit a small standard deviation (sd) showing the result ranges are more precise and give better performance using frame-based in both two-class and multiclass analyses.

Table 6

Three class classification for dataset 4

Dataset 4 (MEEI)	Classifier	Feature Extraction Method (no. of Coefficients)		Average Accuracy (%) ± sd	Class 1 Accuracy (%) ± sd	Class 2 Accuracy (%) ± sd	Class 3 Accuracy (%) ± sd
FILE - BASED (adasyn)	KNN	DTCWPT (64)	Energy Entropy	78.21 ± 0.77	95.97 ± 1.01	42.09 ± 1.97	96.57 ± 0.72
			Shannon Entropy	71.47 ± 1.12	92.19 ± 1.80	29.40 ± 2.64	94.09 ± 1.12
			Renyi Entropy	77.44 ± 1.18	97.10 ± 0.00	39.10 ± 2.88	95.52 ± 2.63
		MFCC (13)		77.15 ± 0.58	94.93 ± 1.02	44.93 ± 1.64	91.72 ± 1.96
		LPC (10)		71.96 ± 0.92	94.06 ± 1.27	31.04 ± 2.52	89.85 ± 1.46
	SVM	DTCWPT (64)	Energy Entropy	93.38 ± 0.91	99.40 ± 1.26	90.30 ± 1.27	90.45 ± 2.01
			Shannon Entropy	87.26 ± 1.56	86.09 ± 1.72	93.28 ± 1.27	82.27 ± 2.77
			Renyi Entropy	94.09 ± 0.99	94.35 ± 1.99	97.01 ± 0.00	90.90 ± 3.18
		MFCC (13)		90.75 ± 1.01	92.03 ± 1.23	95.07 ± 1.01	84.84 ± 2.95
		LPC (10)		83.82 ± 1.33	78.55 ± 2.54	95.67 ± 0.47	77.50 ± 2.20

Table 6 *(Continued)*

Dataset 4 (MEEI)	Classifier	Feature Extraction Method (no. of Coefficients)		Average Accuracy (%) ± sd	Class 1 Accuracy (%) ± sd	Class 2 Accuracy (%) ± sd	Class 3 Accuracy (%) ± sd
FRAME – BASED (adasyn)	KNN	DTCWPT (64)	Energy Entropy	99.42 ± 0.05	98.51 ± 0.00	99.80 ± 0.13	100 ± 0.00
			Shannon Entropy	99.34 ± 0.06	98.51 ± 0.00	99.59 ± 0.16	100 ± 0.00
			Renyi Entropy	99.43 ± 0.06	98.51 ± 0.00	99.98 ± 0.05	99.85 ± 0.19
		MFCC (13)		99.42 ± 0.02	98.51 ± 0.00	99.82 ± 0.05	100 ± 0.00
		LPC (10)		97.74 ± 0.09	98.62 ± 0.18	96.58 ± 0.29	98.02 ± 0.13
	SVM	DTCWPT (64)	Energy Entropy	99.44 ± 0.07	98.51 ± 0.00	100 ± 0.00	99.87 ± 0.21
			Shannon Entropy	99.48 ± 0.02	98.51 ± 0.00	99.98 ± 0.05	100 ± 0.00
			Renyi Entropy	99.47 ± 0.04	98.47 ± 0.10	100 ± 0.00	100 ± 0.00
		MFCC (13)		99.48 ± 0.00	98.51 ± 0.00	100 ± 0.00	100 ± 0.00
		LPC (10)		98.53 ± 0.12	98.47 ± 0.23	99.12 ± 0.19	98.02 ± 0.20

Table 7

Three class classification for dataset 5

Dataset 5 (SVD)	Classifier	Feature Extraction Method (no. of Coefficients)		Average Accuracy (%) ± sd	Class 1 Accuracy (%) ± sd	Class 2 Accuracy (%) ± sd	Class 3 Accuracy (%) ± sd
FILE - BASED (adasyn)	KNN	DTCWPT (64)	Energy Entropy	83.52 ± 0.50	100 ± 0.00	51.70 ± 1.48	98.03 ± 0.40
			Shannon Entropy	84.34 ± 0.30	100 ± 0.00	53.87 ± 0.70	98.42 ± 0.39
			Renyi Entropy	85.23 ± 0.38	100 ± 0.00	56.44 ± 1.12	98.75 ± 0.35
		MFCC (13)		87.38 ± 0.51	100 ± 0.00	64.74 ± 1.38	97.10 ± 0.39
		LPC (10)		85.33 ± 0.66	100 ± 0.00	61.49 ± 1.65	94.95 ± 0.76
	SVM	DTCWPT (64)	Energy Entropy	98.80 ± 0.26	100 ± 0.00	96.80 ± 0.59	99.56 ± 0.43
			Shannon Entropy	94.95 ± 0.61	100 ± 0.00	90.41 ± 0.81	94.43 ± 1.16
			Renyi Entropy	98.32 ± 0.39	100 ± 0.00	96.96 ± 0.75	98.00 ± 0.78
		MFCC (13)		96.77 ± 0.32	100 ± 0.00	97.58 ± 0.25	92.85 ± 0.82
		LPC (10)		93.36 ± 0.41	100 ± 0.00	90.05 ± 0.73	90.00 ± 1.60

Table 6 *(Continued)*

Dataset 5 (SVD)	Classifier	Feature Extraction Method (no. of Coefficients)		Average Accuracy (%) ± sd	Class 1 Accuracy (%) ± sd	Class 2 Accuracy (%) ± sd	Class 3 Accuracy (%) ± sd
FRAME – BASED (adasyn)	KNN	DTCWPT (64)	Energy Entropy	99.59 ± 0.01	100 ± 0.00	98.78 ± 0.03	100 ± 0.00
			Shannon Entropy	99.53 ± 0.03	100 ± 0.00	98.62 ± 0.06	99.98 ± 0.03
			Renyi Entropy	99.58 ± 0.03	100 ± 0.00	98.75 ± 0.09	100 ± 0.00
		MFCC (13)		99.63 ± 0.01	100 ± 0.00	98.89 ± 0.03	100 ± 0.00
		LPC (10)		97.39 ± 0.08	100 ± 0.00	94.06 ± 0.15	98.08 ± 0.14
	SVM	DTCWPT (64)	Energy Entropy	99.65 ± 0.01	100 ± 0.00	98.97 ± 0.00	99.99 ± 0.02
			Shannon Entropy	99.61 ± 0.02	99.98 ± 0.03	98.93 ± 0.06	99.93 ± 0.03
			Renyi Entropy	99.65 ± 0.01	99.99 ± 0.02	98.97 ± 0.00	99.99 ± 0.02
		MFCC (13)		99.64 ± 0.00	99.94 ± 0.00	98.97 ± 0.00	100 ± 0.00
		LPC (10)		99.04 ± 0.05	99.94 ± 0.00	97.57 ± 0.10	99.57 ± 0.09

Table 8
Accuracy of the methods for multiclass analysis (file-based)

Database / Method		Accuracy (%)			
		Class 1	Class 2	Class 3	Average
MEEI	Proposed DT-CWPT	94.35	97.01	90.90	94.09
	IDP (Muhammad et al., 2017)	99.10	94.30	94.50	95.97
SVD	Proposed DT-CWPT	100.00	96.80	99.56	98.80
	IDP (Muhammad et al., 2017)	99.50	95.90	95.10	96.83

Note: that the proposed class definition is as defined in Table 1

CONCLUSION

This work investigated feature extraction based on the DT-CWPT using energy and entropy measures tested with two classifiers, k-NN and SVM. The DT-CWPT performance as a feature extraction tool was proven to be reliable to detect the presence of diseases of the vocal fold. The proposed features yielded promising results and surpassed the conventional MFCC and LPC performance for file-based approach. A new set of features (real and imaginary coefficients) from the signal decomposition contribute to produce the best overall performance in detecting specific pathologies. The proposed system can be used to discriminate between two-class (normal and abnormal) and multiclass samples of voice pathologies. The experimental results using the proposed DT-CWPT features for the two-class analysis achieved 100% and 99.94% accuracy for MEEI and SVD database, respectively. Meanwhile, 99.48% for MEEI database and 99.65% for SVD database were achieved in multiclass. In future, it is hoped that more pathological samples can be obtained from these databases and also from other available databases so that more other specific pathology can be diagnosed and use worldwide. Feature optimisation can also be employed to further optimise the features obtained from DT-CWPT. It may include feature reduction and feature selection optimisation method.

ACKNOWLEDGEMENT

This work was done in part with data from the SVD database: http://www.stimmdatenbank.coli.uni-saarland.de/. The authors would like to thank the anonymous reviewers for their valuable comments.

REFERENCES

Abdullah, R., Muthusamy, H., Vijean, V., Abdullah, Z., & Kassim, F. N. C. (2019). Real and complex wavelet transform approaches for Malaysian speaker and accent recognition. *Pertanika Journal of Science and Technology*, *27*(2), 737-752.

Akbari, A., & Arjmandi, M. K. (2014). An efficient voice pathology classification scheme based on applying multi-layer linear discriminant analysis to wavelet packet-based features. *Biomedical Signal Processing and Control*, *10*(1), 209-223.

Alim, S. A., & Rashid, N. K. A. (2018). Some commonly used speech feature extraction algorithms. In R. Lopez-Ruiz (Ed.), *From natural to artificial intelligence-algorithms and applications* (pp. 4-22). London, UK: IntechOpen.

Ankışhan, H. (2018). A new approach for detection of pathological voice disorders with reduced parameters. *Electrica*, *18*(1), 60-71.

Barry, W. J., & Pützer, M. (2007). *Saarbruecken voice database*. Institute of Phonetics, University of Saarland. Retrieved July 9, 2018, from http://www.stimmdatenbank.coli.uni-saarland.de/

Bayram, I., & Selesnick, I. W. (2008). On the dual-tree complex wavelet packet and M-band transforms. *IEEE Transactions on Signal Processing*, *56*(6), 2298-2310.

Cao, X. C., Chen, B. Q., Yao, B., & He, W. P. (2019). Combining translation-invariant wavelet frames and convolutional neural network for intelligent tool wear state identification. *Computers in Industry*, *106*, 71-84.

Chang, C. C., & Lin, C. J. (2011). LIBSVM: A library for support vector machines. *ACM Transactions on Intelligent Systems and Technology (TIST)*, *2*(3), 1-27.

Godino-Llorente, J. I., Gomez-Vilda, P., Sáenz-Lechón, N., Blanco-Velasco, M., Cruz-Roldán, F., & Ferrer-Ballester, M. A. (2005). Support vector machines applied to the detection of voice disorders. *Lecture Notes in Computer Science*, *3817*, 219-230.

Haidong, S., Junsheng, C., Hongkai, J., Yu, Y., & Zhantao, W. (2019). Enhanced deep gated recurrent unit and complex wavelet packet energy moment entropy for early fault prognosis of bearing. *Knowledge-Based Systems, 188*, 1-14.

Harar, P., Galaz, Z., Alonso-Hernandez, J. B., Mekyska, J., Burget, R., & Smekal, Z. (2018). Towards robust voice pathology detection: Investigation of supervised deep learning, gradient boosting, and anomaly detection approaches across four databases. *Neural Computing and Applications*, *7*, 1-11.

Hariharan, M., Polat, K., & Yaacob, S. (2014). A new feature constituting approach to detection of vocal fold pathology. *International Journal of Systems Science*, *45*(8), 1622-1634.

Hariharan, M., Sindhu, R., Vijean, V., Yazid, H., Nadarajaw, T., Yaacob, S., & Polat, K. (2018). Improved binary dragonfly optimization algorithm and wavelet packet based non- linear features for infant cry classification. *Computer Methods and Programs in Biomedicine*, *155*(December), 39-51.

He, H., Bai, Y., Garcia, E. A., & Li, S. (2008). ADASYN: Adaptive synthetic sampling approach for imbalanced learning. *Proceedings of the International Joint Conference on Neural Networks*, *3*, 1322-1328.

Huang, X., Acero, A., Hon, H. W., & Foreword By-Reddy, R. (2001). *Spoken language processing: A guide to theory, algorithm, and system development*. Upper Saddle River, United States: Prentice Hall PTR.

Lim, W. J., Muthusamy, H., Vijean, V., Yazid, H., Nadarajaw, T., & Yaacob, S. (2018). Dual-tree complex wavelet packet transform and feature selection techniques for infant cry classification. *Journal of Telecommunication, Electronic and Computer Engineering (JTEC)*, *10*(1-16), 75-79.

Majidnezhad, V. (2015). A novel hybrid of genetic algorithm and ANN for developing a high efficient method for vocal fold pathology diagnosis. *Eurasip Journal on Audio, Speech, and Music Processing*, *1*, 1-11.

Martinez, D., Lleida, E., Ortega, A., Miguel, A., & Villalba, J. (2012). Voice pathology detection on the Saarbrücken Voice Database with calibration and fusion of scores using multifocal toolkit. *Communications in Computer and Information Science*, *328*, 99-109.

Mekyska, J., Janousova, E., Gomez-Vilda, P., Smekal, Z., Rektorova, I., Eliasova, I., … & López-de-Ipiña, K. (2015). Robust and complex approach of pathological speech signal analysis. *Neurocomputing*, *167*, 94-111.

Muhammad, G., Alsulaiman, M., Ali, Z., Mesallam, T. A., Farahat, M., Malki, K. H., … & Bencherif, M. A. (2017). Voice pathology detection using interlaced derivative pattern on glottal source excitation. *Biomedical Signal Processing and Control*, *31*, 156-164.

Ngo, H., & Mehrubeoglu, M. (2010). Effect of the number of LPC coefficients on the quality of synthesized sounds. *International Journal of Engineering Research and Innovation, 2*(2), 11-16.

Patil, H. A. (2019). Combining evidences from variable teager energy source and mel cepstral features for classification of normal vs. pathological voices. *European Signal Processing Conference*, *2019-September*(2), 1-5.

Qu, J., Zhang, Z., & Gong, T. (2016). A novel intelligent method for mechanical fault diagnosis based on Dual-tree Complex Wavelet Packet Transform and multiple classifier fusion. *Neurocomputing*, *171*, 837-853.

Saidi, P., & Almasganj, F. (2015). Voice disorder signal classification using M-Band wavelets and support vector machine. *Circuits, Systems, and Signal Processing*, *34*(8), 2727-2738.

Selesnick, I. W., Baraniuk, R. G., & Kingsbury, N. C. (2005). The Dual-tree complex wavelet transform. *IEEE Signal Processing Magazine*, *22*(6), 123-151.

Serbes, G., Aydin, N., & Gulcur, H. O. (2013). Directional dual-tree complex wavelet packet transform. *Proceedings of the Annual International Conference of the IEEE Engineering in Medicine and Biology Society, EMBS*, *2211*, 3046-3049.

Shafik, A., Elhalafawy, S. M., Diab, S. M., Sallam, B. M., & Abd El-samie, F. E. (2009). A wavelet based approach for speaker identification from degraded speech. *International Journal of Communication Networks and Information Security*, *1*(3), 52-58.

Srinivasan, V., Ramalingam, V., & Arulmozhi, P. (2014). Artificial neural network based pathological voice classification using MFCC features. *International Journal of Science, Environment and Technology*, *3*(1), 291-302.

Teixeira, J. P., Oliveira, C., & Lopes, C. (2013). Vocal acoustic analysis–jitter, shimmer and hnr parameters. *Procedia Technology*, *9*, 1112-1122.

Vikram, C. M., & Umarani, K. (2013). Pathological voice analysis to detect neurological disorders using MFCC and SVM. *International Journal of Advanced Electrical and Electronics Engineering, (IJAEEE)*, *4*, 87-91.

Virtanen, T., Singh, R., & Raj, B. (Eds.). (2012). *Techniques for noise robustness in automatic speech recognition*. Chichester, UK: John Wiley & Sons.

Pertanika J. Sci. & Technol. 28 (3): 859 - 878 (2020)

PERTANIKA JOURNALS

SCIENCE & TECHNOLOGY

Journal homepage: http://www.pertanika.upm.edu.my/

Health Risk Assessment among Adult and Children on Potential Air Pollutants Released from the Petrochemical Plant in Malaysia: The Result of Air Modelling

Mohd Shahrol Abd Wahil*, Wong Chin Mun, Abdullah Aliff Abdul Wahab and Hasni Ja'afar

Department of Community Health, Faculty of Medicine, UKM Medical Centre, 56000 Kuala Lumpur, Malaysia

ABSTRACT

Malaysia is the world's third largest exporter of liquified natural gas and the second largest oil and natural gas producer in Southeast Asia, following Indonesia. The potential air pollutants released from the industry may affect the health of the population. The primary objective of this study was to determine the potential health risk among the population in the zone of impact. This was a comparative case study between controlled and uncontrolled emissions based on the air dispersion modelling. Hazard quotient (HQ) was used to assess non-carcinogenic risk, while lifetime cancer risk (LCR) was used to assess carcinogenic risk. All ambient air pollutant levels were within permissible levels and adhered to the standard. The HQ for hydrogen sulphide and benzene was less than one in all scenarios. The LCR for benzene was acceptable in all scenarios. Advanced pollution prevention equipment should be installed within the gas emission system to treat the final emission to meet prescribed permissible limits. Continuous ambient air monitoring and effective control measures should be practiced to ensure the sustainability of clean air. The health risk assessment showed no risk of developing malignancy and non-cancer disorder among the workers and general population living surround the petrochemical plants. This allows the development of the petroleum refinery plants to be continued.

Keywords: Air modeling, health risk assessment, oil refinery, petrochemical plants, pollutants

ARTICLE INFO

Article history:
Received: 05 January 2020
Accepted: 27 March 2020
Published: 16 July 2020

E-mail addresses:
drshahrolaw@yahoo.com (Mohd Shahrol Abd Wahil)
chinmun0204@yahoo.com (Wong Chin Mun)
drabdullahaliff@gmail.com (Abdullah Aliff Abdul Wahab)
drmhasni1965@gmail.com (Hasni Ja'afar)
* Corresponding author

INTRODUCTION

Oil was first discovered in the Miri district of Sarawak in the early 1900s by one of the biggest oil and gas (OG) companies in the world. The oil exploration offshore

ISSN: 0128-7680
e-ISSN: 2231-8526

© Universiti Putra Malaysia Press

of Sarawak found success in 1962, followed by the very first oil field discovery offshore of Peninsular Malaysia in 1971 (Hamdan et al., 2005). That oil discovery promoted opportunity and encouraged more companies to invest in the upstream, midstream and downstream oil industries, including Malaysia's proud OG company, Petroliam Nasional Berhad, which was formed in 1974 in accordance with the Petroleum Act of 1974 (Federal Government Gazette, 1974). The government of Malaysia has contributed significantly towards policy and macroeconomic planning to secure the sustainable and long-term success of the oil and gas industry.

Malaysia is the world's third largest exporter of liquified natural gas and the second largest oil and natural gas producer in Southeast Asia, following Indonesia. As of January 2017, Malaysia held proven oil reserves of 3.6 billion barrels, the fourth largest reserve in Asia Pacific after China, India and Vietnam. Petroleum and other liquid production in 2016 was estimated to be 744,000 barrels per day, a 15% increase since 2013 (U.S Energy Information Administration, 2017). One of the petrochemical plants located in Peninsular Malaysia has the capacity to produce 300,000 barrels per day (Rahman, 2018). With the addition of petrochemical plants, total production of specialty petroleum products will be 3.15 million metric tonnes per year (Malaysian Petrochemicals Association, 2016).

Benzene is a simple cyclic organic compound that occurs naturally in crude oil and is a constituent of petrol (Duarte-Davidson et al., 2001). The petroleum refinery industry is a major source of benzene in the environment. Previous studies have shown the association between exposure to benzene and potential adverse health effects involving the reproductive system (including pregnancy outcomes), respiratory system, nervous system, haematological system and immune system (Gist & Burg, 1997; Marchetti et al., 2011; Protano et al., 2012; Reutman et al., 2002; Smith, 2010). Benzene is a known human carcinogen (IARC, 2018). There is sufficient evidence to support the association between benzene exposure and haematopoietic malignancy, acute myeloid leukaemia, myelodysplastic syndromes, and lymphoma and childhood leukaemia (Smith, 2010). In fact, these malignancies can even occur at low benzene concentrations (Rinsky et al., 1987).

Hydrogen sulphide is a colourless gas with a characteristic odour of rotten eggs that can be found at low concentrations in the petroleum refining industries. The impurities in crude oil include oxygen, sulphur, nitrogen and other heavy metals (Jafarinejad, 2016), while in petroleum products, almost all of the sulphur content comprise hydrogen sulphide, carbonyl sulphide and carbon sulphide (Stumpf et al., 1998). Previous human studies suggested that the respiratory and nervous systems were the most sensitive targets of hydrogen sulphide toxicity (ATSDR, 2016). Exposure to lower concentrations can result in less severe neurological and respiratory effects. Reported neurological symptoms include headache and fatigue and effects on concentration, balance, memory, cognition, motor function and mood (depression). Reported respiratory effects include nasal irritation, sore throat, cough, dyspnoea and alteration in lung function tests (Bahadori, 2014; Lewis &

Copley, 2015; Lim et al., 2016). Hydrogen sulphide is considered a non-human carcinogen because of limited human and animal studies available to prove the carcinogenicity of the substance (ATSDR, 2016).

Children can be considered as a specific subgroup within public health regulations that are more sensitive than the average adult. With regard to susceptibility to toxicants, differences between children and adults may result from a combination of toxicokinetic, toxicodynamic and exposure factors (Schwenk et al., 2003). Children have a faster ventilation rate than adults, and they have relatively greater lung volume compared to body surface area. Chemical disposition including lipid and water content of the body and quantity of plasma protein binding sites differs between children and adults and tends to increase the volume of distribution for many chemicals, leading to lower blood concentrations and longer chemical half-lives (Daston et al., 2004). Young children are also not fully developed in terms of metabolic and renal clearance. Taking into consideration these unique characteristics found in children, their health risk assessment is different than that for adults.

In one of the states in Peninsular Malaysia, the residential areas are now in close proximity to the petrochemical plants, providing an opportunity to evaluate the health effects of a single source of pollution. These petrochemical refinery plants are the only large pollution source in the region of these residential areas. Therefore, the primary objective of this study was to determine the potential health risk for the people at the project site as well as at the surrounding residential areas by measuring the quantitative risk assessment for potential air pollutants using an air dispersion model for controlled and uncontrolled emission.

METHODS

This is a comparative case study between controlled and uncontrolled emissions based on the air dispersion modelling done for a new proposed petrochemical and refinery integrated plants project (Figure 1) from the detailed environmental impact assessment (DEIA) conducted in the year 2012.

Baseline ambient air monitoring was carried out at a total of 14 monitoring stations at the project site, site boundaries and sensitive receptors within a 5 km radius in November 2012. A total of 10 parameters was monitored: total suspended particulates (TSP), particulate matter (PM_{10}), sulphur dioxide (SO_2), nitrogen dioxide (NO_2), mercury (Hg), hydrogen chloride (HCl), chlorine gas (Cl_2), hydrogen sulphide (H_2S), carbon monoxide (CO) and benzene (C_6H_6). The ambient air samples were collected by drawing air from the surrounding area through an absorbent media via a pre-calibrated portable pump stationed at the monitoring point. The high-volume sampler method was used to collect the air samples for TSP and PM_{10}. The air samples were then sent for laboratory analysis.

Figure 1. Location of petrochemical and refinery plants. Place (A): Village LB, place (B): Village RBB, place (C): Residence RJ, place (D): Village RSK. Places A, B, C and D are the areas with the highest predicted pollutant concentration during normal and abnormal operation simulations based on air dispersion modelling.

The point sources of air emissions during the operational phase were identified. A total of 68 stacks consisting of heater stacks, specific process stacks, steam and power generation stacks, and flaring stacks will release a variety of air pollutants. The major components of the air pollutants released from the proposed project are total suspended particles, nitrogen dioxide, sulphur dioxide, hydrogen sulphide and benzene. The simulation for air pollution exposure was carried out; one was done at a location close to the proposed project site, and another was done near 28 residential areas. Residential area is defined as a land use in which housing or residences predominate, which may also be used for the purpose of administrative, commercial, education, medical, sanitary, entertainment, or any purpose which the State Authority may think fit to authorize (Department of Environment Malaysia, 2012). Residential areas in this study include villages and residences surround the proposed project site within 5 km radius zone of impact.

Two emissions scenarios were simulated for each location which are:

(a) Normal operation - The exposure when the air pollution control device is functioning (controlled emission).
(b) Abnormal operation - The exposure to air pollution without the control device (uncontrolled emission).

The model used was the U.S American Meteorological Society/Environmental Protection Agency Regulatory Model (AERMOD) for pollution aerial dispersion (Seangkiatiyuth et al., 2011). The Gaussian Dispersion Model was used to estimate the pollutant dispersion distance based on the variation of the stack heights. To cover all receptors within a 5 km radius from the project site boundary, results in contours were illustrated on an 18 km × 10 km cartesian grid with 200 metre spacing. The results of the modelling are presented in an air pollutant contours diagram for different parameters with average times and scenarios for development. The air dispersion results were a secondary data that published for the project and were compared with the regulation guidelines. The reliability of the model had been endorsed by the Department of Environment Malaysia.

Specific guidelines were used as a reference for ambient air level monitoring. The guidelines used herein were the Recommended Malaysia Ambient Air Quality Standard 2015 (Department of Environment Malaysia, 2013), the Arizona Ambient Air Quality Guidelines 1999 (Arizona Department of Health Services, 1999), Ontario's Ambient Air Quality Criteria 2012 (Ontario Ministry of the Environment, 2012), and the WHO Air Quality Guidelines for Particulate Matter, Ozone, Nitrogen Dioxide and Sulphur Dioxide 2005 (World Health Organization, 2005).

Exposure Scenarios

Several exposure scenarios were simulated:

(a) Scenario 1 - Inhalation exposure of air pollutants among adults within project site during normal operation.
(b) Scenario 2 - Inhalation exposure of air pollutants among adults within project site during abnormal operation.
(c) Scenario 3 - Inhalation exposure of air pollutants among adults at surrounding residential areas during normal operation.
(d) Scenario 4 - Inhalation exposure of air pollutants among adults at surrounding residential areas during abnormal operation.
(e) Scenario 5 - Inhalation exposure of air pollutants among children at surrounding residential areas during normal operation.
(f) Scenario 6 - Inhalation exposure of air pollutants among children at surrounding residential areas during abnormal operation.

Risk Assessment of the Pollutant

Chronic Daily Intake for Inhalation. In general, the chronic daily intake of air pollutants through inhalation can be calculated by Equation 1 (United States Environment Protection Agency, 1989, 2009):

$$CDI_{inh} = C \times \frac{R_{inh} \times ET \times EF \times ED}{BW \times AT} \qquad [1]$$

Where, CDI_{inh} = Chronic daily intake for inhalation (mg/kg-day)
C = Concentration of air pollutant (mg/m^3)
R_{inh} = Inhalation rate (m^3/day)
ET = Exposure time (hours/24 hours)
EF = Exposure frequency (days/year)
ED = Exposure duration (years)
BW = Body weight (kg)
AT = Averaging time (days)

The concentration value (C) is based on the air dispersion modelling results. This concentration value is first converted from units of µg/m^3 to mg/m^3 (United States Environment Protection Agency, 2005). There were certain assumptions made in this study, as shown in Table 1. Physiologically, children inhale less than adults because of lower lung volume capacity than adults. Inhalation rates (R_{inh}) are calculated by the amount of the carrier medium crossing the boundary per unit time, measured as m^3 of air breathed per day. The estimated inhalation rate for children is 5 m^3/day, and for adults is 15 m^3/day (Du et al., 2013; Hong et al., 2017). The average body weight (BW) for Malaysian children aged 6 and 10 years old (Sandjaja et al., 2018) and adults (Lim et al., 2000) are approximately 13 kg, 19 kg and 58 kg respectively. However, in view of the prevalence of obesity in Malaysia increasing over the years for both children and adults (Naidu et al., 2013; Tan et al., 2019), therefore, the estimated average body weights for children and adults in this study were 20 kg and 70 kg respectively.

The pollutant exposure among children was not calculated for the project site since they were neither working nor staying at the petrochemical plants. According to the Malaysian Employment Act of 1955, an employee cannot be required under his or her contract of service to work more than eight hours in one day and 48 hours in one week. As an example, one of the petrochemical plants on the east coast of Peninsular Malaysia runs 24 hours a day seven days a week, which requires four different shift groups with each shift period lasting for 12 hours and individual shift workers generally working four shifts per week (Bahrin et al., 2004). Therefore, the exposure time (ET) in this example is 12 hours per

Table 1
Specific assumptions for exposure

Factor	Definition	Standard Unit	Scenario Specific Assumption		
			Within Project Site	Surrounding Communities	
			Adult	Children	Adult
*During Normal Operation Simulation					
C	Concentration of the pollutant	$\mu g/m^3$			
R_{inhal}	Inhalation rate	m^3/day	15	5	15
BW	Average body weight	kg	70	20	70
ET_{proj}	Exposure time	hours/24 hours	12	24	24
EF_{proj}	Exposure frequency	days/year	208	350	350
ED	Exposure duration	years	25	6	30
$AT_{noncarc}$	Average time (Non-carcinogen)	days	ED x 365 days	ED x 365 days	ED x 365 days
AT_{carc}	Average time (carcinogen)	days	70 years × 365 days	70 years × 365 days	70 years × 365 days
*During Abnormal Operation Simulation					
R_{inhal}	Inhalation rate	m^3/day	15	5	15
BW	Average body weight	kg	70	20	70
ET_{proj}	Exposure Time	hours/24 hours	12	24	24
EF_{proj}	Exposure frequency	days/year	2	2	2
ED	Exposure duration	years	25	6	30
$AT_{noncarc}$	Average time (Non-carcinogen)	days	ED x 365 days	ED x 365 days	ED x 365 days
AT_{carc}	Average time (carcinogen)	days	70 years × 365 days	70 years × 365 days	70 years × 365 days

day, and exposure frequency (EF) is four days per week for 52 weeks, or 208 days/year. An abnormal operation is expected to occur at least two times (days) per year.

The residential areas surrounding the project site are mostly villages, and the residents typically spend most of their lives in their village. Local activities involve agriculture, livestock, forestry, fisheries, culture, the local economy and tourism. The estimated exposure frequency for village residents in this study was 350 days per year, taking into account the period that the residents spend time outside of the area for activities such as vacation and festival celebration. The exposure duration (ED) was estimated at 30 years for non-carcinogen effects, so the average time (AT) was the number of days in 30 years. For carcinogenic effects, the risk is expressed as the excess probability of developing cancer over a lifetime, which is approximately 70 years by default.

Inhalation Reference Dose. The reference concentration (RfC) is an estimation of the maximum permissible risk to the human population through daily exposure, taking into consideration sensitive groups during a lifetime. The threshold RfC value can be used to indicate whether there are adverse health effects during a human lifetime. RfC is typically expressed as the chemical weight (mg) per volume (m^3) of air. Since the units for CDI_{inh} are in mg/kg-day, the RfC should be converted to reference dose (RfD_{inh}) in order to calculate the unitless hazard quotient (HQ). The risk screening environmental indicator (RSEI) method uses the standard adult human exposure factor for inhalation rate (20 m^3/day) and a body weight of 70 kg to convert the RfC (mg/m^3) to dosage units (mg/kg-day). The RfC value for each air pollutant is based on the United States Environment Protection Agency's Integrated Risk Information System (IRIS) as shown in Table 2. The conversion is calculated by the following Equation 2 (United States Environment Protection Agency, 2015):

$$RfD_{inh} = RfC \times \frac{1}{BW} \times R_{inh} \qquad [2]$$

Where, RfD_{inh} = Inhalation reference dose (mg/kg-day)
RfC = Reference concentration (mg/m^3)
BW = Body weight (kg)
R_{inh} = Inhalation rate (m^3/day)

Inhalation Cancer Slope Factor. The inhalation unit risk (IUR) is the upper-bound excess lifetime cancer risk estimated to result from continuous exposure to carcinogens at a concentration of 1 mg/m^3 in the air. The IUR is obtained from the database of the United States Environment Protection Agency's IRIS (United States Environment Protection Agency, 2005). The IUR is given in units of $\mu g/m^3$, which must be converted into units of mg/m^3 (multiplication by 1000). Similar to the RfC, the IUR expressed in units of exposure

Table 2
RfC values for potential air pollutants released from the industry

Air Pollutants	RfC (mg/m^3)	Reference
Total Suspended Particle (TSP)	Not available	-
Sulphur Dioxide (SO_2)	Not available	-
Nitrogen Dioxide (NO_2)	Not available	-
Hydrogen Sulphide (H_2S)	0.002	US EPA's IRIS 2003
Benzene (C_6H_6)	0.030	US EPA's IRIS 2003

RfC: Reference concentration
US EPA's IRIS: United States Environment Protection Agency's Integrated Risk Information System

(mg/m^3) must be converted to units of dose (mg/kg-day) for the calculation of toxicity relative to weight. An inhalation rate of 20 m^3/day and a body weight of 70 kg are used in Equation 3 (United States Environment Protection Agency, 2015):

$$CSF_{inh} = IUR \times BW \times \frac{1}{R_{inh}} \quad [3]$$

Where, CSF_{inh} = Inhalation cancer slope factor (1/(mg/kg-day))
IUR = Inhalation unit risk (1/(mg/m^3))
BW = Body weight (kg)
R_{inh} = Inhalation rate (m^3/day)

Hazard Quotient Estimation. For non-carcinogenic health effects of air pollutants, the risk is expressed as HQ, which is the average daily exposure divided by the reference dose. An HQ of less than 1 is considered safe, and adverse effects are unlikely even for sensitive populations (Equation 4) (United States Environment Protection Agency, 2009).

$$HQ = \frac{CDI_{inh}}{RfD_{inh}} \quad [4]$$

Where, HQ = Hazard quotient (unitless)
CDI_{inh} = Chronic daily intake for inhalation (mg/kg-day)
RfD_{inh} = Inhalation reference dose (mg/kg-day)

Lifetime Cancer Risk Estimation. Since benzene is the only confirmed human carcinogenic (category A) pollutant among the potential pollutant emissions in this study, the slope factor was used to calculate the cancer risk. The lifetime cancer risk (LCR) indicates the probability that an individual will develop cancer over a lifetime (70 years by default) as a result of exposure to a specific carcinogen. A cancer risk of one in a million (1×10^{-6}) means that if one million people are exposed, one cancer case would be expected. The United States Environment Protection Agency considers values within the range of 1×10^{-6} to 1×10^{-4} to be acceptable cancer risk for regulatory purposes. The LCR is calculated as in Equation 5 (United States Environment Protection Agency, 2009):

$$LCR = CDI_{inh} \times CSF_{inh} \quad [5]$$

Where, LCR = Lifetime cancer risk (unitless)
CDI_{inh} = Chronic daily intake for inhalation (mg/kg-day)
CSF_{inh} = Inhalation cancer slope factor $(mg/kg\text{-}day)^{-1}$

RESULTS

Ambient Air Monitoring

The results of the ambient air monitoring are shown in Table 3. For each air pollutant, despite the highest ambient air level chosen from the ambient air monitoring station locations (total of 14 stations), the concentration level was within permissible levels and adhered to the guidelines. The highest ambient air level for most of the air pollutants were recorded at monitoring station (AN1), located at the north-western boundary of the project site. The highest ambient air level for ammonia nitrogen (0.344 mg/m^3) and benzene (0.008 mg/m^3) were recorded at monitoring station (AN8), located one km north of the project site. The highest ambient air level for hydrogen chloride (0.208 mg/m^3) was recorded at the project site.

Predicted Maximum Ambient for Air Pollutants from Air Dispersion Modelling

The predicted maximum levels during normal and abnormal operation were predicted using air dispersion modelling at two different locations; the proposed project site and surrounding residential areas located within a 5 km radius (Table 4). Sulphur dioxide, nitrogen dioxide and hydrogen sulphide concentration levels were found to be higher than permissible levels during the abnormal operation simulation at the proposed project site with values

Table 3
Ambient air levels for air pollutants

Air Pollutants	Unit	Averaging Time (Hours)	Highest Ambient Air Level	Permissible Level
Total Suspended Particle (TSP)	µg/m^3	24	66.000[a]	260.000*
Particulate Matter (PM_{10})	µg/m^3	24	59.000[a]	150.000*
Sulphur Dioxide (SO_2)	ppm	24	<0.001[a]	0.100[#]
Nitrogen Dioxide (NO_2)	ppm	24	<0.001[a]	0.100[#]
Mercury (Hg)	µg/m^3	24	<0.001[a]	2.000[#]
Ammonia Nitrogen (NH_3N)	mg/m^3	8	0.344[b]	100.000[#]
Hydrogen Chloride (HCl)	mg/m^3	8	0.208[c]	20.000[#]
Chlorine Gas (Cl_2)	mg/m^3	8	<0.001[a]	10.000[#]
Hydrogen Sulphide (H_2S)	ppm	8	<1.000[a]	7.000[#]
Carbon Monoxide (CO)	ppm	8	<5.000[a]	10.000*
Benzene (C_6H_6)	mg/m^3	8	0.008[b]	Not available

The highest ambient air level for each air pollutant was chosen among 14 monitoring stations (AN1 until AN14) at the project site, site boundaries and sensitive receptors within a 5 km radius for the purpose of ambient air monitoring.
a: Location AN1- At north-western boundary of the project site
b: Location AN8- Approximately 1.0 km north of the project site
c: Location AN9- Within the project site, near the existing dump site
*: Recommended Malaysia Ambient Air Quality Standard 2015
#: Ontario's Ambient Air Quality Criteria 2012

of 106.4 μg/m^3, 190.7 μg/m^3 and 47.2 μg/m^3 respectively. A similar pattern was found at surrounding residential areas where nitrogen dioxide and hydrogen sulphide concentrations were found to be higher than permissible levels during the abnormal operation simulation in village RSK and village RBB with values of 96.8 μg/m^3 and 19.1 μg/m^3 respectively. The predicted maximum ambient air for all air pollutants were acceptable at all areas (within project site and residential areas) during normal operation.

Non-Cancer Risk Assessment

HQ for each air pollutant was calculated based on simulated scenario given (Scenario 1 to 6) as shown in Table 5. In general, the HQ for hydrogen sulphide and benzene were less than one in all scenarios indicating that the non-carcinogenic risk for human exposure to both air pollutants are deemed as acceptable. The highest HQ for hydrogen sulphide was 8.0×10^{-2} in scenario 5. The lowest HQ for hydrogen sulphide was 3.9×10^{-2} in scenario 4. The highest HQ for benzene was 3.9×10^{-1} in scenario 5. The lowest HQ for benzene was 3.2×10^{-3} in scenario 2. The HQ for children (scenario 5 and 6) was higher than adult (scenario 3 and 4) due to difference in body weight between these children and adult. The HQ for other air pollutants (total suspended particles, sulphur dioxide and nitrogen dioxide) cannot be calculated since the RfC of these air pollutants were not available in the database.

Table 4
Air dispersion modelling for potential air pollutants released from the industry

Air Pollutant	Pollutant Concentration (μg/m^3)				
	Total Suspended Particle (TSP)	Sulphur Dioxide (SO_2)	Nitrogen Dioxide (NO_2)	Hydrogen Sulphide (H_2S)	Benzene (C_6H_6)
Averaging Time (Hours)	24	24	24	24	8
Guideline Value	260.000*	105.000*	75.000*	7.000#	Not available
At project site					
Existing Baseline	30.000	3.000	2.000	0.000	0.300
Normal Operation	35.100	27.600	53.300	0.470	14.600
Abnormal Operation	174.100	106.400	190.700	47.200	47.100
At surrounding communities					
Existing Baseline	97.000	3.000	2.000	0.000	6.700
Normal Operation	98.300[a]	20.700[b]	35.500[b]	0.190[b]	13.800[b]
Abnormal Operation	127.700[a]	61.300[c]	96.800[d]	19.100[b]	26.100[b]

The highest air pollutant level for each simulation (normal and abnormal operation) surround the project site was chosen among the 28 communities.
a: Village LB- Within 500 m south of the project site
b: Village RBB- Approximately 2 km east of the project site
c: Residence RJ- Approximately 700 m south-eastern of the project site
d: Village RSK- Approximately 3 km east of the project site
*: Recommended Malaysia Ambient Air Quality Standard 2015
#: Ontario's Ambient Air Quality Criteria 2012

Table 5
Hazard quotient for potential air pollutants released from the industry

Scenario	Total Suspended Particle (TSP)			Sulphur Dioxide (SO_2)			Nitrogen Dioxide (NO_2)			Hydrogen Sulphide (H_2S)			Benzene (C_6H_6)		
	CDI (mg/kg-day)	RfD (mg/kg-day)	HQ (Unit-less)	CDI (mg/kg-day)	RfD (mg/kg-day)	HQ (Unit-less)	CDI (mg/kg-day)	RfD (mg/kg-day)	HQ (Unit-less)	CDI (mg/kg-day)	RfD (mg/kg-day)	HQ (Unit-less)	CDI (mg/kg-day)	RfD (mg/kg-day)	HQ (Unit-less)
Scenario 1	2.1×10^{-3}	-	-	1.7×10^{-3}	-	-	3.3×10^{-3}	-	-	2.9×10^{-5}	5.7×10^{-4}	5.0×10^{-2}	8.9×10^{-4}	8.6×10^{-3}	1.0×10^{-1}
Scenario 2	1.0×10^{-4}	-	-	6.2×10^{-5}	-	-	1.1×10^{-4}	-	-	2.8×10^{-5}	5.7×10^{-4}	4.8×10^{2}	2.8×10^{-5}	8.6×10^{-3}	3.2×10^{-3}
Scenario 3	2.0×10^{-2}	-	-	4.3×10^{-3}	-	-	7.3×10^{-3}	-	-	3.9×10^{-5}	5.7×10^{-4}	6.8×10^{-2}	2.8×10^{-3}	8.6×10^{-3}	3.3×10^{-1}
Scenario 4	1.5×10^{-4}	-	-	7.2×10^{-5}	-	-	1.1×10^{-4}	-	-	2.2×10^{-5}	5.7×10^{-4}	3.9×10^{-2}	3.1×10^{-5}	8.6×10^{-3}	3.6×10^{-3}
Scenario 5	2.4×10^{-2}	-	-	5.0×10^{-3}	-	-	8.5×10^{-3}	-	-	4.6×10^{-5}	5.7×10^{-4}	8.0×10^{-2}	3.3×10^{-3}	8.6×10^{-3}	3.9×10^{-1}
Scenario 6	1.7×10^{-4}	-	-	8.4×10^{-5}	-	-	1.3×10^{-4}	-	-	2.6×10^{-5}	5.7×10^{-4}	4.6×10^{-2}	3.6×10^{-5}	8.6×10^{-3}	4.2×10^{-3}

CDI: Chronic daily intake
RfD: Reference dose
HQ: Hazard Quotient

Cancer Risk Assessment

For the cancer risk assessment, benzene was the only toxicant classified as a known human carcinogen in the United States Environment Protection Agency Classification and the IARC Classification. Therefore, the cancer risk assessment was calculated only for benzene as shown in Table 6. In general, the LCR for benzene was lower than value of 1×10^{-6} in all scenarios, indicating that the risk of developing benzene-related malignancy over a lifetime duration of 70 years is very minimal. The highest LCR for benzene was 3.3×10^{-8} in scenario 3. The lowest LCR for benzene was 8.4×10^{-11} in scenario 6. The HQ for children (scenario 5 and 6) was lower than adult (scenario 3 and 4) due to difference in exposure duration between these children and adult.

Table 6
Lifetime cancer risk for benzene released from the industry

	Benzene (C_6H_6)		
Scenario	CDI (mg/kg-day)	CSF (mg/kg-day)$^{-1}$	LCR (Unitless)
Scenario 1	3.2×10^{-4}	2.7×10^{-5}	8.7×10^{-9}
Scenario 2	9.9×10^{-6}	2.7×10^{-5}	2.7×10^{-10}
Scenario 3	1.2×10^{-3}	2.7×10^{-5}	3.3×10^{-8}
Scenario 4	1.3×10^{-5}	2.7×10^{-5}	3.6×10^{-10}
Scenario 5	2.8×10^{-4}	2.7×10^{-5}	7.7×10^{-9}
Scenario 6	3.1×10^{-6}	2.7×10^{-5}	8.4×10^{-11}

CDI: Chronic daily intake
CSF: Cancer Slope Factor
HQ: Hazard Quotient

DISCUSSIONS

National standards vary according to health risks, technological feasibility, economic considerations and various other political and social factors, which in turn depend on the level of development and national capability for air quality management (Vahlsing & Smith, 2012). In order to develop a national standard, epidemiological and toxicological studies from locations with similar population sizes and geographical and meteorological factors should be considered. Regardless of the specific values set at the global level (WHO) or in specific regions (United States, Canada and countries in Europe) for ambient air quality standards, Malaysia is an individual country that should design and implement its own national plans based on economic strategies, political wills, local laws and regulations (Green et al., 2002).

There is no fix rule on choosing which air quality standard in the environmental health impact assessment (EHIA). The selection of the air quality standard should consider geographical and meteorological background, economic stability, government policy, and social acceptance. The author decided to choose the Recommended Malaysia Ambient Air

Quality Standard of 2015 (Department of Environment Malaysia, 2013) and the Ontario's Ambient Air Quality Criteria 2012 (Ontario Ministry of the Environment, 2012) from the various established air quality standards and guidelines.

The air dispersion model is a desirable prediction model that can provide estimations not only for mean concentrations but also for peak time-average concentrations in any time interval (Efthimiou et al., 2011). The model is routinely used to provide reliable estimates of air pollutant concentrations over a variety of timescales and areas, including estimating short- and long-term concentrations at sensitive receptor sites. It is also used to provide evidence for predicted concentrations from relevant sources of pollution so that mitigation actions can be applied to areas that are potentially affected. The air dispersion model can allow regulators to assess emissions and evaluate the effectiveness of mitigation strategies prior to permitting operations, and can provide additional information to improve exposure assessments (Douglas et al., 2017).

As shown in the air dispersion modelling, the industry is predicted to release acceptable concentrations of potential air pollutants namely; total suspended particles, sulphur dioxide, nitrogen dioxide, hydrogen sulphide and benzene during normal operations when the control measures for air emissions are functioning adequately. However, if there is a failure in any component of air emission control, the concentration of certain potential air pollutants such as sulphur dioxide, nitrogen dioxide and hydrogen sulphide will exceed acceptable levels, especially at the project site. The employees should be aware and properly trained to mitigate this issue. The concern should be focused on the surrounding population as well because of concentrations of nitrogen dioxide and hydrogen sulphide exceeding the permissible level.

This detailed environmental impact assessment was made in view of the project operating throughout its lifespan which is approximately 30 to 50 years. Any changes in the petrochemical refinery process and operation would subject for a new impact assessment. Therefore, this article is relevant as assumption made that no changes of process taken place to date. The health risk assessment for exposure to toxic pollutants in this study was carried out based on predictions using air dispersion modelling. Hence, the individual health risk assessment could not be calculated since no personal air monitoring was conducted. The values of the HQ and LCR are a general estimation. The HQ for hydrogen sulphide and benzene showed no risk (values less than one) during both operation simulations among adult and children. The LCR value for benzene showed a very low risk of developing benzene-induced haematological malignancy.

Control of Air Pollutants Emission from Petrochemical Plants

The major air pollutants that will be emitted from the petrochemical plants include total suspended particles, sulphur dioxide, nitrogen dioxide, hydrogen sulphide and benzene.

Certain control actions should be performed by the project management. Advanced pollution prevention equipment such as low nitrogen oxide burners, de-nitrogen oxide equipment, de-sulphur oxide equipment and dust collection equipment should be installed within the gas emission systems to treat the final emissions and to meet prescribed permissible limits as stipulated in the Environmental Quality (Clean Air) Regulation of 2014 (Federal Government Gazette, 2014).

Considering the feasibility of control technology, the most achievable control technology is recommended to reduce the emissions of the air pollutants that are anticipated to be produced from the project. The fuel source to be used for the proposed project is either the process gas, low-sulphur fuel oil, or natural gas, so the particulate matter produced from the waste gas is very low (McDonald et al., 2004). In addition, a scrubber or filter is installed to reduce the particulate matter in the waste gas emissions. In order to reduce the concentration of sulphur oxide emissions, process gas, low-sulphur fuel oil and natural gas are used as a fuel source for heater, cracker and boiler firing. Low nitrogen dioxide burners are employed for boiler and heater systems to reduce the flame temperature and hence decrease the generation of nitrogen oxides.

The process tail gas that contains hydrocarbons is treated in the recovery system before it is vented to the atmosphere. In emergency situations, any hydrocarbon in the unrecovered process tail gas is burned by flare. Hydrocarbon removal efficiency of up to 98% can be achieved in the flare burning process (Ismail & Umukoro, 2012). The flare system is equipped with a spare emergency electricity supply system and fuel to the flare system is transported via pressure force, so the efficiency of the flare system is affected during power failures (Bahadori, 2014). Regular maintenance of point sources of emissions should be done to ensure that the plant is operating at its optimum level and to comply with the emissions limits.

Continuous real-time stack emission monitoring by Department of Environment Malaysia should be done strictly as per required by the Environmental Quality (Clean Air) Regulation of 2014 at all point sources of emission in the petrochemical plants. The objectives of continuous monitoring are to ensure that the control devices function at full capacity, to ensure that the gases emitted from the stacks are below permissible level and to serves as the evidence for environmental legislation and enforcement.

Air Pollutants Mitigation

In the event of abnormal operations which may involve failure of the process equipment, the relevant plant should be temporarily shut down until it can resume normal operations. The project management should ensure that the project operation can be terminated within an hour. The failed equipment should then be repaired as soon as possible.

The monitoring of ambient air pollutant levels at the project site and at surrounding residential areas should be conducted and reported regularly by Department of Environment Malaysia. Health surveillance should be done by the nearest district health office to monitor the air pollutant related disease among the nearby population especially cardiovascular and respiratory morbidity and mortality. These data together with ambient air monitoring data are crucial to estimate the burden of disease among communities and to relate with potential air pollutant released from the petrochemical plants. The nearest government health clinic and hospital should be well-prepared and have strong capacity to cope with the unexpected numbers of patients.

During the event of uncontrolled emission of air pollutants, risk communication to the affected community should be delivered effectively. The community has right to know about the incident, the toxicant released, and the possible health risk to them. The company should be transparent not only to their stakeholders and investors, but also to the respective government agency, state authority, workers, public and the mass media. A good risk communication relieves the public panic and ensure effective mitigation action taken. Multi-agencies collaboration including District and State Authority, Department of Environment Malaysia, Ministry of Health Malaysia, Fire and Rescue Department of Malaysia, Royal Malaysia Police, Civil Defence Forces (*Angkatan Pertahan Awam*) and others is needed to ensure effective disaster management. Each agency has their specific function to provide necessary action.

Workers should comply with the safe work practice to minimize the risk to them and the surround people. They should wear appropriate and adequate personal protection equipment (PPE) while performing task at the petrochemical plants. Unsafe act should be avoided at the workplace such as smoking, not wearing appropriate respiratory protection while handling volatile organic compounds, not comply with standard operation procedure (Federal Government Gazette, 1994). The medical surveillance component of the health surveillance programme should be conducted among the workers periodically according to Occupational Safety and Health (Use and Standards of Exposure of Chemicals Hazardous to Health) Regulations 2000 (Federal Government Gazette, 2000) . In the same regulation, the worker should be removed from any work that exposed them to chemical hazardous to health.

Public have their role as well in this mitigation action. They should ensure good indoor air quality at home; avoid tobacco smoking, avoid use of household product-containing volatile organic compound, and others. Air cleaners for home use and office use can provide relief indoor but need to consider cost of purchasing and maintenance. The outdoor activities should be limited to reduce exposure towards the air pollutants. They should take care of their health and to seek medical attention if developed air pollutant-related diseases. Open burning should be prohibited. Public early warning system for example siren and alarm system at the petrochemical plants should be activated to alert the public when indicated.

CONCLUSIONS

In conclusion, the baseline ambient air concentrations for all air pollutants were found to be acceptable and below the permissible levels. The health risk assessment showed no risk of developing malignancy and non-cancer disorder among the workers and general population living surround the petrochemical plants. This allows the project to continue the development of the petroleum refinery plants and to operate at full capacity, providing advanced, efficient and well-maintained engineering control measures. Continuous monitoring by the oil and gas company and government authorities such as the Department of Environment of Malaysia should be done in areas prone to air pollution to fulfil the requirements of the laws and legislation. Oil and gas industries are very crucial to economic growth in Malaysia but should not forget the health complications that may arise from toxicant exposure if the emissions are not controlled.

ACKNOWLEDGEMENTS

The authors would like to thank the Department of Community Health, Faculty of Medicine, National University of Malaysia for the assistance given for this research.

REFERENCES

Arizona Department of Health Services. (1999). *Arizona ambient air quality guidelines (AAAQGs) 1999*. Retrieved March 19, 2020, from http://agriculturedefensecoalition.org/sites/default/files/pdfs/28A_1999_Arizona_Ambient_Air_Quality_Guidelines_1999_Draft.pdf.

ATSDR. (2016). *U.S. department of health and human services, public health service, toxicological profile for hydrogen sulfide and carbonyl sulfide*. Agency for Toxic Substances and Disease Registry. Retrieved March 19, 2020, from https://www.atsdr.cdc.gov/toxprofiles/tp114.pdf.

Bahadori, A. (2014). *Pollution control in oil, gas and chemical plants*. Cham, Switzerland: Springer International Publishing.

Bahrin, J. S., Sajahan, M. H., & Hamad, M. N. (2004). Emergency response programme in a petrochemical company in Malaysia. *Journal of Occupational Safety and Health, 1*(1), 3-8.

Daston, G., Faustman, E., Ginsberg, G., Fenner-Crisp, P., Olin, S., Sonawane, B., … & McLaughlin, T. J. (2004). A framework for assessing risks to children from exposure to environmental agents. *Environmental Health Perspectives, 112*(2), 238-256.

Department of Environment Malaysia. (2012). *Guideline for sitting and zonning of industry and residential areas* (2nd Rev. Ed). Retrieved March 19, 2020, from http://www.doe.gov.my/eia/wp-content/uploads/2012/02/Guidelines-For-Siting-and-Zoning-of-Industry-and-Residental-Areas-2012.pdf.

Department of Environment Malaysia. (2013). *Recommended Malaysia ambient air quality standard of 2015*. Retrieved March 19, 2020, from http://www.doe.gov.my/portalv1/wp-content/uploads/2013/01/Air-Quality-Standard-BI.pdf.

Douglas, P., Hayes, E. T., Williams, W., Tyrrel, S. F., Kinnersley, R., Walsh, K., … & Drew, G. H. (2017). Use of dispersion modelling for environmental impact assessment of biological air pollution from composting: Progress, problems and prospects. *Waste management, 70*, 22-29.

Du, Y., Gao, B., Zhou, H., Ju, X., Hao, H., & Yin, S. (2013). Health risk assessment of heavy metals in road dusts in urban parks of Beijing, China. *Procedia Environmental Sciences, 18*, 299-309.

Duarte-Davidson, R., Courage, C., Rushton, L., & Levy, L. (2001). Benzene in the environment: An assessment of the potential risks to the health of the population. *Occupational and Environmental Medicine, 58*(1), 2-13.

Efthimiou, G., Bartzis, J., Andronopoulos, S., & Sfetsos, A. (2011). Air dispersion modelling for individual exposure studies. *International Journal of Environment and Pollution, 47*(1-4), 302-316.

Federal Government Gazette. (1974). *Legal Notification P.U (B) Act 144: Petroleum Development Act 1974*. Retrieved October 3, 2019, from http://www.agc.gov.my/agcportal/uploads/files/Publications/LOM/EN/Act%20144%20-%20Petroleum%20Development%20Act%201974.pdf.

Federal Government Gazette. (1994). *Legal Notification Act 514: Occupational Safety and Health 1994*. Retrieved March 19, 2020, from https://www.dosh.gov.my/index.php/legislation/acts/23-02-occupational-safety-and-health-act-1994-act-514/file.

Federal Government Gazette. (2000). *Legal Notification P.U (A) 131/2000 Act 514: Occupational Safety and Health (Use and Standards of Exposure of Chemicals Hazardous to Health) Regulations 2000*. Retrieved March 19, 2020, from https://www.dosh.gov.my/index.php/legislation/eregulations/regulations-under-occupational-safety-and-health-act-1994-act-514/522-pua-131-2000-1/file.

Federal Government Gazette. (2014). *Legal Notification P.U (A) 151. Environmental Quality (Clean Air) Regulation 2014*. Retrieved September 16, 2019, from http://www.federalgazette.agc.gov.my/outputp/pua_20140604_P.U.%20%28A%29%20151-peraturan-peraturan%20kualiti%20alam%20sekeliling%20%28udara%20bersih%29%202014.pdf.

Gist, G. L., & Burg, J. R. (1997). Benzene-A review of the literature from a health effects perspective. *Toxicology and Industrial Health, 13*(6), 661-714.

Green, L. C., Crouch, E. A., Ames, M. R., & Lash, T. L. (2002). What's wrong with the National Ambient Air Quality Standard (NAAQS) for fine particulate matter (PM2. 5)? *Regulatory Toxicology and Pharmacology, 35*(3), 327-337.

Hamdan, M. K., Darman, N. B., Husain, D., & Ibrahim, Z. B. (2005, April 5-7). Enhanced oil recovery in Malaysia: Making it a reality. In *SPE Asia Pacific Oil and Gas Conference and Exhibition* (pp. 1-13). Jakarta, Indonesia.

Hong, S. H., Shin, D. C., Lee, Y. J., Kim, S. H., & Lim, Y. W. (2017). Health risk assessment of volatile organic compounds in urban areas. *Human and Ecological Risk Assessment: An International Journal, 23*(6), 1454-1465.

IARC. (2018). *Benzene Volume 120: IARC monographs on the evaluation of carcinogenic risk to humans*. Lyons: International Agency for Research on Cancer. Retrieved March 19, 2020, from http://www.inchem.org/documents/iarc/iarcmono/v120iarc.pdf.

Ismail, O. S., & Umukoro, G. E. (2012). Global impact of gas flaring. *Energy and Power Engineering, 2012*(4), 290-302.

Jafarinejad, S. (2016). Control and treatment of sulfur compounds specially sulfur oxides (SOx) emissions from the petroleum industry: A review. *Chemistry International, 2*(4), 242-253.

Lewis, R. J., & Copley, G. B. (2015). Chronic low-level hydrogen sulfide exposure and potential effects on human health: A review of the epidemiological evidence. *Critical Reviews in Toxicology, 45*(2), 93-123.

Lim, E., Mbowe, O., Lee, A. S., & Davis, J. (2016). Effect of environmental exposure to hydrogen sulfide on central nervous system and respiratory function: A systematic review of human studies. *International Journal of Occupational and Environmental Health, 22*(1), 80-90.

Lim, T., Ding, L., Zaki, M., Suleiman, A., Siti, S., Aris, T., & Maimunah, A. (2000). Distribution of body weight, height and body mass index in a national sample of Malaysian adults. *The Medical journal of Malaysia, 55*, 108-128.

Malaysian Petrochemicals Association. (2016, May 19-20). Malaysia petrochemical country report 2015. In *APIC - The Asia Petrochemical Industry Conference Singapore* (pp. 4-48). Singapore.

Marchetti, F., Eskenazi, B., Weldon, R. H., Li, G., Zhang, L., Rappaport, S. M., … & Wyrobek, A. J. (2011). Occupational exposure to benzene and chromosomal structural aberrations in the sperm of Chinese men. *Environmental Health Perspectives, 120*(2), 229-234.

McDonald, J. D., Harrod, K. S., Seagrave, J., Seilkop, S. K., & Mauderly, J. L. (2004). Effects of low sulfur fuel and a catalyzed particle trap on the composition and toxicity of diesel emissions. *Environmental Health Perspectives, 112*(13), 1307-1312.

Naidu, B. M., Mahmud, S. Z., Ambak, R., Sallehuddin, S. M., Mutalip, H. A., Saari, R., … & Hamid, H. A. A. (2013). Overweight among primary school-age children in Malaysia. *Asia Pacific Journal of Clinical Nutrition, 22*(3), 408-415.

Ontario Ministry of the Environment. (2012). *Ontario's ambient air quality criteria (AAQCs) 2012*. Retrieved March 19, 2020, from http://www.airqualityontario.com/downloads/AmbientAirQualityCriteria.pdf.

Protano, C., Scalise, T., Orsi, G., & Vitali, M. (2012). A systematic review of benzene exposure during pregnancy and adverse outcomes on intrauterine development and birth: still far from scientific evidence. *Annali di Igiene, 24*(6), 451-463.

Rahman, S. (2018). *Developing Eastern Johor: The pengerang integrated petroleum complex*. Singapore: ISEAS-Yusof Ishak Institute.

Reutman, S. R., LeMasters, G. K., Knecht, E. A., Shukla, R., Lockey, J. E., Burroughs, G. E., & Kesner, J. S. (2002). Evidence of reproductive endocrine effects in women with occupational fuel and solvent exposures. *Environmental Health Perspectives, 110*(8), 805-811.

Rinsky, R. A., Smith, A. B., Hornung, R., Filloon, T. G., Young, R. J., Okun, A. H., & Landrigan, P. J. (1987). Benzene and leukemia. *New England Journal of Medicine, 316*(17), 1044-1050.

Sandjaja, S., Poh, B. K., Rojroongwasinkul, N., Bao, K. L. N., Soekatri, M., Wong, J. E., … & Manios, Y. (2018). Body weight and BMI percentiles for children in the South-East Asian Nutrition Surveys (SEANUTS). *Public Health Nutrition, 21*(16), 2972-2981.

Schwenk, M., Gundert-Remy, U., Heinemeyer, G., Olejniczak, K., Stahlmann, R., Kaufmann, W., … & Gelbke, H. (2003). Children as a sensitive subgroup and their role in regulatory toxicology: DGPT workshop report. *Archives of Toxicology, 77*(1), 2-6.

Seangkiatiyuth, K., Surapipith, V., Tantrakarnapa, K., & Lothongkum, A. W. (2011). Application of the AERMOD modeling system for environmental impact assessment of NO2 emissions from a cement complex. *Journal of Environmental Sciences, 23*(6), 931-940.

Smith, M. T. (2010). Advances in understanding benzene health effects and susceptibility. *Annual Review of Public Health, 31*, 133-148.

Stumpf, Á., Tolvaj, K., & Juhász, M. (1998). Detailed analysis of sulfur compounds in gasoline range petroleum products with high-resolution gas chromatography–atomic emission detection using group-selective chemical treatment. *Journal of Chromatography A, 819*(1-2), 67-74.

Tan, S. T., Mohd-Sidik, S., Rampal, L., Ibrahim, N., & Tan, K. A. (2019). Are Malaysians getting fatter and rounder?: An updated systematic review (2009–2015). *Malaysian Journal of Medicine and Health Sciences, 15*(1), 63-77.

U.S Energy Information Administration. (2017). *Country analysis brief: Malaysia*. Retrieved September 11, 2019, from www.eia.gov/beta/international/analysis_includes/countries_long/Malaysia/malaysia.pdf.

United States Environment Protection Agency. (1989). *Risk assessment guidance for superfund volume 1 human health evaluation manual (Part A): Interim final*. Office of Solid Waste and Emergency Response Washington, DC. Retrieved March 19, 2020, from https://www.epa.gov/sites/production/files/2015-09/documents/rags_a.pdf.

United States Environment Protection Agency. (2005). *Human health risk assessment protocol chapter 7: Characterizing risk and hazard*. Multimedia Planning and Permitting Division, Center for Combustion Science and Engineering. Retrieved March 19 2020, from https://archive.epa.gov/epawaste/hazard/tsd/td/web/pdf/05hhrap7.pdf

United States Environment Protection Agency. (2009). *Risk assessment guidance for superfund volume 1: Human health evaluation manual (Part F, Supplemental Guidance for Inhalation Risk Assessment)*. Retrieved March 19, 2020, from https://www.epa.gov/sites/production/files/2015-09/documents/partf_200901_final.pdf.

United States Environment Protection Agency. (2015). *Technical appendix A: Toxicity weights for TRI chemicals and chemical categories*. Retrieved March 19, 2020, from https://www.epa.gov/sites/production/files/2015-12/documents/technical_appendix_a-toxicity_v2.3.4.pdf.

Vahlsing, C., & Smith, K. R. (2012). Global review of national ambient air quality standards for PM 10 and SO 2 (24 h). *Air Quality, Atmosphere and Health, 5*(4), 393-399.

World Health Organization. (2005). W*HO air quality guidelines for particulate matter, ozone, nitrogen dioxide and sulfur dioxide: Global update 2005: Summary of risk assessment*. Retrieved March 19, 2020, from https://apps.who.int/iris/bitstream/handle/10665/69477/WHO_SDE_PHE_OEH_06.02_eng.pdf?sequence=1.

Pertanika J. Sci. & Technol. 28 (3): 879 - 892 (2020)

PERTANIKA JOURNALS

SCIENCE & TECHNOLOGY

Journal homepage: http://www.pertanika.upm.edu.my/

Land Use Change using Geospatial Techniques in Upper Prek Thnot Watershed in Cambodia

Norin Khorn[1], Mohd Hasmadi Ismail[1]*, Norizah Kamarudin[1,2] and Siti Nurhidayu[1,2]

[1]Department of Forestry Science and Biodiversity, Faculty of Forestry and Environment, Universiti Putra Malaysia, 43400 UPM, Serdang, Selangor, Malaysia
[2]Institute of Tropical Forestry and Forest Product (INTROP), Universiti Putra Malaysia, 43400 UPM, Serdang, Selangor, Malaysia

ABSTRACT

Monitoring of land use change is crucial for sustainable resource management and development planning. Up-to-date land use change information is important to understand its pattern and identify the drivers. Remote sensing and geographic information system (GIS) have proven as a useful tool to measure and analyze land use changes. Recent advances in remote sensing technology with digital image processing provide unprecedented possibilities for detecting changes in land use over large areas, with less costs and processing time. Thus, the objective of this study was to assess the land use changes in upper Prek Thnot watershed in Cambodia from 2006 until 2018. Geospatial tools such as remote sensing and GIS were used to process and produce land use maps from Landsat 5 TM, Landsat 7 ETM+ and Landsat 8. The post-classification comparison was conducted for analysing the land use changes. Results show forest area was greatly decreased by 1,162.06 km^2 (33.67%) which was converted to rubber plantation (10.55 km^2), wood shrub (37.65 km^2), agricultural land (1,099.71 km^2), built-up area (17.76 km^2), barren land (3.65 km^2), and water body (14.69 km^2). Agricultural land increased by 1,258.99 km^2 (36.48%), while wood shrub declined by 161.88 km^2 (4.69%). Rubber plantation, built-up area, barren land, and water bodies were increased by 10.55 km^2 (0.31%), 33.64 km^2 (0.97%), 4.87 km^2 (0.14%) and 15.89 km^2 (0.46%), respectively. The decrease of forest and wood shrub had resulted due to population growth (1.8% from 2008 to 2019) and land

ARTICLE INFO

Article history:
Received: 20 March 2020
Accepted: 09 June 2020
Published: 16 July 2020

E-mail addresses:
norinkhorn7@gmail.com (Norin Khorn)
mhasmadi@upm.edu.my (Mohd Hasmadi Ismail)
norizah_k@upm.edu.my (Norizah Kamarudin)
sitinurhidayu@upm.edu.my (Siti Nurhidayu)
* Corresponding author

ISSN: 0128-7680
e-ISSN: 2231-8526

© Universiti Putra Malaysia Press

conversion for agricultural purposes. Hence, this study may provide vital information for wise sustainable watershed's land management, especially for further study on the effect of land use change on runoff in this area.

Keywords: Cambodia, land use change, Prek Thnot watershed, remote sensing-GIS, sustainable management

INTRODUCTION

Knowledge of land use is very crucial for many planning and management activities; and considered as a significant factor for modelling and understanding the earth's surface (Gribb & Czerniak, 2016). In fact, land use changes are affected by both natural phenomena and human activities. Natural events, including continental drift, glaciation, flooding, and tsunamis, and human activities including conversion of forest to agriculture, urban sprawl, and forest plantations have modified the dynamics of land use types worldwide. Land use changes caused by human activities have proceeded much quicker in recent decades than caused by nature. Consequently, almost all ecosystems of the world have significantly has been changed by humans (Giri, 2012). Moreover, timely and accurate information about land use change detection is significantly vital to understand relationships and interfaces between human and natural phenomena for better decision making (Lu et al., 2004). Therefore, data on land use and possibilities for their ideal use is vital for the selection, planning, and implementation of land use schemes to find such increased demands for basic human needs and prosperity.

Land use is one of the most accessible detectable indicators of human interference on land; thus, land use information is essential in any geographical database. Land use has become a sort of "boundary object" between varied disciplines in modern maps. This advancement enhances the intrinsic value of land cover information. Conversely, it poses new challenges for its harmonization and correct use by further enlarging the base of potential users. Any land surface is diverse, and the mapping standards to acquire, represent, and generalize land characteristics are about as varied as the land surface itself (Di Gregorio & O'Brien, 2012).

In many years geospatial technology such as remote sensing and geographic information system (GIS) are primarily tools which widely used for change detection in late decades. Remote sensing is used broadly to detect and monitor land use at varied scales (Giri, 2012; Sohl & Sleeter, 2012). Meanwhile, GIS provides a flexible environment for digital data collection, storage, display and analysis that is needed to detect changes (Lu et al., 2004). Lu et al. (2004) addressed various land use change detection techniques and showed that image differencing, principal component analysis, and post-classification comparison were the most common methods used for change detection. It is likely to demonstrate a model to estimate the trends in land uses in a particular period through the study of past land use changes. It may provide some basis for scientific and practical land-use planning,

management and ecological improvement in a specific study area and instruction for regional socio-economic development. Hence, up-to-date and accurate land cover change information is essential to understand and identify land use changes.

Furthermore, the analysis of land use change detection is still an active research topic, and the development of new techniques continues. For a new change detection technique, it is essential to be capable of implementing it effortlessly and of providing accurate change detection outputs related to trajectory change. Even though a variety of change detection techniques have been advanced, it remains difficult to decide a suitable method to implement accurate change detection for a specific research purpose or study area. Selecting an appropriate change detection technique requires deliberated consideration of the main impact drivers (Lu et al., 2004). In most developing countries like Cambodia, for example, such factors associating with population growth, economic development and competing demands for land have been dominant causes of land use change (Vadrevu et al., 2019). There is a significant statistical correlation between population growth and land use conversion in most African, Asian, and Latin American countries (Lambin & Meyfroidt, 2011; d'Amour et al., 2017). Many studies addressed that a change of land use considerably affected other hydrological matters in the watershed or river basin such as water quality (Kumar et al., 2019), runoff (Samie et al., 2019), soil erosion (Tsegaye, 2019), sedimentation (Munoth & Goyal, 2019) and flooding (Szwagrzyk et al., 2018). Beside Prek Thnot watershed is among the basins in Cambodia that are having the highest risk of impairment which leads to different disasters, such as droughts, flood, pest and diseases, and storms that affect people's food and nutrition security, due to various incompatible land uses (FA & APFNet, 2016). Therefore, the objective of this study was to assess the land use changes in upper Prek Thnot watershed in Cambodia from 2006 until 2018.

MATERIALS AND METHODS

Study Area

Prek Thnot watershed area is about 6,666 km^2 (FA & APFNet, 2016) which partly covers several provinces namely Kampong Speu, Kampot, Koh Kong, Preah Sihanouk, Takeo, Kandal, and Phnom Penh city of the Kingdom of Cambodia. The upstream part of Prek Thnot watershed is in Kampong Speu province. Prek Thnot watershed plays a vital role in providing ecosystem services and supporting the livelihoods and production systems of the downstream communities. The Prek Thnot River flows from the Cardamom Mountains in the southwest of Cambodia towards Bassac River, a part of Mekong River, which is between latitudes 11°00' to 12°10' N and longitudes 103°80' to 105°00' E (Figure 1). It is dominated by a tropical monsoon climate that having two specific seasons, such as the rainy season (May-October) and the dry season (November-April). Generally, the slope of the watershed of Prek Thnot River lies in the eastern facing slope.

The delineated boundary was employed by using watershed delineation tool in ArcGIS 10.4.1 software using digital elevation map (DEM). The geospatial data model was created to produce flow accumulation lines and ultimately delineate a catchment using the Spatial Analyst tools. The watershed delineation was based on the 'eight-pour point' algorithm (Jenson & Domingue, 1988; Jenson 1991), which included pit filling, calculation of flow direction and flow accumulation. From the flow accumulation grids, stream networks were extracted. Streams are defined wherever drainage areas are higher than the specified threshold value. The border was created from 30 m spatial resolution from OpenTopography (http://opentopo.sdsc.edu) to determine the entire land area contributing to flow in a stream. As a result, the study area is in the upper Prek Thnot watershed, which widely locates in Kampong Speu province. It covers 3,450 km^2 and lies between latitudes of 11°00' and 12°10' N and longitudes of 103°40' and 104°20' E (Figure 1).

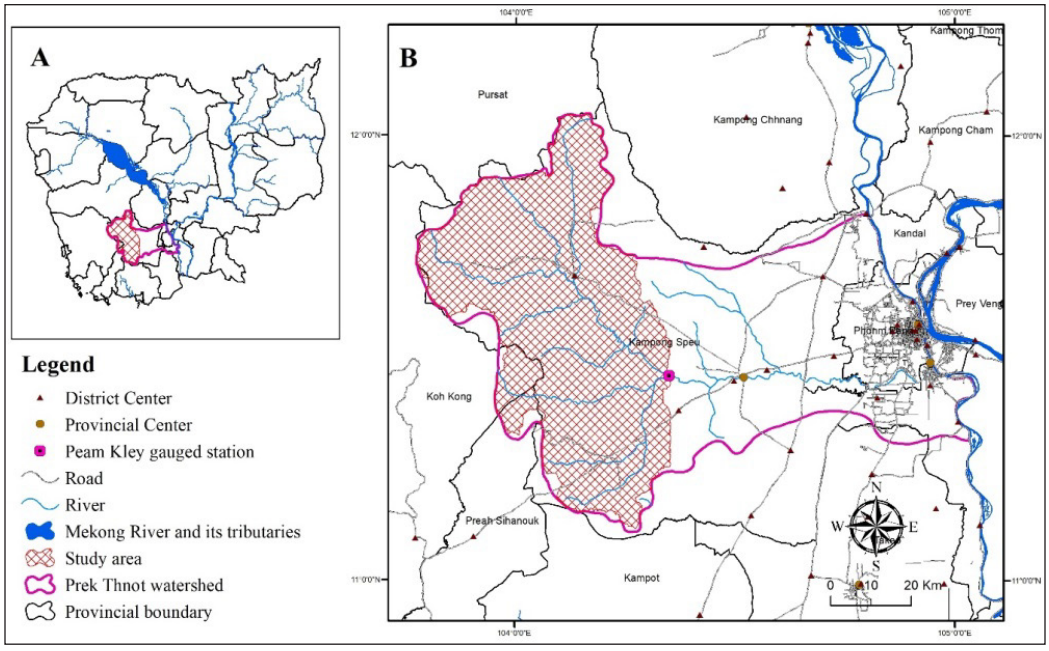

Figure 1. Study area; (A) Cambodia map and (B) Prek Thnot watershed area

Data Source

The land use data in 2006 and 2018 were obtained from remote sensing imageries (Landsat 5 TM, Landsat 7 ETM+ and Landsat 8). These imageries were provided by the Forestry Administration (FA) and the Ministry of Environment (MOE) of the Kingdom of Cambodia. The image processing, classification and accuracies of the land use maps were carried out in collaboration with national and international experts including from FAO-UNREDD, JICA-CAMREDD and international universities, Forestry and Forest Products Research

Institute, Japan (FFPRI) (FA, 2016; MOE, 2018). Maximum likelihood classification (MLC) approach was used for land use change assessment. It was found that MLC was appropriate and most used and convenient to apply with satisfactory accuracy. All maps projection was projected to Universal Transverse Mercator (UTM) coordinate system, zone 48, with World Geocoded System (UTM WGS 84) projection parameters. The overall accuracies reported form the land use classification ranging from 85% to 90%. The original land uses type were classified under the national level scheme for the country based on the classification as shown in Table 1. Based on this classification, there are 17 land use classes were used for the country namely evergreen forest, semi-evergreen forest, deciduous forest, pine forest, forest regrowth, bamboo, tree plantations, rubber plantation, wood shrub, grassland, paddy field, cropland, built-up area, village, rock, sand, and water.

Table 1
Description of land use classes in Cambodia

No	Land use class	Descriptions
1	Evergreen forest	Areas covered by trees maintaining their leaves during the whole year.
2	Semi-evergreen forest	Contain variable percentages of evergreen and deciduous trees.
3	Deciduous forest	Comprised of dry mixed deciduous forest and dry Dipterocarp forests
4	Bamboo	Areas dominated by bamboo
5	Wood shrub	Areas dominated by evergreen and deciduous woodland with a height less than 5 meters
6	Mangrove forest	Areas dominated by Mangroves i.e. coastal salt tolerant species
7	Rear Mangrove	Mostly growing in coastal zone after mangrove spp. Salt tolerant species but only infrequent floods
8	Rubber plantation	Areas currently supporting, and areas reserved for, rubber plantation
9	Flooded forest	This forest type is found in Tonle Sap Lake. Most of the forests are low and disturbed. In many cases, there is only a mosaic remaining
10	Forest regrowth	Areas of naturally regenerated forest where there are clearly visible indication of human activities such as selective logging, areas regenerating following agricultural land use, areas recovering from human induced fire, including: - Forest where it is not possible to distinguish whether planted or naturally regeneration. - Forests with mix of naturally regenerated trees and planted/seeded trees, and where the naturally regenerated trees are expected to constitute more than 50 percent of the growing stock at stand maturity. -Abandoned forest land and bare land which will regrow into forest within ten years
11	Pine tree	The area dominated by coniferous trees
12	Pine plantation	The area dominated by pine tree plantation
13	Oil palm	The area dominated by oil palm tree.
14	Tree plantation	This class includes the following types: Teak, Eucalyptus, Acacia, Jatropha and others

Table 1 *(continue)*

No	Land use class	Descriptions
15	Paddy field	Paddy field is a flooded parcel of arable land used for growing semiaquatic rice
16	Crop land	This category includes arable and tillage land and agro-forestry systems where vegetation falls below the thresholds used for the forest land category
17	Grassland	Grasslands are characterised as lands dominated by grasses rather than large shrubs or trees. It is crucial that the rainfall is concentrated in six or eight months of the year, followed by a long period of drought when fires can occur
18	Built-up area	The patch of land with building and construction
19	Village	The patch of land with houses and garden surrounding house.
20	Rock	Land of naturally exposed rocks or strip mines, quarries and gravel pits
21	Sand	In general, land of sand having thin soil or sand including deserts, dry salt flats, beaches, sand dunes
22	Water	Area of fresh and sea water

Source: (FA, 2016; MOE, 2018)

Reclassification of Land Use

In general, land use reclassification is often used to update existing land use data files, to group land-use types, or to assess water quality impacts or management options regarding alteration to land use over time. Similar characteristics of land use classes can be grouped into a single classification to simplify modelling (www.aquaterra.com/basins3/BASINS%20Utilities/Land%20Use%20Reclassification). In this study, both land use in 2006 and 2008 were reclassified by grouping the identified classes in the study area into seven classes (Table 2). The reclassification is needed in order to synchronise the limitation of satellite imagery resolution with the land use data in a GIS. Land use reclassification was conducted by using ArcGIS 10.4.1 software functions by merging polygons in Table 1 to a new class as developed and described in Table 2.

Table 2
New classes of land use of upper Prek Thnot watershed

No	Land use class	Code	Descriptions
1	Forest	F	Evergreen forest, semi-evergreen forest, deciduous forest, pine forest, forest regrowth, bamboo and tree plantations
2	Rubber plantation	RP	Rubber plantation
3	Wood shrub	WS	Wood shrub and grassland
4	Agricultural land	AL	Paddy field and crop land
5	Built-up area	BU	Built-up area and villages
6	Barren land	BL	Rock and sand
7	Water	W	Water

Land Use Changes Detection

Change detection is a significant process in monitoring and managing natural resources. Urban development provides a quantitative analysis of the spatial distribution of the population of interest (Singh, 1989). One of the important uses of land use data is for change analysis, and various methods have been designed to identify conversion in the land surface (Singh, 1989; Lu et al., 2004). The most apparent method of change detection is a comparative analysis of spectral classification for times t1 and t2 produced independently. The base map of satellite imageries area was prepared by the Forestry Administration (FA) and the Ministry of Environment (MOE) of the Kingdom of Cambodia. The subset images were combined and used to recognize different features in the study area. For image interpretation, ERDAS Imagine and ArcGIS software were used to prepare land use category map of the study area. The post-classification technique was used to assess land use change in this study. The post-classification comparison was conducted by using ArcGIS 10.4.1 software. The percentage change (trend) for each land use type was then calculated by dividing magnitude change by the base year (the initial year) and multiplied by 100 as shown in Equation 1.

$$\text{Percentage change} = \frac{\text{Magnitude of Change}}{\text{Base year}} * 100 \qquad (1)$$

The data of the land-use change from periods of 2006 and 2018 went through the process of overlaying, intersecting and dissolving of vector data layers, thus providing the basis for the evaluation of data applicability for this purpose.

RESULTS AND DISCUSSION

Land Use Status

The Multi-temporal land use of 2006 and 2018, covering seven main classes such as forest, rubber plantation, wood shrub, agricultural land, built-up area, barren land and water (Figure 2). Meanwhile, the spatial distribution pattern of land use, obtained from reclassification, is illustrated in Table 3.

Results from classified 2006 maps indicated that an area occupied by different classes are as follows; forest shared the majority with 2,819.60 km^2 which account for 81.71% and following by agricultural land and wood shrub which were 380.93 km^2 (11.04%) and 239.39 km^2 (6.94%), respectively. Built-up area covered 10.64 km^2, corresponding to 0.31%, while water body and barren land occupied by 0.23 km^2 (0.01%) and 0.09 km^2 (0.00%), accordingly. At the same time, no rubber plantation exists in the study area in 2006. In 2018, forest and agricultural land were estimated to have covered almost the same rate, which was 1,657.54 km^2 (48.03%) and 1,639.91 km^2 (47.52%), respectively. Wood

shrub shared a proportion almost double as built-up area, which was 77.51 km^2 (2.25%) and 44.28 km^2 (1.28%), individually. Meanwhile, rubber plantation was found in the study area with coverage of 10.55 km^2, accounting for 0.31%. Finally, the water body was 16.12 km^2 (0.47%), whereas barren land covered 4.96 km^2 (0.14%) (Table 3).

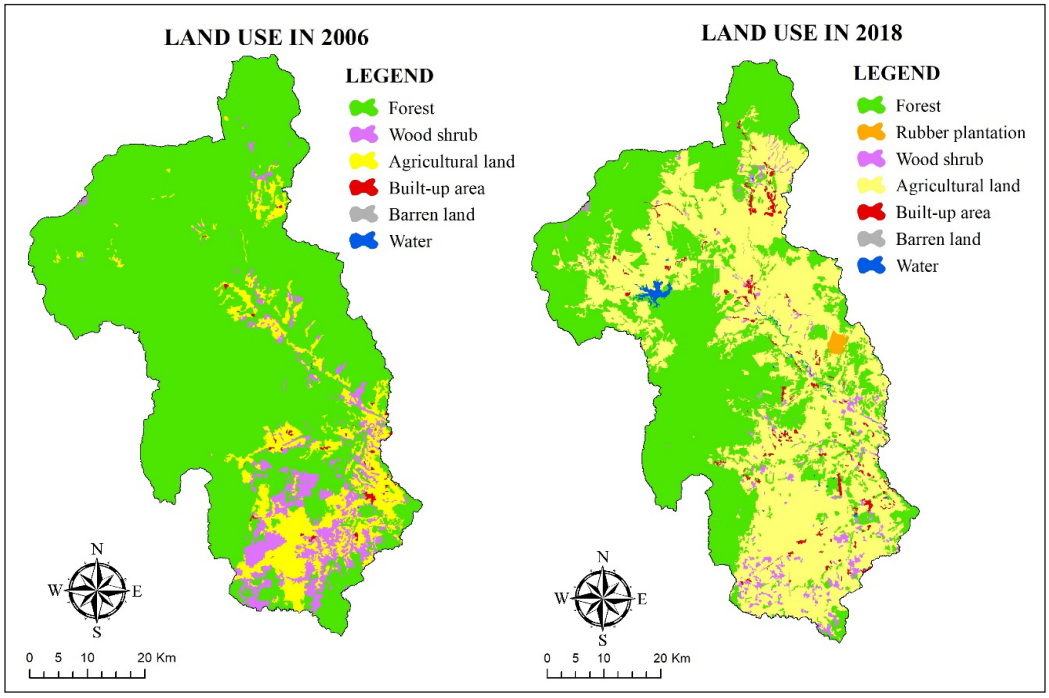

Figure 2. Land use types in 2006 and 2018 in the Prek Thnot watershed area

Table 3
Land use status (2006-2018) in the study area

Land Use Class	2006		2018	
	Area (km^2)	Area (%)	Area (km^2)	Area (%)
Forest	2819.60	81.71	1657.54	48.03
Rubber Plantation	0.00	0.00	10.55	0.31
Wood shrub	239.39	6.94	77.51	2.25
Agricultural land	380.93	11.04	1639.91	47.52
Built-up area	10.64	0.31	44.28	1.28
Barren land	0.09	0.00	4.96	0.14
Water	0.23	0.01	16.12	0.47
Total	**3450.87**	**100**	**3450.87**	**100**

Land Use Changes in Prek Thnot Watershed

Relative land use change in study area was assessed based on data presented in Table 4, 5, and Figure 3. The relative changes showed some irregular pattern in this study area from 2006 to 2018. From 2006 to 2018, forest and wood shrub areas were rapidly declined by 1,162.06 km^2 (33.67%) and 161.88 km^2 (4.69%), respectively. This might be considered as a serious risk to the resource's sustainability of Prek Thnot watershed. However, agricultural land significantly increased by 1,258.99 km^2 (36.48%). Most forest and wood shrub areas were altered into agricultural land. An increase in agricultural land and a decrease in forest and wood shrub regions were affected by the growth in agricultural land requirements. Such factors including sugarcane and other agro-industry crop plantations conversions by economic land concession (ELC) companies and by local people (FA & APFNet, 2016), and an increase of paddy field demands (Chann & Frewer, 2017), all distributed to alteration of these areas. Furthermore, the built-up area increased by 33.64 km^2 which correspond to 0.97% of a total change. It was caused by residential expansion due to population growth and economic development matters. The population growth rate is increased by about 1.8% from 2008 to 2019 (NIS, 2019).

Table 4
The changes in land use from 2006 to 2018

Land Use Class	Net change	
	Area (km^2)	Area (%)
Forest	-1162.06	-33.67
Rubber Plantation	10.55	0.31
Wood shrub	-161.88	-4.69
Agricultural land	1258.99	36.48
Built-up area	33.64	0.97
Barren land	4.87	0.14
Water	15.89	0.46

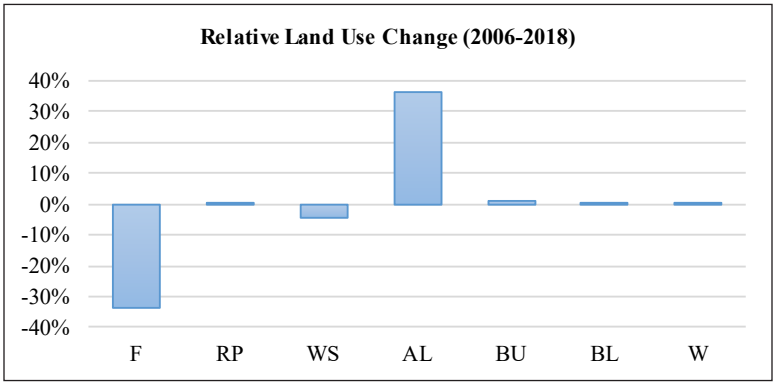

Figure 3. Diagrammatic illustration of relative land use change (2006-2018)

Table 5
Land use change matrix as observed in the study area

	Land Use Classes	2018 Area in km^2							
		F	RP	WS	AL	BU	BL	W	Total 2006
2006 Area in km^2	Forest (F)	**1635.59**	10.55	37.65	1099.71	17.76	3.65	14.69	2819.60
	Rubber plantation (RP)	0.00	**0.00**	0.00	0.00	0.00	0.00	0.00	0.00
	Wood shrub (WS)	16.53	0.00	**26.06**	189.84	6.34	0.29	0.33	239.39
	Agricultural land (AL)	5.39	0.00	13.80	**345.98**	13.86	1.02	0.88	380.93
	Built-up area (BU)	0.03	0.00	0.00	4.38	**6.24**	0.00	0.00	10.64
	Barren land (BL)	0.00	0.00	0.00	0.00	0.09	**0.00**	0.00	0.09
	Water (W)	0.00	0.00	0.00	0.00	0.00	0.00	**0.23**	0.23
	Total 2018	1657.54	10.55	77.51	1639.91	44.28	4.96	16.12	**3450.87**

The rubber plantation increased by 10.55 km^2, representing 0.31% of a net change, while the barren plantation grew moderately by 4.87 km^2 (0.14%). Finally, the water body was rapidly increased from 0.23 km^2 to 16.12 km^2 with a net change of 15.89 km^2, accounting for 0.46% of a total transformation. The installation of a water dam called Tasal Dam in the upper part of the study area might be caused of the increment. Based on the results the land use practices in the study area have changed significantly in 12 years. The land use change in the watershed area was obvious by the decline in the area of forest and wood shrubs and expansion of area by agriculture and built-up area. The alteration or depletion of forested land and wood shrubs may adversely affected water which may prove a limiting factor in the future for both urban growth and agriculture practice the watershed areas (Butt et al., 2015). From now, proper management of the watershed is essential to ensure the watershed area can play their role in socio-economic development of the area.

Sustainable Resource Management

Based on the results, the changes in the forested areas were 34 % from 2006 to 2018. This proportion is represented by 48 % of the total study area. The tendency of changes occurred in the flatland areas rather than highland areas, which focuses on agricultural areas. According to Cambodia National REDD+ Strategy 2017-2026, it was stated that deforestation and forest degradation in Cambodia were mainly driven by (i) uncertain land tenure, land speculation, unauthorized encroachment of forest lands, (ii) rapid expansion of agriculture into forest lands, the grant of large scale agro industrial-economic land concessions, and distribution of land titles under social land concessions between 1996-2012, (iii) unauthorized logging and unsustainable harvesting of forest and non-timber products, (iv) weak forest governance, law enforcement, and monitoring of forest and land-use sector, and (v) other drivers. The others include inadequate implementation of

environmental and social impact assessment regulations and a lack of state land registration and forest estate demarcation.

However, several transformative actions were taken and the sustainable management of national resources, including forestry and primary policy priority, was initiated by the Royal Government of Cambodia. The government is committed to implementing the sustainable management of national resources by adopted National REDD+ Strategy, National Forest Programme, and other governmental policies, strategies and programmes. Strategic plans were designed such as (1) improving management and monitoring of forest resources and forest land use, (2) strengthening implementation of sustainable forest management, and (3) mainstreaming approaches to reduce deforestation, build capacity and engage stakeholders (NRS, 2017). The strategy 1 aimed to strengthen the management of forest conversation areas, to promote forest land tenure through forest land classification, zoning, demarcation, and registration, to enhance law enforcement activities to address unauthorised logging, and encroachment, and to strengthen capacity for data management and establish decision support systems for forest and land-use sector. Strategy 2 focused on enhancing and scaling up community-based forest management, engaging and encouraging the private sector to implement alternative and sustainable supply chains from agro-industrial plantations, expanding afforestation, reforestation and restoration activities, and identifying and implementing alternative and sustainable livelihood development programmes for local communities most dependent on forest resources. Finally, strategy 3 was developed to support mechanisms to mainstream policies and measures that reduce deforestation in relevant government ministries and agencies. It also strengthened capacity, knowledge and awareness of stakeholders to enhance their contribution to reducing deforestation and forest degradation, and to encourage public engagement, participation and consolations in forestry and land use planning, and promote the involvement of multiple stakeholders.

The land use of upper Prek Thnot watershed has been under pressures where the land resources have been transformed into various land uses. This watershed area is situated in fertile plains and is lush with vegetation. An area is an attractive place for agriculture and people to reside. Due to this, the extensive amount of deforestation occurred. Contrary to the deforestation, agriculture area has been increased remarkably from 2006 to 2018, followed by the built-up area. The trend of land use changes found in this study, especially significant percentage decreased on the forest cover will be helpful to policymakers to take appropriate decision to revert the situation and to conserve the watershed area for sustainable development. The socio-economic variables are well-thought-out highly related to the changes in land use of an area (Verburg et al., 2004). Hence incorporating socio-economic and demographic data of the study area along with temporal change pattern would give critical reasoning for land use assessment and management in the area.

CONCLUSION

The land use notably forested land of the upper Prek Thnot watershed has been under various pressures from the surrounding populations. The forests have been decreased severely, and land has been fragmented and converted into several lands uses. The study has irrevocably shown that modifications induced by humans have triggered the processes of land cover conversion. As a result, land use significantly changed in the study area in the period between 2006 and 2018. The analysis showed that there was a rapid decrease in the forested area by 1,162.06 km^2 and wood shrub by 161.88 km^2, while agricultural land significantly increased by 1,258.99 km^2. The same trend occurred to a rubber plantation, built-up area, barren land and water where the areas increased by 10.55 km^2, 33.64 km^2, 4.87 km^2, and 15.89 km^2, respectively. The decrease in forest and wood shrub areas led to an increase in other areas including agricultural land, rubber plantation, built-up area, barren land and water. These changes also are driven by the influenced of the growth of population and land demands for agricultural purposes, such as sugarcane and other agro-industry crop plantations conversions by economic land concession (ELC) companies and by local people (FA and APFNet, 2016), an increase of paddy field demands, residential expansion (Chann and Frewer, 2017), and economic development matters. The sustainable resource management is needed to be instigated in this area based on the availabilities of national strategies, policies and programmes. Therefore, this study may provide vital information for wise sustainable watershed's land management, especially for further study on the effect of land use change on runoff in this watershed area.

ACKNOWLEDGEMENT

The authors are thankful to Southeast Asian Regional Center for Graduate Study and Research in Agriculture (SEARCA) under the Graduate Education Institution Development (GEIDD) Program, and the Forestry Administration and the Ministry of Environment of the Kingdom of Cambodia.

REFERENCES

Butt, A., Shabbir, R., Ahmad, S. S., & Aziz, N. (2015). Land use change mapping and analysis using Remote Sensing and GIS: A case study of Simly watershed, Islamabad, Pakistan. *The Egyptian Journal of Remote Sensing and Space Science, 18*(2), 251-259.

Chann, S., & Frewer, T. (2017). *Commodity frontiers: An ethnographic study of social-environmental interaction of Upper Stung Prek Thnot River Catchment, Eastern Cardamom Mountains*. Phnom Penh, Cambodia: United Nations Development Programme.

Di Gregorio, A., & O'Brien, D. (2012). Overview of land-cover classifications and their interoperability. In C. P. Giri (Ed.), *Remote sensing of land use and land cover: Principles and applications* (pp. 37-47). Boca Raton, Florida: CRC Press.

d'Amour, C. B., Reitsma, F., Baiocchi, G., Barthel, S., Güneralp, B., Erb, K. H., ... & Seto, K. C. (2017). Future urban land expansion and implications for global croplands. *Proceedings of the National Academy of Sciences, 114*(34), 8939-8944.

FA. (2016). *Cambodia forest cover 2014*. Forestry Administration of Cambodia. Retrieved May 22, 2019, from httpps://red.unfccc.int.uploads/53_1_cambodia_forest_cover_resource_2014_english.pdf

FA., & APFNet. (2016). *Watershed Characterization of Prek Thnot Watershed*. Forestry Administration of Cambodia and Asian-Pacific Network for Sustainable Forest Management and Rehabilitation. Retrieved April 20, 2019, from http://47.93.204.26:8082/ uploads/file/20180311/1520780315809470.pdf

Giri, C. P. (2012). Brief overview of remote sensing of land cover. In C. P. Giri (Ed.), *Remote sensing of land use and land cover: Principles and applications* (pp. 3-12). Boca Raton, Florida: CRC Press.

Gribb, W. J., & Czerniak, R. J. (2016). Land use/land cover classification systems and their relationship to land planning. In O. Ahlqvist, D. Varanka, S. Fritz, & K. Janowicz (Eds.), *Land use and land cover semantics: Principles, best pratices, and prospects* (pp. 1-20). Boca Raton, Florida: CRC Press.

Jenson, S. K. (1991). Applications of hydrological information automatically extracted from digital elevation models. *Hydrological Processes, 5*(1), 31-44.

Jenson, S. K., & Domingue, J. O. (1988). Extracting topographic structure from digital elevation data for geographic information system analysis. *Photogrammetric Engineering and Remote Sensing, 54*(11), 1593-1600.

Kumar, P., Dasgupta, R., Johnson, B. A., Saraswat, C., Basu, M., Kefi, M., & Mishra, B. K. (2019). Effect of land use changes on water quality in an ephemeral coastal plain: Khambhat City, Gujarat, India. *Water, 11*(4), 1-15.

Lambin, E. F., & Meyfroidt, P. (2011). Global land use change, economic globalisation, and the looming land scarcity. *Proceedings of the National Academy of Sciences, 108*(9), 3465-3472.

Lu, D., Mausel, P., Brondizio, E., & Moran, E. (2004). Change detection techniques. *International Journal of Remote Sensing*, *25*(12), 2365-2407.

MOE. (2018). *Cambodia forest cover 2016*. Ministry of Envrionment of Cambodia. Retrieved September 30, 2019, from https://redd.unfccc.int/uploads/54_3_ cambodia_forest_cover_resource__2016_english.pdf

Munoth, P., & Goyal, R. (2019). Impacts of land use land cover change on runoff and sediment yield of Upper Tapi River Sub-Basin, India. *International Journal of River Basin Management, 18*(2), 1-13.

NIS. (2019). *General Population Census of the Kingdom of Cambodia 2019: Provisional Population Totals*. Nation Insitute of Statistics of the Ministry of Planning. Retrieved October 1, 2019, from https://www.nis.gov.kh/nis/Census2019/Provisional%20 Population%20Census%202019_English_FINAL.pdf

NRS. (2017). *National REDD+ Strategy 2017-2026*. National REDD+ Strategy. Retrieved February 17, 2020, from http://www.cambodia-redd.org/wp-content/uploads/2017/09/1.-NRS-Final-Eng.pdf

Samie, M., Ghazavi, R., Vali, A., & Pakparva, M. (2019). Evaluation of the effect of land use change on runoff using supervised classified satellite data. *Global NEST*, *21*(2), 245-252.

Singh, A. (1989). Digital change detection techniques using remotely-sensed data. *International Journal of Remote Sensing, 10*(6), 989-1003.

Sohl, T., & Sleeter, B. (2012). Role of remote sensing for land-use and land-cover change modeling. In C. P. Giri (Ed.), *Remote sensing of land use and land cover: Principles and applications* (pp. 225-239). Boca Raton, Florida: CRC Press.

Szwagrzyk, M., Kaim, D., Price, B., Wypych, A., Grabska, E., & Kozak, J. (2018). Impact of forecasted land use changes on flood risk in the Polish Carpathians. *Natural Hazards, 94*(1), 227-240.

Tsegaye, B. (2019). Effect of land use and land cover changes on soil erosion in Ethiopia. *International Journal of Agricultral Secience and Food Technology*, *5*(1), 26-34.

Vadrevu, K., Heinimann, A., Gutman, G., & Justice, C. (2019). Remote sensing of land use/cover changes in South and Southeast Asian Countries. *International Journal of Digital Earth*, *12*(10), 1099-1192.

Verburg, P., Schot, P., Dijst, M., & Veldkamp, A. (2004). Land use change modelling: Current practice and research priorities. *GeoJournal*, *61*, 309-324.

Pertanika J. Sci. & Technol. 28 (3): 893 - 916 (2020)

PERTANIKA JOURNALS

SCIENCE & TECHNOLOGY

Journal homepage: http://www.pertanika.upm.edu.my/

Nano-Sized Adsorbent from Pyrolysed Sago Activated Sludge for Removal of Pb(II) from Aqueous Solution

Nur Aqilah Makshut, Zainab Ngaini*, Rafeah Wahi*, Hasnain Hussain, Nurul Iwani Mahmut and Nurul Qhalila Bahrin

Faculty of Resource Science and Technology, Universiti Malaysia Sarawak, 94300 UNIMAS, Kota Samarahan, Sarawak, Malaysia

ABSTRACT

Increased disposal of heavy metals, including lead (II) (Pb(II)) into the environment calls for a reliable and sustainable solution. In this study, nano-sized biochar from sago activated sludge was proposed for the removal of Pb(II). Sago activated sludge was pyrolysed in a tube furnace followed by a chemical activation to yield nano-sized particles ranging from 45 to 75 nm. The nano-sized biochar obtained was characterised and the influence of pH (2 – 10), initial Pb(II) concentration (1 – 5 mg/L), contact time (30 – 90 mins) and adsorbent dosage (0.1 – 0.5 g) was investigated in a batch adsorption study. Response surface methodology (RSM) approach with central composite design (CCD) was used as statistical tools to optimize the adsorption process by relating the mutual interactions among all studied variables. Characterisation of the prepared adsorbent showed that large surface area was observed on sludge activated carbon (78.863 m^2/g) compared with sludge biochar (8.044 m^2/g) and sludge biomass (1.303 m^2/g). The batch adsorption best fitted the Langmuir isotherm (maximum adsorption capacity, $Q_0 = 3.202 \times 10^{-3}$ mg/g, R-squared value = 0.9308). The RSM indicated that the optimum Pb(II) removal (99.87%) was at 0.5 g of adsorbent, 5 mg/L initial concentration and 30 min contact time. This study is significant because utilisation of sago effluent will reduce sago manufacturing waste by conversion into a value-added product as adsorbent to adsorb Pb(II) in wastewater.

Keywords: Activated carbon, adsorption, nano-sized adsorbent, RSM, sago, tube furnace

ARTICLE INFO

Article history:
Received: 10 February 2020
Accepted: 14 April 2020
Published: 16 July 2020

E-mail addresses:
aqilahmakshut@gmail.com (Nur Aqilah Makshut)
nzainab@unimas.my (Zainab Ngaini)
wrafeah@unimas.my (Rafeah Wahi)
hhasnain@unimas.my (Hasnain Hussain)
nuruliwani.ni@gmail.com (Nurul Iwani Mahmut)
qnorule@yahoo.com (Nurul Qhalila Bahrin)
* Corresponding author

ISSN: 0128-7680
e-ISSN: 2231-8526

© Universiti Putra Malaysia Press

INTRODUCTION

Heavy metal pollution into the aquatic environment including lead (Pb) could cause adverse effects to aquatic habitats as well as humans, resulting in severe mucous irritation, widespread capillaries damage and central nervous system irritation (Ahmad et al., 2009). For example, Pb(II) is refractory and not biologically detoxifiable, and tends to bioaccumulate over time. It may be introduced into water bodies from various sources, such as storage batteries, lead smelting, plating ammunition, ceramic glass industries and tetraethyl lead manufacturing industries (Ahmad et al., 2009).

Many technologies have been introduced to remove Pb(II) in the water, such as physical treatment including coagulation/flocculation and chemical treatment namely chemical precipitation, and ion-exchange and electrochemical process (Amuda et al., 2007). However, there are limitations using these technologies in terms of the treatment cost and effectiveness in removing heavy metals, especially at lower concentrations (Amuda et al., 2007).

Biosorption is commonly reported in the treatment of heavy metals in the wastewater due to its effectiveness and low treatment cost (Ahmad et al., 2009). Biosorption utilizes the ability of a natural sorbent such as agricultural wastes to accumulate heavy metal ions in the aqueous solution by metabolically mediated or physicochemical pathways of uptake (Abbas et al., 2014). There are several biosorbents reported from agricultural wastes such as banana peels (Anwar et al., 2010), palm oil empty fruit bunch (Wahi et al., 2009), sawdust of *Pinus sylvestris* (Taty-Costodes et al., 2003), and Nigerian bamboo (Ademiluyi & Nze, 2016) for the removal of heavy metals from the wastewater. Sludge-based biosorbent was reported to have better average pore diameter (5.62 nm) and mesopore range of 3.13-5.70 nm with higher materials uptake up to 99.7% (Wang et al., 2008; Aliakbari et al., 2016). The utilisation of sludge-based activated carbon for nutrient removal (Yue et al., 2018) or other value-added products such as spirulina cultivation in sago starch factory (Phang et al., 2000) is able to improve waste management in Malaysia in terms of waste disposal cost reduction (Aliakbar et al., 2016).

Sago industry in Malaysia has produced an abundance of agricultural wastes during starch production, which offering potential alternative low-cost materials as biosorbents for the removal of heavy metals such as Pb(II). Approximately 10 – 22 tonnes of sago effluent is generated daily and considered massive compared to the other wastes such as *hampas* and bark which can be reused as value-added products (Ngaini et al., 2013; Wahi et al., 2017a; Ngaini et al., 2014a; Ngaini et al., 2014b; Ngaini et al., 2018). Sago effluent contains high organic content, high biological oxygen demand (BOD), chemical oxygen demand (COD) and other nutrients (Ngaini et al., 2014a) and can be treated *via* the activated sludge process. These benefits meet the suitability of sago effluent to be treated *via* the activated sludge process.

Agricultural waste such as sago activated sludge is a potential feasible and sustainable feedstock for large scale production of nanoparticles for adsorbent purpose. Nanoparticles play a vital role in water treatment, attributing to its excellent properties including small and uniform particle size, high surface area, and composition distribution (Tara et al., 2020). There were limited studies reported on the use of agricultural waste as a source of nanoparticles, and none on sago activated sludge use as nano-sized adsorbent.

Determination and optimization of the nano-sized adsorbent can be done by utilizing the Response Surface Methodology (RSM). It is a statistical method to optimize a certain process by relating the mutual interactions among all variables and providing an estimation of the joined impact of these variables on the results (Kishnor et al., 2006). In addition, a second-order Central Composite Design (CCD) is used to determine and evaluate the optimum variables on the adsorption efficiency. In other words, CCD is used to optimise the parameters with reduced number of experiments while analysing the interactions among parameters (Tan et al., 2008). The analysis of interactions between parameters might take longer time and more experimental runs if the batch adsorption method was applied. Thus, utilising RSM in CCD can improve time and cost management.

In this work, we reported a novel nano-sized adsorbent synthesized from sago activated sludge via pyrolysis and chemical activation method. The physicochemical characterisation, morphology and surface area were characterised, and the adsorptive capability for Pb(II) removal was studied *via* batch adsorption study and optimization of Pb(II) removal was studied using response surface methodology (RSM) approach.

METHODS

Preparation of Sludge Activated Carbon (SAC)

Sago effluent was collected in 20 L tanks from Herdson Sago Industries, Sarawak. Urea (24 g) and phosphoric acid (200 mL) were added into the effluent (20 L) with carbon (C), nitrogen (N), and phosphorus (P) at C:N:P ratio of 100:10:1 (Winkler, 2013). The effluent was aerated for 7 days, filtered and sun-dried to obtain 93.2 g of sludge biomass (SBS). SBS (5 g) was sieved (45 μm) and heated using a tube furnace (1200 Mini Tube Furnace TI-01200-50SL) under N_2 atmosphere at 400°C for 30 min to yield sludge biochar (SBC) (3 g). SBC (3 g) was soaked in NaOH (5 M, 30 mL) for 2 hr. The mixture was filtered and washed to pH 7. The solid was oven-dried at 100°C for 24 hr for further pyrolysis at 500°C for 90 mins. The carbon was treated with HCl (5 M, 5 mL) to remove impregnating salt and washed using distilled water (150 mL) until pH 4. The solid obtained was oven-dried at 100°C for 1 hr to get 2.8 g of SAC and stored in a desiccator for further usage.

Physicochemical Characterisation

Assessment of Water Quality after Activated Sludge Process. The assessment of water quality was carried out based on the pH, Chemical Oxygen Demand (COD), Total Suspended Solids (TSS), ammoniacal nitrogen (AN). The pH of sago effluent was measured using a pH meter and performed in triplicates, where average values were taken.

Determination of Chemical Oxygen Demand (COD). A COD reactor was turned on to reach a thermal temperature of 150°C. About 2 mL of sago effluent were pipetted into a COD vial which contained COD reagent and inverted three times. A blank sample was prepared using 2 mL of deionized water, heated for 2 h and placed on the HACH instrument. The sample of sago effluent was then placed into the holder for COD analysis (Romes, 2009). The COD analyses were performed in triplicates where average values were taken.

Determination of Total Suspended Solids (TSS). A membrane filter (0.45 μm, 47 mm, white grid) was cleaned and weighed. About 300 mL of the water sample was filtered and the filter was dried in the oven at 100°C for 1 h, cooled to room temperature and weighed. The procedures were repeated in triplicates until a constant weight was obtained. The calculation for TSS is shown in Equation 1:

$$\text{Total Suspended Solids, mg/L} = (A - B)\ \text{mg} / (C/1000)\ \text{L} \quad [1]$$

where A is weight of filter + residue (mg), B is weight of filter (mg) and C is volume of filtered sample (L).

Determination of Ammoniacal Nitrogen (AN). Nessler method ranging from 0 to 2.5 mg/L was used for NH_3-N analysis. Two Falcon tubes were filled with 25 mL of water sample and deionised water as a blank. Three drops of polyvinyl alcohol as mineral stabiliser were added dropwise into each falcon tube. About 1.0 mL of Nessler reagent was pipetted into each falcon tube. The blank and sample mixture were placed on the HACH instrument to obtain the value of NH_3-N (Romes, 2009). The AN analysis was performed in triplicates where average values were taken.

Proximate Analysis

The procedure for obtaining the moisture content, volatile matter content, ash content and fixed carbon content of SBS, SBC and SAC was adapted from American Society for Testing Materials (ASTM) D-3173, D-3175 and D-3174, respectively.

Moisture Content. Empty, dried crucible (W_e) was weighed. A certain amount of samples was added into the crucible, weighed and labelled (W_s). The sample was dried at 105°C for 24 h. The sample was dried until a constant weight was obtained. The dried sample was weighed again and denoted as W_d. The moisture content of samples was calculated by using Equation 2:

$$Moisture\ Content\ (\%) = \frac{Ws - Wd}{Ws - We} \times 100\ \% \quad [2]$$

Volatile Matter. Empty dried crucible (W_e) was weighed. A certain quantity of samples was placed into the crucibles, weighed and labelled (W_s). The sample was dried for 7 mins in a furnace at 500°C. The dried sample was then weighed and denoted as W_v. The volatile matter content of samples was calculated by using Equation 3:

$$Volatile\ Matter\ Content\ (\%) = \frac{Ws - Wv}{Ws - We} \times 100 \quad [3]$$

Ash Content. Empty dried crucible was weighed (W_e). The sample was kept dry for 24 hr in a desiccator before the ashing process. The dried sample was placed into the crucible and weighed (W_s). The sample was burnt in a furnace for 3 hr with the first 1 hr at 500°C and the subsequent 2 hr at 700°C. The crucible with the dried sample was labelled (W_a). The ash content was calculated by using Equation 4:

$$Ash\ Content\ (\%) = \frac{W_s - W_a}{W_s - W_e} \times 100\% \quad [4]$$

Fixed Carbon. The fixed carbon content in samples was calculated by using Equation 5:

Fixed Carbon (%)= (% moisture content + % volatile matter + % ash content) [5]

Instrumental Analysis

The characterisation of the functional groups' presence in SBS, SBC and SAC was conducted by using Fourier transform infrared spectroscopy (FTIR) (Thermo Scientific Nicolet IS10 FTIR Spectrometer). Approximately 2 mg of sample in 400 mg dried KBr powder were compressed into a pellet and analysed. The IR spectra were plotted over a frequency range from 400 - 4000 cm^{-1}. The surface morphology and the size of particles were analysed using Transmission Electron Microscope (TEM) (JEOL 1230 Electron Microscope) with magnification 100,000x. The specific surface area was determined using Brunauer-Emmett-Teller (BET) (Quantachrome ASIQC0000-3) with liquid nitrogen adsorption at 77 K.

Batch Adsorption of Pb(II)

Effect of pH on the Adsorption of Pb(II). Pb(II) solution (5 mg/L) was prepared in a 100 mL distilled water. The adsorption was carried out at room temperature with adsorbent dosage 0.5 g. The solution was adjusted to pH 2 – 10 by using HCl (1 M) and NaOH (1 M). The mixture was agitated at 260 rpm for 30 min (Bishnoi et al., 2004). The adsorbent was filtered and analysed using Inductively Coupled Plasma-Optical Emission Spectroscopy (ICP-OES) (Perkin Elmer Optima 8000) (Kumar & Kirtika, 2009).

Effect of Adsorbent Dosage on the Adsorption of Pb(II). Pb(II) solution (5 mg/L) was prepared in a 100 mL distilled water. The adsorption was carried out at room temperature with adsorbent dosage ranging from 0.1 to 0.5 g. The solution was adjusted to pH 8 by using NaOH (1 M). The mixture was agitated at 260 rpm for 30 min (Bishnoi et al., 2004). The adsorbent was filtered and analysed using ICP-OES.

Effect of Initial Concentration on the Adsorption of Pb(II). Pb(II) solution in various concentrations (1 – 5 mg/L) was prepared in a 100 mL distilled water. The experiment was conducted at room temperature. The solution was adjusted to pH 8 by using NaOH (1 M). The adsorbent dosage (0.5 g) was used and agitated at 260 rpm for 30 min. The adsorbent was filtered and analysed using ICP-OES.

Adsorption Isotherms

Adsorption isotherm was used to determine the adsorption characteristic of Pb(II) on SAC. Two types of isotherm model were studied, the Langmuir isotherm and Freundlich isotherm. The Langmuir isotherm was calculated using Equation 6.

$$Langmuir\ isotherm:\ \frac{Ce}{qe} = \frac{1}{Qob} + \frac{Ce}{Qo} \qquad [6]$$

where Ce is the equilibrium concentration of Pb(II) after adsorption and q_e, mg/g is the amount of Pb(II) adsorbed per unit mass of adsorbent at equilibrium. The Q_0 (theoretical maximum adsorption capacity (mg/g)) and *b* (Langmuir adsorption constant (L/mg)) were obtained from the slopes and intercepts of linear plot of (C_e/q_e) versus C_e, respectively (Desta, 2013).

The separation factor or equilibrium parameter (R_L) is essential to predict the affinity between sorbate and sorbent using a separation factor in order to support that the adsorption fits the Langmuir Isotherm (Desta, 2013). R_L can be calculated via Equation 7:

$$Equilibrium\ parameter:\ R_L = \frac{1}{(1 + bCi)} \quad [7]$$

where b is Langmuir constant (L/mg) obtained from the plotted graph Ce/qe against Ce. C_i is the initial concentration of Pb(II) solution in mg/L. The adsorption is deduced as irreversible when the $R_L = 0$, linear when $R_L = 1$, unfavourable when $R_L > 1$ or favourable when $0 < R_L < 1$ (Desta, 2013).

The Freundlich isotherm was calculated by using Equation 8.

$$Freundlich\ isotherm: \log q_e = logK_f + \frac{1}{n} logC_e \quad [8]$$

where, q_e is the amount of Pb(II) adsorbed per unit mass of adsorbent at equilibrium. The K_f is a constant indicative of the adsorption capacity of the adsorbent. The n is an empirical constant connected to the magnitude of the adsorption driving force. The constant value Freundlich, K_f and *n* were obtained from the graph of log q_e against log C_e (Kanawade & Gaikwad, 2011).

Response Surface Methodology (RSM)

The operating variables chosen for RSM in CCD study by using SAC as adsorbent were the adsorbent dosage, initial concentration and contact time. The initial concentration was set from 1 to 5 mg/L. The contact time range was 30 – 90 mins while the adsorbent dosage used ranged from 0.1 to 0.5 g for 50 mL Pb(II) solution volume. The pH of the solution (pH 2) and temperature (STP) were kept constant throughout the experiments. The output parameter was the efficiency of Pb(II) removal in percentage. There were 17 experimental standards generated from Design Expert 7.1.6 (trial version) based on the variable values.

RESULTS AND DISCUSSION

Physicochemical Characterisation

During the aeration process for preparing the SAC, oxygen supply was introduced to the microorganism present in the effluent. The microbes utilized the dissolved oxygen and transformed wastes into more biomass and carbon dioxide (Carrier et al., 2012). Additional nutrients such as phosphorus and urea in the tank were able to provide more nutrients for the microorganisms to grow and clump together (Winkler, 2013). Nitrogen from urea plays an important role in the production of biomass from the activated sludge process. Limited amount of nitrogen influences the filamentous growth, which leads to poor settling process

(Slade et al., 2011). Micronutrients present in the effluent promote higher percentage of methane and carbon dioxide instead of additional biosolids (Amuda et al., 2008).

Pyrolysis of SBS to SBC in the tube furnace at 400°C gave a total carbonisation percentage of 56.4%. High temperature during pyrolysis promotes volatilisation and produces char with a high value of fixed carbon and porosity (Wahi et al., 2017b). The porosity of biochar plays an important factor for excellent adsorption. Sodium hydroxide (NaOH) was used during the activation to produce more porous surfaces (Foo & Hameed, 2012a) and improve sorption properties (Park et al., 2013). NaOH is commonly used as it is cheaper, less corrosive and more environmentally friendly compared with other activating agents such as KOH, $ZnCl_2$, and H_3PO_4 (Perrin et al., 2005).

Assessment of Water Quality after Activated Sludge Process

The water assessment for pH, chemical oxygen demand (COD), total suspended solids (TSS) and ammoniacal nitrogen (AN) was conducted on sago effluent before and after the activated sludge process. The pH of effluent was improved from pH 4 to pH 7. The COD of sago effluent showed a sharp decrease after the activated sludge process from 30.0±0.33 mg/L to 16.67±0.17 mg/L. Reducing 50% of the values indicated better improvement in water quality after the sludge process (Gerardi, 2002). TSS in sago effluent also decreased from 176.6±0.65 mg/L to 153.3±0.54 mg/L. High suspended solids in a water body could block sunlight from penetrating the water and preventing photosynthesis of aquatic plants to occur (Gerardi, 2002). AN also showed reduced amount from 21.0±0.16 mg/L to 0.71±0.55 mg/L. The summary of results for the water assessments can be observed in Table 1.

Table 1
Water assessment on sago effluent before and after the activated sludge process

Assessment	Before process	After process
pH	4	7
COD (mg/L)	30.0±0.33	16.67±0.17
TSS (mg/L)	176.6±0.65	153.3±0.54
AN (mg/L)	21.0±0.16	0.71±0.55

Proximate Analysis. Proximate analysis of SBC and SAC is tabulated in Table 2. The moisture content of SBC reduced from 0.514% to 0.0% after pyrolysis at 500°C, indicating complete removal of volatile matter (Wahi et al., 2017b). SAC yielded low moisture content compared to SBC due to carbonization process, which caused the loss of volatile matter (Rafiq et al., 2016). The longer heating period of biochar is essential to improve the quality and lower moisture content of activated carbon (SAC) (Wahi & Senghie, 2010). A less volatile matter that clogged the pores of biochar caused a decrease in the percentage

of the volatile matter of SBC (0.084%) and SAC (0.001%) (Wahi et al., 2017b). High carbonization temperature released a high amount of volatile matter from breaking of weaker bridges and bonds in organic matrices (Qian et al., 2008).

Ash content in SAC was improved to 99.9% from 99.1% in SBC which indicated that inorganic residue was higher in SAC (Rafiq et al., 2016). The ash content shows a significant increase as the ash remains in the solid fraction whereas the organic matter undergoes thermal decomposition, resulting in the decrease of the fixed carbon content in SBC from 0.30% to 0.08% in SAC (Ronsse et al., 2012).

Table 2
Proximate analysis of SBC and SAC

Proximate analysis	SBC	SAC
Moisture content, %	0.514	0
Volatile matter, %	0.084	0.001
Ash content, %	99.1	99.9
Fixed carbon content, %	0.30	0.08

Instrumental Analysis

Functional Group Analysis. The FTIR spectra of SBS, SBC and SAC are shown in Figure 1. The adsorption peaking at 3408 – 3426 cm^{-1} was attributed to the υ_{O-H} stretching vibration of carboxylic acids, phenols and alcohols in lignin, cellulose and pectin present

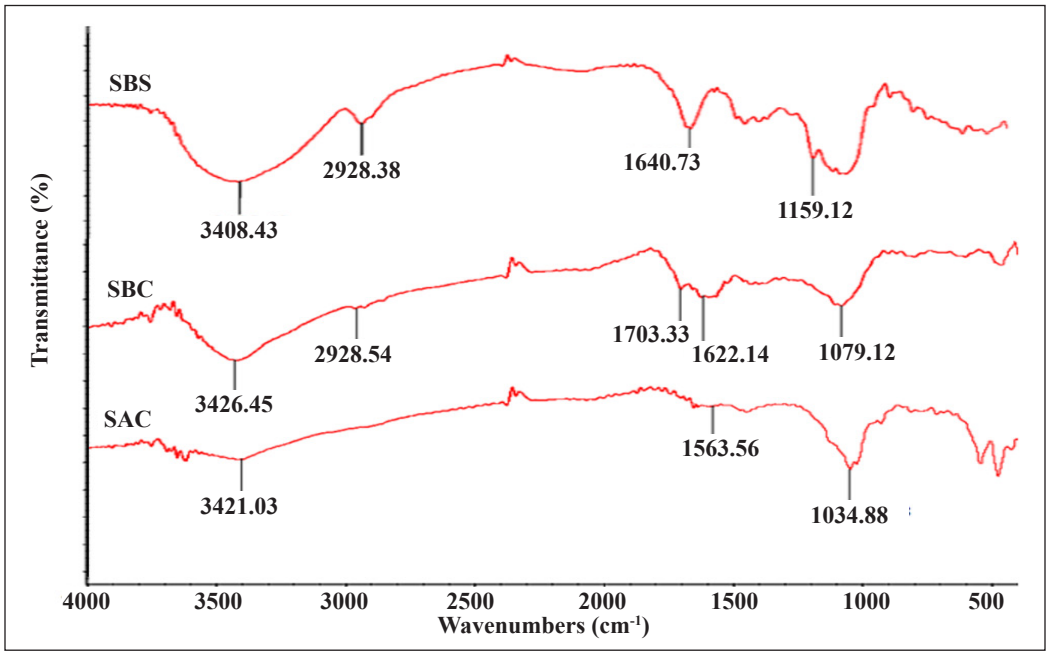

Figure 1. IR Spectra of (a) SBS, (b) SBC and (c) SAC

in SBS (Pathania et al., 2017). The broad O-H peak in SBS (Figure 1a) was reduced after the double carbonisation and activation process (Figure 1b-c). The pyrolysis caused the decomposition of functional groups and liberation of volatile matter during carbonisation (Foo & Hameed, 2012a). A weak peak at 2928 cm^{-1} corresponded to υ_{C-H} ($-CH_2$, $-CH_3$) was observed in SBS and reduced in SBC and SAC after pyrolysis. The peaks at 1622-1703 cm^{-1} could be due to the stretching vibration of $\upsilon_{C=C}$ and υ_{C-O} from lignin and hemicellulose in SBS and SBC and reduced after activation in SAC (Tan et al., 2008). The appearance of strong peaks in the spectra at 1034 - 1079 cm^{-1} was assigned to υ_{C-N} presence in the samples (Stella et al., 2016).

Transmission Electron Microscope (TEM) Analysis. The TEM image of SAC is shown in Figure 2. The pyrolysis of SBS at 400°C in the tube furnace under inert nitrogen atmosphere followed by chemical activations produced spherical, nano-sized particles within the range of 45 - 75 nm. The high temperature of a fast pyrolysis or carbonisation reaction in the tube furnace reduced the size of particles into nano-sized particles (Hedge et al., 2015). The size of carbon particles plays an important role in the adsorption capacity of a composite. Small-sized adsorbent provides a larger surface area which increases the rate of effective collision, increasing the binding probability between sorbent and sorbate, thus increasing the adsorption. The carbon particle size of composite with range 75 – 150 µm was reported to give higher adsorption capacity than that of 850 – 1000 µm (McKay, 1982). Similarly, effective adsorption of heavy metals was reported on carbon with a diameter range of 0.25 – 0.5 mm or lower, and ineffective with diameter >1.25 mm (Ricordel et al., 2001). The higher uptake by smaller particles is due to greater accessibility to pores and larger surface area for mass adsorption per unit weight of carbon (Senthilkumar et al., 2005).

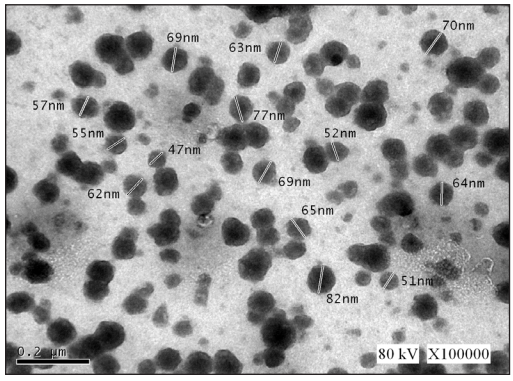

Figure 2. TEM image of SAC

Brunauer Emmett and Teller (BET) Analysis. The surface area of SBS (1.303 m^2/g) was characterised using BET. The surface area increased after pyrolysis from 8.044 m^2/g (SBS) to 78.863 m^2/g (SAC). The results showed a highly significant surface area difference between untreated and treated biochar. The large surface area of SAC was due to the larger pore size of SAC (Rajan et al., 2019). The surface area of SAC is highly dependent on the carbonization temperature with a higher temperature giving larger surface areas (Hu & Srinivasan, 1999). Double physical activation followed by chemical treatment with NaOH

aids in the production of a larger surface area of SAC. The large surface area was due to the intercalation of the carbonate metal from NaOH to the carbon matrix, thus broadening the space between the carbons' atomic layer (Foo & Hameed, 2012b).

Batch Adsorption of Pb(II)

Effect of pH on the Adsorption of Pb(II). The pH of the aqueous suspension of an adsorbent is a crucial factor that controls the adsorption of heavy metals (Gaya et al., 2015). From Figure 3, the highest adsorption occurred at pH 8 (95.06%) while the lowest was at pH 2 (12%). This is plausibly due to at lower pH (<pH 8), the presence of H^+ ions reduces the interaction with the predominant Pb(II) species (El-Ashtoukhy et al., 2008). The adsorption reached equilibrium at pH 8 and decreased at pH 10 due to the negatively charged surface of activated carbon sludge. Soluble hydroxylated complexes were also formed at higher pH, causing competition between the complexes and Pb ions for the binding sites (Ibrahim et al., 2016).

Effect of Adsorbent Dosage on the Adsorption of Pb(II). In this study, a series of batch adsorption experiment was performed to investigate the effect of adsorbent dosage (0.1 – 0.5 g) employing SAC for the adsorption of Pb(II). The activated carbon sludge demonstrated excellent removal efficiency with the increased removal of Pb(II) from 27.4 to 99.78% as the adsorbent dosage increased from 0.1 – 0.5 g. The removal efficiency is commonly corresponding to the surface area and particle size of the adsorbent. Effective adsorption of heavy metals on carbon with a diameter range of 0.25 – 0.5 mm or lower (Ricordel et al., 2001) gave higher uptake due to greater accessibility to pores and larger surface area for mass adsorption per unit weight of carbon (Senthilkumar et al., 2005). High surface area (78.863 m^2/g) of SAC contributed to the excellent adsorption capacity of Pb(II) (McKay,

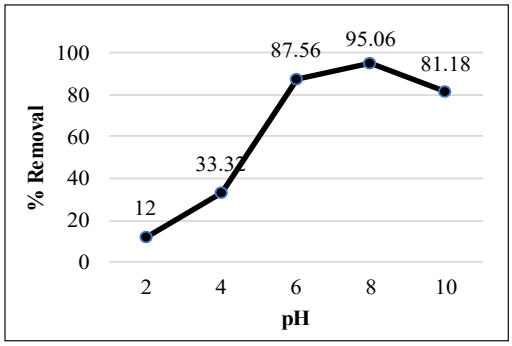

Figure 3. Effect of pH on the Adsorption of Pb(II) (Experimental conditions: Pb(II) concentration: 5 mg/L, adsorbent dosage: 0.5 g/100 mL (0.005 g/mL), adsorption time: 30 min, mixing rate: 260 rpm, pH: 8)

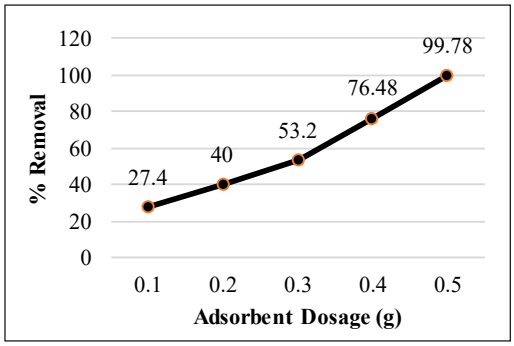

Figure 4. Effect of Adsorbent Dosage on the Adsorption of Pb(II) (Experimental conditions: Pb(II) concentration: 5 mg/L, adsorption time: 30 min, mixing rate: 260 rpm, pH: 8)

1982), with advantage on its nanosize particles (Figure 2). Overall, the percentage of removal increased with the increase in dosage of adsorbent (0.1–0.5 g) (Figure 4). This is due to the higher exchangeable site and surface areas of the adsorbent, which leads to better adsorption capacity (Patil et al., 2011; Gao et al., 2013).

Effect of Initial Concentration on the Adsorption of Pb(II). The adsorption of Pb(II) decreased from 84.18 to 27.18% as the initial concentration of Pb(II) decreased from 1 to 5 mg/L (Figure 5). This trend suggested for the possible monolayer adsorption (Hu et al., 2009) of Pb(II) onto the surface of SAC. At higher concentration, the mass transfer of Pb(II) molecules becomes limited as the availability of binding sites is very low (Mehdizadeh et al., 2014). In fact, initial concentration is an important parameter to promote a driving force and improve mass transfer resistance from aqueous to solid phases adsorbent (Hema & Srinivasan, 2010).

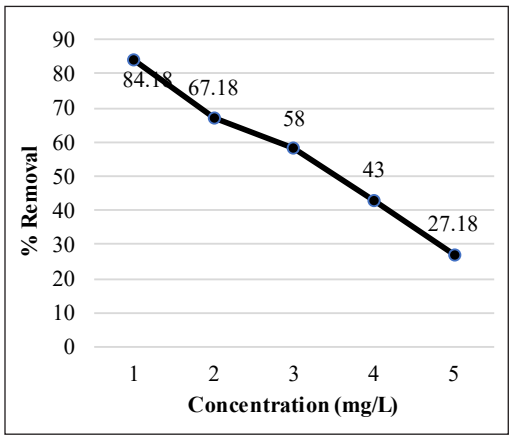

Figure 5. Effect of Initial Concentration on the Adsorption of Pb(II) (Experimental conditions: Pb(II) concentration: 1-5 mg/L, adsorbent dosage: 0.5 g/100 mL (0.005 g/mL), adsorption time: 30 min, mixing rate: 260 rpm, pH: 8)

Adsorption Isotherms

Langmuir Isotherm. The graph of (Ce/qe) against Ce (Figure 6) demonstrated that the experimental data of Pb(II) ions removal by SAC fitted well with Langmuir isotherm (R^2=0.9308), indicating a monolayer adsorption. Langmuir isotherm model proposes a good sorption method of monolayer adsorption on a homogenous adsorbent layer, without any interaction between the adsorbate molecules and adjacent sites (Fat'hi et al., 2014). Table 3 shows that the constant b showed high adsorption energy (0.5108 L/mg), indicating a fast increment in adsorption at low concentrations of adsorbate (Mor et al., 2006).

The maximum adsorption capacity, Q_0 obtained from Langmuir isotherm for removal of Pb(II) by SAC in comparison with other adsorbents is depicted in Table 3.

Table 3
Equilibrium constant of Langmuir Isotherm and Freundlich Isotherm on the removal of Pb(II)

Isotherm	Parameters	Values
Langmuir	Q_0 (mg/g)	3.202×10^{-3}
	b (L/mg)	0.5108
	R^2	0.9308
	R_L	0.999
Freundlich	n	2.5109
	1/n	0.399
	K_f	1.131×10^{-3}
	R^2	0.9084

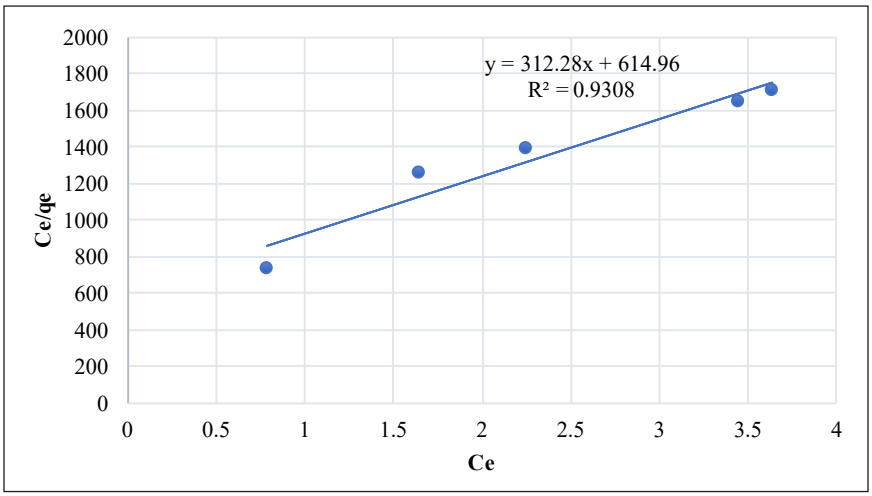

Figure 6. Langmuir isotherm plot for Pb(II) adsorption by SAC (Experimental conditions: Pb(II) concentration: 1-5 mg/L, adsorbent dosage: 0.5 g/100 mL (0.005 g/mL), adsorption time: 30 min, mixing rate: 260 rpm, pH: 8)

The SAC had relatively low adsorption capacity (3.202×10^{-3}) compared to other adsorbents from previous studies. Most of the studies however, were conducted at acidic pH, and higher Pb(II) concentration compared to the present study. One of the plausible reason for the low adsorption capacity of SAC is the adsorption condition, which was conducted at basic pH (pH 8). Previous studies as shown in Table 4 showed that maximum removal of Pb(II) ions is observed at pH 5.6–7.6. At a higher pH, Pb(II) ions form hydroxide precipitate, which consequently decreases the adsorption rate and removal percentage (El-Ashtoukhy et al., 2008). On the other hand, batch adsorption experiments in the present study shows high removal of Pb(II) (maximum removal 99.78%) despite of the low Q_0 value. The high removal percentage might be attributed to the high adsorbent dosage (0.02 g/mL) used for removal of Pb(II) at very low initial concentrations (1-5 mg/L). At high adsorbent dosage more active sites are available for metal uptake (Anwar et al., 2010).

Freundlich Isotherm. Freundlich isotherm for Pb(II) adsorption by SAC is shown in Figure 7 and the corresponding parameters are shown in Table 3. The adsorption intensity, n was 2.51 (n>1). The n value showed the degree of non-linearity between the solution concentration and adsorption. Should the value of n is 1, the adsorption is assumed as linear. If $n < 1$, the adsorption is a chemical process while $n > 1$ is the most common degree on non-linearity obtained due to the distribution of surface sites that causes a decrease in adsorbent-adsorbate interactions as surface density is increasing (Reed & Matsumoto, 1993).

The 1/n value of SAC was 0.399 (Table 3), indicates a normal Langmuir isotherm ($1/n<1$) (Fan et al., 2013) with only a slight intensity of heterogenous layer adsorption

Table 4
Comparison on maximum adsorption capacity, Q_0 obtained from Langmuir isotherm for removal of Pb(II) by different adsorbent

	Adsorbent	Q_0, mg/g	Adsorption condition	Author(s)
(i)	Banana peels	2.18	Pb(II) concentration: 30-80 mg/L Adsorbent dosage: 40 g/L (0.04 g/mL) Adsorption time: 20 min Mixing rate: 100 rpm pH: 5	Anwar et al. (2010)
(ii)	Tamarind wood activated carbon	43.85	Pb(II) concentration: 10-50 mg/L Adsorbent dosage: 2 g/L (0.002 g/mL) Adsorption time: 30 min Mixing rate: 120 rpm pH: 6.5	Acharya et al. (2009)
(iii)	Mesembryanthemum activated carbon	66.67	Pb(II) concentration: 50-1000 mg/L Adsorbent dosage: 1 g/50 mL (0.02 g/mL) Adsorption time: 24 h Mixing rate: 150 rpm pH: 5	Alkherraz et al. (2020)
(iv)	Urea Treated *Leucaena leucocephala* Leaf	90.09	Pb(II) concentration: 50-250 mg/L Adsorbent dosage: 0.02 g/50 mL (0.0004 g/mL) Adsorption time: 30 min Mixing rate: 100 rpm pH: 5	Mansur et al. (2020)
(v)	Magnetic chitosan/graphene oxide composites	76.94	Pb(II) concentration: 0.5-14 mg/L Adsorbent dosage: 0.02 g/25 mL (0.0008 g/mL) Adsorption time: 60 min Mixing rate: 180 rpm pH: 5	Fan et al. (2013)
(vi)	Chitosan-tripolyphosphate beads	57.33	Pb(II) concentration: 20-300 mg/L Adsorbent dosage: 0.20 g/50 mL (0.004 g/mL) Adsorption time: 100 min Mixing rate: 400 rpm pH: 4.5	Ngah & Fatinathan (2010)
(vii)	Sago activated carbon (SAC)	3.202×10^{-3}	Pb(II) concentration: 1-5 mg/L Adsorbent dosage: 0.5 g/100 mL (0.005 g/mL) Adsorption time: 30 min Mixing rate: 260 rpm pH: 8	Present study

(Arami-Nya et al., 2012; Tsai et al., 2001). Gao et al. (2013) suggested at $1/n<1$, adsorption occurred from the interaction between adsorbed molecules with various energies. The ultimate adsorption capacity, K_f was 1.131×10^{-3}, and the R^2 value (0.9084) shows good fitting with Freundlich isotherm.

Both Langmuir and Freundlich isotherms depicted R^2 value larger than 0.900. However, the adsorption of Pb(II) by SAC is best represented by Langmuir isotherm (R^2=0.9308).

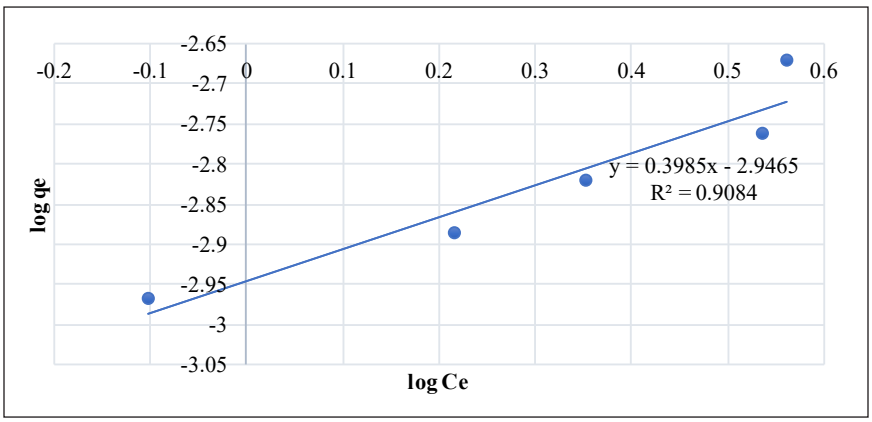

Figure 7. Freundlich isotherm plot for Pb(II) adsorption by SAC (Experimental conditions: Pb(II) concentration: 1-5 mg/L, adsorbent dosage: 0.5 g/100 mL (0.005 g/mL), adsorption time: 30 min, mixing rate: 260 rpm, pH: 8)

The separation factor, R_L obtained was 0.999, indicating that the adsorption of Pb(II) onto SAC was favourable ($0<R_L<1$).

Response Surface Methodology (RSM)

Table 5 shows the design matrix, experimental conditions; initial concentration (A), adsorbent dosage (B) and contact time (C), their ranges and responses which are percentage removal of Pb(II) ions by SAC at pH 2, to simulate the strongly acidic nature of real wastewater containing Pb ions from battery manufacturing industry (Arunlertaree et al., 2007). The Pb(II) ions removal by SAC ranged between 22.55% to 99.87%. Run 3 shows the highest percentage removal of Pb(II) ions (99.87%) was at the following experimental conditions: Pb(II) initial concentration (5 mg/L), adsorbent dosage (0.5 g), contact time (30 min). The lowest percentage removal of Pb(II) ions (22.55%) was at the following experimental conditions: Pb(II) initial concentration (5 mg/L), adsorbent dosage (0.1 g), contact time (90 min). Results from RSM study showed a contradicting Pb(II) percentage removal response compared to the batch adsorption study. The inconsistency was plausibly due to the combination effects of the parameters studied, which was in different adsorbent dosage settings in both studies i.e. 0.5 g SAC/100 mL (0.005 g/mL) Pb(II) solution in batch adsorption study, and 0.5 g SAC/50 mL Pb(II) (0.01 g/mL) solution in RSM study. Higher adsorbent dosage per volume of Pb(II) solution in RSM studies provided more active sites for adsorption of Pb(II) to occur on SAC surface (Mehdizadeh et al., 2014).

The development of the polynomial regression equations by the Design Expert software suggested quadratic model for Pb(II) removal as response of SAC usage as adsorbent. The model was selected based on the highest order polynomial where the additional terms are significant, and the model is not aliased (Arami-Nya et al., 2012). The final empirical model in terms of coded factors is represented in Equation 9.

Table 5
The percent removal of Pb(II) for 17 experimental runs

Standard Run	Parameter			% Removal of Pb(II)*
	Initial concentration (mg/L)	Adsorbent dosage (g)	Contact time (min)	
1	1.00	0.10	30.00	57.58
2	5.00	0.10	30.00	36.89
3	1.00	0.50	30.00	98.55
4	5.00	0.50	30.00	99.87
5	1.00	0.10	90.00	64.58
6	5.00	0.10	90.00	22.55
7	1.00	0.50	90.00	83.96
8	5.00	0.50	90.00	64.56
9	3.00	0.30	60.00	52.73
10	3.00	0.30	60.00	52.09
11	1.00	0.30	60.00	60.88
12	5.00	0.30	60.00	41.55
13	3.00	0.10	60.00	30.05
14	3.00	0.50	60.00	70.54
15	3.00	0.30	30.00	99.65
16	3.00	0.30	90.00	84.65
17	3.00	0.30	60.00	59.43

$$\text{Percentage removal of Pb(II)} = +56.11 - 10.01A + 20.58B - 7.22C + 5.58AB - 5.26AC - 5.32BC - 8.75A^2 - 9.67B^2 + 32.18C^2 \quad [9]$$

The coefficients with one variable, initial concentration (A), adsorbent dosage (B) and contact time (C) represent the effect of the factors on the responses of percent removal of Pb(II). The coeffiecients multiplied between two different variables show the correlation between the two variables and quadratic effect. A positive symbol in front of the terms shows synergistic effect while a negative symbol means antagonistic effect (Chowdhury et al., 2012)

The performance of the model can be concluded by determining the plots of predicted against actual (experimental) percentage removal of Pb(II) (Figure 8). High R^2 value (0.9999) indicates that the experimental data fitted excellently with the developed model. The predicted R^2 was 0.9989, which was in a reasonable range with the adjusted R^2 of 0.9996. A model ratio greater than 4 is needed where the model ratio of 205.459 indicates an adequate signal. Thus, this model can be used to navigate the design space.

The coefficient of variance (CV) value determination is crucial as it shows the ratio between the standard error of estimates with the mean value of the observed response as

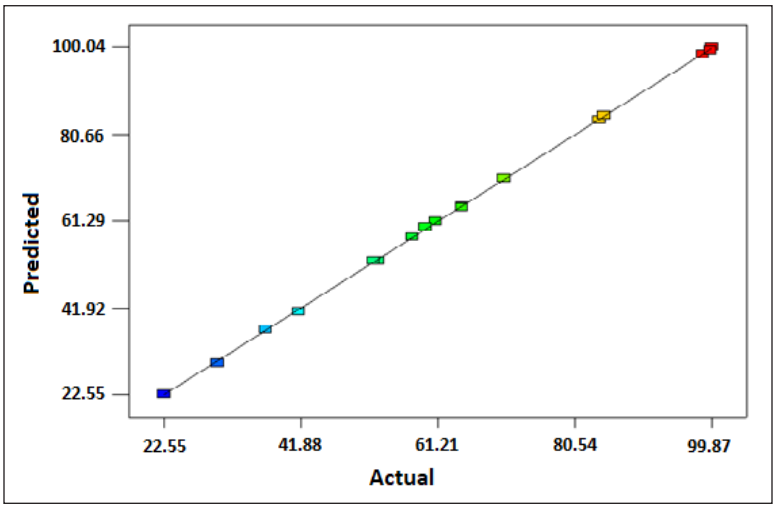

Figure 8. Predicted vs. actual percent removal of Pb(II) using SAC at pH 2 (R^2 = 0.9999, Adjusted R^2 = 0.9996, Predicted R^2 = 0.9989)

a percentage and it measures the reproducibility of the model. The model is considered reasonably reproducible if it is less than 10% (Chowdhury et al., 2012). It was observed that the CV for Pb(II) removal using SAC was 0.73%, indicating a reproducible model.

The 3-dimensional (3D) surface plots for percent removal of Pb(II) based on RSM study are represented in Figure 9. Figure 9 (a), (b) and (c) show the effects of the initial concentration of Pb(II) solution, adsorbent dosage and contact time respectively, on the removal of Pb(II) using SAC at pH 2 and standard room temperature (STP).

Figure 9a shows the effect of the adsorbent dosage and initial concentration on Pb(II) removal. The minimum removal was 36.89% at 0.1 g while the maximum removal was 99.87% at the adsorbent dosage of 0.5 g. The removal of Pb(II) increased as the adsorbent dosage was increased from 0.1 to 0.5 g at a constant concentration of Pb(II) (5 mg/L). At higher adsorbent dosage, more adsorption surfaces are available (Acharya et al., 2009), which subsequently provide more active sites for adsorption to occur (Mehdizadeh et al., 2014).

Figure 9b shows the effect of contact time and initial concentration on the percent removal of Pb(II) when the adsorbent dosage is at a constant (0.1 g). At 90 mins, the highest removal of Pb(II) was 64.68% at 1 mg/L, while the lowest removal of Pb(II) was 22.55% at 5 mg/L. This phenomenon is due to the lower availability of active sites prior to the adsorbent with time, causing limited mass transfer of Pb(II) molecules to the outer surface of adsorbents (Mehdizadeh et al., 2014). The highest removal of Pb(II) in the first 30 min was 57.58% at 1 mg/L while the lowest removal was 36.89% at 5 mg/L. However, at 60 min (3 mg/L), the removal was 30.07%. This phenomenon could be due to the reversibility of the removal process (Ghasemi et al., 2014).

Similar observation was observed on the effect of contact time and adsorbent dosage at the constant concentration of Pb(II) (5 mg/L) (Figure 9c). The maximum removal was 99.87% and slowly reduced to 41.55%, before increasing to 64.56% in 30 – 90 mins. In other words, the shorter time (30 mins) gave the best removal (99.87%) of Pb(II). The removal percentage of Pb(II) in the present study is relatively higher compared to percentage removal of Pb(II) by sawdust of *Pinus sylvestris* (97.6%) (Taty-Costodes et al., 2003) and banana peel (85.3%) (Anwar et al., 2010). The shorter contact time is important for practical wastewater treatment application.

Based on the RSM study, the highest percentage removal of Pb(II) was 99.87% indicating that the optimum conditions of Pb(II) removal was obtained: 0.5 g adsorbent dosage for 50 mL Pb(II) solution, 5 mg/L initial concentration, pH 2 at 30 mins contact time. Acidic condition (pH 2) of the Pb(II) solution may cause SAC fibrous surface to be

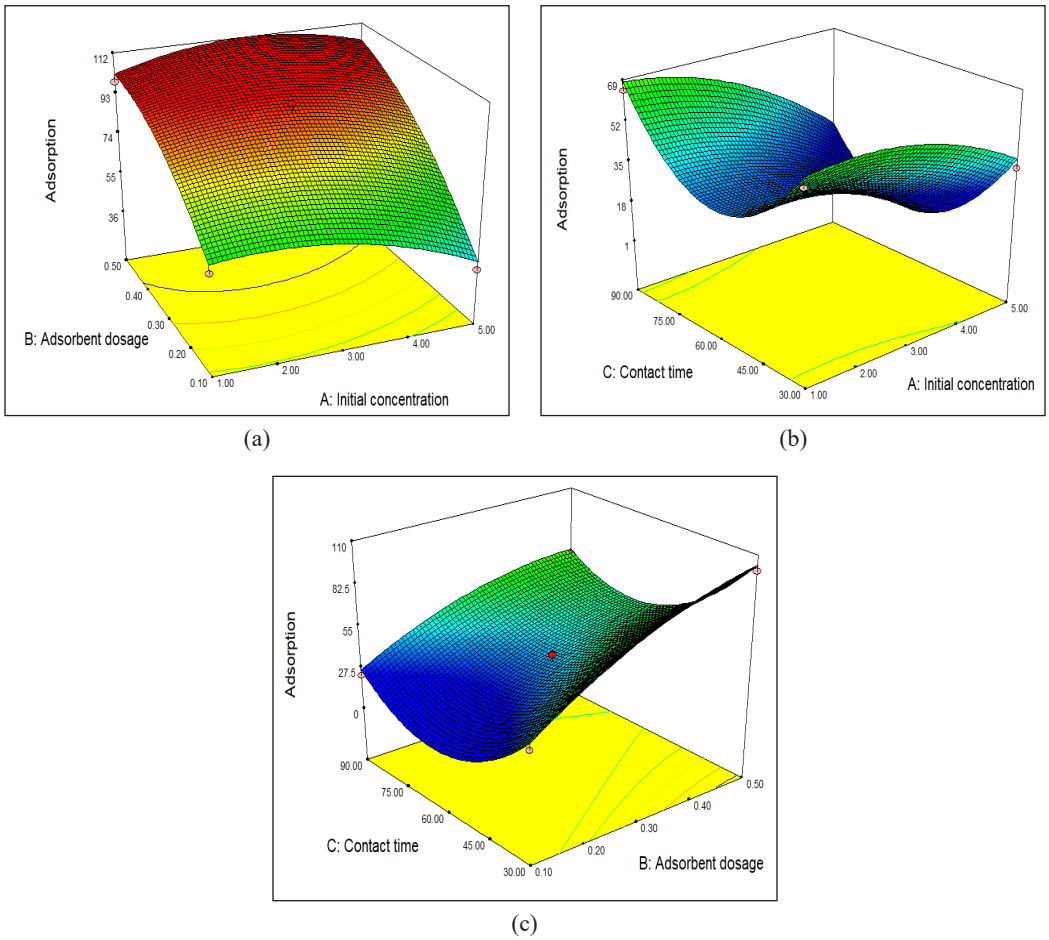

Figure 9. The combined effect of (a) adsorbent dosage and initial concentration with contact time 30 min, (b) contact time and initial concentration with adsorbent dosage 0.1 g, (c) contact time and adsorbent dosage with initial concentration 5 mg/L.

contracted and tightly captured (Arunlertaree et al., 2007), and thus increased the surface area per volume of adsorbent used (Wahi & Senghie, 2010), resulted in an increase of Pb(II) adsorption on SAC surface. In addition, the contact time of 30 min is optimum for maximised adsorption of Pb(II), as shown in previous studies (Taty-Costodes et al., 2003) and banana peel (85.3%) (Anwar et al., 2010)

CONCLUSION

In summary, a spherical nano-sized adsorbent, namely sago activated carbon (SAC) was successfully derived from sago effluent via tube furnace pyrolysis. Characterisation of the prepared adsorbent showed that large surface area was observed on sludge activated carbon (78.863 m^2/g) compared with sludge biochar (8.044 m^2/g) and sludge biomass (1.303 m^2/g). The batch adsorption best fitted the Langmuir isotherm (maximum adsorption capacity, $Q_0 = 3.202 \times 10^{-3}$ mg/g, R-squared value = 0.9308). The RSM indicated that the optimum Pb(II) removal (99.87%) was at 0.5 g of adsorbent, 5 mg/L initial concentration and 30 min contact time. The SAC derived from activated sludge process has the potential to be employed as an adsorbent to reduce the environmental issues related to sago industries.

ACKNOWLEDGEMENTS

The authors would like to thank Universiti Malaysia Sarawak for the research fund (Tun Openg Sago Research Chair: F07/TOC/1742/2018).

REFERENCES

Abbas, S. H., Ismail, I. M., Mostafa, T. M., & Sulaymon, A. H. (2014). Biosorption of heavy metals: A review. *Journal of Chemical Science and Technology, 3*(4), 74-102.

Acharya, J., Sahu, J. N., Mohanty, C. R., & Meikap, B. C. (2009). Removal of lead (II) from wastewater by activated carbon developed from tamarind wood by zinc chloride activation. *Chemical Engineering Journal, 149*(1-3), 249-262.

Ademiluyi, F. T., & Nze, J. C. (2016). Multiple adsorption of heavy metal ions in aqueous solution using activated carbon from Nigerian bamboo. *International Journal of Resource Engineering Technology, 5*(1), 164-169.

Ahmad, A., Rafatullah, M., Sulaiman, O., Ibrahim, M. H., Chii, Y. Y., & Siddique, B. M. (2009). Removal of Cu(II) and Pb(II) ions from aqueous solutions by adsorption of sawdust of Meranti wood. *Desalination, 247*(1-3), 636-464.

Aliakbari, Z., Younesi, H., Ghoreyshi, A. A., Bahramifar, N., & Heidari, A. (2016). Production of sewage-sludge based activated carbons under different post-activation conditions. *Waste and Biomass Valorization, 9*(3), 451-463.

Alkherraz, A. M., Ali, A. K., & Elsherif, K. M. (2020). Equilibrium and thermodynamic studies of Pb(II), Zn(II), Cu(II) and Cd(II) adsorption onto Mesembryanthemum activated carbon. *Journal of Medicinal and Chemical Sciences, 3*(1), 1-10.

Amuda, O. S., Deng, A., Alade, A. O., & Hung, Y. T. (2008). Conversion of sewage sludge to biosolids. *Biosolids Engineering and Management, 7*, 65-119.

Amuda, O. S., Giwa, A. A., & Bello, I. A. (2007). Removal of heavy metal from industrial wastewater using modified activated coconut shell carbon. *Biochemical Engineering Journal, 36*(2), 174-181.

Anwar, J., Shafique, U., Waheed-Uz-Zaman, Salman, M., Dar, A., & Anwar, S. (2010). Removal of Pb(II) and Cd(II) from water by adsorption on peels of banana. *Bioresource Technology, 101*(6), 1752-1755.

Arami-Nya, A., Daud, W. M. A. W., Mjalli, F. S., Abnisa, F., & Shafeeyan, M. S. (2012). Production of microporous palm shell based activated carbon for methane adsorption: modelling and optimisation using response surface methodology. *Chemical Engineering Research and Design, 90*, 776-784.

Arunlertaree, C., Kaewsomboon, W., Kumsopa, A., Pokethitiyook, P., & Panyawathanakit, P. (2007). Removal of lead from battery manufacturing wastewater by egg shell. *Songklanakarin Journal of Scince and Technology 29*(3), 857-868.

Bishnoi, N. R., Bajaj, M., Sharma, N., & Gupta, A. (2004). Adsorption of Cr(VI) on activated rice husk carbon and activated alumina. *Bioresource Technology, 91*(3), 305-307.

Carrier, M., Hardie, A. G., Uras, U., Görgens, J., & Knoetze, J. H. (2012). Production of char from vacuum pyrolysis of south african sugarcane bagasse and its characterisation as activated carbon and biochar. *Journal of Analytical and Applied Pyrolysis, 96*, 24-32.

Chowdhury, Z. Z., Zain, S. M., Khan, R. A., Arami-Nya, A., & Khalid, K. (2012). Process variables optimization for preparation and characterization of novel adsorbent from lignocellulosic waste. *Bioresources, 7*(3), 3732-3754.

Desta, B. M. (2013). Batch sorption experiments: Langmuir and freundlich isotherm studies for the adsorption of textile metal ions onto teff straw (*Eragrostic tef*) agricultural waste. *Journal of Thermodynamics, 2013*, 1-7.

El-Ashtoukhy, E. S. Z., Amin, N. K., & Abdelwahab, O. (2008). Removal of lead(II) and copper(II) from aqueous solution using pomegranate peel as a new adsorbent. *Desalination, 223*(1-3), 162-173.

Fan, L., Luo, C., Sun, M., Li, X., & Qiu, H. (2013). Highly selective adsorption of lead ions by water-dispersible magnetic chitosan/graphene oxide composites. *Colloids and Surfaces B: Biointerfaces*, *103*, 523-529.

Fat'hi, M. R., Asfaram, A., Hadipour, A., & Roosta, M. (2014). Kinetics and thermodynamic studies for removal of acid blue 129 from aqueous solution by almond shell. *Journal of Environmental Health Science and Engineering, 12*(1), 62-68.

Foo, K. Y., & Hameed, B. H. (2012a). Preparation, characterisation and evaluation of adsorptive properties of orange peel based activated carbon via microwave induced K_2CO_3 activation. *Bioresource Technology, 104*, 679-686.

Foo, K. Y., & Hameed, B. H. (2012b). Potential of jackfruit peel as precursor for activated carbon prepared by microwave induced NaOH activation. *Bioresource Technology, 112*, 143-150.

Gao, H., Sun, Y., Zhou, J., Xu, R., & Duan, H. (2013). Mussel-inspired synthesis of polydopamine-functionalised graphene hydrogel as reusable adsorbents for water purification. *ACS Applied Materials Interfaces, 5*(2), 425-432.

Gaya, U. I., Otene, E., & Abdullah, A. H. (2015). Adsorption of aqueous Cd(II) and Pb(II) on activated carbon nanopores prepared by chemical activation of doum palm shell. *SpringerPlus, 4*(1), 1-18.

Gerardi, M. H. (2002). *Nitrification and denitrification in the activated sludge process*. New York, USA: Marcel Dekker Inc.

Ghasemi, M., Khosroshahy, M. Z., Abbasabadi, A. B., Ghasemi, N., Javadion, H., & Fattahi, M. (2014). Microwave-assisted functionalisation of *Rosu canina*-L fruits activated carbon with tetraethylenepentamine and its adsorption behaviour towards Ni(II) in aqueous solution: Kinetic equilibrium and thermodynamic study. *Powder Technology, 274*, 362-371.

Hedge, G., Manaf, S. A. A., Kumat, A., Ali, G. A., Chong, K. F., Ngaini, Z. & Sharma, K. V. (2015). Biowaste sago bark based catalyst free carbon nanospheres: Waste to wealth approach. *ACS Sustainable Chemistry and Engineering, 3*(9), 2247-2253

Hema, M., & Srinivasan, K. (2010). Uptake of toxic metals from wastewater by activated carbon from ago industrial by-product. *Indian Journal of Engineering and Materials Sciences, 17*(5), 373-389.

Hu, Z., & Srinivasan, M. P. (1999). Preparation of high-surface-area activated carbons from coconut shell. *Microporous and Mesoporous Materials, 27*(1), 11-18.

Hu, C., Li, J., Zhou, Y., Li, M., Xue, F., & Li, H. (2009). Enhanced removal of methylene blue from aqueous solution by pummelo peel pretreated with sodium hydroxide. *Journal of Health Science*, *55*(4), 619-624.

Ibrahim, W. M., Hassan, A. F., & Azab, Y. A. (2016). Biosorption of toxic heavy metals from aqueous solution by Ulva lactuca activated carbon. *Egyption Journal of Basic and Applied Sciences, 3*(3), 241-249.

Kanawade, S. M., & Gaikwad, R. W. (2011). Removal of methylene blue from effluent by using activated carbon and water hyacinth as adsorbent. *International Journal of Chemical Engineering Application, 2*(5), 317-319.

Kishnor, K., Ujjval, T., & Patel, K. C. (2006). Application of response surface methodology of optimization of lactic acid production using date juice. *Journal of Microbiology and Biotechnology, 16*(9), 1410-1415.

Kumar, P. S., & Kirtika, K. (2009). Equilibrium and kinetic study of adsorption of nickel from aqueous solution onto Bael Tree leaf powder. *Journal of Engineering Science and Technology, 4*(4), 351-363.

Mansur, N. F., Hanafiah, M. A. K. M., & Ismail, M. (2020). Pb(II) Adsorption onto Urea Treated *Leucaena leucocephala* Leaf Powder: Characterization, Kinetics and Isotherm Studies. *Nature Environment and Pollution Technology, 19*(1), 311-318.

McKay, G. (1982). Adsorption of dyestuffs from aqueous solutions with activated carbon I: Equilibrium and batch contact-time studies. *Journal of Chemical Technology and Biotechnology, 32*(7-12), 759-772.

Mehdizadeh, S., Sadjadi, S., Ahmadi, S., & Outokesh, M. (2014). Removal of heavy metals from aqueous solution using platinum nanoparticles/zeolite-4A. *Journal of Environmental Health Science and Engineering, 12*(1), 1-7.

Mor, S., Ravindra, K., De Vissher, A., Dahiya, R. P., & Chandra, A. (2006). Municipal solid waste characterization and its assessment for potential methane generation: A case study. *Science of The Environment, 371*(1-3), 1-10.

Ngah, W. S. W., & Fatinathan, S. (2010). Adsorption characterization of Pb(II) and Cu(II) ions onto chitosan-tripolyphosphate beads: Kinetic, equilibrium and thermodynamic studies. *Journal of Environmental Management, 91*(4), 958-969.

Ngaini, Z., Azlin, A. R. K. A., Nazlina, S., Hasnain, H., Norhaizat, S., Teng, J. X., & Lawai, V. (2013). Production of fire-retardant sound-absorbing panels from sago waste. *Journal of Tropical Forest Science, 25*(4), 510-515.

Ngaini, Z., Wahi, R., Halimatulzahara, D., & Yusoff, N. A. N. M. (2014a). Chemically modified sago waste for oil absorption. *Pertanika Journal of Science & Technology, 22*(1), 153-161.

Ngaini, Z., Noh, F., & Wahi, R. (2014b). Esterified sago waste for engine oil removal in aqueous environment. *Environmental Technology, 35*(22), 2761-2766.

Ngaini, Z., Noh, F., & Wahi, R. (2018). Facile sorbent from esterified cellulosic sago waste for engine oil removal in marine environment. *International Journal of Environmental Science and Technology, 15*(2), 341-348.

Park, J., Hung, I., Gan, Z., Rojas, O. J., Lim, K. H., & Park, S. (2013). Activated carbon from biochar: influence of its physicochemical properties on the sorption characteristics of phenanthrene. *Bioresource Technology, 149*, 383-389.

Pathania, D., Sharma, S., & Singh, P. (2017). Removal of methylene blue by adsorption onto activated carbon developed from Ficus carida bast. *Arabian Journal of Chemistry, 10*, 1445-1451.

Patil, S., Renukdas, S., & Patel, N. (2011). Removal of methylene blue, a basic dye from aqueous solutions by adsorption using teak tree (Tectona grandis) bark powder. *International Journal of Environmental Science*, *1*(5), 711-725.

Perrin, A., Celzard, A., Albiniak, A., Jasienko-Halat, M., Mareche, J. F., & Furdin, G. (2005). NaOH activation of anthracits: Effect of hydroxide content on pore textures of methane storage ability. *Microporous and Mesoporous Materials, 81*(1-3), 31-40.

Phang, S. M., Miah, M. S., Yeoh, B. G., & Hashim, M. A. (2000). Spirulina cultivation in digested sago starch factory wastewater. *Journal of Applied Phycology, 12*, 395-400.

Qian, Q., Machida, M., & Tatsumoto, H. (2008). Textural and surface chemical characteristics of activated carbons prepared from cattle manure compost. *Waste Management, 28*(6), 1064-1071.

Rafiq, M. K., Bachmann, R. T., Rafiq, M. T., Shang, Z., Joseph, S., & Long, R. (2016). Influence of pyrolysis on physico-chemical properties of corn stover (*zea mays L.*) biochar and feasibility for carbon capture and energy balance. *PLoS ONE, 11*(6), 1-17.

Rajan, Y., Ngaini, Z., & Wahi, R. (2019). Novel adsorbent from sago-grafted silica for removal of methylene blue. *International Journal of Environmental Science and Technology, 16,* 4531-4542.

Reed, B. E., & Matsumoto, M. R. (1993). Modelling cadmium adsorption by activated carbon using the langmuir and freundlich isotherm expressions. *Separation Science and Technology*, *28*(13-14), 2179-2195.

Ricordel, S., Taha, S., Cisse, I., & Dorange, G. (2001). Heavy metals removal by adsorption onto peanut husks carbon: characterization, kinetic study and modelling. *Separation and Purification Technology, 24*(3), 389-401.

Hach-Lange (1989). *Water analysis handbook*. Loveland, CO, USA: HACH, Company.

Ronsse, F., Van, H. S., Dickinson, D., & Prins, W. (2012). Production and characterisation of slow pyrolysis biochar: Influence of feedstock type and pyrolysis conditions. *GCB Bioenergy, 5*(2), 104-115.

Senthilkumar, S., Varadarajan, P. R., Porkodi, K., & Subbhuraam, C. V. (2005). Adsorption of methylene blue onto jute fiber carbon: kinetics and equilibrium studies. *Journal of Colloid and Interface Science, 284*(1), 78-82.

Slade, A. H., Thorn, G. J. S., & Dennis, M. A. (2011). The relationship between BOD:N ratio and wastewater treatability in a nitrogen-fixing wastewater treatment system. *Water Science and Technology, 63*(4), 627-632.

Stella, M. G., Sugumaran, O., Niveditha, S., Ramalakshmi, B., Ravichandran, P., & Seshadri, S. (2016). Production, characterization and evaluation of biochar from pod (*pisum sativum*), leaf (*bassica olerase*) and peel (*citrus sinensis*) wastes. *International Journal of Recycling of Organic Wastes on Agriculture, 5*(1), 43-53.

Tan, I. A. W., Ahmad, A. L., & Hameed, B. H. (2008). Adsorption of basic dye on high-surface-area activated carbon prepared from coconut husk: Equilibrium, kinetic and thermodynamic studies. *Journal of Hazardous Materials, 154*(1-3), 337-346.

Tara, N., Siddiqui, S. I., Rathi, G., Chaudhry, S. A., Inamuddin, & Asiri, A. M. (2020). Nano-engineered adsorbent for the removal of dyes from water: A review. *Current Analytical Chemistry*, *16*, 14-40.

Taty-Costodes, V. C., Fauduet, H., Porte, C., & Delacriox, A. (2003). Removal of Cd(II) and Pb(II) ions from aqueous solutions by adsorption onto sawdust *pinus sylvestis*. *Journal of Hazardous Materials, 105*(1-3), 121-142.

Tsai, W. T., Chang, C. Y., Lin, M. C., Chien, S. F., Sun, H. F., & Hsieh, M. F. (2001). Adsorption of acid dye onto activated carbons prepared from agricultural waste bagasse by $ZnCl_2$ activation. *Chemosphere, 45*(1), 51-58.

Wahi, R., & Senghie, H. (2010). The use of microwave derived activated carbon for removal of heavy metal in aqueous solution. *Journal of Science and Technology, 3*(1), 97-108.

Wahi, R., Chuah, A. L., Nourouzi, M. M., Ngaini, Z., & Choong-Shean-Yaw, T. (2017a). Utilization of esterified sago bark fibre waste for removal of oil from palm oil mill effluent. *Journal of Chemical Engineering, 5*(1), 170-177.

Wahi, R., Zuhaidi, N. F. Q., Yusof, Y., Jamel, J., Kanakaraju, D., & Ngaini, Z. (2017b). Chemically treated microwave-derived biochar: An overview. *Biomass and Bioenergy, 107*, 411-421.

Wahi, R., Ngaini, Z., & Jok, V. U. (2009). Removal of mercury, lead and copper from aqueous solution by activated carbon of palm oil empty fruit bunch. *World Applied Sciences Journal, 5*, 84-91.

Wang, X., Zhu, N., & Yin, B. (2008). Preparation of sludge-based activated carbon and its application in dye wastewater treatment. *Journal of Hazardous Materials, 153*(1-2), 22-27.

Winkler, M. (2013). *Optimal nutrient ratios for wastewater treatment*. Colorado, USA: Hach Company.

Yue, C., Li, L. Y., & Johnston, C. (2018). Exploratory study on modification of sludge-based activated carbon for nutrient removal from stormwater runoff. *Journal of Environmental Management, 226*, 37-45.

Pertanika J. Sci. & Technol. 28 (3): 917 - 935 (2020)

PERTANIKA JOURNALS

SCIENCE & TECHNOLOGY

Journal homepage: http://www.pertanika.upm.edu.my/

Health Risk Assessment on High Groundwater Arsenic Concentration among Adult and Children in Beranang Subdistrict, Malaysia

Mohd Shahrol Abd Wahil*, Abdullah Aliff Abdul Wahab, Wong Chin Mun and Hasni Ja'afar

Community Health Department, Faculty of Medicine, UKM Medical Centre, 56000 Kuala Lumpur, Wilayah Persekutuan, Malaysia

ABSTRACT

Beranang, one of the rural areas of Selangor which still depends on the groundwater as a secondary source of water for drinking and other purposes apart from treated water. The main objective of this study was to evaluate the health risk assessment of arsenic ingestion through groundwater consumption among Beranang residents in Selangor. Five houses with a functioning electrical pump-assisted tube well were chosen for the sampling, which occurred in February 2019. The groundwater samples were taken at each sampling point and stored at room temperature during transport to the laboratory within 24 hours. The groundwater samples were analyzed using the ICP-MS method. Both hazard quotient (HQ) and lifetime cancer risk (LCR) were calculated based on the formula provided by the US EPA (United States Environment Protection Agency). Arsenic concentration in the groundwater samples was higher than the WHO Drinking Guideline and Malaysia Raw Water Standard in all houses. The mean concentration was 46.90 µg/L with maximum and minimum concentrations of 54.40 µg/L and 23.70 µg/L, respectively. The concentration was approximately 2- to 6- fold in all houses with 100% prevalence of contaminated tube wells. The health risk degree of children was higher than that of adults on the whole, indicating that children

ARTICLE INFO

Article history:
Received: 5 January 2020
Accepted: 20 February 2020
Published: 16 July 2020

E-mail addresses:
drshahrolaw@yahoo.com (Mohd Shahrol Abd Wahil)
drabdullahaliff@gmail.com (Abdullah Aliff Abdul Wahab)
chinmun0204@yahoo.com (Wong Chin Mun)
drmhasni1965@gmail.com (Hasni Ja'afar)
*Corresponding author

ISSN: 0128-7680
e-ISSN: 2231-8526

© Universiti Putra Malaysia Press

suffer much higher risks than adults. The health risk degree through oral exposure was higher than dermal exposure. Despite the fact that the groundwater is not suitable for drinking, however, there is no health risk through dermal exposure.

Keywords: Arsenic, groundwater, hazard quotient, health risk assessment, lifetime cancer risk

INTRODUCTION

Arsenic is a metalloid that occurs naturally as one of the most abundant elements in the earth's crust and is a component of more than 200 minerals (Mandal & Suzuki, 2002). In the groundwater, this heavy metal can be derived from natural sources as a result of weathering and erosion of bedrock and ore deposits (Demirak et al., 2006; Muhammad et al., 2010). The pollution of groundwater by arsenic may also be due to human activities, for examples; agricultural sectors involve the use of fertilizers and pesticides, mining activities, land development, the addition of solutes to groundwater systems, or human-induced flow-system changes (Avila-Sandoval et al., 2018). High concentration of arsenic in the groundwater can cause deterioration of drinking water quality and is adverse to human health. Arsenic is classified as a class A carcinogen based on sufficient evidence from human data (United States Environment Protection Agency, 1991).

Human exposure to arsenic occurs mainly through ingestion of arsenic-contaminated drinking water (Rahman et al., 2009). Groundwater contamination by arsenic is one of the major environmental health concerns in many countries, especially within communities that are still dependent on the tube wells as their primary source of drinking water (Chen & Ahsan, 2004; Muhammad et al., 2011; Wongsasuluk et al., 2014). The contamination of groundwater by arsenic in Bangladesh in 2000 was the largest poisoning of a population in history. It is estimated that approximately half of the 125 million people of the Bangladeshi population are at risk of drinking contaminated water (Smith et al., 2000).

Arsenic contamination in drinking water is of great concern for public health because of its effects on human health. Pregnant women and their fetuses are at risk of intoxication; previous human and animal studies have shown reproductive and developmental toxicity due to arsenic exposure (Abdul et al., 2015). In addition to acute poisoning, arsenic causes skin, lung, and bladder malignancy and has non-cancer effects on the integumentary, cardiovascular, pulmonary, nervous, endocrine, and reproductive systems (Brown & Ross, 2002).

In Malaysia, rural areas make up 70% of the total land area (231,180 square km or 23 million hectares) consisting of agricultural areas, forests, village settlements, beaches and islands. Rural community is defined as a settlement that covers all types of villages and small settlements of less than 10,000 people, features agricultural sectors and natural resources such as forest and water bodies. According to Statistic Canada 1996, rural and

small town refers to individuals in towns or municipalities outside of the commuting zone of larger urban centers with 10,000 or more population (Department of Statistic Malaysia, 2010). As for 2018, there were 7.8 million rural residents which comprised 24.4% of total Malaysia population, and majority of them were *Bumiputra*, and age between 15 - 30 years old. While in Selangor state, there were 435,900 rural residents which comprised 6.7% of total population (Ministry of Rural Development Malaysia, 2018). Beranang is an example of rural area in Hulu Langat district. It was gazetted as one of the seven sub-districts of Hulu Langat district in the National Land Code (Hulu Langat Land Office, 2018).

National coverage of water supply was 95.3% of the total population in 2016, and increased to 95.5% in 2017, with greater portion of the urban population has access to water supply as compared to rural population (Ministry of Rural Development Malaysia, 2018). Over the years, there are increasingly frequent occurrences of dry spells and water crises in Peninsular Malaysia, particularly Malacca and Selangor, and some parts of East Malaysia (Ahmed et al., 2014). Due to frequent occurrence of water crisis, the affected residents struggled for secondary source of water supply. In Beranang, the residents spent out-of-pocket money for electrical pump-assisted tube wells to overcome the crisis.

Access to information about the health risk assessment of arsenic exposure in Malaysia is limited despite reported cases of arsenic-related skin cancer due to groundwater consumption in 1990s (Jidon, 1993). The health risk assessment is used to determine whether exposure to arsenic, at any dose, can cause an increase in the incidence of adverse effects on human health. Therefore, the main objective of this study was to evaluate the health risk assessment of groundwater Arsenic consumption among Beranang residents in Selangor.

METHODS

This is a cross-sectional study that was conducted in February 2019 in Beranang, Hulu Langat, Selangor among houses equipped with shallow electrical pump-assisted tube wells.

Study Location Background

Hulu Langat district is the fifth largest (out of nine total districts) in Selangor, Malaysia. This district covers the area of 82,620 hectares and consists of seven sub-districts (Ampang, Beranang, Cheras, Hulu Langat, Hulu Semenyih, Semenyih and Kajang). Beranang was chosen due to its proximity to UKM Community Health Service Centre for undergrad and postgrad training and desirable population who consumed groundwater from the tube well until present despite having primary source of water supply from tap water. Beranang covers 6,184 hectares area of total 14,071 population (Department of Statistic Malaysia, 2000). The land use pattern of Beranang is mainly resident housing area and agriculture consists of palm oil plantation, rubber plantation, vegetables and local fruits. Beranang

river is one of the principle tributaries of Langat River. Some parts of this sub-district are mainly a forest area. The industrial sectors are distributed in the industrial hub-zone which is located three km from the study area.

Sample Collection and Laboratory Analysis

Five houses equipped with shallow electrical pump-assisted tube wells with a depth of 10 to 30 meters were purposely chosen for groundwater sampling in this study as shown in Figure 1. The coordinates of each house are as follows: House 1: 2.886748°N, 101.882698°E, House 2: 2.889236°N, 101.886726°E, House 3: 2.889438°N, 101.886581°E, House 4: 2.888878°N, 101.886177°E and House 5: 2.888853°N, 101.885757°E. The equipment used included a 60 mL volume dispensing bottle.

Groundwater collection bottles with plastic caps were used. The bottles were washed with 2.0% nitric acid (HNO_3) for 24 hours followed by a rinse with deionized water to prevent contamination. For each house, two 60 mL samples of groundwater were taken; tap spout after purging of the water and kept at room temperature, then transported immediately to the laboratory within 24 hours. During preparation, 2 mL of concentrated nitric acid and 5 mL hydrochloric acid (HCl) were added to the filtered water samples and heated gently at 95°C until the remaining volume of the solution was between 15 and 20 mL. The solutions were then allowed to cool before dilution with ultra-pure water to a volume of 100 mL. Subsequently, samples were filtered using 0.45 µm syringe filters. All reagents were of analytical reagent grade. Ultra-pure water was used for all dilutions. The element standard solutions from Perkin Elmer that were used for the calibrations were prepared by diluting

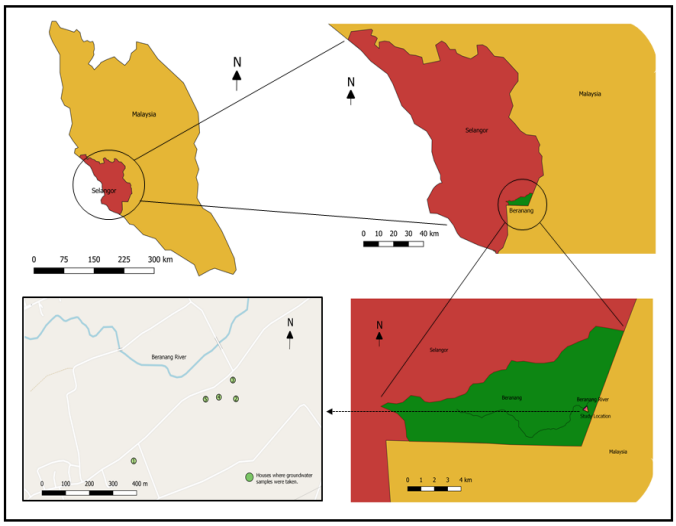

Figure 1. Study location

the multi-element Inductively Coupled Plasma Mass Spectrometry (ICP-MS) Calibration Standard 3 solutions of 10 mg/mL. The preparation and analysis of samples was done in UKM environment laboratory using an ICP-MS ELAN 9000 machine.

Exposure Scenarios

Several exposure scenarios were simulated (Table 1 and Table 2)

1. Scenario 1 - Oral exposure of arsenic: Ingestion through drinking from well water
2. Scenario 2 - Dermal exposure of arsenic: Whole body contact through bathing using well water
3. Scenario 3 - Dermal exposure of arsenic: Hands contact through washing dishes using well water
4. Scenario 4 - Dermal exposure of arsenic: Combined hands and feet contact through washing vehicle using well water

The wells are mostly secondary sources of drinking water for those homes. Since the major consumption for drinking is still from treated water, therefore, the groundwater intake rate for an individual would be approximately 1 L per day for adult and 0.5 L for children (United States Environment Protection Agency, 2019). From verbal survey, all house respondents use groundwater for other domestic purposes as well. Among all domestic activities, a person is mostly in contact with groundwater through bathing, washing dishes and washing vehicles. Watering plants using well water for instance, do not expose the person toward groundwater. Hence, the dermal absorbed dosage (DAD) is calculated for such major events in routine daily activities.

While bathing, the whole-body surface area is in contact with the water. While washing dishes, only both hands are in contact with the water. Same goes to washing car, where both hands and feet are wet with groundwater during the activity. Surface area of the skin are differed between adult and children, where adult have larger surface area than children. Different body parts have different size of surface area. For example, feet have larger surface area than hands (United States Environment Protection Agency, 2011). Average person including adult and children, he or she having shower for 15 minutes, 2 times per day (in the morning and the evening); washing dishes for 15 minutes, 3 times per day (every meal - breakfast, lunch and dinner); washing vehicle for 30 minutes, once per week.

Most of the rural residents spend their time at the village area and mainly involve in agriculture activities, hence, the exposure towards arsenic among consumer would be 350 days per year for 30 years. The exposure duration for children is 6 years (United States Environment Protection Agency, 2004). The average body weight for Asian population is lesser than the average weight for Caucasian, the author chose 60 kg as reasonable body weight for adult and 15 kg for children (Du et al., 2013; Lim et al., 2000). The average

Table 1

Specific Assumptions for Exposure for Adult

Factor	Definition	Standard Unit	Scenario Specific Assumption				Reference
			Ingestion	Dermal Absorption			
			Scenario 1	Scenario 2	Scenario 3	Scenario 4	
C	Concentration of arsenic	µg/L					This study
IR	Intake rate of water	(L/day)	1	-	-	-	US EPA 2019
K_p	Dermal permeability coefficient of arsenic in water	cm/hour	-	1.00E-03	1.00E-03	1.00E-03	US EPA 2004
T_{event}	Event duration (hour/event)	(hour/event)	-	0.25	0.25	0.5	This study
SA	Surface area of the skin	cm^2	-	20,600 (Whole body)	1,070 (Hands)	2,440 (Hands and Feet)	US EPA 2011
EV	Exposure event	(event/day)	-	2	3	1/7 (Once per week)	This study
EF	Exposure frequency	days/year	350	350	350	350	This study
ED	Exposure duration	years	30	30	30	30	US EPA 2004
BW	Average body weight	kg	60	60	60	60	Du et al. 2013, Lim et al 2000
$AT_{noncarc}$	Average time (Non-carcinogen)	days	ED x 365 days	ED x 365 days	ED x 365 days	ED x 365 days	US EPA 2004
AT_{carc}	Average time (carcinogen)	days	70 years × 365 days	70 years × 365 days	70 years × 365 days	70 years × 365 days	US EPA 2004

*US EPA = United States Environment Protection Agency

Table 2

Specific Assumptions for Exposure for Children

Factor	Definition	Standard Unit	Scenario Specific Assumption				Reference
			Ingestion		Dermal Absorption		
			Scenario 1	Scenario 2	Scenario 3	Scenario 4	
C	Concentration of arsenic	µg/L					This study
IR	Intake rate of water	(L/day)	0.5	-	-	-	US EPA 2019
K_p	Dermal permeability coefficient of arsenic in water	cm/hour	-	1.00E-03	1.00E-03	1.00E-03	US EPA 2004
T_{event}	Event duration (hour/event)	(hour/event)	-	0.25	0.25	0.5	This study
SA	Surface area of the skin	cm^2	-	10,800 (Whole body)	500 (Hands)	1,250 (Hands and Feet)	US EPA 2011
EV	Exposure event	(event/day)	-	2	3	1/7 (Once per week)	This study
EF	Exposure frequency	days/year	350	350	350	350	This study
ED	Exposure duration	years	6	6	6	6	US EPA 2004
BW	Average body weight	kg	15	15	15	15	Du et al. 2013, Lim et al 2000
$AT_{noncarc}$	Average time (Non-carcinogen)	days	ED x 365 days	ED x 365 days	ED x 365 days	ED x 365 days	US EPA 2004
AT_{carc}	Average time (carcinogen)	days	70 years × 365 days	70 years × 365 days	70 years × 365 days	70 years × 365 days	US EPA 2004

*US EPA = United States Environment Protection Agency

time used in non-carcinogen risk calculation for children is 2190 days (6 years x 365 days), for adult is 10,950 days (30 years x 365 days), while in non-carcinogen risk calculation for children or adult is 25,550 days (70 years x 365 days) (United States Environment Protection Agency, 2004).

Health Risk Assessment

Average Daily Dosage through Ingestion. Average daily dose (ADD) of arsenic in drinking water was calculated by the following Equation 1 (United States Environment Protection Agency, 1989):

$$ADD = \frac{C \times IR \times EF \times ED \times F_c}{BW \times AT} \quad [1]$$

Where,
- ADD = Average daily dosage (mg/kg-day)
- C = Concentration of toxicant (µg/L)
- IR = Intake rate of water (L/day)
- ED = Exposure duration (Year)
- EF = Exposure frequency (Days/year)
- F_c = The factor for conversion from µg to mg (0.001)
- BW = Body weight (kg)
- AT = Average time (Days)

Dermal Absorbed Dosage. Dermal absorbed dosage (DAD) of arsenic through water contact was calculated based on the formula given by US EPA as following Equation 2 (United States Environment Protection Agency, 2004):

$$DAD = \frac{C \times K_p \times T_{event} \times SA \times EV \times EF \times ED \times F_{c1} \times F_{c2}}{BW \times AT} \quad [2]$$

Where,
- DAD = Dermal absorbed dosage (mg/kg-day)
- C = Concentration of toxicant (µg/L)
- K_p = Dermal permeability coefficient of arsenic in water (cm/hour)
- T_{event} = Event duration (hour/event)
- SA = Surface area of the skin (cm^2)
- EV = Event frequency (Event/day)
- EF = Exposure frequency (Days/year)
- ED = Exposure duration (Year)
- F_{c1} = The factor for conversion from µg to mg (0.001)
- F_{c2} = The factor for conversion of unit (L/1000 cm^3) (0.001)
- BW = Body weight (kg)
- AT = Average time (Days)

Hazard Quotient (HQ) Estimation. For non-carcinogenic effects, the risk is expressed as a hazard quotient (HQ), the ratio between the exposure and the reference dose (RfD). The HQ value above 1 is considered to be a health risk. The RfD is based on the assumption that thresholds exist for certain toxic effects. The oral reference dose for arsenic is 0.0002 mg/kg-day, while the dermal absorption reference dose is 0.000190 mg/kg-day. The formula for estimating target HQ through ingestion is following Equation 3 (United States Environment Protection Agency, 1989):

$$HQ = \frac{ADD}{RfD} \quad [3]$$

Where, HQ = Hazard quotient (unitless)
ADD = Average daily dosage (mg/kg-day)
RfD = Reference dose (mg/kg-day)

The formula for estimating target HQ through dermal absorption is following Equation 4 (United States Environment Protection Agency, 2004):

$$HQ = \frac{DAD}{RfD} \quad [4]$$

Where, HQ = Hazard quotient (unitless)
DAD = Dermal absorbed dosage (mg/kg-day)
RfD = Reference dose (mg/kg-day)

Lifetime Cancer Risk (LCR) Estimation. The lifetime cancer risk (LCR) was used to assess carcinogenic effect of the toxicant exposed to the human. The LCR was calculated using the formula provided by the US EPA (United States Environment Protection Agency, 1996). The ADD was calculated the same way that had been mentioned in the section above. The cancer slope factor for oral arsenic exposure is 1.50 $(mg/kg\text{-}day)^{-1}$, while cancer slope factor for dermal arsenic exposure is 3.66 $(mg/kg\text{-}day)^{-1}$ (United States Environment Protection Agency, 1991). The risk is expressed as an excess probability of contracting cancer over a lifetime of 70 years. A one in a million (1.00E-06) cancer risk means that if one million people are exposed, one additional cancer case would be expected. The US EPA cancer risk considered acceptable for regulatory purposes is within the range of 1.00E-06 to 1.00E-04. The formula for estimating target LCR through ingestion is as following Equation 5 (United States Environment Protection Agency, 1989):

$$LCR = ADD \times CSF \quad [5]$$

Where, LCR = Lifetime cancer risk (unitless)
ADD = Average daily dose (mg/kg-day)
CSF = Cancer slope factor $(mg/kg\text{-}day)^{-1}$

The formula for estimating target LCR through dermal absorption is as following Equation 6 (United States Environment Protection Agency, 2004):

$$LCR = DAD \times CSF \quad [6]$$

Where, LCR = Lifetime cancer risk (unitless)
DAD = Dermal absorbed dosage (mg/kg-day)
CSF = Cancer slope factor $(mg/kg\text{-}day)^{-1}$

RESULTS

Arsenic Concentration in Groundwater

Surprisingly, arsenic concentration in the groundwater was found to be higher than WHO Guidelines for Drinking Water Quality (10.00 µg/L), Malaysia Recommended Raw Water Quality (10.00 µg/L), and Malaysia Drinking Water Quality Standard (10.00 µg/L), in all houses (Figure 2). The mean concentration of arsenic was 46.90 µg/L, the highest concentration recorded was 54.40 µg/L in house 4 and the lowest concentration was 23.70 µg/L in house 1.

Estimation of Potential Health Risks

Non-Cancer Risk Assessment. The HQ values for each of the scenario; drinking, bathing, washing dishes and washing vehicle among adult and children are listed in Table 3. In general, children have higher risk of non-carcinogenic effect compared to adult in all four

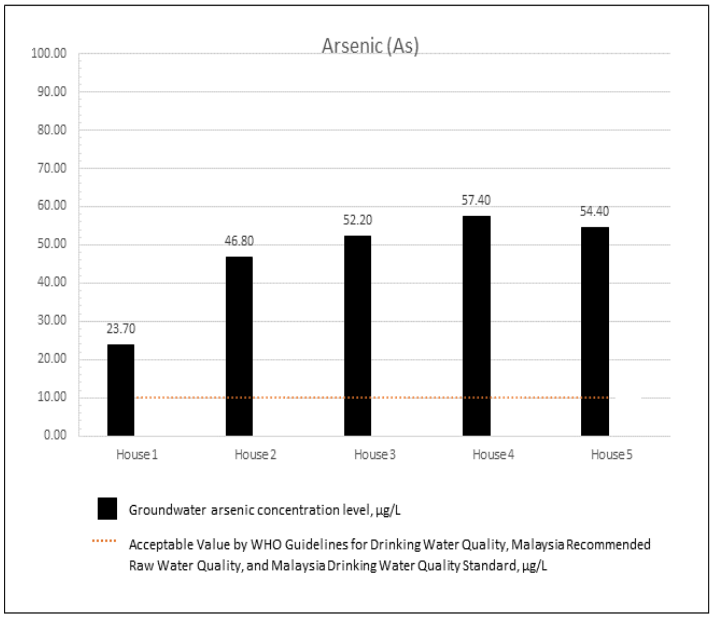

Figure 2. Groundwater arsenic concentration level in each house

scenarios. Out of total houses, member of house 4 have the highest risk. Scenario 1 posed the highest risk, followed by scenario 2, scenario 3, and scenario 4 accordingly. As shown, the HQ values were more than one for all houses in scenario 1 with the range between 1.89E+00 and 4.59E+00 among adult, and the range of 3.79E+00 and 9.17E+00 among children. The risk of getting arsenic related disease in long term is higher than those who do not consume the groundwater.

The HQ values were less than one in scenario 2. The HQ values for adult range between 2.05E-02 and 4.97E-02. The HQ values for children ranged between 4.31E-02 and 1.04E-01. The HQ values were less than one in scenario 3. The HQ values for adult ranged between 1.60E-03 and 3.87E-03. The HQ values for children were range between 3.00E-03 and 7.24E-03. The HQ values were less than one in scenario 4. The HQ value for adult were range between 3.47E-04 and 1.72E-03. These activities (bathing, washing dishes and washing vehicles) do not pose any risk of developing arsenic related disease. Therefore, these activities are considered safe when in contact with groundwater.

Cancer Risk Assessment. The LCR values for each of the scenario; drinking, bathing, washing dishes and washing vehicles among adult and children are listed in Table 4. In general, adult have higher risk of getting arsenic related malignancy as compared to children, contradict with the non-cancer risk assessment findings as mention above, due to short duration of exposure among children (6 years) compared to adult (30 years).

The LCR values for scenario 1 among adult ranged from 2.43E-4 to 5.90E-4, these values were beyond the acceptable range. The risk of developing arsenic related malignancy are between 2.4 and 5.9 in 10,000 adult population. The LCR values for drinking scenario among children were unacceptable in all houses except house 1. The LCR value in house 2, house 3, house 4 and house 5 were range between 1.92E-4 and 2.36E-4. The risk

Table 3

Arsenic concentration and hazard quotient for each scenario among adult and children

House	Arsenic Conc. (µg/L)	RfD_{inges} (mg/kg-day)	RfD_{derm} (mg/kg-day)	Ingestion	
				Scenario 1	
				HQ Adult	HQ Children
1	*23.70	2.00E-04	1.90E-04	1.89E+00	3.79E+00
2	*46.80	2.00E-04	1.90E-04	3.74E+00	7.48E+00
3	*52.20	2.00E-04	1.90E-04	4.17E+00	8.34E+00
4	*57.40	2.00E-04	1.90E-04	4.59E+00	9.17E+00
5	*54.40	2.00E-04	1.90E-04	4.35E+00	8.69E+00

Table 3 *(Continued)*

House	Dermal Absorption					
	Scenario 2		Scenario 3		Scenario 4	
	HQ Adult	HQ Children	HQ Adult	HQ Children	HQ Adult	HQ Children
1	2.05E-02	4.31E-02	1.60E-03	3.00E-03	3.47E-04	7.12E-04
2	4.05E-02	8.50E-02	3.16E-03	5.90E-03	6.86E-04	1.41E-03
3	4.52E-02	9.48E-02	3.52E-03	6.59E-03	7.65E-04	1.57E-03
4	4.97E-02	1.04E-01	3.87E-03	7.24E-03	8.41E-04	1.72E-03
5	4.71E-02	9.88E-02	3.67E-03	6.86E-03	7.98E-04	1.63E-03

*Exceed the limit of WHO Guideline (Drinking Water) and Malaysia Guideline (Raw Water)

Table 4

Arsenic concentration and lifetime cancer risk for each scenario among adult and children

House	Arsenic Conc. (µg/L)	CSF_{inges} (mg/kg-day)	CSF_{derm} (mg/kg-day)	Ingestion	
				Scenario 1	
				LCR Adult	LCR Children
1	*23.70	1.50	3.66	2.43E-04	9.74E-05
2	*46.80	1.50	3.66	4.81E-04	1.92E-04
3	*52.20	1.50	3.66	5.36E-04	2.15E-04
4	*57.40	1.50	3.66	5.90E-04	2.36E-04
5	*54.40	1.50	3.66	5.59E-04	2.24E-04

Table 4 *(Continued)*

House	Dermal Absorption					
	Scenario 2		Scenario 3		Scenario 4	
	LCR Adult	LCR Children	LCR Adult	LCR Children	LCR Adult	LCR Children
1	2.45E-05	2.57E-06	4.77E-07	1.78E-07	1.04E-07	4.24E-08
2	4.83E-05	5.07E-06	9.42E-07	3.52E-07	2.04E-07	8.38E-08
3	5.39E-05	5.65E-06	1.05E-06	3.93E-07	2.28E-07	9.35E-08
4	5.93E-05	6.22E-06	1.16E-06	4.32E-07	2.51E-07	1.03E-07
5	5.62E-05	5.89E-06	1.09E-06	4.09E-07	2.38E-07	9.74E-08

*Exceed the limit of WHO Guideline (Drinking Water) and Malaysia Guideline (Raw Water)

of developing arsenic related malignancy are between 1.9 and 2.4 in 10,000 children population.

The LCR values for scenario 2 were acceptable for both adult and children population. The LCR values for adult range between 2.45E-05 and 5.93E-05. The risk of developing arsenic related malignancy are between 2.5 and 5.9 in 100,000 adult population. The LCR values for children range between 2.57E-06 and 6.22E-06. The risk of developing arsenic related malignancy are between 2.6 and 6.2 in 1000,000 children population.

The LCR values for scenario 3 were acceptable for both adult and children population. The LCR values for adult range between 4.77E-07 and 1.16E-06. The risk of developing arsenic related malignancy are between 4.8 and 11.6 in 10,000,000 adult population. The LCR values for children range between 1.78E-07 and 4.32E-07. The risk of developing arsenic related malignancy are between 1.8 and 4.3 in 10,000,000 children population.

The LCR values for scenario 4 were acceptable for both adult and children population. The LCR values for adult range between 1.04E-07 and 2.51E-07. The risk of developing arsenic related malignancy are between 1.0 and 2.5 in 10,000,000 adult population. The LCR values for children range between 4.24E-08 and 1.03E-07. The risk of developing arsenic related malignancy are between 4.2 and 10.3 in 100,000,000 children population. The risk was too minimal and negligible.

DISCUSSIONS

Possible Source of Contamination

The study found, unexpectedly, that the groundwater of all houses was contaminated with arsenic. It may be due to combination of natural and anthropogenic source mainly from agricultural activities such as palm oil plantation and rubber plantation using pesticides and fertilizer. The use of phosphate fertilisers is also one of the causes of release of arsenic into the groundwater system. Laboratory studies suggest that phosphate that is used on soils contaminated by leaded arsenate can produce arsenic into groundwater. A study done in Kedah state found that the high concentration of arsenic in groundwater in the area was believed to be attributed to by activities of agricultural development using phosphate fertilisers and pesticides (Shamsuddin et al., 2019). There are no arsenic related mining activities in the study area, indicating that mining contamination is not the cause of the high-arsenic groundwater.

Arsenic concentration in the groundwater exceeded the WHO guideline for drinking water. The arsenic level was tremendously high by approximately 2- to 6-fold in all houses with 100% prevalence of contaminated tube-wells, a maximum concentration level of

57.40 µg/L. Highest levels of arsenic in groundwater were reported in other parts of Asia such as Afghanistan (500 µg/L), Bangladesh (2500 µg/L), Nepal (150 µg/L) , Pakistan (2580 µg/L), China (500 µg/L), Taiwan (1820 µg/L), and Mongolia (500 µg/L), in which the contaminations were mostly due to natural process; reductive dissolution and alluvial sedimentation (Ali et al., 2019). While in Malaysia, a study done in Sabah state revealed higher levels of arsenic of the well water samples than the values in the WHO health-based guidelines with the prevalence of tube wells contaminated with arsenic was 19%, a maximum concentration of 22.80 µg/L, however, the source of contamination was not mentioned (Kato et al., 2010).

Exposure Rate among House Respondents

The main difference in health risk among exposed house respondents is due to the difference in the daily average exposure dose. The higher the daily average exposure dose, the higher will be the risk. Adults and children in the model have obvious different factors which contribute to the value of average daily intake (exposure). These main factors include; intake rate, exposure duration, body surface area and body weight as calculated according to the standard equations. The average daily exposure dose of groundwater arsenic for adults is higher than that for children. Average daily intake through oral exposure is higher than dermal exposure due to dermal permeability of arsenic in the water may limit the absorption of arsenic into the body as compared to oral ingestion. Oral absorption kinetics has generally been described as a simple first-order process in most arsenic models, reflecting the rapid appearance of arsenic in the blood following oral administration. Bio-accessibility of inorganic arsenic in water through oral ingestion is almost 100% (Kenyon & Clewell III, 2015). Arsenic absorption through dermal depends on the body surface area which in contact with groundwater arsenic. The larger body surface area, the higher concentration of arsenic will be absorbed.

Degree of Health Risk among Exposed House Respondent

The non-carcinogenic risk of arsenic for children is significantly higher than the risk for adults. In general, HQ for children was 2 times more than HQ for adult in all scenarios, and in all houses. The non-cancer risk was mainly caused by oral exposure which is, approximately 90 times, 1180 times, and 5400 times as compared to whole body dermal exposure, hands dermal exposure and combined hands and feet dermal exposure respectively.

In contrast with non-carcinogenic risk, the risk for adult is higher than the risk for children. In general, LCR for adult was 2.5 times more than children through oral exposure, hands dermal exposure, and combined hands and feet dermal exposure. While, LCR for adult was much higher, 10 times more than children through whole body dermal contact in

view of enormous difference of average daily exposure. The body surface area for adult is 20600 cm^2 and body surface area of children is 10800 cm^2. The carcinogenic risk is mainly caused by oral exposure which is, approximately 10 times, 50 times, and 2300 times as compared to whole body dermal exposure, hands dermal exposure and combined hands and feet dermal exposure respectively.

Study done in China showed similar trend for degree of health risk between adult and children, where the non-cancer risk and cancer risk were mainly caused by oral exposure, which are, approximately 200 times and 100 times higher than the dermal exposure respectively (Zhang et al., 2019).

Health Effect of Arsenic

Low to moderate levels of arsenic exposure (10 - 300 µg/L) through drinking water has adverse health effects to human include skin lesions, cardiovascular disease, neurological complications, diabetes, respiratory complications, hepatic and renal dysfunction including mortality due to chronic diseases. An estimation of approximately 100 million population all around the world are exposed to arsenic levels more than 50 µg/L. Symptoms of acute exposure develop rapidly, usually exposed to high dose (concentration) of arsenic, whereas clinical symptoms of chronic arsenic exposure develop over a prolonged period of lower concentration arsenic exposure. In acute arsenic intoxication, organ damage could occur and may lead to death (Abdul et al., 2015).

Arsenic is a well-known teratogen and affects foetus development. Arsenic affects the male and female sex organs and may cause fertility issues in both genders. Spontaneous abortions, still birth, perinatal mortality, neonatal mortality, low birth weight, and preterm birth were reported to have a strong association with low to moderate (<1 - 3585 µg/L) concentration of arsenic ingestion during pregnancy (Abdul et al., 2015). Moreover, arsenic ingestion (<100 µg/L) may lead to tumorigenesis in various body parts such as skin, bladder, kidneys, lungs and liver. Effects of arsenic exposure are distinctly divided into four stages. They are preclinical, clinical, internal complications and malignancy stages (Abdul et al., 2015). In this study, all house respondents have high risk of developing health effect of arsenic through chronic oral exposure.

Arsenic Removal Technology

Tube well water is still an option for drinking and other domestic purposes in other rural areas of Malaysia. There are various cost-effective techniques for arsenic removal from drinking water. The US EPA has identified the best available technologies with maximum arsenic removal of more than 95%; ion exchange, activated alumina, reverse osmosis, modified coagulation, modified lime softening, electrodialysis reversal, and oxidation/

filtration (Han et al., 2003). For the treatment of shallow tube well water with a depth of 10 to 30 metres in rural areas of Malaysia, the main concern would be the cost of tube well maintenance and reagent and residue handling. Effective and applicable water treatment technology for arsenic removal with the existing infrastructure of tube wells in a rural setting such as ALCAN activated alumina and BUET activated alumina have advantages: almost all arsenic removed, no costly filter media or maintenance is needed, affordable and readily available hardware, it improves colour and taste of the water as iron is removed, and iron can be a visible indicator for arsenic presence and help with water quality monitoring (Van Halem et al., 2010).

Groundwater and Health Monitoring

The monitoring of groundwater quality should be done continuously by various agencies such as the Drinking Water Quality Surveillance Unit, the Engineering Services Division, the Ministry of Health Malaysia, and the Department of Environment Malaysia. Collaboration between the agencies in terms of sharing of information is vital to ensure effective groundwater quality surveillance. Health monitoring should be done periodically among high-risk groups to look for arsenic-related diseases and malignancies. This can be carried out by the nearest district health office. We suggest the extension of this activity to other parts of Malaysia where the consumption of groundwater is still practised. Frequent and effective health education about disease prevention can be given to targeted groups in the population by the health promotion team of district health offices.

Limitation

The purposive sampling method was used to select the houses equipped with a tube well because not many of the houses use well water as their drinking water supply. The purpose of this study was to assess the existing (few, but at risk) houses that use well water. A very small number of samples is not suitable for random sampling. Furthermore, this self-funded study also limits the number of samples because of laboratory costs. Structured survey was not done as the main objective of the study was to assess the possible health risk of Arsenic exposure among the residents who have been using well water for quite long time (chronic effect). The simulation scenarios proposed in this study was based on the verbal survey from respondent of all purposely chosen house. Despite the estimated exposure rate (from simulation scenarios) being weak, this information can be used for risk communication for affected residents and the calculation to measure the risk can be used in similar situation in the future. Due to the lack of long-term monitoring data, the consistency of the groundwater arsenic content is undetermined in term of time period.

CONCLUSIONS

There are crucial conclusions that can be summarized from the finding of this study. The data demonstrate high groundwater arsenic contamination in Beranang, Hulu Langat district, Selangor. The health risk degree of children was higher than that of adults on the whole, indicating that children suffer much higher risks than adults. The health risk degree through oral exposure was higher than dermal exposure. As for dermal exposure, the risk degree through whole body contact was higher than limbs contact. Groundwater arsenic in the study area mainly originates from the agriculture activities using pesticides and fertilizers. The naturally high arsenic concentration in the existing groundwater could be burdened by intense industrialization, rapid urbanization and land usage come to place.

ACKNOWLEDGMENTS

The authors would like to thank the Department of Community Health, Faculty of Medicine, National University of Malaysia for the assistance given for this research.

REFERENCES

Abdul, K. S. M., Jayasinghe, S. S., Chandana, E. P., Jayasumana, C., & De Silva, P. M. C. (2015). Arsenic and human health effects: A review. *Journal Environmental Toxicology and Pharmacology, 40*(3), 828-846.

Ahmed, F., Siwar, C., & Begum, R. A. (2014). Water resources in Malaysia: Issues and challenges. *Journal of Food, Agriculture and Environment, 12*(2), 1100-1104.

Ali, W., Rasool, A., Junaid, M., & Zhang, H. (2019). A comprehensive review on current status, mechanism, and possible sources of arsenic contamination in groundwater: A global perspective with prominence of Pakistan scenario. *Environmental Geochemistry and Health, 41*(2), 737-760.

Avila-Sandoval, C., Júnez-Ferreira, H., González-Trinidad, J., Bautista-Capetillo, C., Pacheco-Guerrero, A., & Olmos-Trujillo, E. (2018). Spatio-temporal analysis of natural and anthropogenic arsenic sources in groundwater flow systems. *International Journal of Environmental Research and Public Health, 15*(11), 1-18.

Brown, K. G., & Ross, G. L. (2002). Arsenic, drinking water, and health: A position paper of the American council on science and health. *Regulatory Toxicology and Pharmacology, 36*(2), 162-174.

Chen, Y., & Ahsan, H. (2004). Cancer burden from arsenic in drinking water in Bangladesh. *American Journal of Public Health, 94*(5), 741-744.

Demirak, A., Yilmaz, F., Tuna, A. L., & Ozdemir, N. (2006). Heavy metals in water, sediment and tissues of Leuciscus cephalus from a stream in southwestern Turkey. *Journal Chemosphere, 63*(9), 1451-1458.

Department of Statistic Malaysia. (2000). *Population distribution by local authority areas and mukims*. Population and Housing Cencus of Malaysia. Retrieved January 31, 2020, from https://www.mycensus.gov.my/index.php/census-product/publication/census-2000/652-population-distribution-by-local-authority-areas-and-mukims-2000.

Department of Statistic Malaysia. (2010). *Report on definition of urban and rural areas in population and housing census 2010*. Retrieved January 31, 2020, from https://www.rurallink.gov.my/wp-content/uploads/2015/05/23.pdf

Du, Y., Gao, B., Zhou, H., Ju, X., Hao, H., & Yin, S. (2013). Health risk assessment of heavy metals in road dusts in urban parks of Beijing, China. *Procedia Environmental Sciences, 18*, 299-309.

Han, B., Zimbron, J., Runnells, T., Shen, Z., & Wickramasinghe, S. (2003). New arsenic standard spurs search for cost effective removal techniques. *Journal American Water Works Association, 95*(10), 109-118.

Hulu Langat Land Office. (2018). *Hulu Langat district profile*. Retrieved January 31, 2020, from https://www.selangor.gov.my/hululangat.php/pages/view/125

Jidon, A. (1993). Skin cancer caused by chronic arsenical poisoning-a report of three cases. *Medical Journal of Malaysia, 48*(1), 87-92.

Kato, M., Onuma, S., Kato, Y., Thang, N. D., Yajima, I., Hoque, M. Z., & Shekhar, H. U. (2010). Toxic elements in well water from Malaysia. *Journal Toxicological and Environmental Chemistry, 92*(9), 1609-1612.

Kenyon, E. M., & Clewell III, H. J. (2015). Toxicokinetics and pharmacokinetic modeling of arsenic. In J. C. States (Ed.), *Arsenic: Exposure sources, health risks, and mechanisms of toxicity* (pp. 495-509). Hoboken, New Jersey: John Wiley & Sons, Inc.

Lim, T., Ding, L., Zaki, M., Suleiman, A., Siti, S., Aris, T., & Maimunah, A. (2000). Distribution of body weight, height and body mass index in a national sample of Malaysian adults. *The Medical Journal of Malaysia, 55*, 108-128.

Mandal, B. K., & Suzuki, K. T. (2002). Arsenic round the world: A review. *Talanta, 58*(1), 201-235.

Ministry of Rural Development Malaysia. (2018). *Basic data ministry of rural development Malaysia*. Retrieved January 31, 2020, from https://www.rurallink.gov.my/wp-content/uploads/2019/04/DATA-ASAS-KPLB-2018_FINAL.pdf

Muhammad, S., Shah, M. T., & Khan, S. (2010). Arsenic health risk assessment in drinking water and source apportionment using multivariate statistical techniques in Kohistan region, northern Pakistan. *Journal Food and Chemical Toxicology, 48*(10), 2855-2864.

Muhammad, S., Shah, M. T., & Khan, S. (2011). Health risk assessment of heavy metals and their source apportionment in drinking water of Kohistan region, northern Pakistan. *Journal Microchemical, 98*(2), 334-343.

Rahman, M. M., Ng, J. C., & Naidu, R. (2009). Chronic exposure of arsenic via drinking water and its adverse health impacts on humans. *Environmental Geochemistry and Health, 31*(1), 189-200.

Shamsuddin, M. K. N., Sulaiman, W. N. A., Ramli, M. F. B., & Kusin, F. M. (2019). Geochemical characteristic and water quality index of groundwater and surface water at Lower River Muda Basin, Malaysia. *Arabian Journal of Geosciences, 12*(9), 1-27.

Smith, A. H., Lingas, E. O., & Rahman, M. (2000). Contamination of drinking-water by arsenic in Bangladesh: A public health emergency. *Bulletin of the World Health Organization, 78*, 1093-1103.

United States Environment Protection Agency. (1989). *Risk assessment guidance for superfund volume 1 human health evaluation manual (Part A): Interim final*. Office of Solid Waste and Emergency Response Washington, DC. Retrieved January 31, 2020, from https://www.epa.gov/sites/production/files/2015-09/documents/rags_a.pdf.

United States Environment Protection Agency. (1991). *Integrated Risk information system (IRIS), chemical assessment summary for arsenic*. Retrieved August 15, 2019, from https://cfpub.epa.gov/ncea/iris/iris_documents/documents/subst/0278_summary.pdf

United States Environment Protection Agency. (1996). Proposed guidelines for carcinogen risk assessment. *Office of Research and Development, U.S. Environmental Protection Agency, Washington, DC, 61*(79), 17960-18011.

United States Environment Protection Agency. (2004). *Risk assessment guidance for superfund volume I: Human health evaluation manual (Part E, Supplemental guidance for dermal risk assessment)*. EPA/540/R/99/005(OSWER 9285.7-02EP), PB99-963312. Retrieved January 31, 2020, from https://rais.ornl.gov/documents/RAGS_E_EPA540R99005.pdf.

United States Environment Protection Agency. (2011). *Chapter 7 dermal exposure factors: Exposure factors handbook 2011 edition*. Washington, DC, EPA/600/R-09/052F, 2011. Retrieved January 31, 2020, from https://www.nrc.gov/docs/ML1400/ML14007A666.pdf.

United States Environment Protection Agency. (2019). *Exposure factors handbook chapter 3 (update): Ingestion of water and other select liquids*. Washington, DC, EPA/600/R-18/259F, 2019. Retrieved January 31, 2020, from https://ofmpub.epa.gov/eims/eimscomm.getfile?p_download_id=538153.

Van Halem, D., Olivero, S., de Vet, W., Verberk, J., Amy, G., & van Dijk, J. (2010). Subsurface iron and arsenic removal for shallow tube well drinking water supply in rural Bangladesh. *Journal Water Research, 44*(19), 5761-5769.

Wongsasuluk, P., Chotpantarat, S., Siriwong, W., & Robson, M. (2014). Heavy metal contamination and human health risk assessment in drinking water from shallow groundwater wells in an agricultural area in Ubon Ratchathani province, Thailand. *Journal Environmental Geochemistry Health, 36*(1), 169-182.

Zhang, Y., Xu, B., Guo, Z., Han, J., Li, H., Jin, L., ... & Xiong, Y. (2019). Human health risk assessment of groundwater arsenic contamination in Jinghui irrigation district, China. *Journal of Environmental Management, 237*, 163-169.

Pertanika J. Sci. & Technol. 28 (3): 937 - 950 (2020)

PERTANIKA JOURNALS

SCIENCE & TECHNOLOGY

Journal homepage: http://www.pertanika.upm.edu.my/

Construction of 3D-Terrain Model from Contour Lines using Parameterized B-Spline ruled Surface

Muhammad Ammad and Ahmad Ramli*

School of Mathematical Sciences, Universiti Sains Malaysia, 11800, Penang, Malaysia

ABSTRACT

In this paper work, three-dimensional terrain models were reconstructed from two-dimensional contour lines. Firstly, spatial curves were generated from contour lines using parameterized cubic B-spline curve interpolation. Then surfaces were constructed by using B-spline ruled surface. In the reconstruction process, some issues such as keyholes and branching may arise. Therefore, we propose a method that handles the branching object to construct a bilinear patch by following the proposed data point's extraction algorithm. We also solved keyholes issues by retaining the same knot vector condition on B-spline ruled surface. Results are also demonstrated for models with branching and without branching.

Keywords: 3D-terrain model, B-spline, contour lines, parameterization method, surface reconstruction

INTRODUCTION

Construction of 3D surface from 2D contour is very important for rapid prototyping and NC Machining in Computer Aided Design (CAD), medical imaging such as Computed Tomography (CT) and Geographical Information System (GIS) in order to be visualized for further analysis and planning. Numerous methods have been proposed in reconstructing of surfaces because it involves lots of area such as manufacturing, engineering, medical and geoinformatic. In surface reconstruction, type of data will determine the approach that is going to be used. In topographic map, shape of earth surface is represented by contour lines which is a distinguishing feature of a topographic map. Contour lines are imaginary lines connecting point of equal elevation to show the shape of terrain and topography of the landscape.

Different techniques on surface reconstruction from 2D contour have been addressed in the past but some complexities

ARTICLE INFO

Article history:
Received: 06 January 2020
Accepted: 30 March 2020
Published: 16 July 2020

E-mail addresses:
mammad343@yahoo.com (Muhammad Ammad)
alaramli@usm.my (Ahmad Ramli)
* Corresponding author

ISSN: 0128-7680
e-ISSN: 2231-8526

© Universiti Putra Malaysia Press

are common like continuity, planarity, rapid changing, multifurcation, and keyholes (Meyers et al., 1992). Keyholes actually cause a problem with triangulation process which is due to the irregular placement of point on contour (Sunderland et al., 2015) and surface continuity can be achieved by applying contour interpolation method such as performing Hermite interpolation along the gradient paths (Hormann et al., 2003).

For branching object, fast reconstruction method by Shin and Jung (2004) is implemented to generate original geometry by connecting the vertices with edges between two consecutive slices. Straight skeleton method is used to create faces on key contour by linking the key contour lines in GIS map for generating 3D terrain (Salvatore & Guitton, 2004; Sugihara & Murase, 2017).

The complexity of many geometric operations greatly depends on the method of representation. Some information related to most commonly method of representing surfaces such as implicit (Guo et al., 2010; De Araújo et al., 2015; Akenine et al., 2018), parameterized B-spline and NURBS (Lim & Haron, 2014; Zhang 2016; Bhattarai et al., 2017) are also taken into account. The parameterized form is more natural for designing and representing shape in the computer as compared to implicit (Brigger et al., 2000). The construction of surface using parameterized B-spline and radial basis function from scattered data points was discussed by Jie et al. (2016). Tensor product of B-spline interpolation can also be used as a modern acquisition technique for reconstruction of surfaces (Vaitkus & Várady, 2018). As a parametric function B-spline possesses considerable geometric significance for constructing a ruled surface, such constructions are fundamental to many CAD systems (Jha, 2008). One basic problem in the study of the parametric curve is to approximate a curve with lower degree curve segment (Amirfakhrian, 2012). However, some geometric feature such as singular point cannot be preserved. In this study our aim was to reconstruct smooth surface. So we used parameterized B-spline curve interpolation to recreate contour lines. Then by using B-spline ruled surface, we constructed surfaces on each contour. The issues related to branching object was resolved by creating a bilinear patch. In order to construct bilinear patch to fill the space between branching objects, we also proposed a data extraction algorithm. The results and comparison of our method are also discussed in detail.

The organization of the paper is as follows. Section 2 discussed previous methods related to terrain model, followed by Section 3 where definition of B-spline are presented. In Section 4 methodology and computation of proposed method is stated. In Section 5 and 6 continuity constraints and the results are discussed respectively. Finally, conclusion and future work are presented in Section 7.

LITERATURE REVIEW

Straight skeleton method by Aichholzer et al. (1995) is defined as an appropriate shrinking process for the polygon. In contour map, altitude is an important element especially for the hilly area. As altitude increases, the map of contour line is redefined. After retreating the map, if contour lines cross itself at a certain height, then one possible way to manage contour lines or polygon is by the process of division of polygon. Contour polygon is divided into two or more polygons. By this approach the polygon will change topologically during the retreating process and gradually it will reduce the size of the polygon. In this case, this method is quite useful for splitting the edge or shrinking edges to zero, making it neighboring edges adjacent. This shrinking process gives a hierarchy of nested polygons and from such polygons B-spline curves are formed, which further examine the processing of 3D terrain model as a last step. This method takes some time to reconstruct the object.

In key contour polygon (Sugihara & Murase, 2017), to create a 3D terrain model, a physical simulation is performed which uses a more realistic environment such as town model based on the 3D terrain model. Some modifications such as land formation and site preparation require construction of 3D model on these sites. This is mostly done manually by labor and it takes enormous time but in the case of key contour polygon with given elevation, in order to automate laborious step the faces connecting contour are automatically formed by using the geographic information system and CG integrated system followed by straight skeleton method and thus automatically 3D terrain model is created.

Fast reconstruction (Shin & Jung, 2004) is also an automatic reconstruction method for constructing a 3D terrain model from a 2D contour line, which does not take into account matching region and clefts due to the degraded performance and long processing time. This method is totally based on triangle strips that are generated from a single tiling operation for a simple region that does not contain branches, but it also be useful for branching. If there are branches, then contour lines are converted into several sub-contour as a partition. By considering a number of vertices and their spatial distribution the geometry of the contour line will be reconstructed by connecting the vertices with edges on adjacent contour slices or lines. In this way, in less time a most realistic model can be formed by using this fast reconstruction method. However this method may be favorable for branching surfaces and is highly rated over other methods due to its quick execution. The algorithm used in this study has restriction that the center of gravity of a contour line should be located on its interior region. Therefore unnatural structure can be observed for some models.

DEFINITIONS

The B-spline curve of degree d (order d+ 1) with control points $P_0, P_1, \ldots, P_n$ and knot values $t_0, t_1, \ldots, t_m$ is defined on the interval [a, b] = $[t_d, t_{m-d}]$ by Equation 1

$$B(t) = \sum_{i=0}^{n} P_i N_{i,d}(t) \quad [1]$$

where $N_{i,d}(t)$ is the basis function of degree *d*. The underlying core of B-spline is its basis function.

B-spline basis function of degree *d*, defined by knot vector $t_0, t_1, \ldots, t_m$ are defined recursively as Equation 2 and 3

$$N_{i,0}(t) = \begin{cases} 1, & if\ t \in [t_i, t_{i+1}) \\ 0, & otherwise \end{cases} \quad [2]$$

$$N_{i,d}(t) = \frac{t - t_i}{t_{i+d} - t_i} N_{i,d-1}(t) + \frac{t_{i+d+1} - t}{t_{i+d+1} - t_{i+1}} N_{i+1,d-1}(t) \quad [3]$$

for $i=0,\ldots, n$ and $d \geq 1$.

If the list of data points $Q_i, i \in [0, \mathrm{n}]$ are given, then the B-Spline curve interpolation of order *k* is to find the knot vector $T = (T_0, T_1, \ldots, T_{n+k-1}, T_{n+k})$, the parametric values t_i, for each $Q_i, i \in [0, \mathrm{n}]$ and the control points P_i such that the resulting B-spline curve $B(t)$ has the property as in Equation 4

$$B(t_i) = Q_i, i \in [0, n] \quad [4]$$

B-spline surface is an extension of B-spline curve. The most common kind of B-spline surface is the tensor product surface. Let $N_{i,d}(s)$ be the B-spline basis function of degree *d* with knot vector $s_0, s_1, \ldots, s_m$ and let $N_{j,e}(t)$ be the B-spline basis function of degree *e* with knot vector $t_0, t_1, \ldots, t_q$. A mathematical description of tensor product of B-spline surface with control points $P_{i,j}$ ($0 \leq i \leq n = m-d-1, 0 \leq j \leq p = q-e-1$) is defined by Equation 5

$$S(s,t) = \sum_{i=0}^{n} \sum_{j=0}^{p} P_{i,j} N_{i,d}(s) N_{j,e}(t) \quad [5]$$

for $(s,t) \in [s_d, s_{m-d}] \times [t_e, t_{q-e}]$.

A B-spline ruled surface is formed from two spatial curves *B(s)* and *C(s)* when point on each curve corresponding to the parameters are joined by a line. Consider two B-spline curves $B(s) = \sum_{i=0}^{n} b_i N_{i,d}(s)$ and $C(s) = \sum_{j=0}^{n} c_j N_{j,d}(s)$. The curves are assumed to have the same degree and to be defined on the same knot vector $s_0, s_1, \ldots, s_m$. The constructed B-spline ruled surface, linear in *t-direction*, is given by Equation 6

$$S(s,t) = \sum_{i=0}^{n} \sum_{j=0}^{1} P_{i,j} N_{i,d}(s) N_{j,1}(t) \qquad [6]$$

the surface has knot vector s_0, s_1, ... , s_m in *s-direction* and *0,0,1,1* in *t-direction.*

A digital terrain model (DTM) is a digital representation of ground surface landform using a set of height over 2D points residing on a reference surface to produce topographic map. A common mathematical representation for DTMs includes regularly spaced grid (2D raster or Matrix form), irregularly distributed 2D points (variable point distance), contour and Fourier series.

METHODS

Computation of B-Spline Ruled Surface

A 3D terrain model was constructed from 2D contour by using B-spline ruled surface. Firstly, the contour line needed to be extracted as a set of points. The data points on contour lines were interpolated by using parameterized method on cubic B-spline curve (Ammad & Ramli, 2019).

The next step was to create a surface from one slice of the contour line which was represented by a B-spline curve, to its adjacent slice using B-spline ruled surface by fulfilling all necessary and required condition. In this way, all required segment of surfaces were created between adjacent slices. The problem arising here was the closure of surface, because surface constructed by B-spline ruled surface remained open in *t-direction* at the top in fact. In *s-direction* periodic B-spline was used to reconstruct closed curves but it was much difficult to use periodic curves in *t-direction*. The idea used was to extend the surface to a single vertex (summit vertex) on top of the last contour. Another solution could be to cap the open surface with another surface but some joining problem may arise (Jaillet et al., 2001). When we chose that vertex, then the B-spline curve focused to a single point was created and the control points were summit vertex with required multiplicity. So, we generated an extra segment of surface which produced a more realistic look of 3D-terrain model. In the final step, all portions were connected into a single form which was the 3D terrain model from 2D contour line.

The computation of the B-spline ruled surface is not trivial. Special attention is required related to parameters, knots and degree of B-spline curve while constructing a ruled surface. Assume two spatial B-spline curves (Equation 7 & 8]

$$B(s) = \sum_{i=0}^{n} b_i N_{i,d}(s) \qquad [7]$$

and

$$C(s) = \sum_{j=0}^{n} c_j N_{j,d}(s) \qquad [8]$$

are defined over the same knots $s_0, s_1, \ldots, s_m$ and have the same degree d with control points b_i and c_j. B-spline surfaces are the tensor product in nature, so it is required that the two boundary curves to have the same degree and defined over the same knot values. We want to construct a ruled surface by using both curves, which is ruled in *t-direction* and there is a linear combination between these two curves. Furthermore in B-spline ruled surface, the interpolation is between the points of equal parameter values, not point of equal arc length. Because ruling according to parameter value is achieved by B-spline but not achieved by arc length due to the geometrically different surface, the constructed B-spline surface from same degree curves, defined on same knot vector, linear in *t-direction* is given by Equation 9

$$S(s,t) = \sum_{i=0}^{n} \sum_{j=0}^{1} P_{i,j} N_{i,d}(s) N_{j,1}(t) \qquad [9]$$

Before implementing Equation [9] the following conditions must be fulfilled for both curves with degree d_1 and d_2 respectively.

1. Parameter range should be the same for both curves.
2. If $d_1 = d_2$ then set $d = d_1$, If $d_1 \neq d_2$ then set $d = \max\{d_1, d_2\}$, and raise the lower degree curve to d by using degree rising algorithm.
3. If knot vector of both curves are different then use knot insertion algorithm or knot refinement algorithm to obtain identical knot vector.

Branching Object

It is always a difficult task to deal with branching surfaces. We cannot reconstruct branching surfaces with general B-spline ruled surface. However, we present a method to handle this case. In our solution, we splitted the body contour into two parts (Left and Right) at common points, because for simplifying the branching process we needed to use patches to obtain the satisfying result of the branching process. By splitting the body contour into left and the right part we got two patches, one from the left part of body contour connected to the curve b1, that interpolated left branching contour and second from the right part of body contour connected to the curve b2, that interpolated right branching contour as shown in Figure 1. These two patches make the joint between the body and the branches. The center patch fills the space between the left and right patch to provide a smooth surface that lies on existing contours.

In order to generalize our work, we proposed an Algorithm 1 to numerically find the required data points in constructing the bilinear patch. Given a list of data points p_i, q_j, and r_k of left branch, right branch and body contour respectively, then the algorithm extract the required points *a, b,* R_k and R_l, where *a* is the point of left branching contour, *b* on right branching contour, while points R_k and R_l are on body contour. The data points are shown in Figure 2 (a). The algorithm work in three steps. In first step, the user get the

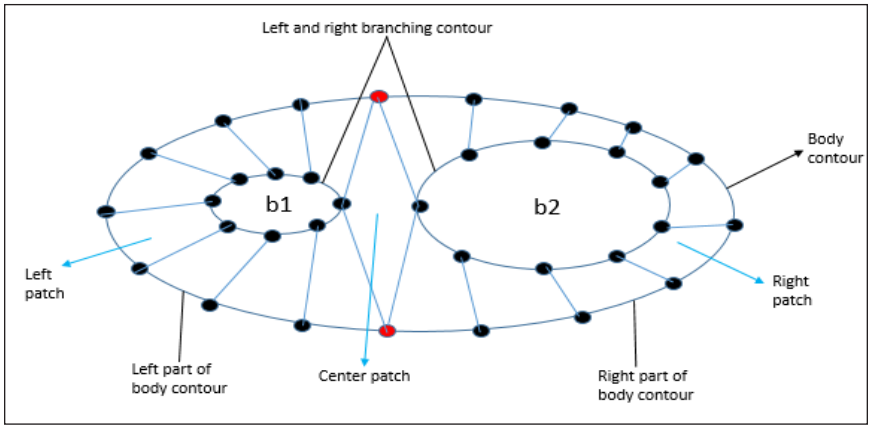

Figure 1. Skeleton of joining branches with trunk

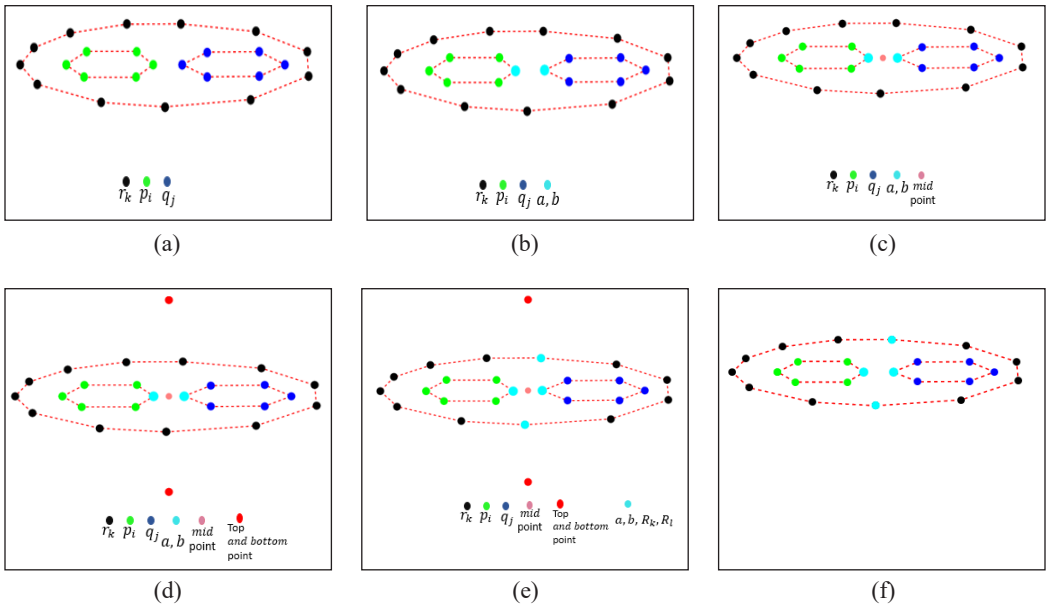

Figure 2. Step wise extraction of points for bilinear patch using Algorithm 1 (a) representation of data points. (b) Implementation of Step-1: branching points with minimum distance is marked by a and b, shown as cyan points. (c) Midpoint of a and b in marked by a pink point. (d) Step-2: top and bottom points shown as red points. (e) Step-3: Cyan points on body contour have minimum distance from top and bottom point, represented as R_k, R_l. (f) Extracted data points are represented by cyan points.

pair of points that have minimum distance, resulted *a* and *b* points as shown in Figure 2 (b). Then the midpoint of these two points is shown in Figure 2 (c). In second step the algorithm find the maximum distance of two points in body contour and compute the top (and bottom) point by adding (subtracting) maximum distance, $\boldsymbol{\alpha}$ to midpoint. The top and bottom points are shown in Figure 2 (d). In the final step, the algorithm search the points that have minimum distance from top and bottom points to all points on body contour and gives the points R_k and R_l as shown in Figure 2 (e). So the final extracted points are given in cyan color shown in Figure 2 (f).

Algorithm 1: Algorithm for finding data points for bilinear patch

Input:
$p_i = (x_i, y_i, z_i)$, $i = 1,2,\ldots,length(p)$
$q_j = (x_j, y_j, z_j)$, $j = 1,2,\ldots,length(q)$
$r_k = (x_k, y_k, z_k)$, $k = 1,2,\ldots,length(r)$
Result: $\{a, b, R_k, R_l\}$

Step 1- Initialization;
While $i=1$ *to* $length(p)$, $j=1$ *to* $length(q)$ **do**
  If $dist(p_i, q_j) \leq minDist(p_i, q_j)$ **then**
    closestpair : $(a=p_i, b=q_j)$;
    Return: a, b;
  end
end
$Midpoint = mid(a, b)$

Step 2- Initialization;
Let $R_1=r_k$, $R_2=r_l$
While $k=1$ *to* $length(r)$-1, $l=k+1$ *to* $length(r)$ **do**
  If $dist(R_1, R_2) \geq maxDist(R_1, R_2)$ **then**
    $\alpha = maxDist\ (R_1, R_2)$;
    Return: α ;
  end
end
$top = Midpoint + \alpha$
$bottom = Midpoint - \alpha$

Step 3- Initialization;
Let $R_k=r_k$, $R_l=r_l$
While $k=1$ *to* $length(r)$, $l=1$ *to* $length(r)$ **do**
  If $dist(top, R_k) \leq minDist(top, R_k)$, $dist(bottom, R_l) \leq minDist(bottom, R_l)$ **then**
    topclosestpoint: R_k;
    bottomclosestpoint: R_l;
    Return: R_k, R_l ;
  end
end

Creating a Bilinear Patch

We used B-spline ruled surface to create the left surface patch and right surface patch shown in Figure 3. Note that for this case with 4 points, the only possibility to fill the space (center patch) between these patches is to fill with a bilinear patch.

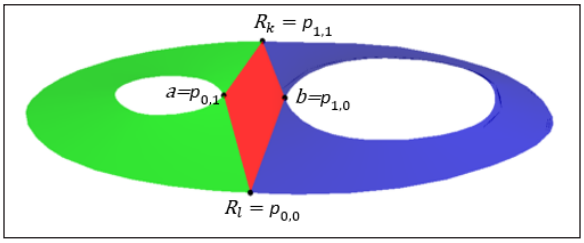

Figure 3. A closed view joining patches with bilinear patch

Given four points, $P_{0,0}$, $P_{0,1}$, $P_{1,0}$, $P_{1,1}$ then the ruled surface defined by the line segment joining $P_{0,0}$ and $P_{0,1}$ and the line segment joining $P_{1,0}$ and $P_{1,1}$ is a bilinear surface shown in Figure 1. In B-spline form the surface is as in Equation 10

$$S(s,t) = \sum_{i=0}^{1}\sum_{j=0}^{1} P_{i,j}N_{i,1}(s)N_{j,1}(t) \qquad [10]$$

with knot vector *0,0,1,1* in both directions. We can also obtain the bilinear surface in Bezier form by replacing the B-spline basis functions by the linear Bernstein basis functions.

So the center patch which was a bilinear surface patch is created by using Equation [10] and the remaining space is filled by this patch. By joining all the three patches we got a smooth branching surface and the final result is shown in Figure 3.

Continuity

In the construction of 3D-terrain model by using B-spline ruled surface, one should also check the continuity constraints in order to join all patches seamlessly. In achieving G^0 continuity between all patches, most scheme set the same degree and knot vector for all patches of B-spline (Milroy et al., 1995). By doing this, all adjacent patches share their control points along the boundaries. So, G^0 continuity is achieved trivially. In our study, in order to check G^0 continuity we also followed the theorem stated as:

Let $B(u,t)$ and $C(v,t)$ be two B-spline surfaces defined as:

$$B(u,t) = \sum_{i=0}^{m}\sum_{j=0}^{n} b_{i,j}N_{j,p}(u)N_{i,q}(t)$$

$$C(v,t) = \sum_{i=0}^{m} \sum_{j=0}^{g} c_{i,j} N_{j,r}(v) N_{i,q}(t)$$

where $b_{i,j}$, $c_{i,j}$ are the control points in E^3, and the B-spline basis functions $N_{j,p}(u)$ with degree p, $N_{i,q}(t)$ with degree q, $N_{j,r}(v)$ with degree r are defined on the non-periodic knot vector U, V and T.

The sufficient and necessary conditions of G^0 continuity between $B(u,t)$ and $C(v,t)$ is:

$$b_{i,0} = c_{i,0}$$

then $B(0,t) = C(0,t)$, namely $B(u,t)$ and $C(v,t)$ are G^0 continuous with common boundary curve $C(t)$.

However in branching model, when we attached the bilinear patch to fill the space, it also shared the boundary control points between neighboring patches which guaranteed the G^0 continuity.

RESULTS AND DISCUSSIONS

The results of three different reconstructed 3D-terrain model from 2D-contour lines have been discussed in this section. These models are directly reconstructed from interpolated contour line shown in Figure 4 (b) using B-spline ruled surface and the work is done with programming software Mathematica V.10.2. For the quality of our automatic reconstruction method, we also produced results of the complex object (e.g branching model) along with a simple matching region. In branching object, each branch was reconstructed independently and then the bilinear patch was used to make joint and fill the space between trunk and branches.

Model-1

This is one type of non-branching model and the contour lines of this model include valley, ridges and hill. The boundaries are also sprawling at some points which indicate the ridges position as shown in Figure 4 (a).

The reconstruction process of such type of model having valley and ridges is not an easy task. The user can face discontinuity between adjacent patches of B-spline ruled surface if the selected position of interpolated points is more in inside position or more in outside position. The wrong selected position of interpolated points especially at valley position can also create an edge at joining position of adjacent patches. The reconstructed model with and without meshes is shown in Figure 4 (c) and (d) respectively.

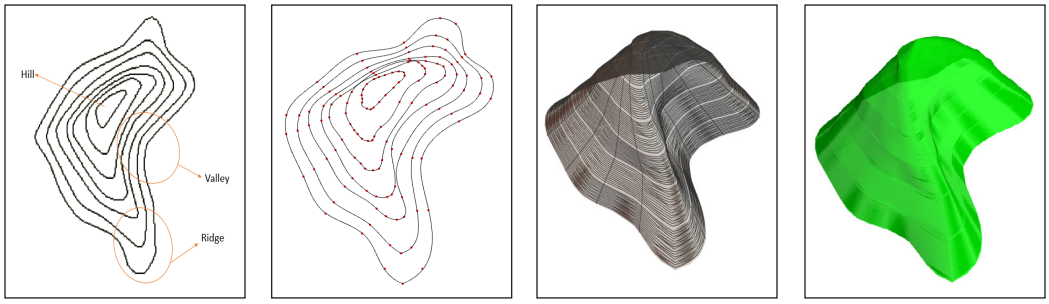

(a) (b) (c) (d)

Figure 4. Reconstructed Model-1 by B-spline ruled surface; (a) contour lines; (b) Recreated contour lines using B-spline curve interpolation; (c) Aligned model with meshes; and (d) shaded image without meshes

Model-2

This is one type of a branching model and contour lines of this model include valley, ridges, hill and saddle. Most of the researchers call branching model a complex model, because the reconstruction process of branching model is much difficult and it produces many error such as key holes and continuity problem at the region of trunk joining with branches. The result obtained by applying B-spline ruled surface with necessary and sufficient condition and after creating a bilinear patch to join branching and trunk with G^0 continuity between adjacent patches is shown in Figure 5 (c and d) with and without mesh respectively. In Figure 5 the branching part joining with trunk indicates the saddle and we can clearly see through the shaded image that our technique produces good result also for saddle region.

Model-3

This is also a non-branching model of knife edged hill that consists of 7 contour lines and the top contour line indicates a knife edge hill. The elevation change is not quick between contour lines that shows a shallow slope. The reconstruction process of these type of models

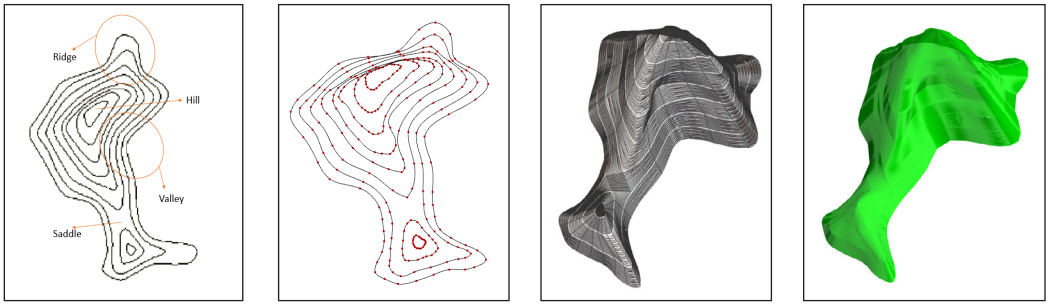

(a) (b) (c) (d)

Figure 5. Reconstructed Model-2 by B-spline ruled surface: (a) contour lines; (b) Recreated contour lines using B-spline curve interpolation; (c) Aligned model with meshes; and (d) shaded image without meshes

are very easy and possibilities of any type of errors are very rare. The resulting graph of model-3 is shown in Figure 6.

However, our method performs as well as Shin and Jung (2004) while using a different approach and a different process of dealing with branching object along with simple region. Moreover, Shin and Jung (2004) used the concept that the center of gravity of contour line should be in its interior region which might produce unnatural results for some models. But in our case there is no restriction in computation of B-spline ruled surfaces for reconstructing the surfaces.

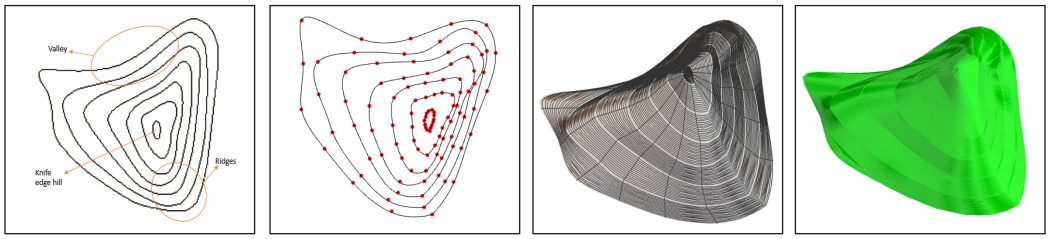

(a) (b) (c) (d)

Figure 6. Reconstructed Model-3 by B-spline ruled surface: (a) contour lines; (b) Recreated contour lines using B-spline curve interpolation; (c) Aligned model with meshes; and (d) shaded image without meshes

CONCLUSION

In this paper we used B-spline ruled surface to reconstruct the three-dimensional terrain model from two-dimensional contour lines. Our method started with the recreation of contour lines by using parameterized B-spline curve interpolation and ended up with the construction of ruled surface patches on each contour with G^0 continuity between all patches. We applied our method to both simple and complex region (branching object) and our method produced similar results to previous methods while using a different technique without the restriction that the location of the core of gravity of the contour line should be in its interior region, which could produce unnatural structure for some designs. The one drawback of the proposed method is that in branching object, the maximum achievable continuity between bilinear patch with its neighboring patches is G^0 but in the simple region, it can be higher than G^0. However, in future work, this method may be improved to reconstruct more complex objects such as saddle and ridges with higher continuity. Also, we can look into the connectivity between patches to preserve G^1 continuity.

ACKNOWLEDGEMENT

This work was supported by Universiti Sains Malaysia under RUI grant no. 1001/PMATHS/8011014.

REFERENCES

Aichholzer, O., Aurenhammer, F., Alberts, D., & Gärtner, B. (1995). A novel type of skeleton for polygons. *Journal of Universal Computer Science, 1*(12), 752-761.

Akenine-Mo, T., Haines, E., & Hoffman, N. (2018). *Real-time rendering*. New York, NY: AK Peters/CRC Press.

Amirfakhrian, M. (2012). Approximation of 3D-parametric functions by bicubic B-spline functions. *International Journal of Mathematical Modelling and Computations, 2*(3), 211-220.

Ammad, M., & Ramli, A. (2019, July 16-19). Cubic B-Spline curve interpolation with arbitrary derivatives on its data points. In *2019 23rd International Conference in Information Visualization–Part II* (pp. 156-159). Adelaide, Australia.

Bhattarai, S., Vichare, P., & Dahal, K. (2017, October 25-27). Performance comparison of adapted Delaunay triangulation method over NURBS for surface optimization problems. In *31st Annual European Simulation and Modelling Conference, ESM 2017* (pp. 76-80). Lisbon, Portugal.

Brigger, P., Hoeg, J., & Unser, M. (2000). B-spline snakes: A flexible tool for parametric contour detection. *IEEE Transactions on Image Processing, 9*(9), 1484-1496.

De Araújo, B. R., Lopes, D. S., Jepp, P., Jorge, J. A., & Wyvill, B. (2015). A survey on implicit surface polygonization. *ACM Computing Surveys (CSUR), 47*(4), 1-39.

Guo, G., Wu, X., Wang, M. Y., & Wu, J. (2010, August 4-7). Fast implicit surface reconstruction method based on normal constraints. In *2010 IEEE International Conference on Mechatronics and Automation* (pp. 1783-1788). Xi'an, China.

Hormann, K., Spinello, S., & Schröder, P. (2003, November 19-21). C1-continuous terrain reconstruction from sparse contours. In *Proceedings of the Vision, Modeling, and Visualization Conference 2003 (VMV 2003)* (Vol. 3, pp. 289-297). München, Germany.

Jaillet, F., Shariat, B., & Vandorpe, D. (2001). Smooth reconstruction of branching objects with B-splines. *Revue internationale de CFAO et d'in-formatique graphique, 16*(2), 183-201.

Jha, K. (2008). Construction of branching surface from 2-D contours. *International Journal of CAD/CAD, 8*, 1-15.

Jie, L. K., Ramli, A., & Majid, A. A. (2016). A comparison study between b-spline surface fitting and radial basis function surface fitting on scattered points. *Jurnal Teknologi, 78*(6-5), 103-107.

Lim, S. P., & Haron, H. (2014). Surface reconstruction techniques: a review. *Artificial Intelligence Review, 42*(1), 59-78.

Meyers, D., Skinner, S., & Sloan, K. (1992). Surfaces from contours. *ACM Transactions on Graphics (TOG), 11*(3), 228-258.

Milroy, M. J., Bradley, C., Vickers, G. W., & Weir, D. J. (1995). G1 continuity of B-spline surface patches in reverse engineering. *Computer-Aided Design, 27*(6), 471-478.

Salvatore, S., & Guitton, P. (2004). Contour line recognition from scanned topographic maps. *Journal of Winter School of Computer Graphics, 12*(1-3), 419-426.

Shin, B. S., & Jung, H. S. (2004). Fast reconstruction of 3d terrain model from contour lines on 2d maps. In *Asian Simulation Conference* (pp. 230-239). Heidelberg, Germany: Springer.

Sugihara, K., & Murase, T. (2017, September 20-22). Automatic generation of a 3D terrain model from key contours. In *2017 International Conference on Cyberworlds (CW)* (pp. 111-117). Chester, UK.

Sunderland, K., Woo, B., Pinter, C., & Fichtinger, G. (2015, March 18). Reconstruction of surfaces from planar contours through contour interpolation. In *Medical Imaging 2015: Image-Guided Procedures, Robotic Interventions, and Modeling* (Vol. 9415, p. 94151R). Florida, United States.

Vaitkus, M., & Várady, T. (2018). Parameterizing and extending trimmed regions for tensor-product surface fitting. *Computer-Aided Design, 104*, 125-140.

Zhang, Y. J. (2016). *Geometric modeling and mesh generation from scanned images* (Vol. 6). Boca Raton, Florida: CRC Press.

Pertanika J. Sci. & Technol. 28 (3): 951 - 966 (2020)

PERTANIKA JOURNALS

SCIENCE & TECHNOLOGY

Journal homepage: http://www.pertanika.upm.edu.my/

Extra Derivative Implicit Block Methods for Integrating General Second Order Initial Value Problems

Mohammed Yousif Turki[1], Fudziah Ismail[2,3]* and Norazak Senu[2,3]

[1]Department of Mathematics, Faculty of Education and Pure Sciences, AL-Anbar University, Iraq
[2]Department of Mathematics, Faculty of Science, Universiti Putra Malaysia,
43400 UPM, Serdang, Selangor, Malaysia
[3]Institute for Mathematical Research, Universiti Putra Malaysia, 43400 UPM, Serdang, Selangor, Malaysia

ABSTRACT

This paper focuses on the construction of two-point and three-point implicit block methods for solving general second order Initial Value Problems. The proposed methods are formulated using Hermite Interpolating Polynomial. The block methods approximate the numerical solutions at more than one point at a time directly without reducing the equation into the first order system of ordinary differential equations. In the derivation of the method, the higher derivative of the problem is incorporated into the formula to enhance the efficiency of the proposed methods. The order and zero- stability of the methods are also presented. Numerical results presented show the efficiency of these methods compared to the existing block methods.

Keywords: Block methods, extra derivative, second order IVPs

INTRODUCTION

Many researchers have focused on the block method for directly solving general second order initial value problems (IVPs), whereby the IVPs are not reduced to system of first order IVPs. Awoyemi et al. (2011) used the collocation technique to develop block linear multistep methods to solve second order IVPs. Majid et al. (2012) used two-point block method to solve general second order IVPs. Badmus (2014) developed an efficient seven-point hybrid block method for the direct solution of general second order IVPs. Abdelrahim and Omar (2016) developed a single-step hybrid block method of order five, for directly solving second order ordinary differential equations (ODEs). For

ARTICLE INFO

Article history:
Received: 12 February 2020
Accepted: 23 April 2020
Published: 16 July 2020

E-mail addresses:
moh9883@yahoo.com (Mohammed Yousif Turki)
fudziah_i@yahoo.com.my (Fudziah Ismail)
norazak@upm.edu.my (Norazak Senu)
* Corresponding author

ISSN: 0128-7680
e-ISSN: 2231-8526

© Universiti Putra Malaysia Press

solving the same type of problems, Ramos et al. (2016), developed an efficient Falkner-type method of order two and three. Waeleh and Majid (2017) derived block method to solve second order IVPs using variable stepsize code. Nasir et al. (2018) presented the diagonal block method of order four, for solving the second-order boundary value problems with Robin boundary conditions. While Singh and Ramos (2019) derived an optimized two-step hybrid block method which was formulated in variable step-size mode for integrating the general second order IVPs directly.

In most of the previously mentioned work, the methods did not have the extra derivative in the formulation of the methods. The aim of having the extra derivative in the formulation of the method is that, numerical solutions which are very accurate can be obtained. Furthermore, most of the block methods in the literature were derived using collocation and interpolation technique and some of them were derived using linear operator, which require more computational effort.

In this paper, we derived the methods using integration technique which was much simpler than the collocation and linear operator techniques. Previous work on block method which were derived using integration technique, only used Newton interpolation for the function on the right-hand side of the integration. In this research the function was replaced by Hermite interpolation, so that the extra derivatives of the problems to be solved could be included into the formula. Here, block methods with extra derivative are derived for directly solving the general second order ODEs (Equation 1).

$$y'' = f(t, y, y'), \qquad y(a) = y_0, y'(a) = y_0' \quad a \le t \le b \tag{1}$$

The first derivative of f with respect to t can be written as

$$y''' = f'(t, y, y') = f_t + y' f_y + f f_{y'} = g(t, y, y').$$

Hermite Interpolating Polynomial P, can be defined by Equation 2:

$$P(t) = \sum_{i=0}^{n} \sum_{k=0}^{m_{i-1}} f_i^{(k)} L_{i,k}(t), \tag{2}$$

where $f_i = f(t_i), t_i = a + ih,\ i = 0,1,\ldots,n$ and $h = \frac{b-a}{n}$, n is a positive integer. $L_{i,k}(t)$ is the generalized Lagrange polynomial which can be defined by

$$L_{i,m_i}(t) = \ell_{i,m_i}(t), i = 0,1,\ldots,n,$$

$$\ell_{i,k}(t) = \frac{(t - t_i)^k}{k!} \prod_{j=0, j\neq i}^{n} \left(\frac{t - t_j}{t_i - t_j}\right)^m j, i = 0,1,\ldots,n, k = 0,1,\ldots,m_i.$$

And recursively for $k = m_i - 2, m_i - 3, \ldots, 0$.

$$L_{i,k}(t) = \ell_{i,k}(t) - \sum_{v=k+1}^{m_i-1} \ell_{i,k}^{(v)}(t_i) L_{i,v}(t).$$

MATERIALS AND METHODS

Derivation of the Methods

In two-point block method, the interval $[a, b]$ contains two points for each block. To evaluate the first point, y_{n+1} and y'_{n+1} at t_{n+1}, we integrate (1) once and twice over the interval $[t_n, t_{n+1}]$, which gives Equation 3

$$\int_{t_n}^{t_{n+1}} y'' \, dt = \int_{t_n}^{t_{n+1}} f(t, y, y') dt. \tag{3}$$

and Equation 4

$$\int_{t_n}^{t_{n+1}} \int_{t_n}^{t} y' \, dt \, dt = \int_{t_n}^{t_{n+1}} \int_{t_n}^{t} f(t, y, y') dt \, dt. \tag{4}$$

Let $t_{n+1} = t_n + h$ and substituting into Equation 3 and 4, we have Equation 5 and 6

$$y'(t_{n+1}) = y'(t_n) + \int_{t_n}^{t_{n+1}} f(t, y, y') dt, \tag{5}$$

$$y'(x_{n+1}) = y(t_{n+1}) = y(t_n) + h\, y'(t_n) + \int_{t_n}^{t_{n+1}} (t_{n+1} - t) f(t, y, y') \, dt. \tag{6}$$

Then, $f(t, y, y')$ in Equation 5 and 6 will be replaced by Hermite Interpolating Polynomial in Equation 2 which is defined by $P_2(t)$ as follows (Equation 7):

$$\begin{aligned} P_2(t) = {} & [(\frac{t - t_{n+1}}{t_n - t_{n+1}})^2 (\frac{t - t_{n+2}}{t_n - t_{n+2}})^2 + (\frac{2}{t_n - t_{n+1}})(\frac{2}{t_n - t_{n+2}})(t - t_n)(\frac{t - t_{n+1}}{t_n - t_{n+1}})^2 \\ & (\frac{t - t_{n+2}}{t_n - t_{n+2}})^2] f_0 + [(\frac{t - t_{n+1}}{t_n - t_{n+1}})^2 (\frac{t - t_{n+2}}{t_n - t_{n+2}})^2] f_1 + [(\frac{t - t_n}{t_{n+2} - t_n})^2 \\ & (\frac{t - t_{n+1}}{t_{n+2} - t_{n+1}})^2 + (\frac{2}{t_{n+2} - t_{n+1}})(\frac{2}{t_{n+2} - t_n})(t - t_{n+2})(\frac{t - t_n}{t_{n+2} - t_n})^2 \\ & (\frac{t - t_{n+1}}{t_{n+2} - t_{n+1}})^2] f_2 + [(t - t_n)(\frac{t - t_{n+1}}{t_n - t_{n+1}})^2 (\frac{t - t_{n+2}}{t - t_{n+2}})^2] g_0 + [(t - t_{n+1}) \\ & (\frac{t - t_n}{t_{n+1} - t_n})^2 (\frac{t - t_{n+2}}{t_{n+2} - t_n})^2] g_1 + [(t - t_{n+2})(\frac{t - t_n}{t_{n+2} - t_n})^2 (\frac{t - t_{n+1}}{t_{n+2} - t_{n+1}})^2] g_2 \end{aligned} \tag{7}$$

Where f_0, f_1 and f_2 are the function f (Equation 1) at the first, second and third point of the interpolation, while g_0, g_1 and g_2 are the derivatives respectively (Equation 8).

Let $t = t_{n+2} + s\,h$ and

$$s = \frac{t - t_{n+2}}{h}. \tag{8}$$

Taking $dt = h\,ds$ and change the limit of integration from –2 to –1 in Equation 5 and 6 we obtain Equation 9 and 10

$$y'(x_{n+1}) = y'(x_n) + \int_{-2}^{-1}[\, f_0 L_{0,0}(s) + f_1 L_{1,0}(s) + f_2 L_{2,0}(s) + g_0 L_{0,1}(s) + g_1 L_{1,1}(s) + g_2 L_{2,1}(s)]\, h\, ds, \tag{9}$$

$$y(x_{n+1}) = y(x_n) + hy'(x_n) + \int_{-2}^{-1}(-h - sh)\,[f_0 L_{0,0}(s) + f_1 L_{1,0}(s) + f_2 L_{2,0}(s) + g_1 L_{1,1}(s) + g_2 L_{2,1}(s)]\, h\, ds\,. \tag{10}$$

where

$$L_{0,0}(s) = (\tfrac{s^2}{4}(s+1)^2 + \tfrac{3}{4}s^2(s+2)(s+1)^2),\ L_{1,0}(s) = s^2(s+2)^2,$$

$$L_{2,0}(s) = \tfrac{1}{4}((s+2)^2(s+1)^2 - 3s(s+2)^2(s+1)^2),$$

$$L_{0,1}(s) = h(\tfrac{s^2}{4}(s+2)(s+1)^2),\ L_{1,1}(s) = h(s^2(s+1)(s+2)^2),$$

$$L_{2,1}(s) = h(\tfrac{s}{4}(s+1)^2(s+2)^2).$$

Evaluating the integrals in Equation 9 and 10 produces the first formula of the two-point implicit block method as follows (Equation 11 and 12):

$$y'_{n+1} = y'_n + \frac{h}{240}[101f_n + 128f_{n+1} + 11f_n] + \frac{h^2}{240}[13g_n - 40g_{n+1} - 3g_{n+2}] \tag{11}$$

$$y_{n+1} = y_n + hy'_n + \frac{h^2}{42}[13f_n + 7f_{n+1} + f_{n+2}\Big] + \frac{h^3}{1680}[59g_n - 128g_{n+1} - 11g_{n+2}] \tag{12}$$

Integrating Equation 1 once and twice over the $[t_{n+1}, t_{n+2}]$ to obtain the approximate solutions of y_{n+2} and y'_{n+2}, we have Equation 13

$$\int_{t_{n+1}}^{t_{n+2}} y'' \, dt = \int_{t_{n+1}}^{t_{n+2}} f\,(t,y,y')dt. \tag{13}$$

and Equation 14

$$\int_{t_{n+1}}^{t_{n+2}} \int_{t_{n+1}}^{t} y' \; dt \, dt = \int_{t_{n+1}}^{t_{n+2}} \int_{t_{n+1}}^{t} f\,(t,y,y')dt \, dt. \tag{14}$$

Taking $t_{n+2} = t_{n+1} + h$ and substituting into Equation 13 and 14 we have Equation 15 and 16

$$y'(t_{n+2}) = y'(t_{n+1}) + \int_{t_{n+1}}^{t_{n+2}} f\,(t,y,y')dt \tag{15}$$

$$y(t_{n+2}) = y(t_{n+1}) + hy'(t_n) + \int_{t_{n+1}}^{t_{n+2}} (t_{n+2} - t) f\,(t,y,y')dt \tag{16}$$

Replaced $f(t,y,y')$ in Equation 15 and 16 by Hermite Interpolating Polynomial in Equation 7 and changing the limit of integration from –1 to 0 in Equation 15 and 16, we obtain Equation 17 and 18

$$\begin{aligned} y'(x_{n+2}) = y'(x_{n+1}) + \int_{-1}^{0} [\, & f_0 L_{0,0}(s) + f_1 L_{1,0}(s) + f_2 L_{2,0}(s) \\ & + g_0 L_{0,1}(s) + g_1 L_{1,1}(s) + g_2 L_{2,1}(s)]\, h \, ds. \end{aligned} \tag{17}$$

$$\begin{aligned} y(x_{n+2}) = y(x_{n+1}) + hy'(x_{n+1}) + \int_{-1}^{0} (-sh)[& f_0 L_{0,0}(s) + f_1 L_{1,0}(s) \\ & + f_2 L_{2,0}(s) + g_0 L_{0,1}(s) + g_1 L_{1,1}(s) + g_2 L_{2,1}(s)]\, h \, ds. \end{aligned} \tag{18}$$

Evaluating the integrals in Equation 17 and 18, produces the second formula of the two-point implicit block method as follows (Equation 19 and 20):

$$y'_{n+2} = y'_{n+1} + \frac{h}{240}[11f_n + 128f_{n+1} + 101f_{n+2}] + \frac{h^2}{240}[3g_n + 40g_{n+1} - 13g_{n+2}]. \tag{19}$$

$$y_{n+2} = y_{n+1} + hy'_{n+1} + \frac{h^2}{1680}[37f_n + 616f_{n+1} + 187f_{n+2}] + \frac{h^3}{80}[5g_n + 76g_{n+1} - 16g_{n+2}]. \tag{20}$$

We denote the formula as two-point second derivative block implicit method or 2PSDBI(2).

In the three-point block, each block contains three points. The values of y_{n+1}, y_{n+2} and y_{n+3} at the point t_{n+1}, t_{n+2} and $t_{n+3}1$ are calculated concurrently in a block. The approach is similar to the derivation of the two-point implicit method. Equation 1 will be integrated once and twice over the intervals $[t_n, t_{n+1}]$, $[t_{n+1}, t_{n+2}]$ and $[t_{n+2}, t_{n+3}]$ to obtain the approximate solutions of y_{n+1}, y'_{n+1}, $y_{n+2}, y'_{n+2}, y_{n+3}$ and y'_{n+3}. Define $P_3(t)$ as follows (Equation 21):

$$P_3(t) = [(\frac{t-t_{n+1}}{t_n-t_{n+1}})(\frac{t-t_{n+1}}{t_n-t_{n+1}})(\frac{t-t_{n+3}}{t_n-t_{n+3}})^2 + ((\frac{-1}{t_n-t_{n+1}}) + (\frac{-1}{t_n-t_{n+2}}) + (\frac{-2}{t_n-t_{n+3}}))$$

$$((t-t_n)(\frac{t-t_{n+1}}{t_n-t_{n+1}})(\frac{t-t_{n+2}}{t_n-t_{n+2}})(\frac{t-t_{n+3}}{t_n-t_{n+3}})^2)]f_0 + [(\frac{t-t_n}{t_{n+1}-t_n})^2(\frac{t-t_{n+2}}{t_{n+1}-t_{n+2}})(\frac{t-t_{n+3}}{t_{n+1}-t_{n+3}})^2]f_1 +$$

$$[(\frac{t-t_n}{t_{n+2}-t_n})^2(\frac{t-t_{n+1}}{t_{n+2}-t_{n+1}}) \quad (\frac{t-t_{n+3}}{t_{n+2}-t_{n+3}})^2]f_2 + [(\frac{t-t_n}{t_{n+3}-t_n})^2(\frac{t-t_{n+1}}{t_{n+3}-t_{n+1}})(\frac{t-t_{n+2}}{t_{n+3}-t_{n+2}}) - ((\frac{2}{t_{n+3}-t_n})$$

$$+(\frac{1}{t_{n+3}-t_{n+1}}) + (\frac{1}{t_{n+3}-t_{n+2}}))((t-t_{n+3})(\frac{t-t_n}{t_{n+3}-t_n})^2(\frac{t-t_{n+1}}{t_{n+3}-t_{n+1}})(\frac{t-t_{n+2}}{t_{n+3}-t_{n+2}}))]f_3$$

$$+((t-t_n)(\frac{t-t_{n+1}}{t_n-t_{n+1}})(\frac{t-t_{n+2}}{t_n-t_{n+2}})(\frac{t-t_{n+3}}{t_n-t_{n+3}})^2)g_0 + ((t-t_{n+3})(\frac{t-t_n}{t_{n+3}-t_n})^2(\frac{t-t_{n+1}}{t_{n+3}-t_{n+1}})(\frac{t-t_{n+2}}{x_{n+3}-x_{n+2}}))g_3. \quad (21)$$

Hermite Interpolating Polynomial in Equation 21 will interpolate $f(x, y, y')$ and let $t = t_{n+3} + s\,h$ and $s = \frac{t-t_{n+3}}{h}$. For each evaluation of y_{n+1}, y'_{n+1}, y_{n+2}, y'_{n+2} and y_{n+3}, y'_{n+3}, we obtained the formulae which can be written as follows (Equation 22, 23, 24, 25, 26 and 27):

$$y'_{n+1} = y'_n + \frac{h}{6480}[3463f_n + 3537f_{n+1} - 783f_{n+2} + 263f_{n+3}] + \frac{h^2}{1080}[97g_n - 17g_{n+3}], \quad (22)$$

$$y_{n+1} = y_n + h\,y'_n + \frac{h^2}{45360}[16384f_n + 7857f_{n+1} - 2376f_{n+2} + 815f_{n+3}] + \frac{h^3}{7560}[388g_n - 53g_{n+3}], \quad (23)$$

$$y'_{n+2} = y'_{n+1} + \frac{h}{80}[-7f_n + 47f_{n+1} + 47f_{n+2} - 7f_{n+3}] + \frac{h^2}{360}[-11g_n + 11g_{n+3}], \quad (24)$$

$$y_{n+2} = y_{n+1} + h\,y'_{n+1} + \frac{h^2}{15120}[-715f_n + 5832f_{n+1} + 3051f_{n+2} - 608f_{n+3}] + \frac{h^3}{2520}[-41g_n + 36g_{n+3}], \quad (25)$$

$$y'_{n+3} = y'_{n+2} + \frac{h}{6480}[263f_n - 783f_{n+1} + 3537f_{n+2} + 3463f_{n+3}] + \frac{h^2}{1080}[17g_n - 97g_{n+3}], \tag{26}$$

$$y_{n+3} = y_{n+2} + h\,y'_{n+2} + \frac{h^2}{1680}[38f_n - 115f_{n+1} + 626f_{n+2} + 291f_{n+3}] + \frac{h^3}{2520}[22g_n - 97g_{n+3}]. \tag{27}$$

This method is denoted as three-point second derivative block implicit method or 3PSDBI(2).

Order and Error Constant

The local truncation error associated with the normalized form of the proposed method can be defined as the linear difference operator (Equation 28)

$$L[\psi(t); h] = \sum_{i=0}^{k}[\alpha_i\psi(t+jh) - h\beta_i\psi'(t+jh) - h^2\gamma_i\psi''(t+jh) - h^3\delta_i\psi'''(t+jh)]. \tag{28}$$

Further detail can be seen in Fatunla (1995). Assuming that $\psi(t)$ is sufficiently differentiable, Equation 28 can be expanded as a Taylor series expansion about the point t to obtain the expression $L[\psi(t); h] = \mathbb{C}_0\psi(t) + \mathbb{C}_1 h\psi'(t) + \ldots + \mathbb{C}_p h^p\psi^{(p)}(t) + \ldots$, where the constant coefficients $\mathbb{C}_p, p = 0,1,\ldots$ are given as follows (Equation 29):

$$_0 = \sum_{i=0}^{k}\alpha_j, \quad \mathbb{C}_1 = \sum_{i=0}^{k} j\,\alpha_j - \sum_{i=0}^{k}\beta_j,$$
$$\vdots$$
$$\mathbb{C}_p = \frac{1}{p!}\sum_{i=0}^{k} j^p\,\alpha_j - \frac{1}{(p-1)!}\sum_{i=0}^{k} j^{p-1}\,\beta_j\ - \frac{1}{(p-2)!}\sum_{i=0}^{k} j^{p-2}\,\gamma_j - \frac{1}{(p-3)!}\sum_{i=0}^{k} j^{p-3}\,\delta_j, p = 3,4 \tag{29}$$

It can be said that the proposed method has order p if $\mathbb{C}_0 = \mathbb{C}_1 = \ldots \mathbb{C}_p = \mathbb{C}_{p+1} = 0, \mathbb{C}_{p+2} \neq 0$. Therefore, $\mathbb{C}_{p+2}$ is the error constant and $\mathbb{C}_{p+2}h^{p+2}\psi^{(p+2)}(t_n)$ is the principal local truncation error at the point t_n.

The formulae of the two-point implicit block method given by Equation 11, 12, 19 and 20 can be written in the form of a matrix as follows:

$$\begin{bmatrix} 0 & 0 & 0 & 0 \\ 0 & -1 & 1 & 0 \\ 0 & 0 & 0 & 0 \\ 0 & 0 & -1 & 1 \end{bmatrix}\begin{bmatrix} y_{n-1} \\ y_n \\ y_{n+1} \\ y_{n+2} \end{bmatrix} = h\begin{bmatrix} 0 & 1 & -1 & 0 \\ 0 & 1 & 0 & 0 \\ 0 & 0 & 1 & -1 \\ 0 & 0 & 1 & 0 \end{bmatrix}\begin{bmatrix} y'_{n-1} \\ y'_n \\ y'_{n+1} \\ y'_{n+2} \end{bmatrix} +$$

$$h^2\begin{bmatrix} 0 & \frac{101}{240} & \frac{128}{240} & \frac{11}{240} \\ 0 & \frac{18}{42} & \frac{7}{42} & \frac{1}{42} \\ 0 & \frac{11}{240} & \frac{128}{240} & \frac{101}{240} \\ 0 & \frac{37}{1680} & \frac{616}{1680} & \frac{187}{1680} \end{bmatrix}\begin{bmatrix} f_{n-1} \\ f_n \\ f_{n+1} \\ f_{n+2} \end{bmatrix} + h^3\begin{bmatrix} 0 & \frac{13}{240} & \frac{-40}{240} & \frac{-3}{240} \\ 0 & \frac{59}{1680} & \frac{-128}{1680} & \frac{-11}{1680} \\ 0 & \frac{3}{240} & \frac{40}{240} & \frac{-13}{240} \\ 0 & \frac{5}{840} & \frac{76}{840} & \frac{-16}{840} \end{bmatrix}\begin{bmatrix} g_{n-1} \\ g_n \\ g_{n+1} \\ g_{n+2} \end{bmatrix}$$

Or Equation 30

$$\alpha Y_m = h\beta Y'_m + h^2\gamma F_m + h^3\delta G_m \tag{30}$$

where α, β, γ and δ are the (4x4) matrix coefficients of Y_m, Y'_m, F_m and G_m respectively.

By substituting these matrices into Equation 29 we have

$$C_0 = \mathbb{C}_1 = \mathbb{C}_2 = \mathbb{C}_3 = \mathbb{C}_4 = \mathbb{C}_5 = \mathbb{C}_6 = \mathbb{C}_7 = \bar{0},$$

where $\bar{\mathbf{0}}$ is the zero vector which can be written as $\bar{0} = [0,0,0,0]^T$.

For $p = 8$, it is found that $\mathbb{C}_8 \neq \bar{\mathbf{0}}$. Hence, the two-point implicit block method has order $p = 6$ with error constant $\mathbb{C}_8 = [\frac{1}{9450}, \frac{1}{17280}, \frac{1}{9450}, \frac{29}{604800}]^T$. For the three-point implicit block method, given by Equation 22, 23, 24, 25, 26 and 27, the formulae can be written in the form of a matrix as in Equation 30, where α, β, γ and δ are matrices (6x6) and

$$\alpha = \begin{bmatrix} 0 & 0 & 0 & 0 & 0 & 0 \\ 0 & 0 & -1 & 1 & 0 & 0 \\ 0 & 0 & 0 & 0 & 0 & 0 \\ 0 & 0 & 0 & -1 & 1 & 0 \\ 0 & 0 & 0 & 0 & 0 & 0 \\ 0 & 0 & 0 & 0 & -1 & 1 \end{bmatrix}, \beta = \begin{bmatrix} 0 & 0 & 1 & -1 & 0 & 0 \\ 0 & 0 & 1 & 0 & 0 & 0 \\ 0 & 0 & 0 & 1 & -1 & 0 \\ 0 & 0 & 0 & 1 & 0 & 0 \\ 0 & 0 & 0 & 0 & 1 & -1 \\ 0 & 0 & 0 & 0 & 1 & 0 \end{bmatrix},$$

$$\gamma = \begin{bmatrix} 0 & 0 & \frac{3463}{6480} & \frac{3537}{6480} & \frac{-783}{6480} & \frac{263}{6480} \\ 0 & 0 & \frac{16384}{45360} & \frac{7857}{45360} & \frac{-2376}{45360} & \frac{815}{45360} \\ 0 & 0 & \frac{-7}{80} & \frac{47}{80} & \frac{47}{80} & \frac{-7}{80} \\ 0 & 0 & \frac{-715}{15120} & \frac{5832}{15120} & \frac{3051}{15120} & \frac{-608}{15120} \\ 0 & 0 & \frac{263}{6480} & \frac{-783}{6480} & \frac{3537}{6480} & \frac{3463}{6480} \\ 0 & 0 & \frac{38}{1680} & \frac{-115}{1680} & \frac{626}{1680} & \frac{291}{1680} \end{bmatrix}, \delta = \begin{bmatrix} 0 & 0 & \frac{97}{1080} & 0 & 0 & \frac{-17}{1080} \\ 0 & 0 & \frac{388}{7560} & 0 & 0 & \frac{-53}{7560} \\ 0 & 0 & \frac{-11}{360} & 0 & 0 & \frac{11}{360} \\ 0 & 0 & \frac{-41}{2520} & 0 & 0 & \frac{36}{2520} \\ 0 & 0 & \frac{17}{1080} & 0 & 0 & \frac{-97}{1080} \\ 0 & 0 & \frac{22}{2520} & 0 & 0 & \frac{-97}{2520} \end{bmatrix},$$

$$Y_m = \begin{bmatrix} y_{n-2} \\ y_{n-1} \\ y_n \\ y_{n+1} \\ y_{n+2} \\ y_{n+3} \end{bmatrix}, Y'_m = \begin{bmatrix} y'_{n-2} \\ y'_{n-1} \\ y'_n \\ y'_{n+1} \\ y'_{n+2} \\ y'_{n+3} \end{bmatrix}, F_m = \begin{bmatrix} f_{n-2} \\ f_{n-1} \\ f_n \\ f_{n+1} \\ f_{n+2} \\ f_{n+3} \end{bmatrix}, G_m = \begin{bmatrix} g_{n-2} \\ g_{n-1} \\ g_n \\ g_{n+1} \\ g_{n+2} \\ g_{n+3} \end{bmatrix}.$$

By substituting these matrices into (29) we have, $\mathbb{C}_0 = \mathbb{C}_1 = \cdots \mathbb{C}_6 = \mathbb{C}_7 = \bar{0}$,

It is found that, the three-point implicit block method has order $p = 6$ and error constant is $\mathbb{C}_8 = [\frac{97}{100800}, \frac{269}{604800}, \frac{-113}{100800}, \frac{-113}{201600}, \frac{97}{100800}, \frac{313}{604800}]^T$.

Zero-Stability of the Methods

For the two-point implicit block method, substituting Equation 11 into Equation 19, we have Equation 31

$$y'_{n+2} = y'_n + \frac{h}{15}[7f_n + 16f_{n+1} + 7f_{n+2} + \frac{h^2}{15}[g_n - g_{n+2}] \quad (31)$$

And also by substituting Equation 11 and 12 into Equation 20, we have Equation 32

$$y_{n+2} = y_n + 2hy'_n + h^2[\frac{79}{105}f_n + \frac{16}{15}f_{n+1} + \frac{19}{105}f_{n+2}] + h^3[\frac{2}{21}g_n - \frac{16}{105}g_{n+1} - \frac{4}{105}g_{n+2}]. \quad (32)$$

The first characteristic polynomial of the two-point implicit block method is given by,

$\rho(R) = \det[RA^{(0)} - A^{(1)}] = 0$, where

$$A^{(0)} = \begin{bmatrix} 1 & 0 & 0 & 0 \\ 0 & 1 & 0 & 0 \\ 0 & 0 & 1 & 0 \\ 0 & 0 & 0 & 1 \end{bmatrix} \text{ and } A^{(1)} = \begin{bmatrix} 0 & 0 & 1 & 0 \\ 0 & 0 & 0 & 1 \\ 0 & 0 & 1 & 0 \\ 0 & 0 & 0 & 1 \end{bmatrix}.$$

$$\rho(R) = \det \begin{bmatrix} R & 0 & -1 & 0 \\ 0 & R & 0 & -1 \\ 0 & 0 & R-1 & 0 \\ 0 & 0 & 0 & R-1 \end{bmatrix} = 0,$$

$R^2(R-1)^2 = 0, R = 0,0,1,1, |R| \leq 1.$

For the three-point implicit block method, substituting Equation 22 into Equation 24, to obtain Equation 33

$$y'_{n+2} = y'_n + h\left[\frac{181}{405}f_n + \frac{17}{15}f_{n+1} + \frac{7}{15}f_{n+2} - \frac{19}{405}f_{n+3}\right] + \frac{h^2}{135}[8g_n + 2g_{n+3}]. \quad (33)$$

Substituting Equation 22 and 23 into Equation 25, we obtain Equation 34

$$y_{n+2} = y_n + 2hy'_n + h^2[\frac{481}{567}f_n + \frac{116}{105}f_{n+1} + \frac{1}{35}f_{n+2} + \frac{52}{2835}f_{n+3}] + \frac{h^3}{945}[118g_n - 8g_{n+3}]. \quad (34)$$

Substituting Equation 33 into Equation 26, we have Equation 35

$$y'_{n+3} = y'_n + h\left[\frac{39}{80}f_n + \frac{81}{80}f_{n+1} + \frac{81}{80}f_{n+2} + \frac{39}{80}f_{n+3}\right] + \frac{h^2}{40}[3g_n - 3g_{n+3}] \quad (35)$$

And also by substituting Equation 33 and 34 into Equation 27, we have Equation 36

$$y_{n+3} = y_n + 3hy'_n + h^2[\frac{369}{280}f_n + \frac{243}{112}f_{n+1} + \frac{243}{280}f_{n+2} + \frac{81}{560}f_{n+3}] + h^3[\frac{27}{140}g_n - \frac{9}{280}g_{n+3}]. \quad (36)$$

The first characteristic polynomial of the three-point implicit block method is given as

$\rho(R) = \det[RA^{(0)} - A^{(1)}] = 0,$

where

$$A^{(0)} = \begin{bmatrix} 1 & 0 & 0 & 0 & 0 & 0 \\ 0 & 1 & 0 & 0 & 0 & 0 \\ 0 & 0 & 1 & 0 & 0 & 0 \\ 0 & 0 & 0 & 1 & 0 & 0 \\ 0 & 0 & 0 & 0 & 1 & 0 \\ 0 & 0 & 0 & 0 & 0 & 1 \end{bmatrix} \text{ and } A^{(1)} = \begin{bmatrix} 0 & 0 & 0 & 0 & 1 & 0 \\ 0 & 0 & 0 & 0 & 0 & 1 \\ 0 & 0 & 0 & 0 & 1 & 0 \\ 0 & 0 & 0 & 0 & 0 & 1 \\ 0 & 0 & 0 & 0 & 1 & 0 \\ 0 & 0 & 0 & 0 & 0 & 1 \end{bmatrix}$$

$$\rho(R) = \det\begin{bmatrix} R & 0 & 0 & 0 & -1 & 0 \\ 0 & R & 0 & 0 & 0 & -1 \\ 0 & 0 & R & 0 & -1 & 0 \\ 0 & 0 & 0 & R & 0 & -1 \\ 0 & 0 & 0 & 0 & R-1 & 0 \\ 0 & 0 & 0 & 0 & 0 & R-1 \end{bmatrix} = 0,\ R^6 - 2R^5 + R^4 = 0,$$

$R = 0,0,0,0,1,1, |R| \leq 1.$

According to Ackleh et al. (2009), the two-point and three-point implicit block methods are zero-stable, since, the characteristic polynomial $\rho(\xi)$ has a modulus less than or equal to one, and that the multiplicity of the roots with modulus one be at most two.

RESULTS AND DISCUSSION

In this section, based on the new methods, codes in C-programming language are developed for solving general second order ordinary differential equation problems and the numerical results are compared when the same set of problems are solved using the existing methods. The comparisons are made with block methods of almost the same order and the same or higher step number. The values of $y'_{n+1}, y_{n+1}, y'_{n+2}, y_{n+2}$ in the two-point method and $y'_{n+1}, y_{n+1}, y'_{n+2}, y_{n+2}, y'_{n+3}$ and y_{n+3} in the three-point method are approximated using the predictor-corrector equations. Where Taylor method is used as the predictor equation, this is the same as in the implementation of other implicit block methods in the literature, see Majid et al. (2006) for further details. We are also using Taylor method for the predictor equations in the implementation of the comparison methods, hence it is a very fair comparison. The predictor equations using Taylor method for the two point method can be written as Equation 37,

$$y'^{p}_{n+m} = y^{p}_{n+(m-1)} + h\, f^{c}_{n+(m-1)},$$
$$y^{p}_{n+m} = y^{p}_{n+(m-1)} + h\, y'^{p}_{n+(m-1)} + \frac{h^2}{2!} f^{c}_{n+(m-1)}, \quad (37)$$

$$f^{p}_{n+m} = f(t_{n+m}, y^{p}_{n+m}, y'^{p}_{n+m}),$$
$$g^{p}_{n+m} = f'(t_{n+m}, y^{p}_{n+m}, y'^{p}_{n+m}).\ m = 1,2.$$

Problem 1 :

$y'' = 2y - y'.\ y(0) = 0,\ \ y'(0) = 1,\ \ [0,10].$

Exact Solution: $y(t) = \frac{e^{t} - e^{-2t}}{3}.$

Problem 2 :

$$t^2y'' + ty' + (t^2 - 0.25)y = 0.\ y(1) = \sqrt{\frac{2}{\pi}}sin1,\ \ y'(1) = \frac{2cos1 - sin1}{\sqrt{2\pi}},\ \ [1,8].$$

Exact Solution: $y(t) = \sqrt{\frac{2}{\pi t}}sin(t).$

Problem 3:

$y'' - t(y')^2 = 0.\ y(0) = 1,\ \ y'(0) = \frac{1}{2},\ \ [0,1].$

Exact Solution: $y(t) = 1 + \frac{1}{2}ln(\frac{2+t}{2-t}).$

Problem 4 :

$y''_1 = -y_2 + sin\pi t, \qquad y_1(0) = 0, \ y'_1(0) = -1,$

$y''_2 = -y_1 + 1 - \pi^2 sin\pi t, \quad y_2(0) = 1, \ y'_2(0) = 1 + \pi, \ [0,5].$

Exact Solution: $y_1(t) = 1 - e^t, y_2(t) = e^t + sin\pi t.$

Problem 5:

$y''_1 = \frac{-y_1}{r^3}, \qquad y_1(0) = 1, \ y'_1(0) = 0,$

$y''_2 = \frac{-y_2}{r^3}, \quad y_2(0) = 0, \ y'_2(0) = 1, \ r = \sqrt{y_1^2 + y_2^2}, \ [0,10].$

Exact Solution: $y_1(t) = cos(t), y_2(t) = sin(t).$

Problem 6:

$y'' = 100y, \ y(0) = 1, \ y'(0) = -10, \ [0,2].$

Exact Solution: $y(t) = e^{-10t}.$

From the set of test problems, problems 1, 2 and 4 are linear problems. Problems 3 and 5 are nonlinear problems and problem 6 is a mildly stiff problem. Problem 5 is also the two body problem which determines the motion of two objects interact with each other.

Notations used are:

h : step size.
Time : time in seconds.
Max Error : maximum error $|y(t_i) - y_i|$.
2PSDBI(2) : New two-point implicit second derivative block method of order six.
3PSDBI(2) : New three-point implicit second derivative block method of order six.
Majid(2) : Order three, Two-point implicit block method in Majid et al. (2012).
Omar : Order five, Implicit Four-point block method in Omar and Adeyeye (2016)
Awoyemi(2): Order four, Implicit Three-point modified block method in Awoyemi et al. (2011).
Mukhtar(2) : Four- point implicit block method in Mokhtar et al. (2012).

1.2345(-6) means $1.2345 \text{x} 10^{-6}$. Numerical results for 2PSDBI(2) are given in Figure 1 to 6, whereas for 3PSDBI(2) are given in Figure 7 to 12 respectively.

For methods with less algebraic order usually the accuracy is less but the total computational time is also less since it has less function evaluations or less number of steps in the formula. For method with higher algebraic order the accuracy is more but the computational time is also more because there are more steps and more function

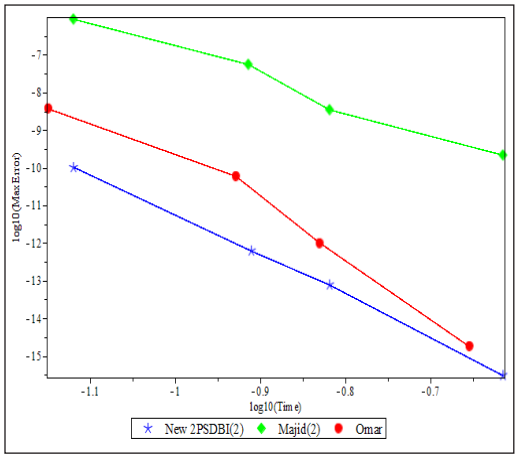

Figure 1. Efficiency curves (2PSDBI(2)) for Problem 1

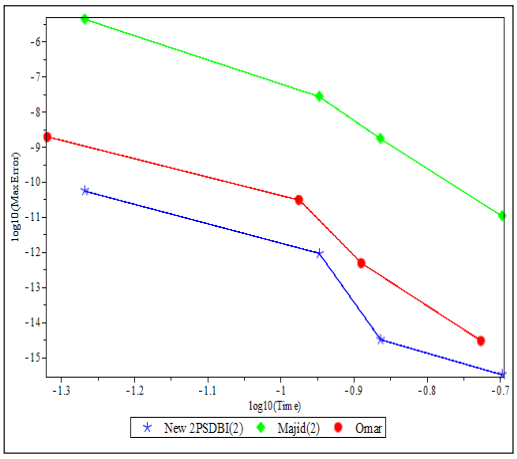

Figure 2. Efficiency curves (2PSDBI(2)) for Problem 2

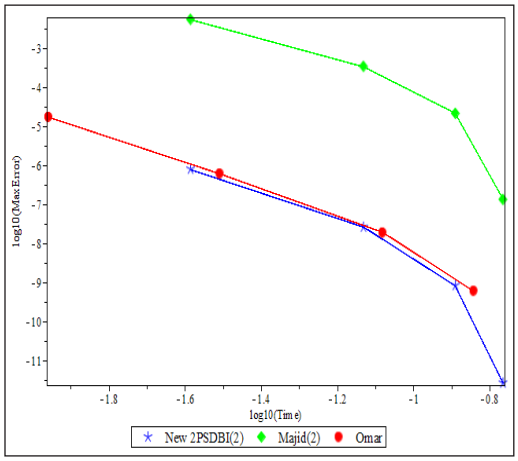

Figure 3. Efficiency curves (2PSDBI(2)) for Problem 3

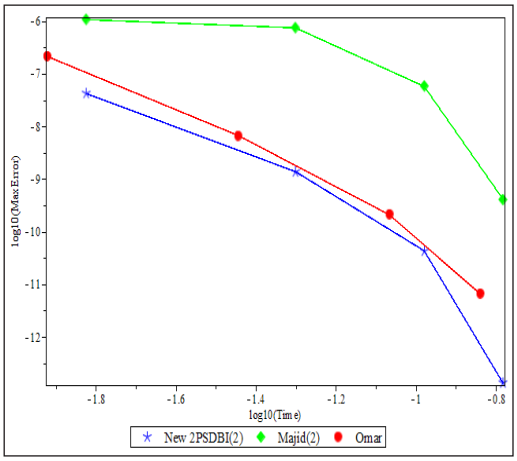

Figure 4. Efficiency curves (2PSDBI(2)) for Problem 4

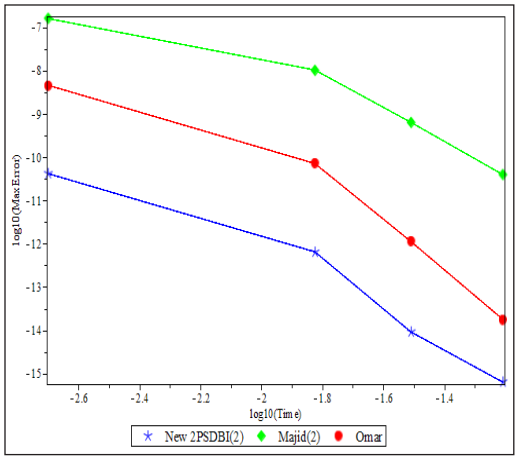

Figure 5. Efficiency curves (2PSDBI(2)) for Problem 5

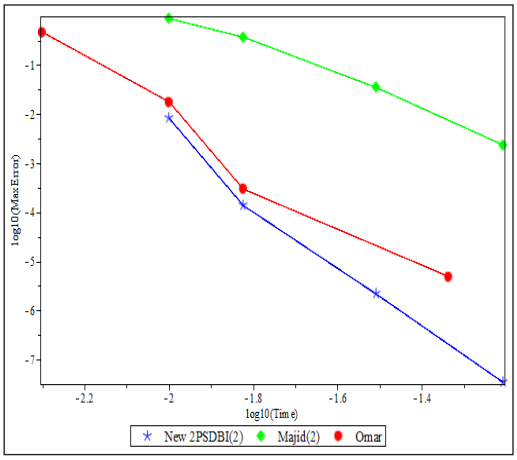

Figure 6. Efficiency curves (2PSDBI(2))for Problem 6

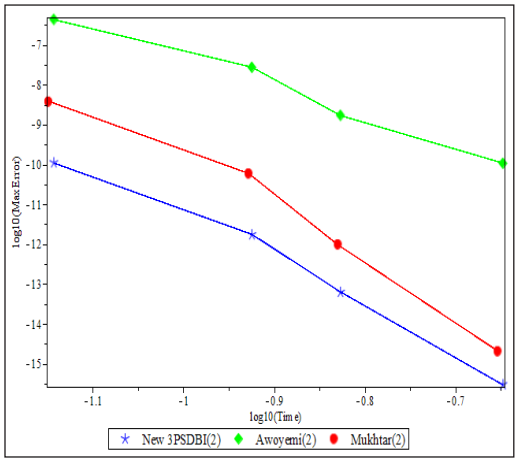

Figure 7. Efficiency curves (3PSDBI(2)) for Problem 1

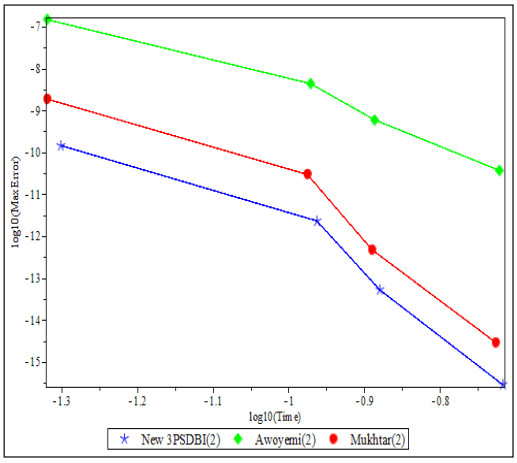

Figure 8. Efficiency curves (3PSDBI(2)) for Problem 2

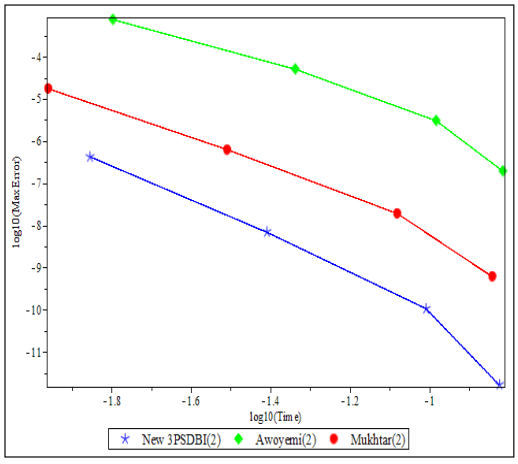

Figure 9. Efficiency curves (3PSDBI(2)) for Problem 3

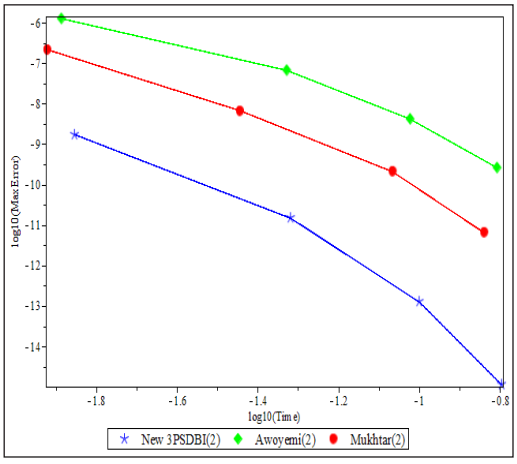

Figure 10. Efficiency curves (3PSDBI(2)) for Problem 4

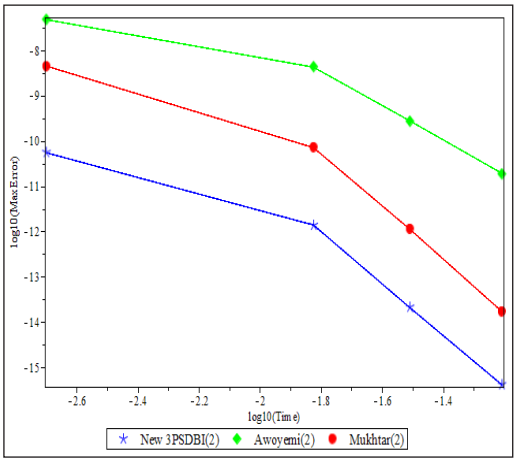

Figure 11. Efficiency curves (3PSDBI(2)) for Problem 5

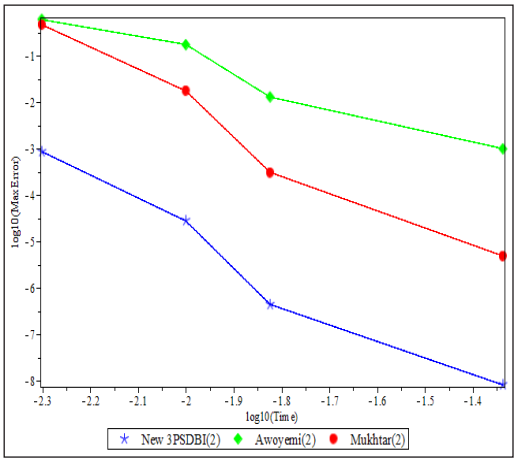

Figure 12. Efficiency curves (3PSDBI(2)) for Problem 6

evaluations in the formula. Thus, the right technique of measuring the efficiency of certain numerical methods is by using the efficiency curves. Figure1 to 12, showed the efficiency curves, where the common logarithm of the maximum global errors were plotted versus the computational time. From the efficiency curves given in Figure 1 to 6, it is observed that 2PSDBI(2) method is the most efficient compared to Majid(2) and Omar for solving the same set of test problems, since a smaller global maximum error can be attained for the same total of computational time. The same observation can be seen in Figure 7 to 12, it is obvious that the new 3PSDBI(2) method performed better than Awoyemi(2) and Mukhtar(2) methods.

CONCLUSION

We presented the construction of two and three-point extra derivative implicit block methods for directly solving general second order IVPs. The order and zero-stability of the methods are given. The methods are then used to solve linear, nonlinear and mildly stiff IVPs. From the efficiency curves, we can be conclude that the proposed methods performed noticeably more efficient than the existing methods, though the methods of comparisons are of the same nature as the proposed methods, that is block in nature and can directly solve general second order IVPs. Therefore, the proposed methods have a very high potential to be an efficient numerical methods for integrating general second order IVPs.

ACKNOWLEDGEMENT

We gratefully acknowledged Universiti Putra Malaysia for the financial assistance received through Putra Research Grant, vote number 9543500.

REFERENCES

Abdelrahim, R., & Omar, Z. (2016). Direct solution of second order ordinary differential equations using a single-step hybrid block method of order five. *Mathematical and Computational Applications, 21*(2), 1-12.

Ackleh, A. S., Allen, E. J., Kearfott, R. B., & Seshaiyer, P. (2009). *Classical and modern numerical analysis: Theory methods and practice.* Boca Raton, Flrida: CRC Press.

Awoyemi, D., Adebile, A., Adesanya, A., & Anake, T. A. (2011). Modified block method for the direct solution of second order ordinary differential equations. *International Journal of Applied Mathematics and Computation, 3*, 181-188.

Badmus, A. (2014). An efficient seven-point hybrid block method for direct solution $y'' = f(x, y, y')$. *Journal of Advances in Numerical Mathematics and Computer Sciences, 2014*, 2840-2852.

Fatunla, S. O. (1995). A class of block methods for second order IVPs. *International Journal of Computer Mathematics, 55*(1-2), 119-133.

Majid, Z. A., Mokhtar, N. Z., & Suleiman, M. (2012). Direct two-point block one-step method for solving general second-order ordinary differential equations. *Mathematical Problems in Engineering, 2012*, 1-16.

Majid, Z. A., Suleiman, M., & Omar, Z. (2006). 3-point block method for solving ordinary differential equations. *Bulletin of the Malaysian Mathematical Sciences Society, 29*(1), 23-31.

Mokhtar, N. Z., Majid, Z. A., Ismail, F., & Suleiman, M. (2012). Numerical solution for solving second order ordinary differential equations using block method. *International Journal of Modern Physics, 9*, 560-565.

Nasir, N. M., Majid, Z. A., Ismail, F., & Bachok, N. (2018). Diagonal block method for solving two-point boundary value problems with robin boundary conditions. *Mathematical Problems in Engineering, 2018*, 1-12.

Omar, Z., & Adeyeye, O. (2016). Order five block method for the solution of second order boundary value problems. *Indian Journal of Science and Technology, 9*(31), 1-4.

Ramos, H., Singh, G., Kanver, V., & Bhatia, S. (2016). An efficient variable step-size rational Falkner-type method for solving special second order IVP. *Applied Mathematics and Computation, 291*, 39-51.

Singh, G., & Ramos, H. (2019). An optimized two-step hybrid block method formulated in variable step-size mode for integrating $y'' = f(x, y, y')$. *Numerical Mathematics-Theory Methods and Applications, 12*(2), 640-660.

Waeleh, N., & Majid, Z. A. (2017). Numerical algorithm of block method for general second order ODEs using variable stepsize. *Sains Malaysiana, 46*(5), 817-824.

Pertanika J. Sci. & Technol. 28 (3): 967 - 981 (2020)

PERTANIKA JOURNALS

SCIENCE & TECHNOLOGY

Journal homepage: http://www.pertanika.upm.edu.my/

Palm Oil Trend Analysis via Logic Mining with Discrete Hopfield Neural Network

Alyaa Alway[1], Nur Ezlin Zamri[1], Mohd Shareduwan Mohd Kasihmuddin[2], Mohd. Asyraf Mansor[1]* and Saratha Sathasivam[2]

[1]School of Distance Education, Universiti Sains Malaysia, 11800, Penang, Malaysia
[2]School of Mathematical Sciences, Universiti Sains Malaysia, 11800, Penang, Malaysia

ABSTRACT

Analyzing commodity prices contributes greatly to traders, economists and analysts in ascertaining the most feasible investment strategies. Limited knowledge about the price trend of the commodities indeed will affect the economy because commodities like palm oil and gold contribute a huge source of income to Malaysia. Therefore, it is important to know the optimal price trend of the commodities before making any investments. Hence, this paper presents a logic mining technique to study the price trend of palm oil with other commodities. This technique employs 2-Satisfiability based Reverse Analysis Method (2-SATRA) consolidated with 2-Satisfiability logic in Discrete Hopfield Neural Network (DHNN2-SAT). All attributes in the data set are represented as a neuron in DHNN which will be programmed based on a 2-SAT logical rule. By utilizing 2-SATRA in DHNN2-SAT, the induced logic is generated from the commodity price data set that explains the trend of commodities price. Following that, the performance evaluation metric; error analysis and accuracy will be calculated based on the induced logic. In this case, the experimental result has shown that the best-induced logic identifies which trend will lead to an increase in the palm oil price with the highest accuracy rate.

Keywords: 2-Satisfiability, Hopfield neural network, logic mining

ARTICLE INFO

Article history:
Received: 18 January 2020
Accepted: 18 March 2020
Published: 16 July 2020

E-mail addresses:
alyaalway@student.usm.my (Alyaa Alway)
ezlinzamri@student.usm.my (Nur Ezlin Zamri)
shareduwan@usm.my (Mohd Shareduwan Mohd Kasihmuddin)
asyrafman@usm.my (Mohd. Asyraf Mansor)
saratha@usm.my (Saratha Sathasivam)
* Corresponding author

INTRODUCTION

In 1870, oil palm was founded as an ornamental plant in Malaysia before being marketed at Tennamaram Estate, Selangor, in 1917 (Nambiappan et al., 2018). Naturally, palm oil is known as the most profitable industrial production. In the early 1960s, palm oil production grew quickly. Due to

ISSN: 0128-7680
e-ISSN: 2231-8526

© Universiti Putra Malaysia Press

that, palm oil has been a significant subsection of Malaysia's economy, adding 37.9% of the agricultural industry to domestic product development (Department of Statistics Malaysia, 2019). The global resolution of the palm oil industry has established the palm oil industry in Malaysia as one of the biggest contributors to domestic product growth in the world (Balu et al., 2018). Malaysia is currently the second-largest palm oil producer and exporter after Indonesia (Kushairi et al., 2019). Approximately 20 million tons of crude palm oil is produced annually (Ismail, 2013). Despite being the top producing crops, the subsector for palm oil encounters several difficulties. The difficulties including lower production of palm oil, lower exports, greater demand for palm oil and lower prices of palm oil (Kushairi et al., 2019). Besides that, the rise and fall of commodities price influence the performance of the subsector of the palm oil (Songsiengchai et al., 2020). Bakar (2009) stated that Malaysia currently suffered poor returns in agricultural production and the stagnant commodity prices were escalating. Learning less about the price trend would impact the economy as a whole, as Malaysia still depends on these resources to expand economically. Some researchers (Baruník & Malinska, 2016; Alameer et al., 2019) had reported that understanding the price trend in advance would support the interest group in decisions making (buying or selling). In this scenario, the government should create a countermeasure if the drop in the commodity price is inevitable. Since this has become a major problem that needs to be tackled, therefore, it is crucial to evaluate the palm oil price trend before making any decisions or investments.

Artificial Intelligence (AI) is widely used in agriculture applications (Mekonnen et al., 2020) and planning marketing strategies (Davenport et al., 2020). The common method in extracting the important information about one data set is by using data mining integrated with AI. Nonetheless, several types of research have discovered a more precise model for the extraction of information through integrating Artificial Neural Network (ANN) such as Kasihmuddin et al. (2018) and Kho et al. (2020). Usage of ANN occurring in different disciplines varying from market share to commodity price. The usage of ANN has proven its effectiveness against statistical methods in forecasting commodity prices, especially in energy fuels (Rahman, 2012) and metal prices (Abdullah & Wahid, 2010). The work by Khamis and Wahab (2016) presents that ANN is the best model in forecasting the price of crude palm oil. Moreover, the study conducted by Ramakrishnan et al. (2017) utilizes ANN with other statistical models to examine the effective interplays between commodity prices and the exchange rate for Malaysia. Discrete Hopfield Neural Network (DHNN) is a recurrent ANN that is popularized by Hopfield and Tank (1985) to tackle several problems of constraint optimization. The operation in the DHNN can be described as follows (Nájera et al., 2020): (1) A data is inserted and shared with the input layer. (2) This transmits it to the middle layers that change their status. (3) Choose each neuron that is updated at random. (4) A state of equilibrium is achieved. (5) The pattern of activation is transferred

to the output layer. DHNN has a content addressable memory (Liu et al., 2006) and mimics the human brain (Haykin, 1994).

According to Mainzer (2020), most of the general problem-solving methods are successfully represented in a formal logical rule. There is a technical procedure in extracting the information from the logical formulas. It has been shown that logic mining can maps information into the logical form (Kowalski, 1979). Satisfiability (SAT) logic is capable of transforming problems into a mathematical representation. Cook (1971) had introduced a non-deterministic problem known as *k*-SAT logic. Sathasivam et al. (2014) had suggested a higher order of Horn Satisfiability (HORN-SAT) combining different forms of *k*-SAT logic representation because HORN-SAT was considered as a good logical representation as this logic guarantees satisfiable property. Another representation of *k*-SAT logic is 3-Satisfiability (3-SAT) logic. Iverson (1962) stated that any real-life problem could be reduced to 3-SAT to reveal the behavior of the data set. Besides that, in the work of Mansor et al. (2019), they utilized 3-SAT in a new modified Hopfield Neural Network (HNN) called Elliot HNN by implementing an Artificial Immune System (AIS) to solve optimization task. The work by Kasihmuddin et al. (2019) has successfully implemented 2-Satisfiability in logic mining to examine the behavior of real-life data set of students' performances which attained better accuracy than most existing model. In this case, the choice of suitable logical rules to be incorporated into the neural network plays a significant role in logic mining.

Several researchers incorporate DHNN with logic mining because of its effectiveness in solving optimization problems (Abdullah & Sathasivam, 2005). Thus, in our framework, we utilized logic mining with DHNN in investigating the price trend of commodities. As mentioned earlier, it is proven that by using the logic mining technique, we can transform any information into the logical rules. Sathasivam and Abdullah (2011) introduced the incorporation of logic with reverse analysis in DHNN. AN extended work by Kasihmuddin et al. (2018) improved the existing model by implementing 2-Satisfiability based Reverse Analysis Method (2-SATRA) in classifying the condition of the diabetic patient. Furthermore, Mansor et al. (2018) utilized 3-SATRA incorporated with DHNN in evaluating numerous cardiovascular diseases data set. The application of 2-SATRA in Kho et al. (2020) revealed the best logical rule that represented the behavior among the gameplay or objectives in the League of Legends game. 2-SATRA is also known as an efficient logic mining technique to obtain the best-induced logic that reveals the link between the attributes inside a real-life data set. As for our case, the proposed 2-SATRA will discover the logical relationship between palm oil prices with other commodities. Hence, this paper proposed the logic mining technique named 2-SATRA incorporate with DHNN technique to identify the price trend of palm oil.

However, there is no current study that executes logic mining in examining the price trend of the commodities. Most of the current studies only emphasize an individual

commodity instead of doing a comparison with other commodities. The contributions of this research presented as follows: (1) To represent commodity price data into 2-SAT logical rules. (2) To implement 2-SATRA with DHNN to extract the information of the commodity price data set. (3) To investigate the relationship between commodity price data set by analyzing the interpretation of induced logic. Therefore, through our findings, we can provide information on which price trend commodity encourages the fluctuation of palm oil prices. The generated induced logic from our mechanism could aid and explain in layman terms for economists and traders of which resources affect our nation's economic growth. The structure of this paper is organized as follows. Section 2 presents a brief description of the materials and methods used such as Boolean satisfiability and Discrete Hopfield Neural Network. Section 3 demonstrates the implementation of 2-SATRA into our proposed model and provides all the information involved. In Section 4, the results from various performance evaluation metrics were discussed in detail and conclusions are finally presented in Section 5.

MATERIALS AND METHOD

Boolean Satisfiability (SAT)

Generally, Boolean satisfiability or satisfiability (SAT) is defined as logical rule with conjunction of clauses which consists of disjunction of literals with each literals or variables can be either true or false. There are three components of the fundamental SAT logical rule presented as follows (Kasihmuddin et al., 2017):

1. SAT formula comprises of a set of q literals or variables, $\left(x_1,...,x_q\right)$ within each clause. Note that l_i only complies with bipolar representation of $\{-1,1\}$ and all the variables are connected by logical operator $OR\ (\vee)$.
2. Literals or variables can represent the variable itself, M or the negation of the variable, $\neg M$.
3. Comprises of a set of k different clauses, $\left(C_1,C_2,C_3,...,C_k\right)$ where each distinct clauses contains q literals and will be connected by logical operator $AND\ (\wedge)$.

In other notation, this work comprises limited number of literals, which is two ($q=2$), namely as; 2-Satisfiability (2-SAT) logical rule, A_{2-SAT}. The general formulation of A_{2-SAT} is shown in Equation 1:

$$A_{2-SAT} = \wedge_{i=1}^{k} C_i \tag{1}$$

where $C_i = \vee_{j=1}^{2}(x_{ij}, y_{ij})$ and k represents the number clauses denoted by Conjunctive Normal Form (CNF) formula. Further explanation of three cases of A_{2-SAT} is presented as follows, where according to Equation 2:

$$A_{2-SAT} = (U \vee \neg V) \wedge (W \vee X) \wedge (\neg Y \vee \neg Z) \tag{2}$$

Case 1. Satisfiable when $(U, V, W, X, Y, Z) = (1,-1,1,1,-1,-1)$ which concludes that A_{2-SAT} is true when $A_{2-SAT} = 1$.
Case 2. Unsatisfiable when $(U, V, W, X, Y, Z) = (-1,1,1,1,-1,-1)$ in resulting $A_{2-SAT} = -1$.
Case 3. Equation 2 achieved the full inconsistency when $(U, V, W, X, Y, Z) = (-1,1,-1,-1,1,1)$.
This work will utilize the symbolic representation of A_{2-SAT} into our framework of 2-SAT and DHNN to represent the commodity price data set and implement reverse analysis to unveil the price trend of palm oil in Malaysia from the year 2008-2019. There is no recent research in integrating A_{2-SAT} with reverse analysis in order to investigate the relationship of related commodities such as gold, crude petroleum and timber with the inconsistent price of palm oil in Malaysia which plays a major role to our economic growth as the second largest palm oil exporter in the world.

2-Satisfiability in Discrete Hopfield Neural Network (DHNN)

Over the years, HNN has become one of the leading neural networks utilized by many researchers and neural networkers due to its structure flexibility and variability to act as an extensive network to solve optimization tasks. Initially, HNN was introduced by Hopfield and Tank in 1985, where HNN acted as a platform to solve multiple NP problems. HNN is a fully connected recurrent neural network without self-feedback. The utilization of HNN varies in terms of application versatility, from; obesity detection (Nájera et al., 2020), stability analysis (Shen et al., 2020), face recognition (Swapna et al., 2020) and financial forecasting (Del Ángel, 2020). This work is focusing on implementing A_{2-SAT} to represent the commodity price data set, therefore, the mechanism of discrete HNN (DHNN) is favourable as it is an auto associative memory network which could interpret functions of a memory to a neural network model (Shevchuk, 2016). The general DHNN characteristics utilized in this work are the input and output patterns are in discrete vector, specifically in bipolar state $\{-1,1\}$ (Kasihmuddin et al., 2017). Other than that, each neuron connection or synaptic weights are depicted as $W_{ij}^{(2)}$ where DHNN has symmetrical weights therefore it has zero diagonal elements with no self-connections between the neurons, $W_{ij}^{(2)} = W_{ji}^{(2)}$. Note that, the synaptic weights are calculated by using Abdullah method (1993). The fundamental neurons update formulated in DHNN is shown as follows (Equation 3):

$$S_i = \begin{cases} 1 & ,if \sum_j W_{ij} S_j \geq \phi \\ -1 & ,Otherwise \end{cases} \quad (3)$$

Note that S_j is the state of unit j and ϕ is the predetermined threshold value of unit *i*. The structure of local field formulated by Abdullah (1993) complies with DHNN which cater a case of higher order of neurons connections as shown in Equation 4 with updating rule presented in Equation 5 presented as follows:

$$h_i(t) = \sum_{j=1, i \neq j}^{N} W_{ij}^{(2)} S_j + W_i^{(1)} \quad (4)$$

$$S_i(t+1) = sgn[h_i(t)] \quad (5)$$

Note that $W_{ij}^{(2)}$ is the second order synaptic weight where else $W_i^{(1)}$ is the first order synaptic weight. The sgn is a signum function to squash the output of neurons, where in this case, we utilized Hyperbolic Tangent Activation Function (HTAF) (Mansor & Sathasivam, 2016).

The utilization of Lyapunov energy function to affirm the stability of DHNN (Sathasivam & Abdullah, 2010) in generating the optimized induced logic, $A_i^{induced}$ is formulated in Equation 6 and Galán-Marín & Muñoz-Pérez (2001) also emphasized on the dynamics of Hopfield network must be determined by the energy theorem mechanism stated as follows:

$$H_{A_{2-SAT}} = -\frac{1}{2} \sum_{i=1, i \neq j}^{N} \sum_{j=1, i \neq j}^{N} W_{ij}^{(2)} S_i S_j - \sum_{i=1}^{N} W_i^{(1)} S_j \quad (6)$$

Energy Theorem: *In a Hopfield neural network, any changes by the updating rule in Equation 6 in the components of the results in a decrease in the Lyapunov energy function.*

DHNN provides a central memory feature or content addressable memory to store synaptic weights in a matrix form and best logic, A_{best} to be later retrieved in the testing phase. The significance of implementing DHNN with A_{2-SAT} is the extensive yet straightforward framework that could generate a plausible induced logic which explicitly emphasizes the price trend of palm oil. From the produced $A_i^{induced}$, we could ascertain which commodity affects the rise and fall of palm oil price. Currently, there is no work in incorporating DHNN with $A_i^{induced}$ in order to investigate the influence of palm oil with respect to other significant commodities.

Implementation of DHNN2-SATRA Model

Each commodity can be interpreted as a neuron in DHNN and integrated based on A_{2-SAT}. Therefore, the implementation of DHNN2-SAT in Reverse Analysis Method is called 2-Satisfiability based Reverse Analysis Method (2-SATRA). The research done by Sathasivam and Abdullah (2011) had shown that they had succeeded in inducing all possible logical rules that explained the behavior of one data set by proposing a reverse analysis method. After that, Kasihmuddin et al. (2018) had revised the traditional method resulting to 2-SATRA so that more logical rules and learning methods could be applied to reliably generalize the behavior of the data set. Further to this, 2-SATRA is an effective logic mining tool to find best-induced logic from the commodity price data set that explains

the behavior of the data set which in this case is the trend of palm oil price. The flow of this experiment can be seen in the Figure 1. All simulations were measured in two parts; training stage and testing stage. Root mean square error (RMSE) and mean absolute error (MAE) would be calculated in the training stage to test the performance of DHNN2-SAT model. The formulation of RMSE, MAE and accuracy are as follows (Equation 7 & 8):

$$RMSE = \sum_{i=1}^{n} \sqrt{\frac{1}{n}(\rho - o)} \tag{7}$$

$$MAE = \sum_{i=1}^{n} \frac{1}{n} |\rho - o| \tag{8}$$

where ρ is the total number of clauses in A_{2-SAT}, o is the number of satisfied clauses in A_{2-SAT} and n is the number of iteration before $\rho = o$. The lowest value of RMSE and MAE indicates the best performance DHNN2-SAT model. In the testing stage, accuracy (α) will be computed to investigate the capability of 2-SATRA in our DHNN2-SAT model. We describe α formulation as follows (Equation 9):

$$\alpha = \frac{A_i^{induced}}{N_{A_{test}}} \times 100\% \tag{9}$$

where $A_i^{induced}$ is the induced logic and $N_{A_{test}}$ is the number of testing data. By computing α, the best induced logic is attained that explains the behavior of the commodity data set.

In this paper, a real-life data set of Malaysia's commodities price with 7 types of commodities would be exerted in the established 2-SATRA. The commodities price ranged from the year 2009 until 2018. The real data set use multivariate data. A total of 120 data were adopted where 60% of the data was training data while the rest was for testing data (Kho et al., 2020). Seven attributes were used in A_{2-SAT} logical rule and by using permutation, different combinations of the clause were obtained so that the highest accuracy could be attained. The information of the data set is presented in Table 1. The computational simulation was conducted on Dev C++ Version 5.11 for Windows 10 in 4GB RAM with Intel Core i3. The same device would be used throughout the simulation to avoid any biases. Table 2 shows all the parameters involved in DHNN2-SAT.

RESULT AND DISCUSSION

This work exhibits an extensive network to predict the price trend of palm oil by entrenching A_{2-SAT} with DHNN. The role of A_{2-SAT} is to generalize the trend of the commodity price data set through a comprehensive logical system that could be utilized in explaining the trend in layman representation. DHNN2-SAT with the aid of reverse

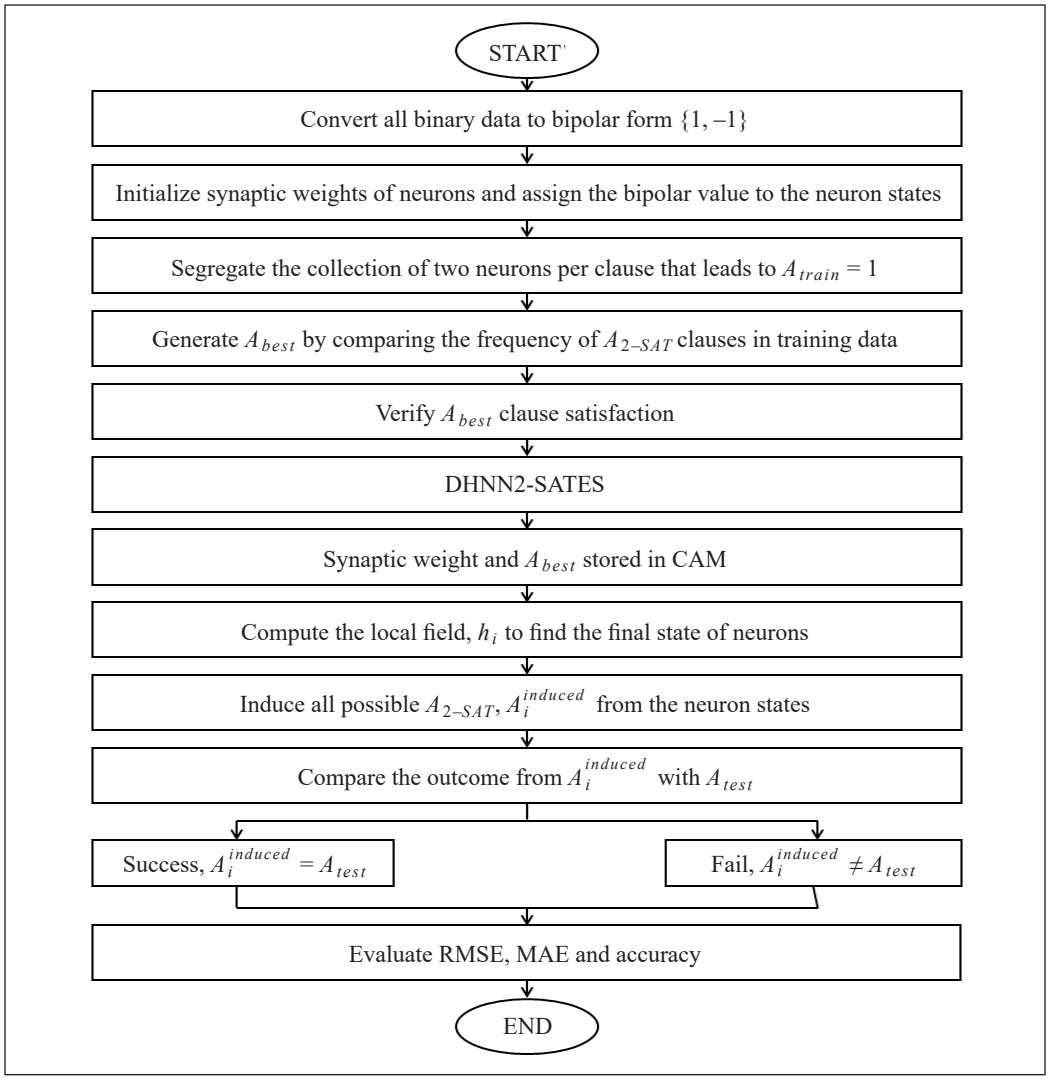

Figure 1. Implementation of DHNN2-SATRA

Table 1
List of commodities

Attributes	Name of Commodities	Source
A	Palm oil	Malaysian Palm Oil Board (2019)
B	Cocoa bean	Malaysian Cocoa Board (2019)
C	Gold	GoldBroker (2019)
D	Crude petroleum	CEIC (2018)
E	Black & white pepper	CEIC (2018)
F	Timber	Malaysia Timber Industry Board (2019)
G	Latex	Malaysian Rubber Board (2019)

Table 2
List of parameters in DHNN2-SAT (Sathasivam et al., 2013)

Parameter	Parameter value
Number of trial	100
Neuron combination	100
Tolerance value	0.001

analysis method, generated induced logic to display explicit manner of which commodities is held accountable for the rise and fall of palm oil price. Table 3 demonstrates the value of RMSE and MAE computed in the training stage for different number of neurons (*NN*). Table 4 exhibits the lists of induced logic after permutating the attributes in commodities data. In Table 4, 9 sets were obtained and determined by permutation, where the different set of induced logic produced different values of accuracy. The optimized induced logic was selected from the induced logic with the highest accuracy.

As depicted in Table 3, we can conclude that the best performance of the DHNN2-SAT model was reported at $NN = 9$ as it yields the least value of RMSE and MAE. The value of errors would be increased as the *NN* increased. This is because of our local searching technique only effective when it incorporates a low value of *NN*. Some researchers (Kasihmuddin et al., 2018; Mansor et al., 2018) suggest increasing the number of neurons to increase the accuracy of 2-SATRA. Nevertheless, the higher value of both errors; RMSE and MAE will be achieved as we increase the *NN* due to DHNN2-SAT requires more iteration to obtain the satisfying interpretation of 2-SAT. The best induced logic represented as $A_5^{induced}$, depicts the commodities of affecting the price trend of palm oil with the highest accuracy. The distinction between this work with other approaches is the utilization of permutation attributes in DHNN2-SAT. The role of attributes permutation is to increase the possibility and verify the network's accuracy by employing a different arrangement of the commodities that contribute to A_{2-SAT}. The attributes permutation showed different generated $A_i^{induced}$ with varies accuracy which we could magnify that the optimized induced logic was selected by observing the highest accuracy attained. Worth mentioning that, the formulated induced logical rule that explains the trend of palm oil prices is considered optimal because the expected global minima ratio is always approximately 1 (Kasihmuddin et al., 2017).

Throughout our findings of $A_5^{induced}$, the extracted information predicts the price of gold influence the price of palm oil. In this case, when the price of gold increases, the price of palm oil will also increase. This finding has a good agreement with the work of Cashin et al. (1999) which indicated that the palm oil price was correlated with gold. On the other hand, the palm oil price would affect others commodities price. The price of cocoa bean, crude petroleum, and latex increased as the palm oil price increases. Hence, the extracted

Table 3
Performance Evaluation of 2-SATRA in Training Stage

NN	RMSE	MAE
9	1.1905	0.8326
18	3.459	2.7523
27	7.4095	6.4491
36	10.8389	10.1037
45	14.3233	13.7653
54	17.5107	17.1898
63	20.727	20.5647
72	23.781	23.6072
81	26.827	26.7267
90	29.8942	29.8518

Table 4
Performance evaluation of 2-SATRA in testing stage

Sets	Induced Logic, $A_i^{induced}$	Accuracy (%)
1	$A_1^{induced} = (D \vee B) \wedge (\neg F \vee G) \wedge (E \vee C)$	72
2	$A_2^{induced} = (D \vee B) \wedge (G \vee C) \wedge (E \vee \neg F)$	60
3	$A_3^{induced} = (B \vee D) \wedge (G \vee C) \wedge (E \vee \neg F)$	60
4	$A_4^{induced} = (B \vee C) \wedge (D \vee \neg E) \wedge (\neg F \vee G)$	66
5	$A_5^{induced} = (B \vee C) \wedge (D \vee \neg E) \wedge (\neg F \vee G)$	75
6	$A_6^{induced} = (G \vee B) \wedge (C \vee D) \wedge (\neg E \vee \neg F)$	66
7	$A_7^{induced} = (\neg D \vee E) \wedge (F \vee G) \wedge (\neg B \vee C)$	72
8	$A_8^{induced} = (\neg F \vee \neg G) \wedge (B \vee C) \wedge (D \vee E)$	66
9	$A_9^{induced} = (D \vee \neg E) \wedge (\neg F \vee G) \wedge (B \vee C)$	75

logical rule is successfully identifying the key components that contribute to the palm oil price trend. Another interesting perspective, the optimal logical rule reported that the price of palm oil would stabilize if the price of the crude oil returned to the threshold price. The price of latex was observed to influence the price of palm Oil. According to Udomraksasakul and Rungreunganun (2018), the price of latex has reached a new low since 2010 and this pattern can be observed in the price of palm oil. In this case, regression analysis such as Weijermars and Sun (2018) and Kasihmuddin et al. (2017) are required to confirm the claim made by logical rule. The price of pepper and timber shows an inverse correlation relative to palm oil where the price of pepper and timber will reduce when the price of

palm oil increases. The proposed method is incomparable with the existing work such as Cortez et al. (2018) and Li et al. (2019) because these studies only emphasized on the price trend of palm oil without considering the performance of other commodities. In this case, the value of accuracy is sufficient to validate the performance of 2-SATRA. However, the generated induced logic is still significant to predict the trend of the commodities for the other subsequent year, by entrenching new set of the data entries. The limitation of this work is we only consider the price trend instead of the actual price for commodities. Hence, the increase and decrease of the palm oil price were denoted by 1 and -1 respectively.

Other than that, A_{2-SAT} in this work, depicts the decreasing price trend in palm oil. Hence, alteration of A_{2-SAT} formulation in DHNN2-SAT is required to comply with $A_i^{induced} = -1$. This perspective requires the utilization of other non-Satisfiable formula such as maximum *k*-SAT (MAX*k*-SAT). Ultimately, the induced logic can help the traders, analysts, economist and strategists in deciding the most feasible investment strategies. Investors could also utilize the induced logic to provide an expert discussion regarding on stock market and their potential profit. Industrial players and policymakers can benefit from the generated induced logic to improve the developments of national economic growth.

CONCLUSION

In a nutshell, this paper carries out several important processes to finally obtained a beneficial result that shows which commodities affect the increase in palm oil price. First, A_{2-SAT} is incorporated in DHNN (DHNN2-SAT) as a single logic mining. Every attribute in the commodity price data set is represented in terms of DHNN2-SAT. After that, the training stage in DHNN2-SAT will be intensified by using the local searching technique. Next, this process is extended by integrating DHNN2-SAT with 2-SATRA that operates as a logic mining tool to conclude the logical rule of the commodity price data set. As a consequence, this paper will generate the best induced logic based on the highest accuracy attained to emphasize the behavior of the data set which concluded all objectives presented in this experiment have been successfully achieved. The outcome of this experiment establishes the desired price trend for palm oil with the highest accuracy. In the future, our research can be improved by using different types of searching techniques such as genetic algorithm, imperialist competitive algorithm, artificial immune system, and ant colony optimization. The effectiveness of these searching techniques is different and has its advantages. Furthermore, this research can also explore different logical rule such as Maximum Satisfiability (MAX*k*-SAT) by considering $A_{train} = -1$.

ACKNOWLEDGEMENT

This research was funded by Fundamental Research Grant Scheme (FRGS), Ministry of Education Malaysia, grant number 203/PJJAUH/6711751.

REFERENCES

Abdullah, R., & Wahid, M. B. (2010). *World palm oil supply, demand, price and prospects: Focus on Malaysian and Indonesian palm oil industry.* Kajang, Malaysia: Malaysian Palm Oil Board Press.

Abdullah, W. A. T. W. & Sathasivam, S. (2005, December 1-3). Logic mining using neural networks. In *Proceedings of the International Conference on Intelligent Systems* (pp. 1-6). Kuala Lumpur, Malaysia.

Abdullah, W. A. T. W. (1993). The logic of neural networks. *Physics Letters A*, *176*(3-4), 202-206.

Alameer, Z., Elaziz, M. A., Ewees, A. A., Ye, H., & Jianhua, Z. (2019). Forecasting gold price fluctuations using improved multilayer perceptron neural network and whale optimization algorithm. *Resources Policy*, *61*, 250-260.

Bakar, B. B. (2009, September 27-28). The Malaysian agricultural industry in the new millennium: Issues and challenges. In *International Conference on Malaysia: Malaysia in Global Perspective* (pp. 337-356). Cairo University, Egypt.

Balu, N., Azman, I., Hashim, N., Ismail, I., Shahari, D. N., & Idris, N. A. N. (2018). Malaysia: 100 years of resilient palm oil economic performance. *Journal of Oil Palm Research*, *30*(1), 13-25.

Baruník, J., & Malinska, B. (2016). Forecasting the term structure of crude oil futures prices with neural networks. *Applied Energy*, *164*, 366-379.

Cashin, P. A., McDermott, C. J., & Scott, A. M. (1999). *The myth of comoving commodity prices.* Washington, DC: International Monetary Fund.

CEIC. (2018). *Malaysia exports: By selected commodities*. Retrieved January 01, 2020, from https://www.ceicdata.com/en/malaysia/exports-by-selected-commodities.

Cook, S. A. (1971, May 3-5). The complexity of theorem-proving procedures. In *Proceedings of the third annual ACM symposium on Theory of computing* (pp. 151-158). Shaker Heights, Ohio.

Cortez, C. T., Saydam, S., Coulton, J., & Sammut, C. (2018). Alternative techniques for forecasting mineral commodity prices. *International Journal of Mining Science and Technology*, *28*(2), 309-322.

Davenport, T., Guha, A., Grewal, D., & Bressgott, T. (2020). How artificial intelligence will change the future of marketing. *Journal of the Academy of Marketing Science*, *48*(1), 24-42.

Del Ángel, R. G. (2020). Financial time series forecasting using Artificial Neural Networks. *Revista Mexicana de Economía y Finanzas Nueva Época REMEF*, *15*, 105-122.

Department of Statistics Malaysia. (2019). *Selected agricultural indicators.* Retrieved January 01, 2020, from https://www.dosm.gov.my.

Galán-Marín, G., & Muñoz-Pérez, J. (2001). Design and analysis of maximum Hopfield networks. *IEEE Transactions on Neural Networks, 12*(2), 329-339.

GoldBroker. (2019). *Gold price in Malaysian Ringgit - Malaysia*. Retrieved January 01, 2020, from https://www.goldbroker.com/charts/gold-price/myr.

Haykin, S. (1994). *Neural networks: A comprehensive foundation*. Upper Saddle River, NJ: Prentice Hall PTR.

Hopfield, J. J. & Tank, D.W. (1985). Neural computation of decisions in optimization problems. *Biological Cybernetics*, *52*(3), 141-152.

Ismail, A. (2013). The effect of labour shortage in the supply and demand of palm oil in Malaysia. *Oil Palm Industry Economic Journal, 13*(2), 15-26.

Iverson, K. E. (1962, May 1-3). A programming language. In *Proceedings of the spring joint computer conference* (pp. 345-351). San Francisco, California.

Kasihmuddin, M. S. M., Mansor, M. A., & Sathasivam, S. (2017). Hybrid genetic algorithm in the Hopfield network for logic satisfiability problem. *Pertanika Journal of Science and Technology*, *25*(1), 139-152.

Kasihmuddin, M. S. M., Mansor, M. A., & Sathasivam, S. (2018). Satisfiability based reverse analysis method in diabetes detection. In *AIP Conference Proceedings* (Vol. 1974, No. 1, p. 020020). Melville, NY: AIP Publishing LLC.

Kasihmuddin, M. S. M., Mansor, M. A., & Sathasivam, S. (2019, December). Students' performance via satisfiability reverse analysis method with Hopfield Neural Network. In *AIP Conference Proceedings* (Vol. 2184, No. 1, p. 060035). Melville, NY: AIP Publishing LLC.

Khamis, A., & Wahab, A. (2016). Comparative study on predicting crude palm oil prices using regression and neural network models. *International Journal of Science and Technology, 5*(3), 88-94.

Kho, L. C., Kasihmuddin, M. S. M., Mansor, M., & Sathasivam, S. (2020). Logic mining in league of legends. *Pertanika Journal of Science and Technology*, *28*(1), 211-225.

Kowalski, R. (1979). *Logic programming for problem solving*. New York, NY: Elsevier Science Publishing.

Kushairi, A., Ong-Abdullah, M., Nambiappan, B., Hishamuddin, E., Bidin, M. N. I. Z., Ghazali, R., ... & Parveez, G. K. A. (2019). Oil palm economic performance in Malaysia and R&D progress in 2018. *Journal of Oil Palm Research*, *31*(2), 165-194.

Li, X., Shang, W., & Wang, S. (2019). Text-based crude oil price forecasting: A deep learning approach. *International Journal of Forecasting*, *35*(4), 1548-1560.

Liu, Y., Wang, Z., & Liu, X. (2006). Global exponential stability of generalized recurrent neural networks with discrete and distributed delays. *Neural Networks*, *19*(5), 667-675.

Mainzer, K. (2020). Logical thinking becomes automatic. In K. Mainzer (Ed.), *Artificial intelligence-When do machines take over?* (pp. 15-45). Berlin, Heidelberg: Springer.

Malaysia Timber Industry Board. (2019). *Malaysia timber industry board*. Retrieved January 01, 2020, from http://www.mtib.gov.my/en/.

Malaysian Cocoa Board. (2019). *Ministry of plantation industries and commodities*. Retrieved January 01, 2020, from https://www.koko.gov.my/lkm/index.cfm.

Malaysian Palm Oil Board. (2019). *The official portal of Malaysian palm oil board*. Rerieved January 01, 2020, from http://www.mpob.gov.my/.

Malaysian Rubber Board. (2019). *Malaysian rubber board*. Retrieved January 01, 2020, from http://www.lgm.gov.my/.

Mansor, M. A., & Sathasivam, S. (2016, June). Performance analysis of activation function in higher order logic programming. In *AIP Conference Proceedings* (Vol. 1750, No. 1, p. 030007). Melville, NY: AIP Publishing LLC.

Mansor, M. A., Kasihmuddin, M. S. M., & Sathasivam, S. (2019). Modified artificial immune system algorithm with Elliot Hopfield neural network for 3-satisfiability programming. *Journal of Informatics and Mathematical Sciences, 11*(1), 81-98.

Mansor, M. A., Sathasivam, S., & Kasihmuddin, M. S. M. (2018, June). Artificial immune system algorithm with neural network approach for social media performance metrics. In *AIP Conference Proceedings* (Vol. 1974, No. 1, p. 020072). Melville, NY: AIP Publishing LLC.

Mekonnen, Y., Namuduri, S., Burton, L., Sarwat, A., & Bhansali, S. (2020). Machine learning techniques in wireless sensor network based precision agriculture. *Journal of the Electrochemical Society*, *167*(3), 1-11.

Nájera, M. A. C., Mechaca, J. L., Martínez, S. I., Villanueva, J. D. T., & Vega, D. A. M. (2020). Prevention of obesity using Hopfield networks in patients with obese ancestry. *International Journal of Combinatorial Optimization Problems and Informatics*, *11*(2), 61-66.

Nambiappan, B., Ismail, A., Hashim, N., Ismail, N., Nazrima, S., Idris, N. A. N., ... & Kushairi, A. (2018). Malaysia: 100 years of resilient palm oil economic performance. *Journal of Oil Palm Research, 30*(1), 13-25.

Rahman, A. K. A. (2012). *Impact of palm oil supply and demand on crude palm oil price behavior.* Kelana Jaya, Malaysia: Malaysian Palm Oil Board Press.

Ramakrishnan, S., Butt, S., Chohan, M. A., & Ahmad, H. (2017, July 16-17). Forecasting Malaysian exchange rate using machine learning techniques based on commodities prices. In *2017 International Conference on Research and Innovation in Information Systems (ICRIIS)* (pp. 1-5). Langkawi, Malaysia.

Sathasivam, S., & Abdullah, W. A. T. W. (2010). The satisfiabilty aspect of logic on little Hopfield network. *American Journal of Scientific Research, 2010*(7), 90-105.

Sathasivam, S., & Abdullah, W. A. T. W. (2011). Logic mining in neural network: Reverse analysis method. *Computing*, *91*(2), 119-133.

Sathasivam, S., Fen, N. P., & Velavan, M. (2014). Reverse analysis in higher order Hopfield network for higher order horn clauses. *Applied Mathematical Sciences, 8*(13), 601-612.

Sathasivam, S., Ng, P. F., & Hamadneh, N. (2013). Developing agent based modelling for reverse analysis method. *Journal of Applied Sciences, Engineering and Technology*, *6*(22), 4281-4288.

Shen, W., Zhang, X., & Wang, Y. (2020). Stability analysis of high order neural networks with proportional delays. *Neurocomputing*, *372*, 33-39.

Shevchuk, A. V. (2016). Artificial intelligence and intellectualization: New prospects for economic development. *Міжнародний науковий журнал" Науковий огляд"*, *4*, 1-9.

Songsiengchai, P., Sidique, S. F., Djama, M., & Azman-Saini, W. N. W. (2020). Asymmetric adjustments in the Thai palm oil market. *Kasetsart Journal of Social Sciences*, *41*(1), 220-225.

Swapna, M., Sharma, Y. K., & Prasad, B. M. G. (2020). A survey on face recognition using convolutional neural network. In *Data Engineering and Communication Technology* (pp. 649-661). Singapore: Springer.

Udomraksasakul, C., & Rungreunganun, V. (2018). Forecasting the price of field latex in the area of Southeast Coast of Thailand using the ARIMA Model. *International Journal of Applied Engineering Research*, *13*(1), 550-556.

Weijermars, R., & Sun, Z. (2018). Regression analysis of historic oil prices: A basis for future mean reversion price scenarios. *Global Finance Journal*, *35*, 177-201.

Pertanika J. Sci. & Technol. 28 (3): 983 - 1008 (2020)

PERTANIKA JOURNALS

SCIENCE & TECHNOLOGY

Journal homepage: http://www.pertanika.upm.edu.my/

Modified Imperialistic Competitive Algorithm in Hopfield Neural Network for Boolean Three Satisfiability Logic Mining

Nur Ezlin Zamri[1], Alyaa Alway[1], Mohd. Asyraf Mansor[1], Mohd Shareduwan Mohd Kasihmuddin[2]* and Saratha Sathasivam[2]

[1]School of Distance Education, Universiti Sains Malaysia, 11800 USM, Penang, Malaysia
[2]School of Mathematical Sciences, Universiti Sains Malaysia, 11800 USM, Penang, Malaysia

ABSTRACT

Artificial neural networks (ANNs) are actively utilized by researchers due to their extensive capability during the training process of the networks. The intricate training stages of many ANNs provide a powerful mechanism in solving various optimization or classification tasks. The integration of an ANN with a robust training algorithm is the supreme model to outperform the existing framework. Therefore, this work presented the inclusion of three satisfiability Boolean logic in the Hopfield neural network (HNN) with a sturdy evolutionary algorithm inspired by the Imperialist Competitive Algorithm (ICA). In general, ICA stands out from other metaheuristics as it is inspired by the policy of extending the power and rule of a government/country beyond its own borders. Existing models that incorporate standalone HNN are projected as non-versatile frameworks as it fundamentally employs random search in its training stage. The main purpose of this work was to conduct a comprehensive comparison of the proposed model by using two real data sets with an elementary HNN with exhaustive search (ES) versus a HNN with a standard evolutionary algorithm, namely- the genetic algorithm (GA). The performance evaluation of the proposed model was analyzed by computing plausible errors, such as root mean square error (RMSE), mean absolute error (MAE),

ARTICLE INFO

Article history:
Received: 1 January 2020
Accepted: 18 March 2020
Published: 16 July 2020

E-mail addresses:
ezlinzamri@student.usm.my (Nur Ezlin Zamri)
alyaalway@student.usm.my (Alyaa Alway)
asyrafman@usm.my (Mohd. Asyraf Mansor)
shareduwan@usm.my (Mohd Shareduwan Mohd Kasihmuddin)
saratha@usm.my (Saratha Sathasivam)
*Corresponding author

ISSN: 0128-7680
e-ISSN: 2231-8526

© Universiti Putra Malaysia Press

global minima ratio (R_m), computational time (CT) and accuracy (Q). The computational simulations were carried out by operating the different numbers of neurons in order to validate the efficiency of the proposed model in the training stage. Based on the simulations, the proposed model was found to execute the best performance in terms of attaining small errors and efficient computational time compared to other existing models.

Keywords: 3-satisfiability, Hopfield neural network, imperialist competitive algorithm, logic mining

INTRODUCTION

The inception of artificial neural networks (ANNs) has initiated a variety of capable models, which act as a useful tool in solving specific tasks such as classification, prediction, and pattern recognition (Ghaleini et al., 2019). Many of the recent developments have assembled different takes in refining the existing ANN models, specifically by integrating them with proficient searching techniques in order to intensify the quality of their standalone framework. In general, ANN possesses comprehensive structure of training and testing stages, thus emerging as one of the most efficient tools in finding patterns and extracting information to solve real-life applications. They are implemented in tasks such as solar radiation forecasting (Benali et al., 2019), risk analysis (Shi et al., 2019), fault detection (Dybkowski & Klimkowski, 2019), and quantitative analysis (Li et al., 2019a). Accordingly, ANNs can be described in many forms; one of them is the feedback-inducing recurrent networks. In particular, Hopfield neural network (HNN) is a recurrent neural network resembling the operations of human memory (Hureira & Vartanian, 2019). Proposed by Hopfield and Tank in 1985, its ability to manage nonlinear patterns by its training and testing capabilities is especially useful for interpreting complex real-life problems. In recent years, HNN has been widely used by many researchers as it has a deliberately sturdy component of content addressable memory (CAM) (Kong et al., 2019) and emits a degree of convergence by utilizing an energy function (Kasihmuddin et al., 2019). However, the fundamental HNN employs dated heuristics in its training stage, namely the exhaustive search (ES). Nievergelt (2000) had discovered that ES was not considered as a robust search technique as it exerted a random search mechanism, which increased the tendency of overfitting and showed the lack of variations (Lim & Bang, 2010). As such, Mansor et al. (2019) had proposed the incorporation of Elliot Hopfield Neural Network (EHNN) with a modified artificial immune system algorithm (AIS), thus ameliorating the performance of the HNN elementary model. Other than that, Genitha and Vani (2019) had proposed an integrated framework of modified genetic algorithm (GA) with the HNN approach for a super-resolution mapping of satellite images, thereby instigating greater accuracy compared to a primary HNN model. GA is a computational processing algorithm inspired by Darwin's model, namely a survival for the fittest model (Feng et al., 2019). Furthermore,

Jayashree and Kumar (2019) had underlined mutation and crossover as the key traits of GA in order to extract information and prioritize feature selection. Consequently, it is one of the prevalent metaheuristics used by many neural networkers, substantiating its compatibility for a comparison with the Imperialist Competitive Algorithm (ICA) mechanism. The common ground in these works is the homogenization of the HNN framework with other evolutionary algorithms to enhance the HNN training stage in producing a better HNN mechanism. In order to introduce an all-rounded model, HNN can implement more vigorous metaheuristics in its training stage.

Generally, ICA is an evolutionary algorithm motivated by human socio-political behaviors. Imperialism is known as the practice of a government/country to grow stronger and rule beyond its territory, whereby the imperialist's main vision is to increase the number of colonies. The main components of ICA consist of the initial empires, assimilation, revolution, and imperialist competition (Li et al., 2019b). A work by Tashayo et al. (2019) had inaugurated its use to forecast the maximum surface settlement (MMS) induced by tunneling in civil projects. Meanwhile, Gerist and Maheri (2019) had proposed an approach to solve damage detection problems, specifically by utilizing ICA and resulting in a great performance of the convergence rate and better identification of the global optima both. Therefore, it can be concluded that employing ICA is an endless potential, ranging from industrial planning, scheduling, and decision-making to machine learning (Atashpaz-Gargari & Lucas, 2007). However, it is commonly used by researchers to explicitly acquire a solution to a problem, rather than making use of it to generate a learning model for the problem. A research by Abdechiri and Meybodi (2011) had emphasized the credibility of HNN in utilizing ICA to solve the propositional satisfiability (SAT) problem. However, the work is not suitable for solving real data sets. Therefore, in the current work, the proposed model employs ICA in the training stage to overcome the complexity of checking clause satisfaction, generate variation, and vast searching space in order to solve two real-life data sets acquired from UCI repository.

Due to the comprehensibility of the HNN framework, researchers have considered it as a black box model or a symbolic system. Taking this fact into consideration, the execution of logic learning in HNN has delineated many versatile models, primarily from the work of Abdullah (1992) that incorporates logic programming on HNN. The work presented an extensive HNN framework to cater for the optimization of logical consistency. Abdullah (1992) had accordingly proposed an optimized logic learning through synaptic weights, which was called the Abdullah (WA) method. In layman terms, logic programming illustrates the symbolic knowledge that will be "trained" by the HNN model. The primary work by Sathasivam (2012) had further fostered Abdullah's (1992) proposal by implementing first-order logic in a neuro-symbolic integration model, which attained more than 90% of global minimum energy (Kasihmuddin et al., 2019). Several

compelling logical rules such as the 2-Satisfiability (2-SAT) (Kasihmuddin et al., 2017a) and Maximum Satisfiability (MAX-*k*SAT) (Mansor et al., 2017) have been successfully embedded in HNN. Its application with propositional satisfiability logic is boundless, ranging from Very Large Scale Integration (VLSI) circuit configuration (Mansor et al., 2016) and Bezier curves satisfiability model (Kasihmuddin et al., 2016). For this work, the incorporation of the 3-Satisfiability (3-SAT) propositional logic is utilized due to its ability to achieve a higher probability of satisfied interpretation compared to Horn Satisfiability (Horn-SAT) and 2-SAT. Thus, the proposed HNN-ICA model is incorporated with 3-SAT in order to solve real-life applications.

Currently, no recent approach is available to thoroughly compare the performance of ICA with other metaheuristics in solving real-life data sets. This is crucial; as an evolutionary algorithm catering for variation and larger searching space in comparison with random search, ICA has to verify its distinctive features that can lead a better training model compared to other metaheuristics. Therefore, the contributions of this research are presented as follows: (1) to introduce the formulation of ICA with 3-SAT logic programming, (2) to initiate a model with the integration of HNN with ICA as a robust tool in order to solve optimization tasks by comparing it with two other searching techniques (i.e., GA and ES), (3) to implement reverse analysis with the proposed model of HNN-3SATICA in order to cater to real-life applications. The construction of the proposed model HNN-3SATICA shows better performance in the training stage and successfully interprets real-life datasets to detect the factors that are more prominent than others contributing to the optimization problems.

MATERIALS AND METHOD

3-Satisfiability Logic (3-SAT)

Propositional satisfiability or SAT logic is perceived as a logical rule that consists of clauses containing literals or variables. General satisfiability logic (*k*-SAT) can signify the capability to represent real-life applications (Kasihmuddin et al., 2019). This work utilized discrete HNN which catered neurons in bipolar representation $\{1,-1\}$ (Kasihmuddin & Sathasivam, 2016). Hansen et al. (2019) had emphasized on the generalization of *k*-SAT logical rule, P_{k-SAT} can be reduced to 3-SAT, P_{3-SAT} logical rule. The general formula of P_{3-SAT} is given as in Equation (1):

$$P_{3-SAT} = \wedge_{i=1}^{m} Z_i \tag{1}$$

where P_{3-SAT} is a 3-SAT that consists of clause Z_i shown in Equation (2):

$$Z_i = \vee_{j=1}^{3} \left(x_{ij}, y_{ij}, z_{ij} \right) \tag{2}$$

whereby n literals and m clauses denoted by Conjunctive Normal Form (CNF) formula. The general structure of P_{3-SAT} (Mansor et al., 2017) can be summarized as follows:

i. A set of m clauses in a Boolean formula, where $Z_1, Z_2, ..., Z_m$ and clauses will be connected with logical AND operator $\wedge$.
ii. Each clause consists of only literals will be combined by logical OR operator $\vee$. In the P_{3-SAT} formula, we only considered three literals in each clause.
iii. Boolean Satisfiability formula composes an array of n literals, $u_1, u_2, ..., u_n$, where $u_i \in \{1, -1\}$ in each clause. Note that in this work, n is equal to 3.
iv. The literals can be the variable itself or the negation of the variable, for example A or $\neg A$.

Further extension of P_{3-SAT}, an example of P_{3-SAT} is shown as follows:

$$P_{3-SAT} = (A \vee \neg B \vee C) \wedge (D \vee E \vee F) \wedge (\neg G \vee H \vee \neg I) \tag{3}$$

Equation (3) is satisfiable since it gives truth value resulting to $P_{3\text{-}SAT}$=1. According to Equation (3), if the neuron states read $(A, B, C, D, E, F, G, H, I) = (-1, 1, 1, 1, 1, 1, 1, -1, 1)$, the formula will be unsatisfiable or $P_{3-SAT} = -1$. In this research, P_{3-SAT} will be embedded to the proposed model, HNN-3SATICA in comparison with different learning algorithms. P_{3-SAT} will cater the modified networks to unveil the true pattern or behaviour of the real data sets involved. Note that P_{3-SAT} is a symbolic form representation thus it is appropriate to be integrated in these networks as HNN is a non-symbolic platform.

Hopfield Neural Network (HNN)

HNN is a recurrent neural network, without hidden layer that mimics human biological brain. HNN structure of interconnected neurons and a powerful feature of CAM are crucial in solving various optimization and combinatorial tasks (Kong et al., 2019). The proposed model consists of structured N neurons, each of which is represented by an Ising variable. The neurons in discrete HNN are utilized in bipolar representation whereby $S_i \in \{1, -1\}$ (Sathasivam, 2010). The fundamental overview for the bipolar neuron state activation in HNN is shown in Equation (4):

$$S_i = \begin{cases} 1 & , \ if \ \sum_j W_{ij} S_j \geq \omega \\ -1 & , \text{otherwise} \end{cases} \tag{4}$$

where W_{ij} refers to synaptic weight of the neuron from unit j to i. S_j is the state of neuron j and ω is the predefined threshold value. Barra et al. (2018) specified that $\omega = 0$ to verify the network's energy decreases and ascertain our network to achieve plausible results. The connection in Hopfield net contains no connection with itself $W_{jj} = W_{ii} = 0$ (symmetrical). HNN model has similar intricate details to the Ising model of magnetism (Neelakanta & DeGroff, 1994). As the neuron states are termed in bipolar form, the neuron

rotates towards the magnetic field, resulting in the neurons to rotate until the equilibrium is achieved. Hence, the dynamic of HNN (considering all the neurons involved) is asynchronously changed according to $S_i \rightarrow \text{sgn}\left[h_i(t)\right]$, where h_i is the local field of the neurons connection. Motivated by Sathasivam et al. (2011), the sum of the field induced by each neuron is given in Equation (5):

$$h_i = \sum_{k=1,k\neq j}^{N} \sum_{j=1,j\neq k}^{N} W_{ijk} S_j S_k + \sum_{j=1,j\neq i}^{N} W_{ij} S_j + W_i \tag{5}$$

Thus, the biggest task of local field is to evaluate the final bipolar state of neurons and generate all possible P_{3-SAT} induced logic that was obtained from the final state of neurons. One of the most prominent features of HNN is the fact that it always converges in some cases, as illustrated by the following theorem (Hopfield, 1982).

Theorem 1. Let N be a neural network of order n and be defined by $N = (W, T)$ where W is an $n \times n$ matrix with element W_{ij} and T is a vector of dimension n, where element t depicted as the threshold attached to node i. The network will always converge to a stable state when running in serial mode; only one neuron can change the state at any time instantly, if the diagonal elements of W are non-negative.

Moreover, the subsequent state updating rule can be represented as in Equation (6)

$$S_i(t+1) = \text{sgn}\left[h_i(t)\right] \tag{6}$$

whereby sgn represents the signum function to squash the output of neurons, where this paper utilized Hyperbolic Tangent Activation Function (HTAF) (Mansor & Sathasivam, 2016). The following Equation (7) represents the Lyapunov energy function in HNN (Mansor et al., 2018a).

$$L_{P_{3-SAT}} = -\frac{1}{3} \sum_{i=1,i\neq j\neq k}^{N} \sum_{j=1,i\neq j\neq k}^{N} \sum_{k=1,i\neq j\neq k}^{N} W_{ijk} S_i S_j S_k - \frac{1}{2} \sum_{i=1,i\neq j}^{N} \sum_{j=1,i\neq j}^{N} W_{ij} S_i S_j - \sum_{i=1}^{N} W_i S_i \tag{7}$$

The energy value computed from the Equation (7) will be authenticated as global or local minimum energy. The network will provide the filtering mechanism and produce the correct solution when the induced neurons state reached global minimum energy. There are limited works to combine HNN and ICA as a single computational network. Thus, the robustness of ICA helps to improve training process in HNN.

Imperialist Competitive Algorithm (ICA)

The pioneering work of ICA was presented by Atashpaz-Gargari and Lucas (2007), who stated that it was an algorithm inspired by imperialistic competition. Generally, all inspired countries are divided into two parts, namely the imperialist states and colonies, which tackle a list of operations such as initialization, assimilation, revolution, and imperialist

competition. This can lead to a better searching technique compared to other metaheuristics. The main purpose of ICA is to drive the colonies to converge to a global minimum solution, which is believed to have shown vigorous mechanisms in solving optimization tasks (Mollajan et al., 2019). It is set to be different compared to other metaheuristics as its features function to ease the performing neighborhood movements in both the continuous and discrete search spaces (Hosseini & Al Khaled, 2014). The application of ICA is infinitely many, such as ship design optimization (Peri, 2019), engineering design optimization (Aliniya & Keyvanpour, 2019), slope stability prediction (Koopialipoor et al., 2019), and heat and power dispatch problem (Davoodi & Babaei, 2019).

This work is focusing on utilizing ICA to find the maximum fitness of countries that will increase the number of satisfied clauses in the training stage. Its implementation with HNN is addressed as follows (Abdechiri & Meybodi, 2011):

Step 1. Forming initial empires (Initialization)
Each solution is shown by an array called country. Note that, in an N-dimensional optimization tasks, a country is denoted as $1\times N$ array. This array predefined as Equation (8):

$$C_{Nj} = \begin{cases} 1 & , \ rand[0,1] \geq 0.5 \\ -1 & , \text{otherwise} \end{cases} \tag{8}$$

whereby C_i is the country and C_{Nj} is the number of variables to be considered of interest about a country. Each empire E_i comprises N number of countries which represents the state of P_{3-SAT} as shown in Equation (9):

$$E_i = \left(C_1^{Ei}, C_2^{Ei}, ..., C_N^{Ei}\right) \tag{9}$$

Step 2. Fitness Evaluation
Each country's fitness is calculated based on the clauses by using Equation (10):

$$f_{C_i^{E^i}} = \sum_{i=1}^{NZ} Z_i \tag{10}$$

$f_{C_i^{E^i}}$ denoted as fitness of each C_i in E^i, Z_i is the clause in P_{3-SAT} and NZ is the total number of clauses.

Step 3. Colonies moving towards imperialist (Assimilation)
We select the imperialist, T^{E_i} from the country, $C_i^{E_i}$ with the highest $f_{C_i^{E^i}}$ and the rest will remain as colonies by using Equation (11).

$$C_i^{E_i} = \begin{cases} T^{E_i}, & \max\left[f_{C_i^{E^i}}\right] \\ C_i^{E_i}, & \text{otherwise}, \ i = rand[1, N] \end{cases} \tag{11}$$

Other remaining countries and colonies will be allocated to respective empires where each colonies population is randomized.

Step 4. Revolution

When revolution occurs, the rest of the colonies, $C_i^{E_i}$ inside an empire E_i will be randomized according to the following Equation (12):

$$C_{ij}^{E_i} = \begin{cases} 1 & , \ rand[0,1] \geq 0.5 \\ -1 & , \text{otherwise} \end{cases} \tag{12}$$

to offer colonies acquiring better position that will attain higher chances of redeeming its place to take over the reigning empire by replacing the current imperialist, T^{E_i}. In order for revolution to take place, the fitness for each $C_i^{E_i}$ will be computed by using Equation (10) and the new imperialist T^{E_i} will be selected based on Equation (11).

Step 5. Imperialist Competition

This feature of ICA sets apart ICA from other metaheuristics. In this process, imperialistic competition occurs among all imperialist in order to acquire power of each empires $V_N^{E^i}$ as in Equation (13):

$$V_{E_i} = f_{T^{E_i}} - \varepsilon f_{T^{E_i}} + \frac{1}{N-1} \sum_{i=1}^{N} f_{C_i^{E_i}} \tag{13}$$

whereby $f_{T^{E_i}}$ represents the fitness of each imperialist. According to Atashpaz-Gargari & Lucas (2007), $\varepsilon = 0.05$ is chosen as an optimal value for this study. Empires that show no power will fall in this competition and the surviving imperialist will be the one that has the highest power. Worth mentioning that, if the power for a particular empire is within $\left|V_{E_i} - V_{\phi}\right| \leq \lambda$, T^{E_i} will be chosen as the final neurons states for P_{3-SAT}. Note that λ will be predetermined by users. Step 4 and Step 5 will be repeated until termination criteria $f_{T^{E_i}} = NZ$ is been met. The state of T^{E_i} will be stored as CAM. In this paper, we modified the ICA of the pioneering work (Atashpaz-Gargari & Lucas, 2007) that utilized ICA to solve a continuous problem into bipolar representation to solve NP problems. A work on implementing ICA with HNN for solving Satisfiability problem was executed by Abdechiri & Meybodi (2011), however it only catered to simulated data set. Figure 1 depicts the summary of ICA from Step 1 until Step 5. This research extends the work of ICA by implementing HNN and P_{3-SAT} logical rule with reverse analysis in solving real data sets.

Genetic Algorithm (GA)

In this paper, GA will be applied into HNN-3SAT or abbreviated as HNN-3SATGA in order to compare with other searching techniques, HNN-3SATICA and HNN-3SATES. GA is a popular optimization algorithm that was inspired by Darwin's evolutionary theory to find a formula or optimized answer in order to predict or match patterns (Esfe et al., 2019).

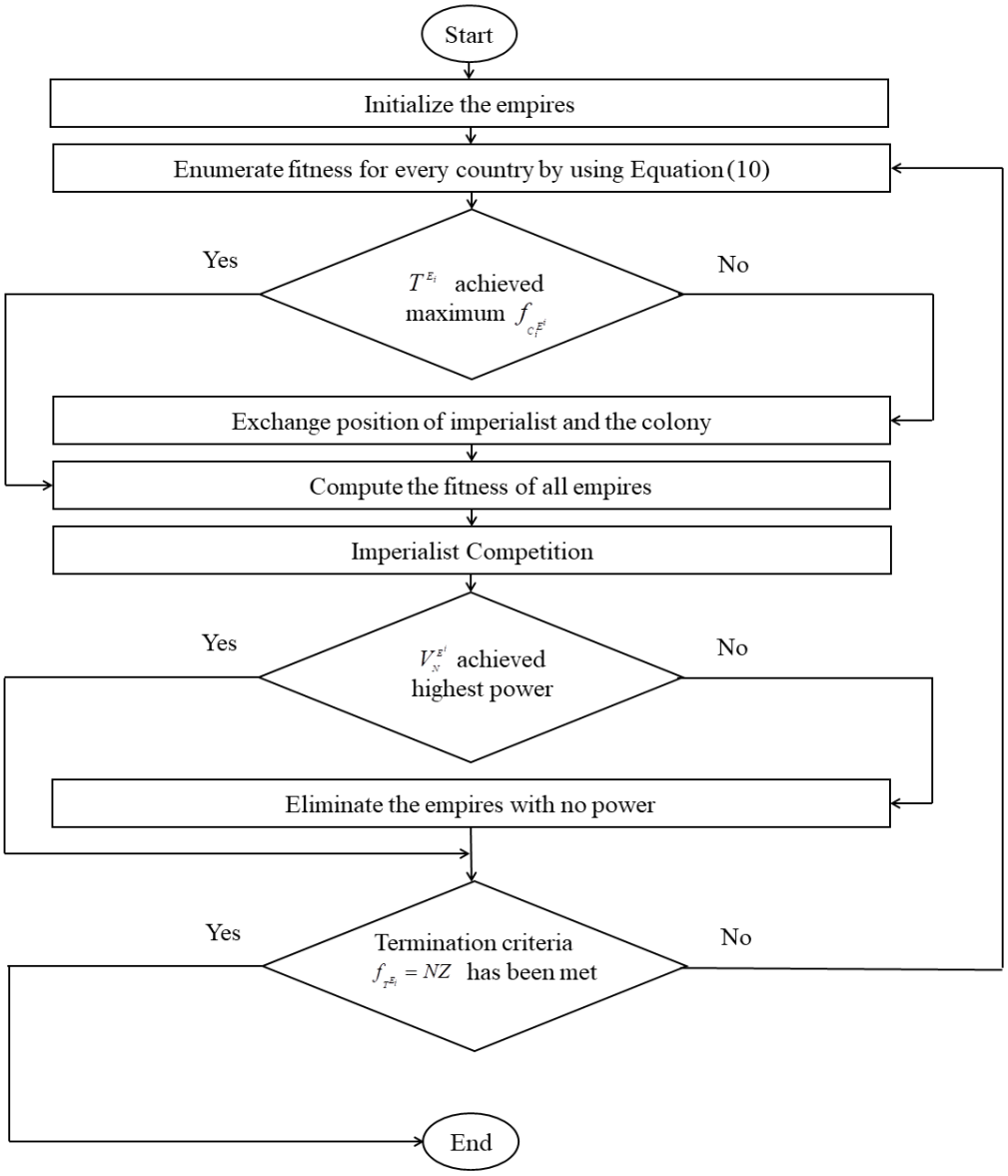

Figure 1. Summary of ICA

The phases of HNN-3SATGA are as follows (Mansor et al., 2019):

Step 1. Initialization
Initialize 100 random chromosomes (Cr_i) as bipolar interpretation where each element of $\{1,-1\}$ is denoted by True and False. Every Cr_i portrays the possible interpretation for P_{3-SAT} .

Step 2. Cr_i Fitness Computation
Fitness of the Cr_i in GA is typically being calculated by using fitness function. Thus, the fitness computation is based on the satisfiability of the clauses in P_{3-SAT} . Hence, the maximum fitness manifests the effectiveness of the training process.

Step 3. Cr_i Selection

Select y Cr_i (in our case $y=10$) containing P_{3-SAT} information with the highest fitness out of 100 Cr_i to undergo the crossover process.

Step 4. Crossover
Two Cr_i are selected and separated during the crossover phase from 10 selected Cr_i . Furthermore, by joining both parts of the paternal Cr_i , a child Cr_i is produced. Hence, the second child is therefore generated by the addition of the primary and secondary segment and vice versa (Luke, 2013).

For example:

Before crossover

$Cr_1 = -1-1-1111-1-1-1$

$Cr_2 = -1-1-11-11-1-1-1$

After crossover

$Cr_1 = -1-1-1-1-1-1-1-1-1$

$Cr_2 = -1-1-11-11111$

Therefore, the Cr_i fitness for the new generated Cr_i can be determined.

Step 5. Mutation
Mutation is an integral optimization operator in the GA which shifts Cr_i patterns, ensuring that the population is not trapped at local minima. This is the random process of altering specific genes of the Cr_i . As an illustration:

Before mutation

$Cr_3 = -1-1-11-11111$

After mutation

$Cr_3 = 1-1-11-11111$

The first part of the Cr_i was flipped from -1 to 1. Thus, a better Cr_i might be generated after mutation. The fitness value for a newly formed Cr_i will be computed. The current Cr_i will repeat the first step if the fitness value does not achieve maximum fitness.

IMPLEMENTATION

Performance Evaluation Metrics

The performance of the proposed model in executing logic mining will implement several performance metrics such as root mean square error (RMSE), mean absolute error (MAE), global minima ratio (R_m), computational time (CT) and accuracy (Q).The list of parameter names in performance evaluation metrics is shown in Table 1. Meanwhile, the list of parameter values used in R_m depicts in Table 2.

Root Mean Square Error (RMSE)

Overall, RMSE is a prediction metric utilized by neural networkers to enumerate the predicted value of a model with observed value. RMSE formulation utilized in this work is shown in Equation (14):

$$RMSE = \sum_{i=1}^{n} \sqrt{\frac{1}{n}(f_x - f_y)^2} \tag{14}$$

Mean Absolute Error (MAE)

According to Willmott and Matsuura (2005), MAE capable of evaluating good error estimation by showing a uniformly distributed error. MAE formulation consists of the absolute value of the difference between the estimated values and the actual values (Chai & Draxler, 2014). A good model will attain low values of RMSE and MAE. The equation of MAE is shown in Equation (15):

$$MAE = \sum_{i=1}^{n} \frac{1}{n} \left| f_x - f_y \right| \tag{15}$$

Global Minima Ratio (R_m)

The global minimum ratio is the generalized metric for evaluating the efficiency of the solutions. Tolerance value will filter each calculated final energy of the neurons in HNN. The final energy is assumed as global minimum energy if the final energy of the model within the tolerance value (Sathasivam, 2010). The Equation (16) of R_m is shown as follows:

$$R_m = \frac{1}{ab} \sum_{i}^{n} N_{L_{P_{3-SAT}}} \tag{16}$$

Computational Time (*CT*)

Computational time is used to determine the effectiveness of the proposed models. The

value for CT will be measured in SI unit of second (s). The Equation (17) of CT is shown below:

$$CT = TrainingTime(s) + TestingTime(s) \tag{17}$$

whereby $TrainingTime$ and $TestingTime$ are depicted as the total time to execute the HNN-3SAT models in training and testing phase respectively. In the work by Kho et al. (2020), CT was utilized for HNN-2SAT model because it implies the capability and stability of the model.

Accuracy (Q)

The accuracy is used to assess the models ability to train the data set. The Equation (18) of Q is shown below:

$$Q = \frac{P_{induced}^{Correct}}{N_{P_{test}}} \times 100\% \tag{18}$$

Table 1

List of parameters in performance evaluation metrics

Parameter	Parameter name	Parameter	Parameter name
f_x	Total number of clauses	$N_{L_{P_{3-SAT}}}$	Number of global minimum energy
f_y	Number of satisfied clause	$N_{L_{P_{3-SAT}}}$	Number of global minimum energy
n	Number of iteration before $f_x = f_y$	$N_{P_{test}}$	Number of testing data
a	Number of trials	$P_{induced}^{Correct}$	Correct induced logic
b	Number of neuron combination		

Table 2

List of parameters in R_m

Parameter	Parameter value
a	100
b	100
Tolerance value	0.001 (Sathasivam, 2010)

Experimental Setup

The utilization of P_{3-SAT} will aid in discovering valuable information on real data sets. Many works of literature have surfaced in explaining that information and patterns can be represented in a logical form. The use of reverse analysis method to extract significant information from a particular data set has been introduced by Sathasivam and Abdullah (2011) by considering the CNF logical rule. Motivated by the work of Mansor et al. (2018b), more systematic logic mining techniques incorporating P_{3-SAT} in HNN have been proposed. Following this, the 3-SAT-based Reverse Analysis Method (3-SATRA) is employed in HNN-3SATICA to generate an optimized induced logical rule from several prominent data sets. In this case, raw data are translated into P_{3-SAT} and then embedded and processed by HNN-3SAT. By pursuing this, the induced P_{3-SAT} will be used to classify the outcome of the dataset. The comprehensive 3-SATRA via HNN-3SATICA is depicted in Figure 2.

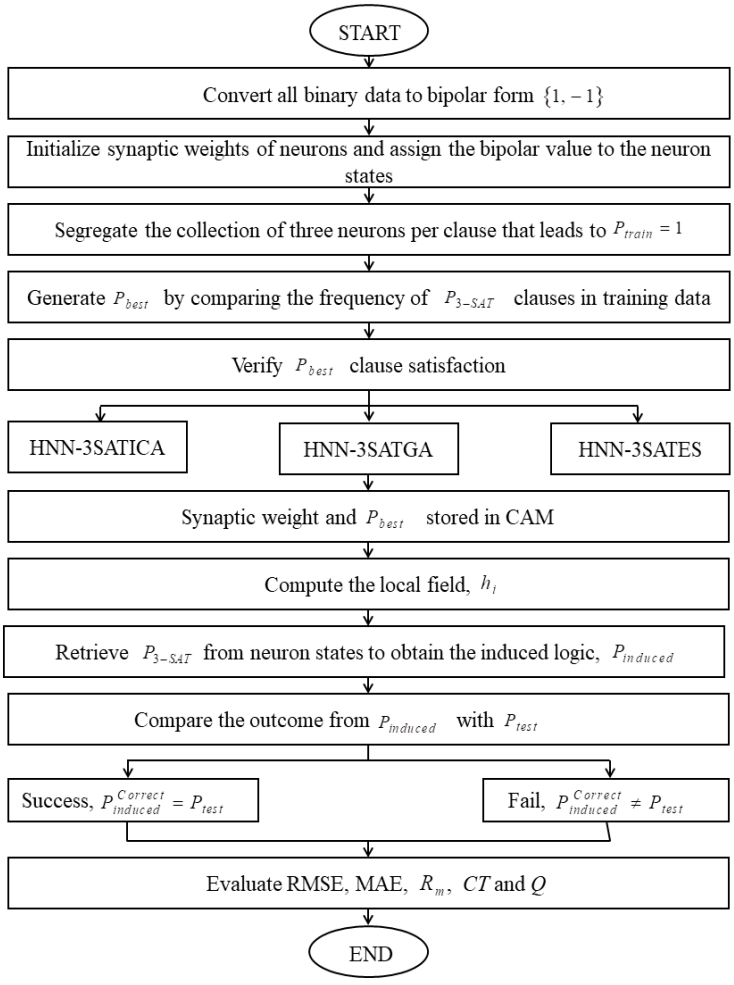

Figure 2. Implementation of 3-SATRA in HNN-3SATICA

In this paper, two different real data sets from different fields occupied the constructed 3-SATRA, namely the Bach Choral Harmony data set (BCHDS) and German Credit data set (GCDS). All data sets were taken from the UCI machine learning repository website and each of them had different purposes. Nine attributes were used in this paper and all real data sets used multivariate data. In this experiment, the aim was to analyze a comprehensive comparison of accuracy between HNN-3SATICA and other existing models such as GA, ES, and researchers utilizing the same data sets. The information about BCHDS and GCDS is shown in Table 3 and 4.

Table 3

List of attributes for each data sets

Data Set	Details of each attributes			Output $P_{3\text{-}SAT}$
BCHDS (Haque et al., 2019)	*A*	:	Pitch for Key "C-M"	To identify the distinction between good harmony and bad harmony for musician.
	B	:	Pitch for Key "E-m"	
	C	:	Pitch for Key "B-m"	
	D	:	Pitch for Key "A-m"	
	E	:	Pitch for Key "F-m"	
	F	:	Pitch for Key "G-M"	
	G	:	Pitch for Key "A-M"	
	H	:	Bass	
	I	:	Meter	
GCDS (Liu et al., 2019)	*A*	:	Credit History	To distinguish bank's customer of having a good or bad credit risks.
	B	:	Status of existing checking account	
	C	:	Saving account/bonds	
	D	:	Personal status	
	E	:	Age	
	F	:	Housing	
	G	:	Number of existing credits at this bank	
	H	:	Telephone	
	I	:	Foreign worker	

As mentioned earlier, the literals can be the variable itself or the negation of the variable; for example, A or $\neg A$. Thus, as the work implemented real-life data sets, the negation literals represented attributes that did not affect the output of P_{3-SAT} and *vice versa* for non-negate literals.

Table 4
Method used in existing model

Data Set	Method
BCHDS	AdaBoost
GCDS	Support Machine Vector (SVM)

The source code was developed through Dev C++ Version 5.11 in 8GB RAM with Intel Core i5 to acquire a good comparison between all proposed models. The same device was used during simulation to avoid bias; using the same device rendered the simulation comparable as the memory (RAM) and processor had the same power. Another factor that can trigger bias is a different compiler for each learning algorithm, which may lead to different computational times or anomaly in error values. Moreover, to avoid bias, the number of neurons chosen for the simulations showed the same combination of $9 \leq NN \leq 72$ for all learning algorithms. The threshold for simulation was set to 24 hours according to Kasihmuddin et al. (2016). All outputs exceeding 24 hours of computation time were omitted due to the simulation, which would eventually break down in finding the satisfied clause interpretation, $E_{P_{3-SAT}} = 0$. Table 5, 6 and 7 show all parameters involved in the proposed models.

Table 5
List of parameters in HNN-3SATES (Sathasivam, 2012)

Parameter	Parameter value
Neuron Combination (*b*)	100
Number of Trial (*a*)	100
Tolerance Value (*Tol*)	0.001
Number of String	100
Selection Rate	0.1

Table 6
List of parameters in HNN-3SATGA (Kasihmuddin et al., 2017b)

Parameter	Parameter value
Neuron Combination (*b*)	100
Number of Trial (*a*)	100
Tolerance Value (*Tol*)	0.001
Selection Rate	0.1
Mutation Rate	0.01
Generation	1000

Table 7
List of parameters in HNN-3SATICA

Parameter	Parameter value
Neuron Combination (b)	100
Number of Trial (a)	100
Tolerance Value (Tol)	0.001
Initial Empires	10
Parameter (ε)	0.05
Termination Value (λ)	0.05

RESULT AND DISCUSSION

The effectiveness of implementing ICA in the training stage of the HNN-3SAT model was investigated in this paper. The proposed mode of HNN-3SATICA in comparison with existing models that utilized GA (Kasihmuddin et al., 2017b) and ES (Sathasivam, 2012) embedded two real-life data sets, which were retrieved from the UCI Machine Learning Repository platform. The investigation of a model's performance can be separated into two parts. The first important part is to examine the quality of the solution generated by different searching techniques, specifically by employing the suitable training errors. Second, one should analyse the robustness and efficiency of the proposed model by comparing the CT and Q needed to execute the models' respective mechanisms. Accordingly, five performance evaluation metrics were involved in analyzing the training and testing stages of the modified models, as presented in the Performance Evaluation section. Therefore, this research's main contribution was the display of HNN-3SATICA competency in outperforming the existing models.

In this section of result analysis for BCHDS, it could be concluded that the outcomes attained by HNN-3SATICA for RMSE and MAE showed a consistent value of zero (Figure 3 & 4), thereby indicating ICA providing a better and well-trained HNN framework. However, the results were identical to HNN-3SATGA. Similarly, HNN-3SATES projected larger errors as the number of neurons increased. The incorporation of ES underlined the lack of modification undertaken in the training stage of the fundamental HNN. For the R_m, it is likely to be a better model when it is prone to the value of 1 (Sathasivam, 2011). From Figure 5, all models are approaching to 1 even by manipulating different numbers of neurons. The trend showed the capability of the training methods deployed by HNN-3SAT to attain the global minimum energy by having R_m closer to 1. From Figure 6, it can be deduced that all models exhibit less CT compared to the assigned threshold time. Regardless, HNN-3SATICA executed less CT compared to other models, thereby displaying

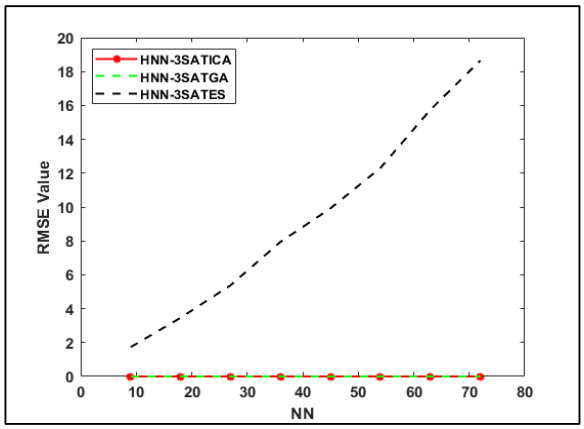

Figure 3. RMSE value of HNN-3SAT models for BCHDS

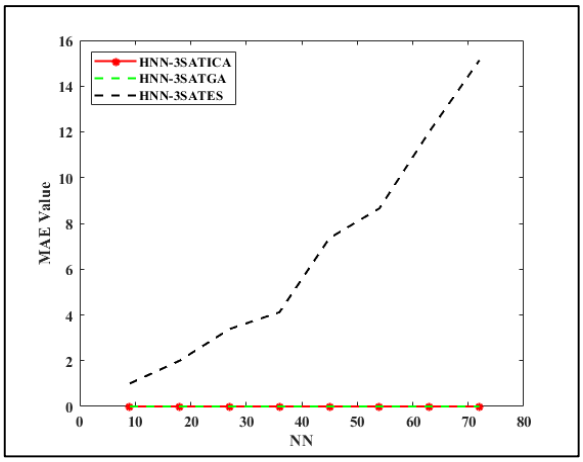

Figure 4. MAE value of HNN-3SAT models for BCHDS

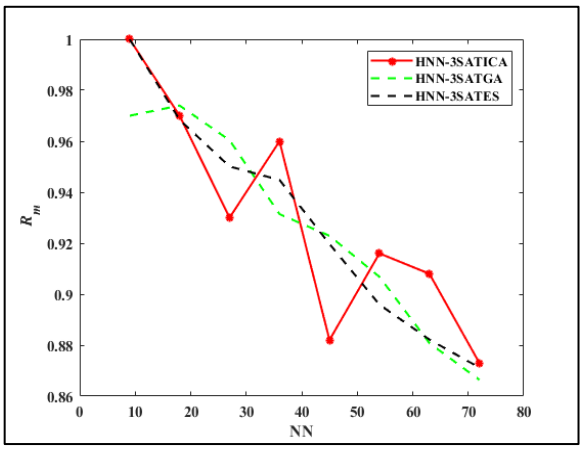

Figure 5. R_m of HNN-3SAT models for BCHDS

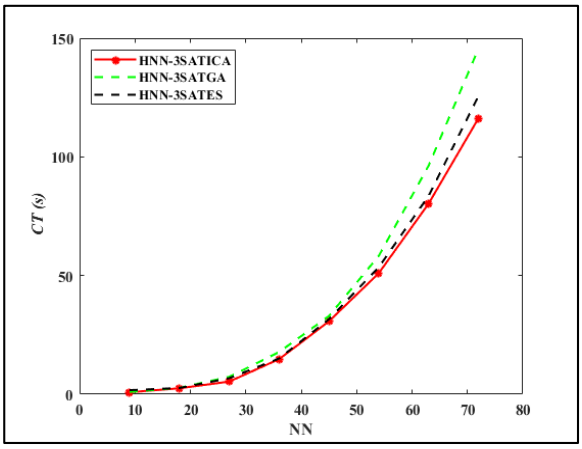

Figure 6. CT of HNN-3SAT models for BCHDS

Table 8
Accuracy of HNN-3SATICA with other existing models

Data Set	HNN-3SATICA	Sathasivam (2012)	Kasihmuddin et al. (2017b)	Haque et al. (2019)
BCHDS	61%	54%	61%	56.72%

the effectiveness of ICA during the training stage with different levels of complexity. Table 8 outlines the accuracy of all models that utilized BCHDS, whereby HNN-3SATICA and HNN-3SATGA are observed to enumerate the same value of accuracy. Both models achieved 61% of accuracy, which demonstrated their respective capability in attaining an optimized induced logic for BCHDS. Besides, HNN-3SATES and the work by Haque et al. (2019) both generate an accuracy value less than 60%. The accuracy for both methods was not promising, particularly for HNN-3SATES. It is due to the non-optimized induced logic generated at the end of the executions. By executing the simulation of HNN-3SATICA for BCHDS, the induced logic attained by HNN-3SATICA can be observed as per Equation (19) below:

$$P_{induced}^{Correct} = \left(\neg A \vee B \vee \neg C\right) \wedge \left(D \vee E \vee \neg F\right) \wedge \left(G \vee H \vee I\right) \tag{19}$$

whereby from Equation (19), in order to produce a good harmony, attributes A, C, and F are insignificant to be scrutinize. However, such attributes like B, D, E, G, H and I would lead the harmonization to be out of tune.

In comparison with the result analysis of BCHDS, GCDS showed better result of HNN-3SATICA with other existing models. Figure 7 reveals the RMSE values attained by HNN-3SATGA and HNN-3SATES as relatively increasing as the number of neurons increased. However, HNN-3SATICA persistently achieved zero RMSE values despite the

incremental number of neurons. Furthermore, the MAE analysis for all models yielded comparatively similar outcomes to the illustration of RMSE analysis. From Figures 7 and 8, the execution of the ICA mechanism is significant to aid the standalone HNN with a vigorous training stage to achieve $E_{P_{3-SAT}} = 0$. Unfortunately, both HNN-3SATGA and HNN-3SATES revealed an inclining trend of errors for their MAE and RMSE outcomes both, showing the incompetency of the GA and ES mechanisms to accommodate a higher number of neurons as the complexity increased. The analysis of R_m in GCDS (Figure 9) shows that most of the models are able to generate at most 100% of global minimum solutions, except for HNN-3SATGA. Although two different data sets from different fields were utilized, the findings of R_m achieved by all models depicted indistinguishable results. Figure 10 displays that the *CT* for HNN-3SATGA and HNN-3SATES requires more time compared to HNN-3SATICA. This was due to the proposed model offering a larger search space, which contributed to a more efficient HNN framework. In Table 9, the induced logic generated by HNN-3SATICA in the testing stage records an accuracy of 83%. This finding set forth its ability to acquire an optimized induced logic that could best represent the GCDS data set. Contrary to this, HNN-3SATGA, HNN-3SATES, and SVM methods deployed by Liu et al. (2019) have achieved lower accuracy compared to HNN-3SATICA. This is attributable to ICA mechanism's function to attain $E_{P_{3-SAT}} = 0$, which can lead to a better training stage in the resulting construction of an optimized induced logic. Equation (20) displays the induced logic attained by HNN-3SATICA at $NN = 54$ until $NN = 72$:

$$P_{induced}^{Correct} = \left(\neg A \vee B \vee \neg C\right) \wedge \left(D \vee E \vee \neg F\right) \wedge \left(G \vee H \vee I\right) \tag{20}$$

From Equation (20), one can distinguish whether a customer is a good credit risk or not, whereby attributes such as *A* and *D* can exhibit a fair credit status. Here, the credit history and personal status were very important to know their credit management and liability. Other than that, the induced logic could reveal insignificant and trivial attributes such as *C* and *I* in order to sort out which customer was a good or bad credit risk.

The training stage played a prominent role in enhancing the standalone HNN framework. From the HNN-3SATICA results obtained in Figure 3 and 4 and Figure 7 and 8, the capability of ICA is portrayed by improving the HNN training stage to attain a good solution. The deviation of error was generally smaller than the other counterparts due to the optimization operator employed in ICA. Assimilation and revolution in ICA played a big role to generate fewer iterations in obtaining $E_{P_{3-SAT}} = 0$. Apart from this, the fewer iterations indicated that less RMSE and MAE were generated from the model. However, the results attained for HNN-3SATGA and HNN-3SATES were larger than the proposed model, particularly in GCDS. They both employed undeniably ineffective searching method compared to ICA, especially ES. In particular, ES used random search where the number of neurons increases, the complexity also increases. Thus, ES contributes to

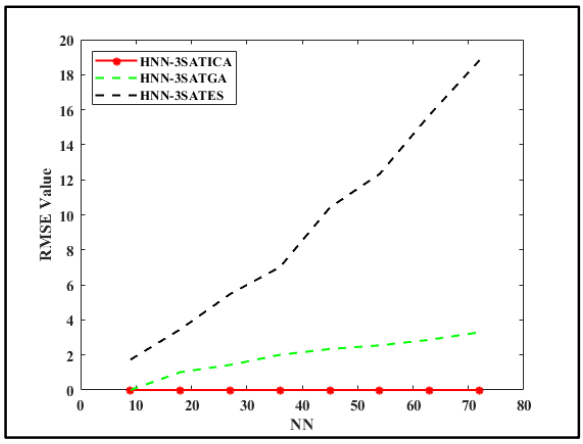

Figure 7. RMSE value of HNN-3SAT models for GCDS

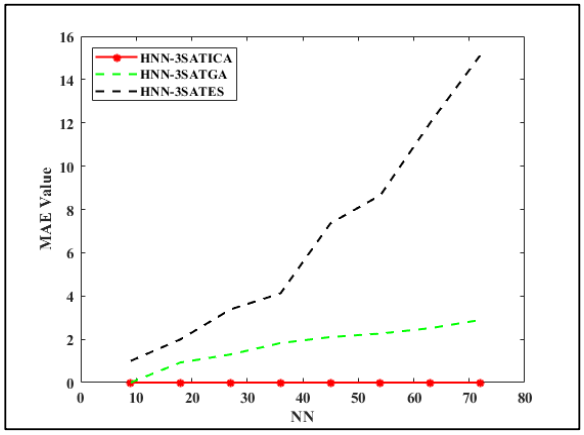

Figure 8. MAE value of HNN-3SAT models for GCDS

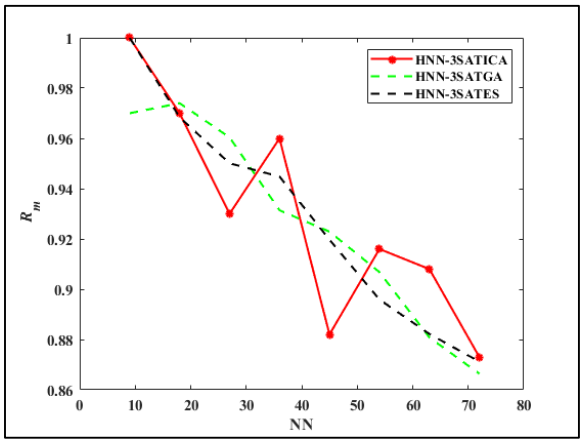

Figure 9. R_m of HNN-3SAT models for CGDS

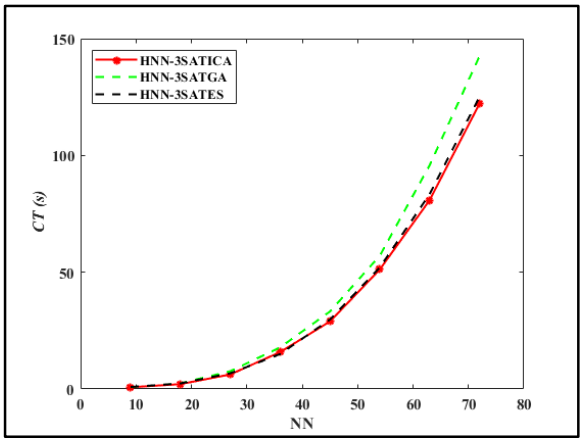

Figure 10. CT of HNN-3SAT models for BCHDS

Table 9

Accuracy of HNN-3SATICA with other existing models

Data Set	HNN-3SATICA	Sathasivam (2012)	Kasihmuddin et al. (2017b)	Liu et al. (2019)
GCDS	83%	71%	82%	75.7%

generate larger errors. Figures 5 and 9 showcase the R_m obtained by all models, which are relatively identical even as the number of neurons increased. Therefore, this ensured the proposed model reached the global minimum energy without any complications. This fact displayed the versatility and relevancy of the ICA mechanism to accomplish close achievement as the existing models.

CT is predefined as the expanse of time needed for the network to complete the overall computational process. Therefore, it is significant to identify a model's performance efficiency affirmation (Xiao et al., 2017). From Figures 6 and 10, it is discovered that CT needed to execute HNN-3SATICA is lesser than other existing models. In contrast, with HNN-3SATES, HNN-3SATICA attained faster execution due to the ICA algorithm that had fewer parameters compared to ES. However, for ES, the number of neurons was gradually increasing and thus more CT was required due to its nature of brute force that needed more iterations. Thereby resulting in overfitting the solution. HNN-3SATICA was set apart from other models as it achieved a satisfactory percentage of accuracy for both BCHDS and GSDS data sets. Based on the results in Table 9, it can be concluded that ICA plays a vital role in the proposed model to generate better-induced logic, which reflects the precision of the modified network. The reason for ICA being able to fulfill such factor is due to the optimization operator in it, which introduces a larger search space and variations of solution that contribute to an effective training stage.

The limitation of HNN-3SATICA is that this modified framework only caters to bipolar representation and only utilizes the multivariate type of data sets. Further extension can be done by utilizing the binary form of entries and incorporating other types of data sets, such as time-series. Other than that, this modified network only utilized one type of SAT, namely 3-SAT. Therefore, one can incorporate more than one or other types of SAT, such as 2-SAT, MAX-*k*SAT, and *k*-SAT. The main drawback of HNN-3SATICA is its tendency of overfitting, which lacks the variability of generated induced logic. In the current context, overfitting indicates that as the search algorithm becomes more complex in the training phase, the solution will produce inaccurate and biased results (Reunanen, 2003). To overcome such aspect, an alteration of the data sets is crucial. Rearrangement and permutation of the attributes with a randomized selection of attributes should be implemented. The no-free lunch theorem (Wolpert & Macready, 1997) states that there are no absolute or specific algorithms that can be utilized to solve any problems. However, in this research, it was found that HNN-3SATICA worked exceptionally well for GCDS. On the contrary, the HNN-3SATICA and HNN-3SATGA worked well for BCHDS.

CONCLUSION

In this research, the formulation of constructing ICA in 3-SAT proved to be adequate to represent the mechanism that involves in ICA and the implementation of ICA with standalone HNN framework with reverse analysis proved to be effective in solving real life data sets. Through this approach, we have successfully presented a modified model of HNN-3SATICA which presented ICA role in generating variations and broad searching space. Particularly in this research, assimilation and revolution components of ICA provided a better solution in checking $E_{P_{3-SAT}} = 0$ which modify the training stage of a fundamental HNN framework. The proposed HNN-3SATICA model was trained and tested by using two real life data sets, in comparison with two different searching techniques; HNN-3SATGA and HNN-3SATES. The performance evaluation between these models was analysed by employing different performance metrics such as RMSE, MAE, global minima ratio, computational time and accuracy. The analysis of the results displayed the competency of the proposed model, HNN-3SATICA for all chosen performance evaluation metrics. We have successfully accomplished all objectives as presented based on the performance of our proposed model. Computational simulations for all models were specifically difficult towards larger number of neurons. However, the constructed proposed model, HNN-3SATICA showed good potential and a better training mechanism compared other metaheuristics and regular HNN framework. Extended research is required to further enhance HNN-3SATICA model by employing the same mechanism to other types of recurrent neural networks, such as Elman and Kohonen neural network. Other than that, we can utilize other types of propositional logic such as *k*-SAT and MAX-*k*SAT.

ACKNOWLEDGEMENT

This research was funded by Fundamental Research Grant Scheme (FRGS), Ministry of Education Malaysia, grant number 203/PMATHS/6711804 and Universiti Sains Malaysia.

REFERENCES

Abdechiri, M., & Meybodi, M. R. (2011, February 26-28). A hybrid Hopfield network-imperialist competitive algorithm for solving the SAT problem. In *3rd International Conference on Signal Acquisition and Processing (ICSAP 2011)* (Vol. 2, pp. 37-41). Singapore.

Abdullah, W. A. T. W. (1992). Logic programming on a neural network. *International Journal of Intelligent Systems*, *7*(6), 513-519.

Aliniya, Z., & Keyvanpour, M. R. (2019). CB-ICA: A crossover-based imperialist competitive algorithm for large-scale problems and engineering design optimization. *Neural Computing and Applications*, *31*(11), 7549-7570.

Atashpaz-Gargari, E., & Lucas, C. (2007, September 25-28). Imperialist competitive algorithm: An algorithm for optimization inspired by imperialistic competition. In *2007 IEEE Congress on Evolutionary Computation* (pp. 4661-4667). Singapore.

Barra, A., Beccaria, M., & Fachechi, A. (2018). A new mechanical approach to handle generalized Hopfield neural networks. *Neural Networks*, *106*, 205-222.

Benali, L., Notton, G., Fouilloy, A., Voyant, C., & Dizene, R. (2019). Solar radiation forecasting using artificial neural network and random forest methods: Application to normal beam, horizontal diffuse and global components. *Renewable Energy*, *132*, 871-884.

Chai, T., & Draxler, R. R. (2014). Root mean square error (RMSE) or mean absolute error (MAE)?–Arguments against avoiding RMSE in the literature. *Geoscientific Model Development*, *7*(3), 1247-1250.

Davoodi, E., & Babaei, E. (2019). A modified imperialist competitive algorithm for combined heat and power dispatch. *Computational Intelligence in Electrical Engineering, 10*(1), 1-18.

Dybkowski, M., & Klimkowski, K. (2019). Artificial neural network application for current sensors fault detection in the vector controlled induction motor drive. *Sensors*, *19*(3), 1-16.

Esfe, M. H., Amiri, M. K., & Bahiraei, M. (2019). Optimizing thermophysical properties of nanofluids using response surface methodology and particle swarm optimization in a non-dominated sorting genetic algorithm. *Journal of the Taiwan Institute of Chemical Engineers*, *103*, 7-19.

Feng, L., Ong, Y. S., & Gupta, A. (2019). Genetic algorithm and its advances in embracing memetics. In *Evolutionary and Swarm Intelligence Algorithms* (pp. 61-84). Cham, Switzerland: Springer.

Genitha, C. H., & Vani, K. (2019). A hybrid approach to super-resolution mapping of remotely sensed multi-spectral satellite images using genetic algorithm and Hopfield neural network. *Journal of the Indian Society of Remote Sensing*, *47*(4), 685-692.

Gerist, S., & Maheri, M. R. (2019). Structural damage detection using imperialist competitive algorithm and damage function. *Applied Soft Computing*, *77*, 1-23.

Ghaleini, E. N., Koopialipoor, M., Momenzadeh, M., Sarafraz, M. E., Mohamad, E. T., & Gordan, B. (2019). A combination of artificial bee colony and neural network for approximating the safety factor of retaining walls. *Engineering with Computers*, *35*(2), 647-658.

Hansen, T. D., Kaplan, H., Zamir, O., & Zwick, U. (2019, June 23-26). Faster k-SAT algorithms using biased-PPSZ. In *Proceedings of the 51st Annual ACM SIGACT Symposium on Theory of Computing* (pp. 578-589). Phoenix, Arizona, USA.

Haque, M. R., Saud, A. A., Annajiat Yasmin, B., & Hossain, S. (2019). *Solving multi-class classification tasks with classifier ensemble based on clustering* (Bachelor Degree). United International University, Bangladesh.

Hopfield, J. J. (1982). Neural networks and physical systems with emergent collective computational abilities. *Proceedings of the national academy of sciences*, *79*(8), 2554-2558.

Hopfield, J. J., & Tank, D. W. (1985). "Neural" computation of decisions in optimization problems. *Biological Cybernetics*, *52*(3), 141-152.

Hosseini, S., & Al Khaled, A. (2014). A survey on the imperialist competitive algorithm metaheuristic: implementation in engineering domain and directions for future research. *Applied Soft Computing*, *24*, 1078-1094.

Hureira, D., & Vartanian, C. (2019). Machine learning and neural networks for real-time scheduling. *Recent Advances in Real-Time Systems as of 2019, 1*, 1-7.

Jayashree, J., & Kumar, S. A. (2019). Evolutionary correlated gravitational search algorithm (ECGS) with genetic optimized Hopfield neural network (GHNN)–A hybrid expert system for diagnosis of diabetes. *Measurement*, *145*, 551-558.

Kasihmuddin, M. S. B. M., & Sathasivam, S. (2016). Accelerating activation function in higher order logic programming. In *AIP Conference Proceedings* (Vol. 1750, No. 1, p. 030006). New York, USA: AIP Publishing.

Kasihmuddin, M. S. M., Mansor, M. A., & Sathasivam, S. (2016). Bezier curves satisfiability model in enhanced Hopfield network. *International Journal of Intelligent Systems and Applications*, *8*(12), 9-17.

Kasihmuddin, M. S. M., Mansor, M., & Sathasivam, S. (2017a). Robust artificial bee colony in the Hopfield network for 2-satisfiability problem. *Pertanika Journal of Science and Technology*, *25*(2), 453-468.

Kasihmuddin, M. S. M., Mansor, M. A., & Sathasivam, S. (2017b). Hybrid genetic algorithm in the Hopfield network for logic satisfiability problem. *Pertanika Journal of Science and Technology*, *25*(1), 139-152.

Kasihmuddin, M. S. M., Mansor, M. A., Basir, M. F. M., & Sathasivam, S. (2019). Discrete mutation Hopfield neural network in propositional satisfiability. *Mathematics*, *7*(11), 1-21.

Kho, L. C., Kasihmuddin, M. S. M., Mansor, M., & Sathasivam, S. (2020). Logic mining in league of legends. *Pertanika Journal of Science and Technology*, *28*(1), 211-225.

Kong, D., Hu, S., Wang, J., Liu, Z., Chen, T., Yu, Q., & Liu, Y. (2019). Study of recall time of associative memory in a memristive Hopfield neural network. *IEEE Access*, *7*, 58876-58882.

Koopialipoor, M., Armaghani, D. J., Hedayat, A., Marto, A., & Gordan, B. (2019). Applying various hybrid intelligent systems to evaluate and predict slope stability under static and dynamic conditions. *Soft Computing*, *23*(14), 5913-5929.

Li, F., Ge, L., Dan, W., Gu, Y., He, Q., & Sun, K. (2019a, April 12-15). Application of improved variable learning rate back propagation neural network in energy dispersion x-ray fluorescence quantitative analysis. In *2019 IEEE 4th International Conference on Cloud Computing and Big Data Analysis (ICCCBDA)* (pp. 428-432). Chengdu, China.

Li, M., Lei, D., & Xiong, H. (2019b). an imperialist competitive algorithm with the diversified operators for many-objective scheduling in flexible job shop. *IEEE Access*, *7*, 29553-29562.

Lim, S., & Bang, H. (2010). Waypoint planning algorithm using cost functions for surveillance. *International Journal of Aeronautical and Space Sciences*, *11*(2), 136-144.

Liu, Y., Ghandar, A., & Theodoropoulos, G. (2019, May 4-5). A metaheuristic strategy for feature selection problems: Application to credit risk evaluation in emerging markets. In *2019 IEEE Conference on Computational Intelligence for Financial Engineering and Economics (CIFEr)* (pp. 1-7). Shenzhen, China.

Luke, S. (2013). *Essentials of metaheuristics*. Raleigh, USA: Lulu Press.

Mansor, M. A. B., Kasihmuddin, M. S. B. M., & Sathasivam, S. (2017). Robust artificial immune system in the Hopfield network for maximum k-satisfiability. *International Journal of Interactive Multimedia and Artificial Intelligence*, *4*(4), 63-71.

Mansor, M. A., & Sathasivam, S. (2016). Performance analysis of activation function in higher order logic programming. In *AIP Conference Proceedings* (Vol. 1750, No. 1, p. 030007). New York, USA: AIP Publishing.

Mansor, M. A., Kasihmuddin, M. S. M., & Sathasivam, S. (2016). VLSI circuit configuration using satisfiability logic in Hopfield network. *International Journal of Intelligent Systems and Applications (IJISA)*, *8*(9), 22-29.

Mansor, M. A., Kasihmuddin, M. S. M., & Sathasivam, S. (2019). Modified artificial immune system algorithm with Elliot Hopfield neural network for 3-satisfiability programming. *Journal of Informatics and Mathematical Sciences*, *11*(1), 81-98.

Mansor, M. A., Sathasivam, S., & Kasihmuddin, M. S. M. (2018a). Artificial immune system algorithm with neural network approach for social media performance metrics. In *AIP Conference Proceedings* (Vol. 1974, No. 1, p. 020072). New York, USA: AIP Publishing.

Mansor, M. A., Sathasivam, S., & Kasihmuddin, M. S. M. (2018b). 3-satisfiability logic programming approach for cardiovascular diseases diagnosis. In *AIP Conference Proceedings* (Vol. 1974, No. 1, p. 020022). New York, USA: AIP Publishing.

Mollajan, A., Memarian, H., & Quintal, B. (2019). Imperialist competitive algorithm optimization method for nonlinear amplitude variation with angle inversion. *Geophysics*, *84*(3), 81-92.

Neelakanta, P. S., & DeGroff, D. (1994). *Neural network modeling: Statistical mechanics and cybernetic perspectives*. Florida, USA: CRC Press.

Nievergelt, J. (2000). Exhaustive search, combinatorial optimization and enumeration: Exploring the potential of raw computing power. In *International Conference on Current Trends in Theory and Practice of Computer Science* (pp. 18-35). Heidelberg, Germany: Springer.

Peri, D. (2019). Hybridization of the imperialist competitive algorithm and local search with application to ship design optimization. *Computers and Industrial Engineering*, *137*, 1-11.

Reunanen, J. (2003). Overfitting in making comparisons between variable selection methods. *Journal of Machine Learning Research*, *3*, 1371-1382.

Sathasivam, S. (2010). Upgrading logic programming in Hopfield network. *Sains Malaysiana*, *39*(1), 115-118.

Sathasivam, S. (2011). Learning rules comparison in neuro-symbolic integration. *International Journal of Applied Physics and Mathematics*, *1*(2), 129-132.

Sathasivam, S. (2012). First order logic in neuro-symbolic integration. *Far East Journal of Mathematical Sciences*, *61*(2), 213-229.

Sathasivam, S., & Abdullah, W. A. T. W. (2011). Logic mining in neural network: Reverse analysis method. *Computing 91*(2), 119-133.

Sathasivam, S., Hamadneh, N., & Choon, O. H. (2011). Comparing neural networks: Hopfield network and RBF network. *Applied Mathematical Sciences*, *5*(69), 3439-3452.

Shi, J., Zhu, Y., Khan, F., & Chen, G. (2019). Application of Bayesian regularization artificial neural network in explosion risk analysis of fixed offshore platform. *Journal of Loss Prevention in the Process Industries*, *57*, 131-141.

Tashayo, B., Behzadafshar, K., Tehrani, M. S., Banayem, H. A., Hashemi, M. H., & Nezhad, S. S. T. (2019). Feasibility of imperialist competitive algorithm to predict the surface settlement induced by tunneling. *Engineering with Computers*, *35*(3), 917-923.

Willmott, C. J., & Matsuura, K. (2005). Advantages of the mean absolute error (MAE) over the root mean square error (RMSE) in assessing average model performance. *Climate Research 30*(1), 79-82.

Wolpert, D. H., & Macready, W. G. (1997). No free lunch theorems for optimization. *IEEE Transactions on Evolutionary Computation, 1*(1), 67-82.

Xiao, L., Wang, X. H., Wang, B. Z., Zheng, G., & Chen, P. (2017). An efficient hybrid method of iterative mom-po and equivalent dipole-moment for scattering from electrically large objects. *IEEE Antennas and Wireless Propagation Letters*, *16*, 1723-1726.

Pertanika J. Sci. & Technol. 28 (3): 1009 - 1026 (2020)

PERTANIKA JOURNALS

SCIENCE & TECHNOLOGY

Journal homepage: http://www.pertanika.upm.edu.my/

Impact of Meteorological Factors on Rice Growth Stages and Yield

Peter David Kulyakwave [1,2], Shiwei Xu[1]* and Wen Yu[1]

[1]Agricultural Information Institute, Chinese Academy of Agricultural Sciences, Beijing, 100081, China
[2] Department of Research, Training, and Market Development, National Service Headquarters. Box 1694. Dar Es Salaam, Tanzania

ABSTRACT

Weather variability poses threats to rural crop producers in Tanzania. This research aimed to find the impact of weather variation on the growth stage and yield of rice in Tanzania. The analyses were done using rice yield data and weather variables from 1981-2017. The approaches used were; decomposing rice yields into yield tendency and yield weather, stepwise integral regression for identification of significant yield model, and applied Fisher's meteorological regression and Chebyshev polynomial function to compute coefficients for weather factors. From the results, other than the non-natural factors, rainfall, maximum and minimum temperature, and sunshine significantly affect rice yield from sowing to harvest stage. The effect of rainfall, sunshine, maximum and minimum temperature coefficients on the rice yield differ by growth stage. An increase of 1 millimeter of rainfall at the sowing-seedling stage increased rice yield by 2.7 kg/ha. In the sowing-seedling stage, the temperature had a stronger positive influence on the rice yield as with every 1°C in average maximum temperature increased the rice yield by 674.1 kg/ha. The minimum temperature coefficient had stronger influences in the vegetative, tillering –booting stages, thus, with 1°C increase in average minimum temperature, the rice yield increased by 70.1 kg/ha and 420.7 kg/ ha respectively. In the flowering –grain formation stage, the maximum temperature had a greater influence on rice yield, that is, as 1°C increased, the rice yielded increased by 674.7 kg/ha. The sunshine duration had a higher influence on the harvesting stage.

ARTICLE INFO

Article history:
Received: 5 November 2019
Accepted: 31 March 2020
Published: 16 July 2020

E-mail addresses:
pkulyakwave822@yahoo.com (Peter David Kulyakwave)
xushiwei@caas.cn (Xu Shiwei)
yuwen@caas.cn (Yu Wen)
*Corresponding author

ISSN: 0128-7680
e-ISSN: 2231-8526

© Universiti Putra Malaysia Press

Increased 1-hour duration of sunshine increased rice yield by 495.95 kg /ha. Finally, a meteorological rice model, which could be used for rice yield forecasting in the region, was developed.

Keywords: Meteorological factors, natural and non-natural factors, rice, weather, yield

INTRODUCTION

Weather factor variations have significant impacts on most agricultural crop productions as already witnessed by the farming communities (Vaghefi et al., 2013). Changes and variations of the common meteorological factors such as precipitation, maximum and minimum temperature, sunshine, and humidity pose threats to crop performances, from the growth stages to the expected outputs; thus, they have direct cause to food insecurity all over the world (Thi et al., 2015). Rice is among the crops that are sensitive to any weather variations particularly with water, light, and heat (Shannon & Motha, 2015). It should be noted that rice crop requires more water than any other crop. Water is needed at the time of transplanting and much water is needed during the growing period. In addition to water, rice cultivation needs an average temperature and sunlight, especially during the ripening period.

In Tanzania, rice production is mainly dependent on rainfall (Adhikari et al., 2015; Katengile et al., 2018). About 71% of rice produced in the country is under the rain-fed system, however, the system has been vulnerable to weather shocks. Only a small portion of rice is produced through irrigation water (Katambara et al., 2016). The continuous dependence on rain-fed production substantiates the existing high relationship between rice production and weather factors (Ngailo et al., 2016). Although many studies continue to urge scientists to carry out more researches because of the existing relationships between rice crop and the influences of weather factors on the phenological progresses, studies on the weather-crops relationship are few in Tanzania (Hat & Prueger, 2015; Islam et al., 2016; Johansson et al., 2015; Lizumi & Ramankutty, 2015; Siebert et al., 2017). The available studies have centered on the impacts of climate change on crops. The few recent studies have focused only on the long effects of the climatic change to other cereal crops other than rice (Mkonda, 2014; Mkonda & He, 2017; Msongaleli et al., 2017; Mtongori, et al, 2016). Other studies have focused on the impact of weather variability on agricultural crop production and economic activities. These studies range from agriculture (Dell et al., 2014), infrastructures (Gelete & Gokcekus, 2018; Moretti & Loprencipe, 2018), investment, political, export and imports (Chatzopoulos et al., 2019), industrial products and conflicts (Peter, 2014). From these studies, the influence of weather on production emerges. For example, it was reported that for each 1^{o}C rise in temperature reduced agricultural export

in developing countries by 2.0 to 2.7% (Benjamin et al., 2012) and that for each increase of 1°C reduced industrial outputs between 2.0 to 2.6 percent (Hsiang, 2014). Similarly, it was revealed that rainfall and temperature variability had a significant negative impact on crop growth and output level especially in developing countries (Burke, 2010; Dell et al., 2014). On an interesting note, it was reported that the rise in temperatures and decrease in rainfall had negative influences in political stability and conflicts which generally affected economic performances in Sub-Saharan Africa (Bruckner & Ciccone, 2011; Zhao et al., 2017).

Several studies that have shown the relationship between the cumulative influences of climatic factors on crop production. For example, Zhao et al. (2017) established the relationship between the maximum and minimum temperatures, and the rice yield in China. Similar studies in China concluded that weather had positive and negative contributions on peanut yield in Hebei on winter wheat in Weishan County (Wen et al., 2014; Yu et al., 2015). Mirzabaev (2013), who assessed the effect of weather variability on agricultural revenue in Central Asia, found that weather variability had a relatively high negative impact.

Rice crop undergoes several growth stages that help to identify its life cycle. Scholars generally agree that rice growth is separated into stages that are associated with either vegetative or reproductive development (Sridevi & Chellamuthu, 2015; Weng et al., 2017). The relationship between weather-related factors and their variability at each rice growth stage has a worth impact on rice yield. This is, however, made possible by analyzing the yield contributed by weather fluctuation (Y_w) as deduced from the difference between actual rice yield (Y_a) and trend yield (Y_t). Basically, *Yt* is the yield from other attributes other than natural ones such as technological progress, seeds, management practices, and government policies. As a subject of concern to crop specialists, the weather is known as an input in crop production (Paltasingh, 2012). However, while it is possible for researchers to quantify and measure other production inputs, it has not been possible for weather variables (Abdul-rahaman & Ebenezer, 2017). Therefore, the main objective of this study was to determine the influence of weather-related factors including the rainfall, maximum and minimum temperature, and sunshine on the rice growth cycle. Most of the previous cited empirical approaches used the Ricardian and Hedonic models on estimating impacts of weather on crop production. Nevertheless, the Ricardian models are mostly used to explain the variations of values of land per ha across different geographical conditions including very few weather parameters and are limited for the permanent crops (Mamane & Malam, 2015). On similar views, most of the studies involving the uses of the Hedonic models rely on analyzing variables on sale prices for land allocations and its produces as well as some environmental attributes (Salman et al., 2016). In the real sense, the aforementioned models used the temperature and rainfall variables to estimate the aggregate impact of weather variables on crop production and to the entire economy. In the current study, we

have determined the impact of the respective weather variables and the resulting weather yield at each rice growth stage by using the econometric methods based on Fisher's (1925) ideas and Chebyshev Polynomial Function.

MATERIALS AND METHODS

The study used secondary data pertaining to rice production and weather statistics. A collection of rice yield data series from the study region for the past 36 years (1981-2017) was obtained from different sources that include the Tanzania government agencies namely; Tanzania Ministry of Agriculture, Food Security and Cooperative (MAFC), Ministry of Industry and Trade (MOIT), and National Bureau of Statistics (NBS). Meteorological data that include the average monthly rainfall (mm), monthly maximum and minimum temperature (^{o}C), and sunshine (Hours) for 36 years, were obtained from the Tanzania Meteorological Authority (TMA).

Profile of the Study Region

Mbeya is among the oldest regions situated in the Southern Highlands of Tanzania. It is situated between latitude 70 and 90 31' to the south of equator and Longitude 320 and 350 east of Greenwich. The region is among the leading regions in terms of agricultural outputs in Tanzania. It has a tropical climate that supports the growth of many cereal crops such as rice, maize, wheat, and sorghum. The region's annual rainfall ranges from 650 - 1200 mm with the experience of a dry and cold spell between June and September. The tropical climate, rainfall distribution, and variations in temperature favor rice production. Rice cultivation is undertaken in a large area of the region including Mbarali and Kyela Districts.

Research Method

In this research, the traditional classical production function was used where the dependent variable rice yield *Ya* is a function of a set of various independent variables (Dell et al., 2014). The assumption is *Ya* is the result of natural factors such as (weather variables; rainfall, sunshine, maximum and minimum temperature), and non-natural factors including change in technology, farm management, fertilizer application, seed varieties, pesticides, policy and labor. Therefore, in this study, the statistical relationship between the rice yield and the two components; natural and non-natural factors were considered.

This study accommodated previous concepts from different researchers including Yu et al. (2015) and Zhao et al. (2017). It also reviewed a recent study by Jiayu et al. (2018) who had reported on the existing statistical relationship between meteorological factors and crop yield. The study further stressed on to detach weather yield from the actual yield as yield due to weather variations. In addition, the actual yield is defined as the sum of the trend yield which is a measure of technology advancement and management, and weather yield due to weather factors variation. In accordance with that, accommodating a

similar approach in this research, weather yield was computed from the difference between actual yield and linear trend-yield. This study's central idea was to establish a significant statistical relationship between weather yield and weather-related yield coefficients and weather factors as opposed to previous findings cited in this paragraph that used only the weather factors to explain their impact on crop yield. Owing to the idea that in the study region rice is transplanted in early January and matures in July of the same year, therefore, the study considered a total of seven 7 months and five growth stages.

Actual, Trend, and Meteorological Yield Model Setting

The actual yield Y_a (Equation 1) was computed from crop production and weather factors in time series data which enabled the researchers to set up the required model. More so, the actual yield was obtained from traditional classical production function as a combination of natural factors (Y_w) and non-natural factors (technology advancement, farm managements, fertilizer application, seed varieties, pesticides, policy and labor) at a specified duration of time. Henceforth, the trend yield is refered to as a yield due to the effect of the non-natural factors including farmers' interventions and technological application with time (Zhao et al., 2017). Likewise, Paltasingh (2012) and Jiayu et al. (2018) defined weather yield as the yield realized from the relative contribution of weather factors on crop performance. Therefore, the relationship was developed as follows (Equation 1, 2 and 3):

$$Y_a = Y_T + Y_w + \mu \quad [1]$$

Where Y_a is the actual rice yield, Y_T is the trend yield, Y_w is the weather yield, and μ is an error term.

$$Y_T = f(t) \quad [2]$$

Where f(t) shows the function of a particular year t

$$Y_w = \sum_{q=0}^{n} \sum_{p=0}^{m} f(w_{p,q}) \quad [3]$$

Therefore q is the growth stages of the rice plant, p is the weather factors (in this study we denoted as x1= rainfall (rf), x2= maximum temperature (tmax), x3=minimum temperature (trmin), and x4=sunshine (ss), $w_{p,q}$ is the weather variable by growth stage, and $f(w_{p,q})$ is the function of weather variables and respective yield variations.

In order to calculate the variations in different yield, we introduced the concept of initial yield or the Standard yield, and the relationship could be derived as follows (Equation 4, 5 and 6):

$$Y_{a0} = Y_{T0} + Y_{w0} + \mu \quad [4]$$

$$Y_{T0} = f(t_0) \quad [5]$$

$$Y_{w0} = \sum_{q=0}^{n} \sum_{p=0}^{m} f(\overline{w}_{p,q}) \quad [6]$$

Whereas Y_{a0} denote the base or standard rice crop yield, Y_{T0} denote the base trend yield or is the yield contributed by the non-natural factors, and Y_{w0} is the weather yield which is the result of the average weather variables.

Fisher Integral Regression Model

Fisher (1925) gave a respectable statistical regression model that could be used to compute the relationship between weather- yields and weather factors at different crop growth stages. In addition, he provided the possibilities for ascertaining the quantitative relationship among variables and their coefficients in the model. This study applied Fisher's regression model to establish the quantitative relationships between the weather yield as a dependent variable on weather-related attributes. The model requires to have the following Equation 7 which is the advancement of Equation 4:

$$\hat{y}_{pt} = \alpha_0 + \int_0^{\tau} a1j\ (t)x_1(t)dt + \int_0^{\tau} a2j\ (t)x_2(t)dt + \int_0^{\tau} a3j\ (t)x_3(t)dt + \int_0^{\tau} a4j\ (t)x_4(t)dt \quad [7]$$

Where, $\hat{y}pt$ = Weather yield, a_0= Constant, τ = growth stage of rice as it count from 0 as sowing stage with j^{th} independent period, a_1, a_2, a_3, and a_4, are the regression coefficients of explanatory variables (x_1=rainfall, x_2=maximum temperature, x_3=minimum temperature, x_4=sunshine respectively) , t= is time, τ = is (the rice 'jth' growth durations), and $x_n(t)$ denote the function of independent variable in the model.

From Equation 7, the effect of each weather factor was computed from the sowing stage to the harvest stage. Thereafter, we acknowledged the Chebyshev-orthogonal polynomial function to solve regression coefficients in linear function form as in Equation 8:

$$a_i(t) = \sum_j \alpha_{ij}\varphi_{ji} \quad [8]$$

Whereby φ_{ij} is j = 1, 2, 3,…5. and $\alpha_i(t)$ is a regression coefficient of x_n, as a functional form of rice growth stage and time, which is approximated by Chebyshev polynomial as in Equation 9:

$$\hat{y} = \alpha_0 + \sum_i \sum_j \alpha_{ij} p_{ji} \quad [9]$$

This resulted in Equation 10 for independent variable effect on yield:

$$p_{ji} = \int_0^{\tau} x_i(t)\varphi_j dt \quad [10]$$

Since the intention was to solve φ, the Chebyshev polynomial matrix was used to consider the total rice growth stages as given in Equation 10.

RESULTS

Descriptive Analyses

Table 1 describes the statistical behavior of the rice yield earned, rainfall, the maximum and minimum temperature and sunshine for the period of 1981-2017. The mean rice yield is 2748.2 kg/ha. However, the results show significant variations among seasons as portrayed by the yield range (7785.3 kg/ha) which is the difference between the maximum and minimum yield (Yan et al., 2018).

Table 1

Descriptive statistics of the rice yield, rainfall, sunshine, maximum and minimum temperatures

Statistics	Rice yield (kg/ha)	Rainfall (mm) from January-July						
		Jan	Feb	Mar	Apr	May	Jun	Jul
Mean	2783.2	152.3	129.3	202.1	152.0	135.7	77.6	13.8
SD	1276.3	73.5	50.8	76.8	67.4	82.4	59.4	19.2
CV	0.5	0.5	0.4	0.4	0.4	0.6	0.8	1.4
Minimum	666.7	40.3	54.1	76.3	19.3	2.8	0.0	1.0
Maximum	852.0	340.4	237.9	451.3	363.9	329.7	192.1	72.2
Range	7785.3	300.1	183.8	375.0	344.6	326.9	192.1	72.2

Statistics	Rice yield (kg/ha)	Sunshine (hr) from January-July						
		Jan	Feb	Mar	Apr	May	Jun	Jul
Mean	2783.2	6.5	7.0	6.9	7.2	8.2	9.3	9.6
SD	1276.3	1.5	1.7	1.0	1.0	0.8	0.8	0.7
CV	0.5	0.2	0.2	0.2	0.1	0.1	0.1	0.1
Minimum	666.7	2.9	2.8	4.5	4.6	6.5	7.6	7.9
Maximum	852.0	9.4	9.5	8.6	9.1	9.7	10.4	10.8
Range	7785.3	6.5	6.7	4.1	4.5	3.2	2.8	2.9

Statistics	Rice yield (kg/ha)	Temperature maximum (^{o}C) January-July						
		Jan	Feb	Mar	Apr	May	Jun	Jul
Mean	2783.2	23.7	24	24.1	23.4	22.8	22.2	22.1
SD	1276.3	0.8	0.9	0.6	0.6	0.6	1.1	0.7
CV	0.5	0	0	0	0	0	0.1	0
Minimum	666.7	22	21.8	22.9	22.2	21.9	20.8	20.6
Maximum	852	25	25.6	26	24.5	23.8	27	23.7
Range	7785.3	3.0	3.8	3.1	2.3	1.9	6.2	3.1

Table 1 *(Continued)*

Statistics	Rice yield (kg/ha)	Temperature minimum (°C) January-Jul						
		Jan	Feb	Mar	Apr	May	Jun	Jul
Mean	2783.2	14.5	14.4	14	12.6	9.8	6.7	5.9
SD	1276.3	0.6	0.6	0.7	0.8	0.8	1.8	1.2
CV	0.5	0	0	0.1	0.1	0.1	0.3	0.2
Minimum	666.7	13.2	13.1	12.7	9.6	8.1	4.2	3.3
Maximum	852	15.9	16.2	15.5	14	11.2	15.1	7.8
Range	7785.3	2.7	3.1	2.8	4.4	3.1	10.9	4.5

Source. Tanzania Meteorological Authority (TMA)

The rainfall data attest to have noticeable variations among the months. For instance, the mean rainfall was the lowest in July with 13.8 mm and the highest with 202.1 mm in March. Basing on the differences, the rainfall range was 375 mm and 72.2 mm for July and March respectively which portray a significant difference not only between months but also within months. In order to understand the degree of variability among the weather variables, the authors calculated the corresponding coefficients of variability (CV) as a ratio of the standard deviation (SD) to the mean. Therefore, 0.4 as a minimum CV was obtained for the month of February, March and April and 1.4 as maximum CV the month of July. Henceforth, it reveals that from February to April the degree of rainfall variation was relatively low compared to other months while the highest rainfall variability was in July. Regarding sunshine, the minimum variability was observed during February (2.8 hrs) while the maximum was in July with (10.8 hrs). Based on temperature variability minimum temperature was observed on 3.3°C in June and the maximum was 27°C in July.

Trend Yield Determination

The trend yield is sparing of important as it shows the level of technological advancement and acceptance and other non-natural attributes including (farm management, fertilizer application, seed varieties, pesticides, policy, labor) which increase rice yields with time. As a result, trend yield was obtained from the regression equation (Equation 2) of rice yield in kg/ha obtained from Tanzania as a function of time in years from 1981-2017 as presented in Table 2. The result in Tables 2 implies that the time in years (t) was significant positively to explain the linear trend yield at 5% probability level. Therefore, there was an increment of the line of yield increase by 44.6 multiplied by time t in years as calculated for the period of years 1981-2017.

Table 2

Regression results of rice yield over time (years) y=f (t (years))

yield	Coef.	Std. Err.	t	P>t
time	44.601	20.243	2.2	0.035**
_cons	1990.01	400.29	4.97	0.000***

*** 1% significant level, ** 5% significant level

Thus, from the regression results in Table 2, we could obtain Equation 11 as our true linear trend yield model as shown below.

$$Y_t = 1990 + 44.60 * t \quad [11]$$

Where Y_t is the intended linear trend yield showing the linear incremental of yield over time, the value 1990 is the constant of the model equation, and t is the time in years.

Therefore by solving the Equation 11 which resulted from the regression Table 2, Figure 1 shows the behavior of the actual yield and the yield for the period from 1981 to 2017 was obtained. The result is similar to the trend established in (Paltasingh, 2012). The difference between the actual yield and trend yield as explained in this work is what we refer to as weather yield that is a function of weather or meteorological factors.

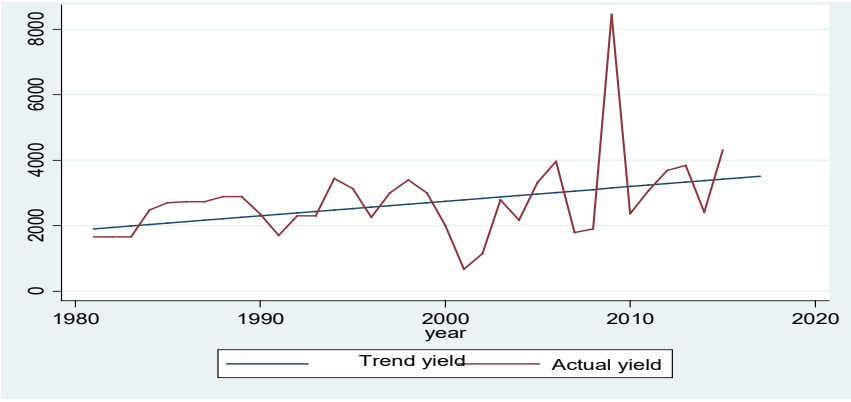

Figure 1. Actual yield and linear trend yield from the year 1981-2017

Determination of Coefficients of the Variables

Table 3 illustrates the regression results of the rice growth stages with respect to the weather factors. The regression summary demonstrates that the rainfall, maximum and minimum temperatures, and the sunshine have a significant influence on various rice growth stages. Further, it shows that the R^2 is 53%, this means that the weather factors including rainfall, temperature maximum, and sunshine explained well the variation in rice growth stages.

Table 3

Regression results for the weather- yield with weather factors on the growth stage

s/n	Growth stage	Predictor Variables	Coef	Std. Err	t	P>|t|
1	Sowing - seedling	rf0	2.708**	1.261	2.150	0.041
		tmax0	137.947**	61.571	2.240	0.033
2	Late seedling - tillering	ss1	71.845**	27.284	2.630	0.014
3	Jointing - booting	ss2	56.078**	23.320	2.400	0.023
4	Flowering - grain formation	tmax3	-89.367***	20.455	-4.370	0.000
5	Maturity - harvesting	tmin4	5.844***	1.595	3.660	0.001
		Constant	-22209.89**	10655.530	-2.080	0.046

*** P<0.01, **P<0.05, *P<0.1; F=0.001, R^2=0.53, Adj R^2=0.42, DW=2.4 Rainfall stage 1= rf0, Maximum temperature stage1= tmax0, Sunshine stage 2=ss1, Sunshine stage 3=ss2, maximum temperature stage 4=tmax3 minimum temperature stage 5=tmin4,

From Table 3, Equation 12 was obtained as a yield weather model for the study region. Also, we solved for Chebyshev yield coefficients (φij) by using the coefficients of significant variables and the resulting yield coefficients are presented in Table 4.

$$Yw = -22209.890 + 2.708 * rf0 + 137.947 * trmax0 + 71.845 * ss1 + 56.078 * ss2 - 89.367 * trmax3 + 5.844 * trmin4 \quad [12]$$

Table 4

The yield coefficients for weather-related factors on rice yield by growth stage from the Chebyshev Polynomial function

Month	Growth stage	Rainfall (kg/ha/mm)	Sunshine (kg/ha/hr)	Temperature minimum (kg/ha/°C)	Temperature maximum (kg/ha/ °C)
Jan	Sowing-Seedling	2.7	64.9	210.4	674.1
Feb			-143.7	-490.9	-398.3
Mar	Vegetative		-240.1	70.1	-398.3
Apr	Tillering - booting		-224.3	420.7	137.9
May	Flowering-Grain formation		-96.4	70.1	674.1
Jun	Maturity -		143.7	-490.9	674.1
Jul	Harvesting		495.9	210.4	-398.3

DISCUSSION

This study aimed to establish the relationships between weather factors -yield coefficients on the rice yield by growth stages in the Mbeya region. Thus based on the results, a discussion on how coefficients of weather factors affected rice yield on various growth stages is presented in this section. As a preamble, while all other significant weather factors demonstrate to vary with growth stages (Belloumi, 2014; Zhao & Fitzgerald, 2013), the rainfall yield coefficient influenced rice yield on only sowing-seedling stage. In our findings, rainfall demonstrated to have a significant effect at the sowing - seedling stages. It was found that each 1 mm increase of the average rainfall could increase 2.7 kg/ha of the rice yield. This result indicates that any deviation from this amount can lead to a negative impact on rice yield. This finding echoes (Zhao & Fitzgerald, 2013) observation in their study of climate change and its implications to edible rice yield.

Sowing to the Seedling Stage

Rainfall. In the study areas, rice planting is done from early January. This month experience the mean rainfall of 152.3 mm (Table 1), thus, enough to support seedling development. The result in (Table 4) shows that the rainfall yield coefficient was 2.7 kg/ha/mm implying that, every 1 mm increases of rainfall at the sowing –seedling stage, the rice yield increased 2.7 kg/ha. These findings are consistent with the findings of Jiayu et al. (2018) conducted in China, and also Vaghefi et al. (2013).

Sunshine. Sunshine is essential to balance water through evaporation. Conversely, moderate sunshine is required by rice plants at different growth stages for optimal output. Table 4 shows that the sunshine yield coefficient influence rice yield positively in the sowing-seedling stage. This implied that as sunshine duration increased by 1-hr during the sowing-seedling stage the rice yield increased 64.9 kg/ha. This fact goes in line with our expectations that rice seed requires warm moisture to support seed rapture and emerging at the early stages of germination. This is similar to Opin et al.'s (2015) observations that optimum sunshine is required to catalyze seeds metabolism and create a reasonable environment for seeds germination. However, it was illustrated that increased sunshine duration in hours was disadvantageous for late planting because it reduced rice yield by 143.7 kg/ha.

Minimum and Maximum Temperatures. Both minimum and maximum temperatures appear to be essential for rice growth especially at the early stages of planting and germination. The results indicate that their positive yield coefficients of 210.4 kg/ha/ ^{o}C and 674.1 kg/ha/ ^{o}C benefited rice yield respectively. Also, as demonstrated in Table 4, each 1^{o}C increase of the minimum and maximum temperature enhances rice yield by 210.4 kg/ha

and 674.1 kg/ha respectively from planting to the seedling. Both minimum and maximum temperatures are essential because rice grows well in an area with a temperature between 20°C to 27°C which is a characteristic of the tropical climate. Our findings concur with the findings by Krishnan et al. (2011) who found that rice survived up to 6 days under a low temperature below 15°C, and 2 days at the maximum between 27°C -37°C, while, there was no germination at the temperature above 45°C. In the case of the delayed planting, the rice yield decreased by 490.9 kg/ha and 398.3 kg/ha for each increase of 1°C in minimum and maximum temperature respectively. Generally, it implied that in the sowing-seedling stage the maximum temperature yield coefficient had a relatively stronger influence on rice yield than the other weather factors.

Vegetative Stage

Sunshine. The findings have revealed that excess sunshine duration at the vegetative stage is detrimental to rice development. This implies that as sunshine duration increased by 1 hour in the vegetative stage decreased rice yield by 240.1 kg/ha. In line with these findings, Opin et al. (2015) upheld that during the vegetative stage plants needed sunshine for development. However, if sunshine duration exceeded the required level, the plant lost color and hibernated on the ground, that is, if the situation prolongs it can cause delayed plant growth and or plant death.

Minimum Temperatures. The minimum temperature yield coefficient in the vegetative growth stage influenced rice yield positively (Table 4). The analyses indicate that if the minimum temperature was increased by 1°C during the vegetative stage, therefore, the rice yield increased 70.1 kg/ha. A similar claim was reported by Yaoje et al. (2017) as they narrated that the minimum temperature benefited rice with steady growth and enough nutrients. Henceforth, among the weather variables, the minimum temperature had a stronger influence in the vegetative growth stage to influence rice yield positively.

Maximum Temperatures. It was demonstrated that as the maximum temperature increased by 1°C during the vegetative stage decreased rice yield by 398.3 kg/ha. The current finding is contrary to the findings of (Ajetombi & Binuomote, 2014; Yaojje et al., 2017) at different times reported that higher temperatures during the early vegetative stage facilitated faster rice growth and yields.

Tillering and Booting

Sunshine. The influence of the sunshine yield coefficient on rice yield at this stage was negative. It was indicated that as sunshine duration increased by 1-hour in March decreased rice yield by 224.3 kg/ ha. It is apparently proven that at this stage, rice demands extra water for growth and for preparing the plant for the flowering process. Due to a negative

but strong correlation between sunshine and rainfall, therefore, rainfall is required to benefit rice yield. Further, since at this stage the average rainfall was 152.04 mm (Table 1), scholars (Zhao et al., 2017) insisted that care should be taken here as rice did not demand too much water. They recommended at least 2.5 cm height of rainfall water which was sufficient to support the tillering and booting stage.

Minimum and Maximum Temperature. On the one hand, the minimum temperature yield coefficient was positive (420.7 kg/ha/^{o}C), which had a stronger influence on the rice yield in the tillering and booting stage. This means an increase in average minimum temperature by 1^{o}C in the tillering and booting stage increased rice yield by 420.7 kg/ha. Consequently, an increase in maximum temperature by 1^{o}C would increase the rice yield by 137.9 kg/ha. Therefore, these findings declared that in the tillering and booting stage the average minimum temperature had more influence on the rice yield than the other weather factors. As illustrated in Figure 2 and the minimum and maximum temperatures had almost similar behavior. That is, while the minimum temperature was increasing, the maximum temperature was curving upward from negative to the positive quadrant. Our findings agree with Yu (2016) who reported a similar scenario in Hainan-China. The behavior demonstrated by the maximum temperature benefits the flowering stage. This current finding is similar to Oh-e et al. (2007) and Kaur and Attwal (2017) observation that the variations of maximum and minimum temperature had different responses in terms of crop yields in China and India respectively.

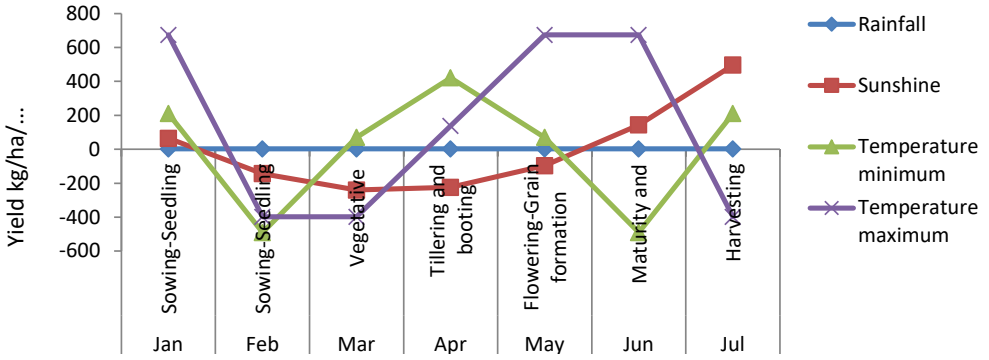

Figure 2. Impact of the yield coefficients of the rainfall (kg/ha/mm), sunshine (kg/ha/hr), maximum and minimum temperatures (kg/ha/◦C) on rice yield by growth stage.

Flowering - Grain Formation Stage

Sunshine. The yield coefficient of average sunshine in the flowering stage was negative (Table 4). It indicated that having a longer sunshine duration at this growth stage could reduce rice yield by 96.4 kg/ha. Under normal circumstances, high sunshine at this stage precludes normal flowering as it induces stress to the rice plant, and hence fewer grains

formation. This finding concurs with Li-quan et al. (2016) who revealed that minimum day sunshine was conducive in early stages to support photosynthesis and flowering development. However, it is advantageous for the late flowering stage where an increase of sunshine duration will increase yield by 143.7 kg/ha.

Minimum and Maximum Temperature. The positive yield coefficient of minimum temperature indicates that an average increase by 1°C could facilitate flowering and grain formation for enhanced rice yield up to 70.1 kg/ha at flowering and early grain formation stage. Meanwhile, an increase of 1°C in an average maximum temperature increased rice yield by 674.1 kg/ha at flowering and grain stage especially from April, and by 674.1 kg/ha in May. Although rice plants can relatively tolerate an increase in temperature at the flowering stage, this increase had a positive impact on grains formation and increased rice yield 674.1 kg/ha. This observation contradicts the earlier findings of Hat and Prueger (2015) and Chaturvedi et al. (2017) who reported that high temperature was detrimental during the grain formation stage of plant development.

Maturity - Harvest Stage

Sunshine. The sunshine yield coefficients were positive in maturity and harvesting stages which benefited the rice yield. As is shown, in (Figure 2), sunshine exhibits a sharp increase from June and reaches a peak in July. Therefore, the sunshine was very necessary at maturity because the grain is characterized by a full of moisture, thus, adequate sunshine is required to decrease the moisture as rice grains are ready for harvesting. Also, as it was shown in Table 4, an increase of 1 hour of sunshine duration would increase rice yield 495.9 kg/ha (harvesting stage) in July. Additionally, in this final stage (harvesting stage) sunshine was a major rice yield determinant than the other weather factors due to a relatively higher yield coefficient (495.9 kg/ha/hr). In a similar study, Dunand and Saichuk (2012) maintained that sunshine was crucial during seeds maturity and pre-harvesting seed since rice needs to attain 15 to 18% and 18 to 21% of moisture content of grain on the main stem and crop grain respectively.

Minimum Temperature. Furthermore, the rice yield coefficients for minimum temperature were negative in the maturity stage but positive in the harvesting stage. It was demonstrated that an increase of 1°C minimum temperature was detrimental to the grain's maturity, thus, decreased rice yield 210.4 kg/ha in June. The impact was contrary to the harvesting stage as a similar increase of 1°C benefited rice yield 210.4 kg/ha. This indicates essentiality for the minimum temperature to facilitate normal grains ripening and maturity. A similar trend was commented by Jiayu et al. (2018), although, they added the situation could differ depending on locations.

Maximum Temperature. The results indicate that rice yield increased by 674.1 kg/ha at each average increase of 1^{o}C maximum temperature at the maturity stage. However, in the harvesting month of July, the maximum temperature reduced rice yield by 398.3 kg/ha at each 1^{o}C increase of maximum temperature. This is similar to Oh-e et al. (2007) and also Zhao and Fitzgerald (2013) assertion. In practice, it is very obvious that high temperatures has a significant negative impact on rice yield from flowering to maturity. For example, Fankhauser and McDermott (2016) observed that high temperatures during the final stages of rice growth could disrupt both morphology and biochemical status of rice grains.

CONCLUSION

The study has revealed that the previous weather data (rainfall, sunshine, maximum and minimum temperatures) have significantly influenced the rice yield in the Mbeya Region. The results from the Fisher Regression Model and Chebyshev Polynomial Function have confirmed that different weather factors have affected rice yield at different rice growth stages. In addition, the developed weather rice yield model from this study could be useful for regional rice yield forecasting. At this end, the study recommends necessary efforts to curb the impacts of weather variability on rice crop yield to be taken. The efforts involve; planning for water harvesting, investing in irrigation technology, and investing in the local community awareness of weather-driven impacts on rice production. Also the introduction of crop risk awareness and management at local levels. Since this study focused on the few meteorological factors namely; the rainfall, sunshine duration, and temperatures, we recommend further studies on other meteorological factors to be undertaken to rice crop and other agricultural crops in Tanzania.

ACKNOWLEDGMENT

This article was supported by the CAAS Science and Technology Innovation Project (number: CAAS-ASTIP-2018), founded by the Chinese Academy of Agricultural Sciences.

REFERENCES

Abdul-rahaman, I., & Ebenezer, O. (2017). Climate variability and sustainable food production. *Ghana Journal of Geography, 9*(2), 80-83.

Adhikari, U., Nejadhashemi, A. P., & Woznicki, S. A. (2015). Climate change and eastern Africa: A review of impact on major crops. *Food and Energy Security, 4*(2), 110-132.

Ajetombi, J., & Binuomote, S. (2014). An investigation of the effect of climate change on selected cereal crops yield in Nigeria: A ricardian analysis. *Continental Journal of Agricultural Science, 8*(3), 38-48.

Belloumi, M. (2014). Eastern and Southern African countries investigation of the impact of climate change on agricultural production in eastern and southern African countries. *Classification Q54; Q18, 54*(July), 1-29.

Benjamin A. O., Dell, M., & Benjamin, F. J. (2012). Temperature shocks and economic growth: Evidence from the last half century. *American Economic Journal, 4*(3), 66-95.

Bruckner, M., & Ciccone, A. (2011). Rain and the democratic window of opportunity. *Econometrica, 79*(3), 923-947.

Burke, P. J. (2010). Do output contractions trigger democratic change? *American Economic Journal of Macroeconomics, 2*(4), 124-157.

Chaturvedi, A. K., Bahuguna, R. N., Shah, D., & Singh, M. P. (2017). High temperature stress during flowering and grain filling offsets beneficial impact of elevated CO_2 on assimilate partitioning and sink- strength in rice. *Scientific Reports, 7*(8227), 1-14.

Chatzopoulos, T., Pérez, I., Zampieri, M., & Toreti, A. (2019). Climate extremes and agricultural commodity markets: A global economic analysis of regionally simulated events. *Weather and Climate Extremes, 27*, 1-14.

Dell, M., Benjamin, F. J., Benjamin, A. O., & Muqaddimah, G. (2014). What do we learn from the weather? The new climate–economy literature. *Journal of Economic Literature, 52*(3), 740-798.

Dunand, R., & Saichuk, J. (2012). Rice growth and development. InJ. Saichuk (Ed.), *Louisiana rice production handbook* (pp. 41-53). Baton Rouge, Louisiana: Louisiana State University Agricultural Center.

Fankhauser, S., & McDermott, T. K. J. (2016). *The economics of climate –resilient development*. Cheltenham, UK: Edward Elgar Publishing.

Fisher, R. A. (1925). Statistical methods for research workers. In S. Kotz & N. L. Johnson (Eds.), *Breakthroughs in statistics* (pp. 66-70). New York, NY: Springer.

Gelete, G., & Gokcekus, H. (2018). The economic impact of climate change on transportation assets. *Journal of Environmental Pollution and Control, 1*(1), 1-6.

Hat, J. L., & Prueger, J. H. (2015). Temperature extremes: Effect on plant growth and development. *Weather and Climate Extremes, 10*(2015), 4-10.

Hsiang, S. M. (2014). Temperatures and cyclones strongly associated with economic production in the Caribbean and Central America. *Proceedings of the National Academy of Sciences, 107*(35), 15367-15372.

Islam, S., Cenacchi, N. T. B., Sulser, S., Gbegbelegbe, G., Hareau, U., & Kleinwechter, K. W. (2016). Structural approaches to modeling the impact of climate change and adaptation technologies on crop yields and food security. *Global Food Security, 10*(2016), 63-70.

Jiayu, Z., Shiwei, X., Ganqiong, L., Yongen, Z., Jianzhai, W., & Jiajia, L. (2018). The influence of meteorological factors. *Crop Science, 852*(April), 837-852.

Johansson, R., Luebehusen, E., Morris, B., Shannon, H., & Meyer, S. (2015). Monitoring the impacts of weather and climate extremes on global agricultural production. *Weather and Climate Extremes, 10*(2016), 65-71.

Katambara, Z., Mng, M., Chambi, C., & Malley, Z. (2016). Characteristics of rice produced under direct and indirect SRI practices in Chimala area in Mbarali District. *Journal of Agriculture and Sustainability, 9*(1), 15-30.

Katengile, R. J., Ngelenge, H. S., & Businderi, I. M. (2018). Socio-economic and field performance evaluation of different rice varieties under system of rice intensification in Morogoro, Tanzania. *Agricultural Research and Technology, 17*(2), 1-5.

Kaur, K., & Attwal, K. (2017). Factors affecting paddy pant at different growth stages. *International Journal Advanced Technology in Engineering Science, 4*(5), 193-199.

Krishnan, P., Ramakrishnan, B., Reddy, K. R., & Reddy, V. R. (2011). High-temperature effects on rice growth, yield, and grain quality. *Advances in Agronomy, 111*(December), 87-206.

Li-quan, J., Yan-zhen, W. U., Shi-teng, Z., Yun-xia, W. Z., Jian-guo, H. U., & Yu-long, W. (2016). Effects of CO_2 enrichment and spikelet removal on rice quality under open-air field conditions. *Journal of Integrative Agriculture, 15*(9), 2012-2022.

Lizumi, T., & Ramankutty, N. (2015). How do weather and climate in fluence cropping area and intensity ? *Global Food Security, 4*(2015), 46-50.

Mamane, B. G. H., & Malam, M. M. N. (2015). A ricardian analysis of the impact of temperature and rainfall variability on agriculture in Dosso and Maradi regions of Niger Republic. *Agricultural Sciences, 6*, 724-733.

Mirzabaev, A. (2013). Impacts of weather variability and climate change on agricultural revenues in central Asia. *Journal of International Agriculture, 52*(2013), 242-246.

Mkonda, M. Y., & He, X. (2017). Yields of the major food crops: Implications to food security and policy in Tanzania's semi-arid agro-ecological zone. *Sustainability, 9*(8), 7-15.

Mkonda, M. (2014). Rainfall variability and its association to the trends of crop production in Mvomero District, Tanzania. *European Scientific Journal, 10*(20), 15-18.

Moretti, L., & Loprencipe, G. (2018). Climate change and transport infrastructures: State of the art. *Sustainability, 10*(11), 1-18.

Msongaleli, B. M., Tumbo, S. D., Kihupi, N. I., & Rwehumbiza, F. B. (2017). Performance of sorghum varieties under variable rainfall in central Tanzania*. International Scholarly Research Notices, 2017*, 1-10.

Mtongori, H. I., Stordal, F., & Benestad, R. E. (2016). Evaluation of empirical statistical downscaling models' skill in predicting Tanzanian rainfall and their application in providing future downscaled scenarios. *Journal of Climate, 29*(9), 3231-3252.

Ngailo, J. A., Mwakasendo, J. A., Kisandu, D. B., & Tippe, D. E. (2016). Rice farming in the southern highlands of Tanzania: Management practices, socio-economic roles and production constraints. *European Journal of Research in Social Sciences, 4*(3), 5-11.

Oh-e, I., Saitoh, K., & Kuroda, T. (2007). Effects of high temperature on growth, yield and dry-matter production of rice grown in the paddy field. *Plant Production Science, 10*(4), 412-422.

Opin, C., Potuschak, T., & Bachmair, A. (2015). Seedling germination: Seedlings follow sunshine and fresh air cell migration: Recoiling from an embrace. *Current Biology, 25*, 565-566.

Paltasingh, K. (2012). Measuring weather impact on crop yield using aridity index: Evidence from Odisha. *Agricultural Economics Research Review, 25*(13), 205-216.

Peter, H. G. (2014). Water, drought, climate change, and conflict in Syria. *American Meteorological Society, 6*(2014), 331-340.

Salman, K., Ghaffar, A., Syed, A. S., Abbas, U. J., Dawood, J., & Fayaz, M. (2016). A hedonic analysis of agricultural land prices in Pakistan's Peshawar District. *Asian Journal of Agriculture and Rural Development, 6*(4), 59-67.

Shannon, H. D., & Motha, R. P. (2015). Managing weather and climate risks to agriculture in North America, central America and the Caribbean. *Weather and Climate Extremes, 10*(2015), 50-56.

Siebert, S., Webber, H., & Rezaei, E. E. (2017). Weather impacts on crop yields - searching for simple answers to a complex problem. *Environment Research Letters, 12*(2017), 5-8.

Sridevi, V., & Chellamuthu, V. (2015). Impact of weather on rice – A review. *International Journal of Applied Research, 1*(9), 825-831.

Thi, N., Jintrawet, A., & Promburom, P. (2015). Impacts of seasonal climate variability on rice production in the central highlands of Vietnam. *Italian Oral Surgery, 5*(2015), 83-88.

Vaghefi, N. M., Nasir, S., Radam, A., & Rahim, K. A. (2013). Modeling the impact of climate Change on rice production: An overview. *Journal of Applied Sciences, 13*(24), 5649-5660.

Wen, Y., Shiwei, X., Liu, S., Ahamed, A., & Wang, Yu. (2014). Meteorological impact on the winter wheat yield in weishan China. *Journal of Applied Science, 13*(14), 2740-2742.

Weng, F., Zhang, W., Wu, X., Xu, X., Ding, Y., & Li, G. (2017). Impact of low-temperature, overcast and rainy weather during the reproductive growth stage on lodging resistance of rice. *Nature Publishing Group, 2017*(April), 1-9.

Yan, M., Liu, P., Zhang, C., Zheng, Y., & Wang, X. (2018). Quantitative research on the relationship between yield of winter wheat and agroclimatological resources. *Earth and Environmental Science, 108*(2018), 4-11.

Yaojie, C., Min, L., Wenzhong, W., Minglu, M., & Yaoxiu, F. (2017). Effects of climate change on winter wheat yield in Wenshui County. *Journal of Arid Land Resources and Enviroment, 7*(2017), 6-15.

Yu, W. (2016). Could rice yield change be caused by weather ? *Journal of Agricultural Chemistry and Environment, 5*(01), 31-37.

Yu, W., Shiwei, X., Wen, Y., Ahmed, A. G., & Guogang, X. (2015). Application of modified fisher integral model on the influence of meteorological factors on peanut yield in Hebei of China. *International Journal of Agricultural and Food Research, 4*(2), 3-7.

Zhao, C., Liu, B., Piao, S., Wang, X., Lobell, D. B., Huang, Y., … & Durand, J. L. (2017). Temperature increase reduces global yields of major crops in four independent estimates. *Proceedings of the National Academy of Sciences, 114*(35), 9326-9331.

Zhao, X., & Fitzgerald, M. (2013). Climate Change: Implications for the yield of edible rice. *PLoS ONE, 8*(6), 1-9.

Pertanika J. Sci. & Technol. 28 (3): 1027 - 1048 (2020)

PERTANIKA JOURNALS

SCIENCE & TECHNOLOGY

Journal homepage: http://www.pertanika.upm.edu.my/

Performance of HEC-HMS and ArcSWAT Models for Assessing Climate Change Impacts on Streamflow at Bernam River Basin in Malaysia

Habibu Ismail[1,2], Md Rowshon Kamal[1]*, Lai Sai Hin[3] and Ahmad Fikri Abdullah[1]

[1]Department of Biological and Agricultural Engineering, Faculty of Engineering, Universiti Putra Malaysia, 43400 UPM Serdang, Selangor, Malaysia
[2]Department of Agricultural and Bio-Resources Engineering, Ahmadu Bello University, Zaria 2222, Nigeria
[3]Department of Civil Engineering, Faculty of Engineering, University of Malaya, 50603 Kuala Lumpur, Wilayah Persekutuan Kuala Lumpur, Malaysia

ABSTRACT

Hydrological models are reliable tools that have been extensively used for hydrological studies. However, the complexity of some of these models has been a major setback, which affects their performance. This study compared Hydrologic Engineering Corps Hydrologic Modeling System (HEC-HMS) with most widely applied Soil Water Assessment Tool (ArcSWAT) model and used to assess impacts of climate change on streamflow at Bernam Basin, Malaysia for 2010-2039, 2040-2069 and 2070-2099 to the baseline period (1976-2005) using an ensemble of ten GCMs under three RCP scenarios (RCPs 4.5, 6.0 and 8.5). The models performed satisfactorily. However, HEC-HMS performed better compared to ArcSWAT with 0.74, 0.71, 4.21 and 0.37; and 0.71, 0.69, 5.32 and 0.31 for R^2, NSE, PBIAS and RSR, respectively, during the calibration and validation periods. Future periods suggest a decreasing pattern in streamflow, with a higher percentage (−5.94%) expected for the RCP 8.5 scenario in the late century (2080s) during dry season period. In the wet season, streamflow decreases in all future periods except for RCP4.5 where it is expected to increase (0.36%). Therefore, the Basin may likely experience tremendous pressure in the late century due to low streamflow, particularly in dry season months.

Keywords: ArcSWAT, climate change, flow regime, HEC-HMS, hydrological model

ARTICLE INFO

Article history:
Received: 29 January 2020
Accepted: 24 April 2020
Published: 16 July 2020

E-mail addresses:
habfta@yahoo.com (Habibu Ismail)
rowshon@upm.edu.my (Md Rowshon Kamal)
laish@um.edu.my (Lai Sai Hin)
ahmadfikri@upm.edu.my (Ahmad Fikri Abdullah)
* Corresponding author

ISSN: 0128-7680
e-ISSN: 2231-8526

© Universiti Putra Malaysia Press

INTRODUCTION

Climate change brings a severe impact on water resources, which affects many watersheds. Changes in rainfall and temperature patterns threaten phases of hydrological cycle, disturb the ecosystem, affect agricultural production and increase the vulnerability (Schlenker et al., 2007). Conversely, ground-water level shows significant variability due to climate change with drastic decline as reported by Sivarajan et al. (2019). As pressure on the world's freshwater resources increases, many river basins will face both increasing freshwater scarcity and increasing pollution. Therefore, adaptation strategies under the new realities of climate change are one of the most important challenges in the 21st century for global water and food security. Due to spatial and temporal variations in climate, water availability in different water catchments in the world has been affected and there are occurance of flooding in many áreas. For example, severe flooding has frequently affected Malaysia, especially during the boreal winter moonsoon (Hamzah et al., 2019; Ibadullah et al., 2019). Therefore, it is imperative for the country to have a reliable and skilful early warning system of both weather and flood events. The general circulation models (GCMs) are currently the most reliable tools for assessing the changes in climate. However, regional hydrological changes can only be predicted by using hydrological models to simulate hydrological impacts of climate change at basin scales, using downscaling techniques (Jiang et al., 2007).

It is quite hard to manually quantify and regulate streamflow at different sections of a channel in a large irrigation scheme, resulting in inadequate delivery between wáter supply and irrigation demand. Hydrological models are essential tools that facilitate the streamflow monitoring for adequate water allocation for industrial, domestic and agricultural purposes, particularly when projecting the impacts of variability in climate. However, some models are more reliable particularly when handling ungauged stations or stations with poor input data, which is a common situation in most of the watersheds. Abdulkareem et al. (2018), highlighted details of hydrological models used in Malaysia, about 65% of the studies applied semi-distributed and distributed hydrological models. Out of these 65% of the modelling studies, 60% applied HEC-HMS model due to its least input parameters followed by ArcSWAT model (20%) and MIKE-SHE (9%).

The Bernam River Basin is the primary source of irrigation supply for the Tanjung Karang Rice Irrigation Scheme, which is the fourth largest in Malaysia. The hydrological processes of this river basin under climate change are paramount to the planning and management of the irrigation scheme's potential water requirements. Water shortage is an annual issue for the scheme. An imbalance between water supply from the upstream and the water demand at the intake of the scheme is often experienced (DID, 2018).

Among the hydrological models, the use of ArcSWAT in streamflow simulation and forecast for present and projected climate scenarios has been extensive (Ajayi, 2017; Alansi et al., 2009; Dlamini et al., 2017; Dlamini et al., 2016; Lai & Arniza, 2011). However, the

difficulty in data preparation into ArcSWAT format and the high number of parameters required to run the model are some of its major weakness (Abbaspour et al., 2007a), particularly for ungagged stations, where data is scarce . MIKE-SHE has an advantage in terms of seamless integration of all the important processes of the hydrological cycle (Refsgaard et al., 1995). However, it requires extensive model data and physical parameter that may not be available all the time, which make the model setup difficult. Amin et al. (2017) applied the Watershed Environmental Hydrology (WEHY) model to assess future climate change impact on hydrologic processes of watershed. The model requires detailed topographic information and simulations are conducted on model computational units. HEC-HMS is an open-source hydrological modeling software for simulating precipitation-runoff processes of watershed systems (Ghorbani et al., 2016; Kabiri, 2014; Mohammed et al., 2011; Razi et al., 2010; Yusop et al., 2007). Among the advantages of the model over other hydrological models is the various options in methods selection, to compute different hydrological responses for watershed development. Previous studies have extensively applied HEC-HMS model to examine the impacts of future climate projections on water resources (Chu & Steinman, 2009; Kabiri et al., 2015). Hydrological modeling studies (Alansi et al., 2009; Dlamini et al., 2017) were carried out in the study area using different model. Thus, the need to evaluate HEC-HMS and ArcSWAT models as different hydrological models perform best in certain hydrological catchments. Therefore, this study assesed the performance of these models for climate change impacts assessment on streamflow in Bernam River Basin Malaysia.

MATERIALS AND METHODS

Study Area

The Bernam River Basin is an agro-hydrological watershed situated at the boundary between the States of Perak and Selangor, Malaysia (Figure 1). The mean elevation is about 950 m above sea level. The climate of the area is a humid tropic that is largely characterized by the two predominant rainfall seasons, dry season (January–June) and the wet season (July–December) (Deni et al., 2010). The average annual rainfall in the region is about 2,000 mm, and its distribution is mostly between the months of October–January and only to a limited extent over April–May. The distribution of rainfall is unpredictable between the months of January–August. The mean maximum and minimum temperatures are 31.5°C and 22.3°C, respectively.

Downscaling of GCMs Variables

Adoption of multi-models is essential and recommended for impact studies and adaptation strategies (Ghosh & Mujumdar, 2007; New & Hulme, 2000), because single GCM does not

Figure 1. Typical view of Upper Bernam River Basin (UBRB), Malaysia

actually provide useful information in assessing the climate change impacts. Therefore, ten global climate projections were acquired from Program for Climate Model Diagnosis and Inter-comparison (PCMDI). A baseline period (1976-2005) was adopted and three future periods of 30-year time segments were defined as the 2020s (2010-2039), 2050s (2040-2069) and 2080s (2070-2099) for the ten GCMs under three Representative Concentration Pathways (RCPs) scenarios (RCP 4.5, RCP 6.0, and RCP 8.5). The spatial resolution from the output of GCMs cannot give a good climate change scenario to a target watershed because GCMs operate on a large spatial scale. Therefore, downscaling is required to represent the impact of climate change on a catchment área. A Climate-smart Decision Support System (CSDSS) for downscaling hydro-meteorological variables, which was developed by Rowshon et al. (2019), was used to downscale the extracted GCMs outputs. The CSDSS was built in MATLAB environment using First-order Markov Chain Model and "Delta change factor" statistical downscaling method. In the First-order Markov

Chain Model, the occurence of rainfall is characterized by two transition probabilities; the probability of a wet day preceded by a dry day $P_{(dw)}$ and the probability of a wet day preceded by wet day $P_{(ww)}$, as given in Equations 1 and 2. The two transition probabilities were estimated from the observed rainfall series and were constant for a given month but differ from one month to the other.

$$P_{dw} = P\{wet\ on\ day\ (t) \mid dry\ on\ day\ (t-1)\} \quad [1]$$

$$P_{ww} = P\{wet\ on\ day\ (t) \mid wet\ on\ day\ (t-1)\} \quad [2]$$

In order to simulate the occurrence of rainfall, $P_s(t)$, on day t, a random number, U_t was generated using MATLAB program and compared with the critical transition probability, P_c, depending on the preceding day's $(t-1)$ rainfall (Equation 3).

$$P_c = \begin{cases} P_{dw}\ if\ P_s(t-1) = d \\ P_{ww}\ if\ P_s(t-1) = w \end{cases} \quad [3]$$

Where, w = wet day and d = dry day. A wet day is simulated when the random number is less than the critical probability, otherwise it is simulated as a dry day (Equation 4).

$$P_s(t) = \begin{cases} w\ if\ U_t \leq P_c \\ d\ if\ U_t > P_c \end{cases} \quad [4]$$

The variation in the amount of rainfall on wet days is defined using a probability density function, which best describes the amount of rainfall. The gamma distribution (Equation 5), which is the most popular distribution widely used in rainfall studies (Dlamini et al., 2015) was adopted in this study. The gamma distribution is fitted to all days modeled as wet days and a threshold value of 1 mm was considered for Malaysia due to the high humidity condition (Deni et al., 2010; Zin et al., 2010).

$$f(x) = \frac{\left(x/\beta\right)^{\alpha-1} exp\left(-x/\beta\right)}{\beta\Gamma(\alpha)}; \alpha, \beta > 0; x > 0 \quad [5]$$

Where, α is a shape parameter, β is a scale parameter, and $\Gamma(\alpha)$ represents the gamma function. The maximum likelihood estimators were used to estimate the gamma parameters (Haan, 1977).

Rainfall generator models are evaluated on the basis of how well they preserve the statistical properties of the original data. Daily observed rainfall datasets for 30 years (1976-2005) were used to calculate representative parameters for model evaluation. The data was provided in the model to compute area specific parameters from the generated

daily series by running the model 100 times. This was done so that the statistical properties of the synthetic data would be close to the distribution of the original dataset. A number of statistical properties of the synthetic data describing rainfall occurrence, quantity and distribution (including monthly mean rainfall, standard deviation, rainy days, wet/dry spells and annual maximum rainfall) was calculated. Deteils procedure of the probability distribution and statistical properties could be found in other study (Dlamini et al., 2015).

In the "Delta change factor" method, the mean values of GCM simulated baseline and future climates were estimated using Equations 6 and 7:

$$\overline{GCM_b} = \sum_{i=1}^{Nb} GCM_{bi}/N_b \quad [6]$$

$$\overline{GCM_f} = \sum_{i=1}^{Nf} GCM_{fi}/N_f \quad [7]$$

Where, $\overline{GCM_b}$ and $\overline{GCM_f}$, GCM_b and GCM_f are the mean values and values from GCM baseline and GCM future climate scenario, respectively. N_b and N_f are the total number of values in the downscaling for baseline and future periods, respectively.

Subsequently, monthly additive (CF_{add}) and multiplicative Change Factor (CF_{mul}) changes between the baseline and future periods in the equivalent climate variable of interest are calculated for the GCM grid box using Equations 8 and 9. Relative change factors are used in the case of rainfall (ΔP), derived from the ratio of projected-to-baseline averages, while absolute change factors are used for temperature, solar radiation, relative humidity and wind speed (ΔV), by subtracting the GCMs averages representing baseline from the future.

$$CF_{Rain} = \left(\bar{P}_{GCM,fut,m} \Big/ \bar{P}_{GCM,base,m} \right) \quad [8]$$

$$CF_{var} = \left(\bar{V}_{GCM,fut,m} - \bar{V}_{GCM,base,m} \right) \quad [9]$$

Finally, local scaled future climate values were obtained by applying the Change Factors using Equations 10 and 11. This involves superimposing the change factors suggested by the GCM-scenario combinations to the daily baseline time series to give perturbed climate series.

$$P_{adj,fut,d} = P_{obs,d} \times CF_{Rain} \quad [10]$$

$$V_{fut,d} = V_{obs,d} + CF_{var} \quad [11]$$

Where, *P* and *V* are the rainfall and climate variables, respectively, the subscrip; *adj,fut,d* denotes the downscaled future daily variable; *obs,d* denotes daily observations; CF denotes calculated additive and multiplicative change factors for rainfall and climate variables; *GCM,fut,m* and *GCM,base,m* are the average monthly values of GCM output and baseline periods, respectively.

A simulation dialog window appears after clicking on a specific command button from the CSDSS main dialog window to generate daily sequences of hydro-meteorological variables as shown in Figure 2. The program was validated using the observed and simulated monthly average values for the baseline period. The outputs can be generated as daily time series and long-term monthly time scale, and can be viewed from the "*Analysis and Statistics*" button as tables and graphs.

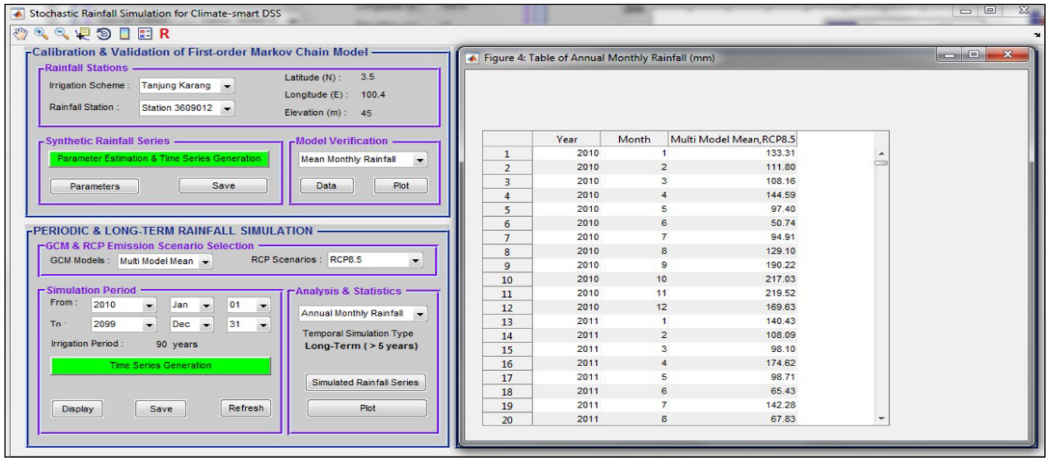

(a)

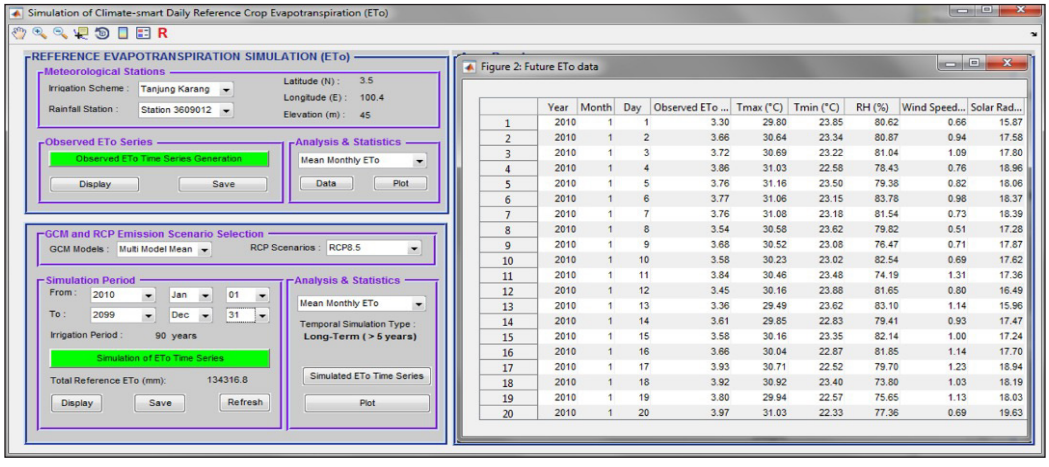

(b)

Figure 2. Windows for downscaling daily climatic variables time-series (2010-2099): (a) Daily rainfall generation; and (b) Daily temperature, relative humidity, wind speed and solar radiation

Hydrological Modeling for Bernam River Basin

Two hydrological models HEC-HMS and ArcSWAT were adopted in this study based on their availability and accuracy. The models require two types of data for hydrological simulation, the spatial and hydro-climatic data. The spatial data include digital elevation model (DEM), soil and land use maps of the área. The DEM was downloaded from DIVA-GIS website while soil and land use maps were obtained from the Department of Agriculture (DOA) Malaysia. A gridded daily climate dataset including rainfall, minimum and maximum temperature, relative humidity, wind speed and solar radiation for 1976-2005 was obtained from the Water Resources and Hydrology Division, Department of Irrigation and Drainage (DID) Malaysia. The gridded data, covering the entire Peninsular Malaysia was developed by Wong et al. (2011), at a spatial resolution of 5 km based on Angular Distance Weighting (ADW) procedure. Further detail procedure of the data processing and development can be found in Wong et al. (2009) and Wong et al. (2011). Daily discharge records (m^3/s) of the Bernam watershed were taken at gauging station known as SKC. The systematic approach for the study is depicted in Figure 3.

HEC-HMS Setup for the Bernam River

The sub-basin element in HEC-HMS model conceptually represents interactions of infiltration, surface runoff and subsurface processes. Priestly-Taylor method was used to compute the potential evapotranspiration, ET (mm/day) as mostly used in continuous simulation using HEC-HMS (Meenu et al., 2013). The model is expressed as in Equation 12:

$$ET = \frac{\Delta}{\lambda \Delta + \gamma}(R_n - G) \quad [12]$$

Where, $\alpha = 1.26$, λ is latent heat of evaporation (MJ/kg), R_n is net radiation at crop surface (MJ m^{-2} day^{-1}), G is soil heat flux density (MJ m^{-2} day^{-1}), Δ is slope vapour pressure curve (kPa $°C^{-1}$), γ is Psychrometric constant (kPa $°C^{-1}$).

The Deficit and Constant Loss (DCL) method was used to compute the runoff-volume (loss). It uses one layer to account for continuous changes in moisture and requires only four parameters namely initial deficit, maximum deficit, constant rate and percentage of impervious área. The method is simple, requires lesser-input parameters and is yet to be applied for climate change study in Malaysia. The DCL parameters were obtained from the land use and soil grids of the area using HEC-GeoHMS, a GIS extension of HEC-HMS. The DCL method was combined with simple canopy and surface methods. The canopy method accounts for precipitation intercepted by plants from one storm to another, which subsequently evaporates and the water extracted by the plants through the process of transpiration. The surface method on the other hand accounts for the maximum amount of water that held on the soil before surface runoff begins.

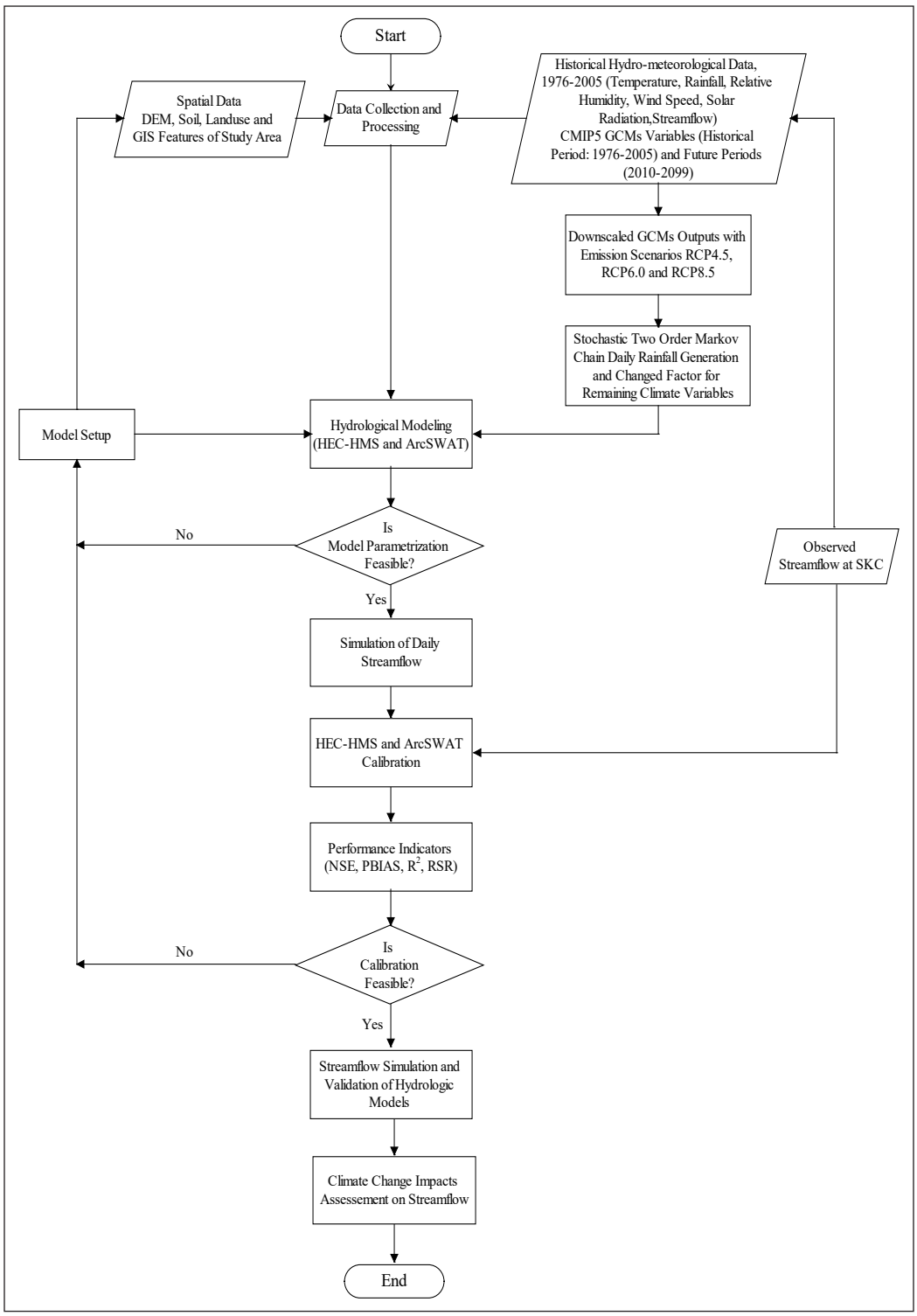

Figure 3. Framework for the projection of hydrologic response under climate change.

Soil Conservation Service Unit hydrograph (SCS-UH) method was used for the transformation of precipitation excess into point runoff. The unit hydrogrph (UH) diischarge, U_t is given as a ratio to the UH peak discharge, U_p, for any time t, a fraction of T_p, the time to UH peak (Equation 13 & 14).

$$U_p = C\frac{A}{T_p} \quad [13]$$

$$T_p = \frac{\Delta t}{2} + t_{lag} \quad [14]$$

Where, A is the watershed area, C is the conversión constant (2.08), Δt is duration of excess precipitation and t_{lag} is the basin lag.

The baseflow in each sub-basin was modeled using constant monthly-varying method. In this method, the program represents baseflow as a constant flow but may vary monthly. The monthly flows were approximated from the long-term series of monthly-observed flow data and were added to the direct runoff, computed from rainfall for each time step of the simulation. The channel flow was computed using Muskingum routing method. The method consists of two parameters; the travel time through the reach, K and a weighing factor, X. The parameters K and X were estimated using the channel geometry. The travel time, K (hr) was computed using Equation 15 (Griffin, 1994):

$$K = \frac{L}{3600Vw} \quad [15]$$

Where, L is the reach length (m), and V_w is the flood wave velocity (m/s).

ArcSWAT Setup for the Bernam River

The ArcSWAT model requires spatial and climatic data. A similar spatial and gridded data set used for HEC-HMS was input to the model. To setup the model, climate data was prepared into ArcSWAT format using Microsoft excel and uploaded to the weather generator (WGEN) user in ArcSWAT mother folder. A look-up table for rainfall was created using the locations of the rainfall stations in the área. The DEM was uploaded to ArcSWAT interface to créate stream network and delineated the catchment boundary. Land use and soil data was processed and reclassified within ArcGIS with the aid of notepad ++ to fit the classes that are compatible to the ArcSWAT land use and soil database, respectively. Subsequently, a land use look-up table was created and attached to the ArcSWAT database to serve as a link between the land cover data of the basin and that of ArcSWAT database. ArcSWAT mother folder consists of soil user covering USA. Therefore, a soil look-up table was created and attached to the ArcSWAT database to serve as a link between the soil data of the basin

and that of ArcSWAT database. Other properties of the soil like soil depth, texture, etc., for the ArcSWAT database were obtained from other sources (Lai, 2001; Wong, 1970). The delineated catchment was sub-divided into sub-basins and hydrologic response units (HRUs), which contain combinations of land use and soil attributes. Finally, the model was evaluated using the discharge data.

Calibration and Validation of Hydrological Models

Monthly streamflow records of 30 years (1976-2006) were used for evaluating the performance of the HEC-HMS and ArcSWAT models. Out of the 30 years records, 18 years (1981-1998) was used for the calibration while 8 years (1999-2006) used for the validation with 5 years warm-up period in each. In both calibration and validation periods, the monthly observed and simulated discharges from the models were compared. Manual and automatic calibration techniques was applied to optimize HEC-HMS parameters. ArcSWAT Calibration and Uncertainty Procedures (SWAT-CUP) software developed by Abbaspour et al. (2007b) was used to perform calibration, validation and sensitivity analysis of ArcSWAT model. Four statistical criteria were employed to evaluate the hydrological goodness of fit; Coefficient of determination (R^2), Nash-sutcliffe Efficiency (NSE), Percent Bias (PBIAS) and Root mean square error-standard deviation ratio (RSR), by comparing the observed streamflow with the models simulated values. NSE is the ratio of the mean square error between observed and simulated values to the variance of the observed data. NSE value 1 indicates the perfect prediction of model. The PBIAS measures the average tendency of the simulated results to be higher or lower than the observed data. Simulated value is over-estimated when the value is negative and under-estimated when it is positive. RSR varies from optimal value of zero, which indicates zero root mean square error (RMSE) or residual variability and therefore accurate model simulation, to a large positive value. The smaller the value of RSR, the greater the ability of the model to simulate the hydrological characteristics of a basin and viceversa (Equation 16, 17, 18 & 19).

$$R^2 = \left(\frac{\sum_{i=1}^{n} \left(P_i^{obs} - P_i^{mean}\right)\left(P_i^{sim} - P_i^{mean}\right)}{\left[\sum_{i=1}^{n} \left(P_i^{obs} - P_i^{mean}\right)^2 \sum_{i=1}^{n} \left(P_i^{obs} - P_i^{sim}\right)^2\right]^{0.5}} \right)^2 \quad [16]$$

$$NSE = 1 - \frac{\sum_{i=1}^{n} \left(Q_{O_i} - Q_{S_i}\right)^2}{\sum_{i=1}^{n} \left(Q_{O_i} - \bar{Q}_O\right)^2} \quad [17]$$

$$PBIAS = \frac{\sum_{i=1}^{n} \left(Q_{oi} - Q_{si}\right)}{\sum_{i=1}^{n} Q_{oi}} \times 100\% \quad [18]$$

$$RSR = \frac{\sqrt{\sum_{i=1}^{n}(Q_{obs} - Q_{sim})^2}}{\sqrt{\sum_{i=1}^{n}(Q_{obs} - \overline{Q_{obs}})^2}} \quad [19]$$

Where, *Qo,i, Qs,i* are the *i* th observed and simulated discharges respectively; $\overline{Qo}$ = mean observed discharge; P_i^{obs} and P_i^{sim} are observed and simulated flows, respectively; P^{mean} is the mean of observed flow; *n* is the total number of reference data points.

Simulation of Future Impacts of Climate Change

To project the future flow regime in the Bernam basin, the downscaled GCMs outputs for the baseline (1976-2005) and future (2010-2099) periods, which include rainfall, temperature, solar radiation, relatve hummidity and wind speed were used as input to the validated HEC-HMS model (Figure 3). Flow simulation was performed for each RCP scenario for 30-year time segments centered on the three future periods. For long-term analysis, data was prepared in accordance with the 'period change' approach by defining future periods as (i) 2020s (2010-2039), (ii) 2050s (2040-2069) and (iii) 2080s (2070-2099), to analyze change from a defined baseline period.

Flow Regime

Three streamflow classes were assessed and studied how they were influenced with the change in climate at the Basin as presented in Table 1. The classes studied for streamflow are high-flow disturbances, low-flow disturbances and flow variability. There are three variables for the high-flow disturbance streamflow: a high-flow disturbance (Q1.67), a duration of flood (FLDDUR), and a seven-day maximum-flow (7QMAX). The high-flow disturbance calculation was based on the most dominant channel forming flow (known as bankfull).

Low-flow disturbance streamflow indicators comprise of baseflow index (BFI), for a baseflow variable change measurement and a minimum 7-day (7QMIN) variable. Flow variability streamflow indicators include temporal shifts in peak flows (TSQPEAK) and coefficient of variation (DAYCV).

RESULTS AND DISCUSSION

Downscaling of GCMs Variables

The stochastic rainfall model was validated using the observed station rainfall in the study catchment prior to application for future simulation. The model demonstrated good performance in the simulation of different rainfall statistics. Estimated transition probabilities and gamma parameters (Figure 4) derived from the observed period (1976-2005) indicated that during the dry season (January to June), the probability of not receiving

Table 1
Streamflow regime variables for climate changes impacts assessment

Variable Name	Symbol	Definition	Streamflow Classification
High-Flow disturbance	Q1.67	Flow of magnitude exceeding return interval of 1.67 years based on a log-normal distribution	High-Flow disturbance
Duration of flood	FLDDUR	The average number of days of flow equal to or exceeding Q1.67 per year	
7-day maximum flow	7QMAX	The average annual maxima of 7 day means of daily mean streamflow	
Base flow index	BFI	The ratio of the smallest annual daily flow to the mean daily flow multiplied by 100 over a water year	Low-flow disturbance
7-day minimum flow	7QMIN	The average annual minima of 7 day means of daily mean streamflow	
Coefficient of variation	DAYCV	The ratio of the standard deviation of daily flows to the average of daily flows multiplied by 100 during a water year	Flow variability
Temporal shifts in peak flows	TSQPEAK	Shifts of peak flows in timing and magnitude	

rains was high if there was no rain the previous day, and the chance of receiving rains when it was raining the previous day increased during the wet season (July to December). The estimated values of α ranged from 0.83 to 0.96 and 0.73 to 1.11, respectively during the dry and wet seasons. Whilst β ranged from 13.09 to 19.93 and 14.27 to 20.60 for the same seasons. The simulated mean monthly rainfall matched quite well with the observed rainfall with R^2 value of 0.98. In addition, the simulation results closely resembled the actual rainfall pattern of the área, where most of the rain fell during the wet season while lower rainfall occured during the dry season. In Figure 4, P00 is the probability of not receiving rains if there was no rain in the previous day; P01 is the probability of not receiving rains if there was rain the previous day; P11 is the probability of receiving rains when it was raining the previous day; and P10 is the probability of receiving rains when it was not raining the previous day.

Temperature (maximum and minimum) and rainfall are among the key climatic variables that bring about the change in climate of an area. They have greatest effect on the estimation of irrigation wáter demand (Goodarzi & Eslamian, 2018). The future temperature increases due to climate change effects as presented in Table 2. The mean máximum temperature was predicted to increase under RCPs 4.5, 6.0 and 8.5 by an average of 1.18^{o}C, 1.14^{o}C and 1.97^{o}C, respectively compared to the baseline period. The largest increment (3.25 ^{o}C) was noticed from the most severe scenario (RCP8.5) in the late century (2080s). Similarly, the projected minimum temperature increased by 1.27^{o}C, 1.21^{o}C and 2.08 ^{o}C for the same future periods. The rate of change in the minimum temperature was slightly higher than the maximum temperature. This result inferred that in the future, the

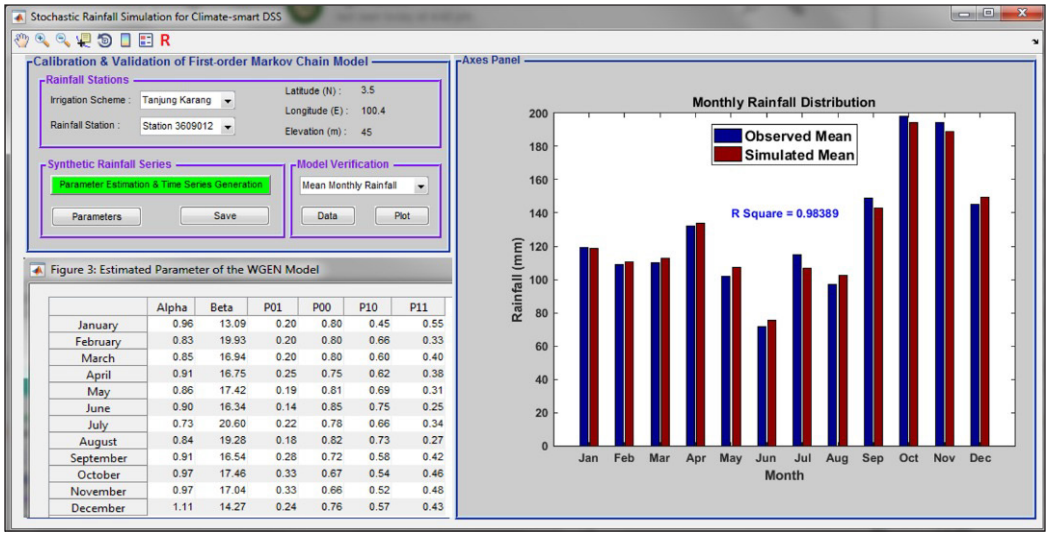

	Alpha	Beta	P01	P00	P10	P11
January	0.96	13.09	0.20	0.80	0.45	0.55
February	0.83	19.93	0.20	0.80	0.66	0.33
March	0.85	16.94	0.20	0.80	0.60	0.40
April	0.91	16.75	0.25	0.75	0.62	0.38
May	0.86	17.42	0.19	0.81	0.69	0.31
June	0.90	16.34	0.14	0.85	0.75	0.25
July	0.73	20.60	0.22	0.78	0.66	0.34
August	0.84	19.28	0.18	0.82	0.73	0.27
September	0.91	16.54	0.28	0.72	0.58	0.42
October	0.97	17.46	0.33	0.67	0.54	0.46
November	0.97	17.04	0.33	0.66	0.52	0.48
December	1.11	14.27	0.24	0.76	0.57	0.43

Figure 4. Validation of First-order Markov Chain model for rainfall generation

basin is anticipated to be warmer, especially during the dry season months. Mean surface temperature was also projected to increase in previous studies (Meinshausen et al., 2011; Tangang et al., 2012).

In the other hand, rainfall may slightly increase in the wet season (July to December) and decrease in the dry season (January to June) during the future period. The wet season average changes are projected to be 1.0%, 0.8% and 2.4% under RCPs 4.5, 6.0 and 8.5 scenarios, respectively with a range of 0.2% for RCPs 4.5 and 6.0 in the 2050s to 2.7% for the RCP8.5 in the 2080s. Whereas, the average changes for the dry season are -2.4%, -3.2% and -3.7% under RCPs 4.5, 6.0 and 8.5 scenarios, respectively.

Table 2
Projected changes in temperature under multi-model projections based on RCP scenarios

Period	Changes in temperature under RCPs		
	RCP4.5	RCP6.0	RCP8.5
Maximum temperature (°C)			
2020s	0.68	0.52	0.82
2050s	1.29	1.06	1.85
2080s	1.57	1.85	3.25
Average	1.18	1.14	1.97
Minimum temperature (°C)			
2020s	0.71	0.62	0.92
2050s	1.36	1.16	1.95
2080s	1.75	1.85	3.36
Average	1.27	1.21	2.08

Hydrological Modeling

The performance of HEC-HMS and ArcSWAT models was assesed using monthly average discharge data. The models performed satisfactorily both during calibration and validation periods as the values are greater than 0.5 (Moriasi et al., 2007) as shown in Figure 5. However, HEC-HMS performs better in the watershed compared to ArcSWAT model with 0.74, 0.71, 4.21 and 0.37; and 0.71, 0.69, 5.32 and 0.31 for R^2, NSE, PBIAS and RSR, respectively, during the calibration and validation periods and ArcSWAT model is 0.67,

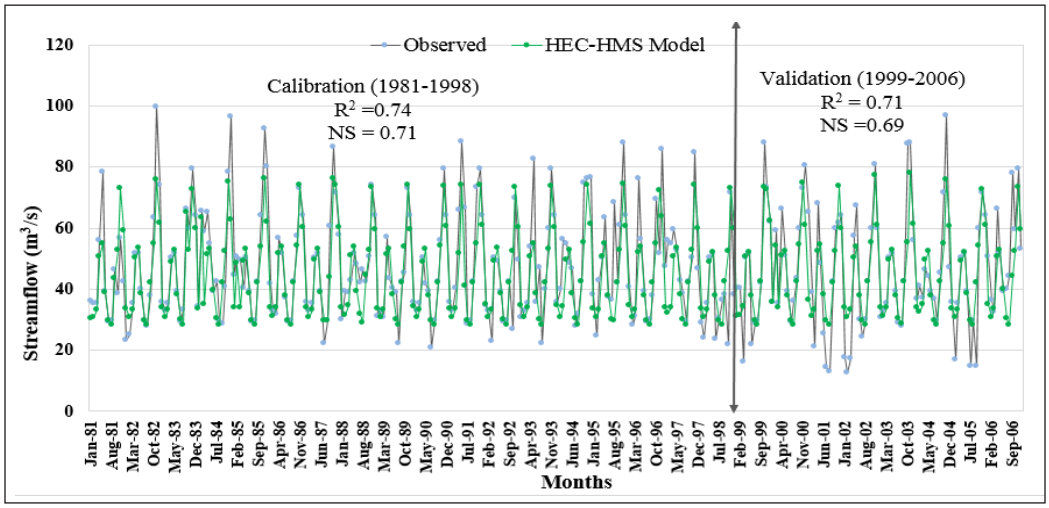

(a)

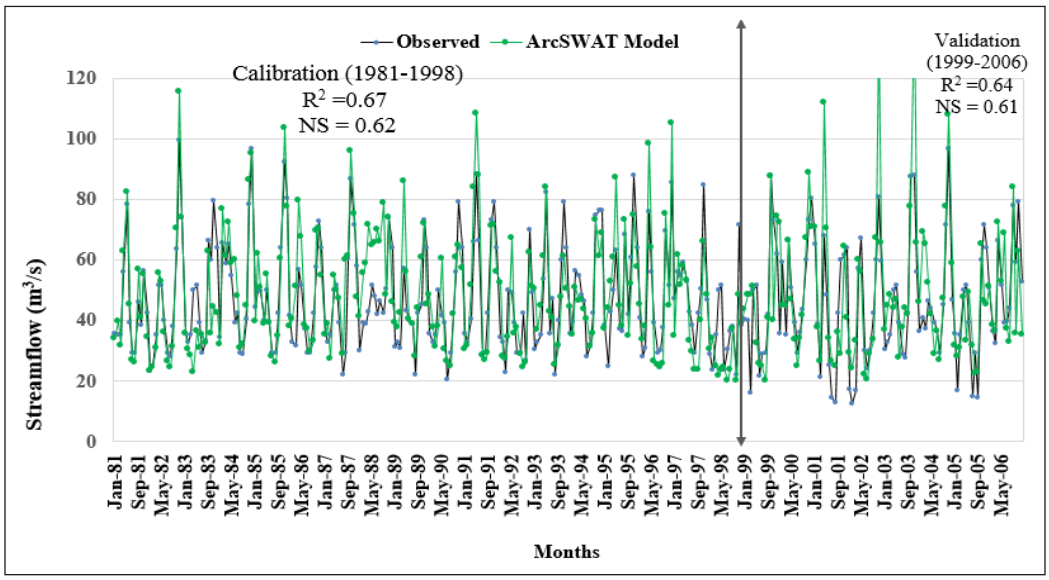

(b)

Figure 5. Simulated and observed monthly discharge for Bernam river basin: (a) HEC-HMS model; and (b) ArcSWAT model

0.62, -5.4 and 0.64; and 0.64, 0.61, -4.2 and 0.65 for the same model efficiency. This might be associated with complexity in ArcSWAT input parameters, which rendered calibration difficult. Similar trend was obtained by Dlamini et al. (2017) when ArcSWAT model failed to simulate high peak discharges in some months in the same basin.

The average percentage of impervious area computed using the DCL method for the delineated sub-basins was 3.83%, which indicates that the portion where all contributing precipitation runs off, with no infiltration, evaporation or other volume losses in Bernam basin is small, likely due to the type of forest in the area. Initial deficit, maximum deficit and constant rate, which signify the properties of soil in the área were found to be among the sensitive parameters in HEC-HMS. The sensitivity analysis was conducted by varying one parameter at a time from -50% to 50% with increments of 10%, keeping all other parameters constant. The soil layer within the sub-basins would require average of 39.4mm (initial déficit) to saturate to maximum storage and can hold about 49.5mm (máximum déficit). The infiltration rate when the soil layer is saturated (constan trate) was estimated to be 49mm/hr.

A consistent under-prediction of peak flows with much higher values and over-prediction of flows with much lesser value was noticed in HEC-HMS and *vice-versa* for the ArcSWAT model during the evaluation. Meenu et al. (2013) reported a similar trend when HEC-HMS failed to simulate peak flows. HEC-HMS also failed to reproduce peak flows in late winter and early spring runoff (Gyawali & Watkins, 2012). The observed discharge data in the study area is associated with large variations in some of the years, with a difference up to about 70m^3/s in some similar months across the years, which is possible for the models to either under-estimate or over-estimate such discharge values, in trying to fit well with the observed v alues. Similarly, Dlamini et al. (2017) noticed challenge using ArcSWAT model and concluded that the problem was attributed to the poor quality of the data in the watershed. However, HEC-HMS has to be applied with caution in the area especially for flood analysis.

Impacts of Climate Change on Future Streamflow

Sequence to the results from the models evaluation, HEC-HMS model was applied to predict the climate change impacts in the basin. The changes in major rice farming (dry and wet) season results are assessed. The changes were the differences relative to the baseline period (1976-2005) for the three 30-year defined future period (2020s, 2050s and 2080s). The changes in future streamflow at Bernam river basin was more pronounced during the dry season period as presented in Table 3. This is expected because warmer temperature during the dry season usually increases the rate of evapotranspiration more compared to wet season period, which consequently affects the future streamflow. The average changes under RCP 4.5, RCP 6.0 and RCP 8.5 are −0.40%, −1.68% and −5.71%, respectively, during

the dry season. In general, the future periods indicate a decreasing streamflow trend in this season, with a higher percentage (−5.94 %) predicted in the late century (2080s) under the RCP 8.5 scenario. Similarly, in the wet season, streamflow decreases in all future periods except for RCP4.5 where is expected to increase (0.36%). The average changes under RCP6.0 and 8.5 are −0.67% and −3.83%, respectively. Though the changes in streamflow is not much, the basin might suffer water pressure, particularly during the dry season period. A study by Dlamini et al. (2017) in the same watershed using ArcSWAT model reported future streamflow to decrease in the dry season months and increase in some months during the wet season. Also, Alansi et al. (2009) used ArcSWAT model to forcast streamflow due to landuse changes in the same catchemet. The flow depths decreased during low flow months. Similar decrease in annual streamflow was observed by Chien et al. (2013). Arnell and Reynard (1996) also reported a decrease in annual streamflow in the wettest scenarios and decline in the driest scenarios. The highest changes in streamflow during the wet season was -8.97% under worst-case scenario (RCP8.5) in 2020s period.

The streamflow projections in this study were based on predicted changes in hydro-climatic parameters. However, other factors like human activities, particularly related to land transformations might also have impacts on the hydrologic cycle in the area. Therefore, it is recommended to integrate projected land use changes in future hydrologic modeling studies in the área.

Table 3
Projected changes in streamflow under multi-model projections based on RCP scenarios

Period	Changes (%) in streamflow		
	RCP 4.5	RCP 6.0	RCP 8.5
Dry Season			
2020s	-0.40	-1.70	-5.66
2050s	-0.63	-1.90	-5.54
2080s	-0.18	-1.44	-5.94
Average	-0.40	-1.68	-5.71
Wet Season			
2020s	0.19	-0.84	-3.92
2050s	0.59	-0.47	-3.67
2080s	0.31	-0.71	-3.90
Average	0.36	-0.67	-3.83

Flow Regime

The assessment of climate-induced shifts in high flow disturbances indicated that all parameters that assess high flow disturbances (Q1.67, FLD-DUR and 7QMAX) showed a decrease in the future irrespective of the emission scenario (Table 4). The Q1.67 in the baseline period showed a decrease of about 5% to 6% during the future period under the

RCPs scenarios. Flood duration (FLD-DUR) decreased from 6 days during the baseline period to an average of less than one day in all the future periods under the three emission scenarios. Although the pattern of change in 7QMAX with years is not clear, however, for the three emission scenarios, results indicate that the average of the seven maximum runoffs in the future will shift by 6% on average. Though the changes in streamflow is not much, the basin might suffer water pressure, particularly during the dry season period.

Table 4
Projected annual flow regimes under multi-model projections based on RCP scenarios

High Flow Disturbance									
	Q1.67 (%)			FLDDR (HR)			7QMAX (%)		
Scenarios	2020s	2050s	2080s	2020s	2050s	2080s	2020s	2050s	2080s
RCP 4.5	-5.71	-5.69	-5.72	10.24	14.36	14.24	-6.05	-6.08	-6.51
RCP 6.0	-5.15	-5.57	-6.00	10.36	14.24	14.48	-5.80	-6.23	-6.51
RCP 8.5	-5.90	-6.29	-6.32	12.48	14.24	13.36	-5.73	-6.51	-7.06
Low Flow Disturbance									
	BFI (%)			7QMIN (m^3/s)					
Scenarios	2020s	2050s	2080s	2020s	2050s	2080s			
RCP 4.5	64.14	64.00	64.00	28.33	28.33	28.67			
RCP 6.0	64.10	64.01	64.30	28.33	28.30	28.30			
RCP 8.5	64.20	64.10	64.81	28.30	28.30	28.31			
Flow Variability									
	DAYCV (%)			TSQPEAK (%)					
Scenarios	2020s	2050s	2080s	2020s	2050s	2080s			
RCP 4.5	31.17	32.70	32.70	-0.24	-0.65	0.41			
RCP 6.0	32.20	32.71	32.00	-1.99	-2.36	-0.71			
RCP 8.5	32.60	32.70	31.00	-2.65	-2.72	-4.94			

Climate-induced shifts in low-flow disturbances were also assessed. The findings showed that the indicators quantifying low-flow disturbances (BFI and 7QMIN) had minor changes in the future for all emission scenarios. Historical and future streamflow data indicate that the 7QMIN and median of BFI at the study area is 28 m^3/s and 64%, respectively. This implies that the flow in the Bernam River Basin is stable and not susceptible to drying.

The DAYCV defines total flow variability without taking into account the temporal sequence flow variation. Baseline and future data indicate that the DAYCV median at the study catchment is about 33%, suggesting a small rate of streamflow change. The future peak flows were not temporally shifted from the baseline period for all the future periods irrespective of the RCP scenario. Conversely, the magnitude of the future monthly peak flows has decreased from baseline peak flow with a range of 0.24% to 4.94%, through the

three future periods under the RCP scenarios. These results inferred that Bernam basin may not face an increase in the frequency of floods but the magnitude of future peak flows might slightly decrease.

CONCLUSION

Hydrologic processes in the Bernam watershed were simulated by employing two hydrological models, namely ArcSWAT and HEC-HMS. The statistical results of the evaluation during both calibration and validation show that the models performed satisfactorily. HEC-HMS model (with DCL method), with less input data is easy to calibrate and therefore gives better statistical values compared to ArcSWAT model. A consistent under-prediction of peak flows with much higher values was noticed in HEC-HMS model, which was also reported by other studies. Therefore, HEC-HMS has to be applied with caution in the study area especially for flood analysis. Temperature is projected to increase in future periods with higher rate during the dry season period. This inferred that in the future, the basin is anticipated to be warmer, especially during the dry season months. In the other hand, rainfall may slightly increase in the wet season (July to December) and decrease in the dry season (January to June) during the future period. Future periods indicate a decreasing streamflow trend in dry season, with a higher percentage (−5.94 %) predicted in the late century (2080s) under the RCP 8.5 scenario. In the wet season, streamflow decreases in all future periods except for RCP4.5 where is expected to increase. Though the changes in streamflow is not much, the basin might suffer water pressure, particularly during the dry season period.

ACKNOWLEDGEMENTS

This research was supported by Universiti Putra Malaysia (Putra Grant No: 9678600) and the Ministry of Higher Education (FRGS Grant No: FRGS/1/2019/WAB01/UPM/02/37; 5540207). The authors wish to acknowledge the Department of Irrigation and Drainage (DID) and the National Hydraulic Research Institute of Malaysia (NAHRIM) for providing hydro-meteorological data.

REFERENCES

Abbaspour, K. C., Vejdani, M., Haghighat, S., & Yang, J. (2007a, December 10-13). SWAT-CUP calibration and uncertainty programs for SWAT. In *MODSIM 2007 International Congress on Modelling and Simulation, Modelling and Simulation Society of Australia and New Zealand* (pp. 1596-1602). Canberra, Australia.

Abbaspour, K. C., Yang, J., Maximov, I., Siber, R., Bogner, K., Mieleitner, J., & Srinivasan, R. (2007b). Modelling hydrology and water quality in the pre-alpine/alpine Thur watershed using SWAT. *Journal of Hydrology, 333*(2-4), 413-430.

Abdulkareem, J., Pradhan, B., Sulaiman, W., & Jamil, N. (2018). Review of studies on hydrological modelling in Malaysia. *Modeling Earth Systems and Environment*, *4*(4), 1577-1605.

Ajayi, J. O. (2017). *Modelling the impact of climate change on hydrology and water resources in the Niger-South Sub-catchment of the Niger River Basin, Nigeria.* (PhD Thesis), Universiti Putra Malaysia, Malaysia.

Alansi, A., Amin, M., Abdul Halim, G., Shafri, H., & Aimrun, W. (2009). Validation of SWAT model for stream flow simulation and forecasting in Upper Bernam humid tropical river basin, Malaysia. *Hydrology and Earth System Sciences Discussions, 6*(6), 7581-7609.

Amin, M., Shaaban, A., Ercan, A., Ishida, K., Kavvas, M., Chen, Z., & Jang, S. (2017). Future climate change impact assessment of watershed scale hydrologic processes in Peninsular Malaysia by a regional climate model coupled with a physically-based hydrology modelo. *Science of the Total Environment, 575*, 12-22.

Arnell, N., & Reynard, N. (1996). The effects of climate change due to global warming on river flows in Great Britain. *Journal of Hydrology, 183*(3-4), 397-424.

Chien, H., Yeh, P. J. F., & Knouft, J. H. (2013). Modeling the potential impacts of climate change on streamflow in agricultural watersheds of the Midwestern United States. *Journal of Hydrology, 491*, 73-88.

Chu, X., & Steinman, A. (2009). Event and continuous hydrologic modeling with HEC-HMS. *Journal of Irrigation and Drainage Engineering, 135*(1), 119-124.

Deni, S. M., Suhaila, J., Zin, W. Z. W., & Jemain, A. A. (2010). Spatial trends of dry spells over Peninsular Malaysia during monsoon seasons. *Theoretical and Applied Climatology, 99*(3-4), 357-371.

Dlamini, N., Rowshon, M., Saha, U., Lai, S., Fikri, A. Z., & Zubaidi, J. (2015). Simulation of future daily rainfall scenario using stochastic rainfall generator for a rice-growing irrigation scheme in Malaysia. *Asian Journal of Applied Sciences, 3*(05), 492-506.

Dlamini, N. S., Kamal, M. R., Soom, M. A. B. M., Mohd, M. S. F. b., Abdullah, A. F. B., & Hin, L. S. (2017). Modeling Potential Impacts of Climate Change on Streamflow Using Projections of the 5th Assessment Report for the Bernam River Basin, Malaysia. *Water, 9*(3), 1-23.

Dlamini, N. S., Rowshon, M. K., Fikhri, A., Lai, S. H., & Mohd, M. S. F. (2016, August 23). Modelling the streamflow of a river basin using enhanced hydro-meteorological data in Malaysia. In *III International Conference on Agricultural and Food Engineering 1152* (pp. 291-298). Kuala Lumpur, Malaysia.

Ghorbani, K., Wayayok, A., & Abdullah, A. F. (2016). Simulation of flood risk area in kelantan watershed, Malaysia using numerical model. *Jurnal Teknologi, 78*(1-2), 51-57.

Ghosh, S., & Mujumdar, P. (2007). Nonparametric methods for modeling GCM and scenario uncertainty in drought assessment. *Water Resources Research, 43*(7), 1-19.

Goodarzi, M., & Eslamian, S. (2018). Performance evaluation of linear and nonlinear models for the estimation of reference evapotranspiration. *International Journal of Hydrology Science and Technology, 8*(1), 1-15.

Griffin, R. H. (1994). Department of the army EM 1110-2-1417. *Analysis, 5*(6), 5-5.

Gyawali, R., & Watkins, D. W. (2012). Continuous hydrologic modeling of snow-affected watersheds in the Great Lakes basin using HEC-HMS. *Journal of Hydrologic Engineering, 18*(1), 29-39.

Haan, C. T. (1977). *Statistical methods in hydrology.* Ames, Iowa: The Iowa State University Press.

Hamzah, F. M., Yusoff, S. H. M., & Jaafar, O. (2019). L-moment-based frequency analysis of high-flow at Sungai Langat, Kajang, Selangor, Malaysia. *Sains Malaysiana, 48*(7), 1357-1366.

Ibadullah, W. M. W., Tangang, F., Juneng, L., & Jamaluddin, A. F. (2019). Practical predictability of the 17 December 2014 heavy rainfall event over East Coast of Peninsular Malaysia using WRF model. *Sains Malaysiana, 48*(11), 2297-2306.

Jiang, T., Chen, Y. D., Xu, C.Y., Chen, X., Chen, X., & Singh, V. P. (2007). Comparison of hydrological impacts of climate change simulated by six hydrological models in the Dongjiang Basin, South China. *Journal of Hydrology, 336*(3-4), 316-333.

Kabiri, R. (2014). Simulation of runoff using modified SCS-CN method using GIS system, case study: Klang watershed in Malaysia. *Research Journal of Environmental Sciences, 8*(4), 178-192.

Kabiri, R., Bai, V. R., & Chan, A. (2015). Assessment of hydrologic impacts of climate change on the runoff trend in Klang Watershed, Malaysia. *Environmental Earth Sciences, 73*(1), 27-37.

Lai, S. H. (2001). *Application of swat hydrological model with GIS interface to Upper Bernam River Basin* (Doctoral dissertation). Universiti Putra Malaysia, Malaysia.

Lai, S. H., & Arniza, F. (2011). Application of SWAT hydrological model to upper Bernam River Basin (UBRB), Malaysia. *IUP Journal of Environmental Sciences, 5*(2), 7-19.

Meenu, R., Rehana, S., & Mujumdar, P. (2013). Assessment of hydrologic impacts of climate change in Tunga–Bhadra river basin, India with HEC-HMS and SDSM. *Hydrological Processes, 27*(11), 1572-1589.

Meinshausen, M., Smith, S. J., Calvin, K., Daniel, J. S., Kainuma, M., Lamarque, J. F., … & Riahi, K. (2011). The RCP greenhouse gas concentrations and their extensions from 1765 to 2300. *Climatic Change, 109*(1-2), 213-241.

Mohammed, T. A., Said, S., Bardaie, M. Z., & Basri, S. N. (2011). Numerical simulation of flood levels for tropical rivers. *IOP Conference Series: Materials Science and Engineering, 17*, 1-10.

Moriasi, D. N., Arnold, J. G., Van Liew, M. W., Bingner, R. L., Harmel, R. D., & Veith, T. L. (2007). Model evaluation guidelines for systematic quantification of accuracy in watershed simulations. *Transactions of the ASABE, 50*(3), 885-900.

DID. (2018). *National water balance management system (NAWABS) for Sungai Bernam Basin*. The Ministry of National Resources and Environment, Malaysia (NRE), The Government of Malaysia: Department of Irrigation and Drainage.

New, M., & Hulme, M. (2000). Representing uncertainty in climate change scenarios: A Monte-Carlo approach. *Integrated Asessment, 1*(3), 203-213.

Razi, M. A. M., Ariffin, J., Tahir, W., & Arish, N. A. M. (2010). Flood estimation studies using hydrologic system (HEC-HMS) for Johor River, Malaysia. *Journal of Applied Sciences, 10*(11), 930-939.

Refsgaard, J., Storm, B., & Mike, S. (1995). *Computer models of watershed hydrology*. Colorado, USA: Water Resources Publication.

Rowshon, M., Dlamini, N., Mojid, M., Adib, M., Amin, M., & Lai, S. (2019). Modeling climate-smart decision support system (CSDSS) for analyzing water demand of a large-scale rice irrigation scheme. *Agricultural Water Management, 216*, 138-152.

Schlenker, W., Hanemann, W. M., & Fisher, A. C. (2007). Water availability, degree days, and the potential impact of climate change on irrigated agriculture in California. *Climatic Change, 81*(1), 19-38.

Sivarajan, N. A., Mishra, A. K., & Rafiq, M. (2019). Examining climate change impact on the variability of ground water level: A case study of Ahmednagar district, India. *Journal of Earth System Science, 128*(5), 122-128.

Tangang, F. T., Juneng, L., Salimun, E., Sei, K., & Halimatun, M. (2012). Climate change and variability over Malaysia: Gaps in science and research information. *Sains Malaysiana, 41*(11), 1355-1366.

Wong, C., Venneker, R., Jamil, A., & Uhlenbrook, S. (2011). Development of a gridded daily hydrometeorological data set for Peninsular Malaysia. *Hydrological Processes, 25*(7), 1009-1020.

Wong, C., Venneker, R., Uhlenbrook, S., Jamil, A., & Zhou, Y. (2009). Variability of rainfall in Peninsular Malaysia. *Hydrology and Earth System Sciences Discussions, 6*(4), 5471-5503.

Wong, I. F. T. (1970). *Reconnaissance soil survey of Selangor*. Kuala Lumpur, Malaysia: Ministry of Agriculture and Lands.

Yusop, Z., Chan, C. H., & Katimon, A. (2007). Runoff characteristics and application of HEC-HMS for modeling stormflow hydrograph in oil palm catchment. *Water Science Technology, 56*(8), 41-48.

Zin, W. Z. W., Jamaludin, S., Deni, S. M., & Jemain, A. A. (2010). Recent changes in extreme rainfall events in Peninsular Malaysia: 1971-2005. *Theoretical and Applied Climatology, 99*(3-4), 303-314.

Pertanika J. Sci. & Technol. 28 (3): 1049 - 1061 (2020)

PERTANIKA JOURNALS

SCIENCE & TECHNOLOGY

Journal homepage: http://www.pertanika.upm.edu.my/

Load Balancing using Enhanced Multi-Objective with Bee Colony Optimization in Cloud Networks

Abhikriti Narwal* and Sunita Dhingra

Department of Computer Science and Engineering, University Institute of Engineering and Technology, Maharshi Dayanand University, Rohtak Haryana, India

ABSTRACT

In the course of recent decades, cloud computing has turned into a hot research point for the logical, scholastic and mechanical networks. It is a wide-ranging term used to depict an extra class of framework-based enrolling that occurs over the web. The distributed computing principally plans to give capable access to remote and geologically disseminated assets. The other important purpose of cloud service providers is to gain maximum profit and use resources efficiently. As cloud technology is evolving day by day and confronts numerous challenges, one of them being uncovered is scheduling. Scheduling refers to a set of policies to control the order of work to be performed by a system. Every task needs a scheduling strategy which is assigned by the system in order to get executed by the processor. Procedures are vigorous to plan the trades for accomplishment. Job scheduling procedures supposed to be the most assumed difficulties in the cloud computing domain. The survey of existing papers reveals the better makespan time but cannot guarantee the proper balancing of load. To overcome this issue, Enhanced Multi-Objective Load balancing Scheduling Algorithm (EMOLB_LB) is proposed which uses Bee Colony Optimization algorithm for the analysis and balancing of load with more objective functions to sort the tasks and improvise the performance in terms of cost and time. The existing scheduling technique, Enhanced Multi-Objective Scheduling Algorithm (EMOSA) uses only non-dominating strategy for sorting the tasks but load management is not taken into consideration which is further optimized by proposing EMOLB_LB

ARTICLE INFO

Article history:
Received: 28 November 2019
Accepted: 12 March 2020
Published: 16 July 2020

E-mail addresses:
abhikritiin@gmail.com (Abhikriti Narwal)
sunitadhingramdu@rediffmail.com (Sunita Dhingra)
*Corresponding author

ISSN: 0128-7680
e-ISSN: 2231-8526

© Universiti Putra Malaysia Press

technique. The experimental results were analysed and compared with various existing techniques like Multi Objective Scheduling algorithm (MOSA), EMOSA and showed that the EMOLBA_LB technique was better than the earlier techniques in term of each performance attribute like average waiting time by 2.934 %, processing cost by 17.6% and processing time by 20.5%.

Keywords: Bee colony optimizations, cloud computing, MOSA (Multi Objective Scheduling algorithm)

INTRODUCTION

Cloud computing is an extension of parallel computing, distributed computing and grid computing[1]. The most recent movements in distributed framework are able to assemble our expert to offer a progressively versatile system. Distributing processing is the premature advancement which depends upon pay per-use criteria. It is enlisting point of view where requests, information, data transmission and IT associations are given over the Internet. The objective of the cloud association suppliers is to utilize assets effectively and accomplish the most phenomenal favourable position. The enduring evolution of cloud computing in IT has led several explanatory remarks on cloud computing. The US National Institute of Standards and Technology (NIST) defines the cloud computing as:"Cloud computing is a model enabling ubiquitous, convenient, on-demand network access to a shared pool of configurable computing resources (e.g., networks, servers, storage, applications, and services) that can be rapidly provisioned and released with minimal management effort or service provider interaction" (Narwal & Dhingra, 2016). There are hundred millions of gadgets associated with the web that are using a considerable amount of distributed computing administrations day by day as it provides a flexible and easy way to keep and retrieve data and files. Distributed computing is a promising and up-coming advancement which allows the customers to pay as they require. It engages encouraging of inescapable applications from client, exploratory, and business regions. Distributed computing is advancing utility-arranged IT organizations to customers around the globe (Foster et al., 2008). The creating cost of tuning and managing PC structures is provoking out-sourcing of business organizations to core interests. The features of distributed framework fuse on self-association, broad structure, asset pooling, smart flexibility and assessed association (Xiao et al., 2014). On intrigue self-association, it recommends that clients (ordinarily affiliations) can ask for and deal with their own particular computing assets. Distributed framework is an accumulation of two phrasings in the situation of figuring innovation with computing resources. It is an investor of diverse assets.

Scheduling refers to the way of assigning errands to resources that require the quality constraints (Singh et al., 2014). As countless customers offer cloud assets and dispatch

1 http://www.cncloudcomputing.co.

their assignments to the cloud, it has turned into a test to plan these undertakings. Thus, work planning is a hotly debated issue in conveyed and distributed computing. It is the procedure through which the processes and threads are mapped to resources by utilizing the accesses (Tripathy & Patra, 2014). The necessity of scheduling appears due to the prerequisite of performing multitasking and multiplexing. If scheduling is done properly then they can boost the interpretation of a system (Bhatia & Sharma, 2015). It is singular significant factor for providing better performance by a system. Scheduling refers to the planning or relegating a job to Virtual Machines (VM) in such a way keeps the usage upsurge (Narwal & Dhingra, 2016). A skillful scheduling scheming progresses the wide-ranging simulator presentation and supports facility of supplier to furnish fine quality parameters constraint. An elite VM dole out with the high-quality constraint. Data Centre Broker takes the solicitations from the client and transfers the solicitation to the VM which best suites the need and quality of service contention. Piecemeal a decent quality task is allotted to a low Quality of Service (QoS) VM which prompts the unfortunate procedure of assets and this abuses the Service level contention (Kowsik & Rajakumari,2014). So, an effective task scheduling calculation ought to be executed at the broker.

RELATED WORK

There are different studies adjacent the utilization of headway techniques of scheduling in cloud computing. To resolve the issues of existing procedures and falling the completion, an optimized priority based method has been proposed by Ghanbari and Othman (2012), taking into consideration of various principles and decision making rules to find out the job which is to be mapped to the specific VM by using various QoS parameters. In 2012, Zhan and Huo had projected an assessment relating to the utilization of improvised Particle Swarm

Optimization (PSO) solidified with Scheduling Algorithm (SA) in scheduling the resources of distributed systems to reorganize the scheduling procedure, by evolving the joining pace and using extent of compensations. Lakra and Yadav (2015) had introduced a scheduling procedure using multi objective functions to check the task dominance with purpose of mapping the task to the machine which would enhance throughput of the scheduler by reducing the completion time. To demonstrate the competence of the procedure based on optimization, Mathukiya and Gohel (2015) had discussed the multi-objective task scheduling algorithm for improvising the output of the scheduler and introduced non-dominated sorting for requesting of tasks. In order to minimize the expense of the processing, Guo et al. (2012) had defined a model for user's requirements scheduler in cloud framework taking into account on heuristic calculation based on the behaviour of particles, rely on small portion value rule. Patel and Bhoi (2014) had projected a precedence based scheduling procedure keeping with the purpose of accomplish better makespan and consistency of jobs by utilizing iterative system. Multi criteria and numerous

attribute decision making model were utilized to achieve better execution. Singh and Kalra (2014) had introduced an intricate thought regarding Genetic Algorithm (GA) and its various versions propounded as scheduling of user's requirement in cloud framework and changed the initial population of GA using Enhanced Max-Min which reduces the finish time of all the jobs and balanced the load as well. Lawrence and Silas (2013) proposed a resource scheduling methodology using potentially all pair-wise rankings of all possible alternatives (PAPRIKA). PAPRIKA method evaluates fairness based on user satisfaction. This method makes use of both task matrix and resource matrix. Priority of the resource is calculated with respect to a threshold value. Tasks are then mapped to the resource that gives higher user satisfaction, thus improving resource utility and minimizing the allocation time. Abdullah and Othman (2013) tried to use the Divisible Load Theory (DLT) to design efficient strategies to minimize the overall processing time for scheduling jobs in cloud computing. In this research homogeneous processors are considered and a closed form solution is derived to assign fractions to each processors. The research has tried to schedule the jobs in such a way that quality of service (QOS) parameters can achieve maximum benefit and results in minimizing the overall total cost. Bini and Sindhu (2015) propounded Hyper-Heuristic scheduler on Cloud constructed assemblies. Optimization procedures of GA and SA are in the solution of procedures pool and can be considered as traditional heuristic procedures. In addition, the combined solution of Differential Algorithm (DA) and GA minimizes the execution and the makespan (Bini & Sindhu, 2015). Kanani and Maniyar (2015) had inspected a transitory survey of Max-Min scheduler. The paper had propounded procedure which was familiar to evade downsides of Max-Min calculation to decrease the finish time and manufactured the asset utilization with seeing customer need, so that the prioritize task was accomplished foremost as demonstrated by its need. Job with better priority would be accomplished foremost than other subordinate exertion needs with the target that user's superlative position could be achieved all the additional total (Kanani & Maniyar, 2015). Raja and Sekar (2016) ran a better credit-based scheduling algorithm by means of the constraints like user priority, task length and deadline constraints. The new results show a significant improvement in the consumption of resources with speedy response time. Within the experimental result, the projected rule shows higher result than the present rule. Credits area unit accustomed cut back the build span of the task and execute all the task in cloud (Ru & Keung, 2013). Zalavadiya and Vaghela (2016) had projected technique showing the priority tasks area unit far from the overladen virtual machine and that they area unit allotted to below loaded virtual machine. It helps to scale back the minimum completion time, quantity of waiting time of tasks in queue is token and win higher resource utilization. This paper concludes that the minimum quantity of your time is taken to execute the tasks and higher resource utilization (Silberschatz et al, 2014). Shameer and Subhajini (2017) had incontestable the correct use of load reconciliation

techniques to extend the performance of the system and cut back the price and energy. Increased Bee Colony rule primarily based multi-objective task planning technique is given and its performance is verified and tested by the CloudSim stimulator. Also, through the experimental analysis, the simplest performance is shown for the projected work (Raja & Sekar, 2016). Vijay and Ghita (2017) had mentioned about the operating of planning algorithms which discusses about the shortest job initial, timeserving load reconciliation and generalised priority rule. They were placed to check the various condition and things and were assessed addicted to parameters, as an example, cost and makespan (Zalavadiya & Vaghela, 2016).The author has explained improvised multi objective scheduling by assigning the job using non dominating sort to the best optimized machine in the list to achieve the best results by diminishing processing time of the solution (Narwal & Dhingra, 2019). Narwal and Dhingra (2017) had discussed the comparative analysis of EMOSA and credit based scheduling algorithm. These algorithms are analysed based on performance parameters and on different scenarios. Also explained that optimization algorithms can be combined to make the results more accurate (Vijay & Ghita, 2017).

METHODOLOGY

The concept has been taken from Shameer and Subhajini (2017). EMOSA gained the best results of scheduling by comparing it with other scheduling procedures, but still it does not take into consideration of load balancing while mapping the machines to the tasks. EMOSA algorithm works with the principle of non-dominating sorting i.e. the tasks are sorted on the basis of multiple objective functions including length, file size and output file size of the task. It uses these objectives to check which task dominates the other tasks and based on this criterion, the best one is ranked highest among all and all other tasks are sorted in this order (Narwal & Dhingra, 2017). Then the organized errands are planned to the virtual machine. The arrangement of these enormous number of undertakings is an amazingly essential and challenging exertion for cloud. The crucial point of planning is to achieve cloud accomplishment of jobs to the extent of recovering output, load adjustment, QoS, financial practicality and the ideal activity time. The concept of load balancing was not taken into consideration i.e. whether that particular virtual machine to the cloudlet is going to be mapped is overloaded or underloaded. Therefore, in order to achieve efficient consumption of cloud resources, the problem of load balancing needed to be resolved. For this, the concept of load balancing was merged with the scheduling algorithm by introducing a Honey Bee Optimization algorithm to achieve the balancing of virtual machines.

In this paper, before mapping the tasks to the virtual machine, load on that particular machine was calculated. Based on the load, underloaded and overloaded machines were evaluated then their demands and supplies were calculated which helped to assign the various tasks to the machine. For the balancing of load, Bee Colony optimization approach was used; in which bees were tasks and the food for the bees was the virtual machines i.e. need to map bees with their best food nest.

Proposed Algorithm

Load Balancing using Bee colony approach works in four different modules:
1. Calculating Load of VM

$$\text{Load}_i = \frac{\text{N} * \text{Length of tasks}}{\text{VM\_MIPS}}$$

Here N is the Number of jobs and VM_MIPS is the Million Instructions per second rate of the virtual machines.

a)VM Capacity is evaluated using:

$$Capacity = No\ of\ PE_s * MIPS\ of\ PE_s + Bandwidth\ of\ VM_s$$

b) Load and Capacity of Virtual Machine can be premeditated from the given two equations:

$$\text{LOAD}_{\text{datacenter}} = \sum \text{Load}$$
$$\text{CAPACITY}_{\text{datacenter}} = \sum \text{Capacity}$$

c)Using the equations below processing time of virtual machine and datacenter (PTdatecenter) can be premeditated:

$$\text{PT}_{\text{vm}} = \frac{\text{Load}}{\text{Capacity}}$$

$$\text{PT}_{\text{vm}} = \frac{\text{Load}_{\text{datacenter}}}{\text{Capacity}_{\text{datacenter}}}$$

d) Standard Deviation (SD) for the load can be evaluated using

$$SD = \sqrt{\frac{1}{N}\sum_{i=0}^{N}(X_i - \overline{X})^2}$$

Where X_i is Processing Time and $\overline{X}$ is the average Processing Time of the virtual machine

2) Using the above SD calculations, comparison of SD with some threshold value rabges between 0-1, can define whether the machine needs load balancing or not. Following conditions defines the procedure for the same.

if (SD>threshold) {
Overloaded =True; load balancing is needed as the machine is overloaded.}
Else if (SD<threshold) {
Underloaded =True; load balancing is not needed here.}

3) Overloaded machines search for the underloaded machines to share their load i.e. they demand for the capacity for machine which can take the overloaded tasks

Demand_OverLoadedVM = Load – Capacity_VM

4) Underloaded machines search for the overloaded machines to take the load of overloaded machine i.e. they supply the capacity which can be taken by the overloaded tasks

Supply_OverLoadedVM = Capacity_VM-Load

RESULT AND DISCUSSIONS

The proposed approach had been simulated using JAVA JDK Netbeans IDE with cloudsim 3.0 simulator. The results had been analysed on various workloads with different number of virtual machines and cloudlets compared with other existing techniques including First Come First Serve (FCFS), Shortest-Job-First (SJF), MOSA (multi-objective scheduling algorithm), EMOSA (Enhanced multi-objective scheduling algorithm) in terms of average waiting time, total processing cost and total processing time (Table 1).

Table 1
List of Constraints for Investigation of Consequences

CloudSim Objects	Input Specifications	Value
Job	Len_Cloudlet	100-20000
	Number._of_Cloudlets	10-2000
Virtual Machine	Count_of_Vm	3-100
	MIPS_Vm	250-2000
	VM_Memory	512-2048
	VM_BW	500-1000
	Pes_Count	1-4
Server (Datacenter)	Number_of._Datacenters	2-5
	Hosts_Count	2-6

Analysis in terms of Average Waiting Time

Average Waiting Time (AWT) is the time the task has to wait for the virtual machine. Average waiting Time is defined using the below Equation 1:

$$\frac{\sum_{i=0}^{no\ of\ cloudlets} cloudlet.waitingtime()cloudlet.WaitingTime}{No.of\ Cloudlets} \quad (1)$$

Figure 1 and Table 2 show the comparison results of Average Waiting Time of the propounded algorithm EMOLB_LB with other existing algorithms. Figure 1 shows that the proposed algorithm performs better than the other procedures. For workload with 60 vms and 500 cloudlets, the AWT is 0. 4913 ms , EMOSA (Narwal & Dhingra, 2017) is having

Table 2

Simulation results of EMOSA_LB in terms of AWT

[Virtual Machine, Cloudlets]	First Come First Serve	Shortest Job First	Multi Objective Scheduling	E-Multi Objective Scheduling	EMOLB_LB
[3,9]	0.7591	0.6598	0.4469	0.4067	0.3625
[3,50]	0.7096	0.5964	0.4284	0.3947	0.3796
[30, 200]	1.98694	0.8026	0.5694	0.4954	0.4498
[40, 300]	1.42684	0.8569	0.5967	0.5036	0.4874
[60, 500]	1.52146	0.8832	0.5712	0.5169	0.4913

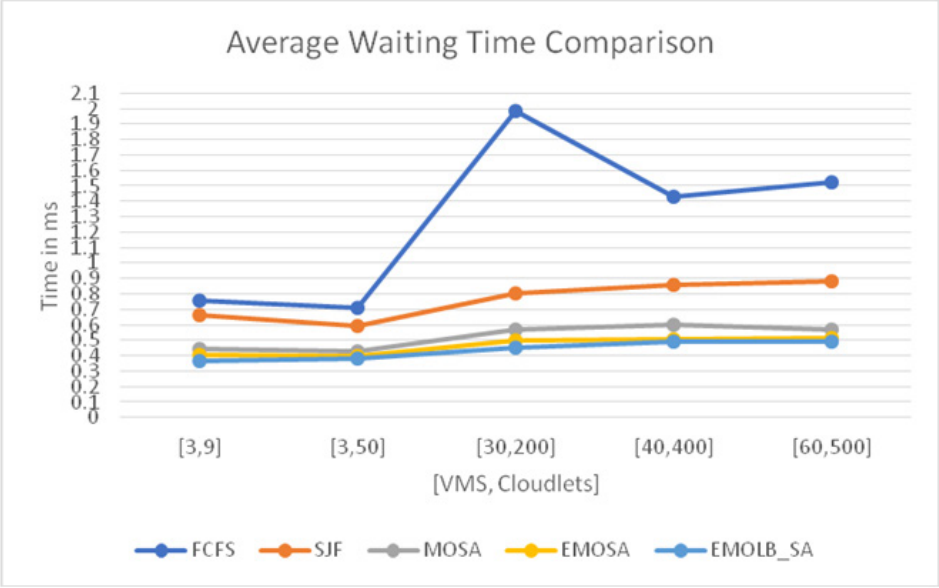

Figure 1. AWT of EMOLB_SA in contrast with EMOSA, MOSA, FCFS and SJF

0.5169 ms, MOSA (Lakra & Yadav, 2015) is 0.5712 ms, SJF (Ru & Keung, 2013) is 0.8832 ms and FCFS (Silberschatz et al., 2014) is 1.52146 ms. Similarly, for other workloads, the propounded EMOLB_LB performs better than other methods. The average waiting time improvement over the existing EMOSA scheduling technique is 2.934% approximately.

Analysis in terms of Processing Cost

It is the rate essential by the task to accomplish on the machine. Total Processing Cost can be denoted by below Equation 2

$$Total\ Processingcost = \sum DataCenterCharateristics_{costpermemory} * VM_{RAM} \quad (2)$$

Table 3

Simulation consequences of EMOSA_LB in relation to processing cost

[Virtual Machine, Cloudlets]	First Come First Serve	Shortest Job First	Multi Objective Scheduling	E-Multi Objective Scheduling	EMOLB_LB
[3,9]	309.9	298.3	220.18	117.9	107.7
[3,50]	596.36	546.36	524.6	315.3	211.7
[30, 200]	8569.3	6895.3	6369.365	6132.69	5880.94
[40, 300]	14012.05	10315.05	9704.36	9584.78	7232.99
[60, 500]	38569.75	21600.56	18695.34	18201.69	17037.92

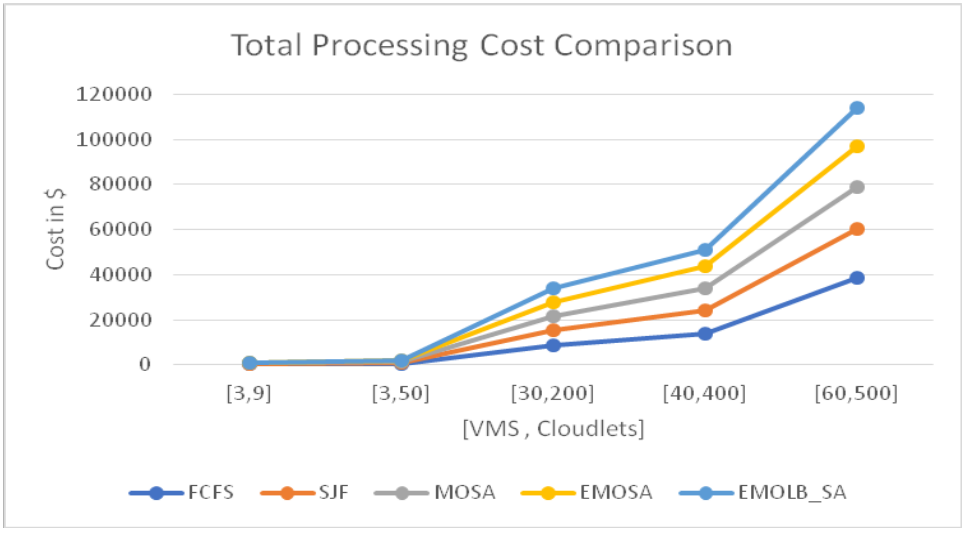

Figure 2. Total processing cost of EMOLB_SA with EMOSA, MOSA SJF and FCFS

Figure 2 and Table 3 show the comparison results of Total Processing Cost of the propounded algorithm EMOLB_LB with other existing algorithms. Figure 2 shows that the proposed algorithm performs better than the other procedures. For workload with

60 vms and 500 cloudlets, the TPC is 17037.92, EMOSA (Narwal & Dhingra, 2017) is having 18201.69, MOSA (Lakra & Yadav, 2015) is 18695.34, SJF (Ru & Keung, 2013) is 21600.56 and FCFS (Silberschatz et al., 2014) is 38569.75. Similarly, for other workloads, the propounded EMOLB_SA performs better than other methods. The Total Processing Cost improvement over the existing EMOSA scheduling technique is 17.6% approximately.

Analysis in terms of Processing Time

It is the period occupied by the machine to accomplish the job on particular virtual machine. Total Processing time is depicted using the below mentioned Equation 3

$$Total\ Processing_{time} = \sum cloudlet_{length} / (vm_{MIPS} * no_{ofPES}) \quad (3)$$

Table 4

Simulation consequences of EMOSA_LB in relation to processing time

[Virtual Machine, Cloudlets]	First Come First Serve	Shortest Job First	Multi Objective Scheduling	E-Multi Objective Scheduling	EMOLB_LB
[3,9]	4003.64	3994.37	3745.89	3438.65	1402.055
[3,50]	24778.39	23965.54	22648.31	21325.32	10792.71
[30, 200]	196547.2	189624.2	151847.73	124920.7	101918.2
[40, 300]	532652.37	465287.61	386547.97	346215.4	131059.3
[60, 500]	958634.62	935697.25	9.16E+05	894631.17	142625.8

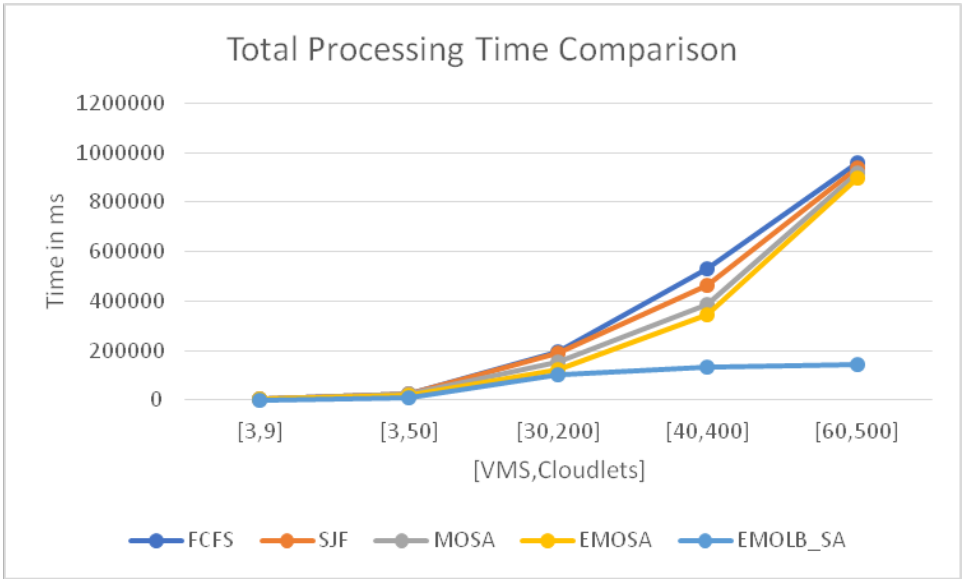

Figure 3. Total processing time of EMOLB_SA with EMOSA, MOSA SJF and FCFS

Figure 3 and Table 4 show the comparison results of Total Processing Time of the propounded algorithm EMOLB_LB with other existing algorithms. Figure 3 shows that the propounded algorithm performs better than the other procedures. For workload with 60 vms and 500 cloudlets, the TPT is 142625.8 ms, EMOSA (Narwal & Dhingra, 2017) is having 894631.17 ms, MOSA (Lakra & Yadav, 2015) is 916358.66 ms, SJF (Ru & Keung, 2013) is 935697.56 ms and FCFS (Silberschatz et al., 2014) is 958634.62 ms. Similarly, for other workloads, the propounded EMOLB_LB performs better than other methods. The Total Processing time improvement over the existing EMOSA scheduling technique is 20.5% approximately.

CONCLUSION

In this paper an effective adjustment of Enhanced Multi-objective task algorithm with Load balancing for a task scheduling has been done. The propounded algorithm is replicated in cloudsim simulator using netbeans IDE and shows that the results are better than the existing procedures Various calculations had been performed in order to minimize the aggregate processing time, cost and average waiting time of a given arrangement of tasks and comparisons of results had been performed with already existing algorithms. The Proposed algorithm increases the efficiency, throughput and accuracy of resource utilization on the cloud network. This proposed technique is ideal for task scheduling which provides the best scheduling solution in an optimal processing time. The future extension is to comprehend and to enhance the proposed calculation by using resource aware and more load balancing algorithms.

ACKNOWLEDGEMENT

The authors are sincerely thankful to the Vice Chancellor and Registrar of Maharshi Dayanand University, Rohtak for all the support to pursue the Doctorate of Research.

REFERENCES

Abdullah, M., & Othman, M. (2013). Cost-based multi-QoS job scheduling using divisible load theory in cloud computing. *Procedia Computer Science, 18*, 928-935.

Bhatia, A., & Sharma, R. (2015). An analysis report of workflow scheduling algorithm for cloud environment. *International Journal of Computer Applications, 119*(12), 21-25.

Bini, B. T., & Sindhu, S. (2015). Scheduling in cloud based on hyper-heuristics. International *Journal for Research in Applied Science & Engineering Technology, 3*, 380-383.

Foster, I., Zhao, Y., Raicu, I., & Lu, S. (2008, November 12-16). Cloud computing and grid computing 360-degree compared. In *2008 Grid Computing Environments Workshop* (pp. 1-10). Austin, TX, USA.

Ghanbari, S., & Othman, M. (2012). A priority based job scheduling algorithm in cloud computing. *Procedia Engineering, 50*(0), 778-785.

Guo, L., Zhao, S., Shen, S., & Jiang, C. (2012). Task scheduling optimization in cloud computing based on heuristic algorithm. *Journal of Networks, 7*(3), 547-553.

Kanani, B., & Maniyar, B. (2015). Review on max-min task scheduling algorithm for cloud computing. *Journal of Emerging Technologies and Innovative Research, 2*(3), 781-784.

Kowsik, P., & Rajakumari, K. (2014). A Comparative Study on Various Scheduling Algorithms in Cloud Environment. *International Journal of Innovative Research in Computer and Communication Engineering, 2*(11), 112-121.

Lakra, A. V., & Yadav, D. K. (2015). Multi-objective tasks scheduling algorithm for cloud computing throughput optimization. *Procedia Computer Science, 48*, 107-113.

Lawrance, H., & Silas, S. (2013). Efficient Qos based resource scheduling using PAPRIKA method for cloud computing. *International Journal of Engineering Science and Technology, 5*(3), 638-643.

Mathukiya, E. S., & Gohel, P. V. (2015). Efficient QoS Based Tasks Scheduling using multi-objective optimization for cloud computing. *International Journal of Innovative Research in Computer and Communication Engineering, 3*(8), 7169-7173.

Narwal, A., & Dhingra, S. (2016). A systematic review of scheduling in cloud computing framework. *International Journal of Advanced Studies in Computers, Science and Engineering, 5***(7)**, 1-9.

Narwal, A., & Dhingra, S. (2017). Enhanced task scheduling algorithm using multi-objective function for cloud computing framework. In *International Conference on Next Generation Computing Technologies* (pp. 110-121). Singapore: Springer.

Narwal, A., & Dhingra, S. (2019). Performance analysis of multiobjective algorithms for cloud computing framework. *Journal of Advanced Research in Dynamical and Control Systems, 11*(05-Special Issue), 2093-2099.

Patel, S. J., & Bhoi, U. R. (2014, August 27-29). Improved priority based job scheduling algorithm in cloud computing using iterative method. *In 2014 Fourth International Conference on Advances in Computing and Communications* (pp. 199-202). Cochin, India.

Raja, K., & Sekar, G. (2016). An algorithm for credit based scheduling in cloud computing environment depending upon deadline strategy. *IOSR Journal of Computer Engineering (IOSR-JCE), 2*(8), 70-76.

Ru, J., & Keung, J. (2013, June 4-7). An empirical investigation on the simulation of priority and shortest-job-first scheduling for cloud-based software systems. In *2013 22nd Australian Software Engineering Conference* (pp. 78-87). Melbourne, VIC, Australia.

Shameer, A. P., & Subhajini, A. C. (2017, September 8-9). Throughput maximization on efficient load balancing in cloud task scheduling using enhanced bee colony algorithm. In *2017 International Conference on Current Trends in Computer, Electrical, Electronics and Communication (CTCEEC)* (pp. 294-298). Mysore, India.

Silberschatz, A., Galvin, P. B., & Gagne, G. (2014). *Operating system concepts essentials*. Hoboken, New Jersey: John Wiley & Sons, Inc.

Singh, R. M., Paul, S., & Kumar, A. (2014). Task scheduling in cloud computing. *International Journal of Computer Science and Information Technologies (IJCSIT), 5*(6), 7940-7944.

Singh, S., & Kalra, M. (2014). Task scheduling optimization of independent tasks in cloud computing using enhanced genetic algorithm. *International Journal of Application or Innovation in Engineering and Management, 3*(7), 2319-4847.

Tripathy, L., & Patra, R. R. (2014). Scheduling in cloud computing. *International Journal on Cloud Computing: Services and Architecture (IJCCSA), 4*(5), 21-7.

Vijay, Y., & Ghita, B. V. (2017, July). Evaluating cloud computing scheduling algorithms under different environment and scenarios. In *2017 8th International Conference on Computing, Communication and Networking Technologies (ICCCNT)* (pp. 1-5). IEEE.

Xiao, P., Hu, Z., Liu, D., Zhang, X., & Qu, X. (2014). Energy-efficiency enhanced virtual machine scheduling policy for mixed workloads in cloud environments. *Computers and Electrical Engineering, 40*(5), 1650-1665.

Zalavadiya, K., & Vaghela, D. (2016). Honey bee behavior load balancing of tasks in cloud computing. *International Journal of Computer Applications, 139*(1), 16-19.

Zhan, S., & Huo, H. (2012). Improved PSO-based task scheduling algorithm in cloud computing. *Journal of Information and Computational Science, 9*(13), 3821-3829.

Pertanika J. Sci. & Technol. 28 (3): 1063 - 1080 (2020)

PERTANIKA JOURNALS

SCIENCE & TECHNOLOGY

Journal homepage: http://www.pertanika.upm.edu.my/

Spectrum Efficiency of Modulation Schemes for Network Optimization in 5GHz Dense Environments

Mina Malekzadeh

Faculty of Electrical and Computer Engineering, Hakim Sabzevari University, Sabzevar, Iran

ABSTRACT

For reliable data transmission, 802.11ax standard employs various orders of modulation schemes with a forward error correction method performing different coding rates (CR). Higher-order modulation schemes can enhance the data rate, but at the same time increasing the possibility of data corruption and bit error occurrence. Moreover, in wireless communications, each modulation scheme can be used with different guard intervals and channel bandwidths. A shorter guard interval increases the data rate at the cost of increasing the interferences and data loss. A longer guard interval solves the issue but at the cost of the performance reduction due to wasting the useful bandwidth. With regards to channel bandwidth, although wider channels increase the data rate, they are subject to more signal interference. This can get even worse in the high-density deployment of 802.11ax where many users are placed in close distance and the signal interferences are strong. Thus, aside from the modulation orders and coding rates parameters, the efficiency of modulation schemes relies on the channel bandwidth and guard interval which demands the proper selection of these parameters. Consequently, this work proposes a simulation model to optimize the performance of the 802.11ax network regarding the modulation schemes under high-density conditions. The model includes all available modulation schemes and their corresponding coding rates along with the channel bandwidth and guard interval. The model is further implemented and the most efficient values for performance optimization are determined on the basis of bit error rate, throughput and its efficiency, end-to-end delay, loss ratio, and jitter.

Keywords: Bit error rate (BER), coding rate, forward error correction (FEC), performance optimization

ARTICLE INFO

Article history:
Received: 6 February 2020
Accepted: 21 April 2020
Published: 16 July 2020

E-mail address:
m.malekzadeh@hsu.ac.ir

ISSN: 0128-7680
e-ISSN: 2231-8526

© Universiti Putra Malaysia Press

INTRODUCTION

The high-efficiency wireless (HEW) 802.11ax standard officially launched at the end of 2019 to improve wireless communication in dense environments where a large number of users are transmitting data simultaneously on the same connection link. To achieve the objectives, the standard employs different parameters, among which is higher-order modulation schemes compared to the previous wireless standards (Otsuka et al., 2019). The modulation algorithms encode data bits into symbols and transmit them using a carrier signal by modifying its properties. In order to provide the reliability of the data, the modulation schemes employ the forward error correction (FEC) method with different coding rates (CR). The FEC adds redundant information to control occurring errors in the data and the CR is a fraction that determines how much of the data is redundant (Vijay & Malarkodi, 2019; Bellaltaa & Szott, 2019). The CR is denoted as the ratio k/n which indicates that for every k bits of useful information, the coder generates n bits of data, of which n-k are redundant.

The 802.11ax standard includes a variety of modulation schemes with different coding rates as follows (Vijay & Malarkodi, 2019; Adame et al., 2019):

- The binary phase-shift keying (BPSK) with two different symbols and one bit per symbol. It includes a single coding rate of 1/2.
- The quadrature phase-shift keying (QPSK) with four different symbols and two bits per symbol. It includes two different coding rates of 1/2 and 3/4.
- The quadrature amplitude modulation (QAM) with the following variants:
    - The 64-QAM encodes data with 64 different symbols and six bits per symbol. It includes 2/3, 3/4, and 5/6 coding rates.
    - The 256-QAM encodes data with 256 different symbols and eight bits per symbol. It includes 3/4 and 5/6 coding rates.
    - The 1024-QAM encodes data with 1024 different symbols and ten bits per symbol. It includes 3/4 and 5/6 coding rates.

Theoretically, increasing the number of symbols in modulation schemes will increase the overall speed because more bits of data are transmitted per each symbol. However, this happens at the cost of receiver sensitivity and range reduction. The sensitivity shows how well a device can receive the signals, hence, reducing the receiver sensitivity increases the possibility of data corruption and bit error rate (BER) that indicate the loss of data and the number of bit errors per unit of time, respectively (Naik & Reddy, 2017). Furthermore, in wireless communications, each modulation scheme can be used with different guard intervals and channel bandwidths. Practically, aside from the modulation orders and coding rates, the efficiency of modulation schemes relies on channel bandwidths and guard intervals.

The guard interval is the time spacing between the symbols to avoid inter-symbol interference. The 802.11ax standard supports short, medium, and long guard intervals (Deng et al, 2017). Utilizing a shorter guard interval, on one hand, increases the data rate (the rate at which the data is transmitted), but on the other hand, it increases the symbols interferences due to reducing the spacing between the symbols and hence results in higher data loss. In the 802.11ax network, any type of data with different requirements is transmitted over for which the guard interval value is set regardless of the type. In this context, if the data is real-time, a shorter guard interval can increase the interferences and cause data loss, for which the real-time data has zero tolerance (D-Link, 2013). In order to solve this issue, the longer guard intervals can be utilized in the networks but at the cost of performance reduction due to allocating useful bandwidth as the space between the symbols instead of using them for data transmission (Vijay & Malarkodi, 2019). Thus, a choice has to be made on high dense deployment of 802.11ax to determine and apply the proper guard interval based on the network requirements regarding the specific modulation schemes. The channel bandwidth is the other parameter affecting the efficiency of the modulation schemes in the network as it controls the rate of data transfer. The 802.11ax standard provides wide and narrow channels (Vijay & Malarkodi, 2019; Deng et al, 2017). Although utilizing wider channels will provide higher data rates and consequently, optimize the overall network performance, they are subject to more signal interference. This can get even worse in the high-density deployment of 802.11ax where many users are placed in close distance and the signal interferences are already high. In this context, it is essential to determine the efficiency of all available channel bandwidths and identify the best selection for high-density 802.11ax network in conjunction with the specific modulation schemes.

Rochim and Sari (2016) studied the fifth-generation mobile networks (5G) and examined the efficiency of higher-order modulation schemes in these networks. The performance of 1024-QAM and 4096-QAM with 1/3, 1/2, 2/3, and 3/4 coding rates were compared with QPSK to 256-QAM. The results were obtained in terms of bit error rate, whereas 802.11ax HEW network, channel bandwidths, guard intervals, and other performance metrics were not taken into account. The QPSK to 256-QAM modulation schemes over 802.11ac networks were investigated in Khan et al. (2016). The functionality was investigated for different channel bandwidths from 20 to 160 MHz as a function of payload size and the number of stations. The SNR and error rates were measured for comparison purposes, though 802.11ax networks, guard intervals, and other metrics were not evaluated. Weller et al. (2019) compared the throughput performance of 1024-QAM with 256-QAM in 802.11ax. Despite that, other modulation schemes, channel bandwidths, and performance metrics were not implemented. The effectiveness of modulation schemes was evaluated in Masiukiewicz (2019) to compare 802.11ax throughput with 802.11ac and 802.11n by varying the channel bandwidth as 40, 80, and 160 MHZ. However,

measurement of other metrics and also the implementation of the narrower channels, including 20MHz and 40MHz were not verified. The BPSK to 256-QAM modulation schemes were evaluated in Hoefel and Bejarano (2016) over the 802.11ax network. The measurement results with regard to error rates and SNR were provided, nonetheless, implementation of other higher-order modulation schemes and performance metrics were not available. A testbed was set up by Codau et al. (2017) for the throughput evaluation of modulation schemes in the 802.11ac network. However, the experimental evaluation did not include 802.11ax and other essential performance measurements. Likewise, a testbed was also presented in Sheshadri and Koutsonikolas (2017) over 802.11ac to obtain the loss ratio in the presence of modulation schemes. The performance of 802.11af standard over 6MHz channel bandwidth was analyzed in Brioso et al. (2018). The efficiency of BPSK to 256-QAM modulation schemes were measured in connection with throughput. However, 802.11ax and other performance metrics were not included. Assessment of LTE cellular network was provided in Naik and Reddy (2017) to determine the performance under different modulation schemes, including QPSK, 16-QAM, and 64-QAM. The SNR results as a function of bit error rate were presented without regard to guard intervals, other metrics, higher-order modulations, and 802.11ax networks. The MATLAB simulator was used in Ghosh (2016) for the analysis of LTE modulation schemes, including QPSK, 16-QAM, and 64-QAM. The SNR and BER results were obtained, but no evaluation over 802.11ax was performed. Rochim and Sari (2016) took into consideration the efficiency of BPSK to 64-QAM modulation schemes in 802.11ac and compared them with those of 802.11n. However, the performance assessment of 802.11ax with its available modulation schemes was not verified. The possible modulation schemes in 802.11ax for vehicle-use were implemented in Akbilek et al. (2018). The performance of the schemes was compared regarding the SNR and error rate. However, the assessment did not involve channel bandwidths, guard intervals, and other performance metrics such as throughput, loss ratio, end-to-end delay, and jitter.

From the related works, there is a lack of a comprehensive study to identify the performance of all available modulation schemes for the 802.11ax network in relation to the available channel bandwidths and guard intervals. Thus, on the basis of this background, this work proposed a model to initially identify the efficiency of the available modulation schemes in line with all the channel bandwidths, coding rates, and guard intervals for the 802.11ax network and determine the best-suited selections for performance optimization under high-density conditions. Three main contributions of this work are: first, to examine different orders of all available modulation schemes in line with coding rates and identify the best selections, second, to assess the performance of all the available guard intervals and identify the best-suited values, third, to resolve the significance of channel bandwidths on performance variations and determine the best values for performance optimization. The

rest of the work is organized as follows. Section 2 provides details regarding the simulation model and parameters. Section 3 presents the results and Section 4 concludes the work.

MATERIALS AND METHODS

This work proposed a model to optimize the performance of 802.11ax networks in high dense deployment regarding the efficiency of modulation schemes. The model developed an 802.11ax network in the 5GHz spectrum frequency band using the network simulator version 3 (NS3.29). The network included an 802.11ax-enabled access point to which 100 users were connected to create a high-density area. Furthermore, the network included an application server which generated data at the rate of 2Mbps. The data was transmitted from the application server to all the users simultaneously in a downlink direction. A simplified presentation of the simulated 802.11ax is provided in Figure 1.

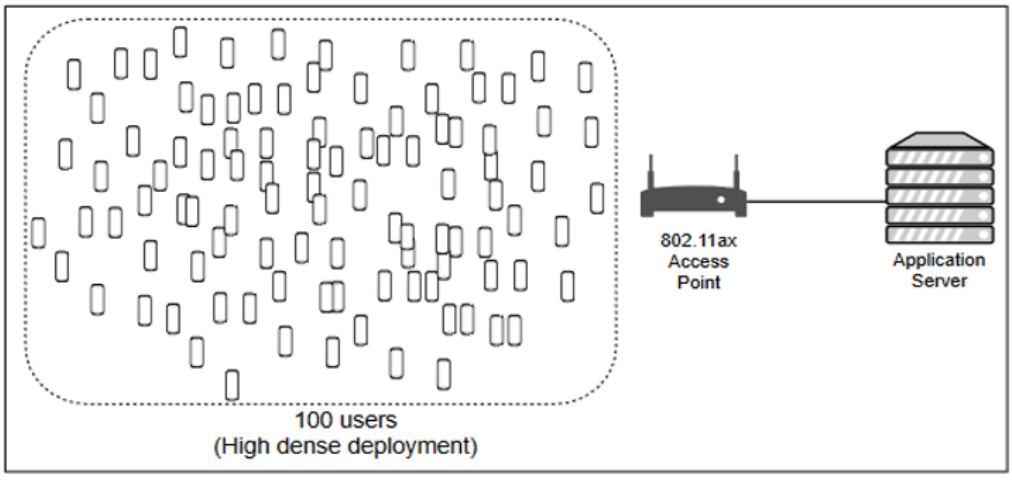

Figure 1. The 802.11ax simulation environment

For encoding of the data, the model included all modulation schemes that were supported by the 802.11ax standard. The modulation algorithms (MA) supported by the model and the corresponding coding rates (CR) are as follows:

- MA=BPSK, CR=1/2.
- MA=QPSK, CR=1/2 and 3/4.
- MA=16-QAM, CR=1/2 and3/4.
- MA=64-QAM, CR=2/3, 3/4, and 5/6.
- MA=256-QAM, CR=3/4 and 5/6.
- MA=1024-QAM, CR=3/4 and 5/6.

Furthermore, in 802.11ax, each modulation scheme can be used with different guard intervals and channel bandwidths. Thus, the model supports the following channel bandwidth (CW) and guard intervals (GUI):

- CW= 20MHz, 40MHz, 80MHz, and 160MHz.
- GUI=800ns, 1600ns, and 3200ns.

The internet protocol (IP) at the network layer used by the model to transmit the encoded data was version 6 (IPv6) due to offering more IP addresses which were required in dense networks with large number of devices. Moreover, the propagation loss model was Friis and the propagation delay was Constant Speed. The number of transmitting and receiving spatial streams was one as defined by default in the 802.11ax standard. The model evaluation was done based on BER, end-to-end-delay, packet loss ratio, and throughput and its efficiency. The throughput efficiency was measured as the difference between the application and simulation throughputs (Masiukiewicz, 2019). A summary of the main simulation parameters is provided in Table 1.

Table 1
Simulation parameters

Parameter name	Parameter description
Network standard	802.11ax
Radio band frequency	5GHz
User density	100 users (high-density)
Modulation schemes	BPSK, QPSK, 16-QAM, 64-QAM, 256-QAM, 1024-QAM
Corresponding FEC coding rate	1/2, 3/4, 2/3, 5/6
Propagation loss model	Friis
Propagation delay	Constant Speed
Traffic pattern	UDP Streaming
Network protocol	IPv6
Application data rate	2Mbps

RESULTS AND DISCUSSIONS

This section presents the results from the implementation of the model and determines the proper parameter selection for the performance optimization of 802.11ax with dense users.

BPSK with 1/2 Coding Rate

The binary phase-shift keying modulation scheme with two different symbols and one bit per symbol using 1/2 coding rate was implemented with all four channel bandwidths and three available guard intervals. The results are provided in Figure 2.

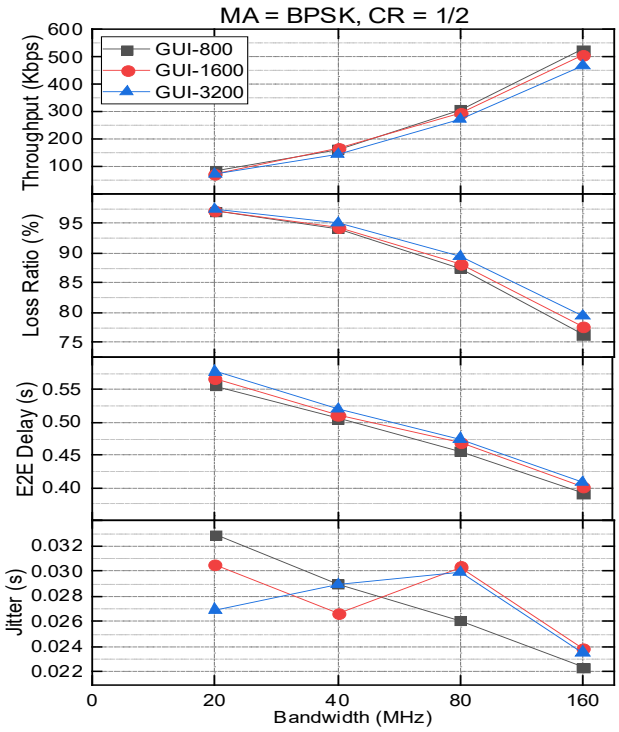

Figure 2. BPSK scheme with 1/2 coding rate

As we mentioned, the application data rate was 2Mbps in all the simulation scenarios. Comparing this rate with the archived throughput by BPSK showed that the algorithm was not able to provide a high-level performance for the end-users. Moreover, based on the results we observed that changing the guard interval from small to larger values did not significantly affect the performance of real-time applications. In contrast, the results confirmed a significant effect of the wider channels on the performance improvement of the end-users. In this context, the least performance was achieved by 20MHz channel bandwidth while 160MHz channel resulted in the best performance. When channel bandwidth was selected 20MHz, the functionality of BPSK compared to application data rate reduced to about 5% which was extremely low. In contrast, using 160MHz under high-density conditions provides 25% functionality for the end-users of real-time applications. Thus, although the result shows the inefficiency of the BPSK modulation scheme in high dense areas, the algorithm performed better when wider channels are used. The throughput efficiency of BPSK relating to the channel width and the guard interval index is provided in Table 2.

Table 2

BPSK throughput efficiency comparison

CW (MHz)	Efficiency, η (%)		
	GUI=800ns	GUI=1600ns	GUI=3200ns
20	4.19	3.68	3.45
40	8.13	8.23	7.23
80	15.31	14.66	13.68
160	26.37	25.28	23.30

QPSK with 1/2 and 3/4 Coding Rates

This section implements the quadrature phase-shift keying with four different symbols and two bits per symbol. Since the scheme supports two distinct coding rates including 1/2 and 3/4, the model implements both of them in line with four existing channel bandwidths and three guard intervals. The results of 1/2 and 3/4 coding rates are provided in Figure 3 (left) and (right), respectively.

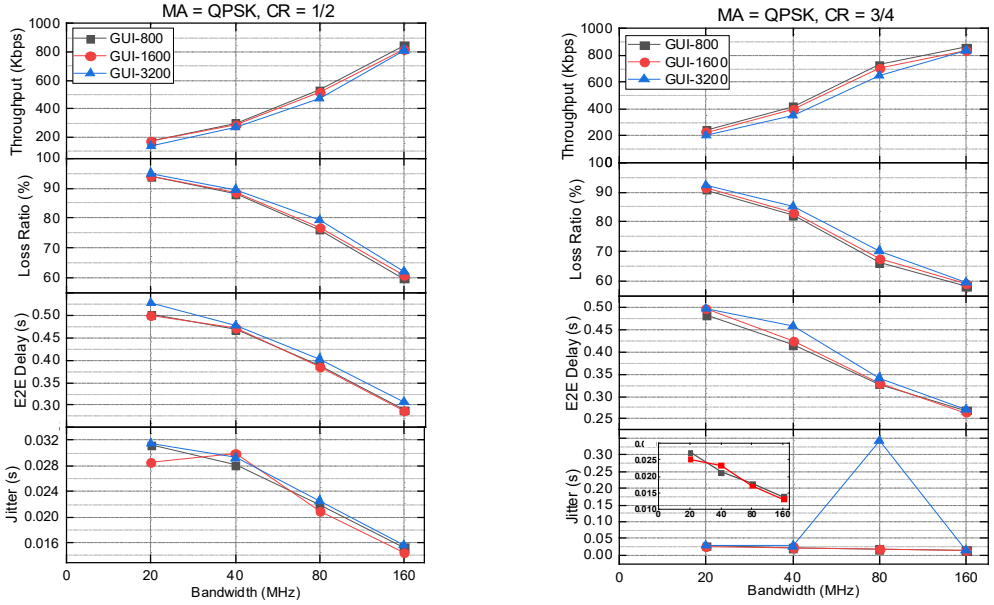

Figure 3. QPSK scheme with 1/2 (left) and 3/4 (right) coding rates

Regardless of the coding rates, the QPSK results showed its better performance compared to BPSK as it provided 40% improvement of the application data rate at the best consideration. Moreover, the results are consistent with BPSK in the context of better performance of the end-users with wider channels, unlike guard interval values which do not have a considerable effect. The comparison over the 1/2 and 3/4 coding rates shows

that when QPSK algorithm was used with 3/4 coding rate, real-time applications provided better services for the end-users in terms of throughput, delay, and loss ratio. However, jitter results showed otherwise for 80MHz channels which provided significantly high jitter values compared to other bandwidths and compared to 1/2 coding rate. This proved that using 80MHz channels for jitter-sensitive applications in high dense 802.11ax was not efficient as it highly degraded the performance of these services. The throughput efficiency of QPSK with 1/2 and 3/4 coding rates relating to the channel width and guard interval is provided in Table 3.

Table 3
QPSK throughput efficiency comparison

CR	CW (MHz)	Efficiency, η (%)		
		GUI=800ns	GUI=1600ns	GUI=3200ns
1/2	20	8.42	8.47	6.80
	40	14.91	14.51	13.53
	80	26.60	25.86	23.60
	160	42.19	40.96	40.69
3/4	20	12.20	11.29	10.24
	40	20.77	19.78	17.61
	80	36.47	35.44	32.51
	160	43.09	41.95	41.65

16-QAM with 1/2 and 3/4 Coding Rates

This section implements the quadrature amplitude modulation scheme with 16 different symbols and four bits per symbol. The scheme supported two distinct coding rates including 1/2 and 3/4, hence, the model implemented them for the available channel bandwidths and guard intervals for the high dense deployment of 802.11ax. The results from the implementation of 16-QAM with 1/2 and 3/4 coding rates are provided in Figure 4 (left) and (right), respectively.

The obtained results show interesting findings. It was observed that while increasing the order of modulation from 4 (QPSK) to 16 (16-QAM) did not affect the widest channels (160MHz), it enhanced the performance of the narrower channels including 20, 40, and 80MHz. This is because the 802.11ax in the model is under highly dense conditions with 100 users that are exchanging heavy loads of real-time traffic simultaneously on the network. This will bring the network to its ultimate capacity and cannot go beyond that. The level of performance improvement of the narrow channels increased, even more, when 3/4 coding rate was utilized by the 16-QAM scheme compared to 1/2 coding rate. In this context, different guard interval values provide a close level of performance and their variations

do not considerably change the experience of the end-users. Thus, when utilizing the 16-QAM scheme in the high dense deployment of 802.11ax network, deploying the 3/4 coding rate with 80 and 160MHz channel bandwidth is best-suited with any available value for the guard interval. The throughput efficiency of 16-QAM with 1/2 and 3/4 coding rates relating to the channel width and guard interval is provided in Table 4.

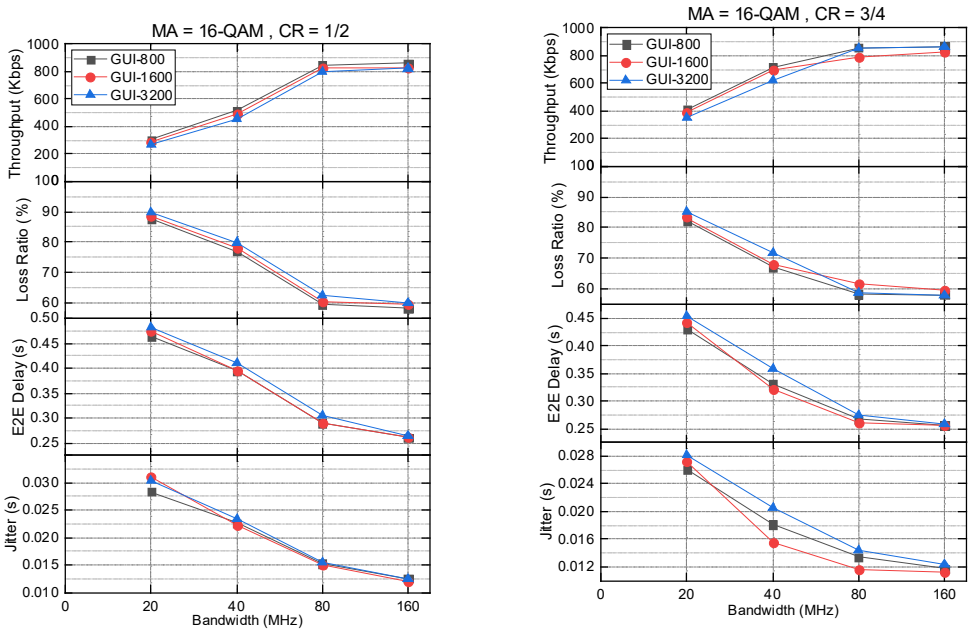

Figure 4. 16-QAM scheme with 1/2 (left) and 3/4 (right) coding rates

Table 4

16-QAM throughput efficiency comparison

CR	CW (MHz)	Efficiency, η (%)		
		GUI=800ns	GUI=1600ns	GUI=3200ns
1/2	20	15.12	14.32	13.21
	40	25.86	24.73	22.89
	80	42.24	41.41	39.78
	160	43.05	41.49	41.17
3/4	20	20.54	19.45	17.52
	40	35.73	34.92	31.05
	80	42.92	39.32	42.90
	160	43.13	41.55	43.14

64-QAM with 2/3, 3/4, and 5/6 Coding Rates

This section increases the order of the quadrature amplitude modulation scheme to 64 different symbols and six bits per symbol while the possible coding rates are 2/3, 3/4, and 5/6. The model implemented the three coding rates in accordance with the four available channel bandwidths and three guard intervals. The results from the implementation of 64-QAM with 2/3, 3/4, and 5/6 coding rates are provided in Figure 5 (left), (middle), and (right), respectively.

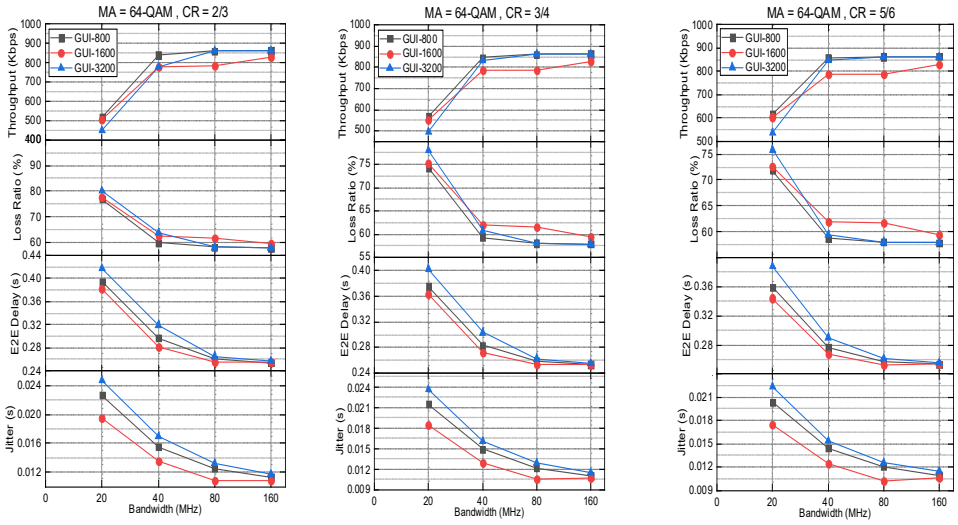

Figure 5. 64-QAM scheme with 2/3 (left), 3/4 (middle), and 5/6 (right) coding rates

The results show the efficiency of 64-QAM scheme to enhance the performance achieved by the narrower channels to a level close to wider channels. In this context, the 40MHz channel achieved similar performance as 80 and 160MHz channels. Moreover, unlike before, different values of guard intervals result in different performance achievements under similar conditions. The longer guard interval value increases delay and jitter to which real-time applications have zero tolerance. Additionally, increasing the guard interval decreases the throughput and increases loss ratio which is not suitable for high-speed demand applications. With regard to different coding rates, they do not considerably change the performance. The end-users' experience using 2/3 coding rate is at a similar level as 3/4 and 5/6 coding rates. Therefore, to enhance the performance of high-density 802.11ax networks using 64-QAM, employing 40, 80, and 160 MHz channel bandwidth with the shortest guard interval (800ns) is the best combination while coding rate's impact is not significant. The throughput efficiency of 64-QAM with 2/3, 3/4, and 5/6 coding rates relating to the channel width and guard interval is provided in Table 5.

Table 5

64-QAM throughput efficiency comparison

CR	CW (MHz)	Efficiency, η (%)		
		GUI=800ns	GUI=1600ns	GUI=3200ns
2/3	20	25.86	25.12	22.42
	40	42.05	38.88	38.95
	80	43.05	39.32	43.09
	160	43.14	41.55	43.22
3/4	20	28.39	27.59	24.69
	40	42.36	39.33	41.64
	80	43.11	39.36	43.12
	160	43.19	41.52	43.20
5/6	20	30.87	30.17	26.81
	40	42.85	39.31	42.39
	80	43.12	39.35	43.16
	160	43.16	41.55	43.18

256-QAM with 3/4 and 5/6 Coding Rates

This section increases the order of quadrature amplitude modulation to 256 different symbols and eight bits per symbol with the existing coding rates as 3/4 and 5/6. Accordingly, the model implements the 256-QAM modulation scheme with the two available coding rate, four channel bandwidths, and three guard intervals. The results for 3/4 and 5/6 coding rates are presented in Figure 6 (left) and (right), respectively.

The results show different findings than before. For all the previous modulation schemes in the model ranging from BPSK to 256-QAM, increasing the bandwidth of channel results in increasing the performance so that the highest performance is achieved by 160MHz channel. However, the results prove otherwise in 256-QAM algorithm. When 256-QAM used 3/4 coding rate, the highest performance in terms of throughput and loss ratio was achieved for 40 and 80 MHz channel bandwidths. However, with reference to delay and jitter, the best performance belongs to the 160MHz channel. Thus, with 3/4 coding rate, for the bandwidth demanded applications the 40 and 80 MHz channels were suitable while for delay-sensitive application, 160MHz channel was suited more. Turning now to 5/6 coding rate appeared some similarities and some differences with 3/4 coding rate. While the best channel bandwidths for 256-QAM with 3/4 coding rate were 40 and 80 MHz, for 5/6 coding rate, the best channel bandwidths are 20, 40, and 80 MHz for bandwidth-demand applications. Moreover, for delay-sensitive applications, like before, using 160MHz channels were more suitable. With respect to guard interval, the 5/6 coding rate was less sensitive to guard interval values while in 3/4 coding rate using a shorter guard

interval improved the performance. The throughput efficiency of 256-QAM with 3/4 and 5/6 coding rates relating to the channel width and guard interval is provided in Table 6.

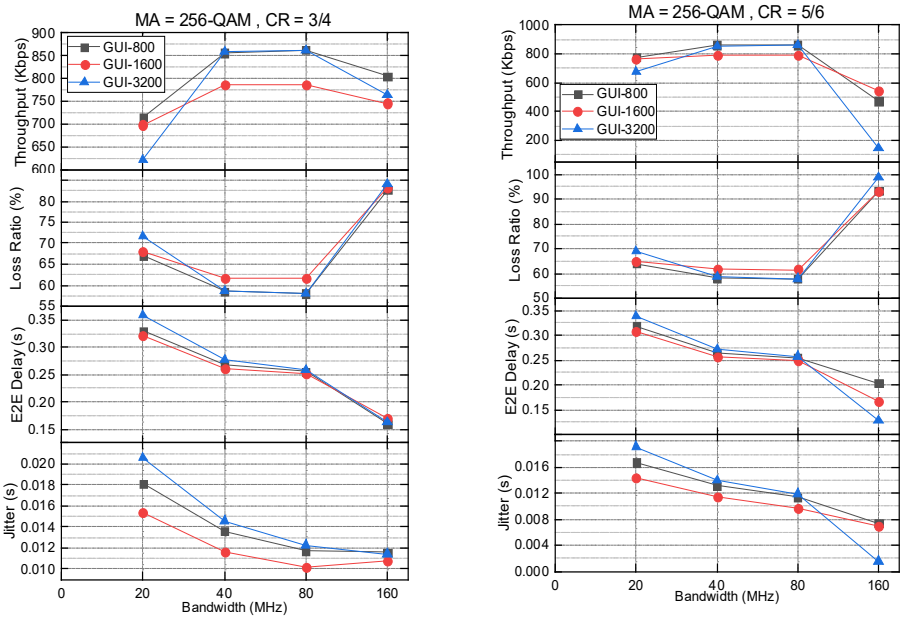

Figure 6. 256-QAM scheme with 3/4 (left) and 5/6 (right) coding rates

Table 6

256-QAM throughput efficiency comparison

CR	CW (MHz)	Efficiency, η (%)		
		GUI=800ns	GUI=1600ns	GUI=3200ns
1/2	20	35.72	34.92	31.05
	40	42.84	39.36	42.92
	80	43.12	39.37	43.14
	160	40.25	37.30	38.23
3/4	20	38.82	38.10	33.70
	40	43.06	39.36	42.81
	80	43.14	39.38	43.21
	160	23.56	27.21	7.21

1024-QAM with 3/4 and 5/6 Coding Rates

The last modulation scheme supported by the proposed model was 1024-QAM which had 1024 different symbols, ten bits per symbol, and two coding rates as 3/4 and 5/6. The model took all these parameters into account and implemented them to identify the most suitable

values to be used in the high dense deployment of 802.11ax networks. The results for 3/4 and 5/6 coding rates are provided in Figure 7 (left) and (right), respectively.

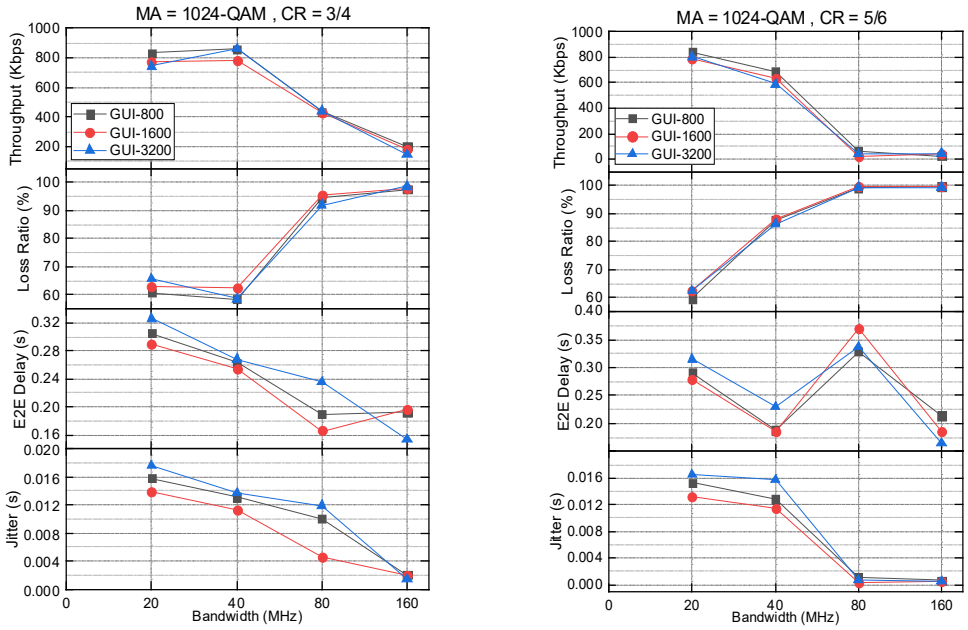

Figure 7. 1024-QAM scheme 3/4 (left) and 5/6 (right) coding rates

The above results prove that very high order modulation is not suitable for high-density areas that utilize wider channels for higher speed. Regardless of the coding rate value, two narrower channels, 20 and 40 MHz bandwidths fulfilled a better throughput and loss ratio performance compared to the wider 80 and 160 MHz channels. Furthermore, in 3/4 coding rate, a similar throughput and loss ratio values were achieved by 20 and 40 MHz channels while in 5/6 coding rate, the 80 and 160 MHz channels achieved similar throughput and loss ratio. In contrast, with respect to delay and jitter results, the wider channels can meet the demand of delay-sensitive applications as they provide less delay and jitter values. The best delay and loss ratio performance for 3/4 coding rate was achieved by 80 and 160 MHz channels while for 5/6 coding rate, the least delay belongs to 40 and 160 MHz. In this context, the jitter results of 80 and 160 MHz channels provided equal results. Like before, the lower coding rate is more responsive to guard interval values. For 3/4 coding rate, the longer guard intervals reduced the performance to a higher extent than in 5/6 coding rate. The throughput efficiency of 1024-QAM with 3/4 and 5/6 coding rates relating to the channel width and guard interval is provided in Table 7.

Table 7

1024-QAM throughput efficiency comparison

CR	CW (MHz)	Efficiency, η (%)		
		GUI=800ns	GUI=1600ns	GUI=3200ns
1/2	20	41.63	38.87	37.19
	40	43.03	39.28	43.02
	80	21.69	21.27	22.03
	160	10.05	9.04	7.24
3/4	20	42.17	39.24	40.27
	40	34.59	31.98	29.50
	80	3.06	0.86	2.00
	160	1.20	2.01	2.25

Bit Error Rate (BER) Occurrence

In this section we compare the bit error rate (BER) comparison of all the modulation schemes. The results are provided in Figure 8.

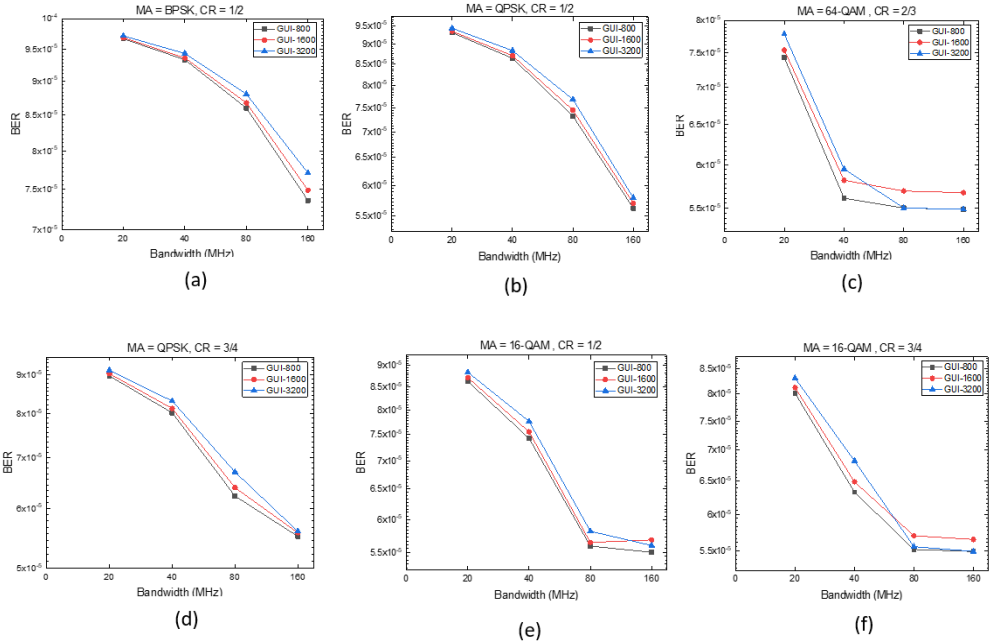

Figure 8. BER comparison of modulation schemes (a) BPSK-1/2, (b) QPSK-1/2, (c) QPSK-3/4, (d) 16-QAM-1/2, (e) 16-QAM-3/4, (f) 64-QAM-2/3

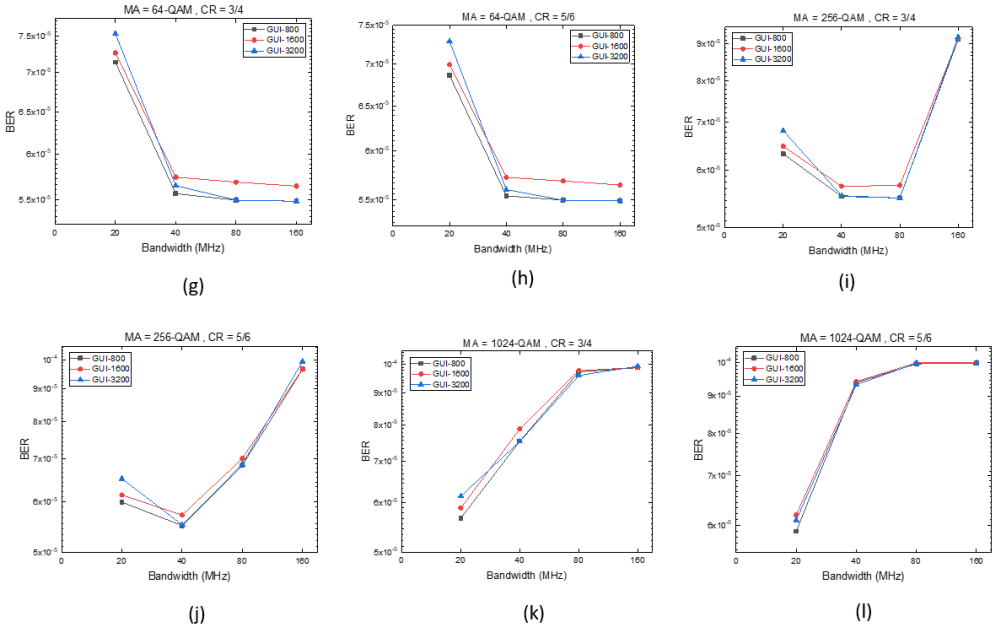

Figure 8(Continued). BER comparison of modulation schemes (g) 64-QAM-3/4, (h) 64-QAM-5/6, (i) 256-QAM-3/4, (j) 256-QAM-5/6, (k) 024-QAM-3/4, (l) 024-QAM-5/6

Typically, the acceptable BER values were below 10e-5 (Feukeu et al., 2013). Thereby, the above results show that all the obtained BER values were within the acceptable range. The results show a direct relationship between the order of modulation and BER reduction so that the worse BER values were obtained using the BPSK and the best values were obtained by the 1024-QAM with 5/6 coding rate. Concerning the channel width, for the lower order modulation from BPSK to 64-QAM, as the channel width increased, the BER decreased significantly. However, in the higher-order modulation from 256-QAM to 1024-QAM, the results were opposite so that lower BER values belonged to narrower channels.

CONCLUSIONS

This work proposes a model to optimize the performance of 802.11ax networks under high-density conditions regarding the available modulation schemes and their corresponding coding rates. The model further includes different combinations of guard interval and channel bandwidth parameters. The model is implemented and the results are measured to determine the proper values for the network optimization. The results show that utilizing wider channels and shorter guard intervals do not necessarily optimize the 802.11ax networks that are under heavy loads of a large number of users. The modulation schemes from BPSK to 64-QAM are able to improve the network performance in line with increasing the bandwidth of channels. In this context, the best performance is accomplished by 64-QAM with 40, 80, and 160 MHz channels with 5/6 coding rate. However, for higher-

order modulation including 256-QAM and 1024-QAM, the results prove otherwise. In this regard, the least amount of data rate obtained by 256-QAM is attained for the widest channel as 160MHz. Likewise, the least data rate of 1024-QAM is gained for 80 and 160 MHz channels. Furthermore, on the basis of the results, we do not observe a significant effect of guard interval values on performance enhancement of high-density 802.11ax. Although the shorter guard interval can improve the overall performance to some extent, the level of improvement is not remarkable. With regard to the bit error occurrence, the BER results are consistent with others so that for the lower order modulation, from BPSK to 64-QAM, as the channel width increases, significantly better performance in terms of lower BER values is achieved. However, for the higher-order modulation i.e. 256-QAM and 1024-QAM, the lower BER values belong to the narrower channels.

ACKNOWLEDGEMENT

The author wishes to acknowledge and extend their gratitude to the network simulator community for all the support and assistance given.

REFERENCES

Adame, T., Carrascosa, M., & Bellalta, B. (2019, April 24-26). The TMB path loss model for 5 GHz indoor WiFi scenarios: On the empirical relationship between RSSI, MCS, and spatial streams. In *2019 IEEE Wireless Days Conference* (pp. 1-8). Manchester, United Kingdom.

Akbilek, A., Pfeiffer, F., Fuenfer, M., Langer, F., & Napholz, B. (2018, November 14-15). Analysis of IEEE 802.11ax high efficiency WLANs for in-vehicle use. In *2018 Proceedings of the 15th Wireless Congress: Systems and Applications* (pp. 1-9). Munich, Germany.

Bellaltaa, B., & Szott, K. K. (2019). AP-initiated multi-user transmissions in IEEE 802.11ax WLANs. *Elsevier Ad Hoc Networks*, *85*(15), 145-159.

Brioso, J. G., Bañacia, A. S., Sawada, H., Ishizu, K., Ibuka, K., Matsumura, T., & Kojima, F. (2018, November 25-28). Vehicle to vehicle communications at suburban environment using IEEE 802.11af compliant devices. In *2018 Proceedings of the IEEE 21st International Symposium on Wireless Personal Multimedia Communications* (pp. 85-89). Chiang Rai, Thailand.

Codau, C., Voina, A., Pastrav, A., Hedesiu, H., & Chirap, C. (2017, September 21-23). Experimental evaluation of the IEEE 802.11ac standard using NI USRP 2954R. In *2017 Proceedings of the IEEE 16th RoEduNet Conference: Networking in Education and Research* (pp. 1-9). Targu Mures, Romania.

Deng, D. J., Lin, Y. P., Yang, X., Zhu, J., Li, Y. B., Luo, J., & Chen, K. C. (2017). IEEE 802.11ax: Highly efficient WLANs for intelligent information infrastructure. *IEEE Communications Magazine*, *55*(12), 52-59.

D-Link. (2013). *Wireless AC1200 dual band access point*. Retrieved Faburary 2, 2020, from https://eu.dlink.com/-/media/business_products/dap/dap-1665/manual/dap_1665_a1_manual_v1_00_eu.pdf.

Feukeu, E. A., Djouani, K., & Kurien, A. (2013). An MCS adaptation technique for doppler effect in IEEE 802.11p vehicular networks. *Elsevier Procedia Computer Science, 19*(1), 570-577.

Ghosh, S. (2016). Performance evaluation of different coding and modulation scheme in LTE using different bandwidth and correlation levels. *Wireless Personal Communications*, *86*(2), 563-578.

Hoefel, R. P. F., & Bejarano, O. (2016). On application of PHY layer abstraction techniques for system level simulation and adaptive modulation in IEEE 802.11ac/ax systems. *Journal of Communication and Information Systems*, *31*(1), 198-210.

Khan, G. Z., Gonzalez, R., Park, E. C., & Wu, X. W. (2016, February 19-22). Analysis of very high throughput (VHT) at MAC and PHY layers under MIMO channel in IEEE 802.11ac WLAN. In *2016 Proceedings of the IEEE 19th International Conference on Advanced Communication Technology* (pp. 877-888). Bongpyeong, South Korea.

Masiukiewicz, A. (2019). Throughput comparison between the new HEW 802.11ax standard and 802.11n/ac standards in selected distance windows. *International Journal of Electronics and Telecommunications*, *65*(1), 79-84.

Naik, K. P. K., & Reddy, A. K. (2017). Performance evaluation of LTE communication system under different modulation schemes. *International Journal of Innovative Technology*, *5*(2), 425-429.

Otsuka, H., Tian, R., & Senda, K. (2019). Transmission performance of an OFDM-based higher-order modulation scheme in multipath fading channels. *Journal of Sensor and Actuator Networks*, *8*(2), 1-15.

Rochim, A. F., & Sari, R. F. (2016, October 3-5). Performance comparison of IEEE 802.11n and IEEE 802.11ac. In *2016 Proceedings of the IEEE International Conference on Computer, Control, Informatics and its Applications* (pp. 54-59). Tangerang, Indonesia.

Sheshadri, R. K., & Koutsonikolas, D. (2017, May 1-4). On packet loss rates in modern 802.11 networks. In *2017 Proceedings of the IEEE INFOCOM 2017 Conference on Computer Communications* (pp. 1-8). Atlanta, USA.

Vijay, B. T., & Malarkodi, B. (2019). High-efficiency WLANs for dense deployment scenarios. *Sādhanā*, *44*(33), 1-14.

Weller, D., Mensenkamp, R. D., Vegt, A. V. D., Bloem, J. W. V., & Laat, C. D. (2019). Wi-Fi 6 performance measurements of 1024-QAM and DL OFDMA. *Semantic Scholar, 2019*, 1-7.

Pertanika J. Sci. & Technol. 28 (3): 1081 - 1090 (2020)

PERTANIKA JOURNALS

SCIENCE & TECHNOLOGY

Journal homepage: http://www.pertanika.upm.edu.my/

Evaluation of Ketoconazole Tablet Prepared using Dry Granulation Technique with Filler-Binder Excipients and Disintegration Agent

Dwi Setyawan*, Nisma Abdurahman Bawazier, Dini Retnowati and Diajeng Putri Paramita

Department of Pharmaceutics, Faculty of Pharmacy, Universitas Airlangga, 60115 Surabaya, Indonesia

ABSTRACT

Ketoconazole is one of high-dose treatment drugs with flowability issue so that it is commonly formulated using wet granulation technique. However, the technique impacts stability of ketoconazole which it changes in color upon solvent usage. This research was conducted to study tablet quality of ketoconazole as function of certain excipients in dry granulation technique. Combination of spray dried lactose (SDL) and Avicel® PH-102 as filler-binder excipients and sodium starch glycolate (SSG) as a disintegration agent were used for the purpose. Ketoconazole tablets were formulated based on 2^2 factorial design. Evaluation was performed on tablet properties, then statistically analyzed using Minitab® software. Tablet hardness and disintegration time increased in increasing level of filler combination and SSG concentration, but a decrease was observed for friability and % dissolved ketoconazole. Both filler combination and disintegration agent exhibited insignificant effect toward tablet properties evaluated. According to overlay contour plot, it is predicted that the optimum formulation of ketoconazole tablet can be set into SDL-Avicel® PH-102 ratio of at least 3:1 or higher and SSG concentration is higher than 3.5%.

Keywords: Avicel PH-102, dry granulation, ketoconazole, sodium starch glycolate, spray dried lactose

ARTICLE INFO

Article history:
Received: 04 November 2019
Accepted: 13 April 2020
Published: 16 July 2020

E-mail addresses:
dwisetyawan-90@ff.unair.ac.id (Dwi Setyawan)
nismazbd@gmail.com (Nisma Abdurahman Bawazier)
dini-r@ff.unair.ac.id (Dini Retnowati)
diajeng-putri-paramita@ff.unair.ac.id (Diajeng Putri Paramita)
* Corresponding author

INTRODUCTION

Ketoconazole is one of API that generally administered orally in tablet dosage form. Tablets are popular dosage form as for patient convenience, good stability, easy and low-cost manufacturing (Taneri et al., 2010; Gohel & Jogani, 2005). Tablet manufacturing involves compression of

ISSN: 0128-7680
e-ISSN: 2231-8526

© Universiti Putra Malaysia Press

powder mixture consisting of drug(s) and excipients. Tablet should possess certain properties in accordance with specifications required, i.e. tablet hardness, friability, disintegration time and dissolution (Edge et al., 2002).

Ketoconazole is a wide-spectrum antifungal drug derived from imidazole group. Based on the physicochemical properties, ketoconazole is classified in Biopharmaceutics Classification System (BCS) class II for drugs with low aqueous solubility yet high permeability (Viçosa et al., 2009). Ketoconazole is extremely hydrophobic with high molecular weight that leads to poor flowability and difficulty during compaction (Jacobs et al., 2016; Molaei et al., 2018). Suitable manufacturing process for this kind of drug is wet granulation technique so it can be compacted into a good tablet (Consiglieri et al., 2010; Javaheri et al., 2014). However, the resulting tablet shows a change in color, indicating instability issue due to photochemical reaction that becomes prominent after solvent exposure (Mhaske & Sahasrabudhe, 2011; Staub et al., 2010). Therefore, it is necessary to determine an appropriate technique in order to improve flowability without generating stability problem.

We suggested dry granulation technique as alternative solution to manufacture ketoconazole tablet, with spray dried lactose (SDL) and Avicel® PH-102 were used as filler-binder excipient in combination and sodium starch glycolate (SSG) was used as disintegration agent in the formulation of ketoconazole tablet. Dry granulation utilizes mechanical energy to promote powder agglomeration via compression (slugging) or compaction (roller compaction) and requires no solvent (Shanmugam, 2015). SDL is modified lactose from spray drying process and consisted of α-lactose monohydrate and amorphous lactose. SDL exhibits improved flowability and compaction behavior compared to conventional lactose attributable to smooth spherical particles of SDL, as well as the existence of amorphous lactose (Ruangchayajatuporn et al., 2011). Avicel® PH-102 is brand name of microcrystalline cellulose and the Arabic numerals represent grade of Avicel® PH itself. Avicel® PH-102 has larger mean particle size with coarser surface in comparison with Avicel® PH-101, another grade of microcrystalline cellulose commonly used in drug formulation. Tablet containing Avicel® PH-102 presented higher hardness and lower friability (Bastos et al., 2008). SSG is known as a so-called "super-disintegration agent" from cross-linked starch derivative. SSG acts as disintegration agent by swelling up to 12 folds in less than thirty min when in contact with water, inducing rapid disintegration of the tablet. Hence, for certain cases, SSG is also used to modify dissolution profile (Bhise et al., 2009; Kumar & Saharan, 2017).

In this research, ketoconazole tablet was prepared using dry granulation technique with filler-binder excipients and disintegration agent. Tablet formulation was optimized according to 2^2 factorial design. Evaluation of tablet properties included tablet hardness, friability, disintegration time, and dissolution rate. Effect of filler-binder excipients and

disintegration agent was analyzed using Minitab® software, as well as determination of the optimum formulation.

MATERIALS AND METHODS

Materials

Ketoconazole was obtained from dari Zhejiang East-Asia Pharmaceutical Co. Ltd., China. SDL (DMV International, Netherland), Avicel® PH-102 (Asahi Corp., Japan), SSG (Yung ZIP Chemical Co., China), and other excipients used in formulation were pharmaceutical grade.

Formulation Design

Ketoconazole tablets were formulated according to factorial design 2^2 with two factors, those are filler combination and disintegration agent, in two levels of concentration. Filler combination consisted of SDL and Avicel® PH-102 in weight ratio of 2:1 and 4:1 as the level difference. SSG was used as disintegration agent with two concentrations of 2 and 4%. API composition in each tablet was equal to 200 mg of ketoconazole. Four formulations of ketoconazole tablet can be seen in Table 1.

F1 contained both factors in low level; F2 contained low level of filler combination and high level of disintegration agent; F3 contained high level of filler combination and low level of disintegration agent; and F4 contained high level of both factors. Ketoconazole tablet was prepared using dry granulation technique. Ketoconazole was tumble-mixed first with SLS and a half part of SSG for 5 min, then with SDL and Avicel® PH-102 for 10 min, and with a half part of each talk and magnesium stearate for another 5 min. Slugging was performed on the mixture under compression force of 10 kN. Subsequently, the slugs were grinded into granule using an oscillating granulator Erweka AR-400 (Germany), and sieved through 1 mm mesh sieve. The remaining part of SSG, talk, and magnesium stearate was

Table 1
Formulations of ketoconazole tablet

Component(s)	Function	Composition (% b/b)			
		F1	F2	F3	F4
Ketoconazole	API	66.6	64.6	66.7	64.7
SDL	Filler	18.6	18.6	22.2	22.2
Avicel® PH-102	Filler	9.3	9.3	5.6	5.6
SSG	Disintegration agent	2	4	2	4
SLS	Surfactant	1	1	1	1
Magnesium stearate	Lubricant	1	1	1	1
Talk	Glidan	1.5	1.5	1.5	1.5
Total		100	100	100	100

added into the granule to be mixed homogenously for 5 min. Tablet form was obtained via compressing the granules on 14 mm diameter tablet die using a hydraulic press Natoli NP-RD10A (USA) with compression force of 10 kN.

Tablet Evaluation

Ketoconazole tablet was evaluated for its property of hardness, friability, and disintegration time in replication measurement. Tablet hardness was calculated from five tablets sample of each formula using Erweka TBH-220 hardness tester, Germany. Tablet friability was examined using Erweka TAP-31914 friability tester, Germany. Sample of 10 tablets from each formula was weighed first before rotated on friability tester at a speed of 25 rpm for 4 minutes. Tablet sample was dusted from fines, then re-weighed to calculate the weight loss presented as a percentage.

The disintegration test was carried out using Erweka ZT-501 disintegrator, Germany, with 900 mL of distilled water as disintegration medium at 37±2ºC. Six tablets were placed each in every wire-ended tube in a basket rack assembled on the disintegrator, then covered by transparent disk. The disintegrator was run until all tablets disintegrated completely.

Dissolution Test

Dissolution of ketoconazole tablet was measured using Erweka DT-700 dissolution instrumentation (Germany) with paddle apparatus in dissolution medium of 0.1 N HCl solution. Tablet sample from each formula was inserted into 900 mL dissolution medium and the instrument was run at stirring speed of 50 rpm and temperature of 37±0.5ºC. Sampling was conducted at time interval of 30 minutes and 5.0 mL solution was taken in every sampling that immediately replaced with fresh dissolution medium in the same amount. Then, the solution was filtered through 0.45 μm-pore cellulose nitrate membrane filter. The filtrate was read for the absorbance on Hitachi UH5300 UV-Vis spectrophotometer (Japan) at the maximum wavelength of ketoconazole at 222 nm. % dissolved ketoconazole was obtained through standard calibration curve and was reported as mean from triplicate measurements.

Statistical Analysis

Effect of filler combination and disintegration agent toward ketoconazole tablet properties was statistically analyzed using Minitab® 18 version (Minitab Inc., Australia). Using the software, the optimum formulation for ketoconazole tablet was also determined from the evaluated properties.

RESULTS AND DISCUSSIONS

Formulation of ketoconazole tablet prepared using dry granulation technique was optimized by factorial design approach. Factorial design employs mathematical equation construction to determine experimental procedure as a function of the factor levels, e.g. in two-level factors experiment, it is described as 2^f factorial design (f denotes the number of factors) (Chowdary & Shankar, 2016). Since factors evaluated in this research were filler combination and disintegration, the experiment was based on 2^2 factorial design resulting in four formulations. Table 2 shows the properties of ketoconazole tablet from four formulations. Tablet hardness of all formulations fell in value between 4.6 to 5.0 kP that within range of acceptable value (Fatmawati et al., 2017).

Table 2
The properties of ketoconazole tablet

Tablet Properties	F1	F2	F3	F4
Hardness (kP)	4.83±0.04	4.6±0.27	4.81±0.47	4.93±0.15
Friability (%)	1.00±0.09	0.55±0.20	0.67±0.22	0.74±0.14
Disintegration Time (min)	4.27±1.77	5.14±0.42	5.78±1.86	5.90±1.32
% Dissolved	72.69±1.24	63.79±4.22	80.27±9.54	73.92±4.74

The friability of ketoconazole tablets were mostly below 1% and met specification required (Winarti et al., 2017), except for F1. It is quite possibly caused by the low amount of SDL and SSG that the former possesses plastic deformation behavior of amorphous phase to form compacted tablet and the last belongs to starch derivative with binder property (Rassu et al., 2006; Rowe et al., 2009). During disintegration time test, ketoconazole tablets disintegrated completely under six minutes in all formulations. The result conforms the quality requirement that tablet disintegration should complete within fifteen minutes (Schmid & Löbenberg, 2010). Percentage of dissolution efficiency in 30 minutes (DE_{60}) was calculated as below: 60.07±2.12, 63.16±1.79, 65.02±3.73, and 62.39±1.97 for F1, F2, F3, and F4, respectively. According to the compendium, ketoconazole in tablet dosage form is required to dissolve not less than 80% in thirty minutes (Ministry of Health, 2014). However, only F3 complied with the requirement.

Analysis using Minitab® software obtains pareto charts, main effect plots, and contour plots that describe the effect of the factors on ketoconazole tablet properties statistically. Pareto charts explain the extent of which each factor impacts tablet hardness, friability, disintegration time, and dissolution. Meanwhile, main effect plots show the main effect generated by each factor in different level of concentration and contour plots show the relationship of the factors toward tablet properties evaluated. Figure 1 displays pareto charts of ketoconazole tablet properties. A factor is considered to have significant effect if the graphic bar crosses the red line and none does in our pareto charts. Therefore, both factors

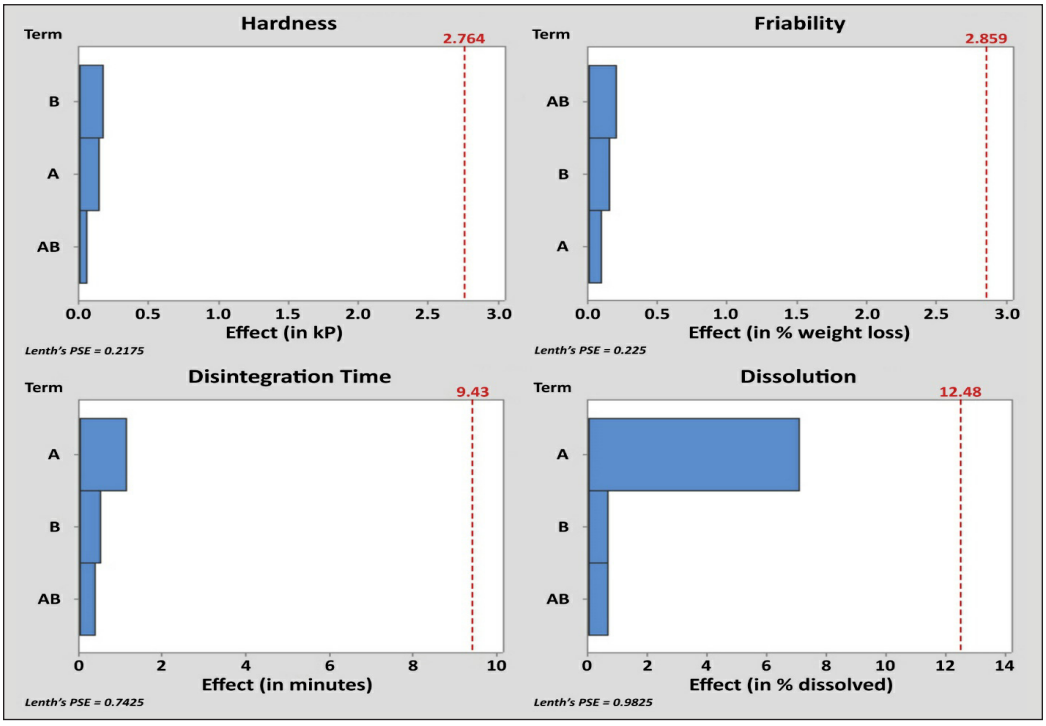

Figure 1. Pareto charts of ketoconazole tablet properties in a function of filler combination (A) and disintegration agent (B) as individual factor or in combination (AB)

used in this research, filler combination and disintegration agent, impact ketoconazole tablet properties in insignificant fashion, as an individual or in combination.

Main effect plots of ketoconazole tablet properties are given in Figure 2. An increment in SDL ratio in filler combination and SSG concentration increases tablet hardness and disintegration time, but decreases friability and % dissolved ketoconazole. Effect of SSG concentration on dissolution seems to be in much lower extent compared to ratio of filler combination. From contour plots shown in Figure 3, we can see combination effect of both factors on tablet properties. Low level of SDL ratio in filler combination and SSG concentration leads to tablet with low hardness and higher value can be obtained at higher level of both factors. Good friability is acquired from tablet with high level of SDL ratio, high level of SSG concentration, or high level of both factors (darker blue zone), as low level of both produces tablet with high friability. Disintegration time can be regulated faster with low level of SDL ratio and SSG concentration, meanwhile % dissolved ketoconazole can be obtained higher at high level of both factors.

Contour plots can be overlaid together to give a graphic seen in Figure 4, from which we can predict the optimum formulation for ketoconazole tablet. The feasible area is white-colored zone on the graphic. So, for manufacturing ketoconazole that readily

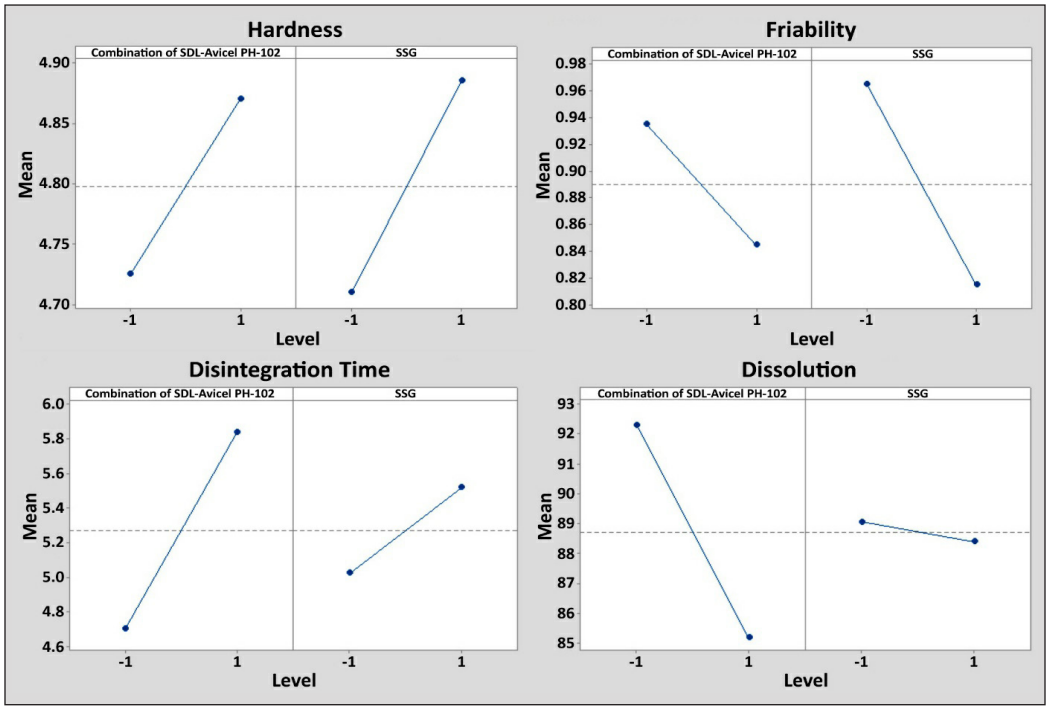

Figure 2. Main effect plots of ketoconazole tablet properties in a function of filler combination and disintegration agent in two levels (-1, low level; +1, high level)

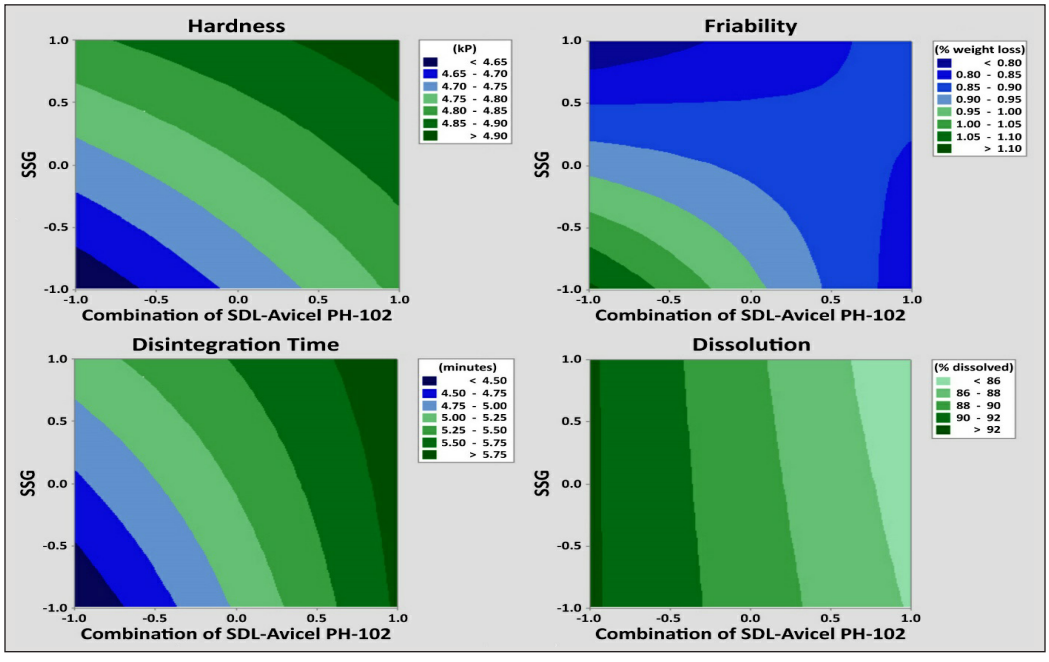

Figure 3. Contour plots of ketoconazole tablet properties in a function of filler combination and disintegration agent in two levels (-1, low level; +1, high level)

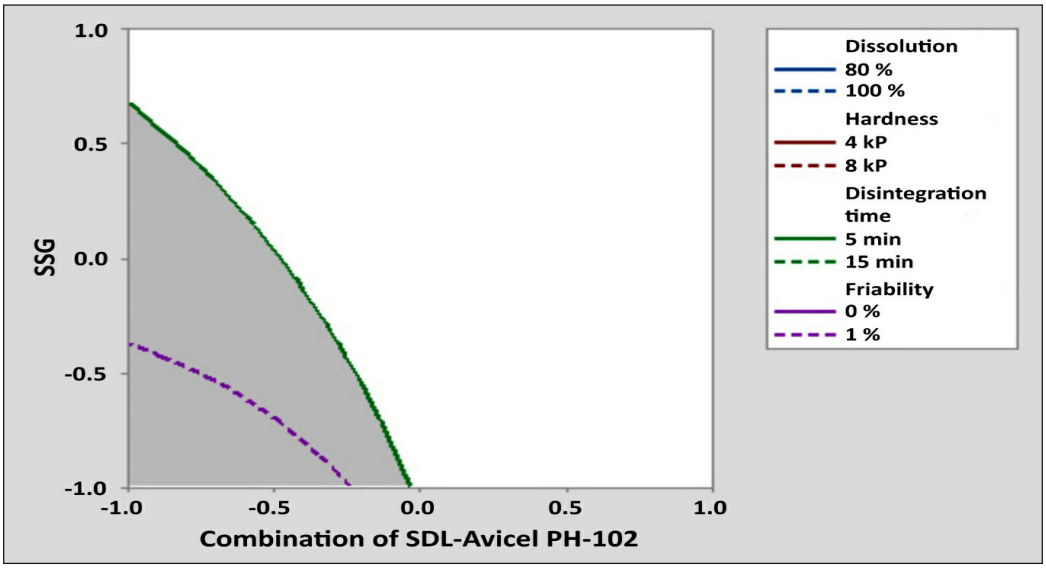

Figure 4. Overlaid contour plot of ketoconazole tablet derived from the evaluated properties (-1, low level; +1, high level)

complies with quality requirements using filler combination of SDL-Avicel® PH-102 and disintegration agent of SSG, SDL-Avicel® PH-102 ratio can be set at least 3:1 or higher and SSG concentration should be higher than 3.5%.

CONCLUSION

To manage stability issue generated from manufacturing ketoconazole tablet with wet granulation, dry granulation technique was explored to formulate ketoconazole tablet. Filler combination of SDL-Avicel® PH-102 and disintegration agent of SSG factors are known to impact tablet properties. Both factors increase tablet hardness and disintegration time, decrease friability and % dissolved ketoconazole, even though it is not significant statistically. Overlaid contour plot allows prediction of the optimum formulation for ketoconazole tablet using combination of SDL and Avicel® PH-102 and disintegration agent of SSG.

ACKNOWLEDGMENT

This research was fully funded by the Ministry of Research, Technology, and Higher Education through grant of Penelitian Dasar Unggulan Perguruan Tinggi (PDUPT) No. 623/UN3.14/LT/2019. This manuscript has been presented at the 2019 international joint symposium of the 8th Asia Pacific Pharmacy Education Network (APPEN) Conference and the 2nd Halal Pharmaceuticals and Cosmetics (HPC) Conference, 8-9 October 2019 at Universitas Airlangga, Surabaya, Indonesia.

REFERENCES

Bastos, M. O., Friedrich, R. B., & Beck, R. C. R. (2008). Effects of filler-binders and lubricants on physicochemical properties of tablets obtained by direct compression: A 2^2 factorial design. *Latin American Journal of Pharmacy, 27*(4), 578-583.

Bhise, S., Chaulang, G., Patel, P., Patel, B., Bhosale, A., & Hardikar, S. (2009). Superdisintegrants as solubilizing agent. *Research Journal of Pharmacy and Technology, 2*(2), 387-391.

Chowdary, K. P. R., & Shankar, K. R. (2016). Optimization of pharmaceutical product formulation by factorial designs: Case studies. *Journal of Pharmaceutical Research, 15*(4), 105-109.

Consiglieri, V. O., Mourão, S., Sampaio, M., Granizo, P., Garcia, P., Martinello, V., ... & Ferraz, H. G. (2010). Improvement of fluconazole flowability and its effect on dissolution from tablets and capsules. *Brazilian Journal of Pharmaceutical Sciences, 46*(1), 115-120.

Edge, S., Steele, D. F., Staniforth, J. N., Chen, A., & Woodcock, P. M. (2002). Powder compaction properties of sodium starch glycolate disintegrants. *Drug Development and Industrial Pharmacy, 28*(8), 989-999.

Fatmawati, D. A., Widjaja, B., & Setyawan, D. (2017). Optimasi tablet levofloksasin yang mengandung bahan pengikat PVP K-30 dan disintegran Vivasol [Optimization of levofloxacin tablet containing PVP K-30 and Vivasol]. *Jurnal Sains Farmasi dan Klinis, 4*(2), 9-15.

Gohel, M. C., & Jogani, P. D. (2005). A review of co-processed directly compressible excipients. *Journal of Pharmacy and Pharmaceutical Sciences, 8*(1), 76-93.

Jacobs, G. A., Gerber, M., Malan, M. M., du Preez, J. L., Fox, L. T., & du Plessis, J. (2016). Topical delivery of acyclovir and ketoconazole. *Drug Delivery, 23*(2), 631-641.

Javaheri, H., Carter, P., & Elkordy, A. A. (2014). Wet granulation to overcome liquisolid technique issues of poor flowability and compactibility: A study to enhance glibenclamide dissolution. *Journal of Pharmaceutics and Drug Development, 2*(3), 1-12.

Kumar, A., & Saharan, V. A. (2017). A comparative study of different proportions of superdisintegrants: Formulation and evaluation of orally disintegrating tablets of salbutamol sulphate. *Turkish Journal of Pharmaceutical Sciences, 14*(1), 40-48.

Mhaske, R. A., & Sahasrabudhe, S. (2011). Identification of major degradation products of ketoconazole. *Scientia Pharmaceutica, 79*, 817-836.

Ministry of Health. (2014). *Farmakope Indonesia* (5th Ed.). Jakarta, Indonesia: Ministry of Health Republic of Indonesia.

Molaei, M., Osouli-Bostanabad, K., Adibkia, K., Shokri, J., Asnaashari, S., & Javadzadeh, Y. (2018). Enhancement of ketoconazole dissolution rate by the liquisolid technique. *Acta Pharmaceutica, 68*(3), 325-336.

Rassu, G., Eissens, A. C., & Bolhuis, G. K. (2006). Tableting properties of an improved spray-dried lactose. *Journal of Drug Delivery Science and Technology, 16*(6), 455-459.

Rowe, R. C., Sheskey, P. J., & Quinn, M. E. (2009). *Handbook of pharmaceutical excipients* (6th Ed.). London, United Kingdom: Pharmaceutical Press.

Ruangchayajatuporn, J., Amornsakchai, T., Sinchaipanid, N., & Mitrevej, A. (2011). Compaction behavior and optimization of spray-dried lactose with various amorphous content. *Journal of Drug Delivery Science and Technology, 21*(2), 175-181.

Schmid, K., & Löbenberg, R. (2010). Influence of the changed USP specifications on disintegration test performance. *Dissolution Technologies, 17*(1), 6-10.

Shanmugam, S. (2015). Granulation techniques and technologies: Recent progresses. *BioImpacts, 5*(1), 55-83.

Staub, I., Flores, L., Gosmann, G., Pohlmann, A., Fröehlich, P. E., Schapoval, E. S., & Bergold, A. M. (2010). Photostability studies of ketoconazole: Isolation and structural elucidation of the main photodegradation products. *Latin American Journal of Pharmacy, 29*(7), 1100-1106.

Taneri, F., Ozcan, I., & Guneri, T. (2010). *In vitro* and *in vivo* evaluation of oral tablet formulations prepared with ketoconazole and hydroxypropyl-beta-cyclodextrin. *Drug Delivery, 17*(3), 152-157.

Viçosa, A. L., Chatah, E. N., Santos, T. C., Jones, L. F. Jr., Dantas, C. B., Dornelas, C. B., ... & Cabral, L. M. (2009). Bioequivalence studies and sugar-based excipients effects on the properties of new generic ketoconazole tablets formulations and stability evaluation by using direct compression method. *Pharmaceutical Development and Technology, 14*(5), 530-539.

Winarti, L., Ameliana L., & Nurahmanto, D. (2017). Formula optimization of orally disintegrating tablet containing meloxicam nanoparticles. *Indonesian Journal of Pharmacy, 28*(1), 53-64.

Pertanika J. Sci. & Technol. 28 (3): 1091 - 1103 (2020)

PERTANIKA JOURNALS

SCIENCE & TECHNOLOGY

Journal homepage: http://www.pertanika.upm.edu.my/

Short Communication

Impact of Chronic Khat Chewing on Carotid Doppler Flow Velocities and Indices in Yemeni Volunteers

Ameen Mohsen Amer[1]*, Elsafi Ahmed Abdalla[2] and Caroline Edward Ayad[2]

[1]*Department of Health Sciences, Faculty of Medicine and Health Sciences, University of Science and Technology, Yemen*
[2]*Sudan University of Science and Technology, College of Medical Radiological Science, Khartoum, Sudan*

ABSTRACT

Chewing Khat is considered as a major deep-rooted sociocultural habit in Yemen. This custom has been causing various health problems. Using Doppler ultrasonography, this study assessed the changes that occurred in bilateral carotid arteries' flow velocities and Doppler indices in Yemenis who regularly chewed Khat for years. Convenient sampling was conducted from August 2017 to August 2018 for 384 participants of whom 179 were excluded and the sample size became 205 participants including 108 (52.7%) Khat chewers and 97 (47.3%) non-Khat chewers. The mean age of the sample was 28.29 ± 7.0 years. In all cases, the carotid Doppler ultrasound scanning protocol, based on the standards of American Institute of Ultrasound in Medicine, was performed to measure carotid Doppler velocities and indices, in addition to internal carotid flow volume. The Khat chewing information of participants was obtained by a standardized questionnaire, and SPSS was used for result analysis. There were differences in systolic velocities between Khat chewers and non-chewers with lower values for the chewers, and they were significant in the right common carotid artery and in the internal carotid artery. The carotid Doppler indices, except the right internal carotid artery, were significantly decreased, and the Right internal carotid artery blood flow volume was significantly increased among Khat chewers compared to that of non-chewers. Moreover among Khat chewers, Doppler indices and most of the peak systolic velocities had a significantly negative correlation with the Khat chewing period. Therefore, this study may provide

ARTICLE INFO

Article history:
Received: 01 December 2019
Accepted: 07 April 2020
Published: 16 July 2020

E-mail addresses:
a.alfalahi@ust.edu, aminalflahi@gmail.com (Ameen Mohsen Amer)
Dr.elsafi@gmail.com (Elsafi Ahmed Abdalla)
carolineayad@yahoo.com (Caroline Edward Ayad)
* Corresponding author

ISSN: 0128-7680
e-ISSN: 2231-8526

© Universiti Putra Malaysia Press

an interpretation of the high prevalence of hemorrhagic stroke among Yemeni population in their middle age, and suggest the mechanism that may cause this type of stroke. More studies are recommended to confirm this finding using the transcranial Doppler technique.

Keywords: Carotid, chronic Khat chewing, Doppler index, Doppler velocity, Yemen

INTRODUCTION

In Yemen, Khat (qat, kat) chewing is considered as a major deep-rooted sociocultural phenomenon. Khat is an evergreen shrub belonging to the Celastraceae family that was named by a botanist, Peter Forsskal who uttered "Catha" (referred to the Catha edulis tree) from the Arabic name "Khat" (Numan, 2012).

Earlier, the clinical observation concluded that Khat had amphetamine-like properties. Then in subsequent chemical analysis, it was suggested that the fresh Khat leaves contained a number of compounds, including phenylalkylamine compounds (alkaloids) such as norpseudoephedrine (cathine) and alpha aminopropiophenone (cathinone) (Hassan et al., 2007). The latter is the main active ingredient in fresh Khat leaves (Kalix, 1990) which is pharmacologically similar and structurally related to amphetamine (Hassan et al., 2007).

Chewing Khat evidently leads to a significant rise of arterial systolic and diastolic blood pressure and pulse rate (Hassan et al., 2005; Hassan et al., 2007; Yehia, 2015), and it is an established risk factor for cardiovascular disease with cigarette smoking (Tesfaye et al., 2008).

Because the regular Khat chewing is associated with the increased diastolic blood pressure resulting from the effect of Cathinone as a peripheral vasoconstrictor, the sustained effect on the cardiovascular system may occur that can contribute to the elevation of blood pressure at the population level (Geta et al., 2019; Mega & Dabe 2017; Getahun et al., 2010; Andualem et al., 2002). Furthermore, the regular intake of Khat is associated with an increased risk of acute myocardial infarction (Al-Motarreb et al., 2005).

The flow velocities were increased and the Doppler indices were decreased when assessing the immediate effect of Khat chewing on Doppler hemodynamics of common carotid arteries (Ibrahim et al., 2017). Doppler ultrasonography scan is non-invasive and appropriate for the bedside examination. With the measuring of flow volumes in the carotid arteries (CAs), this technique has been used to detect extracerebral blood flow among healthy populations. Doppler's indices; resistive index (RI) and pulsatility index (PI) are common parameters for characterizing the waveform to translate the vascular resistance (Ibrahim et al., 2017).

Originally, Pourcelot (1976) introduced RI to assess peripheral vascular diseases. The RI and PI have become important parameters in studying the effect of many diseases on vascularity in different organs, then, according to Ibrahim et al. (2017), they are used to assess the effects of Khat chewing on CAs hemodynamics.

To our knowledge, no study has been investigated the accumulative effects of chronic Khat chewing on CAs hemodynamics. Therefore, the study aimed to determine the effect of chronic Khat chewing on the Doppler flow velocities and indices of CAs in order to estimate its effect on the vascular system and cerebral perfusion.

MATERIALS AND METHODS

For this prospective study, Two radiologists approved the procedures, and a qualified sonographer, who had a Master degree in medical diagnostic ultrasound and seven years field experience, performed imaging of bilateral CAs using Doppler ultrasonography to measure the peak systolic velocity (PSV), end diastolic velocity (EDV), resistivity index (RI), and pulsatility index (PI) among 384 Yemeni participants conveniently selected according to the Table of Krejcie and Morgan (1970). After applying the inclusion and exclusion criteria, the sample size became 205 participants divided into two groups; Khat chewers (n = 108) and non-Khat chewers (n = 97). Then, flow volume was calculated in the bilateral internal carotid arteries (ICAs).

The demographic data were obtained from participants including age, governorate, occupation, and body mass index. Then the information of their chewing Khat habit were collected including the daily duration of chewing in hours and the period of chewing in years using a standardized questionnaire and data collection sheet.

Participants were scanned in the Radiology Department of University of Science and Technology Hospital (USTH), Sana'a, Yemen, from August 2017 to August 2018, using a high-resolution ultrasound system (model: TUS-Aplio 400 / Toshiba-MEC-US) equipped with a linear high frequency probe (Figure 1).

CAs were scanned to determine Doppler parameters in the supine position with supported knees. The operator seated on the right of the patient. The neck scanning was enhanced by tilting and rotating the head away from the side being examined, with possible appropriate adjustment for the head and neck position. Transducer several positions were used to investigate the CAs in the longitudinal and the short-axis (transverse) views that obtained from different anterior and lateral or posterolateral approaches for getting the best view of vessels. Then sweeping of probe was performed to determine the values of Doppler carotid parameters using the manual and automatic calculation software, with beam angle of Doppler was maintained ≤ 60 degrees at all times. All measurements in spectral Doppler were obtained with a small sample volume (≤ 2 mm) and in the center stream of the flow at the area of the greatest velocity shift (Figure 2 and 3).

Figure 1. High-resolution ultrasound system (model: TUS-Aplio 400 / Toshiba-MEC-US)

The blood volume of ICAs was calculated, in 98 participants, by measuring the average peak flow velocity times the cross-sectional area of this circular vessel (Blanco, 2015).

ETHICAL CONSIDERATIONS

Formal approval was obtained from the Research Ethics Committee, Faculty of Medicine and Health Sciences at University of Science and Technology Yemen (USTY) (MECA No.: EAC/UST133), and a written agreement was received from the Radiology Department of the USTH. Then the scanning procedures were explained to the participants before taking written informed consents from them.

By applying the inclusion criteria, the study sample includes Yemeni adults (Khat and non-Khat chewers) on condition that they are non-smokers, non-hypertensive, non-diabetic, and without cardiopulmonary disorders, history of severe dyslipidemia and known kidney diseases so as to avoid significant effect in the extracranial blood flow velocities.

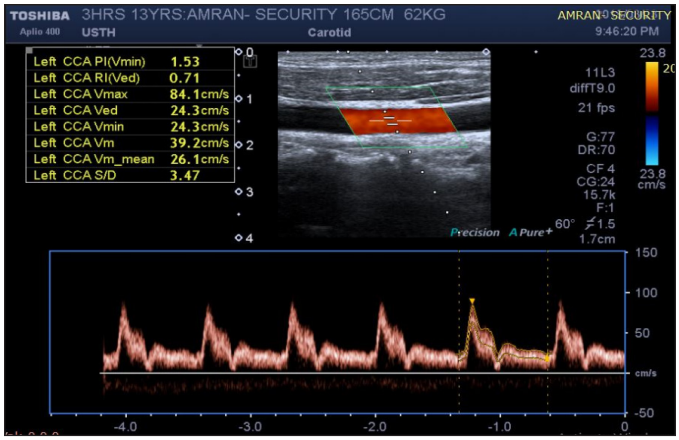

Figure 2. Doppler interrogation of Lt CCA hemodynamics for a Khat chewer participant has a 13 year period of chewing

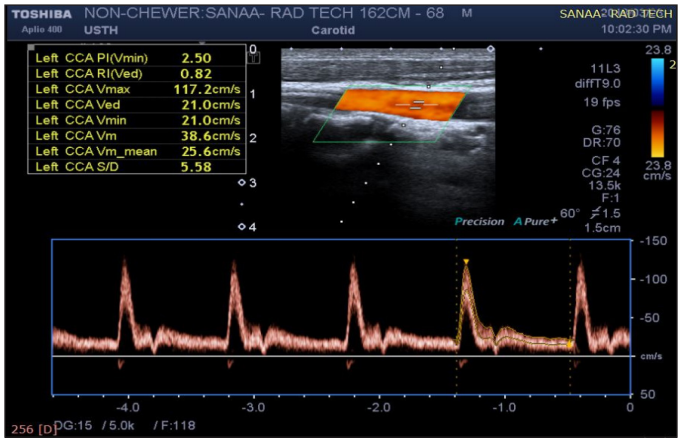

Figure 3. Doppler interrogation of Lt CCA hemodynamics for non-Khat chewer participant

STATISTICAL ANALYSIS

All statistical analyses were achieved by SPSS version 21.0 (SPSS Inc., Chicago, IL, USA). The variables were expressed as mean ± standard deviation. The normality of data was examined using the Kolmogorov-Smirnov test. An Independent sample t-test was used to compare between the variables with respect to the two groups (Khat and non-Khat chewers). Pearson's correlation was also used to analyze the associations among the variables and to determine their significance. After the analysis, the data were presented using figures and tables. A p-value < 0.05 was considered as statistically significant.

RESULTS

The 205 Yemeni participants; 21 (10.2%) females and 185 (89.8%) males were investigated using Doppler ultrasound. The mean age was 28.3 ranging from 16 to 45 years.

This study showed the differences between Khat and non-Khat chewers regarding Doppler parameters, particularly Doppler indices. These differences were significant in PSV of right common carotid artery (RT CCA), internal carotid artery (ICA), and EDV of both external carotid arteries (ECAs), in addition to RI and PI of bilateral CCAs, and ECAs. Moreover, in the chewers' group, the results showed significant correlations between the period of chewing and the carotid Doppler parameters as follows:

A decreased PSV was observed in all bilateral CAs of the Khat chewers' group compared to those of the non-Khat chewers, and was statistically significant only in the RT CCA ($p < 0.001$) and RT ICA ($p = 0.042$).

In the Khat chewers group, the PSV had a significantly negative correlation with the period of chewing only in the RT CCA ($p = 0.01$), left CCA (LT CCA) ($p < 0.001$) and ECA ($p = 0.005$).

A significant increased EDV ($p < 0.001$) was observed only in the bilateral ECAs of Khat chewers' group compared to that of the non-Khat chewers. Furthermore, the EDV in the bilateral ECAs had a significantly positive correlation with the period of chewing in the RT ECA ($p = 0.046$) and LT ECA ($p <0.001$).

There was no significant difference in Doppler parameters between genders in the Khat Chewers group. Moreover, higher carotid flow velocities in males compared to females were observed in the control group. But this trend did not reach statistical significance except that of RT CCA PSV ($p < 0.001$).

The ultrasound Doppler machine automatically calculated the Doppler indices of bilateral CAs. The comparison of RI and PI values between the two groups is demonstrated in Table 1 in which a significant difference was noticed with decreased RI and PI in bilateral CAs of Khat chewers, except in LT ICA.

In the Khat chewers' group, Doppler indices had a significantly negative correlation with the period of chewing in the bilateral CAs, except in the RT ICA RI and LT CCA PI (Table 2, Figures 4 and 5).

Table 1
Comparison of carotids Doppler indices between Khat and non-Khat chewers

Doppler index	**Chewing Status**	**Mean**	**Std. Deviation**	**t-test Sig. (2-tailed)**	**Doppler index**	**Chewing Status**	**Mean**	**Std. Deviation**	t-test Sig. (2-tailed)
RT CCA RI	chewer	0.7739	0.04767	0.026	**RT CCA PI**	chewer	1.9072	0.45763	**0.000**
	non-chewer	0.7884	0.04401			non-chewer	2.2053	0.49456	
RT ICA RI	chewer	0.6143	0.08511	0.012	**RT ICA PI**	chewer	1.0879	0.36626	**0.000**
	non-chewer	0.6457	0.09150			non-chewer	1.3101	0.45799	
RT ECA RI	chewer	0.8190	0.07414	0.000	**RT ECA PI**	chewer	2.3366	0.81658	**0.000**
	non-chewer	0.8625	0.08737			non-chewer	2.8952	1.05374	
LT CCA RI	chewer	0.7584	0.04853	0.000	**LT CCA PI**	chewer	1.8256	0.46958	**0.000**
	non-chewer	0.7861	0.05281			non-chewer	2.1576	0.54098	
LT ICA RI	chewer	0.6079	0.08068	0.701	**LT ICA PI**	chewer	1.1028	0.34266	**0.178**
	non-chewer	0.6124	0.08661			non-chewer	1.1657	0.32052	
LT ECA RI	chewer	0.8143	0.07303	0.001	**LT ECA PI**	chewer	2.1790	0.69968	**0.000**
	non-chewer	0.8528	0.08805			non-chewer	2.8276	0.86916	

Table 2
Correlation between Doppler indices of CAs and period of Khat chewing

Dependent variable		RI						PI					
		RT CCA	**RT ICA**	**RT ECA**	**LT CCA**	**LT ICA**	**LT ECA**	**RT CCA**	**RT ICA**	**RT ECA**	**LT CCA**	**LT ICA**	LT ECA
Period of Khat chewing (yrs.)	**Pearson Correlation**	-0.369**	-0.152	-0.319**	-0.319**	-0.193*	-0.395**	-0.264**	-0.190*	-0.318**	-0.185	-0.285**	**-0.322****
	Sig. (2-tailed)	0.000	0.117	0.001	0.001	0.045	0.000	0.006	0.049	0.001	0.055	0.003	**0.001**
	N	108	108	108	108	108	108	108	108	108	108	108	**108**

** Correlation is significant at the 0.01 level (2-tailed).
* Correlation is significant at the 0.05 level (2-tailed).

In the control group, bilateral CCAs Doppler indices were significantly different between the genders (p =0.01, and 0.008 of RI), and (p =0.001, and 0.002 of PI) for Right and Left respectively.

Table 3
Comparison of internal carotids flow volume between Khat and non-Khat chewers

Doppler Parameter	Chewing Status	N	Mean	Std. Deviation	Sig. (2-tailed)
RT ICA flow	**chewer**	49	433.0524	135.56262	**0.044**
volume (ml/min)	**non chewer**	49	378.3753	129.33580	
LT ICA flow	**chewer**	49	491.1616	145.26714	**0.060**
volume (ml/min)	**non chewer**	49	438.6129	127.82918	

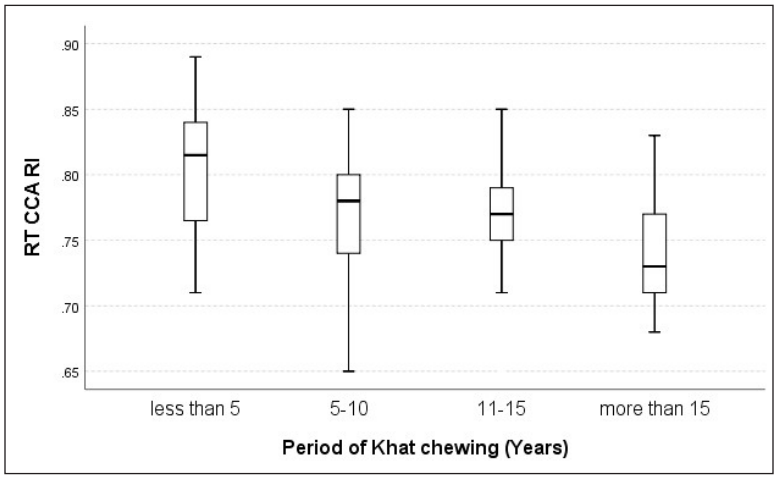

Figure 4. Correlation of right CCA RI with period of Khat chewing

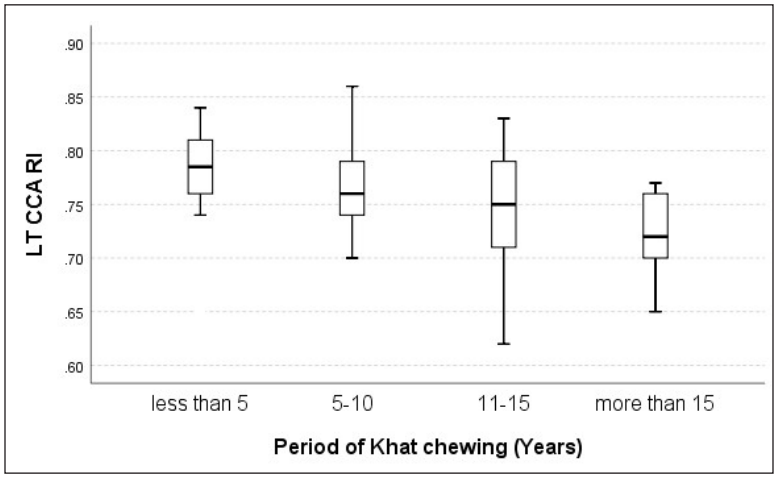

Figure 5. Correlation of left CCA RI with period of Khat chewing

DISCUSSION

This study revealed that the chronic Khat chewing significantly altered the carotids blood hemodynamics by decreasing the PSVs and Doppler indices, in addition to increasing the flow volume as discussed in details below.

In the control group, CAs flow velocities in males were higher compared to females, which supports the previous findings in a healthy adults (Yazici et al., 2005). Also there was no statistical significantly difference in Doppler parameters between genders in the Khat Chewers.

Khat chewing causes increased blood pressure and heart rate (Hassan et al., 2007; Yehia, 2015; Ibrahim et al., 2017), therefore, it is considered a risk factor for cardiovascular complications (Balint et al., 2009; Al-Motarreb et al., 2010; Al Suwaidi et al., 2013).

The decreased PSVs in CAs of Khat chewers compared to those of non-Khat chewers in the current study is consistent with the proven inverse relationship between the velocity and pressure according to physics laws controlling hemodynamics such as Bernoulli principle (Kirsch et al., 2013). This result agrees also with that of Homma et al. (2009) who noticed that the PSV is lower in the hypertensive patient compared to healthy individuals.

These decreased PSVs in the CAs of Khat chewers compared to those of non-Khat chewers were statistically significant in the RT CCA and RT ICA, while the decreased PSVs in addition to the Doppler indices in CAs of Khat chewers was not statistically significant in the LT ICA. This may be attributed, according to Homma et al. (2009), to the probability of slower velocity in the ICA or the effect of anatomical variation in cerebral vessels on ICA, which are anatomically closer in distance to ICA than CCA.

Since Agunloye and Owolabi (2014) reported that the decreased PSVs were associated with stroke, the lower PSVs among Khat chewers in the current study may consolidate that Khat can be a cause of cerebral complications beside causing cardiovascular events (Vanwalleghem et al., 2006; Kulkarni et al., 2012; Balint et al., 2009; Al-Motarreb et al., 2010; Al Suwaidi et al., 2013). Moreover, Ibrahim et al. (2017) indicated that the EDVs in CAs of Khat chewers were mostly increased, which is in line with the current study finding.

To confirm the aforementioned findings, the decrease in RI and PI is mathematically consistent with the decrease in PSVs and the increase in EDVs (Chow et al., 2013). Moreover, the decrease in RI and PI in CAs i.e. leading to low blood resistance in extracranial blood vessels agrees with an increased blood flow volume in bilateral ICAs, that statistically significant in the Right one, of the Khat chewers group compared to non-chewers (Table 3).

Moreover, these findings agree with the results of Ibrahim et al. (2017) who revealed that cerebral perfusion may be affected and increased by Khat chewing.

Since the active gradient in Khat (Cathinone) is pharmacologically similar and structurally related to amphetamine (Wabe, 2011), the decrease in Doppler indices and

increased cerebral perfusion are also noticed as amphetamine impact on cerebral capillary (Russo et al., 1991; Hassan et al., 2007), which may interpret the correlation of amphetamine abuse to hemorrhagic stroke (Westover et al., 2007).

Consequently, a decreased Doppler indices and increased cerebral perfusion may interpret the desirable and acutely psychostimulant effects of Khat chewing including mental alertness, increased energy, wakeful, optimism feelings, increased flow of ideas during activity of studying and enhanced concentration (Balint et al., 2009; Al'Absi, Khalil et al. 2013, Dachew et al., 2015), and also interprets its side effects including intracranial swelling, edema and hemorrhage (Abdul-Mughni et al., 2018).

The correlation between Khat and strokes was proven due to the effect of cathinone on the Central Nervous System (CNS), which finally led to platelets aggregation (Vanwalleghem et al., 2006, Kulkarni et al., 2012). Although this mechanism relates to the ischemic stroke, the mechanism related to the hemorrhagic one correlates with chronic Khat Chewing (Attafi, 2018; Ali et al., 2011; Benois et al., 2009), to the best of our knowledge, has not been established and no study has discussed the cause of increased hemorrhagic strokes among Khat chewers. Nevertheless, it is recommended for further studies (Sallam et al., 2009; Makwana et al., 2017).

Additionally, a study conducted in Sana'a city, Yemen revealed that hemorrhagic strokes happened mostly (51.7%) among patients aged between 15-44 years, and 43.4% of the entire sample were Khat chewers (Sallam et al., 2009). However, another study conducted on Mukalla city, Yemen revealed that the mean age of stroke among the study sample was similar to that noticed in other Middle East countries (Bamekhlah et al., 2014), which was within the 6^{th} and 7^{th} decade with predominance of the ischemic over hemorrhagic type (El-Hajj et al., 2016). This controversial argument resulting from one country can be due to regional and cultural reasons. In Yemeni Northern mountainous areas, Khat is grown and cultivated from hundreds of years (World Bank, 2007; Numan 2012), while it is not cultivated in Southern coastal areas (World Bank, 2007).

Therefore, Khat chewing could be one of the main causes of hemorrhagic stroke in Yemen, and it may become like untreated hypertension (Woo et al., 2004).

Accordingly, this is the first study that reveals and discusses the mechanism of hemorrhagic stroke based on the significantly decreased resistance of extracranial and cranial blood flow among Khat chewers.

When evaluating the Doppler parameters in CAs among the Khat chewers' group itself, it was revealed that the RI, PI and most of the PSVs had a negatively significant correlation with the period of chewing indicating that these Doppler parameters decrease with the increasing period of chewing (Table 2, Figures 4 and 5), which confirmed and supported the previous findings in the comparison between Khat and non-Khat chewers' groups.

These results with the results of Balint et al. (2009), Al-Motarreb et al. (2010) and Al Suwaidi et al. (2013), who reported that chronic Khat chewing has obvious effects on cardiovascular system may strengthen the previous suggested conclusion that Khat could be a risk factor of hemorrhagic stroke. They may also reinforce the interpretation of why the hemorrhagic stroke mostly occurs among younger population in Yemen while it mostly occurs among the elderly in the other Middle East countries (Vanwalleghem et al., 2006; Sallam et al., 2009; Kulkarni et al., 2012; El-Hajj et al., 2016).

Therefore, this study is important and can be a clinical guideline for physicians in preventing or at least decreasing the complications associated with cerebrovascular perfusion resulting from chronic Khat chewing, particularly among those with known cardiovascular disorders.

Further studies are recommended to address the B-mode sonography of carotid arteries and to use transcranial Doppler ultrasound technique which can provide measurements of cerebral blood flow with higher temporal resolution (Markus, 2004).

CONCLUSION

Chronic Khat chewing has mostly significant alterations in the blood flow velocities and Doppler indices of CAs (i.e., decreasing the PSVs, RI, PI, and increasing the EDVs), in addition to increasing Flow Volume of ICAs, which proved the relationship between the regular Khat chewing and stroke. Moreover, the negative correlation between carotid Doppler indices and the period of Khat chewing could help in the illustration of the mechanism through which Khat chewing could be a risk factor of hemorrhagic stroke.

ACKNOWLEDGEMENT

We thank the Radiology Department staff in University of Science and Technology Hospital who facilitated the study participants scanning procedures.

REFERENCES

Abdul-Mughni, A. S., El-Nahla, S. M., Hassan, S. A., & Dessouki, A. A. (2018). Teratogenic effects of Khat (Catha edulis) in New Zealand rabbit. *Journal of Advanced Veterinary and Animal Research*, *5*(1), 25-36.

Agunloye, A. M., & Owolabi, M. O. (2014). Exploring carotid sonographic parameters associated with stroke risk among hypertensive stroke patients compared to hypertensive controls. *Journal of Ultrasound in Medicine*, *33*(6), 975-983.

Al Suwaidi, J., Ali, W. M., & Aleryani, S. L. (2013). Cardiovascular complications of Khat. *Clinica Chimica Acta*, *419*, 11-14.

Al'Absi, M., Khalil, N. S., Al Habori, M., Hoffman, R., Fujiwara, K., & Wittmers, L. (2013). Effects of chronic khat use on cardiovascular, adrenocortical, and psychological responses to stress in men and women. *The American Journal on Addictions, 22*(2), 99-107.

Ali, W. M., Al Habib, K. F., Al-Motarreb, A., Singh, R., Hersi, A., Al Faleh, H., … &Al Suwaidi, J. (2011). Acute coronary syndrome and Khat herbal amphetamine use: An observational report. *Circulation 124*(24), 2681-2689.

Al-Motarreb, A., Al-Habori, M., & Broadley, K. J. (2010). Khat chewing, cardiovascular diseases and other internal medical problems: The current situation and directions for future research. *Journal of Ethnopharmacology*, *132*(3), 540-548.

Al-Motarreb, A., Briancon, S., Al-Jaber, N., Al-Adhi, B., Al-Jailani, F., Salek, M. S., & Broadley, K. J. (2005). Khat chewing is a risk factor for acute myocardial infarction: A case-control study. *British Journal of Clinical Pharmacology*, *59*(5), 574-581.

Andualem, M. A., Hassen, T. S., & Yemane, T. (2002). Effect of Khat (Catha edulis Forsk) on blood pressure & heart rate, a community based study. *Ethiopian Journal of Health Development*, *16*(3), 325-334.

Attafi, M. (2018). Analysis of cathinone and cathine in urine sample of Khat chewer presenting with hemorrhagic stroke. *Journal of Medicinal Chemistry and Toxicology, 3*(1), 15-18.

Balint, E. E., Falkay, G., & Balint, G. A. (2009). Khat–a controversial plant. *Wiener Klinische Wochenschrift*, *121*(19-20), 604-614.

Bamekhlah, R. M., Bin-Nabhan, A. S., & Musaian, N. S. (2014). Risk factors and clinical presentation of stroke in Mukalla, Hadhramout, Republic of Yemen. *Alandalus Journal for Applied Sciences*, *391*(3567), 1-19.

Benois, A., Raynaud, L., Coton, T., Petitjeans, F., Hassan, A., Ilah, A., … & Leberre, J. (2009). Morbidity and mortality after intensive care management of hemorrhagic stroke in Djibouti. *Medecine Tropicale: Revue Du Corps De Sante Colonial, 69*(1), 41-44.

Blanco, P. (2015). Volumetric blood flow measurement using Doppler ultrasound: concerns about the technique. *Journal of Ultrasound, 18*(2), 201-204.

Chow, M. J., Mondonedo, J. R., Johnson, V. M., & Zhang, Y. (2013). Progressive structural and biomechanical changes in elastin degraded aorta. *Biomechanics and Modeling in Mechanobiology*, *12*(2), 361-372.

Dachew, B. A., Bifftu, B. B., & Tiruneh, B. T. (2015). Khat use and its determinants among university students in northwest Ethiopia: A multivariable analysis. *International Journal of Medical Science and Public Health*, *4*(3), 319-323.

El-Hajj, M., Salameh, P., Rachidi, S., & Hosseini, H. (2016). The epidemiology of stroke in the Middle East. *European Stroke Journal*, *1*(3), 180-198.

Geta, T. G., Woldeamanuel, G. G., Hailemariam, B. Z., & Bedada, D. T. (2019). Association of chronic khat chewing with blood pressure and predictors of hypertension among adults in Gurage Zone, Southern Ethiopia: A comparative study. *Integrated Blood Pressure Control, 12*, 33-42.

Getahun, W., Gedif, T., & Tesfaye, F. (2010). Regular Khat (*Catha edulis*) chewing is associated with elevated diastolic blood pressure among adults in Butajira, Ethiopia: A comparative study. *BMC Public Health*, *10*(1), 1-8.

Hassan, N. A. G. M., Gunaid, A. A., & Murray-Lyon, I. M. (2007). Khat [*Catha edulis*]: Health aspects of Khat chewing. *EMHJ-Eastern Mediterranean Health Journal, 13*(3), 706-718.

Hassan, N. A., Gunaid, A. A., El-Khally, F. M., Al-Noami, M. Y., & Murray-Lyon, I. M. (2005). Khat chewing and arterial blood pressure: A randomized controlled clinical trial of alpha-1 and selective beta-1 adrenoceptor blockade. *Saudi Medical Journal*, *26*(4), 537-541.

Homma, S., Sloop, G. D., & Zieske, A. W. (2009). The effect of age and other atherosclerotic risk factors on carotid artery blood velocity in individuals ranging from young adults to centenarians. *Angiology*, *60*(5), 637-643.

Ibrahim, M., Gameraddin, M., & Malik, B. H. A. (2017). Doppler assessment of the effect of chewing Qat on hemodynamics of the common carotid arteries. *Journal of Medical Sciences, 17*(2), 95-101.

Kalix, P. (1990). Pharmacological properties of the stimulant Khat. *Pharmacology and Therapeutics*, *48*(3), 397-416.

Kirsch, J. D., Mathur, M., Johnson, M. H., Gowthaman, G., & Scoutt, L. M. (2013). Advances in transcranial Doppler US: Imaging ahead. *Radiographics*, *33*(1), E1-E14.

Krejcie, R. V., & Morgan, D. W. (1970). Determining sample size for research activities. *Educational and Psychological Measurement, 30*(3), 607-610.

Kulkarni, S. V., Mughani, Y. A. A., Onbol, E. H. A., & Kempegowda, P. (2012). Khat and stroke. *Annals of Indian Academy of Neurology*, *15*(2), 139-140.

Makwana, M. B., Mistri, A., & Patel, V. J. (2017). Physiological assessment of common carotid artery resistive index to evaluate different risk factors for the development of cerebrovascular stroke. *International Journal Of Basic And Applied Physiology*, *6*(1), 60-66.

Markus, H. S. (2004). Cerebral perfusion and stroke. *Journal of Neurology, Neurosurgery and Psychiatry*, *75*(3), 353-361.

Mega, T. A., & Dabe, N. E. (2017). Khat (*Catha edulis*) as a risk factor for cardiovascular disorders: Systematic review and meta-analysis. *The Open Cardiovascular Medicine Journal, 11*, 146-155.

Numan, N. (2012). The green leaf: Khat. *World Journal of Medical Sciences*, *7*(4), 210-223.

Pourcelot, L. (1976). Diagnostic ultrasound for cerebral vascular diseases. In J. Donald & S. Levis (Eds.), *Present and future of diagnostic ultrasound* (pp. 141-147). Rotterdam, Netherlands: Kooyker Scientific Publications.

Russo, K. E., Hall, W., Chi, O. Z., Sinha, A. K., & Weiss, H. R. (1991). Effect of amphetamine on cerebral blood flow and capillary perfusion. *Brain Research*, *542*(1), 43-48.

Sallam, A. R., Al-Aghbari, K., & Awn, H. (2009). The clinical profile of stroke: a Yemeni experience. *Jordan Medical Journal*, *43*(2), 115-121.

Tesfaye, F., Byass, P., Wall, S., Berhane, Y., & Bonita, R. (2008). Peer reviewed: Association of smoking and Khat (*Catha edulis* Forsk) use with high blood pressure among adults in Addis Ababa, Ethiopia, 2006. *Preventing Chronic Disease*, *5*(3), 1-11.

Vanwalleghem, I. E., Vanwalleghem, P. W., & De Bleecker, J. L. (2006). Khat chewing can cause stroke. *Cerebrovascular Diseases*, *22*(2-3), 198-200.

Wabe, N. T. (2011). Chemistry, pharmacology, and toxicology of Khat (*Catha edulis* forsk): A review. *Addiction and Health*, *3*(3-4), 137-149.

Westover, A. N., McBride, S., & Haley, R. W. (2007). Stroke in young adults who abuse amphetamines or cocaine: A population-based study of hospitalized patients. *Archives of General Psychiatry 64*(4), 495-502.

Woo, D., Haverbusch, M., Sekar, P., Kissela, B., Khoury, J., Schneider, A., … & Broderick, J. (2004). Effect of untreated hypertension on hemorrhagic stroke. *Stroke, 35*(7), 1703-1708.

World Bank. (2007). *Yemen toward Qat demand reduction*. Report no. 39738-YE. Washington, D.C.: World Bank.

Yazici, B., Erdogmus, B., & Tugay, A. (2005). Cerebral blood flow measurements of the extracranial carotid and vertebral arteries with Doppler ultrasonography in healthy adults. *Diagnostic and Interventional Radiology, 11*(4), 195-198.

Yehia, M. (2015). *Effects of Qat consumption on blood pressure and cardiac rhythm among hypertensive and ischaemic heart disease subjects* (Doctoral dissertation). University of Khartoum, Khartoum, Sudan.

Pertanika J. Sci. & Technol. 28 (3): 1105 - 1116 (2020)

PERTANIKA JOURNALS

SCIENCE & TECHNOLOGY

Journal homepage: http://www.pertanika.upm.edu.my/

Impact of Lateral Size of Graphene Oxide in Pour Point Depressant Composite on Wax Crystallisation of Model Oil

Muhamad Ridhwan Hafiz Rosdi, Mohd Danial Mohd Johary, Ku Marsilla Ku Ishak and Azlan Ariffin*

School of Materials and Mineral Resources Engineering, Engineering Campus, Universiti Sains Malaysia, 14300 USM, Nibong Tebal, Penang, Malaysia

ABSTRACT

Graphene oxide (GO) is a reliable additive used to improve the wax crystal inhibition performance of pour point depressant (PPD). In understanding the lateral size effect on wax crystal inhibition, PPD emulsions containing graphene oxide of different lateral sizes were prepared. The parameters of pour point reduction (PPR) and dissipated wax crystallisation enthalpy were considered in the assessment of wax inhibition performance. PPR was measured using a pour point tester in accordance to ASTM D-97, while the enthalpy dissipation was evaluated via differential scanning calorimetry (DSC) under cooling cycle. The study revealed that the addition of GO lowered the wax crystallisation enthalpy, as indicated by the lesser amount of precipitated wax present in the model oil. The enthalpy underwent a decrease from 25.04 to 23.97 Jg^{-1} with decreasing GO lateral size. It is evident from the pour point test that the use of different GO lateral sizes significantly affects the wax inhibition, as verified through the highest PPR of 10°C displayed by the EJGO5 sample (with addition of the smallest lateral size of 1 µm). In short, manipulating the GO lateral size in sonicated samples boosted the PPR up to 100% compared to the unsonicated sample (EJGO1). Furthermore, smaller lateral size provides more nucleation site for wax co-crystallisation, hence preventing the neighbouring wax crystals from attaching and forming a looser crystal structure. The thermal characteristics of the PPD

ARTICLE INFO

Article history:
Received: 26 February 2020
Accepted: 22 April 2020
Published: 16 July 2020

E-mail addresses:
piecedue@yahoo.com (Muhamad Ridhwan Hafiz Rosdi)
duerensuke@gmail.com (Mohd Danial Mohd Johary)
ku_marsilla@usm.my (Ku Marsilla Ku Ishak)
srazlan@usm.my (Azlan Ariffin)
*Corresponding author

ISSN: 0128-7680
e-ISSN: 2231-8526

© Universiti Putra Malaysia Press

emulsions were also examined through DSC technique, which revealed that the emulsions thermal properties were unaffected by the addition of GO.

Keywords: Ethylene vinyl acetate, graphene oxide, lateral size, pour point depressant, wax crystallisation

INTRODUCTION

The precipitation of paraffin wax presents significant impacts on the waxy crude oil transportation. Paraffin wax tends to precipitate from oil due to super-saturation which takes place when the temperature of waxy crude oil falls below its wax appearance temperature (WAT) (Deshmukh & Bharambe, 2008; Martínez-Palou et al., 2011; Pedersen & Rønningsen, 2003; Yang et al., 2015). In this instance, chemical treatment such as pour point depressant (PPD) is preferred to hinder the deposition of wax, since chemical treatment is more cost-effective and efficient compared to other techniques. In general, most conventional PPD products formulated in solution are susceptible to solidification at low temperatures. Therefore, the application of PPD solution in cold climates such as the winter season is limited. To solve the PPD solidification issue at room temperature, emulsion technology is often implemented (Razak et al., 2018; Rosdi et al., 2016; Umoruddin et al., 2019).

Admiral et al. (2016) had successfully formulated flowable PPD emulsion at ambient temperature with enhanced viscosity at room temperature, thermal properties at sub ambient temperature, particle size, and stability. However, even though PPD emulsion demonstrates decent thermal and stability performances, the wax inhibition performance remains limited. Recently, graphene and graphene oxide (GO) have attracted the interest and attention of researchers as additives for wax inhibition enhancement. Indeed, the introduction of nano-sized particles into polymers has also been recognised as a well-acknowledged technique for boosting the present polymers properties (Boccaccini et al., 2010; Kim et al., 2017; Zhao et al., 2018). This specific polymer classification, known as polymer nanocomposites, can be utilised in PPD emulsion to increase its performance effectiveness. The addition of GO provides more nucleation site in emulsion, hence preventing the formation of a massive 3-dimensional crystal network structure while simultaneously enhances the flow ability of the emulsion. Al-Sabagh et al. (2016) pointed out that the addition of GO into conventional polymethylmethaacrylate (PMMA) results in superior performance by lowering the apparent viscosity and pour point of crude oil. Similarly, Sharma et al. (2019) demonstrated that significant depression in pour point could be improved with an incorporation of higher percentage GO in PPD-GO additives.

To date, most studies are focussing on the application of GO with particular dosage or concentration as well as its lateral size effects restrictedly towards the mechanical, electrical, and thermal conductivity properties of PPD material (Kim et al., 2017; Li et

al., 2019). Nonetheless, the influence of lateral size of GO on the wax crystallisation of model oil still remains unclear to be discussed. Therefore, in this study, an experiment was constructed to examine the effect of GO lateral size (with different sonication times) on the wax crystallisation behaviour and the wax crystal microstructure of model oil. Moreover, the lateral size impacts on the PPD emulsions thermal properties and stability were also examined to ensure their standard properties were not compromised.

MATERIALS AND METHODS

Materials

The tall oil fatty acid based emulsifier (MWV01), hydrocarbon solvent (Solvesso 150), and xylene utilised in this study were provided by ACME Chemicals (Malaysia) Sdn. Bhd. Meanwhile, the ethylene glycol, ethylene vinyl acetate (EVA, 25% VA content), and diethanolamine were procured from Merck Sdn. Bhd., and the graphene oxide was supplied by Nano Malaysia Berhad. Deionised water on the other hand was directly available in the laboratory.

Graphene Oxide Preparation

Sonication process was chosen in the preparation of the different lateral sizes GO. GO was weighed (0.3 gram) and dispersed in deionised water in a 50 ml glass beaker, producing GO of concentration of 10 mg/L. The beaker was then placed in ice bath to contain the heat generated from the sonication. The sonication amplitude was set to 25%. The designated GO samples as control/unsonicated (GO1) and sonicated (GO2-5) were subjected to respective sonication times, as presented in Table 1.

Table 1
Graphene oxide (GO) sample preparation based on sonication duration parameter

	GO1	GO2	GO3	GO4	GO5
Sonication duration (minutes)	0	10	30	60	100

Sample Preparation

The preparation of nano-hybrid PPD was undertaken by blending together EVA, Solvesso 150, xylene, diethanolamine, MWV01 emulsifier, ethylene glycol, and deionised water at a stirring speed of 600 rpm for 60 minutes at 50 - 60°C. Subsequently, the GO1 sample was added into the mixture accordingly and the mixture was sonicated for 10 minutes. Ice bath was used to ensure the mixture temperature not exceeding 60°C. This emulsion was denoted as EJGO1. As for the EJN sample, no addition of GO was involved. The same procedure was repeated using GO2 - GO5 samples to produce EJGO2 - EJGO5 emulsions accordingly.

Sample Characterisation

Scanning Electron Microscopy (SEM). To prepare the testing sample, a drop of sonicated GO was initially deposited on a silicon wafer (1 x 1 cm) and was left to dry in an oven for approximately 30 min. The silicon wafer, once completely dried, was attached to the sample holder using double-sided copper tape. The sample was then coated with gold to ensure it was in conductive state prior to SEM analysis. The lateral sizes of the GO1, GO2, GO3, GO4, and GO5 samples were measured through the Image J software.

Thermal Properties of PPD Composite Emulsion. The PPD composite thermal properties were assessed using Mettler Toledo (USA) differential scanning calorimeter (DSC) at a low temperature range. The samples were weighed to approximately 8 - 10 mg, then analysed at temperatures between 50°C and -30°C at a cooling/heating rate of 10°C/minute. In the first cycle, the samples were heated from 30°C to 50°C and held at an isothermal temperature of 50°C for 1 min before cooling to -30°C under the same condition as mentioned above.

Performance Evaluation via Pour Point (ASTM D-97). The evaluation was carried out according to the pour point standard of ASTM D97. This standard is generally applied to measure the pour point of any petroleum-based oil. In this evaluation, model oil sample was transferred into a glass tube and was pre-heated up to 50°C, followed by a cooling process to enable the formation of paraffin wax crystals within the model oil. When the sample temperature started to drop, its flow features were observed at every 1°C interval. The glass test tube was then tilted to spot for any model oil movement. Once no more model oil flow was observed (in tilting position), the tube was placed horizontally for approximately 10 seconds. If the test sample did not display any flow behaviour, the pour point was recorded. The pour point reduction (PPR) was then determined based on Equation 1.

$$P_R = P_B - P_{PPD} \quad (1)$$

P_R = Pour point reduction.
P_B = Pour point of untreated model oil.
P_{PPD} = Pour point of treated model oil.

Thermal Analysis of Treated Wax. Differential scanning calorimetry (DSC) has been comprehensively employed in the wax appearance temperature (WAT) investigation. Herein, the untreated/treated samples (8 - 10 mg) were analysed at temperatures between 30°C and -100°C (5°C/min). The samples were cooled from 30°C to -100°C and held at -100°C (isothermal temperature) for 1 min before undergoing heating from -100°C to 30°C at a rate of 5°C/min.

Polarised Optical Microscopy (POM). The microstructure of the untreated/treated waxes in model oil was inspected using BX51 (Olympus Optical Co., Ltd., Japan) polarising

optical microscope. The simulated paraffin wax was heated to 50°C in water bath. Subsequently, approximately 4 µL of the paraffin wax was dropped onto a round glass slide before sandwiching it together with another slide. The round glass slide was then placed on the heating stage and heated to 50°C at a rate of 5°C/min in oxygen environment. The microstructure of the waxes was recorded during the cooling process (1ºC/min) under 100X magnification.

RESULTS AND DISCUSSION

Graphene Oxide Lateral Size Analysis

Scanning electron microscopy (SEM) was conducted to measure the GO lateral size respective of different ultrasonication times. The GO samples were designated as control/ unsonicated (GO1) and sonicated (GO2 - GO5). Figure 1 (A - E) displays the SEM images of all GO samples (GO1 - GO5) at 300X magnification.

Figure 2 on the other hand exhibits the relationship between sonication time and the lateral size of the GO samples. Clearly, a considerable decrement in the GO lateral size was observed between the GO1 (unsonicated) and GO2 (sonicated) samples, of 29 µm and 9 µm respectively. This is because the GO1 (control) sample remained in its stacking manner, which eventually underwent exfoliation into GO nanosheets after sonication. Further increase in sonication time (GO2 - GO5) resulted in proportionate reduction of lateral size to 9 µm, 6µm, 4µm, and 2µm respectively as shown in Figure 2. These findings are supported by the study conducted by Lin et al. (2017) where significant reduction in lateral size was observed at the initial stage of sonication of graphene-based material. The changes in the lateral size of GOs are also in agreement with the observation made from Figure 1.

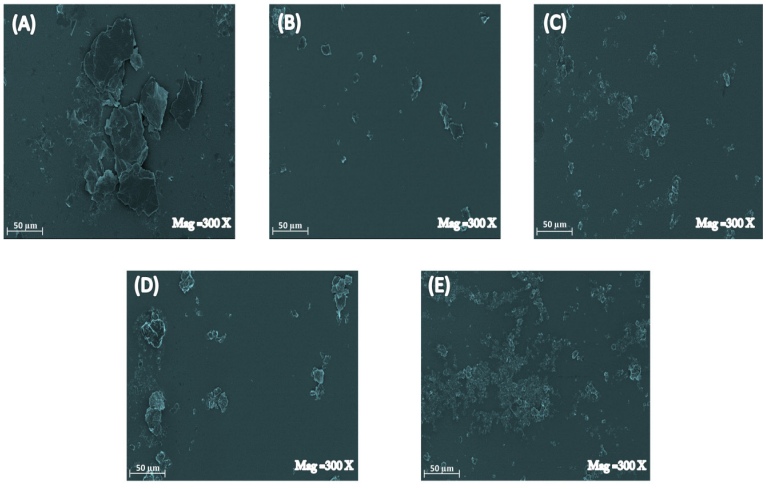

Figure 1. Micrographs of graphene oxide at different sonication times; (A) O minute (GO1); (B) 10 minutes (GO2); (C) 30 minutes (GO3); (D) 60 minutes (GO4); and (E) 100 minutes, at a magnification of 300X

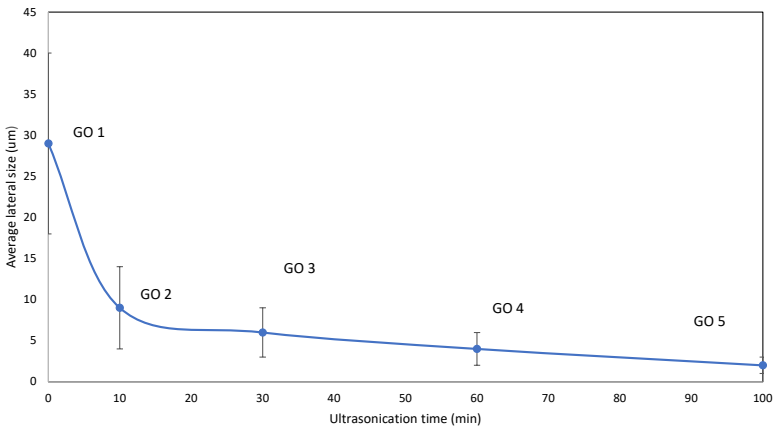

Figure 2. Average lateral sizes of control (GO1)/sonicated (GO2 - GO5) graphene oxide samples subjected to different ultrasonication times

Thermal Properties of PPD Composite Emulsion

Figure 3 displays the DSC heating cycle thermograms of the PPD emulsions with variable graphene oxide lateral sizes (GO1 - GO5). As can be seen, the addition of GO in the PPD emulsions generally lowered their melting point. Moreover, no clear pattern or trend was observed between the samples given the fluctuating thermal readings. However, the PPD emulsions thermal properties were found to remain unaffected (not exceeding EJN) with the addition of GO. EJGO5 displayed the lowest melting temperature, indicating that GO widens the temperature range of PPD emulsion by maintaining the fluidity of the emulsion. Upon heating, the emulsions, particularly EJN, EJGO2, and EJGO4, generated exothermic peaks of -63.51, -84.18, and -80.03°C respectively as presented in Table 2. This suggests that crystallisation had occurred before the melting point was reached. These peaks are referred as the devitrification peaks (Td). Devitrification or recrystallisation that occurs

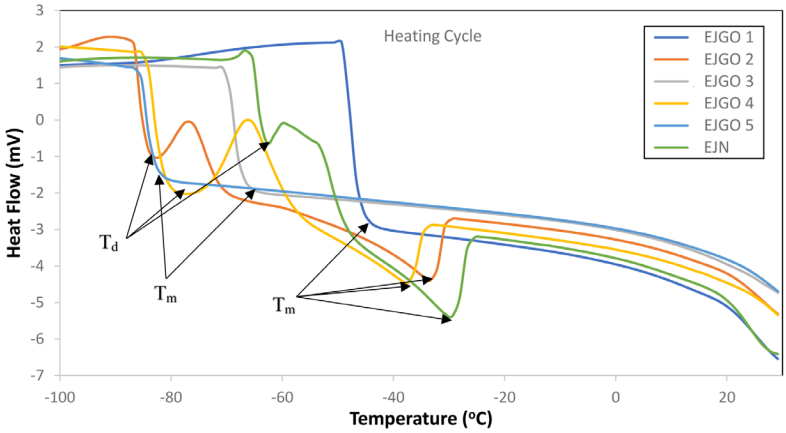

Figure 3. DSC heating cycle thermograms of PPD samples

during the reheating process of sample indicates no formation of ice crystals during its cooling process (Nasir et al., 2018). Accordingly, this phenomenon helps to eliminate the problem of neighbouring droplets collision due to volume expansion from the ice crystals formation. Therefore, the formation of large sized droplets could be avoided, and the stability of emulsions can be enhanced during the temperature cycle.

Pour Point Evaluation (ASTM D-97)

Figure 4 shows the pour point reduction (PPR) of the treated waxes with the EJN and EJGO1 - EJGO5 emulsions. The results indicated that the addition of graphene oxide, particularly in EJGO1 boosted the performance of the additive in reducing the pour point of the model oil to as minimum as 2°C reduction compared to the control sample (EJN). The highest PPR of 10°C was displayed by EJGO5 which has the smallest lateral size of 1 μm. This underlines the impact of lateral size manipulation in boosting the PPR of sonicated emulsions up to 100% compared to the unsonicated sample (EJGO1) which only yielded 5°C PPR.

Theoretically, paraffin chains will adsorb and co-crystallise with polymers. This manifestation modifies the shape and size of the wax crystals. Furthermore, it encourages improvement in performance-wise as displayed by EJGO1 - EJGO5 in Figure 4 which is contributed by the presence of graphene oxide. This material provides secondary nucleation site for wax co-crystallisation. Besides, it also creates repulsive interaction among wax crystals (Al-Sabagh et al., 2016), which allows the wax crystals to remain dispersed without forming interlocking network, hence enhancing the flow-ability of model oil even at lower temperatures. Notably, smaller GO lateral size is achieved with longer ultrasonication duration, which provides more nucleation site for wax precipitation. Consequently, this reduces the tendency of wax particles crystallisation with one another by forming a rigid network that favours the flow improvement at a lower temperature.

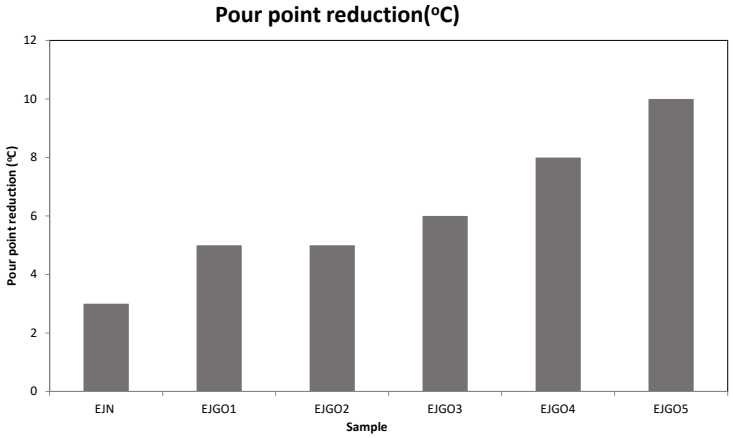

Figure 4. Pour point reduction of model oil injected with 1000 ppm PPD samples

Thermal Analysis of Model Oil

The DSC thermograms and wax crystallisation enthalpy of the wax samples are demonstrated in Figure 5 and Table 3 respectively. Generally, the addition of the control sample (EJN) was seen to increase the wax appearance temperature (WAT) value to about 4.71°C. This portrays the role of EVA as crystal nuclei to stimulate wax crystallisation at the initial stage before providing an inhibition effect.

On the other hand, EJGO5 demonstrated a WAT increment of 2.73°C, which was the lowest among all samples. This indicates that the addition of GO provides better efficiency in the modification of the wax crystallisation process. In addition, GO plays a major role in dispersing and stabilising wax crystals to inhibit aggregation so that high pour reduction can be achieved, as demonstrated in Figure 5. As such, GO provides heterogeneous nucleation sites for wax chains to co-crystallise, resulting in smaller wax aggregates and thus generating well-dispersed aggregates. Hence, the model oil remained in fluid state.

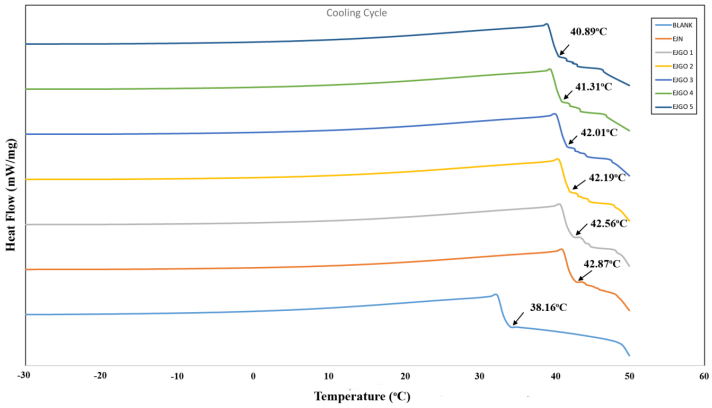

Figure 5. DSC thermograms of wax appearance temperature (WAT) of untreated/treated model oil

Based on Table 3, the samples with GO addition demonstrated lower wax crystal enthalpy values compared with the untreated and treated waxes with the reference sample (EJN). For instance, EJGO1 exhibited an enthalpy of 25.04 Jg^{-1}, lower than those of the untreated and treated EJN of 30.40 and 31.93 Jg^{-1} respectively. Further decrement in enthalpy was observed with the reduction in the lateral size of GO. Herein, the addition of GO decreased the ΔH_f and increased the critical radius (RC) (Yang et al., 2017), where EJGO5 exhibited the lowest enthalpy value of 23.97 Jg^{-1}. Enthalpy information can be used to evaluate the capability of a wax additive. Moreover, a lower enthalpy value indicates lesser amount of wax being precipitated or crystallised. Thus, better pour point inhibition can be achieved.

However, these findings are not aligned with the WAT results, as shown in Figure 5. This phenomenon plausibly arises due to the presence of GO particles which offers

heterogeneous nucleation sites for the aggregation of wax at smaller degrees of super cooling, therefore resulting in a minor escalation in the wax appearance temperature (WAT) readings.

Table 3

Wax crystallisation enthalpy of all samples

SAMPLE	ΔH_{wc} (Jg^{-1})
Untreated wax	30.40
EJN	31.93
EJGO 1	25.04
EJGO 2	25.06
EJGO 3	24.56
EJGO 4	24.34
EJGO 5	23.97

Polarised Optical Microscopy (POM)

The microstructures of the untreated/treated model oil observed at 20°C are as illustrated in Figure 6. As can be seen, the untreated model oil exhibited smaller wax crystal size compared to the treated EJN and EJGO1. A large amount of precipitated wax crystals was present in the untreated sample. The addition of EJN into the model oil had significantly altered the morphology of the wax crystals into larger wax precipitates, whereas the introduction of GO into the model oil resulted in smaller and more dispersed wax crystals as illustrated in Figure 6(C). GO particles are capable to improve the inhibition of wax growth via surface adsorption (Al-Sabagh et al., 2016), where they adsorb onto wax surfaces, causing the wax nuclei irresponsive towards temperature changes. This promotes the aggregation of wax; however in fine small size or in dispersed manner. Subsequently, the interlocking wax network, which is essential for solidification is eliminated.

The wax crystal microstructures of the model oil treated with EJGO1 - EJGO5 were observed and demonstrated in Figure 7. As shown in Figure 7(A), the wax crystals assembled as interlocking wax network. This occurrence shows that EJGO1 which has the highest lateral size of 29 µm exhibited the least efficiency in creating barrier to the formation of interlocking network. After the addition of EJGO2, the formation of wax network became lesser and more dispersed wax particles were observed. The reduced lateral size of GO favours further inhibition of interlocking network of wax crystals, as evident in Figure 7. Furthermore, even with the highest number of crystal aggregates, the wax aggregates in EJGO5 remained dispersed and stabilised given the adsorption of GO with the surplus nucleation site.

Apparently, more wax crystals were formed but in dispersed manner in EJGO5 than EJGO1, as observed by the very limited interlocking wax networks present in the model oil

as shown in Figure 7(E). Therefore, GO is deemed to impede the formation of interlocking crystal network, contributing to a lower pour point temperature. The deviations in wax morphology are in consent with the pour point results portrayed in Figure 4.

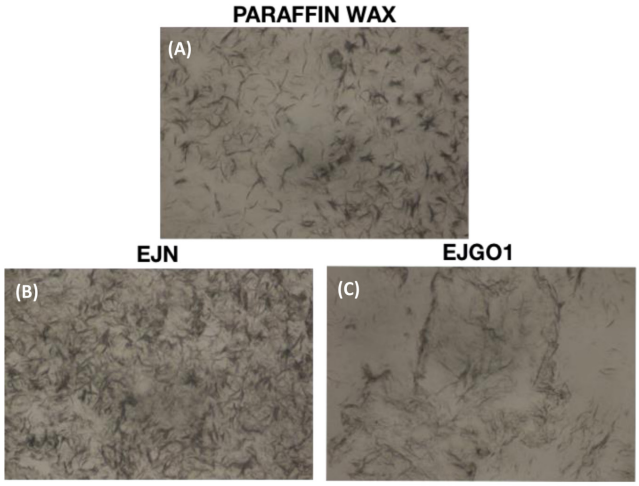

Figure 6. Polarised optical microscope images of the wax crystal microstructures of (A) untreated paraffin wax; (B) treated wax with EJN; and (C) treated wax with EJGO1

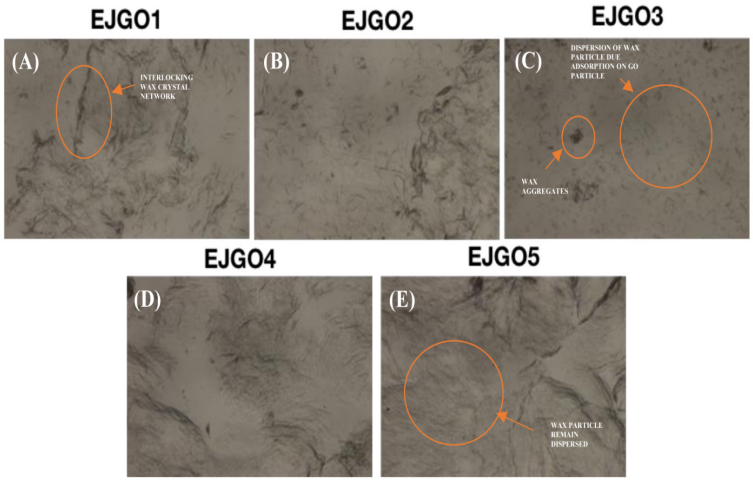

Figure 7. Polarised optical microscope images of wax crystal microstructures of treated waxes with (A) EJGO1; (B) EJGO2; (C) EJGO3; (D) EJGO4; and (E) EJGO5

CONCLUSION

The effects of variable GO lateral sizes on the pour point reduction (PPR) and wax crystallisation of model oil were investigated in this study. The properties of the PPD emulsions of study were also examined where no significant adverse effect was detected. However, contrasting influences of GO lateral size on the WAT and PPR parameters were

observed. It was also found that GO acts as the crystal nucleus to promote wax crystallisation, which eventually increased the WAT of emulsions. Nonetheless, EJGO5 reflected a higher PPR of 10°C compared to the control sample (EJN) of only 3°C. This finding is supported by the lowest wax crystallisation enthalpy of 23.97 Jg^{-1} displayed by EJGO5 which has the smallest GO lateral size. The study further verified that lateral size also played a significant role in altering wax crystallisation. Herein, smaller GO lateral size offers larger surface area for the adsorption of wax crystals, resulting in fewer wax aggregates formed with improved dispersion. Subsequently, improper wax crystals assembly gives rise to delayed formation of interlocking wax crystal network, which invariably reduces the pour point temperature. In conclusion, this study revealed the structure-activity relationship of GO lateral size effects on the thermal properties and microstructure of wax in model oil. The addition of GO in conventional PPD provides a positive boost towards wax crystallisation while retaining the original PPD emulsion thermal properties.

ACKNOWLEDGEMENTS

The authors are deeply indebted to Professor Azlan Ariffin and the laboratory team for their help and guidance throughout the completion of this research and publication. The authors would also like to express appreciation for the financial support awarded by the Ministry of Education Malaysia (MOE) via Fundamental Research Grant Scheme (FRGS) (Grant No. 203/PBAHAN/6071326).

REFERENCES

Admiral, A., Abdullah, M., & Ariffin, A. (2016). Evaluation of emulsified acrylate polymer and its pour point depressant performance. *Procedia Chemistry, 19*, 319-326.

Al-Sabagh, A., Betiha, M., Osman, D., Hashim, A., El-Sukkary, M., & Mahmoud, T. (2016). Preparation and evaluation of poly (methyl methacrylate)-graphene oxide nanohybrid polymers as pour point depressants and flow improvers for waxy crude oil. *Energy and Fuels, 30*(9), 7610-7621.

Boccaccini, A. R., Erol, M., Stark, W. J., Mohn, D., Hong, Z., & Mano, J. F. (2010). Polymer/bioactive glass nanocomposites for biomedical applications: A review. *Composites Science and Technology, 70*(13), 1764-1776.

Deshmukh, S., & Bharambe, D. (2008). Synthesis of polymeric pour point depressants for Nada crude oil (Gujarat, India) and its impact on oil rheology. *Fuel Processing Technology, 89*(3), 227-233.

Kim, J., Kim, S. W., Yun, H., & Kim, B. J. (2017). Impact of size control of graphene oxide nanosheets for enhancing electrical and mechanical properties of carbon nanotube–polymer composites. *RSC Advances, 7*(48), 30221-30228.

Li, H., Wu, X., Cheng, K., Miao, J., Tang, Z., Qiu, H., & Yang, J. (2019). Preparation of graphene oxide with large lateral size and graphene/polyimide hybrid film via in situ "molecular welding" strategy. *Materials Letters, 237*, 168-171.

Lin, Z., Karthik, P., Hada, M., Nishikawa, T., & Hayashi, Y. (2017). Simple technique of exfoliation and dispersion of multilayer graphene from natural graphite by ozone-assisted sonication. *Nanomaterials, 7*(6), 1-10.

Martínez-Palou, R., de Lourdes Mosqueira, M., Zapata-Rendón, B., Mar-Juárez, E., Bernal-Huicochea, C., de la Cruz Clavel-López, J., & Aburto, J. (2011). Transportation of heavy and extra-heavy crude oil by pipeline: A review. *Journal of Petroleum Science and Engineering, 75*(3), 274-282.

Nasir, N., Rosdi, M., & Ariffin, A. (2018). The impact of different antifreeze agents on the thermal properties of ethylene vinyl acetate emulsion. *Polymers for Advanced Technologies, 29*(2), 708-715.

Pedersen, K. S., & Rønningsen, H. P. (2003). Influence of wax inhibitors on wax appearance temperature, pour point, and viscosity of waxy crude oils. *Energy and Fuels, 17*(2), 321-328.

Razak, A. S. A., Gafri, N. F., Razali, M. A. A., Ariff, Z. M., Hamid, Z. A. A., & Ariffin, A. (2018). The impact of monomer loading on poly (methyl methacrylate) nano emulsion as pour point depressant. *Petroleum Science and Technology, 36*(11), 793-800.

Rosdi, M., Ariffin, A., & Ishak, Z. (2016). Optimizing homogenization parameters for improving ethylene vinyl acetate emulsion stability in pour point depressant application. *Journal of King Saud University-Engineering Sciences, 30*(2), 105-115.

Sharma, R., Mahto, V., & Vuthaluru, H. (2019). Synthesis of PMMA/modified graphene oxide nanocomposite pour point depressant and its effect on the flow properties of Indian waxy crude oil. *Fuel, 235*, 1245-1259.

Umoruddin, N., Rosdi, M. H., & Ariffin, A. (2019). Mixed surfactant enabled EVA emulsion for PPD applications. *Journal of Dispersion Science and Technology, 40*(3), 361-368.

Yang, F., Yao, B., Li, C., Shi, X., Sun, G., & Ma, X. (2017). Performance improvement of the ethylene-vinyl acetate copolymer (EVA) pour point depressant by small dosages of the polymethylsilsesquioxane (PMSQ) microsphere: An experimental study. *Fuel, 207*, 204-213.

Yang, F., Zhao, Y., Sjöblom, J., Li, C., & Paso, K. G. (2015). Polymeric wax inhibitors and pour point depressants for waxy crude oils: A critical review. *Journal of Dispersion Science and Technology, 36*(2), 213-225.

Zhao, Z., Yan, S., Lian, J., Chang, W., Xue, Y., He, Z., ... & Han, S. (2018). A new kind of nanohybrid poly (tetradecyl methyl-acrylate)-graphene oxide as pour point depressant to evaluate the cold flow properties and exhaust gas emissions of diesel fuels. *Fuel, 216*, 818-825.

REFEREES FOR THE PERTANIKA
JOURNAL OF SCIENCE AND TECHNOLOGY

VoL. 28 (3) Jul. 2020

The Editorial Board of the Journal of Science and Technology wishes to thank the following:

Abd Muhaimin Amiruddin
(UPM, Malaysia)

Abdullah Hisam Omar
(UTM, Malaysia)

Adibah Mohd Amin
(UPM, Malaysia)

Ambarish Mohapatra
(SIT, India)

Amir Izzwan Zamri
(UMT, Malaysia)

Angelina Chin Yan Mui
(UM, Malaysia)

Arien Heryansyah
(UTM, Malaysia)

Aslina Baharum
(UMS, Malaysia)

Aweng Eh Rak
(UMK, Malaysia)

Badariah Bais
(UKM, Malaysia)

Baharin Azahari
(USM, Malaysia)

Basava Rao Venkata Vudata
(Osmania University, India)

Bhatia Amit
(Amity University, India)

Che Zulzikrami Azner Abidin
(UniMAP, Malaysia)

Chuah Cheng Hock
(UM, Malaysia)

Eddie Shahril Ismail
(UKM, Malaysia)

Ghufran Redzwan
(UM, Malaysia)

Habshah Midi
(UPM, Malaysia)

Hasfalina Che Man
(UPM, Malaysia)

Hassakorn Wattanasarn
(SNRU, Thailand)

Hollena Nori
(UNIMAS, Malaysia)

Hussein Adel Mahmood
(UPM, Malaysia)

Irfan Ahmed Shaikh
(SAU, Pakistan)

Kamarul Ariffin Noordin
(UM, Malaysia)

Kek Sie Long
(UTHM, Malaysia)

Khadijah Hilmun Kamarudin
(UMT, Malaysia)

Khoo Shin Yee
(UM, Malaysia)

Lai Kee Huong
(Sunway University, Malaysia)

Lee Hooi Ling
(USM, Malaysia)

Lim Fong Peng
(UPM, Malaysia)

Loh Su Peng
(UPM, Malaysia)

Maizatul Akmar Ismail
(UM, Malaysia)

Marsyita Hanafi
(UPM, Malaysia)

Martini Mohammad Yusoff
(UPM, Malaysia)

Marzanah Jabar
(UPM, Malaysia)

Md Faisal Md Basir
(UTM, Malaysia)

Md. Mainul Hasan
(PSTU, Bangladesh)

Md. Noordin Abu Bakar
(USM, Malaysia)

Md. Suffian Idris
(UMT, Malaysia)

Mohamad Ikhsan Selamat
(UiTM, Malaysia)

Mohamad Kamarol Mohd Jamil
(USM, Malaysia)

Mohamad Syazarudin Md Said
(UPM, Malaysia)

Mohamad Taufik Hidayat Baharuldin
(UPM, Malaysia)

Mohamadariff Othman
(UM, Malaysia)

Mohd Amin Mohd Soom
(UMS, Malaysia)

Mohd Shahrul Nizam Mohd Danuri
(KUIS, Malaysia)

Mostafa Abdulghafoor Mohammed
(UPB, Romania)

Muhamad Saufi Mohd Kassim
(UPM, Malaysia)

Muhammad Heikal Ismail
(UPM, Malaysia)

Muhammad Nazrul Hakim Abdullah
(UPM, Malaysia)

Mus`ab, Abd. Razak
(UPM, Malaysia)

Muzzneena Ahmad Mustapha
(UKM, Malaysia)

Ng Kok Haur
(UM, Malaysia)

Nik Azuan Nik Ismail
(UKM, Malaysia)

Nik Nor Liyana Nik Ibrahim
(UPM, Malaysia)

Nor Asila Wati Abdul Hamid
(UPM, Malaysia)

Nora Muda
(UKM, Malaysia)

Norhafiz Azis
(UPM, Malaysia)

Normala Halimoon
(UPM, Malaysia)

Nur Fadhilah Ibrahim
(UMT, Malaysia)

Ooi Lu Ean
(USM, Malaysia)

Phang Chang
(UTHM, Malaysia)

Rashima Mahajan
(MRIIRS, India)

Razali Ngah
(UTM, Malaysia)

Rizafizah Othaman
(UKM, Malaysia)

Rohaya Latip
(UPM, Malaysia)

Rosnah Shamsudin
(UPM, Malaysia)

Rosnita Talib
(UPM, Malaysia)

Roya Abedi
(University of Tabriz, Iran)

Ruslan Rainis
(USM, Malaysia)

Ruslan Wirosoedarmo
(Universitas Brawijaya, Indonesia)

Sayed Sayeed Ahmad
(AGU, United Arab Emirates)

Shaifulazuar Rozali
(UM, Malaysia)

Siti Hasana Sapar
(UPM, Malaysia)

Siti Khairunniza Bejo
(UPM, Malaysia)

Tania Islam
(UM, Malaysia)

Tay Chia Chay
(UiTM, Malaysia)

Viv Djanat Prasita
(Universitas Hang Tuah, Indonesia)

Wan Ainun Mior Othman
(UM, Malaysia)

Yusnita Mohd Ali
(UiTM, Malaysia)

Zelina Zaiton Ibrahim
(UPM, Malaysia)

Zulkarami Berahim
(UPM, Malaysia)

Zulkarnain Hassan
(UniMAP, Malaysia)

Yusnita Mohd Ali
(UiTM, Malaysia)

Zelina Zaiton Ibrahim
(UPM, Malaysia)

Zulkarami Berahim
(UPM, Malaysia)

Zulkarnain Hassan
(UniMAP, Malaysia)

AGU	*– Al Ghurair University*
KUIS	*– Kolej Universiti Islam Antarabangsa Selangor*
MRIIRS	*– Manav Rachna International Institute Research & Studies*
PSTU	*– Patuakhali Science and Technology University*
SAU	*– Sindh Agriculture University*
SIT	*– Silicon Institute of Technology*
SNRU	*– Sakon Nakhon Rajabhat University*
UiTM	*– Universiti Teknologi MARA*
UKM	*– Universiti Kebangsaan Malaysia*
UM	*– Universiti Malaya*
UMK	*– Universiti Malaysia Kelantan*
UMS	*– Universiti Malaysia Sabah*
UMT	*– Universiti Malaysia Terengganu*
UniMAP	*– Universiti Malaysia Perlis*
UNIMAS	*– Universiti Malaysia Sarawak*
UPB	*– Politehnica University of Bucharest*
UPM	*– Universiti Putra Malaysia*
USM	*– Universiti Sains Malaysia*
UTHM	*– Universiti Tun Hussein Onn Malaysia*
UTM	*– Universiti Teknologi Malaysia*

While every effort has been made to include a complete list of referees for the period stated above, however if any name(s) have been omitted unintentionally or spelt incorrectly, please notify the Chief Executive Editor, *Pertanika* Journals at executive_editor.pertanika@upm.edu.my

Any inclusion or exclusion of name(s) on this page does not commit the *Pertanika* Editorial Office, nor the UPM Press or the University to provide any liability for whatsoever reason.

Pertanika Journals

Our goal is to bring high quality research to the widest possible audience

INSTRUCTIONS TO AUTHORS

(REGULAR ISSUE)

-- Manuscript Preparation & Submission Guide --

Revised: March 2020

Please read the Pertanika guidelines and follow these instructions carefully. The Chief Executive Editor reserves the right to return manuscripts that are not prepared in accordance with these guidelines.

MANUSCRIPT PREPARATION

Manuscript Types

Pertanika accepts submission of mainly **four** types of manuscripts
- that have not been published elsewhere (including proceedings)
- that are not currently being submitted to other jounals

1. Regular Article

Regular article is a full-length original empirical investigations, consisting of introduction, methods, results and discussion. Original research work should present new and significant findings that contribute to the advancement of the research area. Analysis and Discussion must be supported with relevant references.

Size: Generally, it is expected **not to exceed 6000 words** (excluding the abstract, references, tables and/or figures)**,** a maximum of **80 references**, and **an abstract of less than 250 words.**

2. Review Article

A review article reports critical evaluation of materials about current research that has already been published by organizing, integrating, and evaluating previously published materials. It summarizes the status of knowledge and outline future directions of research within the journal scope. A review article should aim to provide systemic overviews, evaluations and interpretations of research in a given field. Re-analyses as meta-analysis and systemic reviews are encouraged.

Size: Generally, it is expected **not to exceed 6000 words** (excluding the abstract, references, tables and/or figures), a maximum of **80 references,** and **an abstract of less than 250 words.**

3. Short Communications

Each article should be timely and brief. It is suitable for the publication of significant technical advances and may be used to:

(a) reports new developments, significant advances and novel aspects of experimental and theoretical methods and techniques which are relevant for scientific investigations within the journal scope;

(b) reports/discusses on significant matters of policy and perspective related to the science of the journal, including 'personal' commentary;

(c) disseminates information and data on topical events of significant scientific and/or social interest within the scope of the journal.

Size: It is limited to **3000 words** and have a maximum of **3 figures and/or tables, from 8 to 20 references, and an abstract length not exceeding 100 words.** Information must be in short but complete form and it is not intended to publish preliminary results or to be a reduced version of Regular or Rapid Papers.

4. Others

Brief reports, case studies, comments, concept papers, letters to the editor, and replies on previously published articles may be considered.

Language Accuracy

Pertanika **emphasizes** on the linguistic accuracy of every manuscript published. Articles must be in **English** and they must be competently written and presented in clear and concise grammatical English. Contributors are strongly advised to have the manuscript checked by a colleague with ample experience in writing English manuscripts or a competent English language editor.

Author(s) **may be required to provide a certificate** confirming that their manuscripts have been adequately edited. **All editing costs must be borne by the author(s)**.

Linguistically hopeless manuscripts will be rejected straightaway (e.g., when the language is so poor that one cannot be sure of what the authors really mean). This process, taken by authors before submission, will greatly facilitate reviewing, and thus publication.

MANUSCRIPT FORMAT

The paper should be submitted in one column format with at least 4cm margins and 1.5 line spacing throughout. Authors are advised to use Times New Roman 12-point font and *MS Word* format.

1. Manuscript Structure

Manuscripts in general should be organised in the following order:

- **Page 1:** ***Running title***

This page should **only** contain the running title of your paper. The running title is an abbreviated title used as the running head on every page of the manuscript. The running title **should not exceed 60 characters, counting letters and spaces.**

- **Page 2:** ***Author(s) and Corresponding author's information***

General information: This page should contain the **full title** of your paper **not exceeding 25 words**, with name(s) of all the authors, institutions and corresponding author's name, institution and full address (Street address, telephone number (including extension), hand phone number, and e-mail address) for editorial correspondence. **The corresponding author must be clearly indicated with "*".**

Authors' name: The names of the authors should be named **in full without academic titles.** For Asian (Chinese, Korean, Japanese, Vietnamese), please write first name and middle name before surname (family name). The last name in the sequence is considered the surname.

Authors' addresses: Multiple authors with different addresses must indicate their respective addresses separately by superscript numbers.

Tables / figures list: A **list** of number of **black and white / colour figures and tables** should also be indicated on this page. See ***"5. Figures & Photographs"*** for details.

Example (page 2):

***In vivo* Fecundity Evaluation of *Phaleria macrocarpa* Extract Supplementation in Male Adult Rats**

Sui Sien Leong[1]* and Mohamad Aziz Dollah[2]

[1]Department of Animal Sciences and Fishery, Universiti Putra Malaysia, 97008 Bintulu, Sarawak, Malaysia
[2]Department of Biomedical Sciences, Universiti Putra Malaysia, 43400 Serdang, Malaysia

leongsuisien@upm.edu.my (Sui Sien Leong), Contact number
azizdollah@gmail.com (Mohamad Aziz Dollah), Contact number
**Corresponding author*

- **Page 3: *Abstract***

This page should **repeat** the **full title** of your paper with only the **Abstract**, usually in one paragraph and **Keywords.**

Keywords: **Not more than 8 keywords in alphabetical order** must be provided to describe the contents of the manuscript.

- **Page 4: *Text***

A regular paper should be prepared with the headings *Introduction, Methods, Results and Discussions* in this order. The literature review maybe part of or separated from Introduction. A conclusion maybe embeded or separated from Results and Discussions.

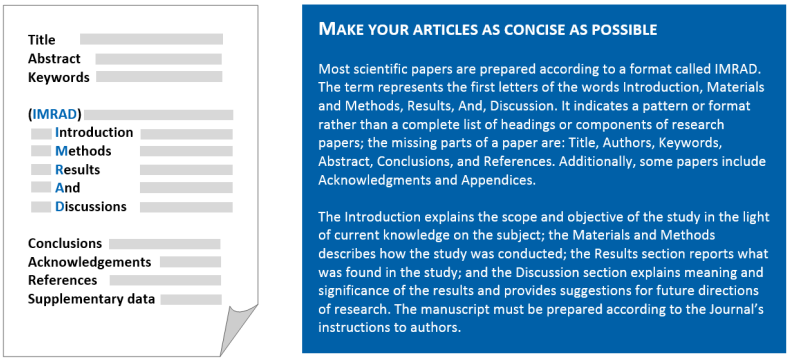

2. *Levels of Heading*

Level of heading	Format
1st	**LEFT, BOLD, UPPERCASE**
2nd	**Flush left, Bold, Capitalise each word**
3rd	**Bold, Capitalise each word, ending with .**
4th	***Bold italic*, Capitalise each word, ending with .**

3. *Equations and Formulae*

These must be set up clearly and should be typed double spaced. Numbers identifying equations should be in square brackets and placed on the right margin of the text.

4. *Tables*

- All tables should be prepared in a form consistent with recent issues of Pertanika and should be numbered consecutively with Roman numerals (Table 1, Table 2).
- A brief title should be provided, which should be shown at the top of each table **(APA format):**

Example: Table 1

PVY infected Nicotiana tabacum *plants optical density in ELISA*

- Explanatory material should be given in the table legends and footnotes.
- Each table should be prepared on a new page, embedded in the manuscript.
- Authors are advised to keep backup files of all tables.

***** Please submit all tables in Microsoft word format only - because tables submitted as image data cannot be edited for publication and are usually in low-resolution.***

5. *Figures & Photographs*

- Submit an **original** figure or photograph.
- Line drawings must be clear, with high black and white contrast.

- Each figure or photograph should be prepared on a new page, embedded in the manuscript for reviewing to keep the file of the manuscript under 5 MB.
- These should be numbered consecutively with Roman numerals (Figure 1, Figure 2).
- Provide a brief title, which should be shown at the bottom of each table **(APA format):**

  Example: Figure 1. PVY-infected *in vitro* callus of *Nicotiana tabacum*

- If a Figure has been previously published, acknowledge the original source and submit written permission form the copyright holder to reproduce the material.
- Authors are advised to keep backup files of all figures.

***** Figures or photographs must also be submitted separately as TIFF, JPEG, because figures or photographs submitted in low-resolution embedded in the manuscript cannot be accepted for publication. For electronic figures, create your figures using applications that are capable of preparing high resolution TIFF files.***

6. Acknowledgement

Any individuals and entities who have contributed should be acknowloedged appropriately.

7. References

References begin on their own page and are listed in alphabetical order by the first author's last name. Only references cited within the text should be included. All references should be in 12-point font and double-spaced.

NOTE: When formatting your references, please follow the ***Pertanika*-APA-reference style** (6th Edition) *(refer to examples)*. Ensure that the references are strictly in the journal's prescribed style, failing which your article will **not be accepted for peer-review**. You may refer to the *Publication Manual of the American Psychological Association* for further details https://apastyle.apa.org/

Examples of reference style are given below:

Books

Books	Insertion in Text	In Reference List
Book with 1-2 authors	**Information prominent' (the author's name is within parentheses):** … (Cochrane, 2007) … Or **'Author prominent' (the author's name is outside the parentheses):** Cochrane (2007) …	Cochrane, A. (2007). *Understanding urban policy: A critical approach.* Malden, United States: Blackwell Publishing.
Book with 3 or more authors (Pertanika's format)	*For all in-text references, list only the firrst author's family name and followed by* 'et al.' **Information prominent' (the author's name is within parentheses):** … (Seeley et al., 2011) … Or **'Author prominent' (the author's name is outside the parentheses):** Seeley et al. (2011) …	Seeley, R., VanPutte, C., Regan, J., & Russo, A. (2011). *Seeley's anatomy & physiology*. New York, United States: McGraw-Hill.

Books	Insertion in Text	In Reference List
Book with 6-7 authors	*For all in-text references, list only the firrst author's family name and followed by* 'et al.' **Information prominent' (the author's name is within parentheses):** … (Bulliet et al., 2011) … Or **'Author prominent' (the author's name is outside the parentheses):** Bulliet et al. (2011) …	Bulliet, R. W., Crossley, P. K., Headrick, D. R., Hirsch, S. W., Johnson, L. L., & Northrup, D. (2011). *The earth and its peoples: A global history* (5th ed.). Boston, United States: Wadsworth.
Book with more than 8 authors	*For all in-text references, list only the first author's family name and followed by* 'et al.' A recent study (Edge et al., 2011) concluded that… Or Edge et al. (2011) concluded that **….**	For books with eight or more authors, please follow the guidelines for journal articles with eight or more authors.
Chapter in edited book	**Information prominent' (the author's name is within parentheses):** … (Richards, 1997) … Or **'Author prominent' (the author's name is outside the parentheses):** Richards (1997) …	Richards, K. C. (1997). Views on globalization. In H. L. Vivaldi (Ed.), *Australia in a global world* (pp. 29-43). Sydney, Australia: Century.
e-book/online book	**Information prominent' (the author's name is within parentheses):** … (Niemann et al., 2004) … Or **'Author prominent' (the author's name is outside the parentheses):** Niemann (2004) …	Niemann, S., Greenstein, D., & David, D. (2004). *Helping children who are deaf: Family and community support for children who do not hear well.* Retrieved June 1, 2019, from http://www.hesperian.org/ publications_download_deaf.php Schiraldi, G. R. (2001). *The post-traumatic stess disorder sourcebook: A guide to healing, recovery, and growth* [Adobe Digital Editions version]. doi:10.1036/0071393722
Editor	**Information prominent' (the author's name is within parentheses):** … (Zairi, 1999) … Or **'Author prominent' (the author's name is outside the parentheses):** Zairi (1999) …	Zairi, M. (Ed.). (1999). *Best practice: Process innovation management.* Oxford, United Kingdom: Butterworth- Heinemann.

Books	Insertion in Text	In Reference List
Several works by same author in the same year	**Information prominent' (the author's name is within parentheses):** … (Fullan, 1996a, 1997b) … Or **'Author prominent' (the author's name is outside the parentheses):** Fullan (1996a, 1996b) …	Fullan, M. (1996a). Leadership for change. In *International handbook for educational leadership and administration.* New York, United States: Kluwer Academic. Fullan, M. (1996b). *The new meaning of educational change.* London, United Kingdom: Casell.
Several authors, different years referred to collectively in your work	**List sources alphabetically by family name in the in-text reference in the order in which they appear in the Reference List.** The cyclical process (Carr & Kemmis, 1986; Dick, 2000) suggests…	Carr, W., & Kemmis, S. (1986). *Becoming critical: Education knowledge and action research.* London, United Kingdom: Falmer Press. Dick, B. (2000). *A beginner's guide to action research.* Retrieved June 1, 2019, from http://www.scu.edu.au/schools/gcm/ar/arp/guide.html

Journals

Journals	Insertion in Text	In Reference List
Journal article with 1-2 authors	**Information prominent' (the author's name is within parentheses):** … (Kramer & Bloggs, 2002)… Or **'Author prominent' (the author's name is outside the parentheses):** Kramer and Bloggs (2002) …	Kramer, E., & Bloggs, T. (2002). On quality in art and art therapy. *American Journal of Art Therapy*, *40*, 218-231.
Journal article with 3 or more authors (Pertanika's format)	*For all in-text references, list only the firrst author's family name and followed by* 'et al.' **Information prominent' (the author's name is within parentheses):** … (Erlo et al., 2008) … Or **'Author prominent' (the author's name is outside the parentheses):** Erlo et al. (2008) …	Elo, A., Ervasti, J., Kuosma, E., & Mattila, P. (2008). Evaluation of an organizational stress management program in a municipal public works organization. *Journal of Occupational Health Psychology*, *13*(1), 10-23. doi: 10.1037/1076-8998.13.1.10

Journal article with 6 - 7 authors	*For all in-text references, list only the firrst author's family name and followed by* 'et al.' **Information prominent' (the author's name is within parentheses):** … (Restouin et al., 2009) … Or **'Author prominent' (the author's name is outside the parentheses):** Restouin et al. (2008) …	Restouin, A., Aresta, S., Prébet, T., Borg, J., Badache, A., & Collette, Y. (2009). A simplified, 96-well–adapted, ATP luminescence–based motility assay. *BioTechniques, 47*, 871–875. doi: 10.2144/000113250
Journal article with more than 8 or more authors	**Information prominent' (the author's name is within parentheses):** … (Steel et al., 2010).. Or **'Author prominent' (the author's name is outside the parentheses):** Steel et al. (2010) …	Steel, J., Youssef, M., Pfeifer, R., Ramirez, J. M., Probst, C., Sellei, R., ... Pape, H. C. (2010). Health-related quality of life in patients with multiple injuries and traumatic brain injury 10+ years postinjury. *Journal of Trauma: Injury, Infection, and Critical Care, 69*(3), 523-531. doi: 10.1097/TA.0b013e3181e90c24
Journal article with DOI	**Information prominent' (the author's name is within parentheses):** … (Shaw et al., 2005).. Or **'Author prominent' (the author's name is outside the parentheses):** Shaw et al. (2005) …	Shaw, K., O'Rourke, P., Del Mar, C., & Kenardy, J. (2005). Psychological interventions for overweight or obesity. *The Cochrane database of systematic reviews* (2). doi:10.1002/14651858.CD003818.pub2

Newspapers

Newspapers	Insertion in Text	In Reference List
Newspaper article – with an author	… (Waterford, 2007)...	Waterford, J. (2007, May 30). Bill of rights gets it wrong. *The Canberra Times*, p. 11.
Newspaper article – without an author	… ("Internet pioneer", 2007) …	Internet pioneer to oversee network redesign. (2007, May 28). *The Canberra Times*, p. 15.
Article in an newsletter	... ("Australians and the Western Front", 2009) ...	Australians and the Western Front. (2009, November). *Ozculture newsletter*. Retrieved June 1, 2019, from http://www.cultureandrecreation.gov.au/ newsletter/

Conference / Seminar Papers

Conference / Seminar Papers	Insertion in Text	In Reference List
Print – *If the paper is from a book, use the book chapter citation format. If it is from regularly published proceedings (e.g. annual), use the Journal article citation format.*	… (Edge, 1996) … Or Edge (1996) …	Edge, M. (1996). Lifetime prediction: Fact or fancy? In M. S. Koch, T. Padfield, J. S. Johnsen, & U. B. Kejser (Eds.), *Proceedings of the Conference on Research Techniques in Photographic Conservation* (pp. 97-100). Copenhagen, Denmark: Royal Danish Academy of Fine Arts.
Online	… (Tester, 2008) … Or Tester (2008) …	Tester, J. W. (2008). The future of geothermal energy as a major global energy supplier. In H. Gurgenci & A. R. Budd (Eds.), *Proceedings of the Sir Mark Oliphant International Frontiers of Science and Technology Australian Geothermal Energy Conference*, Canberra, Australia: Geoscience Australia. Retrieved June 1, 2019, from http://www.ga.gov.au/image_cache/ GA11825.pdf

Government Publications

Government Publications	Insertion in Text	In Reference List
Government as author	**First in-text reference: Spell out the full name with the abbreviation of the body.** … (Department of Finance and Administration [DOFA], 2006) … **Subsequent in-text reference/s:** **Use the abbreviation of the body.** … (DOFA, 2006)…	Department of Finance and Administration. (2006). Delivering Australian Government services: Managing multiple channels. Canberra, Australia: Author.
Government report - online	**First in-text reference: Spell out the full name with the abbreviation of the body.** … (Department of the Prime Minister and Cabinet [PM&C], 2008) … **Subsequent in-text reference/s:** **Use the abbreviation of the body.** … (PM&C, 2008)…	Department of the Prime Minister and Cabinet. (2008). *Families in Australia: 2008.* Retrieved June 1, 2019, from http://www.....

9. General Guidelines

Abbreviations: Define alphabetically, other than abbreviations that can be used without definition. Words or phrases that are abbreviated in the introduction and following text should be written out in full the first time that they appear in the text, with each abbreviated form in parenthesis. Include the common name or scientific name, or both, of animal and plant materials.

Authors' Affiliation: The primary affiliation for each author should be the institution where the majority of their work was done. If an author has subsequently moved to another institution, the current address may also be stated in the footer.

Co-Authors: The commonly accepted guideline for authorship is that one must have substantially contributed to the development of the paper and share accountability for the results. Researchers should decide who will be an author and what order they will be listed depending upon their order of importance to the study. Other contributions should be cited in the manuscript's Acknowledgements.

Copyright Permissions: Authors should seek necessary permissions for quotations, artwork, boxes or tables taken from other publications or from other freely available sources on the Internet before submission to Pertanika. Acknowledgement must be given to the original source in the illustration legend, in a table footnote, or at the end of the quotation.

Footnotes: Current addresses of authors if different from heading may be inserted here.

Page Numbering: Every page of the manuscript, including the title page, references and tables should be numbered.

Spelling: The journal uses American or British spelling and authors may follow the latest edition of the Oxford Advanced Learner's Dictionary for British spellings. Each manuscript should follow one type of spelling only.

SUBMISSION OF MANUSCRIPTS

All submissions must be made electronically using the **online submission system ScholarOne™**, a web-based portal by Clarivate Analytics. For more information, go to our web page and click "**Online Submission**".

Submission Checklist

1. **MANUSCRIPT**:

   Ensure your MS has followed the Pertanika style particularly the first four pages as explained earlier. The article should be written in a good academic style and provide an accurate and succinct description of the contents ensuring that grammar and spelling errors have been corrected before submission. It should also not exceed the suggested length.

2. **DECLARATION FORM:**

- Author has to sign a declaration form. In signing the form, authors declare that the work submitted for publication is orginal, previously unpublished, and not under consideration for any publication elsewhere.

- Author has to agree to pay the publishing fee once the paper is accepted for publication in Pertanika.

Note:

COPYRIGHT FORM: Author will be asked to sign a copyright form when the paper is accepted. In signing the form, it is assumed that authors have obtained permission to use any copyrighted or previously published material. All authors must read and agree to the conditions outlined in the form, and must sign the form or agree that the corresponding author can sign on their behalf. Articles cannot be published until a signed form *(original pen-to-paper signature)* has been received.

Visit our Journal's website for more details at http://www.pertanika.upm.edu.my/

ACCESS TO PUBLISHED MATERIALS

Under the Journal's open access initiative, authors can choose to download free material (via PDF link) from any of the journal issues from Pertanika's website. Under "**Browse Journals**" you will see a link, "*Regular Issue*", "*Special Issue"* or "*Archives*". Here you will get an access to all current and back-issues from 1978 onwards. No hard copy of journals or off prints are printed.

Visit our Journal's website at
http://www.pertanika.upm.edu.my/regular_issues.php for "Regular Issue"
http://www.pertanika.upm.edu.my/cspecial_issues.php for "Special Issue"
http://www.pertanika.upm.edu.my/journal_archives.php for "Archives"

PERTANIKA
JOURNALS

PUBLICATION CHARGE

Upon acceptance of manuscript, a processing fee of RM 750 / USD 250 will be imposed on authors; RM 750 for any corresponding author affiliated to an institution in Malaysia; USD 250 for any corresponding author affiliated to an institution outside Malaysia. Payment must be made online at https://paygate.upm.edu.my/action.do?do=

Any queries may be directed to the **Chief Executive Editor's** office via email to executive_editor.pertanika@upm.edu.my

Medical and Health Sciences

Material Sciences

Pertanika Journal of Science & Technology
Vol. 28 (3) Jul. 2020

Contents

Pertanika Editorial Office, Journal Division,
Putra Science Park,
1st Floor, IDEA Tower II,
UPM-MTDC Technology Centre
Universiti Putra Malaysia
43400 UPM Serdang
Selangor Darul Ehsan
Malaysia
http://www.pertanika.upm.edu.my
E-mail: executive_editor.pertanika@upm.edu.my
Tel : +603 9769 1622/1616

PENERBIT UPM UNIVERSITI PUTRA MALAYSIA PRESS
http://penerbit.upm.my
E-mail: penerbit@upm.edu.my
Tel : +603 9769 8851

ISSN 0128-7680
9 770128 768083 07 >